

Dissertation zur Erlangung des Doktorgrades
der Fakultät für Chemie und Pharmazie
der Ludwig-Maximilians-Universität München

Flexible, multidentate phosphines
in d^{10} -metal complexes

—

A general and simple approach to luminescent
materials

Christin Kirst

aus

Forst/Lausitz, Deutschland

2021

Erklärung

Diese Dissertation wurde im Sinne von §7 der Promotionsordnung vom 28. November 2011 von Herrn Professor Dr. Konstantin L. Karaghiosoff betreut.

Eidesstattliche Versicherung

Diese Dissertation wurde eigenständig und ohne unerlaubte Hilfe erarbeitet.

München, der06.07.2021.....

.....
Christin Kirst

Dissertation eingereicht am08.07.2021.....

1. Gutachterin / 1. Gutachter: Prof. Dr. Konstantin L. Karaghiosoff
2. Gutachterin / 2. Gutachter: Prof. Dr. Thomas M. Klapötke

Mündliche Prüfung am19.08.2021.....

Wer ein Ziel will, darf den Weg nicht scheuen, er sei glatt oder rau.

Theodor Fontane (1819-1898)

Acknowledgment

First and foremost, I would like to take this chance to thank my PhD supervisor Prof. Dr. Konstantin L. Karaghiosoff, Conny, for giving me the opportunity to conduct my PhD theses in his group and for the scientific freedom I was able to enjoy. I am also very grateful to have gotten so many opportunities to visit all kinds of different conferences over the past three years. Every conference was a great opportunity to come into contact with so many researchers and other topics, which has boosted my motivation and inspired my research every time.

Your expertise and knowledge in various fields is truly remarkable. Despite having an abundance of obligations and responsibilities, you always managed to wrap your head around the, sometimes highly complex, topics and ideas I brought to you, and we nevertheless always managed to have productive meetings, which I am very thankful for. On a more personal note, there are many things about you and your way of handling things, that I have always respected and admired. For one, you always manage to create a respectful atmosphere within the meetings by choosing the right words whilst making people feel recognized and understood in a subtle manner, irrespective of any personal or political/societal circumstances. There is most certainly a lot that one can learn from your calm and prudent behavior and always de-escalating, goal-oriented approach. Above and beyond those excellent professional traits and your laissez-faire attitude, that we were all allowed to enjoy, I even more so appreciate your truly warm-hearted and humorous character, which I think comes from a very deep understanding of people and life in general. I sincerely hope that you continue to uphold those values and attributes and finally, I want to, one more time, express my gratitude to you for always being there for me as my mentor and good friend.

Secondly, Prof. Dr. Thomas M. Klapötke is thanked for welcoming me with open arms into his professorial chair and for being the second grader of my thesis. Despite having already mentioned in my publications that I am very grateful for the support you provided over the years, I would also like to take this chance to also thank you for your kind heart, pleasant demeanor and in general all the resources you provided.

Moreover, I want to thank AOR Dr. Burkhard Krumm for NMR measurements, especially of exotic atoms. In general, thanks to the entire NMR team of the inorganic chemistry department, including Ms. Brigitte Breitenstein, for your efforts and in particular for the time-consuming variable temperature NMR measurements.

A big thank you also to Ms. Irene Scheckenbach, whose administrative competence and skills have been essential, not just for the purpose of managing all necessary paperwork, employment and other things for me, but also for guaranteeing the effectiveness of the entire group.

I also owe my gratitude to Dr. Armin Wedel from the Fraunhofer IAP in Potsdam and Dr. Kai Keller from Notion Systems GmbH for believing in this research project and for coming up with an idea for a grant application that also convinced the AiF GmbH to fully fund our joint project, including my PhD studies for two and a half years. We have learned and achieved a lot during this project, which set the foundation for our future work together. In this context, I want to thank Dr. Manuel Gensler (Fraunhofer IAP) for the numerous measurements and the preparation of thin films and devices using the newly developed compounds. Additionally, I am thankful to AR Dr. Jens Petersen from the Julius Maximilian University of Würzburg for the diverse quantum chemical calculations.

My cooperation partners from the physical chemistry department of the LMU, Prof. Dr. Don C. Lamb and M.Sc. Nader Danaf, are thanked for the impressive results achieved by FLIM measurements and in general for the pleasant and successful collaborative work.

Additionally, I want to thank Prof. Dr. Hans Christian Böttcher for our fruitful collaboration and his valuable input.

The members of the research group of Prof. Dr. K. Karaghiosoff are thanked. This includes Dr. Marco Reichel to whom I am very thankful for all the enjoyable and funny moments together, not only during our mutual conference trips. You are one of the kindest persons I know, always having an open ear or giving a helping hand, whenever I needed one. M.Sc. Jonathan Tietze is thanked, who is the newest member of the group and was my first "F-Praktikum" student. He will from now on continue to carry the torch and for sure deliver great results! And of course, also thank you to Dr. Sarah Linert and M.Sc. Mara Egenhöfer for the memorable moments during the conferences and in general, for the friendly atmosphere in the group.

Furthermore, I want to thank the entire research group of Prof. Dr. T. M. Klapötke, including the former (Dr. Ivan Gospodinov, Dr. Cornelia Unger, Dr. Teresa Küblböck, Dr. Anne Friedrichs, Dr. Marcel Holler) and the current members (M.Sc. Greta Bikelyte, M.Sc. Maxi Benz, M.Sc. Max Born, B.Sc. Michael Gruhne, M.Sc. Alexander Harter, M.Sc. Jasmin Lechner, M.Sc. Tobi Lenz, B.Sc. Marcus Lommel, M.Sc. Elena Reinhardt, M.Sc. Maurus Völkl, M.Sc. Alexander Schweiger, M.Sc. Michi Voggenreiter). Additionally, I want to thank the members M.Sc. Alicia Dufter (Liesl), Dr. Dominik Dosch (Dodo) and Stefan Huber (Hubs) for welcoming me so kindly into the lab (D3.103) and for the very pleasant, friendly and joyful working relationship during the past three years. I also want to thank my fellows of the former and current X-ray team, Dr. Maximilian Wurzenberger and M.Sc. Moritz Kofen, for the great organization of the shared spectrometer time. In this connection, I want to thank my former F-Praktikum students and international students: Tom Colgan, Lydia Smith, Marian Ebeling, Lukas Horndasch, Konrad Schönleber and Tim Arcynski.

I am very grateful to Dr. Claudia Müller and Dr. Claudia Göbel, to whom I have been very good friends with throughout our mutual chemistry journey up until this day. Even though we live hundreds of kilometers apart, we always find time not only to chat but also to meet up and for example enjoy Christmas markets and the occasional Wiesn together.

Thank you also to my long-time school friends M.Sc. Christian Will (Willi) and M.Phil. Andrej Wörner for initiating a bet as to who will finish their PhD first. More than a year has passed, and knowing, that Andrej's PhD examination is in October, I can hopefully say with confidence, I have won!

Moreover, I am very grateful to Max, who always motivated and uplifted me when my insecurities kicked in or I just felt very exhausted. Your calmness, love and giant heart really helped me to get to where I am now. I hope, we will continue to walk the way together and support each other for a long time. A big thank you also to Eva, Bernd and Zsanett, for welcoming me so kindly and hearty into your family and for being a great friends and support in stressful times. You are like a second family to me. Also, thank you to Mia, the cutest and prettiest dog. You were a little diva towards others, but we were good buddies and I really miss you.

Abschließend möchte ich mich aus tiefsten Herzen bei meiner Familie bedanken. Ihr habt mich dazu erzogen ein fleißiger, fokussierter und unabhängiger Mensch zu sein, was mir nicht nur dabei geholfen hat meine jetzige Position zu erreichen. Ihr habt mich immer dabei unterstützt meine Träume verwirklichen zu können und das nicht nur finanziell. Ich konnte immer auf euch zählen. Danke für Alles!

Table of content

ACKNOWLEDGMENT	I
1. INTRODUCTION.....	7
1.1. Current state of OLED emitters.....	7
1.2. Sustainable metal complexes for OLED application	9
1.3. Luminescent complexes based on Zn(II)	10
1.4. Luminescent complexes based on Cu(I) and Ag(I)	11
1.5. Functionalized tertiary phosphines and their possible application in OLEDs.....	12
1.6. Novel concept for suitable ligands for luminescent compounds	12
1.7. Synthetic routes to flexible, functionalized phosphines.....	13
1.8. Aim of the thesis.....	14
1.9. References.....	15
2. RESULTS AND DISCUSSION.....	19
2.1. Coordination complexes of di(2-pyridyl)ketone with copper(I) and their formation in solution and under solvent-free conditions	20
2.1.1. Introduction.....	21
2.1.2. Experimental	21
2.1.2.1. General comments	21
2.1.2.2. Synthesis and characterization data for compounds 1–4	22
2.1.2.3. X-ray crystallography.....	23
2.1.2.4. Computational details	24
2.1.3. Results and discussion	24
2.1.3.1. Molecular structures.....	24
2.1.3.2. Solvent-free reactions.....	32
2.1.3.3. UV Vis spectral data	33
2.1.3.4. Hirshfeld surface analysis	33
2.1.4. Conclusion	35
2.1.5. References.....	36
2.2. Copper(I) and silver(I) complexes of bridging bis(quinaldinyl)phenylphosphine oxide ligand	39
2.2.1. Introduction.....	40
2.2.2. Results and discussion	40
2.2.3. Conclusions.....	45
2.2.4. References.....	45
2.3. Investigation of structural changes of Cu(I) and Ag(I) complexes utilizing a flexible, yet sterically demanding multidentate phosphine oxide ligand	46
2.3.1. Introduction.....	47
2.3.2. Results and discussion	48
2.3.2.1. Synthesis and structural characterization of phosphine oxide metal complexes.....	48

2.3.2.2.	<i>NMR characterization of structure and dynamics of phosphine oxide metal complexes in solution.</i>	50
2.3.2.3.	<i>Solid-state NMR characterization of the phosphine oxide metal complexes.</i>	52
2.3.2.4.	<i>Electrochemical characterization of complex 3.</i>	53
2.3.3.	Conclusion	54
2.3.4.	References	55
2.3.5.	Supporting information	58
2.3.5.1.	<i>Synthesis of 2-((trimethylsilyl)methyl)quinoline (A)</i>	58
2.3.5.2.	<i>Synthesis of bis(quinaldinyl)phenylphosphine (1)</i>	58
2.3.5.3.	<i>Synthesis of bis(quinaldinyl)phenylphosphine oxide (2)</i>	59
2.3.5.4.	<i>Synthesis of bis(quinaldinyl)phenylphosphine oxide copper(I) tetrafluoroborate (3)</i>	60
2.3.5.5.	<i>Synthesis of bis(quinaldinyl)phenylphosphine oxide copper(I) hexafluorophosphate (4)</i>	61
2.3.5.6.	<i>Synthesis of bis(quinaldinyl)phenylphosphine oxide silver(I) tetrafluoroborate (5)</i>	61
2.3.5.7.	<i>Synthesis of bis(quinaldinyl)phenylphosphine oxide silver(I) hexafluoroantimonate (6)</i>	63
2.3.5.8.	<i>Crystallographic and refinement data</i>	64
2.3.5.9.	<i>Cyclic voltammetry</i>	67
2.3.5.10.	<i>Hirshfeld surface analysis</i>	67
2.4.	The formation of P–C-bonds utilizing organozinc reagents for the synthesis of aryl- and heteroaryl-dichlorophosphines	69
2.4.1.	Introduction	70
2.4.2.	Results and discussion	71
2.4.3.	Conclusion	75
2.4.4.	Experimental section	75
2.4.5.	References	79
2.4.6.	Supporting Information	80
2.5.	Methods for elucidating the structural-property relationship in luminescent materials	82
2.5.1.	Introduction	83
2.5.2.	Results and discussion	84
2.5.2.1.	<i>Synthesis</i>	84
2.5.2.2.	<i>Structural characterization</i>	85
2.5.2.3.	<i>Photophysical characterization.</i>	86
2.5.2.4.	<i>Lifetime characterization</i>	87
2.5.2.5.	<i>Combining Hirshfeld surface analysis with the FLIM results</i>	89
2.5.3.	Conclusion	91
2.5.4.	References	91
2.5.5.	Supporting information	95
2.5.5.1.	<i>Synthesis</i>	95
2.5.5.2.	<i>Crystallographic data and figures</i>	100
2.5.5.3.	<i>Photophysical spectra</i>	106
2.5.5.4.	<i>Fluorescence lifetime and FLIM images</i>	108

2.6.	Aggregation induced emission in a flexible phosphine oxide and its Zn(II) complexes – a simple approach to blue luminescent materials	115
2.6.1.	Introduction.....	116
2.6.2.	Results and Discussion.....	116
2.6.2.1.	<i>Synthesis and NMR characterization.....</i>	<i>116</i>
2.6.2.2.	<i>Structural characterization.....</i>	<i>117</i>
2.6.2.3.	<i>Photophysical characterization</i>	<i>118</i>
2.6.2.4.	<i>Lifetime characterization.....</i>	<i>120</i>
2.6.2.5.	<i>Combination of Hirshfeld surface analysis with the FLIM results.....</i>	<i>122</i>
2.6.2.6.	<i>Quantum chemical calculations</i>	<i>123</i>
2.6.3.	Conclusion	124
2.6.4.	References.....	125
2.6.5.	Supporting information	127
2.6.5.1.	<i>Synthesis and Characterization</i>	<i>127</i>
2.6.5.2.	<i>Crystallographic data</i>	<i>130</i>
2.6.5.3.	<i>Variable Temperature NMR spectra.....</i>	<i>132</i>
2.6.5.4.	<i>UV/Vis and luminescence images.....</i>	<i>133</i>
2.6.5.5.	<i>Additional FLIM data.....</i>	<i>135</i>
2.6.5.6.	<i>Hirshfeld surface analysis.....</i>	<i>137</i>
2.6.5.7.	<i>Additional computational data</i>	<i>137</i>
2.6.5.8.	<i>Calculated fluorescence and phosphorescence spectra</i>	<i>141</i>
2.7.	Coordination behavior of multidentate phosphine and phosphine oxide ligands towards Zn(II) and their luminescence properties.....	143
2.7.1.	Introduction.....	144
2.7.2.	Results and discussion	145
2.7.2.1.	<i>Design and synthesis of the ligands and complexes.....</i>	<i>145</i>
2.7.2.2.	<i>Molecular and crystal structures.....</i>	<i>146</i>
2.7.2.3.	<i>Hirshfeld surface analysis.....</i>	<i>149</i>
2.7.2.4.	<i>NMR data</i>	<i>150</i>
2.7.2.5.	<i>Variable temperature NMR.....</i>	<i>151</i>
2.7.2.6.	<i>Electrochemical properties.....</i>	<i>154</i>
2.7.2.7.	<i>Photophysical properties.....</i>	<i>154</i>
2.7.2.8.	<i>Theoretical calculations.....</i>	<i>155</i>
2.7.3.	Conclusion	155
2.7.4.	References.....	156
2.7.5.	Supporting information	158
2.7.5.1.	<i>Synthesis of bis(picoly)phenylphosphine zinc(II) chloride (1).....</i>	<i>158</i>
2.7.5.2.	<i>Synthesis of bis(quinaldiny)phenylphosphine zinc(II) chloride (2)</i>	<i>159</i>
2.7.5.3.	<i>Synthesis of bis(picoly)phenylphosphine oxide (3).....</i>	<i>160</i>
2.7.5.4.	<i>Synthesis of bis(picoly)phenylphosphine oxide zinc(II) chloride (4)</i>	<i>161</i>
2.7.5.5.	<i>Synthesis of bis(quinaldiny)phenylphosphine oxide zinc(II) chloride (5)</i>	<i>161</i>
2.7.5.6.	<i>Crystallographic data</i>	<i>165</i>
2.7.5.7.	<i>Electrochemical data.....</i>	<i>167</i>
2.7.5.8.	<i>Photophysical spectra.....</i>	<i>167</i>

2.7.5.9.	<i>Computational details</i>	168
2.8.	Structural diversity of a flexible, multidentate phosphine oxide ligand in Cu(I) and Ag(I) complexes	169
2.8.1.	Introduction.....	170
2.8.2.	Results and discussion.....	170
2.8.2.1.	<i>Synthesis</i>	170
2.8.2.2.	<i>Crystal structures</i>	171
2.8.2.3.	<i>Solution NMR</i>	173
2.8.2.4.	<i>Photophysical data</i>	174
2.8.3.	Conclusions.....	175
2.8.4.	Experimental.....	175
2.8.4.1.	<i>General information</i>	175
2.8.4.2.	<i>General synthesis of bis((4,6-dimethylpyridin-2-yl)methyl)phenylphosphine oxide complexes 1–4</i>	175
2.8.5.	References.....	177
2.8.6.	Supporting information.....	178
2.8.6.1.	<i>Additional figures</i>	178
2.8.6.2.	<i>Crystallographic data</i>	180
2.9.	Coinage metal complexes of bis(quinaldinyl)phenylphosphine – simple reactions can lead to unprecedented results	182
2.9.1.	Introduction.....	183
2.9.2.	Results and discussion.....	183
2.9.2.1.	<i>Synthesis and crystal structures</i>	183
2.9.2.2.	<i>Characterization of the compounds by NMR spectroscopy</i>	189
2.9.3.	Conclusion.....	190
2.9.4.	Experimental Section.....	191
2.9.4.1.	<i>General procedures</i>	191
2.9.4.2.	<i>Synthesis</i>	191
2.9.5.	References.....	193
2.9.6.	Supporting information.....	195
2.9.6.1.	<i>Crystallographic and refinement data</i>	195
2.9.6.2.	<i>Additional figures</i>	197
2.9.6.3.	<i>VT NMR Spectra</i>	199
3.	SUMMARY AND CONCLUSION – KEY FINDINGS	204
3.1.	Functionalized P,N-ligands – small changes, big impacts	204
3.2.	A general approach to dichlorophosphines – an easy and mild route for P-C-bond formation	205
3.3.	Zinc and phosphorus – a luminescent combination	206
3.4.	Copper(I) complexes – from blue to green	208
3.5.	Silver(I) and gold(I) – noble but non-emissive complexes	210
3.6.	Unique ligand properties – first insights into luminescence mechanism	211
3.7.	Primary results of M(III) complexes – an outlook	212

4.	APPENDIX.....	213
4.1.	List of symbols and abbreviations.....	213
4.2.	List of tables	215
4.3.	List of schemes	216
4.4.	List of figures	217
4.5.	List of publications.....	229
4.6.	List of conference contributions	229

1. Introduction

1.1. Current state of OLED emitters

An organic light-emitting diode (OLED) is a semi-conducting device, which is able to emit light when voltage is supplied. The most basic version of an OLED consists of an emission layer which is sandwiched by two conducting layers (Figure 1).^[1] Their inorganic predecessor, the light-emitting diode (LED), was up until now the most essential and indispensable lighting technology used not only in displays but also in general lighting. By now, LEDs have replaced the tried and trusted light bulbs almost completely. LEDs are based on inorganic semiconductor materials such as GaAs, GaN or InGaN. However, they are limited in their application due to their internal structure and composition, which is why LEDs are predominantly used as spotlight sources, OLEDs on the other hand can be used as area light sources. In contrast to LEDs, OLEDs can be manufactured ultra-flat, transparent, flexible and can cover a large substrate. Due to their excellent black levels, high contrasts, high resolution and minimal response times, OLEDs are nowadays predominantly used in displays for mobile phones, instead of LED or LCD based versions.^[2,3] Additionally, OLEDs are even more energy efficient than LEDs as they are self-luminous. Due to their nature, OLED materials can effectively convert up to 100 % of electric energy into light.^[1,4]

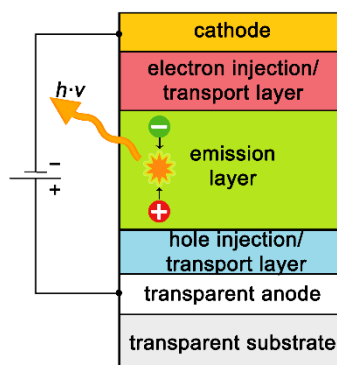


Figure 1. Simplistic scheme of an OLED stack. Layers are not drawn for scale.

Since the 1st generation of OLED was demonstrated in 1987 with an internal quantum efficiency limited to 25 %, the evolution of more efficient and greatly improved materials and devices continued over time (Figure 2).^[5,6] The newest generation utilizes thermally activated delayed fluorescence (TADF) emitters (3rd generation) as exciton generators, which transfer their excitons by Förster resonance energy transfer (FRET) to fluorescent emitters (1st generation).

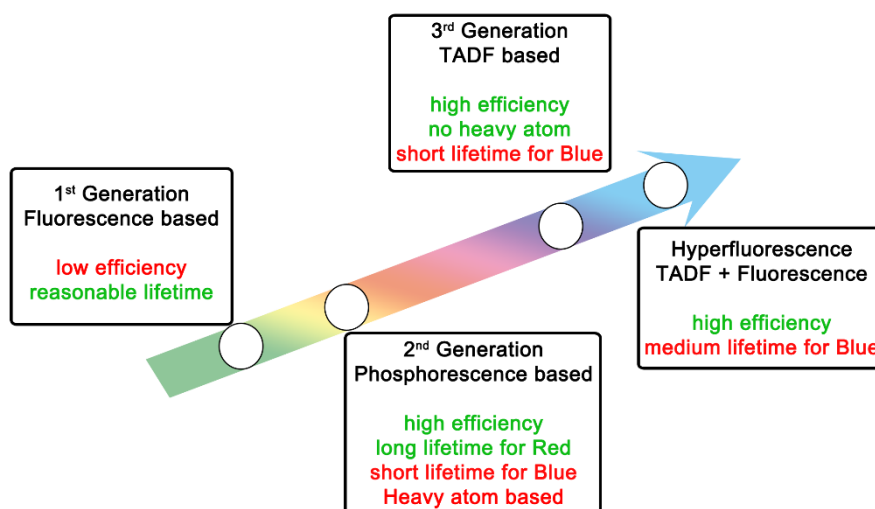


Figure 2. Evolution of OLED emission mechanisms over time.^[6]

This mechanism is called Hyperfluorescence™ (Figure 3) and based on this concept, 100 % internal quantum efficiency can be reached in addition to a high light intensity and color purity.^[7–10] This principle drastically improved the performances and lifetimes of yellow and red OLEDs. However, achieving a high-efficiency and long lifetime for blue OLEDs is still a challenge, even when utilizing Hyperfluorescence™.^[6,11] The problem of blue OLEDs is caused by the necessary high triplet energy and long triplet lifetime. The latter can be reduced by utilizing Hyperfluorescence™ or hybridized local charge transfers (HLCT).^[6] But the high triplet energy can cause bond dissociation, particularly of the vulnerable C–N and/or C(sp²)–C(sp²) bonds, and lead to a faster degradation of the emitter.^[11] Consequently, fundamental research is still needed to optimize the materials and synergies between the different layers of an OLED.

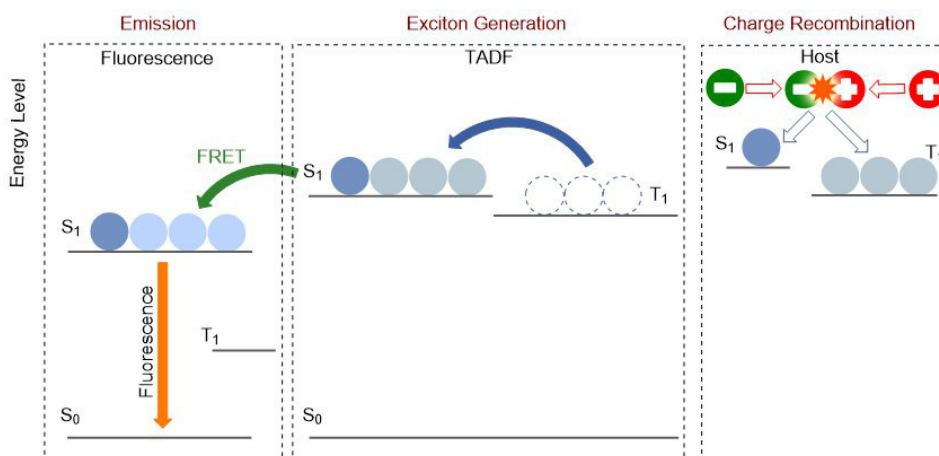


Figure 3. Schematic presentation of Hyperfluorescence™.^[7]

Current research is focusing on the development and synthesis of highly efficient and long-lasting blue-emitting materials.^[6,12] Recent fluorescence and TADF emitters are based on expensive metal complexes^[9,13,14] (Figure 4) and/or large, organic molecules (Figure 5).^[13,15–18] The synthesis of such large, organic TADF emitters is low-yielding and time-consuming and often needs expensive catalysts for the necessary coupling reactions. A scale-up of these procedures to a gram or even kilogram scale is in many cases not feasible from a cost-efficiency standpoint. Another problem of such large organic emitters is, that they oftentimes only show luminescence in solution, but not in thin film or solid state. Especially large molecules tend to have their fluorescence quenched due to tight π - π stacking caused by aggregation in the solid state.^[19]

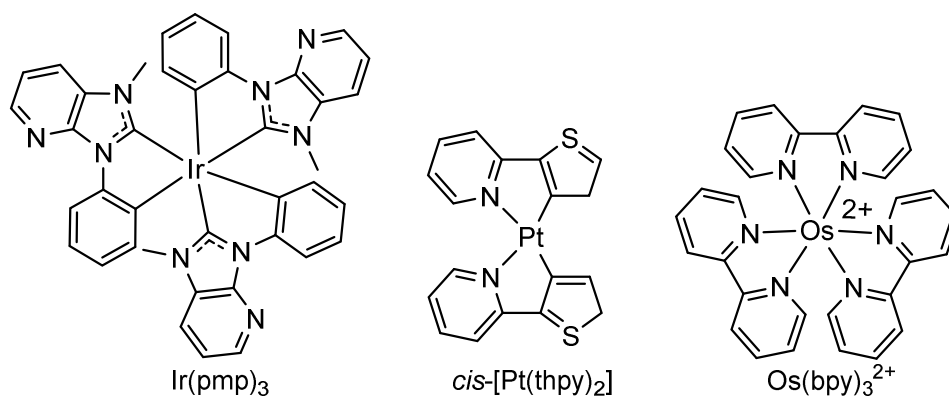


Figure 4. Examples for currently used fluorescence emitters based on heavy metal complexes.

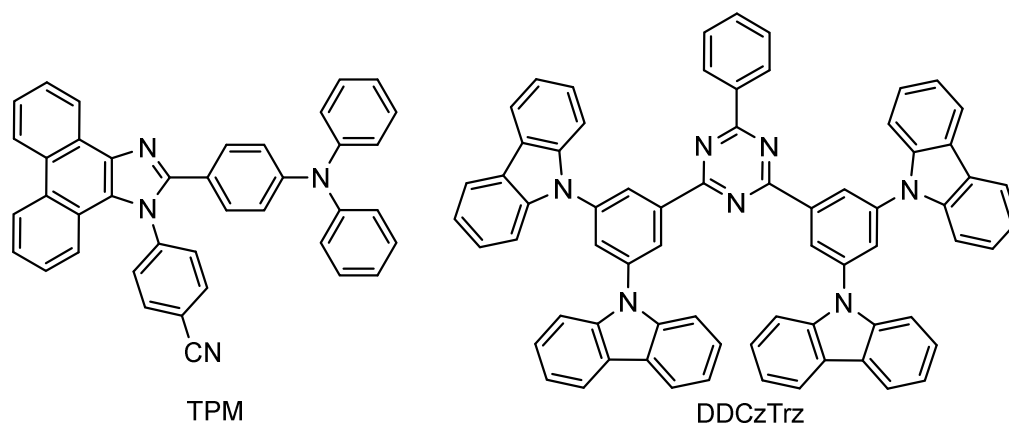


Figure 5. Examples for currently used blue TADF emitters based on large organic molecules.^[20]

Moreover, the currently used fabrication method of OLED materials is based on vacuum deposition techniques requiring sublimatable compounds. However, solution-processed devices fabricated *via* spin coating, screen printing and inkjet printing are growing in popularity due to their application in mass production facilities, making solubility and stability in solution of novel OLED materials a key-factor.^[21,22] Large, organic emitters often lack the necessary solubility in high-boiling solvents, which is needed for solution-processed OLEDs and the consequent industrial series production of OLED panels.^[21]

In summary, alternatives for currently used blue-emitting materials based on cheap, sustainable educts with an easy, scalable synthesis have to be found. Additionally, these compounds need to be highly efficient with regards to their luminescent properties, as well as long-lasting and soluble in high-boiling solvents, in order to make them applicable for printable OLED materials and leverage OLEDs in all kinds of imaginable application areas.

1.2. Sustainable metal complexes for OLED application

This scarcity and price of elements needed for luminescent materials is currently limiting the widespread adoption of OLED technology. Consequently, the interest in luminescent complexes based on cheap, sustainable and low-toxic metals is rising, as suitable alternatives need to be found to replace the currently widely used iridium, platinum or osmium complexes (Figure 6). For fluorescent emitters, alternatives containing Al(III) and Zn(II) and, for phosphorescent or TADF emitters, Cu(I) and Ag(I) are the focus of recent research due to their current prices and availability.^[15–17,23,24]

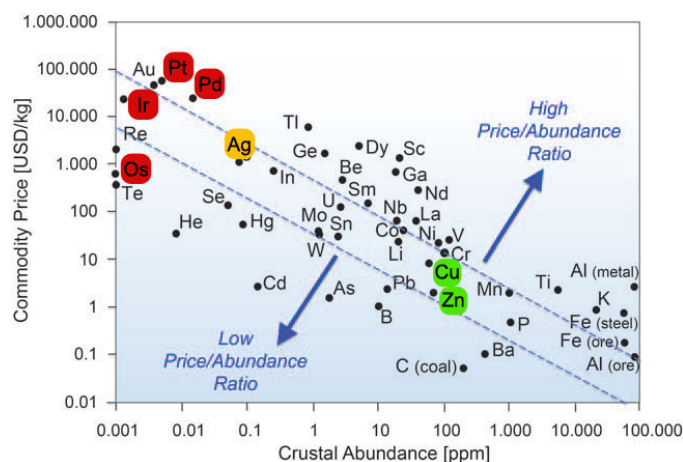


Figure 6. Crustal abundance and price for selected elements based on data from 2013. Picture was modified and taken from ref.^[25]

1.3. Luminescent complexes based on Zn(II)

Zinc in its most stable oxidation state II has a filled d-shell and thus cannot take part in MLCT/LMCT excitations, as it is energetically difficult to further oxidize or reduce Zn(II). Consequently, the luminescence of Zn(II) complexes arises from intra-ligand or ligand-to-ligand electron transitions. When coordinating to a ligand, the zinc(II) atom has the main role of keeping the ligand in a rigid position and a certain orientation, which in return improves the luminescence of the system. Any movement such as vibronic movement is impaired, which otherwise could minimize optoelectronic properties. The luminescent qualities of zinc(II) complexes can be controlled and influenced by modification of the ligand itself.^[23,26–30] The general ligand design was adapted from ligands used in known, very efficiently luminescent Al(III) complexes, e.g. Alq₃ (Figure 7). So typically, nitrogen and oxygen containing heterocycles are used. The emission wavelength of the resulting zinc(II) complexes ranges from UV to blue or even yellow light.^[15,31–33] The problem of currently known luminescent zinc(II) complexes is the low quantum efficiency, which is why their use as hosts is being investigated as well.^[15,34,35] The choice of ligand in luminescent Zn(II) complexes is currently limited to N,O-heterocycles and only a few P,N-ligands have been investigated (Figure 8), which also show a promising emission in the blue to green region of the visible light.^[36–38] To find suitable combinations, alternative ligands need to be created and studied.

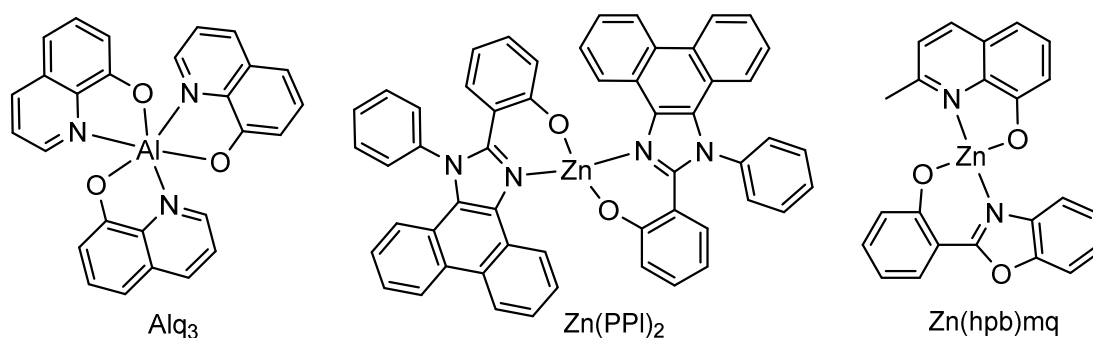


Figure 7. Luminescent Zn(II) complexes known in the literature and Alq₃ on the left in comparison.

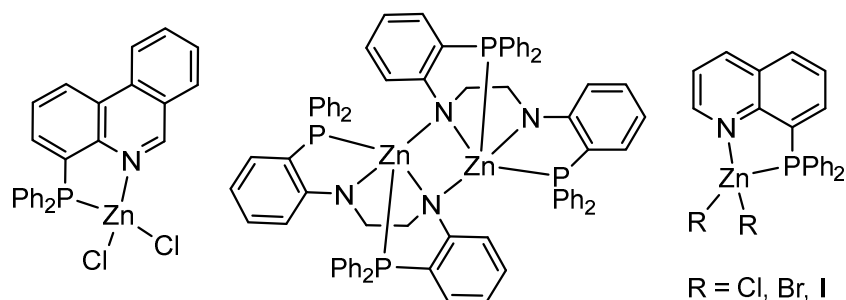


Figure 8. Luminescent Zn(II) complexes containing P,N-ligands.

1.4. Luminescent complexes based on Cu(I) and Ag(I)

Cu(I) complexes can act as TADF materials and harvest both singlet and triplet excitons, which makes them promising competitors of currently used heavy-metal phosphors in addition to being a lot cheaper as well.^[17,39] Blue-emitting materials are easily designed with Cu(I), as it has no unoccupied low-lying d-orbitals due to the filled d-shell, making a $d_{\pi}d_{\sigma^*}$ -quenching impossible, which is the case in Ir, Pt and Os complexes. However, when excited, Cu(I) changes its coordination geometry from tetrahedral to square planar, resulting in an open coordination site, which can in return be occupied by solvent molecules or counterions forming penta-coordinated compounds. This is an undesired property, as it leads to quenching, a slow-down in electron transfer and consequently in thermal and electrochemical instability and reduced luminescent properties.^[40]

For the design of future Cu(I) complexes it is necessary to suppress any geometrical rearrangement of Cu(I) in the complexes during the excited state. This can be achieved by proper ligand design. The ideal ligand should in general offer multiple coordination sites, which can fill the open coordination site during excitation. Additionally, the ligand should, on the one hand, be flexible to be able to adapt to the different coordination geometries of Cu(I) during excitation, but on the other hand, also be bulky enough to minimize geometric changes. A few examples^[4,41–43] which already fulfill these requirements showed promising results in high emission efficiencies and improved quantum yields in addition to the already numerous known luminescent copper(I) complexes reported in the literature (Figure 6, left).^[13,23,24,39,44–46]

On the contrary, luminescent silver(I) complexes are rather rare, though a few examples have been published over the years.^[42,43,47] The d-orbital of Ag(I) is located lower than in Cu(I) and can only contribute to higher electron transitions (triplet state harvesting), which makes the luminescence of Ag(I) complexes highly dependent on the ligand.^[17,48] Here again, a proper ligand design is necessary to realize efficiently luminescent Ag(I) complexes. Highly electron-donating ligands, such as phosphines, are needed to destabilize the d-orbitals of silver(I) and make MLCT possible (Figure 6, right).^[49–51] As pure powders, Ag(I) complexes are sometimes not even emissive due to concentration quenching effects. In solution, the luminescent properties of Ag(I) complexes can be enhanced.^[44]

In summary, research is still ongoing and also needed to find the optimal ligand in synergy with Cu(I) or Ag(I) to create efficiently luminescent compounds.

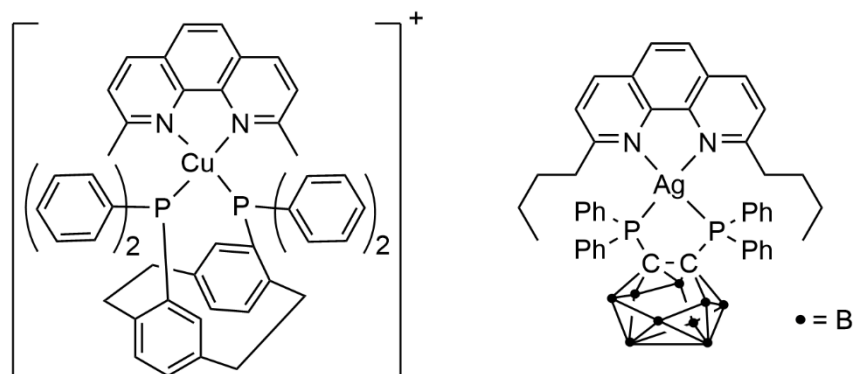


Figure 9. Structures of currently available, efficiently luminescent Cu(I) and Ag(I) complexes.

1.5. Functionalized tertiary phosphines and their possible application in OLEDs.

The development of novel tertiary phosphines (PR_3) with tunable coordination properties towards a variety of metal ions is an important research field in organic phosphorus chemistry and still a focus of ongoing research.^[52–54] With the introduction of nitrogen containing aromatic substituents bound to the phosphorus, multidentate P,N-ligands are formed. These kinds of phosphines possess ambivalent (N/P) Lewis base properties, adjustable coordination abilities, can be made sterically demanding and are in general easy to synthesize. Having additional coordination sides enlarges their potential use in catalytic reactions, which is the reason they are widely used in science and the industry employing transition metal catalysis.^[53,55–64] With the introduction of a CH_2 -group between phosphorus and the attached functionalized, heteroaromatic substituents, the flexibility of the ligand is drastically increased. This facilitates the ligand's ability to adapt its geometry to the present metal ion resulting not only in a versatile coordination chemistry but also in improved properties for the application in transition metal catalysis. Since transition states of metal ions sometimes require different geometrical environments, flexible ligands can adapt their geometry and function as an efficient stabilizer.^[65–69] The advantage of flexible structures in catalysis is an already proven concept for enzymatic systems, Sigman *et al.* recently debated this for a number of other classes of catalysts.^[70–73] However, tertiary, functionalized phosphines are not only useful for catalysis but also as potential hosts or emitters in optoelectronic applications or as ligands in functional materials, such as MOFs.^[38,74–86] Particularly, Artem'ev *et al.* have recently published promising results based on luminescent complexes containing P,N-ligands (Figure 10).^[44,51,78,86–89] They show excellent quantum yields (over 60%), however, these complexes have a rather broad emission wavelength of sometimes over 300 nm, which results in an impure color appearance.

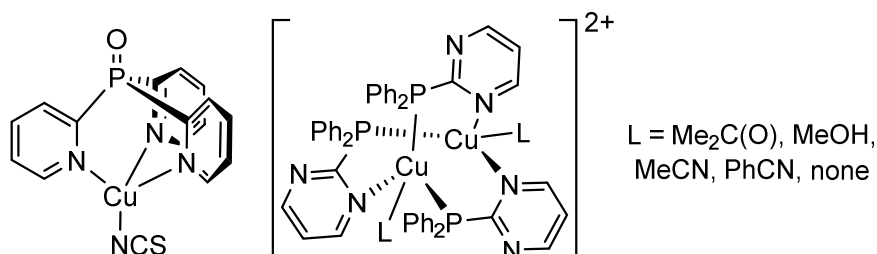


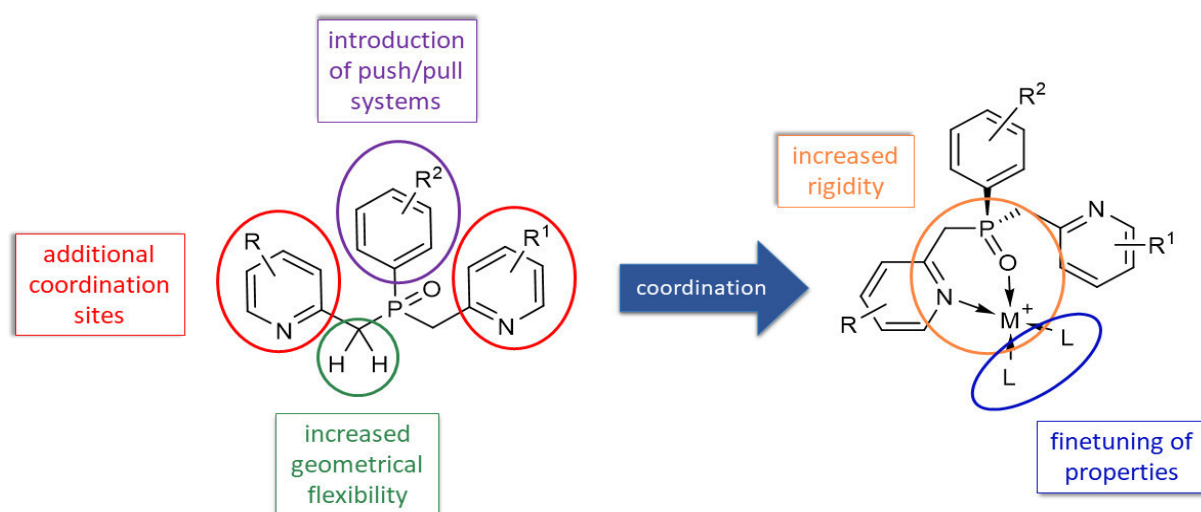
Figure 10. Examples of luminescent complexes published by Artem'ev *et al.*

1.6. Novel concept for suitable ligands for luminescent compounds

The concept for the ligand design of luminescent complexes proposed in this thesis is centered around phosphine (P,N) ligands (Scheme 1). The phosphorus atom in the middle of the molecule has the ability

to act as a central junction connecting the different substituents in one molecule. The general design will combine known trends published in the literature, which can be synergistically adjusted to the needs. For instance, by changing the substituents on the phosphorus, e.g. by introduction of push/pull systems or by extension of the π -system, luminescent properties of the phosphines can easily be tuned (Scheme 1, left).^[78,90]

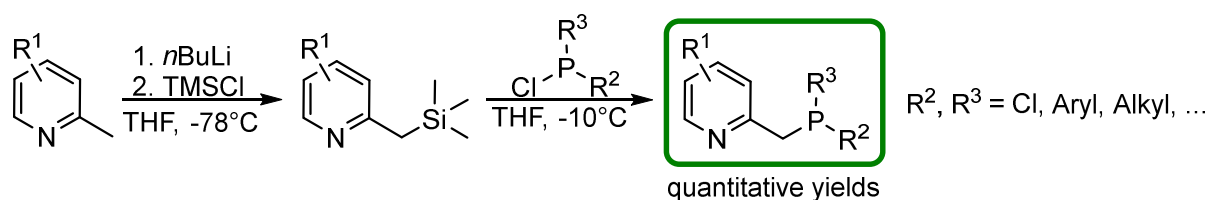
The easy oxidation of phosphines by traces of oxygen or moisture is a disadvantage, which makes phosphine oxides superior due to their improved stability, so phosphine oxide complexes will be prepared and investigated as well. The use of phosphine and phosphine oxides in OLED materials has in general the drawback of the rather labile P–C bond.^[91,92] Through coordination to a metal atom, the P–C bond can be stabilized significantly, which in return will raise the melting and degradation point. Additionally, the flexibility of the functionalized substituents attached to the phosphorus can be lowered by complexation and possible vibration and geometric changes after excitation of the molecule are reduced (Scheme 1, right). The metal center itself can also be beneficial, as it can not only take over the role of the stabilizer of the molecular system, but can also take part in the luminescence process (MLCT or LMCT). Furthermore, the metal center can also provide further coordination sites which can be covered by other ligands with extensive π -systems and finetune the luminescence. Extensive research covering these areas has not been done so far, but it is obvious, that this class of ligands has a great potential.



Scheme 1. General research concept containing phosphine oxide ligands as new OLED materials and possible variation thereof to influence and control the luminescent properties.

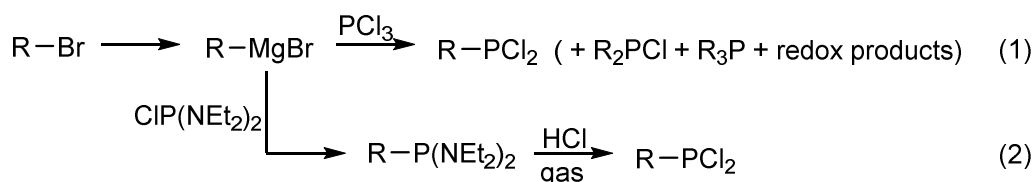
1.7. Synthetic routes to flexible, functionalized phosphines

Multiple ways for the formation of tertiary phosphines have been published over the years and propose a synthesis *via* either the reaction of metal phosphides with alkyl or aryl halides, *via Michael* addition or the reduction of phosphine oxides.^[53,93–95] For the synthesis of phosphines based on the proposed concept (Section 1.6) the most universal and efficient route is the reaction of mono-, di- or trichlorophosphines with trimethylsilylpyridyl derivatives according to Pierre Braunstein *et al.* (Scheme 2).^[96] This synthetic route is superior to the classical way, where the dichlorophosphine is allowed to react directly with the lithiated picolyl derivative, since the reaction's side product is not an inorganic salt (LiCl), but rather a liquid with a low boiling point, that can easily be removed under vacuum (TMSCl). Another benefit is, that this synthesis is scalable, and thus allows for the preparation of the phosphine in quantities of 5 g or more with quantitative yields.



Scheme 2. General synthesis of mono-, bis- and tris-substituted phosphines according to P. Braunstein *et al.*

Dichlorophosphines are needed for the synthesis of bispicolyphosphines (see Section 1.4) according to Braunstein. However, aryl-dichlorophosphines functionalized in the aryl-part are only scarcely available and cannot be synthesized analogous to the Braunstein route via the corresponding silyl-compound. The formation of the P–C-bond in the synthesis of dichlorophosphines is the most critical step, for which several approaches are known, involving multistep protocols wherein the isolation of intermediates is necessary.^[97–100] The most classical route is based on the substitution reaction of phosphorus trichloride with a carbanion (Grignard reagent or an organolithium compound) resulting in the desired dichlorophosphine (see Scheme 3).^[101–103] However, this synthesis often leads to the formation of multiple substitution products and redox reaction products caused by a nucleophilic attack of the organometallic reagent on chlorine (instead of phosphorus). Moreover, some dichlorophosphines tend to dimerize in solution. This causes the additional presence of the corresponding monochlorophosphines and tertiary phosphines in the reaction mixture, which makes the isolation and purification of the desired air and moisture sensitive product very difficult. Additionally, functional groups, such as esters or nitriles, are not tolerated, especially when utilizing organo-lithium reagents. Consequently, the development of a universal and preferably one-pot procedure for the synthesis of differently substituted dichlorophosphines is beneficial not only for the research on P,N-ligands but also in general for organophosphorus compounds.



Scheme 3. Two most common routes for the synthesis of dichlorophosphines.

1.8. Aim of the thesis

In summary, there is a pressing need for alternative ligand systems based on sustainable metal complexes utilizing Cu(I)-, Ag(I)- and Zn(II) salts, which can be used as efficient and durable luminescent materials in printable OLEDs in order to bring OLED technology to the next level.

The ultimate goal of this thesis is, based on the concept discussed in Section 1.6, the development of cheap, efficient, longtime-stable, soluble, green and blue emitting compounds based on P,N ligands or their corresponding phosphine oxides and their resulting Cu(I), Ag(I) and Zn(II) complexes. Consequently, a library of innovative, functionalized P,N-ligands containing aromatic heterocycles as substituents will be prepared. A facile, scalable and high yielding syntheses of these ligands with an easy work-up based on cheap, preferably commercially available starting materials will be developed. In this context, a general approach to the synthesis of dichlorophosphines will be investigated, where preferably the isolation of intermediates is not necessary.

Coordination complexes of the functionalized phosphine and phosphine oxide ligands based on d^{10} metal salts, in particular Cu(I)-, Ag(I)- and Zn(II) salts, will be prepared and their luminescent properties will be investigated. By varying the substituents in the N- and P-containing part of the ligand, the

change in optical properties will be examined. The aim is to gain knowledge about the mechanisms of excitation and emission of these compounds in general.

This thesis is part of a joint project together with the Fraunhofer IAP in Potsdam and Notion Systems GmbH and is funded by the German Federal Ministry for Economic Affairs and Energy on the basis of a decision by the German Bundestag.

1.9. References

- [1] H. Yersin, *Highly Efficient OLEDs with Phosphorescent Materials*, Wiley, 2007.
- [2] F.-M. Xie, J.-X. Zhou, Y.-Q. Li and J.-X. Tang, *J. Mater. Chem. C*, 2020, **8**, 9476–9494.
- [3] T. Tsujimura, *OLED Display Fundamentals and Applications*, John Wiley & Sons, Inc., Hoboken, New Jersey, 2017.
- [4] H. Yersin, *Highly Efficient OLEDs*, Wiley-VCH Verlag GmbH & Co. KGaA, Weinheim, Germany, 2018.
- [5] C. W. Tang and S. A. Vanslyke, *Appl. Phys. Lett.*, 1987, **51**, 913–915.
- [6] J.-H. H. Lee, C.-H. H. Chen, P.-H. H. Lee, H.-Y. Y. Lin, M. K. Leung, T.-L. L. Chiu and C.-F. F. Lin, *J. Mater. Chem. C*, 2019, **7**, 5874–5888.
- [7] J. Adachi, H. Kakizoe, P. K. D. Tsang and A. Endo, *SID Symp. Dig. Tech. Pap.*, 2019, **50**, 95–98.
- [8] Q. Wang, Q.-S. Tian, Y.-L. Zhang, X. Tang and L.-S. Liao, *J. Mater. Chem. C*, 2019, **7**, 11329–11360.
- [9] C. Cebrián and M. Mauro, *Beilstein J. Org. Chem.*, 2018, **14**, 1459–1481.
- [10] H. Yersin, L. Mataranga-Popa, R. Czerwieńec and Y. Dovbii, *Chem. Mater.*, 2019, **31**, 6110–6116.
- [11] S. Schmidbauer, A. Hohenleutner and B. König, *Adv. Mater.*, 2013, **25**, 2114–2129.
- [12] Y. Im, S. Y. Byun, J. H. Kim, D. R. Lee, C. S. Oh, K. S. Yook and J. Y. Lee, *Adv. Funct. Mater.*, 2017, **27**, 1603007.
- [13] C. Bizzarri, F. Hundemer, J. Busch and S. Bräse, *Polyhedron*, 2018, **140**, 51–66.
- [14] T.-T. Bui, F. Goubard, M. Ibrahim-Ouali, D. Gigmes and F. Dumur, *Beilstein J. Org. Chem.*, 2018, **14**, 282–308.
- [15] F. Dumur, *Synth. Met.*, 2014, **195**, 241–251.
- [16] M. G. Kaplunov, S. S. Krasnikova, S. L. Nikitenko and I. K. Yakushchenko, *Mol. Cryst. Liq. Cryst.*, 2014, **589**, 48–55.
- [17] C. Bizzarri, E. Spuling, D. M. Knoll, D. Volz and S. Bräse, *Coord. Chem. Rev.*, 2018, **373**, 49–82.
- [18] B. Wex and B. R. Kaafarani, *J. Mater. Chem. C*, 2017, **5**, 8622–8653.
- [19] L. Zong, Y. Xie, C. Wang, J.-R. Li, Q. Li and Z. Li, *Chem. Commun.*, 2016, **52**, 11496–11499.
- [20] W. C. Chen, C. S. Lee and Q. X. Tong, *J. Mater. Chem. C*, 2015, **3**, 10957–10963.
- [21] Y. Zou, S. Gong, G. Xie and C. Yang, *Adv. Opt. Mater.*, 2018, **6**, 1800568.
- [22] D. Volz, M. Wallesch, S. L. Grage, J. Göttlicher, R. Steininger, D. Batchelor, T. Vitova, A. S. Ulrich, C. Heske, L. Weinhardt, T. Baumann and S. Bräse, *Inorg. Chem.*, 2014, **53**, 7837–7847.
- [23] O. S. Wenger, *J. Am. Chem. Soc.*, 2018, **140**, 13522–13533.
- [24] L. P. Ravaró, K. P. S. Zanoni and A. S. S. de Camargo, *Energy Reports*, 2020, **6**, 37–45.
- [25] M. Reich and P. M. Vasconcelos, *Elements*, 2015, **11**, 305–310.
- [26] S.-C. Yu, C.-C. Kwok, W.-K. Chan and C.-M. Che, *Adv. Mater.*, 2003, **15**, 1643–1647.
- [27] K. G. Vladimirova, A. Y. Freidzon, O. V. Kotova, A. A. Vaschenko, L. S. Lepnev, A. A. Bagatur'yants, A. G. Vitukhnovskiy, N. F. Stepanov and M. V. Alifimov, *Inorg. Chem.*, 2009, **48**, 11123–11130.
- [28] S. F. Liu, Q. Wu, H. L. Schmider, H. Aziz, N. X. Hu, Z. Popović and S. Wang, *J. Am. Chem. Soc.*, 2000, **122**, 3671–3678.
- [29] K. Singh, A. Kumar, R. Srivastava, P. S. Kadyan, M. N. Kamalasanan and I. Singh, *Opt. Mater.*, 2011, **34**, 221–227.

- [30] H.-J. Son, W.-S. Han, J.-Y. Chun, B.-K. Kang, S.-N. Kwon, J. Ko, S. J. Han, C. Lee, S. J. Kim and S. O. Kang, *Inorg. Chem.*, 2008, **47**, 5666–5676.
- [31] A. Gusev, E. Braga, V. Shul'gin, K. Lyssenko, I. Eremenko, L. Samsonova, K. Degtyarenko, T. Kopylova and W. Linert, *Materials*, 2017, **10**, 897.
- [32] I. E. Mikhailov, L. D. Popov, V. V. Tkachev, S. M. Aldoshin, G. A. Dushenko, Y. V. Revinskii and V. I. Minkin, *J. Mol. Struct.*, 2018, **1157**, 374–380.
- [33] Y. Sakai, Y. Sagara, H. Nomura, N. Nakamura, Y. Suzuki, H. Miyazaki and C. Adachi, *Chem. Commun. Chem. Commun*, 2015, **51**, 3181–3184.
- [34] C. S. Oh and J. Y. Lee, *Dye. Pigment.*, 2013, **99**, 374–377.
- [35] Y. Sakai, Y. Sagara, H. Nomura, N. Nakamura, Y. Suzuki, H. Miyazaki and C. Adachi, *Chem. Commun.*, 2015, **51**, 3181–3184.
- [36] T. Tsukuda, C. Nishigata, K. Arai and T. Tsubomura, *Polyhedron*, 2009, **28**, 7–12.
- [37] R. Mondal, P. K. Giesbrecht and D. E. Herbert, *Polyhedron*, 2016, **108**, 156–162.
- [38] S. Bestgen, C. Schoo, B. L. Neumeier, T. J. Feuerstein, C. Zovko, R. Köppe, C. Feldmann and P. W. Roesky, *Angew. Chem.*, 2018, **130**, 14461–14465; *Angew. Chem. Int. Ed.*, 2018, **57**, 14265–14269.
- [39] Y. Liu, S. C. Yiu, C. L. Ho and W. Y. Wong, *Coord. Chem. Rev.*, 2018, **375**, 514–557.
- [40] M. Osawa, I. Kawata, R. Ishii, S. Igawa, M. Hashimoto and M. Hoshino, *J. Mater. Chem. C*, 2013, **1**, 4375–4383.
- [41] R. Czerwieniec, K. Kowalski and H. Yersin, *Dalton Trans.*, 2013, **42**, 9826.
- [42] H. Yersin, R. Czerwieniec, M. Z. Shafikov and A. F. Suleymanova, *Highly Efficient OLEDs*, Wiley-VCH Verlag GmbH & Co. KGaA, Weinheim, Germany, 2018.
- [43] A. Schinabeck, J. Chen, L. Kang, T. Teng, H. H. H. Homeier, A. F. Suleymanova, M. Z. Shafikov, R. Yu, C.-Z. Lu and H. Yersin, *Chem. Mater.*, 2019, **31**, 4392–4404.
- [44] A. V. Artem'ev, M. Z. Shafikov, A. Schinabeck, O. V. Antonova, A. S. Berezin, I. Y. Bagryanskaya, P. E. Plusnin and H. Yersin, *Inorg. Chem. Front.*, 2019, **6**, 3168–3176.
- [45] D. M. Zink, L. Bergmann, D. Ambrosek, M. Wallesch, D. Volz and M. Mydlak, *Transl. Mater. Res.*, 2014, **1**, 015003.
- [46] F. Dumur, *Org. Electron.*, 2015, **21**, 27–39.
- [47] M. Z. Shafikov, R. Czerwieniec and H. Yersin, *Dalton Trans.*, 2019, **48**, 2802–2806.
- [48] C.-C. Hsu, C.-C. Lin, P.-T. Chou, C.-H. Lai, C.-W. Hsu, C.-H. Lin and Y. Chi, *J. Am. Chem. Soc.*, 2012, **134**, 7715–7724.
- [49] M. Z. Shafikov, A. F. Suleymanova, R. Czerwieniec and H. Yersin, *Chem. Mater.*, 2017, **29**, 1708–1715.
- [50] M. Z. Shafikov, A. F. Suleymanova, R. Czerwieniec and H. Yersin, *Inorg. Chem.*, 2017, **56**, 13274–13285.
- [51] A. V. Artem'ev, M. R. Ryzhikov, A. S. Berezin, I. E. Kolesnikov, D. G. Samsonenko and I. Y. Bagryanskaya, *Inorg. Chem. Front.*, 2019, **6**, 2855–2864.
- [52] D. W. Allen, *Phosphines and Related P-C-bonded Compounds*, Royal Society of Chemistry, 2010, **39**.
- [53] E. I. Musina, A. S. Balueva and A. A. Karasik, *Organophosphorus Chemistry*, 2019, **48**, 1–63.
- [54] M. Mizhiritskii, Y. Shpernat and A. J. Robertson, *ChemInform*, 2005, **36**, 26110.
- [55] Y. Xiao, Z. Sun, H. Guo and O. Kwon, *Beilstein J. Org. Chem.*, 2014, **10**, 2089–2121.
- [56] C. G. J. Tazelaar, J. C. Sloopweg and K. Lammertsma, *Coord. Chem. Rev.*, 2018, **356**, 115–126.
- [57] C. A. Tolman, *Chem. Rev.*, 1977, **77**, 313–348.
- [58] J. T. Fleming and L. J. Higham, *Coord. Chem. Rev.*, 2015, **297–298**, 127–145.
- [59] K. N. Gavrilov and A. I. Polosukhin, *Russ. Chem. Rev.*, 2000, **69**, 661–682.
- [60] M. P. Carroll and P. J. Guiry, *Chem. Soc. Rev.*, 2014, **43**, 819–833.

-
- [61] L. Fanfoni, A. Meduri, E. Zangrando, S. Castillon, F. Felluga, B. Milani, *Molecules*, **2011**, *16*, 1804–1824.
- [62] H. Jaafar, H. Li, L. C. Misal Castro, J. Zheng, T. Roisnel, V. Dorcet, J.-B. Sortais, C. Darcel, *Eur. J. Inorg. Chem.*, **2012**, *2012* (22), 3546–3550.
- [63] G. Chelucci, G. Orrù, G. a. Pinna, *Tetrahedron*, **2003**, *59*, 9471–9515.
- [64] P. Braunstein, *J. Organomet. Chem.*, **2004**, *689*, 3953–3967.
- [65] A. Nojiri, N. Kumagai, M. Shibasaki, *J. Am. Chem. Soc.*, **2009**, *131* (10), 3779–3784.
- [66] D. E. Ryan, D. J. Cardin, F. Hartl, *Coord. Chem. Rev.*, **2017**, *335*, 103–149.
- [67] M. Reinmuth, P. Walter, M. Enders, E. Kaifer, H. J. Himmel, *Eur. J. Inorg. Chem.*, **2011**, No. 1, 83–90.
- [68] N. Kumagai, M. Shibasaki, *Angew. Chem.*, **2013**, *125*, 235–246; *Angew. Chem. Int. Ed.*, **2013**, *52* (1), 223–234.
- [69] G. Altenhoff, R. Goddard, C. W. Lehmann, F. Glorius, *J. Am. Chem. Soc.*, **2004**, *126* (46), 15195–15201.
- [70] G. G. Hammes, *Biochemistry*, **2002**, *41* (26), 8221–8228.
- [71] D. Herschlag, *Bioorg. Chem.*, **1988**, *16* (1), 62–96.
- [72] E. Katsoulakou, N. Lalioti, C. P. Raptopoulou, A. Terzis, E. Manessi-Zoupa, S. P. Perlepes, *Inorg. Chem. Commun.*, **2002**, *5* (9), 719–723.
- [73] J. M. Crawford, M. S. Sigman, *Synth.*, **2019**, *51* (5), 1021–1036.
- [74] L. Bergmann, J. Friedrichs, M. Mydlak, T. Baumann, M. Nieger, S. Bräse, *Chem. Commun. (Camb.)*, **2013**, *49* (58), 6501–6503.
- [75] O. Crespo, M. C. Gimeno, A. Laguna, C. Larraz, *Z. Naturforsch.*, **2009**, *64* (11–12), 1525–1534.
- [76] A. Eichhöfer, G. Buth, S. Lebedkin, M. Kühn, F. Weigend, *Inorg. Chem.*, **2015**, *54* (19), 9413–9422.
- [77] I. D. Strel'nik, V. V. Sizov, V. V. Gurzhiy, A. S. Melnikov, I. E. Kolesnikov, E. I. Musina, A. A. Karasik, E. V. Grachova, *Inorg. Chem.*, **2020**, *59* (1), 244–253.
- [78] A. V. Artem'ev, M. R. Ryzhikov, I. V. Taidakov, M. I. M. I. Rakhmanova, E. A. Varaksina, I. Y. Bagryanskaya, S. F. Malysheva, N. A. N. Belogorlova, *Dalton Trans.*, **2018**, *2* (8), 2701–2710.
- [79] C. Han, H. Xu, *Chinese Sci. Bull.*, **2019**, *64* (7), 663–681.
- [80] D. Joly, P. A. Bouit, M. Hissler, *J. Mater. Chem. C*, **2016**, *4* (17), 3686–3698.
- [81] S. N. Arbuzova, P. A. Volkov, N. I. Ivanova, N. K. Gusarova, L. I. Larina, O. N. Kazheva, G. G. Alexandrov, O. A. Dyachenko, B. A. Trofimov, *J. Organomet. Chem.*, **2011**, *696* (10), 2053–2058.
- [82] X. Tan, L. Li, J. Zhang, X. Han, L. Jiang, F. Li, C. Y. Su, *Chem. Mater.*, **2012**, *24* (3), 480–485.
- [83] D. M. Zink, D. Volz, T. Baumann, M. Mydlak, H. Flügge, J. Friedrichs, M. Nieger, S. Bräse, *Chem. Mater.*, **2013**, *25* (22), 4471–4486.
- [84] M. K. Rong, F. Holtrop, J. C. Slootweg, K. Lammertsma, *Coord. Chem. Rev.*, **2019**, *382*, 57–68.
- [85] L. A. Adrio, K. K. Hii, *Organomet. Chem.*, **2009**, *35*, 62–92.
- [86] A. V. Artem'ev, M. I. Rogovoy, D. G. Samsonenko, M. I. Rakhmanova, *Inorg. Chem. Commun.*, **2020**, *115*, 27–30.
- [87] A. V. Artem'ev, M. P. Davydova, A. S. Berezin, M. R. Ryzhikov, D. G. Samsonenko, *Inorg. Chem.*, **2020**, *59* (15), 10699–10706.
- [88] A. V. Artem'ev, E. P. Doronina, M. I. Rakhmanova, A. O. Sutyryna, I. Y. Bagryanskaya, P. M. Tolstoy, A. L. Gushchin, A. S. Mazur, N. K. Gusarova, B. A. Trofimov, *New J. Chem.*, **2016**, *40* (12), 10028–10040.
- [89] A. S. Berezin, A. V. Artem'ev, V. Y. Komarov, A. Y. Baranov, *New J. Chem.*, **2020**, *44* (23), 9858–9862.
- [90] A. V. Artem'ev, A. Y. Baranov, M. I. Rakhmanova, S. F. Malysheva, D. G. Samsonenko, *New J. Chem.*, **2020**, *44* (17), 6916–6922.
- [91] N. Lin, J. Qiao, L. Duan, H. Li, L. Wang, Y. Qiu, *J. Phys. Chem. C*, **2012**, *116* (36), 19451–19457.

- [92] K. Katagiri, Y. Yamamoto, Y. Takahata, R. Kishibe, N. Fujimoto, *Tetrahedron Lett.*, **2019**, 60 (30), 2026–2029.
- [93] I. Wauters, W. Debrouwer, C. V Stevens, *Beilstein J. Org. Chem.*, **2014**, 10, 1064–1096.
- [94] M. Honaker, J. Hovland, R. Nicholas Salvatore, *Curr. Org. Synth.*, **2007**, 4 (1), 31–45.
- [95] E. Podyacheva, E. Kuchuk, D. Chusov, *Tetrahedron Lett.*, **2019**, 60 (8), 575–582.
- [96] A. Kermagoret, F. Tomicki, P. Braunstein, *Dalton Trans.*, **2008**, 22, 2945–2955.
- [97] B. Buchner, L. B. J. Lockhart, *J. Am. Chem. Soc.*, **1951**, 73, 755–756.
- [98] A. Hinke, W. Kuchen, *Phosphorus Sulfur Relat. Elem.*, **1983**, 15 (1), 93–98.
- [99] P. Pellon, J. Hamelin, *Tetrahedron Lett.*, **1986**, 27 (46), 5611–5614.
- [100] J. A. Miles, M. T. Beeny, K. W. Ratts, *J. Org. Chem.*, **1975**, 40 (3), 343–347.
- [101] S. A. Reiter, S. D. Nogai, K. Karaghiosoff, H. Schmidbaur, *J. Am. Chem. Soc.*, **2004**, 126 (48), 15833–15843.
- [102] A. Karaçar, M. Freytag, H. Thönnessen, P. G. Jones, R. Bartsch, R. Schmutzler, *J. Organomet. Chem.*, **2002**, 643–644, 68–80.
- [103] C. Hettstedt, M. Unglert, R. J. Mayer, A. Frank, K. Karaghiosoff, *Eur. J. Inorg. Chem.*, **2016**, 2016 (9), 1405–1414.

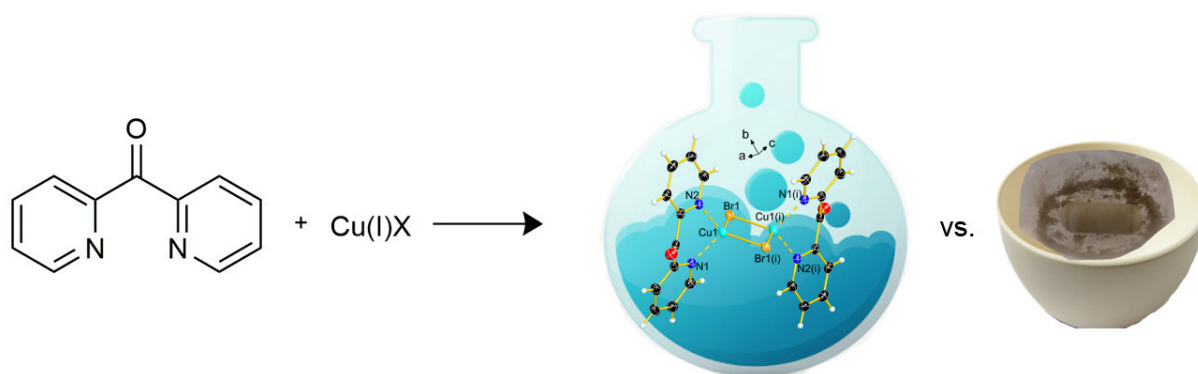
2. Results and discussion

2.1. Coordination complexes of di(2-pyridyl)ketone with copper(I) and their formation in solution and under solvent-free conditions

Christin Kirst, Marco Reichel and Konstantin Karaghiosoff

Published in *Inorg. Chim. Acta* 2021, **514**, 119951–119962.DOI: [10.1016/j.ica.2020.119951](https://doi.org/10.1016/j.ica.2020.119951)

Christin Kirst synthesized all the discussed compounds, performed UV Vis measurements, Hirshfeld surface analysis and single crystal X-ray measurements on compounds **2–4**. She analyzed and evaluated the corresponding data, managed the project and wrote the original draft of the manuscript and implemented the necessary corrections in the final version of the paper.



Abstract: Four copper(I) complexes of the ligand di(2-pyridyl)ketone (dpk) were synthesized using Cu(I)Cl, Cu(I)Br, Cu(I)CN and Cu(I)I in MeCN solution and under solvent-free conditions. The solid compounds show a reaction when mixed without solvent, which is indicated by a rapidly occurring color change. The resulting products were characterized by IR spectroscopy, MS and single crystal X-ray diffraction. In case of the Cu(I)Cl, a 1:2-complex is formed, showing a six-membered, cyclic Cu₃X₃-unit with quasi-boat confirmation. With Cu(I)Br, Cu(I)CN and Cu(I)I, 1:1-complexes are obtained. The Cu(I)Br and Cu(I)I complexes are binuclear and bridged by bromide and iodide anions respectively, resulting in Cu₂Br₂/ Cu₂I₂ halide-bridged square dimers. The copper(I) cation and the cyanide anion of the Cu(I)CN dpk complex are forming a one-dimensional chain bridged by the cyanide groups. The structures were further characterized by Hirshfeld surface analysis, showing the weak interactions in the crystal, which are consistent with the observed physical properties.

2.1.1. Introduction

Copper(I) complexes and clusters are valuable for both physical and biological research and application.^[1] Especially the photochemical and photophysical properties due to their d^{10} electronic configuration and TADF harvesting possibility result in a versatile luminescent behavior.^[2–9] Copper(I) halides and pseudo halides offer a large structural diversity of coordination compounds, arising from the many possible coordination numbers of copper(I) (two, three and four).^[10,11] Copper(I) halides in complexes sometimes tend to aggregate. These aggregates can contain isolated Cu_2X_2 units ($X = Hal$) or even form higher aggregates up to 2D coordination polymers.^[10] When focusing on Cu_3X_3 clusters, only a few are known. Especially six-membered, cyclic Cu_3X_3 -units with a quasi-boat confirmation are rare.^[10,12–14] The synthesis of these types of complexes is mostly done in solution, nevertheless, mechanochemical syntheses of copper(I) complexes with nitrogen containing ligands are also known.^[4,15–17] In general, the solvent-free synthesis of organometallic complexes is an attractive research field, as the reaction conditions are fairly easy and environmentally friendly.^[18] In some cases, it is even possible to synthesize complexes, which have not yet been successfully prepared using solution based procedures.¹⁹

Dipyridylketone (dpk) and a large number of its transition metal clusters and coordination polymers are also attributed great importance in biochemistry and materials science.^[12–24] The application of these metal complexes also in catalysis is constantly increasing, making dpk an interesting ligand.^[28,33,34] Dpk has three potential donor groups and is regarded as a versatile organic ligand, as it can occur in metal complexes in a terminal, monodentate, chelating or bridging role.^[25] This property also allows the use of dpk as a ligand, e.g. in potential anti-cancer agents, when coordinating to a suitable metal ion, like ruthenium.^[35]

There only a few copper(I) complexes of dpk with Cu(I) halogens and pseudohalogens known in the literature.^[34,36,37] Whereas there are several complexes of copper(II) and dpk known.^[25,36,38,39] In other previously reported copper(I) complexes, the dpk ligand reacted and formed addition products with H_2O or alcohols. The resulting ligand is then coordinating to the copper(I) or copper(II).^[21,25,27,40] However, a few copper(I) halide and pseudo halide dpk complexes are still missing, some of which will be discussed herein. We report the synthesis of four copper(I)-complexes containing the ligand dpk. The products were characterized by IR spectroscopy, MS and single crystal X-ray diffraction.

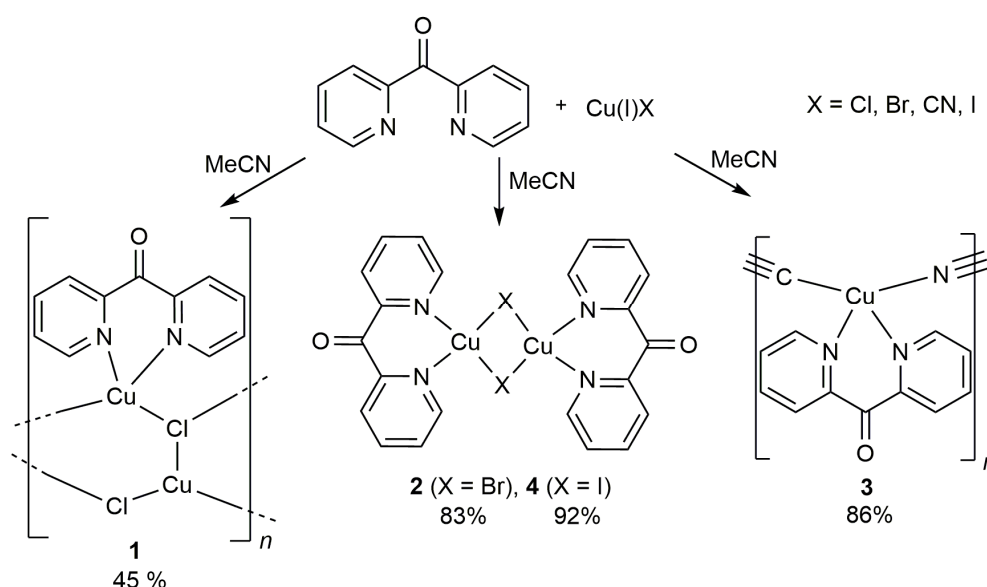
2.1.2. Experimental

2.1.2.1. General comments

All compounds were handled using Schlenk techniques under dry Ar. Unless otherwise specified, all reagents and solvents were purchased from commercial sources and used as received. The solvents dichloromethane, acetonitrile and diethyl ether were dried, freshly distilled and degassed prior to use. As drying agents, calcium hydride was used for dichloromethane, SICAPENT® for acetonitrile, and sodium for diethyl ether. The samples for IR spectroscopy were placed under ambient conditions without further preparation onto a Smith DuraSamplIR II ATR device using a Perkin Elmer BX II FT-IR System spectrometer. Melting points were determined using a Buechi B-540 apparatus using a heating rate of 1 °C per min. ESI measurements were done on a Thermo Finnigan LTQ FT Ultra Fourier Transform Ion Cyclotron Resonance Mass Spectrometer. Elemental analysis was done using an Elementar vario micro cube instrument. UV Vis spectra were recorded on a Varian Cary 500 equipped with a Praying-Mantis-add-on and a photometer ball. Powder diffractograms were recorded on a Huber G644-Guinier diffractometer equipped with a quartz-monochromator (λ -K- $\alpha_1 = 1.54056 \text{ \AA}$).

2.1.2.2. Synthesis and characterization data for compounds 1–4

The synthesis of compounds 1–4 was performed either with solvent or under solvent-free conditions. For the reaction in solution, dpk (0.3 g) was dissolved in dry, degassed acetonitrile (20 mL) and added to the appropriate amount (1:1 reaction) of copper(I) halide/cyanide *via* a cannula (Scheme 4). After stirring for a few minutes, the solution turns orange for compound 3 and dark red in the cases of 1, 2 and 4. For the solvent-free reaction, solid dpk and the appropriate amount of copper(I) halide/cyanide were dried prior to use and combined in a Schlenk flask. After stirring with a stir bar over a period of five minutes, the mixture of the two rather colorless solids slowly changes its color to orange or dark red. The yields of the reactions under solvent-free conditions depend on the reaction time, whereas in solution, the reaction is instantly and leads to the ones mentioned in Scheme 4. All compounds, except 4, decompose in contact with air or moisture and turn green, indicating an oxidation state change of copper(I) to copper(II) making elemental analysis of these compounds difficult.



Scheme 4. Synthesis of the copper(I) complexes 1–4 in solution.

$[\text{Cu}_2(\text{dpk})\text{Cl}_2]_n$ **1**. ESI MS (positive mode, $\text{CH}_3\text{CN}/\text{H}_2\text{O}$): m/z $[\text{C}_{11}\text{H}_8\text{N}_2\text{OCu}^+ + \text{CH}_3\text{CN}] = 288.01935$. IR: $\tilde{\nu}_{\text{max}}$ (cm^{-1}) = 3058 (vw), 2004 (vw), 1660 (s), 1580 (s), 1563 (m), 1463 (w), 1427 (m), 1305 (s), 1276 (s), 1244 (m), 1152 (m), 1092 (m), 1049 (m), 1008 (m), 996 (m), 939 (s), 899 (vw), 825 (m), 783 (w), 769 (w), 741 (vs), 681 (s), 661 (vs), 630 (m), 612 (m), 574 (vw), 529 (vw), 504 (vw), 450 (vw), 425 (vw), 414 (vw). m.p.: 275°C.

$[\text{Cu}_2(\text{dpk})_2\text{Br}_2]$ **2**. ESI MS (positive mode, $\text{CH}_3\text{CN}/\text{H}_2\text{O}$): m/z $[\text{C}_{11}\text{H}_8\text{N}_2\text{OCu}^+ + \text{CH}_3\text{CN}] = 288.01948$. IR: $\tilde{\nu}_{\text{max}}$ (cm^{-1}) = 3051 (vw), 2978 (vw), 1661 (vs), 1579 (s), 1566 (m), 1461 (m), 1427 (m), 1306 (s), 1270 (s), 1244 (m), 1226 (m), 1171 (w), 1149 (w), 1090 (w), 1050 (w), 1010 (m), 995 (w), 941 (s), 903 (w), 825 (m), 765 (w), 742 (vs), 727 (vs), 683 (s), 661 (s), 630 (m), 576 (w), 521 (vw), 504 (vw), 420 (w). m.p.: 245°C.

$[\text{Cu}(\text{dpk})(\text{CN})]_n$ **3**. ESI MS (negative mode, $\text{CH}_3\text{CN}/\text{H}_2\text{O}$): m/z $[\text{C}_{11}\text{H}_8\text{N}_2\text{OCu}^+ + \text{CH}_3\text{CN}] = 288.01935$. IR: $\tilde{\nu}_{\text{max}}$ (cm^{-1}) = 3051 (vw), 2921 (vw), 2121 (m), 2077 (m), 1664 (m), 1583 (m), 1469 (vw), 1431 (m), 1307 (s), 1283 (s), 1245 (m), 1232 (m), 1159 (w), 1095 (m), 1059 (vw), 1017 (s), 979 (vw), 933 (vs), 825 (m), 799 (w), 748 (vs), 678 (s), 663 (vs), 638 (m), 578 (vw), 424 (m). Compound 3 is hardly soluble in any solvents. m.p.: 265°C.

[Cu₂(dpk)₂l₂] **4**. Elemental Anal. Calcd. C₁₁H₈N₂OCuI, C: 35.27, H: 2.15, N: 7.48%. Found: C: 35.21, H: 2.20, N: 7.66%. ESI MS (positive mode, CH₃CN/H₂O): m/z [C₁₁H₈N₂OCu⁺ + CH₃CN] = 288.01962. IR: $\tilde{\nu}_{\max}$ (cm⁻¹) = 3050 (vw), 1652 (m), 1578 (m), 1462 (w), 1428 (w), 1303 (s), 1276 (s), 1229 (vs), 1123 (s), 1053 (s), 982 (s), 932 (s), 905 (m), 826 (s), 741 (vs), 675 (s), 661 (vs), 631(s), 572(w), 524(w), 465 (vw), 419 (s). m.p.: 230°C.

2.1.2.3. X-ray crystallography

Single crystals of the complexes **1–4** suitable for X-ray diffraction measurements could be obtained by diffusion of diethyl ether into the reaction mixture. The crystals were introduced into perfluorinated oil and a suitable single crystal was carefully mounted on top of a thin glass wire. For complex **1**, the data collection was performed with a Bruker D8 Venture TXS system equipped with a multilayer mirror optics monochromator and a Mo K α rotating-anode. Data collection for complexes **2–4** was performed with a Rigaku Oxford Xcalibur 3 diffractometer equipped with a Spellman generator (50 kV, 40 mA) and a Kappa CCD detector, operating with Mo-K α radiation.

For complex **1**, the Bruker SAINT software package utilizing a narrow-frame algorithm was used. Absorption correction using the multi-scan method was applied. Data collection and data reduction for complexes **2–4** were made using the CrysAlisPro software. The structures were solved with SIR2014,^[41] refined with SHELXL-2018/1^[42,43] and finally checked using PLATON^[44] integrated in WinGX.^[45] Non-hydrogen atoms were refined anisotropically. The finalized CIF files were checked with checkCIF. Crystallographic data and structure refinements are listed in Table 1. Molecular plots were performed with DIAMOND 3.2k.^[46] CCDC data are provided free of charge by The Cambridge Crystallographic Data Center: ccdc.cam.ac.uk/structures.

Table 1. Crystallographic and refinement data for complexes **1–4**.

Compound	1	2	3	4
Formula	C ₁₁ H ₈ Cl ₂ Cu ₂ N ₂ O	C ₂₂ H ₁₆ Br ₂ Cu ₂ N ₄ O ₂	C ₁₂ H ₈ CuN ₃ O	C ₂₂ H ₁₆ Cu ₂ I ₂ N ₄ O ₂
Formula weight [g·mol ⁻¹]	382.17	655.29	273.75	749.27
T [K]	111	109	129	127
λ [Å]	0.71073	0.71073	0.71073	0.71073
Crystal system	monoclinic	triclinic	orthorhombic	triclinic
Space group	<i>P</i> 2 ₁ / <i>n</i>	<i>P</i> -1	<i>P</i> 2 ₁ 2 ₁ 2 ₁	<i>P</i> -1
<i>a</i> [Å]	15.5325(12)	7.6133(9)	8.6225(3)	6.7548(5)
<i>b</i> [Å]	3.7473(3)	10.5606(13)	10.1794(4)	8.7556(6)
<i>c</i> [Å]	21.3683(15)	14.1661(17)	12.1640(4)	10.3027(6)
α [°]	90	82.153(4)	90	83.922(5)
β [°]	104.060(2)	82.599(4)	90	71.042(6)
γ [°]	90	83.463(4)	90	75.619(6)
<i>V</i> [Å ³]	1,206.48(16)	1,113.5(2)	1,067.66(7)	558.01(7)
<i>Z</i>	4	2	4	1
Density calcd. [g·cm ⁻³]	2.104	1.954	1.703	2.230
μ [mm ⁻¹]	3.952	5.526	2.028	4.700
<i>F</i> (0 0 0)	752	640	552	356
Crystal size [mm]	0.10 × 0.01 × 0.01	0.07 × 0.05 × 0.03	0.20 × 0.20 × 0.05	0.50 × 0.20 × 0.10
θ range [°]	3.530–28.282	3.184–27.483	3.521–30.503	3.294–30.506

Index ranges	$-20 \leq h \leq 20$ $-4 \leq k \leq 4$ $-28 \leq l \leq 27$	$-9 \leq h \leq 9$ $-13 \leq k \leq 13$ $-18 \leq l \leq 18$	$-12 \leq h \leq 12$ $-14 \leq k \leq 14$ $-17 \leq l \leq 14$	$-9 \leq h \leq 9$ $-8 \leq k \leq 12$ $-14 \leq l \leq 14$
Reflections collected	11,751	15,282	11,211	5,967
Independent reflections	2,941 [$R_{\text{int}} = 0.0430$]	5,078 [$R_{\text{int}} = 0.0332$]	3,247 [$R_{\text{int}} = 0.0413$]	3,402 [$R_{\text{int}} = 0.0278$]
Completeness to theta	98.8 %	99.4 %	99.1 %	99.6 %
Refinement method	Full-matrix least-squares on F^2	Full-matrix least-squares on F^2	Full-matrix least-squares on F^2	Full-matrix least-squares on F^2
Data/restraints/Parameters	2,941 / 0 / 163	5,078 / 0 / 289	3,247 / 0 / 154	3,402 / 0 / 145
R_1/wR_2 ($I > 2 \sigma(I)$)	0.0632/0.1308	0.0266/0.0576	0.0334/0.0700	0.0297/0.0618
R_1/wR_2 (all data)	0.0681/0.1328	0.0354/0.0615	0.0441/0.0754	0.0364/0.0662
Goodness-of-fit on F^2	1.208	1.045	1.037	1.035
larg. diff. peak/hole [$e \cdot \text{\AA}^{-3}$]	1.385/−1.065	0.460/−0.478	0.632/−0.361	1.054/−1.122
CCDC No.	1999022	1999024	1999023	1999021

2.1.2.4. Computational details

Calculations of the IR spectra of the complexes were performed using Gaussian16^[47] starting from X-ray structure coordinates of the complexes and subsequent optimization of the ground state at B3LYP^[48,49] level of theory and with the basis set def2-TZVP^[50,51]. Calculations of the free dpk are based on the crystal structure data by Bock *et al.*^[52] Hirshfeld surface analysis including 2D fingerprint plots of the complexes were done using the CrystalExplorer17 software.^[53] All Hirshfeld surfaces were set to be transparent to allow for the visibility of the molecular structure. The complexes were positioned to highlight specific and significant structural features. Strong intermolecular contacts are visible as red spots in the d_{norm} maps and sharp spikes in the fingerprint plots, respectively.

2.1.3. Results and discussion

2.1.3.1. Molecular structures

The $[\text{Cu}_2(\text{dpk})\text{Cl}_2]_n$ complex **1** crystallizes as brown rods in the monoclinic space group $P2_1/n$ with four formula units per unit cell (Figure 1). Two crystallographically unique copper(I) atoms are present in the Cu_3Cl_3 -unit. One copper(I) cation (Cu1) is tetrahedrally surrounded by two chlorine atoms and two nitrogen atoms of the dpk, whereas the other copper(I) cation (Cu2) adopts a trigonal planar coordination to three chlorine atoms. Both chlorine atoms of the complex are crystallographically unique as well. One chlorine atom (Cl2(i)) is connected to two copper atoms and forms a weak non-classical hydrogen bond ($\text{H4(i)} \cdots \text{Cl2} = 2.789 \text{ \AA}$) to a neighboring hydrogen atom of dpk.^[54] The other chlorine atom (Cl1) is coordinating to three copper atoms and forms a weak non-classical hydrogen bond with a neighboring hydrogen-atom. Polynuclear copper(I) compounds often contain short $\text{Cu} \cdots \text{Cu}$ distances between 2.38–3.2 \AA .^[55] In this case, the $\text{Cu} \cdots \text{Cu}$ distances are much larger and each have a

different length (Cu1...Cu2 3.694(2) Å, Cu1...Cu2(i) 3.304(2) Å and Cu2...Cu2(i) 3.747(3) Å). The copper and chlorine atoms form a six membered ring with alternating positions, wherein five atoms (Cl1–Cu2–Cl2(i)–Cu2(i)–Cl1(i)) lay in a plane and the sixth (Cu1) is angled downwards 72.8° and has a distance of 1.408 Å from the Cl1...Cl1(i) line (Figure 11 and 12). This arrangement is reflecting the different coordination modes of Cu(I) and Cu(II).

The Cu₃Cl₃-rings in the 3D-structure are connected *via* a chain like arrangement linked over two opposing sides and form ribbons, which are surrounded by the dpk ligand (see Figure 13). These ribbons are arranged vertically along the *b* axis and are also linked with each other *via* a second weak non-classical hydrogen bond (H1(iii)...Cl1 = 2.78 Å). The aromatic rings in **1** undergo face-to-face π -stacking with an average distance of 3.494 Å (Figure 12).^[56,57]

According to a review on copper(I) halides of Peng *et al.*¹⁰, only two other complexes ($\{Cu_3Br_3[Co\{S_2CN(CH_2)_4\}_3]\cdot MeCN\}_n$ ^[13] and $[Cu_3Cl_3(ttup)_2]_n$ ^[12]) show a similar structural motive as in **1**, a six-membered cyclic Cu₃X₃-unit with a quasi-boat conformation. In $[Cu_3Cl_3(ttup)_2]_n$, the boat like structure of the Cu₃Cl₃-unit is very distorted, resulting in a very short Cu...Cu distance of 2.783 Å. So complex **1** can only truly be compared to the $\{Cu_3Br_3[Co\{S_2CN(CH_2)_4\}_3]\cdot MeCN\}_n$ complex. The Cu–Cl distances and Cu...Cu distances of **1** follow the same trend as the previously published Cu₃Br₃-compound. Interestingly, in $\{Cu_3Br_3[Co\{S_2CN(CH_2)_4\}_3]\cdot MeCN\}_n$, only four atoms (2 Cu and 2 Br-atoms) of the Cu₃Br₃-unit are located in a plane. The interplanar angles between this plane and the Cu₂Br/Br₂Cu planes, containing the third bromide and copper atom, are 60.2° and 30.7° respectively. The distance of the third bromide and copper atom with respect to the Cu₂Br₂ plane are 1.866 Å and 1.240 Å. The coordination motifs of Cu(I) are the same as in compound **1** (tetrahedrally and trigonal planar). In contrast to **1**, the Cu₃Br₃- and Cu₃Cl₃-units of the previously published complexes are not interconnected.

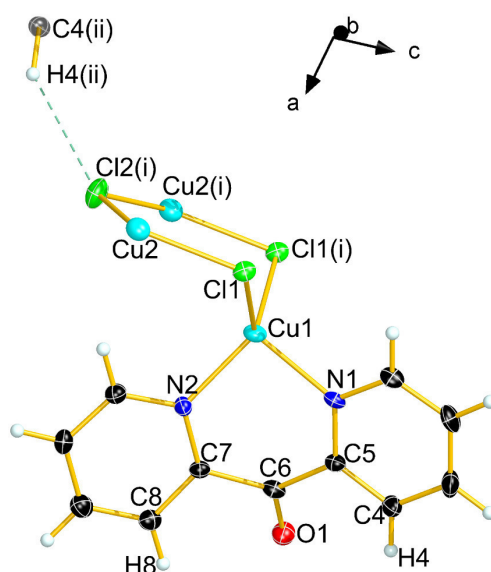


Figure 11. Solid-state molecular structure of **1**. Thermal ellipsoids are set at 50 % probability. Symmetry code: (i) = $x, 1+y, z$; (ii) $-0.5+x, 1.5-y, -0.5+z$.

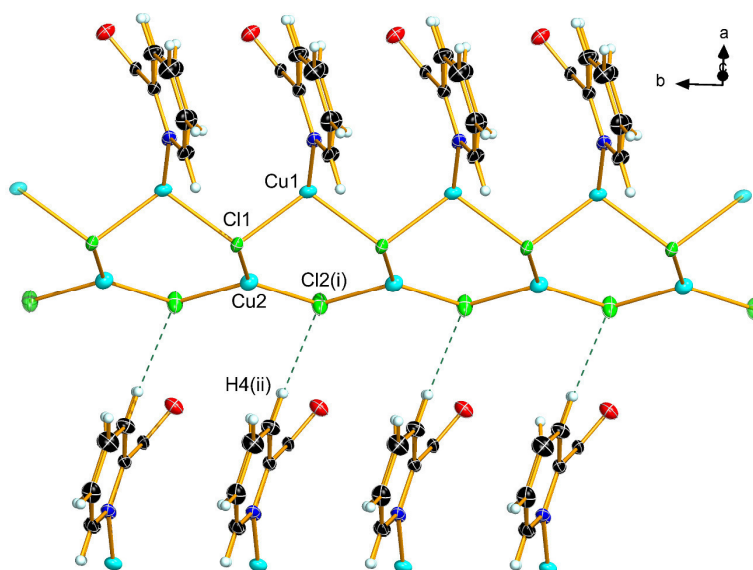


Figure 12. Visualization of the chain-like structure of the Cu_3Cl_3 -units in **1**. Thermal ellipsoids are set at 50 % probability. Symmetry code: (i) $x, 1+y, z$; (ii) $-0.5+x, 1.5-y, -0.5+z$.

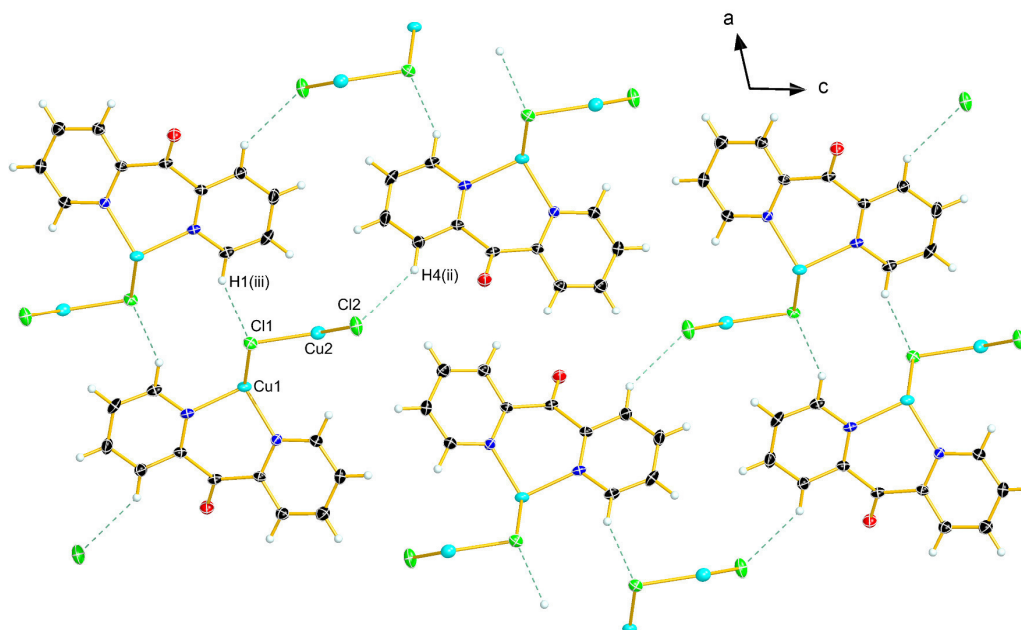


Figure 13. Visualization of the packing arrangement of **1** along the b axis. Thermal ellipsoids are set at 50 % probability. Symmetry code: (ii) $-0.5+x, 1.5-y, -0.5+z$; (iii) $1-x, -y, 2-z$.

$[\text{Cu}_2(\text{dpk})_2\text{Br}_2]$ **2** crystallizes as red blocks in the triclinic space group $P\bar{1}$ with two formula units in the unit cell (Figure 14). **2** is a binuclear copper(I) complex. The two copper(I) cations in **2** are both coordinating tetrahedrally to two nitrogen atoms from the dpk and two bridging bromide anions, resulting in a Cu_2Br_2 halide-bridged square dimer. These types of Cu_2X_2 ($\text{X} = \text{Cl}, \text{Br}, \text{I}$) halide bridged square dimers are very common and have been reported several times with other N -heterocyclic ligands.^[7,14,34,36,58–63] Contrary to complex **1**, the $\text{Cu}\cdots\text{Cu}$ distances in **2** are indeed short (2.569(3) Å and 2.626(3) Å, respectively) as expected for polynuclear copper(I) complexes of this type.^[36,55,58,63–67] The $\text{Br}\cdots\text{Br}$ (4.142(3) Å and 4.195(3) Å) separation is close to the usual Van der Waals contact distance.^[68] The $\text{Cu}-\text{Br}-\text{Cu}-\text{Br}$ -ring forms a parallelogram with internal angles of 63.8° and 116.2° on average. The $[\text{Cu}_2(\text{dpk})_2\text{Br}_2]$ complex forms antiparallel layers in the 3D arrangement (see Figure 15). The single units

of the complex are interconnected *via* face-to-face π -stacking of the pyridine rings, with the shortest distance being 3.020 Å.^[56,57] Moreover, weak hydrogen bonds between the carbonyl oxygen atom and the protons of the neighboring aromatic rings occur, with the shortest O...H distance being 2.64 Å. Additionally, there are non-classical, weak hydrogen bonds between the bromine ions and the protons of the aromatic rings with the shortest Br...H distance being 2.92 Å (see Figure 16).

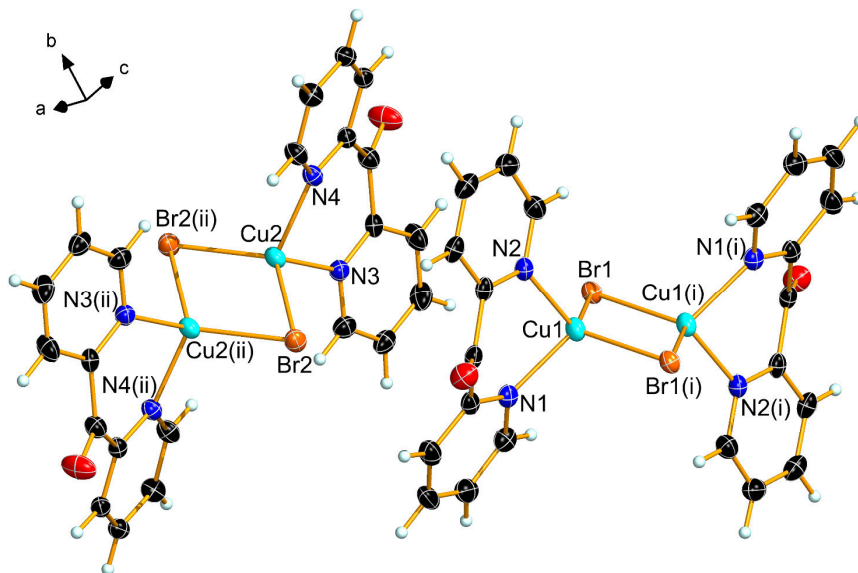


Figure 14. Solid-state molecular structure of **2**. Thermal ellipsoids are set at 50 % probability. Symmetry code: (i) = 1-x, -y, 1-z, (ii) = 2-x, 1-y, -z.

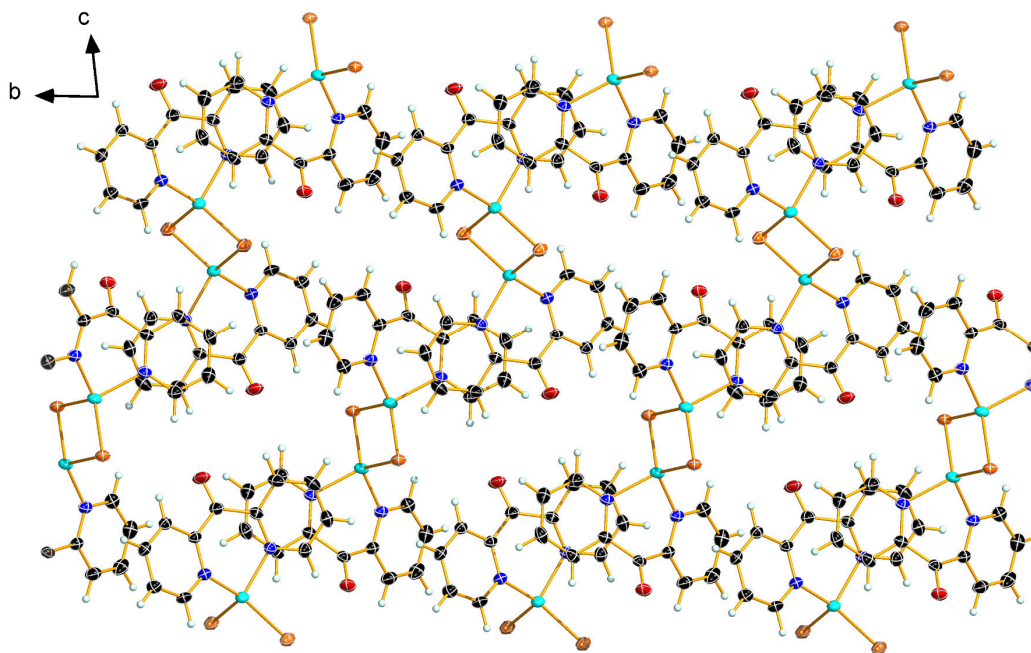


Figure 15. Visualization of the packing arrangement of **2** along the *a* axis. Thermal ellipsoids are set at 50 % probability.

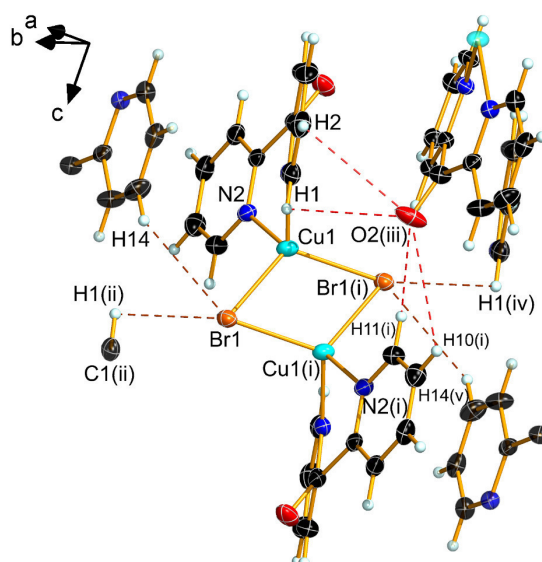


Figure 16. Visualization of the H-bonds of a section in the crystal structure of **2**. Thermal ellipsoids are set at 50 % probability. Symmetry code: (i) = 1-x, -y, 1-z, (ii) = 2-x, -y, 1-z, (iii) = x, -1+y, z, (iv) = -1+x, y, z, (v) = 1-x, -y, 1-z.

[Cu(dpk)(CN)]_n (**3**) crystallizes as red block-like crystals in the orthorhombic space group $P2_12_12_1$ with four formula units in the unit cell (Figure 17). The copper cation in **3** is distorted tetrahedrally coordinated by two nitrogen atoms of the dpk and by one nitrogen and one carbon atom from the cyanide ligand. Although a disorder in terms of exchanged positions of carbon and nitrogen might be expected. There is no indication of such a disorder present in the crystal. This is also reflected by the different distances between copper(I) and the carbon (Cu1–C12 1.896(1) Å) or nitrogen atom (Cu1–N3 1.974(1) Å) of the cyanide unit. The copper(I) cation and the cyanide in **3** are forming a one-dimensional chain bridged by the cyanide groups, similar to other copper(I) cyanide and copper(I) thiocyanate analogues with nitrogen containing ligands (e.g. quinaldine, 2-methylpyridine and pyridine) previously reported. Contact distances and angles in **3** are comparable to the ones reported for similar compounds.^[36,69,70] The alternating spatial positions of the dpk ligands along the copper(I) cyanide-chain are reminiscent of the *syndiotactic* form of polypropylene (see Figure 18).^[71]

In the three-dimensional arrangement, **3** forms zig-zag chains parallel to the *a* axis (see Figure 18 and 19). Furthermore, edge-to-face π - π interactions occur through the aromatic protons of the bound dpk ligand and the aromatic ring of their neighbor at a distance of 2.865 Å (H-to-ring center distance) and an angle of 63.9° (CH to ring plane), which is indicative of a weak interaction.^[56,57] Face-to-face π -interactions between opposing pyridine rings of a single chain are not present, as their distance is larger than 3.8 Å. Offset π -stacking (π - σ attraction at a distance of approximately 3.21 Å) between the pyridine rings of two different chains are stabilizing this arrangement.

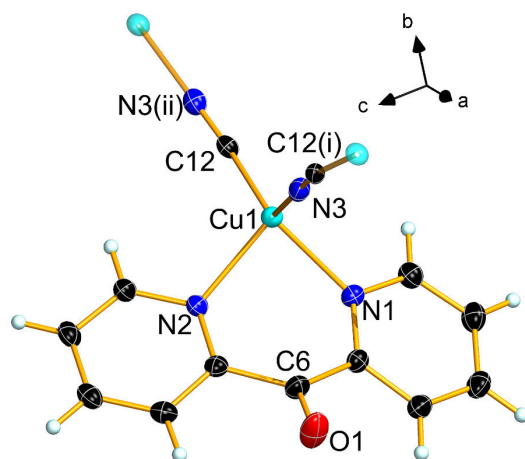


Figure 17. Solid-state molecular structure of **3**. Thermal ellipsoids are set at 50 % probability. Symmetry code: (i) = 0.5+x, 1.5-y, 1-z, (ii) = -0.5+x, 1.5-y, 1-z.

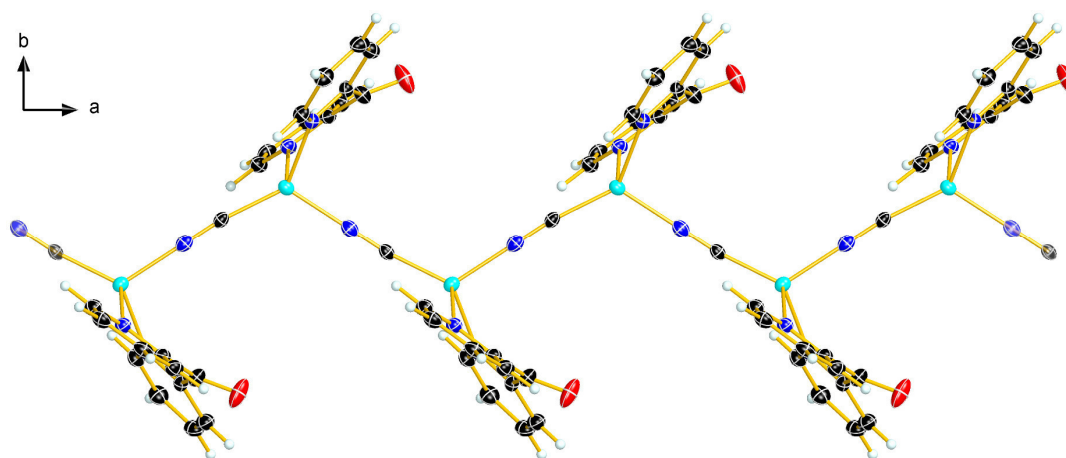


Figure 18. Packing of **3** along the *c* axis showing the *syndiotactic* form. Thermal ellipsoids are set at 50 % probability.

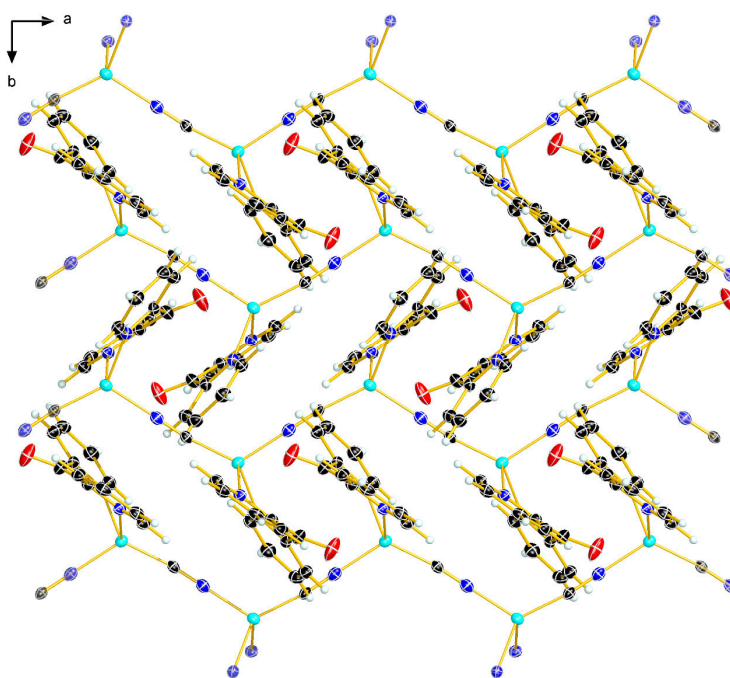


Figure 19. Visualization of the packing arrangement of **3** along the *c* axis. Thermal ellipsoids are set at 50 % probability.

Although a crystal structure of a complex with the composition $[\text{Cu}_2(\text{dpk})_2\text{I}_2]$ has already been published, we noticed crystals with two different shapes under the microscope (Figure 20). On the one hand, plate/square-like crystals were visible, the cell parameters of which correspond to the already reported structure of $[\text{Cu}_2(\text{dpk})_2\text{I}_2]$.^[36] On the other hand, we also noticed rod-shaped crystals, which displayed different cell parameters. These rods of **4** crystallized in the triclinic space group $P\bar{1}$ with one formula unit in the unit cell and have the same chemical composition as the previously published complex. However, the spatial distribution of the dpk ligand in **4** is different, resulting in a different crystal packing. Hence, **4** and the already reported compound are polymorphs.

The copper(I) cation in **4** is tetrahedrally coordinated by two nitrogen atoms and its charge balanced by the two bridging iodide anions. The contact distance between both copper(I) ions $\text{Cu1}\cdots\text{Cu1(i)}$ in **4** is 2.623(2) Å. This is significantly longer than in the other polymorph (2.546(2) Å) and in **2**, but comparable to other Cu^+/Cu^+ dimers like $[\text{Cu}_2\text{I}_2(\text{phen})_2]$, where the $\text{Cu}\cdots\text{Cu}$ distance is 2.663 Å.^[27,45,48,50,52,53,55–58,63] The $\text{I}\cdots\text{I}$ (4.487(3) Å) separation is close to the usual van der Waals contact distance and also smaller as in the other polymorph (4.556(2) Å).^[68]

The four membered Cu-I-Cu-I -ring is a parallelogram with internal angles of 60.6(1)° and 119.4(2)°. The angles at the halogen are much smaller in **4** than in **2**, probably due to the iodide being much larger than the bromide and the Cu-Hal bond lengths being larger in **4** than in **2**. Analogous dimers are found in the crystal of the other polymorph. However, the internal angles of the Cu-I-Cu-I -ring are with 58.4(5)° and 121.6(6)° significantly different when compared to **4**.

In the 3D structure, **4** forms layers wherein the complexes are associated with their neighbor through weak electrostatic non-classical hydrogen bonds between the carbonyl group and the aromatic protons of dpk at a distance of 2.690 Å.^[54] There are face-to-face π - π -interactions observable between neighboring pyridine rings of dpk with an interplanar distance of approximately 2.95 Å. The major difference between the two polymorphs is represented by the packing of the dimeric units in the crystal. In the case of **4**, all dimeric units are oriented in the same way. While in the case of the published polymorph, the orientation of the dimeric units is alternating (see Figure 21).

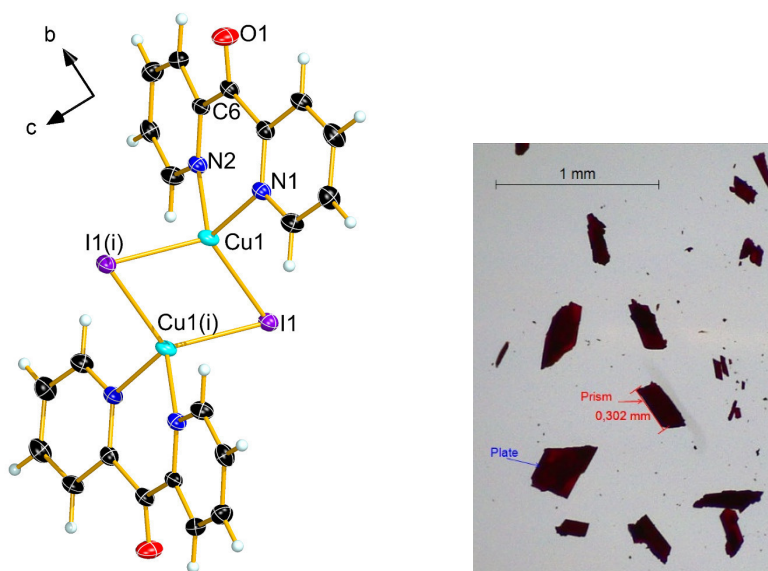


Figure 20. Solid-state molecular structure of **4** (left) and picture of the crystals of **4** under the microscope showing the different crystal shapes (right). Thermal ellipsoids are set at 50 % probability. Symmetry code: (i) = $-x, -y, 1-z$.

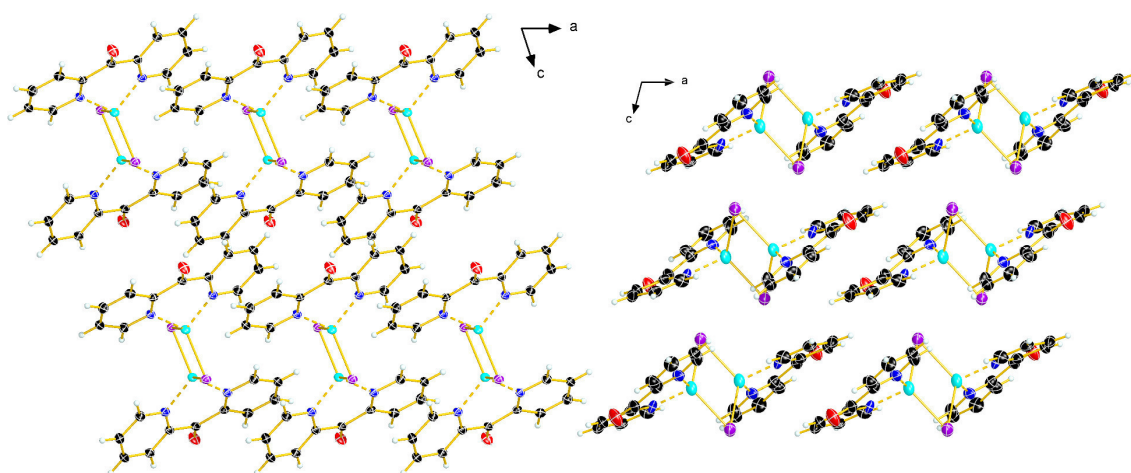


Figure 21. Packing of **4** (left) and the previously published structure (right) visualizing the differently layered structure when comparing both polymorphs. Thermal ellipsoids are set at 50 % probability.

Table 2. Selected bond lengths [Å] and angles [°] of complexes 1–4.

$[\text{Cu}_2(\text{dpk})\text{Cl}_2]_n$ 1	symmetry code: (i) = x, 1+y, z		
C6–O1	1.227(1)	Cu1...Cu2	3.694(2)
C5–C6	1.501(1)	Cu1...Cu2(i)	3.304(2)
C6–C7	1.516(1)	N1–Cu1–N2	95.7(3)
Cu1–N1	2.037(1)	N1–Cu1–Cl1	105.1(2)
Cu1–N2	2.006(1)	N1–Cu1–Cl1(i)	113.1(2)
Cu1–Cl1	2.386(1)	Cl1–Cu1–Cl1(i)	106.1(1)
Cu1–Cl1(i)	2.302(1)	Cu2–Cl2(i)–Cu2(i)	112.8(1)
Cu2–Cl1	2.227(2)	Cl1(i)–Cu2–Cl1	114.9(2)
Cu2–Cl2(i)	2.287(1)	Cu1–Cl1–Cu2	106.4(2)
$[\text{Cu}_2(\text{dpk})_2\text{Br}_2]$ 2	symmetry code: (i) = 1-x, -y, 1-z, (ii) = 2-x, 1-y, -z.		
C6–O1	1.214(1)	Cu1...Cu1(i)	2.626(3)
C5–C6	1.514(1)	Cu2...Cu2(ii)	2.569(3)
C6–C7	1.507(1)	N1–Cu1–N2	93.5(5)
Cu1–N1	2.044(2)	N3–Cu2–N4	93.7(5)
Cu1–N2	2.044(2)	N1–Cu1–Br1	110.1(3)
Cu2–N3	2.029(2)	N2–Cu1–Br1	111.7(4)
Cu2–N4	2.029(2)	N3–Cu1–Br2	105.0(3)
Cu1–Br1	2.448(2)	N4–Cu1–Br2	111.0(4)
Cu1–Br1(i)	2.456(2)	Br1–Cu1–Br1(i)	115.3(4)
Cu2–Br2	2.495(2)	Br2–Cu2–Br2(ii)	117.1(4)
Cu2–Br2(ii)	2.424(2)		
$[\text{Cu}(\text{dpk})(\text{CN})]_n$ 3	symmetry code: (i) = 0.5+x, 1.5-y, 1-z; (ii) = -0.5+x, 1.5-y, 1-z		
C6–O1	1.212(1)	Cu...Cu	5.000(1)
C5–C6	1.509(1)	N1–Cu1–N2	87.8(1)
C6–C7	1.514(1)	N1–Cu1–N3	101.4(1)
Cu1–N1	2.081(1)	N2–Cu1–N3	102.7(1)
Cu1–N2	2.110(1)	C12–Cu1–N2	108.9(1)
Cu1–N3	1.974(1)	N3–Cu1–C12	120.9(1)
Cu1–C12	1.896(1)	Cu1–C12–N3(i)	170.5(1)
N3–C12	1.146(1)	Cu1–N3–C12(ii)	179.9(1)

$[\text{Cu}_2(\text{dpk})_2\text{I}_2]$ 4	symmetry code: (i) = -x, -y, 1-z.		
C6–O1	1.218(1)	Cu1–I1(i)	2.605(1)
C5–C6	1.508(1)	Cu1...Cu1(i)	2.623(2)
C6–C7	1.513(1)	N1–Cu1–N2	93.0(3)
Cu1–N1	2.052(2)	N1–Cu1–I1	112.0(3)
Cu1–N2	2.050(2)	N2–Cu1–I1	109.8(2)
Cu1–I1	2.592(2)	I1–Cu1–I1(i)	119.4(2)

2.1.3.2. Solvent-free reactions

To our surprise, when mixing the copper(I) salt and dpk without solvent in a Schlenk flask, a color change is visible after a few minutes of stirring, indicating a reaction in the solid state has happened (Figure 22). IR spectra of free dpk and the resulting colorful solids were measured and compared to pure dpk^[73], confirming this observation.

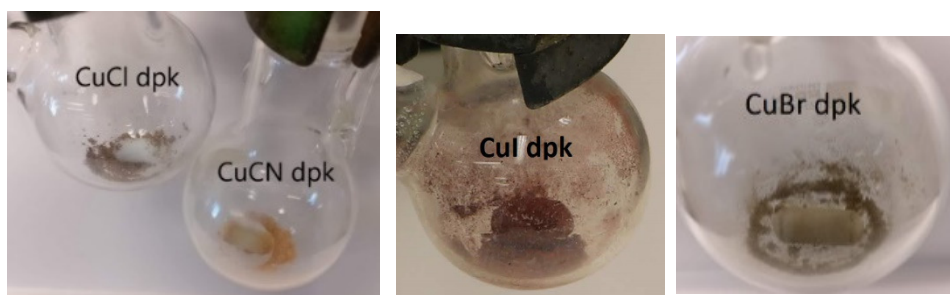


Figure 22. Visualization of the mixtures after combining solid Cu(I)X and dpk.

The calculated IR spectra in the gas phase are in good agreement with the experimental data (Table 3). The IR spectroscopy data of the free dpk are in accordance with the literature values.^[73] Since the dpk molecule in complexes **1–4** is not coordinating to the copper over the oxygen, a drastic change in the C=O stretch vibration is not expected, which is also reflected by the results. The ring stretch- and breathing vibrations of the complexes are significantly reduced in their intensity when compared to free dpk. This is another indicator for the successful solvent-free reaction.

Table 3. Selected IR spectroscopy bands (cm^{-1}) for free dpk and complexes **1–4**.

vibration	free dpk		1		2		3		4	
	expt.	calcd.	expt.	calcd.	expt.	calcd.	expt.	calcd.	expt.	calcd.
C=O stretch	1678 (s)	1749 (vs)	1660 (s)	1724 (vs)	1661 (vs)	1725 (vs)	1664 (m)	1735 (s)	1651 (m)	1720 (s)
py ring stretch	1581 (s)	1613 (w)	1579 (s)	1622 (w)	1579 (s)	1623 (w)	1583 (m)	1628 (m)	1577 (m)	1625 (w)
py ring breathing	993 (s)	1013 (w)	995 (w)	1030 (vw)	992 (s)	1028 (vw)	978 (vw)	1037 (w)	982 (s)	1024 (w)
		944 (s)		966 (vs)		939 (s)		953 (m)		952 (m)
CH out-of-plane stretch	659 (vs)	712 (m)	661 (vs)	712 (w)	661 (vs)	713 (w)	663 (vs)	703 (w)	661 (vs)	699 (m)

Powder diffractometry was done on the solid mixtures after a few hours of stirring to further gain insight into the success of the reactions. All diffractograms, except for **3**, show an incomplete reaction indicated by signals of leftover copper(I) salts and dpk (see Supporting Information for details).

2.1.3.3. UV Vis spectral data

The UV Vis spectra of all compounds after reaction in solution are shown in Figure 23 and are in accordance with the visually observed colors of the solids. They all show broad absorption covering almost the entire visual spectrum. Additionally, all compounds show absorption in the UV spectral part which results mostly from the dpk part of the compounds.

Contrary to some other previously published dpk complexes, the herein presented compounds do not show any luminescence when irradiated with UV light.

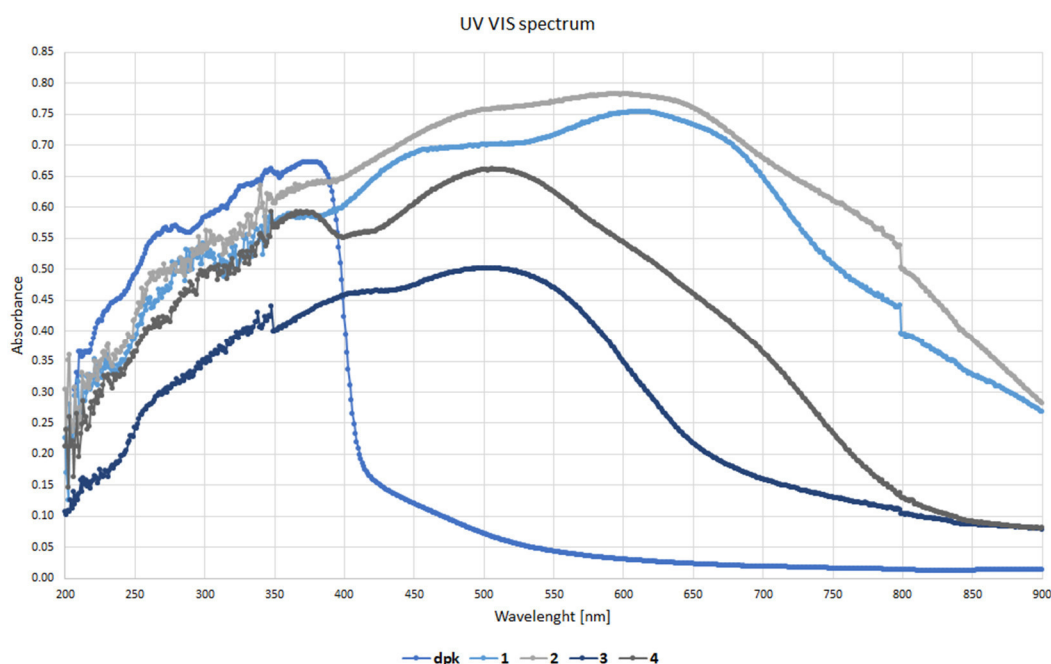


Figure 23. UV Vis spectra of the solid compounds **1–4** and dpk of the reactions in solution.

2.1.3.4. Hirshfeld surface analysis

A quantitative Hirshfeld surface analysis provides information of the different intermolecular interactions based on the respective d_{norm} maps and fingerprint plots of compounds **1–4** (see Figure 24 and Figure 25). The structural motives of compounds **1–4** can easily be divided into two classes, first: chain-structures, and second: dimers. This is also reflected by their fingerprint plots: considering the asymmetric unit, the CuCl-complex **1** shows medium-strong Cu–Cl contacts ($>2.2 \text{ \AA}$) and the CuCN-complex **3** shows very strong C–N contacts ($>1.2 \text{ \AA}$) resulting in polymeric structures. The dimeric structures of **2** and **4** show isolated clusters, with little interactions with other dimeric units.

In general, attractive intermolecular interactions ($\text{O}\cdots\text{H}$, $\text{N}\cdots\text{H}$ and $\text{Hal}\cdots\text{H}$ ($\text{Hal} = \text{Cl}, \text{Br}, \text{I}$)) are present in all structures, as well as weak π - π -interactions, visible as $\text{C}\cdots\text{H}$, $\text{C}\cdots\text{N}$ and $\text{C}\cdots\text{C}$ contacts in the fingerprint plots. Moreover, the number of non-classical hydrogen bonds ($\text{Cl}\cdots\text{H}$ 25.5 % in **1**, $\text{Br}\cdots\text{H}$ 18.0 % in **2** and $\text{I}\cdots\text{H}$ 20.6 % in **4**) is larger than the number of classical hydrogen bonds ($\text{O}\cdots\text{H}$: 5.7 % in **1**, 12.4 % in **2**, 8.4 % in **3** and 9.5 % in **4**) as well as $\text{N}\cdots\text{H}$ contacts (1.4 % in **1**, 4.0 % in **3** and 6.1 % in **4**). The nonclassical hydrogen bonds are weaker, as indicated by their longer contact lengths.

Nevertheless, the different percentage of classical hydrogen bonds in compounds **1–4** is reflected by the similar IR frequencies for the C=O stretching vibration mentioned above (Table 3). Additionally, one should keep in mind, that the Hirshfeld surface analysis does not account for the angle of these interactions.

Except for the C...C contacts in **1** (>3.6 Å), all π - π -interactions are below the values for face-to-face (<3.8 Å), offset (<3.4 Å) and T-shaped (<4.9 Å) π - π -interactions of pyridine/benzene^[57,74] and are therefore structurally relevant. The structure of the CuCl complex **1** has the lowest amount of attractive π - π -interactions (19.1 % >3.1 Å) of all complexes discussed herein. The π - π -interactions in the dimeric structures of **2** and **4** are in sum and strength (**2**: 27.8 % >3.1 Å and **4**: 29.4 % >3.0 Å) very similar. The π - π -interactions in the structure of the CuCN complex **3** are difficult to calculate, as the contributions of the CN ligand to the total amount cannot be easily subtracted.

The structure of the CuCl complex **1** displays, in general, the strongest (2.2 Å) and with 31.2 % also the most intermolecular interactions (O...H and Cl...H), visible as sharp spikes in the fingerprint plot. Thereby, it can be concluded, that **1** has the highest thermal stability, which is confirmed by its melting point (275 °C), being the highest of all four compounds.

It can be further concluded from the Hirshfeld analysis, that the thermal stability of compounds **1–4** decreases in the following order: **1** $>$ **3** $>$ **2** $>$ **4**. The experimental results discussed above are in agreement and show the same trend.

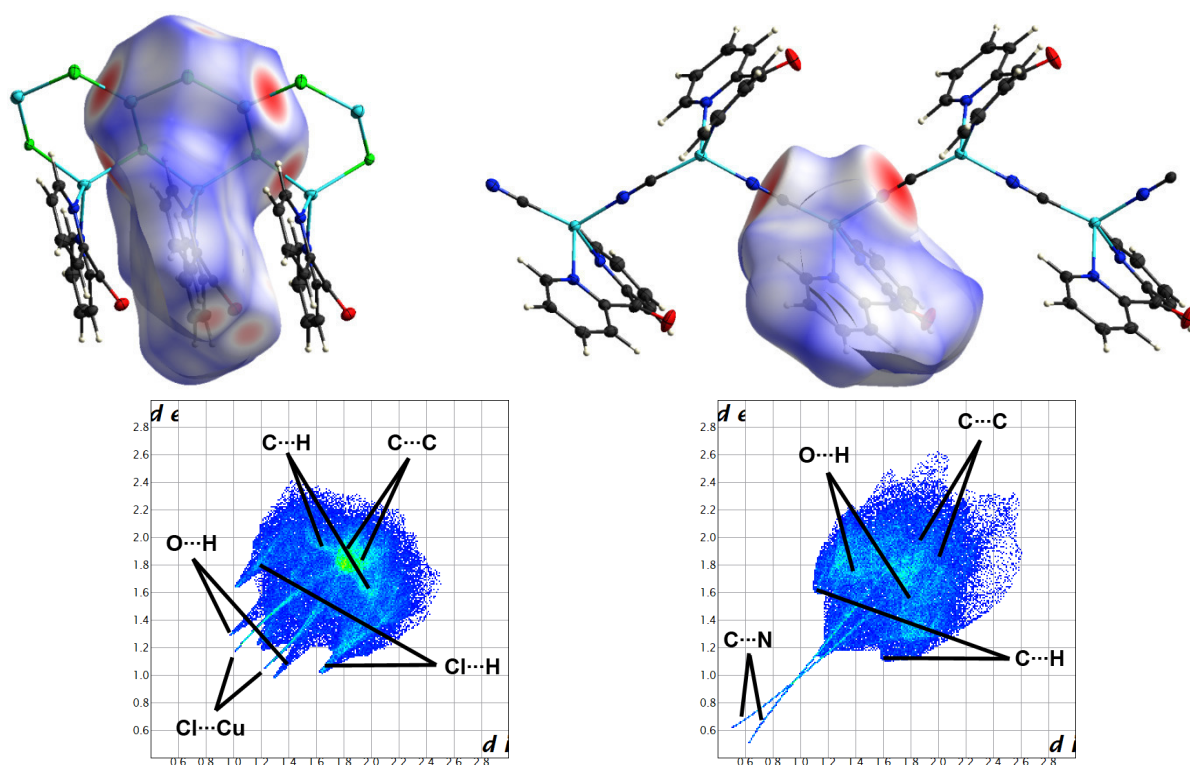


Figure 24. Generated d_{norm} maps (top) and fingerprint plots (bottom) of the chain structures of compound **1** (left) and **3** (right).

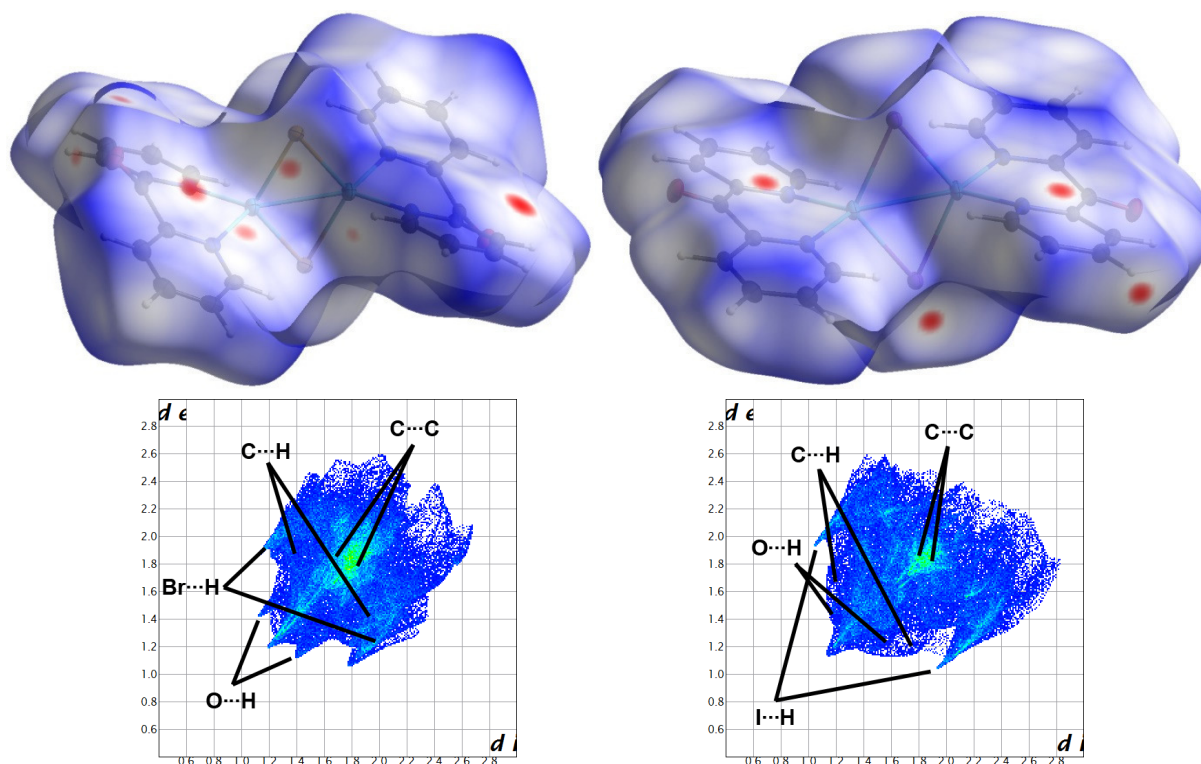


Figure 25. Generated d_{norm} maps (top) and fingerprint plots (bottom) of the dimeric compounds **2** (left) and **4** (right).

2.1.4. Conclusion

In conclusion, we have presented the synthesis of four copper(I) complexes of di(2-pyridyl)ketone in solution. As confirmed by IR spectroscopy, a reaction between the copper(I) salts and dpk also occurs in the solid state without the use of any solvent. The structures of the resulting products from the reaction in solution were determined *via* single crystal X-ray diffraction. They show interesting coordination features in their crystal structures, depending on the counterion. Remarkably, in the case of Cu(I)Cl, although using a 1:1 stoichiometry, a 1:2 complex was isolated. In case of Cu(I)Br, Cu(I)CN and Cu(I)I, a 1:1 complex is formed.

In the crystal, the dpk complexes of Cu(I)Br and Cu(I)I form dimeric structures, while in case of Cu(I)Cl and Cu(I)CN, polymeric structures are obtained. Remarkably, the Cu(I)I structure is a polymorph to an already known compound with the same composition. Both structures deviate in the geometry of the planar Cu_2L_2 -unit and especially in the arrangement of the dimers in the crystal. All structures show π -stacking between the pyridine rings. The Hirshfeld surface analysis clearly shows a difference between the coordination polymers and the dimeric structures and explains the observed values for the C=O stretch vibration and the melting points very well.

All in all, the results highlight the great potential of ligands with multiple coordination sides in regards to the structural diversity of the formed complexes. The utilization of such types of ligands for the generation of distinctive properties of coordination compounds is an important topic in our research group.

CRedit authorship contribution statement

Christin Kirst: Conceptualization, Methodology, Writing – original draft, Investigation. **Marco Reichel:** Formal analysis, Data curation, Visualization, Writing - original draft, Writing - review & editing. **Konstantin Karaghiosoff:** Supervision.

Declaration of Competing Interest

The authors declare that they have no known competing financial interests or personal relationships that could have appeared to influence the work reported in this paper.

Acknowledgements

We thank the Department of Chemistry, Ludwig-Maximilian University of Munich for financial support and especially Prof. T. M. Klapötke for his continuous support over the years. Furthermore, Dr. Peter Mayer is thanked for the single crystal x-ray measurements of small crystals and Lydia Smith for participation in this project.

2.1.5. References

- [1] N. Armaroli, G. Accorsi, F. Cardinali, A. Listorti, In *Photochemistry and Photophysics of Coordination Compounds I. Topics in Current Chemistry*; Springer, Berlin, Heidelberg, **2007**; pp 69–115.
- [2] M. J. Leitzl, D. M. Zink, A. Schinabeck, T. Baumann, D. Volz, H. Yersin, *Top. Curr. Chem.*, **2016**, *374* (3), 25.
- [3] F. Dumur, *Org. Electron.*, **2015**, *21*, 27–39.
- [4] C. Zeng, N. Wang, T. Peng, S. Wang, *Inorg. Chem.*, **2017**, *56* (3), 1616–1625.
- [5] M. J. Leitzl, F. R. Kühle, H. A. Mayer, L. Wesemann, H. Yersin, *J. Phys. Chem. A*, **2013**, *117* (46), 11823–11836.
- [6] A. Y. Baranov, A. S. Berezin, D. G. Samsonenko, A. S. Mazur, P. M. Tolstoy, V. F. Plyusnin, I. E. Kolesnikov, A. V. Artem'ev, *Dalton Trans.*, **2020**, *49* (10), 3155–3163.
- [7] A. V. Artem'ev, M. R. Ryzhikov, I. V. Taidakov, M. I. Rakhmanova, E. A. Varaksina, I. Y. Bagryanskaya, S. F. Malysheva, N. A. Belogorlova, *Dalton Trans.*, **2018**, *47* (8), 2701–2710.
- [8] A. V. Artem'ev, E. P. Doronina, M. I. Rakhmanova, A. O. Sutyryna, I. Y. Bagryanskaya, P. M. Tolstoy, A. L. Gushchin, A. S. Mazur, N. K. Gusarova, B. A. Trofimov, *New J. Chem.*, **2016**, *40* (12), 10028–10040.
- [9] C. M. Brown, V. Carta, M. O. Wolf, *Chem. Mater.*, **2018**, *30* (16), 5786–5795.
- [10] R. Peng, M. Li, D. Li, *Coord. Chem. Rev.*, **2010**, *254* (1–2), 1–18.
- [11] Y. C. Liu, C. I. Li, W. Y. Yeh, G. H. Lee, S. M. Peng, *Inorg. Chim. Acta*, **2006**, *359* (8), 2361–2368.
- [12] L. Chen, L. K. Thompson, S. S. Tandon, J. N. Bridson, *Inorg. Chem.*, **1993**, *32* (19), 4063–4068.
- [13] P. C. Healy, B. W. Skelton, A. H. White, *Dalton Trans.*, **1989**, No. 5, 971–976.
- [14] D. J. Chesnut, A. Kusnetzow, R. R. Birge, J. Zubieta, *Inorg. Chem.*, **1999**, *38* (17), 2663–2671.
- [15] D. Braga, F. Grepioni, L. Maini, P. P. Mazzeo, B. Ventura, *New J. Chem.*, **2011**, *35* (2), 339–344.
- [16] A. Kobayashi, T. Hasegawa, M. Yoshida, M. Kato, *Inorg. Chem.*, **2016**, *55* (5), 1978–1985.
- [17] A. V. Artem'ev, E. P. Doronina, M. I. Rakhmanova, O. A. Tarasova, I. Y. Bagryanskaya, N. A. Nedolya, *Inorg. Chem. Front.*, **2019**, *6* (3), 671–679.
- [18] N. R. Rightmire, T. P. Hanusa, *Dalton Trans.*, **2016**, *45* (6), 2352–2362.
- [19] M. Juribašić, K. Užarević, D. Gracin, M. Ćurić, *Chem. Commun.*, **2014**, *50* (71), 10287–10290.
- [20] H. Zhu, P. Chen, G. Liu, *Org. Lett.*, **2015**, *17* (6), 1485–1488.
- [21] L. Bravo-García, G. Barandika, B. Bazán, M. K. Urriaga, M. I. Arriortua, *Polyhedron*, **2015**, *92*, 117–123.

-
- [22] T. C. Stamatatos, C. G. Efthymiou, C. C. Stoumpos, S. P. Perlepes, *Eur. J. Inorg. Chem.*, **2009**, 3361–3391.
- [23] H. Sartzi, C. C. Stoumpos, M. Giouli, I. I. Verginadis, S. C. Karkabounas, L. Cunha-Silva, A. Escuer, S. P. Perlepes, *Dalton Trans.*, **2012**, 41 (39), 11984–11988.
- [24] G. S. Papaefstathiou, S. P. Perlepes, *Comments Inorg. Chem.*, **2002**, 23 (4), 249–274.
- [25] F. Zhang, C. W. Kirby, D. W. Hairsine, M. C. Jennings, R. J. Puddephatt, *J. Am. Chem. Soc.*, **2005**, 127 (41), 14196–14197.
- [26] C. M. Kepert, G. B. Deacon, N. Sahely, L. Spiccia, G. D. Fallon, B. W. Skelton, A. H. White, *Inorg. Chem.*, **2004**, 43 (9), 2818–2827.
- [27] W. L. Huang, J. R. Lee, S. Y. Shi, C. Y. Tsai, *Transit. Met. Chem.*, **2003**, 28 (4), 381–387.
- [28] M. Bakir, J. A. M. McKenzie, *J. Chem. Soc. Dalt. Trans.*, **1997**, 3 (19), 3571.
- [29] M. Bakir, J. A. M. McKenzie, *J. Electroanal. Chem.*, **1997**, 425 (1–2), 61–66.
- [30] I. J. Bakker, M. C. Feller, R. Robson, *J. Inorg. Nucl. Chem.*, **1971**, 33 (3), 747–754.
- [31] M. C. Feller, R. Robson, *Aust. J. Chem.*, **1968**, 21 (12), 2919–2927.
- [32] M. C. Feller, R. Robson, *Aust. J. Chem.*, **1970**, 23 (10), 1997–2003.
- [33] K. J. Bonnington, F. Zhang, M. M. A. R. Moustafa, B. F. T. Cooper, M. C. Jennings, R. J. Puddephatt, *Organometallics*, **2012**, 31 (1), 306–317.
- [34] A. Basu, A. R. Saple, N. Y. Sapre, *J. Chem. Soc., Dalt. Trans.*, **1987**, No. 7, 1797–1799.
- [35] T. S. Morais, T. J. L. Silva, F. Marques, M. P. Robalo, F. Avecilla, P. J. A. Madeira, P. J. G. Mendes, I. Santos, M. H. Garcia, *J. Inorg. Biochem.*, **2012**, 114, 65–74.
- [36] K. B. Szpakolski, K. Latham, C. J. Rix, J. M. White, *Eur. J. Inorg. Chem.*, **2010**, 2010 (36), 5660–5667.
- [37] M. Munakata, S. Kitagawa, S. Kosome, A. Asahara, *Inorg. Chem.*, **1986**, 25 (15), 2622–2627.
- [38] R. L. Melen, J. M. Rawson, D. J. Eisler, *Polyhedron*, **2012**, 47 (1), 16–23.
- [39] R. A. Mariezcurrena, A. W. Mombrú, L. Suescun, E. Kremer, R. González, *Acta Crystallogr. C*, **1999**, 55 (12), 1989–1991.
- [40] T. C. Stamatatos, V. Tangoulis, C. P. Raptopoulou, A. Terzis, G. S. Papaefstathiou, S. P. Perlepes, *Inorg. Chem.*, **2008**, 47 (18), 7969–7971.
- [41] M. C. Burla, R. Caliendo, B. Carrozzini, G. L. Casciarano, C. Cuocci, C. Giacovazzo, M. Mallamo, A. Mazzone, G. Polidori, *J. Appl. Crystallogr.*, **2015**, 48 (1), 306–309.
- [42] G. M. Sheldrick, *Acta Crystallogr. C*, **2015**, 71 (1), 3–8.
- [43] C. B. Hübschle, G. M. Sheldrick, B. Dittrich, *J. Appl. Crystallogr.*, **2011**, 44 (6), 1281–1284.
- [44] A. L. Spek, *Acta Crystallogr. E*, **2020**, 76, 1–11.
- [45] L. J. Farrugia, *J. Appl. Crystallogr.*, **2012**, 45 (4), 849–854.
- [46] H. Putz, K. Brandenburg, Crystal Impact GbR, Kreuzherrenstr. 102, 53227 Bonn, Germany 2014.
- [47] M. J. Frisch, G. W. Trucks, H. B. Schlegel, G. E. Scuseria, M. A. Robb, J. R. Cheeseman, G. Scalmani, V. Barone, G. A. Petersson, H. Nakatsuji, X. Li, M. Caricato, A. V. Marenich, J. Bloino, B. G. Janesko, R. Gomperts, B. Mennucci, H. P. Hratchian, J. V. Ortiz, A. F. Izmaylov, J. L. Sonnenberg, Williams, F. Ding, F. Lipparini, F. Egidi, J. Goings, B. Peng, A. Petrone, T. Henderson, D. Ranasinghe, V. G. Zakrzewski, J. Gao, N. Rega, G. Zheng, W. Liang, M. Hada, M. Ehara, K. Toyota, R. Fukuda, J. Hasegawa, M. Ishida, T. Nakajima, Y. Honda, O. Kitao, H. Nakai, T. Vreven, K. Throssell, J. A. Montgomery Jr., J. E. Peralta, F. Ogliaro, M. J. Bearpark, J. J. Heyd, E. N. Brothers, K. N. Kudin, V. N. Staroverov, T. A. Keith, R. Kobayashi, J. Normand, K. Raghavachari, A. P. Rendell, J. C. Burant, S. S. Iyengar, J. Tomasi, M. Cossi, J. M. Millam, M. Klene, C. Adamo, R. Cammi, J. W. Ochterski, R. L. Martin, K. Morokuma, O. Farkas, J. B. Foresman, D. J. Fox, *Gaussian 16, Revision C01*, Gaussian Inc., Wallingford CT, **2016**.
- [48] C. Lee, W. Yang, R. G. Parr, *Phys. Rev. B*, **1988**, 37 (2), 785–789.

- [49] P. J. Stephens, F. J. Devlin, C. F. Chabalowski, M. J. Frisch, *J. Phys. Chem.*, **1994**, *98* (45), 11623–11627.
- [50] F. Weigend, R. Ahlrichs, *Phys. Chem. Chem. Phys.*, **2005**, *7* (18), 3297.
- [51] F. Weigend, *Phys. Chem. Chem. Phys.*, **2006**, *8* (9), 1057.
- [52] H. Bock, R. Dienelt, H. Schödel, T. T. H. Van, *Struct. Chem.*, **1998**, *9* (4), 279–288.
- [53] M. J. Turner, J. J. McKinnon, S. K. Wolff, D. J. Grimwood, P. R. Spackman, D. Jayatilaka, M. A. Spackman, *CrystalExplorer17*, University of Western Australia, Australia, **2017**.
- [54] T. Steiner, *Angew. Chem.*, **2002**, *114*, 50–80; *Angew. Chem. Int. Ed.*, **2002**, *41*, 48–76.
- [55] F. A. Cotton, G. Wilkinson, C. A. Murillo, M. Bochmann, *Advanced inorganic chemistry.*, 6th ed., Chichester, **1999**.
- [56] W. B. Jennings, B. M. Farrell, J. F. Malone, *Acc. Chem. Res.*, **2001**, *34* (11), 885–894.
- [57] C. Janiak, *Dalton Trans.*, **2000**, No. 21, 3885–3896.
- [58] I. Jess, C. Näther, *Inorg. Chem.*, **2006**, *45* (18), 7446–7454.
- [59] P. M. Graham, R. D. Pike, M. Sabat, R. D. Bailey, W. T. Pennington, *Inorg. Chem.*, **2000**, *39* (22), 5121–5132.
- [60] N. P. Rath, E. M. Holt, K. Tanimura, *Dalton Trans.*, **1986**, No. 11, 2303.
- [61] A. Johansson, M. Vestergren, M. Håkansson, B. Gustafsson, S. Jagner, *New J. Chem.*, **2004**, *28* (8), 1000–1003.
- [62] X. Yu, J.-H.; Lü, Z.-L.; Xu, J.-Q.; Bie, H.-Y.; Lu, J.; Zhang, *New J. Chem.*, **2004**, *28*, 940–945.
- [63] B. Skelton, A. Waters, A. White, *Aust. J. Chem.*, **1991**, *44* (9), 1207.
- [64] M. Jansen, *Angew. Chem.*, **1987**, *99*, 1136–1149; *Angew. Chem. Int. Ed.*, **1987**, *26*, 1098–1110.
- [65] S. Dinda, A. G. Samuelson, *Chem. - A Eur. J.*, **2012**, *18* (10), 3032–3042.
- [66] P. Pyykkö, *Chem. Rev.*, **1997**, *97* (3), 597–636.
- [67] N. N. Greenwood, A. Earnshaw, *Chemistry of the elements*, Butterworth-Heinemann, **1997**.
- [68] S. S. Batsanov, *Inorg. Mater.*, **2001**, *37* (9), 871–885.
- [69] T. A. Tronic, K. E. DeKrafft, J. L. Mi, A. N. Ley, R. D. Pike, *Inorg. Chem.*, **2007**, *46* (21), 8897–8912.
- [70] G. A. Bowmaker, Effendy, P. C. Junk, B. W. Skelton, A. H. White, *Z. Naturforsch. B*, **2004**, *59* (11–12), 1277–1292.
- [71] J. McMurry, *Organic chemistry*, 2. ed., Brooks/Cole, Pacific Grove, Cal., **1988**.
- [72] N. P. Rath, J. L. Maxwell, E. M. Holt, *Dalton Trans.*, **1986**, No. 11, 2449–2453.
- [73] K. N. Crowder, S. J. Garcia, R. L. Burr, J. M. North, M. H. Wilson, B. L. Conley, P. E. Fanwick, P. S. White, K. D. Siennerth, R. M. Granger, *Inorg. Chem.*, **2004**, *43* (1), 72–78.
- [75] M. O. Sinnokrot, E. F. Valeev, C. D. Sherrill, *J. Am. Chem. Soc.*, **2002**, *124* (36), 10887–10893.

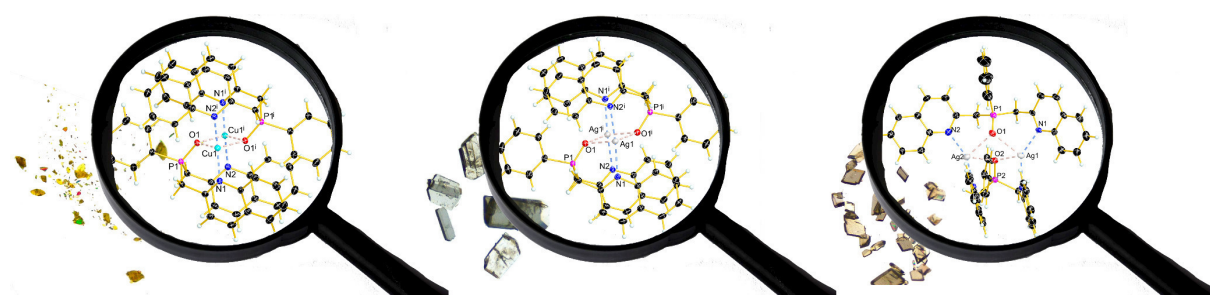
2.2. Copper(I) and silver(I) complexes of bridging bis(quinaldinyl)phenylphosphine oxide ligand

Christin Kirst and Konstantin Karaghiosoff

Published in *Phosphorus, Sulfur Relat. Elem.* 2020, **195**, 918–923.
as a conference proceeding

DOI: [10.1080/10426507.2020.1804162](https://doi.org/10.1080/10426507.2020.1804162)

Christin Kirst synthesized all the discussed compounds and performed the single crystal X-ray measurements. She analyzed and evaluated the corresponding data including the NMR spectroscopy results, managed the project and wrote the original draft of the manuscript and implemented the necessary corrections in the final version of the paper.



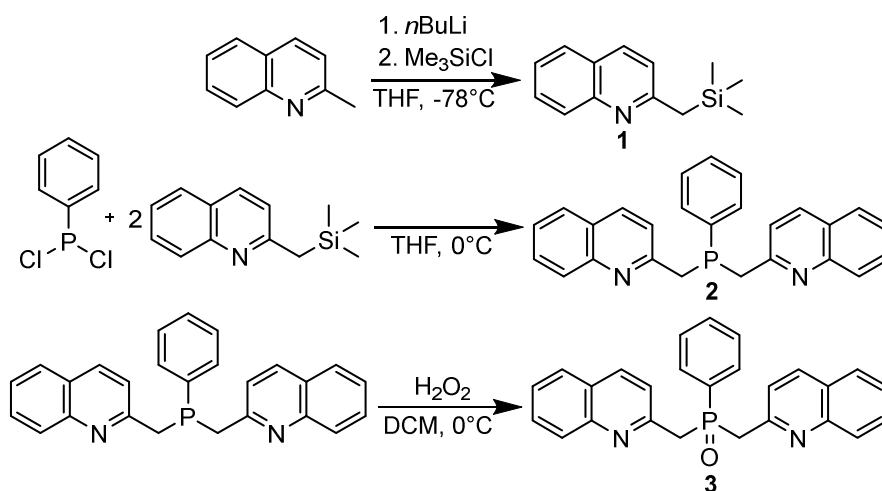
Abstract A novel tertiary phosphine oxide containing two quinaldinyl substituents has been synthesized according to adapted literature procedures. Its coordination properties toward Cu(I) and Ag(I) were investigated and the resulting complexes were analyzed by single crystal X-ray diffraction. Multinuclear complexes are formed, wherein the ligand is bridging across two metal centers. Though for the silver complex, no argentophilic interactions are present. The copper complex was characterized further by multinuclear NMR spectroscopy at variable temperatures.

2.2.1. Introduction

The development of novel, flexible phosphine-based ligands with adjustable coordination properties depending on the offered metal ion is a challenging task in phosphorus chemistry. These types of chelating ligands offer the unique opportunity of generating complexes, wherein one coordination site can be provided on demand for the selective coordination of the ligands within metal assisted chemical reactions, making them crucial for transition metal catalyzed processes in industry and laboratory.^[1–5] Especially tertiary phosphines substituted with at least two picolyl derivatives (P,N-ligands) offer a great variety of metal complexes, which are beneficial for different catalytic reactions (e.g., oligomerizations, dehydrogenations, reductive aminations).^[2,6–8] Different picolyl phosphines (mostly with only one picolyl substituent) or derivatives thereof are already known in the literature, yet their corresponding phosphine oxides are mostly disregarded.^[9]

2.2.2. Results and discussion

The novel bis(quinaldinyl)phenylphosphine oxide ligand was synthesized according to the literature as shown in Scheme 5.^[10,11] After purification via recrystallisation from DCM or acetonitrile **3** is obtained in high yields as a light-beige to white crystalline solid. Compound **3** displays in the ³¹P NMR spectrum (CD₂Cl₂) a signal at 33.9 ppm. The molecular structure of phosphine oxide **3** in the crystal is shown in Figure 26.



Scheme 5. Synthesis of the novel phosphine oxide ligand **3** starting from 2-methylquinoline.

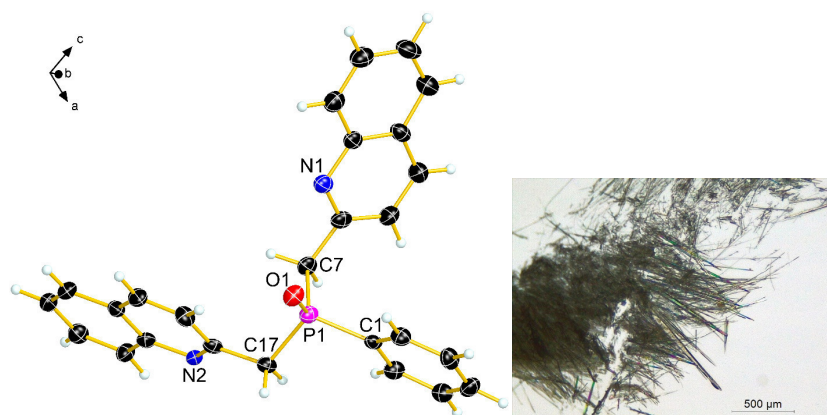


Figure 26. Molecular structure of **3** in the crystal, view of the asymmetric unit (left). Pictures of the needle-like crystals of **3** under the microscope (right). Thermal ellipsoids are drawn at 50 % probability level for all structures. Selected bond lengths [Å] and angles [°]: P1–O1: 1.482(2), O1–P1–C1: 111.6(2), O1–P1–C7: 114.5(2), O1–P1–C17: 113.6(2).

The diastereotopy of the CH₂-protons in **3** can be shown by examining the ¹H NMR spectra in different deuterated solvents. The expected coupling pattern for the AB part of an ABX spin system becomes increasingly visible by raising the polarity of the solvent (Figure 27). These hydrogen atoms are also the most acidic protons of this molecule and form readily non-classical hydrogen bonds (Figure 28). The Cu(I) and Ag(I) complexes of **3** were synthesized as shown in Scheme 6.

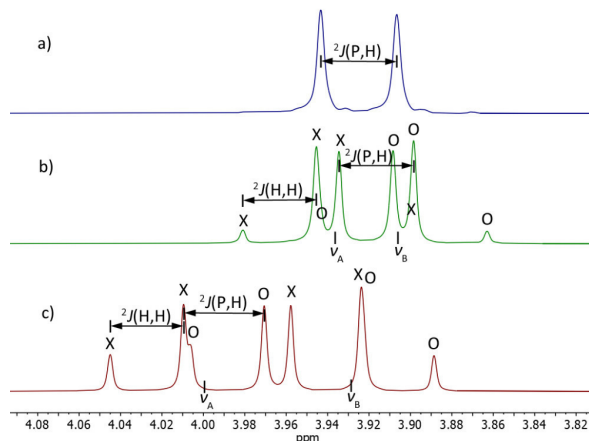


Figure 27. ¹H NMR spectra of **3** in a) CDCl₃ (blue), b) CD₂Cl₂ (green) and c) CD₃CN (red) showing the signals of the CH₂-group.

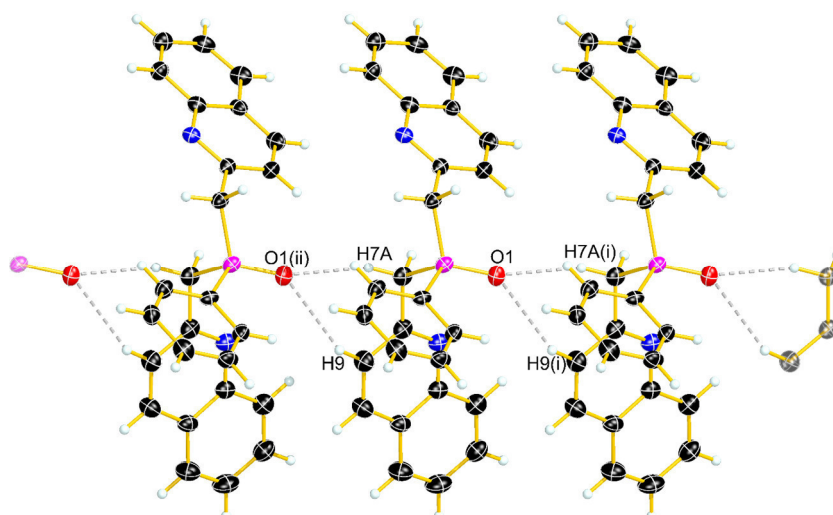
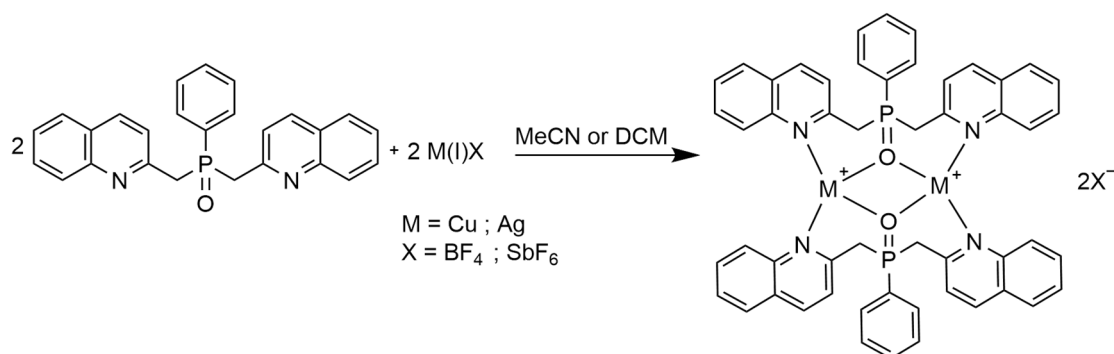


Figure 28. Non-classical hydrogen bonding in the crystal structure of phosphine oxide **3**: H7Aⁱ...O1 2.437(2) Å, H9ⁱ...O1 2.590(2) Å. Symmetry code $i = x, 1+y, z$.



Scheme 6. Synthesis of copper(I) tetrafluoroborate complex **4**, silver(I) tetrafluoroborate complex **5** and silver(I) hexafluorophosphate complex **6** of the phosphine oxide **3** showing the coordination mode of the ligand to the respective metal ions.

The copper(I) tetrafluoroborate complex **4** is obtained as a bright yellow powder and displays in the ^{31}P NMR spectrum a signal at 37.9 ppm (CD_3CN). The silver(I) tetrafluoroborate complex **5** is isolated as a light beige powder and displays in the ^{31}P NMR spectrum a signal at 42.3 ppm (CD_2Cl_2). The silver(I) hexafluoroantimonate complex **6** is obtained as a light beige powder ($\delta^{31}\text{P} = 42.3$ ppm in CD_2Cl_2). All complexes **4-6** could be recrystallized by slow diffusion of diethyl ether into a solution of the complex in acetonitrile or dichloromethane (Figures 29-32). In the case of **6** two different modifications **6a** and **6b** were obtained on recrystallization from dichloromethane and acetonitrile, respectively.

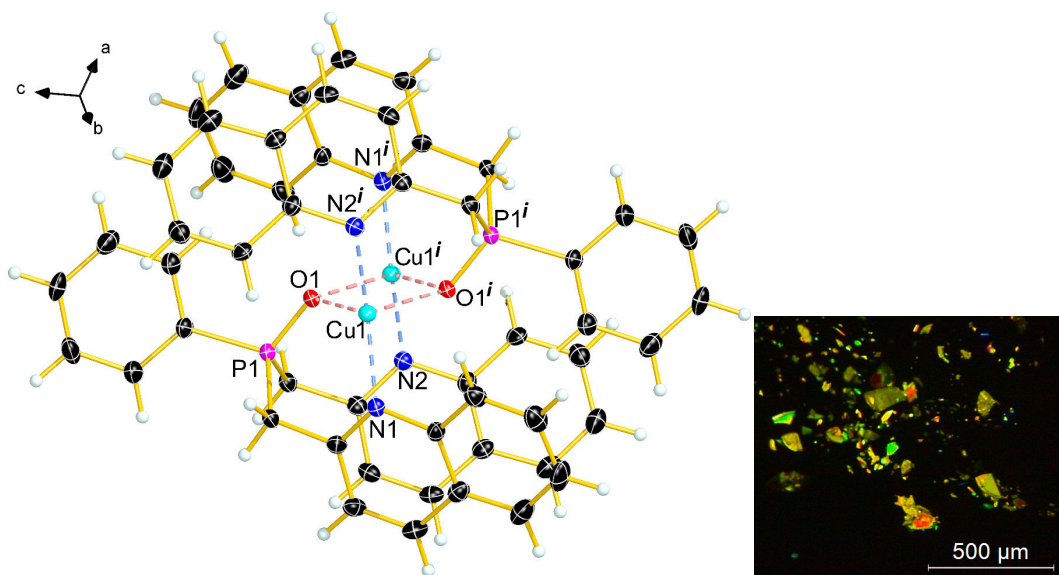


Figure 29. Molecular structure of complex **4** in the crystal; view of the asymmetric unit (left). BF_4 anions were omitted for clarity. View of the crystals of **4** under the microscope through polarization filter (right). Selected bond lengths [\AA] and angles [$^\circ$]: Cu1-N1 : 1.941(2), Cu1-O1 : 2.305(2), $\text{Cu1}^i\text{-N2}$: 1.946(2), $\text{Cu1}\cdots\text{Cu1}^i$: 3.607(4), $\text{O1}\cdots\text{O1}^i$: 2.853(2), Cu1-O1-Cu1^i : 103.3(6). Symmetry code: $i = 2-x, -y, 1-z$.

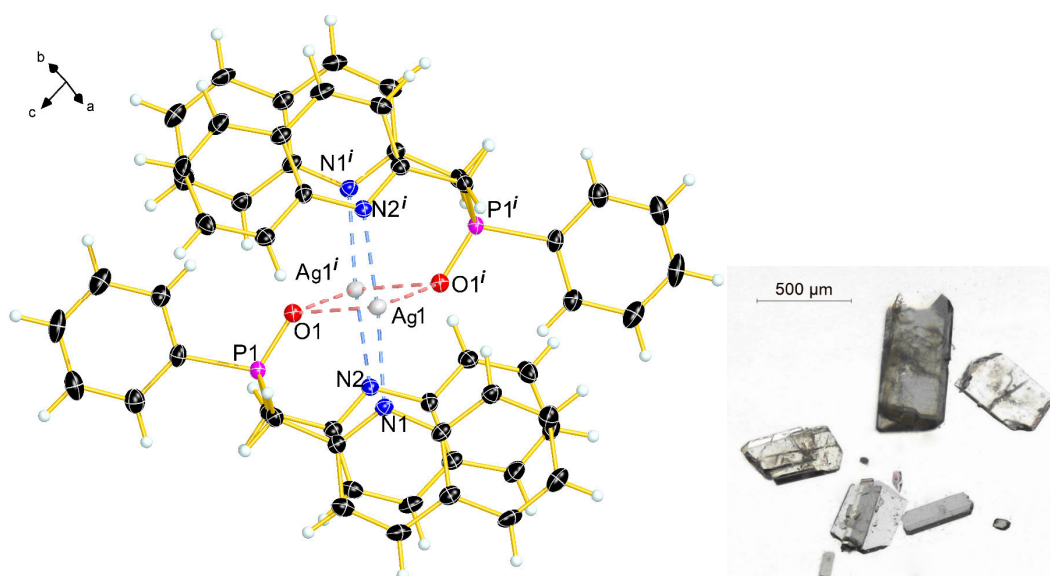


Figure 30. Molecular structure of complex **5** in the crystal; view of the asymmetric unit (left). Solvent molecules and BF_4 anions were omitted for clarity. Pictures of crystals of **5** under the microscope (right). Selected bond lengths [\AA] and angles [$^\circ$]: Ag1-O1 : 2.491(2), Ag1-N1 : 2.230(2), Ag1-N2^i : 2.228(2), $\text{Ag1}\cdots\text{Ag1}^i$: 3.673(4), $\text{O1}\cdots\text{O1}^i$: 3.349(2), Ag1-O1-Ag1^i : 95.3(3). Symmetry code: $i = -x, 1-y, -z$.

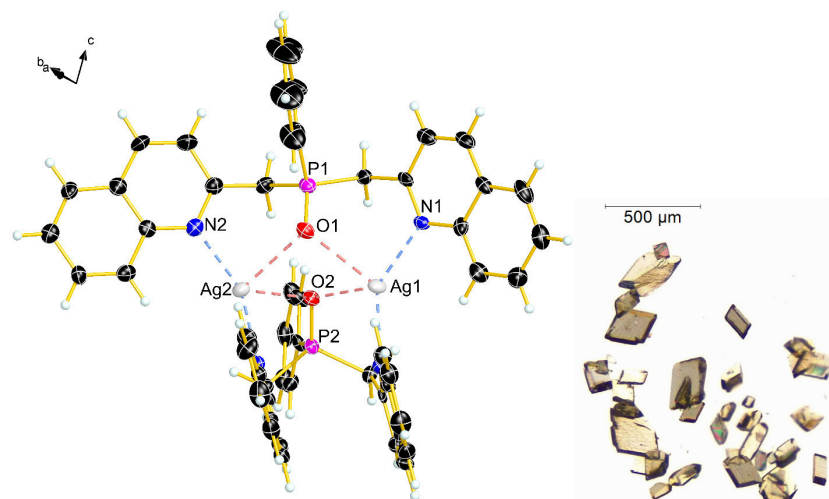


Figure 31. Molecular structure of complex **6a** in the crystal; view of the asymmetric unit (left). Solvent molecules and SbF_6 anions were omitted for clarity. Pictures of the crystals of **6a** under the microscope (right). Selected bond lengths [Å] and angles [°]: O1–Ag1: 2.685(5), O1–Ag2: 2.605(4), Ag1–N1: 2.228(4), Ag1⋯Ag2: 3.792(7), O1⋯O2: 3.199(5), O1–Ag1–N1: 83.1(3), O1–Ag2–N2: 88.5(3), O1–Ag1–O2: 76.0(3), Ag1–O1–Ag2: 91.6(3), Ag1–O2–Ag2: 96.1(3), O1–Ag1–O2–Ag2: –33.5(3).

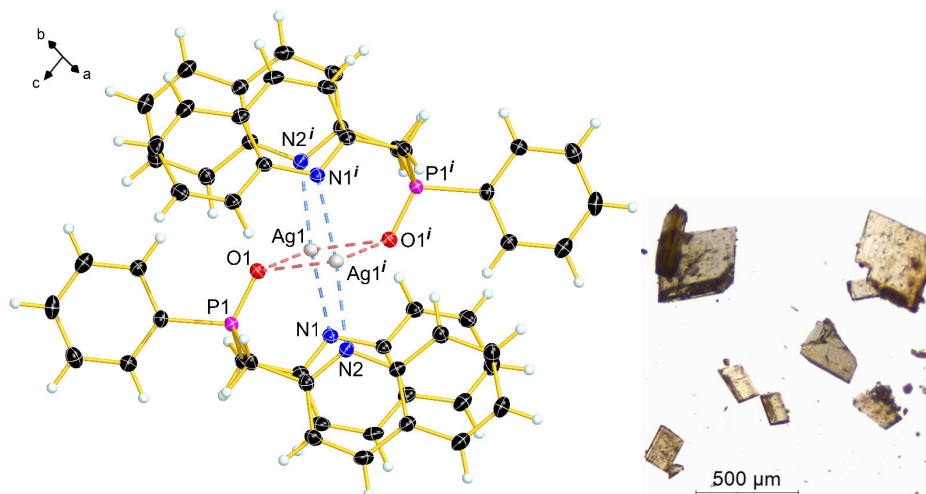


Figure 32. Molecular structure of complex **6b** in the crystal; view of the asymmetric unit (left). Solvent molecules and SbF_6 anions were omitted for clarity. Pictures of the crystals of **6b** under the microscope (right). Selected bond lengths [Å] and angles [°]: O1–Ag1: 2.510(2), Ag1–N1: 2.240(2), Ag1⋯Ag1ⁱ: 3.630(4), O1⋯O1ⁱ: 3.464(2), Ag1–O1–Ag1ⁱ: 92.7(5). Symmetry code: $i = -x, 1-y, -z$.

All complexes display units of two metal atoms (Cu(I), Ag(I)) bridged by two phosphine oxide ligands. The copper(I) ion in **4** as well as the silver(I) ions in **5** and **6b** show a distorted disphenoidal coordination geometry (see-saw geometry). In the case of **6a** the Ag(I) ion is distorted tetrahedrally coordinated. The metal ions are coordinating to both oxygen (equatorial) and nitrogen (axial) atoms of the ligand. The N–M–N angles of 164.0(9)° in **4**, 172.1(7)° in **5** and 170.8(7)° in **6b** are close to the ideal value of 180°. The O–M–O angles are also close to the ideal value of 90° (76.7(6)° in **4**, 84.7(5)° in **5**, 87.1(5)° in **6b**), and the same is true for the O–M–N angles (94.8(8)° in **4**, 91.8(6)° in **5**, 89.0(6)° in **6b**). This see-saw coordination is very rare for copper(I) complexes, less so for silver(I).^[12] In **4**, **5** and **6b** one side of the metal ion is free for further coordination (see Figure 33 and 34). This might be of special interest for possible application in catalysis.

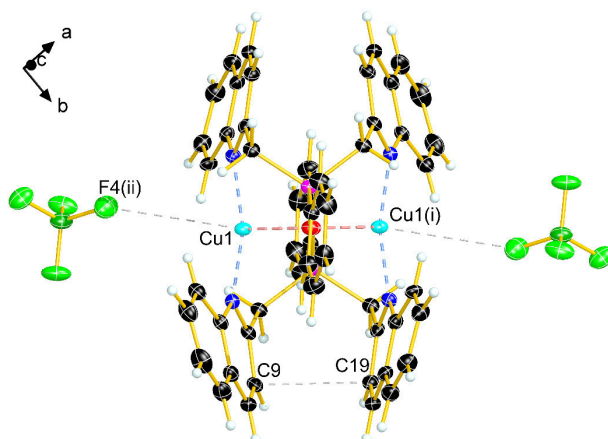


Figure 33. View of the free coordination sides of the metal ions in complex **4**. Selected bond lengths in [Å]: Cu1...F4ⁱⁱ: 4.061(1), C9...C19: 3.055(1). Symmetry code: $ii = x, -1+y, z$.

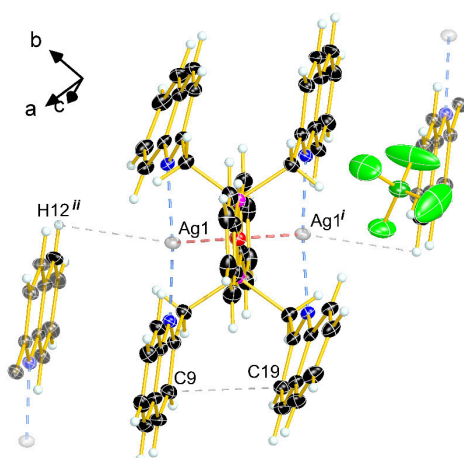


Figure 34. View of the free coordination sides of the metal ions in complex **5**. Selected bond lengths in [Å]: Ag1...H12ⁱⁱ: 3.273(2), C9...C19: 3.237(1). Symmetry code: $ii = 1-x, 1-y, -z$.

To investigate the structural behavior of the complexes in solution, ¹H and ³¹P NMR spectroscopic studies of **4** in CD₃CN at different temperatures were performed (see Figure 35).

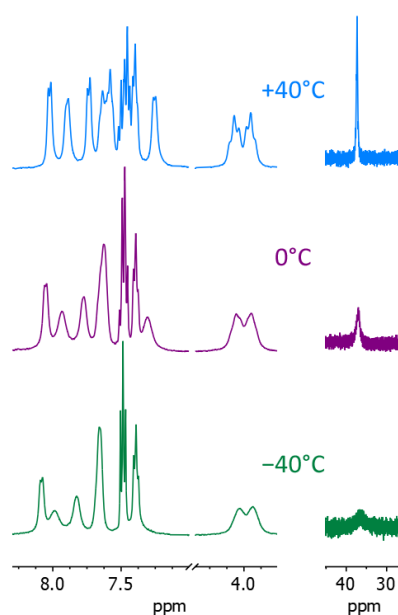


Figure 35. ¹H (left) and ³¹P (right) NMR spectra of complex **4** in CD₃CN at different temperatures.

The quinaldinyl ring and the phenyl ring of the phosphine oxide ligand seem to be quite dynamic in solution as visible in the ^1H NMR spectra (Figure 35). Even at $-40\text{ }^\circ\text{C}$ the dynamical behavior of the complex is still quite fast on the NMR time scale. The diastereotopy of the CH_2 -protons in **4** is clearly visible in the ^1H NMR spectrum at $-40\text{ }^\circ\text{C}$ as indicated by the splitting pattern of the signals.

2.2.3. Conclusions

Although gaining less attention, picolyl phosphine oxide ligands and derivatives thereof show an exciting coordination behavior. One new copper(I) complex and three new silver(I) complexes were obtained wherein the ligand is bridging across two metal centers. So far, a chelating function of the ligand has not been observed. The flexibility of the yet sterically demanding phosphine oxide ligand is shown especially by the different coordination behavior towards Ag(I) in different solvents. Further investigations will be done to clarify the behavior of these complexes in solution.

2.2.4. References

- [1] L. Fanfoni, A. Meduri, E. Zangrando, S. Castillon, F. Felluga, B. Milani, *Molecules*, **2011**, *16*, 1804–1824.
- [2] H. Jaafar, H. Li, L. C. Misal Castro, J. Zheng, T. Roisnel, V. Dorcet, J.-B. Sortais, C. Darcel, *Eur. J. Inorg. Chem.*, **2012**, *2012* (22), 3546–3550.
- [3] Y. Xiao, Z. Sun, H. Guo, O. Kwon, *Beilstein J. Org. Chem.*, **2014**, *10*, 2089–2121.
- [4] D. Zhao, T. M. Neubauer, B. L. Feringa, *Nat. Commun.*, **2015**, 1–7.
- [5] S. Lühr, J. Holz, A. Börner, *ChemCatChem*, **2011**, *3* (11), 1708–1730.
- [6] K. N. Gavrilov, A. I. Polosukhin, *Russ. Chem. Rev.*, **2000**, *69* (8), 661–682.
- [7] A. Mezzetti, *Dalton Trans.*, **2010**, *39*, 7851–7869.
- [8] M. P. Carroll, P. J. Guiry, *Chem. Soc. Rev.*, **2014**, *43* (3), 819–833.
- [9] F. Hung-Low, K. K. Klausmeyer, *Polyhedron*, **2010**, *29* (6), 1676–1686.
- [10] C. Hettstedt, P. Köstler, E. Ceylan, K. Karaghiosoff, *Tetrahedron*, **2016**, *72* (23), 3162–3170.
- [11] A. Kermagoret, F. Tomicki, P. Braunstein, *Dalton Trans.*, **2008**, *22*, 2945–2955.
- [12] G. Venkatachalam, M. Heckenroth, A. Neels, M. Albrecht, *Helv. Chim. Acta*, **2009**, *92* (6), 1034–1045.

2.3. Investigation of structural changes of Cu(I) and Ag(I) complexes utilizing a flexible, yet sterically demanding multidentate phosphine oxide ligand

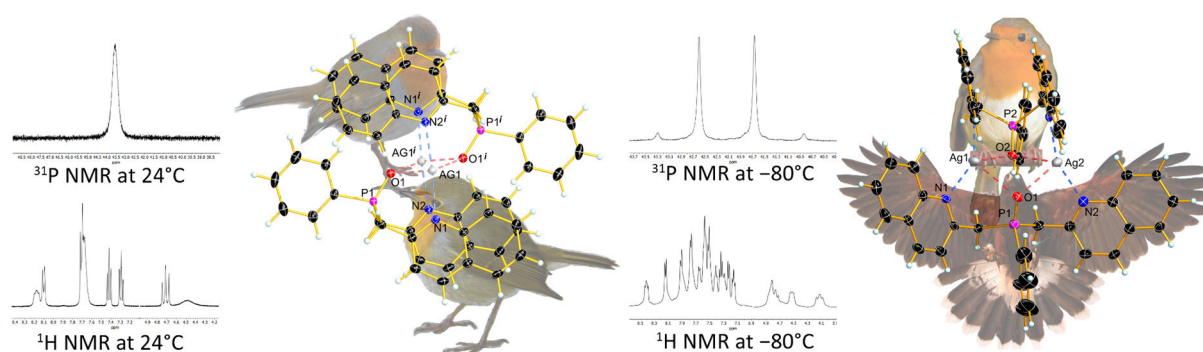
Christin Kirst, Florian Zoller, Thomas Bräuniger, Peter Mayer, Dina Fattakhova-Rohlfing and Konstantin Karaghiosoff

Published in *Inorg. Chem.* 2021, **60**, 2437–2445.

DOI: [10.1021/acs.inorgchem.0c03334](https://doi.org/10.1021/acs.inorgchem.0c03334)

Reprinted (adapted) with permission from *Inorg. Chem.* Copyright (2021) American Chemical Society.

Christin Kirst synthesized all the discussed compounds and performed the single crystal X-ray measurements and Hirshfeld surface analysis. She analyzed and evaluated the corresponding X-ray data and the NMR spectroscopy results in solution. She further managed the project and wrote the original draft of the manuscript, designed the TOC graphic and implemented the necessary corrections in the final version of the paper.



Abstract: The syntheses of a sterically demanding, multidentate bis(quinaldinyl)phenylphosphine oxide ligand and some Cu(I) and Ag(I) complexes thereof are described. By introducing a methylene group between the quinoline unit and phosphorus, the phosphine oxide ligand gains additional flexibility. This specific ligand design induces not only a versatile coordination chemistry but also a rarely observed and investigated behavior in solution. The flexibility of the bird-like ligand offers the unexpected opportunity of open-wing and closed-wing coordination to the metal. In fact, the determined crystal structures of these complexes show both orientations. Investigations of the ligand in solution show a strong dependency of the chemical shift of the CH₂ protons on the solvent used. Variable-temperature, multinuclear NMR spectroscopy was carried out and an interesting dynamic behavior of the complexes is observed. Due to the introduced flexibility, the quinaldinyl substituents change their arrangements from open-wing to closed-wing upon cooling, while still staying coordinated to the metal. This change in conformation is completely reversible when warming up the sample. Based on 2D NMR spectra measured at –80 °C, an assignment of the signals corresponding to the different arrangements was possible. Additionally, the copper(I) complex shows reversible redox activity in solution. The combination of structural flexibility of a multidentate ligand and the positive redox properties of the resulting complexes are key factors for a possible application of such compounds in transition-metal catalysis. *Via* a reorganization of the ligand, occurring transition states could be stabilized and selectivity might be enhanced.

2.3.1. Introduction

The versatile coordinating behavior of hemilabile P-N-compounds is a widely used property, not only in coordination chemistry but also in the fields of catalysis, bioinorganic chemistry or material science.^[1–13] A comprehensive design of such multidentate phosphine ligands is beneficial when trying to provoke or improve specific properties of the resulting metal complex, e.g. luminescence or catalytic activity. A broad variety of phosphine and phosphine oxide ligands with nitrogen containing aromatic substituents directly bonded to phosphorus have been published.^[14–21] Despite the fact that these compounds do not allow for any flexibility of the ligand, they show impressive material properties, such as luminescence or catalytic activity in addition to a rich coordination chemistry.^[22–24] For the application in transition metal catalysis, a certain conformational flexibility of the ligand can be beneficial, as possible transition states can be stabilized more easily.^[25–29] The benefit of flexibility in catalysis has been demonstrated for enzymatic systems, and has recently been discussed for a variety of other catalyst classes by Sigman *et al.*^[30–33] The steric demand of the phosphine ligand when coordinating to a metal can be varied by changing the substituents on phosphorus accordingly. The increased steric demand can result in the ligand bridging across two metal centers, which has been demonstrated previously for some transition metals and can be a promising feature in catalytical application.^[5,34–36] Such ligands can even support metallophilic interactions, which leads to interesting photophysical properties.^[37,38]

By introducing a CH₂-group between phosphorus and the coordinating aromatic substituents, our goal was to create a new class of flexible ligands. These types of ligands should be able to adapt their geometry to the circumstances present in each situation and promise a versatile coordination chemistry. However, the flexibility of the ligand can cause different structural conformations of the metal complexes in solid-state and solution, which can make the investigation of such complexes challenging. Understanding the functional ability and performance of such types of complexes is of great importance. Studies observing different solution and solid-state structures of metal complexes utilizing phosphorus containing ligands have been published mostly in the 1990s.^[39–49] Most of these studies show a dynamic equilibrium in solution between the complex and the dissociated free ligand. A different dynamic in solution has been reported by Klausmeyer *et al.* for silver(I) and copper(I) complexes of bis(picoly)phenylphosphine.^[39] Here, the observed dynamic results from the flexibility of the ligand, which remains coordinated to the metal. The precise knowledge of constitution and conformation is essential for application of a material/compound in solution (e.g. solution processed functional materials or catalysis).^[50–52]

In the present work, the ligand design was adapted in two ways: with the introduction of an additional aromatic ring in the π -system, the ligand becomes sterically more demanding. The additional usage of the phosphine oxide instead of the phosphine is intended to slow down any possible movements and should give a first insight into the types of dynamics in complexes utilizing such flexible ligands.

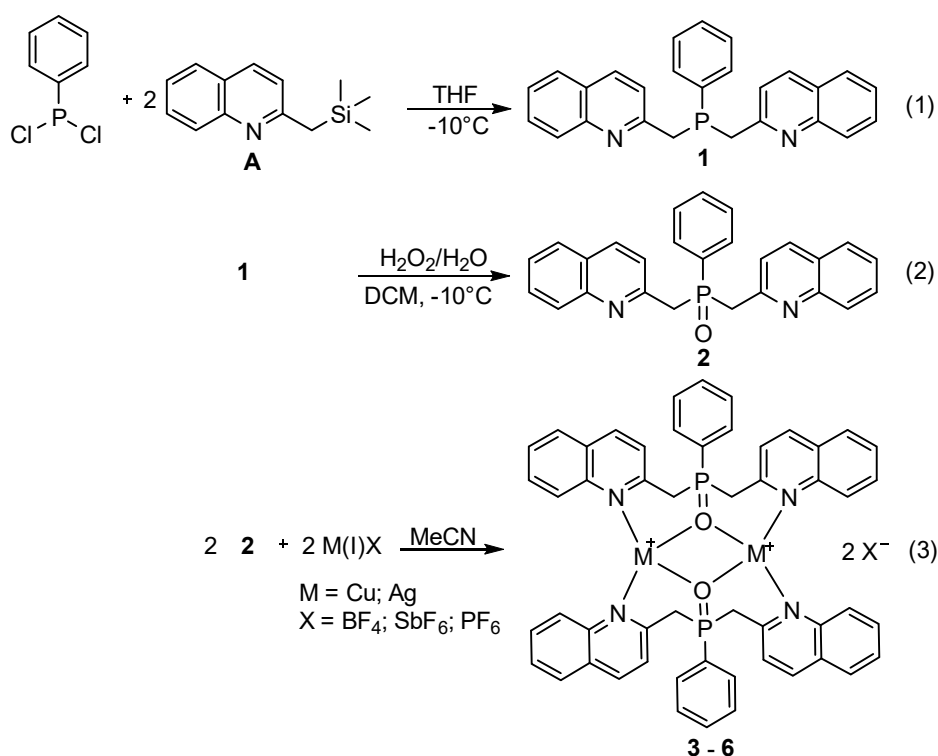
We describe unexpected properties of a novel, flexible, though sterically demanding phosphine oxide ligand and its coordination compounds with selected Cu(I) and Ag(I) salts. These compounds display interesting and reversible conformational changes in solution depending on the temperature, non-coordinating counter ion and also on the solvent used. A thorough investigation of the complexes in solution is done by VT-NMR and electrochemical experiments. By utilizing solid-state NMR and single crystal X-ray crystallography in conjunction with Hirshfeld surface analysis, the solid-state structures could be identified.

The presented results constitute a first, in-depth analysis of the dynamics of flexible ligands in metal complexes. Various cases of application, e.g. in catalysis, could certainly capitalize on the so obtained knowledge.

2.3.2. Results and discussion

2.3.2.1. Synthesis and structural characterization of phosphine oxide metal complexes.

The precursor 2-((trimethylsilyl)methyl)quinoline **A** is synthesized according to the literature.^[53] For the bis(quinaldinyl)phenylphosphine (**1**) as well as for the corresponding phosphine oxide (**2**), the synthesis was adapted according to a similar compound previously published by Braunstein *et al.* and is shown in Scheme 7 (see SI for details).^[54] This reaction allows for the convenient synthesis of large quantities of the phosphine (quantitative yield) in one batch (>5 g). Practically no side reactions take place, allowing for an easy work-up. For the synthesis of **2**, bis(quinaldinyl)phenylphosphine **1** is dissolved in DCM, oxidized utilizing a H₂O₂/water mixture and later isolated in 82 % crystalline yield. For the synthesis of the coinage metal complexes, bis(quinaldinyl)phenylphosphine oxide (**2**) is dissolved in dry, degassed acetonitrile and the resulting mixture transferred *via* a cannula to the respective amount of Cu(I)BF₄, Cu(I)PF₆, Ag(I)BF₄ or Ag(I)SbF₆ under inert gas (see Scheme 7). All complexes can be isolated in high yields (>80 %). The Cu(I) complexes are yellow to orange powders. The complexes are air and moisture sensitive and should be stored under inert gas at ambient temperatures. The Ag(I) complexes are light-beige powders. They are moisture sensitive and should be stored with the exclusion of light.



Scheme 7. Synthesis of bis(quinaldinyl)phenylphosphine (**1**), bis(quinaldinyl)phenylphosphine oxide (**2**) and copper(I) tetrafluoroborate complex (**3**), copper(I) hexafluorophosphate complex (**4**), silver(I) tetrafluoroborate complex (**5**) and silver(I) hexafluoroantimonate complex (**6**) of the phosphine oxide (**2**) showing the coordination mode of the ligand to the respective metal ions.

The molecular structures of compounds **2-6b** of the asymmetric unit in the crystal are shown in Figure 36. The geometry of ligand **2** in the solid state is reminiscent of a bird, with both quinaldinyl substituents being the wings, with one open-wing (containing N1) and the other being closed. Through movement of these wings, the ligand can adapt its coordination geometry to a given metal center. This

impressive behavior is displayed in the crystal structures of the complexes. In all complexes, the binuclear metal (Cu(I), Ag(I)) unit is μ -bridged by two phosphine oxide ligands. Compared to the free phosphine oxide ligand **2**, the P–O bond does slightly elongate when coordinating to the different metal ions (from 1.484 Å in **2** to 1.494–1.501 Å in **3–6b**). The P=O oxygen atom has an additional short contact with one C–H of the quinaldinyl substituent (2.62–2.72 Å in **5–6b**, 3.05–3.16 Å in **3** and **4**). An even longer P–O bond (1.511 Å) and a shorter O \cdots C–H contact (2.44 Å) have been reported for lithium 2-aminobenzothiazolide-diphenylphosphine oxide, which has a partly comparable crystal structure.^[55]

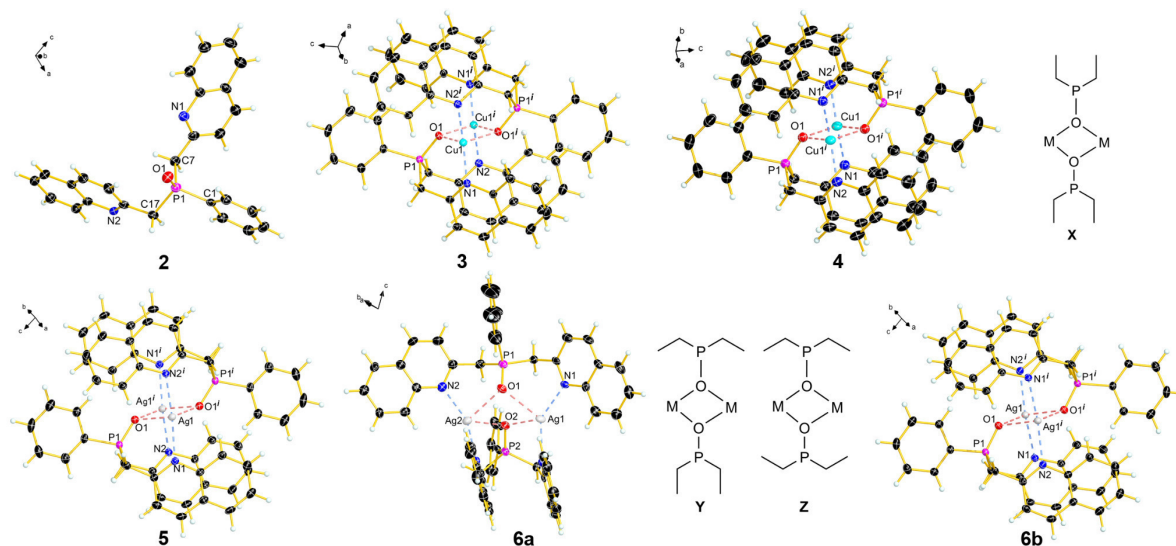


Figure 36. Molecular structures of the asymmetric unit in the crystal of bis(quinaldinyl)phenylphosphine oxide **2**, copper(I) tetrafluoroborate complex **3**, copper(I) hexafluorophosphate complex **4**, silver(I) tetrafluoroborate complex **5** and silver(I) hexafluoroantimonate complexes **6a** and **6b** in addition to a schematic representation of the conformation of the double closed-wing (X), open-wing/closed-wing (Y) and double open-wing (Z) arrangement of the ligand in the complexes. Thermal ellipsoids are drawn at 50 % probability level. Solvent molecules and anions are omitted.

The copper(I) ions in **3** and **4** as well as the silver ions in **5**, **6a** and **6b** are coordinated in a distorted disphenoidal geometry (see-saw geometry) by both oxygen (equatorial) and nitrogen (axial) atoms of the ligands. This see-saw coordination is very rare for copper(I) complexes, less so for silver(I).^[56–60] There are no hydrogen atoms in proximity suitable to complete a possible trigonal bipyramidal or even octahedral geometry around the metal, either *via* agostic or conventional H-bonding to the metal(I) center. The closest atom in proximity to Cu(I) in **3** is the fluorine atom of BF_4^- with a $\text{Cu}\cdots\text{F}$ distance of 4.061(2) Å, in **4** it is the fluorine atom of PF_6^- with a $\text{Cu}\cdots\text{F}$ distance of 4.325(5) Å. For the silver(I) complexes **5** and **6b** the nearest atoms to Ag(I) are the hydrogen atoms of a neighboring quinaldinyl unit ($\text{Ag}\cdots\text{H}$: 3.279(3) Å in **5**, 3.284(2) Å in **6b**). This type of coordination leaves one side of the metal ion free for further coordination. This is an interesting feature, which might be of special interest for a possible application in catalysis.

The two copper ions in **3** and **4** are at a non-bonding distance ($\text{Cu}\cdots\text{Cu}$ = 3.607(4) Å in **3** and 3.533(5) Å in **4**), as the distance is longer than the sum of van der Waals radii (3.46 Å^[61]). The same accounts for the silver ions in **5–6b**: the $\text{Ag}\cdots\text{Ag}$ distances (3.673(4) Å in **5**, 3.792(7) Å in **6a**, 3.630(4) Å in **6b**) are longer than the sum of van der Waals radii (3.54 Å^[61]), so no argentophilic interactions^[62] are present in these complexes.

Earlier, we were comparing the ligand to a flexible bird-like structure. And indeed, we see the different types of double closed-wing (X, Figure 36) and mixed open-wing/closed-wing arrangements (Y, Figure 36) using the same anion (structures **6a** vs. **6b**). If both wings are closed, like in complexes **3–5**

and **6b**, a distortion in the quinaldinyl substituents occurs due to the close proximity of the quinaldinyl rings to each other and the phenyl ring moving slightly in between both quinaldinyl rings (Figure 41 of SI). Such a distortion has been reported before for quinaldine-containing complexes.^[63,64] If the wings are mixed open-wing/closed-wing (**Y**) as in complex **6a**, no distortion appears in any of the quinaldinyl rings, as the phenyl ring is facing far away from the other aromatic systems. The double closed-wing arrangement is supported by π - π -interactions between almost parallel quinaldinyl rings of two neighboring dimers (minimum ring-to-ring distance of 3.113 Å in **3**, 3.280 Å in **4**, 3.357 Å in **5** and 3.377 Å in **6b**).^[65,66]

2.3.2.2. NMR characterization of structure and dynamics of phosphine oxide metal complexes in solution.

The NMR signal of the methylene group is essential for the investigation and validation of the structure of the complexes in solution. In the ligand, both methylene groups are equivalent. Additionally, the protons of one methylene group are diastereotopic and show the typical splitting pattern of an AB part of an ABX spin system (Figure 37, left). The positions of the signals show an impressive dependency on the solvent used, which generates situations ranging from a clear ABX case to a clear A₂X case ($\Delta A = \Delta B$). As described by Braunstein *et al.*^[54] for the similar bis(picoly)phenylphosphine, the ABX pattern is also visible for the phosphine **1** (Figure 37, right), which is in accordance with earlier research from our group.^[53,67] These CH₂-group hydrogen atoms are also the most acidic protons of this molecule. They readily form non-classical hydrogen bonds with neighboring molecules in the solid state (see Figure 42 of SI).

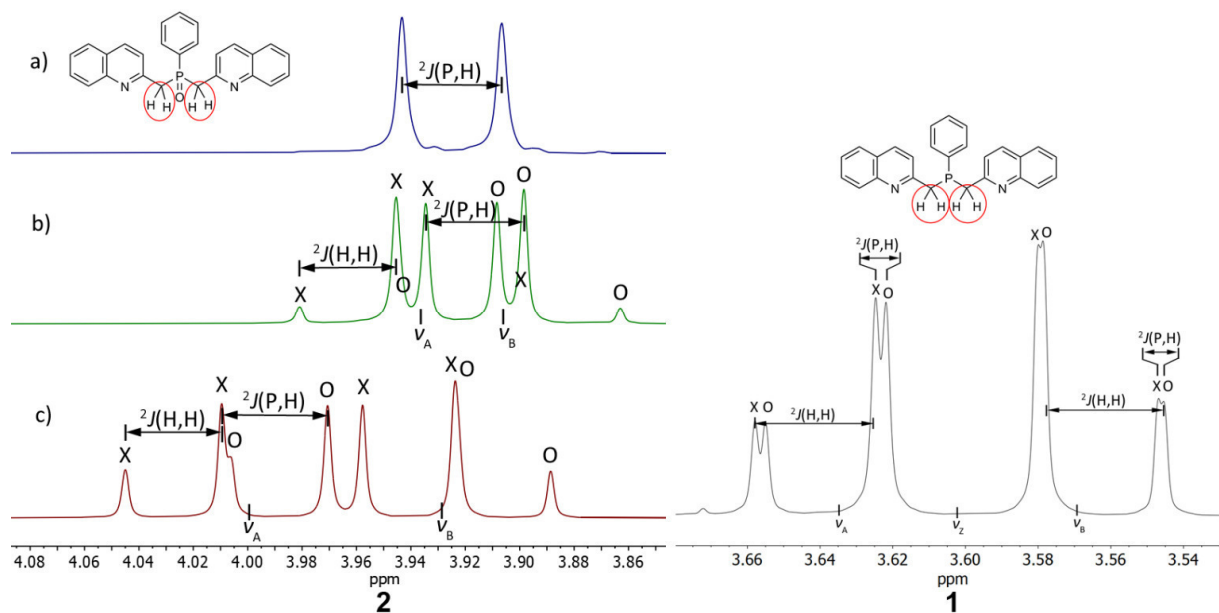


Figure 37. ¹H NMR spectra (left) of phosphine oxide **2** in a) CDCl₃ (blue), b) CD₂Cl₂ (green) and c) CD₃CN (red) showing the signals of the CH₂-group. ¹H NMR spectrum of phosphine **1** in CDCl₃ (right) highlighting the diastereotopy of the CH₂-protons. X and O highlight the different AB sub-spectra.

For the two quinaldinyl substituents of one ligand in the complexes **3–6b**, in solution two different methylene groups should be visible in the ¹H NMR spectrum. However, the ¹H NMR spectra of complexes **3–6b** at RT show the presence of only one set of methylene protons, indicating a dynamic behavior in solution. Consequently, NMR measurements at varying temperatures are recorded to investigate the dynamics of the complexes more closely. Dichloromethane is chosen as the deuterated solvent for the measurements. This solvent is known to be non-coordinating and allows for

measurement temperatures of as low as $-80\text{ }^{\circ}\text{C}$. Selected NMR details of all compounds are shown in Table 4. The ^{31}P NMR spectrum of complex **3** at RT shows a relatively sharp single resonance, which upon cooling to $-80\text{ }^{\circ}\text{C}$, is symmetrically split into two singlets of equal intensity. This indicates the presence of two different phosphorus environments with the same probability at low temperature (Figure 48 of SI). None of these signals correspond to the free ligand. Additionally, in the ^1H NMR spectrum of compound **3** at low temperature, the presence of broad signals for two different methylene groups and additional signals in the aromatic region are now visible. However, in case of the silver complexes, the situation is much clearer, as the ^1H NMR spectra are of higher resolution at low temperature. Both silver complexes **5** and **6** are investigated under the same conditions and show a behavior similar to copper complex **3**. Additional 2D NMR spectra are recorded, to further characterize the situation at $-80\text{ }^{\circ}\text{C}$.

The observations are the following (Figure 38, left and middle): At RT, compound **5** shows one broad phosphorus signal and in the ^1H NMR spectrum one single set of diastereotopic methylene groups (H27, H29) and very broad signals for the phenyl ring, whereas the signals for the quinaldinyl ring are sharp. When cooling down to $-80\text{ }^{\circ}\text{C}$, the resonance of **5** in the ^{31}P NMR spectrum is split into two sharp signals of equal intensity with a temperature of coalescence between 0 and $-20\text{ }^{\circ}\text{C}$.

Table 4. Selected NMR details of the synthesized phosphorus containing compounds **1–6b**. Chemical shifts δ in ppm and in reference to CD_2Cl_2 , if not otherwise stated.

	1 ^a	2 ^b	3 ^c	4 ^d	5 ^e	6 ^f
$^{31}\text{P}\{\text{H}\}$ at RT	-13.9 (CDCl_3)	33.9	44.0	36.2, -141.8 (sept, $^1J_{\text{P-F}} =$ 710.0 Hz) (CD_3CN)	43.6	42.3
$^{31}\text{P}\{\text{H}\}$ at $-80\text{ }^{\circ}\text{C}$			46.4, 40.8		41.7, 42.6	41.4, 42.3

^afree phosphine ligand, ^bfree phosphine oxide ligand, ^c $\text{Cu}(\text{I})\text{BF}_4$ complex, ^d $\text{Cu}(\text{I})\text{PF}_6$ complex, ^e $\text{Ag}(\text{I})\text{BF}_4$ complex, ^f $\text{Ag}(\text{I})\text{SbF}_6$ complex

In the ^1H NMR spectrum at $-80\text{ }^{\circ}\text{C}$, the signals for the methylene group (H27a, H29a and H27b, H29b) and in general for the quinaldinyl rings are split into two different sets in accordance with the two phosphorus signals (Figure 38). The corresponding $^1\text{H}^1\text{H}$ -NOESY and $^1\text{H}^{13}\text{C}$ -HSQC NMR spectra highlighting the CH_2 group of **5** at $-80\text{ }^{\circ}\text{C}$ further confirm the presence of two different sets of quinaldinyl rings (Figure 38, right), with one methylene group displaying a significantly larger diastereotopy than the other (H27a, H29a vs. H27b, H29b). The two sets of signals for the quinaldinyl rings differ mostly in the chemical shift of the proton closest to the CH_2 group (H9a, H11a and H9b and H11b). For one set, it is close to the chemical shift at RT and for the other set, a shift to lower frequencies ($\Delta\delta = 0.4\text{ ppm}$) is observed. The dynamic of the phenyl ring is also slowed down at $-80\text{ }^{\circ}\text{C}$ and the three different signals for the protons in *o*-, *m*- and *p*-position are now observable. When heating the sample, the observations in the ^1H and ^{31}P NMR spectra are reversed back to the initial state at RT.

The variable temperature NMR spectra of **6** show a similar behavior in CD_2Cl_2 and are shown in Figure 38. The chemical shifts of complexes **5** and **6** in the ^{31}P NMR spectra at RT are very similar and thus seem to be independent of the non-coordinating counter ion, indicating the presence of distinct cations and anions in solution. No coupling to $^{107,109}\text{Ag}$ is observed in any of the NMR spectra of the silver complexes.

The differences in the VT-NMR spectra can be explained by the presence of quinaldinyl rings in different orientations with respect to the phenyl ring of the ligands in the complexes. As can be derived from the different polymorphs of **6** in the solid state, the phosphine oxide ligand **2** is very flexible and

can adopt diverse orientations. At RT, both ligands are coordinating to the metal in an open-wing arrangement **Z** shown in Figure 36 ($\delta^1\text{H}$ (H9, H11) = 7.32 ppm at RT). When cooling down, the quinaldinyl substituents of one ligand in the complex rearranges to a closed-wing conformation (**Y**, Figure 36). The proton (H9, H11) consequently moves away from the phenyl ring and out of its shielding cone. This shifts the signal to higher frequencies in the ^1H NMR spectrum ($\delta^1\text{H}$ (H9b, H11b) = 7.65 ppm). The quinaldinyl substituent of the other ligand in the complex remains in the open-wing arrangement (**Y**, Figure 36) and in close proximity to the phenyl ring and its shielding cone, which causes the mentioned proton to shift its signal to lower frequencies ($\delta^1\text{H}$ (H9a, H11a) = 7.22 ppm). This interpretation is supported by the comparison of the chemical shifts of this proton in methylquinaldine (7.30 ppm) and 2-((trimethylsilyl)methyl)quinoline (7.12 ppm) at RT, where the influence of a phenyl substituent is missing completely. This is further confirmed by the ^1H NMR of the phosphine ligand **1** at RT (7.15 ppm), where a similar open-wing conformation is anticipated. Both possible arrangements of the quinaldinyl substituents and the different proximities of the proton to the phenyl ring are visualized in the solid-state by the crystal structure of **6a**. The arrangement with double closed-wings (**X**, Figure 36) would reflect the situation at even lower temperatures.

The observed conformational flexibility of this type of ligand in solution can be of special interest for a possible application in catalysis. This ligand type most likely has the ability to reorganize in order to stabilize any feasible transition states and could thereby enhance selectivity in transition-metal catalysis.

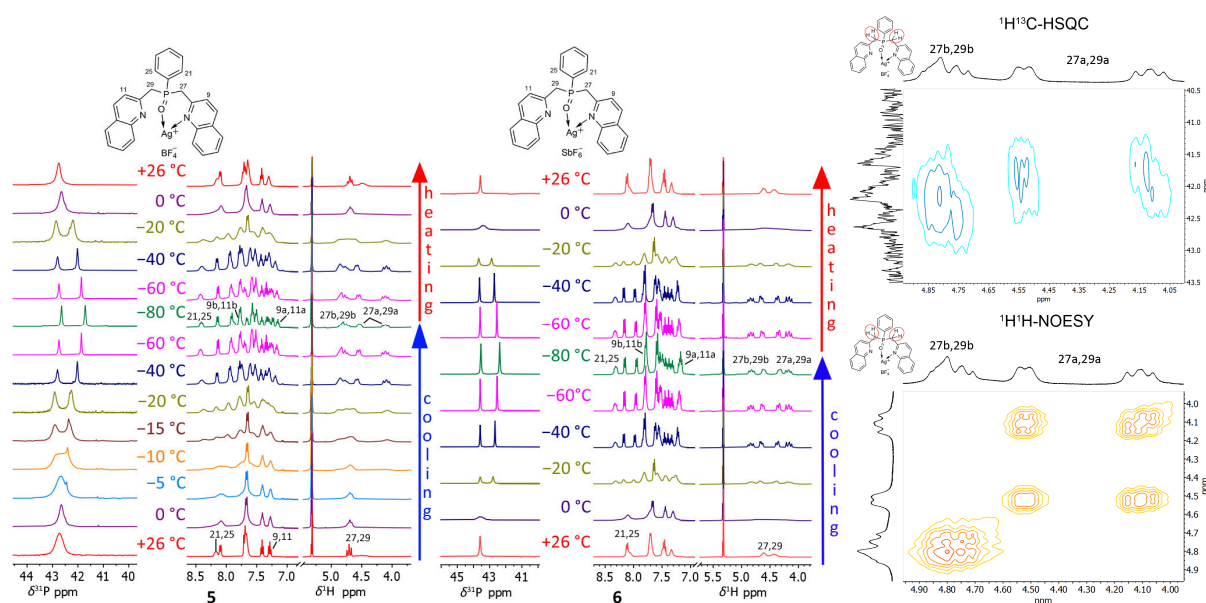


Figure 38. ^{31}P NMR and ^1H NMR of compounds **5** (left) and **6** (middle) in CD_2Cl_2 at different temperatures. $^1\text{H}^1\text{H}$ -NOESY and $^1\text{H}^{13}\text{C}$ -HSQC NMR of the CH_2 group of **5** at -80°C (right).

2.3.2.3. Solid-state NMR characterization of the phosphine oxide metal complexes.

With the aid of solid-state NMR, the chemical shifts of the solid or even crystalline compounds can be compared to its chemical shifts in solution at varying temperatures. The solid-state NMR of the free ligand **2** is congruent with solution NMR. The chemical shift in both ^{31}P NMR spectra is very similar ($\delta^{31}\text{P}$ (CD_2Cl_2) = 33.9 ppm; ^{31}P MAS [20 kHz] δ = 33.5 ppm, Figure 39). However, the results of the ^{31}P MAS NMR of the complexes differ from those achieved in solution NMR (Figure 39). The observed differences in terms of their chemical shifts when comparing solution NMR and SS NMR of the complexes might be due to a distortion and differences in the geometry surrounding phosphorus in

the solid state.^[68] Additionally, Hirshfeld surface analysis indicates an interaction of the counterion with the cationic part of the complex in the crystal (see Figure S11 in SI). This might also have an effect on the chemical shifts observed in the solid-state NMR of the complexes.

The chemical shift visible in the ⁶³Cu MAS NMR of complex **3** is at –329 ppm (Figure 39). In a publication by Tang *et al.*^[69] the solid-state NMR results of different Cu(I) phosphine complexes with different geometries are discussed. The signal with the lowest frequency was reported with –150 ppm for CpCuPEt₃. To the best of our knowledge, solid-state NMR results of similar copper(I) phosphine oxide complexes have not been reported in the literature so far.

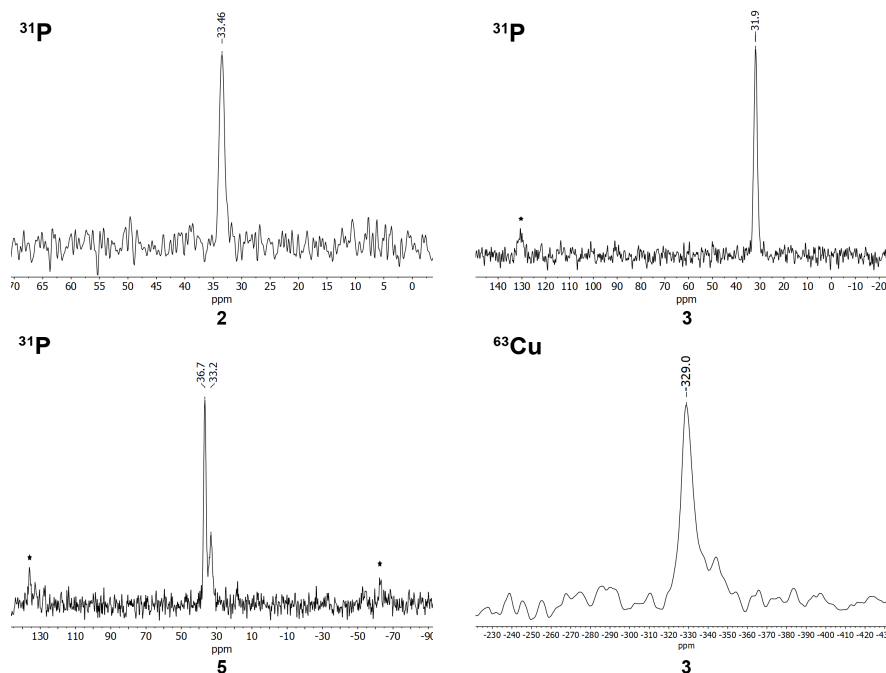


Figure 39. Solid-state ³¹P MAS NMR [20 kHz] of **2**, **3** and **5** and ⁶³Cu MAS NMR [20 kHz] of **3**. Spinning side bands are marked with an asterisk.

2.3.2.4. Electrochemical characterization of complex **3**.

To study the redox activity of complex **3** in solution, complex **3** is dissolved in acetonitrile and studied by cyclic voltammetry. The measurements are performed in a three-electrode cell using a Pt coil as the working electrode, a glassy carbon counter electrode and an Ag/AgNO₃ (0.01 M) reference electrode (Figure 40 and Figure 44 of SI). Complex **3** and the respective ligand are studied in cathodic and anodic scans, respectively, which are performed at potential ranges from 0.5 V to –1.2 V (Figure 40, left) and from 0 V to 2 V (Figure 40, right) using a scan rate of 50 mV s⁻¹.

The ligand alone is electrochemically inactive (Figure 40). In contrast, complex **3** shows several reduction peaks with corresponding re-oxidation peaks in the reverse scan (Figure 40). For complex **3**, during the initial cathodic scan, a broad reduction peak at –0.97 V vs Ag/AgNO₃ composed of two overlapping redox peaks is detected, which become more pronounced and distinctly separated in the subsequent scans (Figure 44 of SI). In the second and the following scans, two pairs of quasi-reversible redox peaks are observed. The first redox couple shows a reduction peak at –1.02 V vs Ag/AgNO₃ and a corresponding re-oxidation peak at –0.42 V vs Ag/AgNO₃. A large separation between the cathodic and anodic peak of 600 mV point to very slow kinetics of charge transfer. The second redox couple shows a reduction peak at –0.90 V with a corresponding oxidation peak at –0.79 vs Ag/AgNO₃, which are followed by a much smaller redox couple with peak reduction and oxidation potentials at 1.14 V and –1.07 V vs Ag/AgNO₃, respectively. The electrochemical activity of complex **3** in cathodic direction

is most probably related to the ligand-assisted redox transformation of the Cu(I)/Cu(0) couple according to information in the literature,^[70] although the reduction products cannot be identified yet. This transformation is electrochemically irreversible for the complex dissolved in acetonitrile, resulting in a deposition of reduction product on the Pt electrode, whose re-oxidation is observed in the reverse scan at potential of -0.50 V vs Ag/AgNO₃. The oxidation behavior of complex **3** is electrochemically slow (quasi-reversible) but chemically stable. In the anodic scan a broad redox couple superimposed on the electrolyte oxidation curve is observed, with oxidation and reduction peaks at 1.10 and 0.51 V vs Ag/AgNO₃, respectively. The oxidation activity of complex **3** is most probably related to the Cu(I)/Cu(II) redox transformation.

These measurements reveal, that complex **3** is redox active and its oxidation and reduction are reversible. The ligand stays connected to the metal during the stressful electrochemical measurements, which is an important property for its potential use as a metal complex in catalytic reactions.

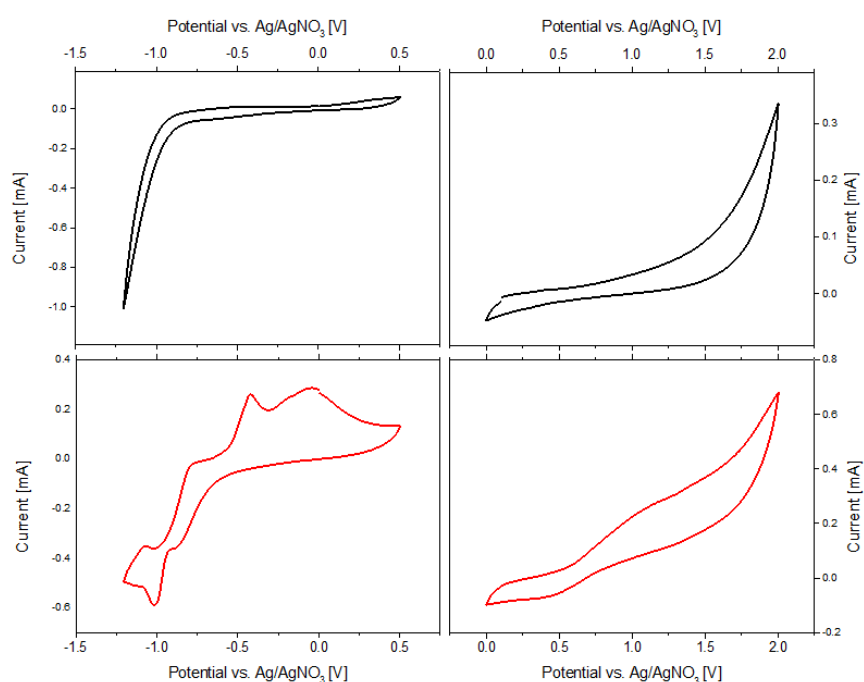


Figure 40. Cyclic voltammograms of complex **3** (red curves) and ligand **2** (black curves) recorded between 0.5– (-1.2) V (left) and 0–2 V (right). The measurements are performed in a three-electrode cell using a Pt coil as working electrode, a glassy carbon counter electrode and an Ag/AgNO₃ (0.01 M) reference electrode at a scan rate of 50 mV s^{-1} .

2.3.3. Conclusion

It is shown that the special type of bis(quinaldinyl)phenylphosphine oxide ligand exhibits a reversible dynamic in solution at different temperatures in its copper(I) and silver(I) complexes, which has not been discussed to this extent so far. An explanation for this phenomenon is given *via* the synergy of a broad variety of complementary analytical methods (VT-NMR, SS NMR, single crystal structures, Hirshfeld surface analysis, cyclic voltammetry). We find, that both quinaldinyl substituents, which are referred to as wings in a figurative sense, are involved in this interesting behavior of the complexes. Their individual flexibility enables different conformations (double open-wing, double closed-wing and mixed) when coordinating to the metal, which are found in the crystal structures of the complexes. The results of the careful examination of the VT-NMR spectra in CD₂Cl₂ point to the transition from an open-wing arrangement at RT to an open-wing/closed-wing arrangement at low temperatures and

exclude a dissociation and reassociation of the complex. The solid-state ^{63}Cu NMR spectrum of complex **3** displays a signal with a chemical shift at very low frequencies. In addition to the conformational flexibility, a first series of electrochemical measurements clearly shows a reversible redox activity for the Cu(I) complex **3** in solution. This indicates a potential application for catalysis, since the complex is stable and does not dissociate under stressful electrochemical conditions.

The combination of advantageous conformational flexibility and electrochemical stability make this new type of bird-like ligand or derivatives thereof possible candidates for transition-metal catalysis. The potential ability of the ligand to reorganize for the purpose of stabilizing any occurring transition states might be crucial to enhance selectivity. However, further mechanistic studies utilizing these types of ligands in catalysis are necessary to evaluate their suitability for this specific case.

ASSOCIATED CONTENT

Supporting Information. Experimental, crystallographic and spectroscopic data is available free of charge *via* the Internet at <http://pubs.acs.org>.

AUTHOR INFORMATION

Corresponding Author

* klk@cup.uni-muenchen.de

Author Contributions

The manuscript was written through contributions of all authors. All authors have given approval to the final version of the manuscript.

Funding Sources

This work was financially supported by the German Federal Ministry for Economic Affairs and Energy on the basis of a decision by the German Bundestag (ZIM, Grant ZF4477702SL7).

Notes

There are no conflicts of interest to declare.

ACKNOWLEDGMENT

The authors gratefully acknowledge the Conversion Excellence cluster (DFG) for support. We further appreciatively acknowledge the financial support by the Department of Chemistry, Ludwig-Maximilian University of Munich. Additionally, we are especially thankful to Prof. Dr. T. M. Klapötke for his continuous support over the years. The entire NMR team at the Ludwig-Maximilian University of Munich including Dr. Burkhard Krumm are thanked for the multi-nuclear and variable temperature NMR measurements.

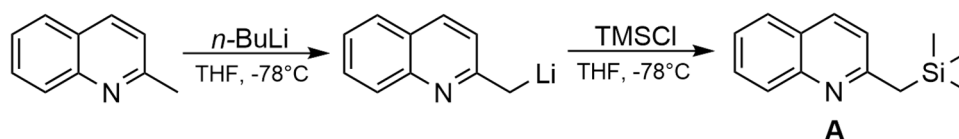
2.3.4. References

- [1] L. Fanfoni, A. Meduri, E. Zangrando, S. Castillon, F. Felluga, B. Milani, *Molecules*, **2011**, *16*, 1804–1824.
- [2] H. Jaafar, H. Li, L. C. Misal Castro, J. Zheng, T. Roisnel, V. Dorcet, J.-B. Sortais, C. Darcel, *Eur. J. Inorg. Chem.*, **2012**, *2012* (22), 3546–3550.
- [3] D. Rosario-Amorin, S. Ouizem, D. A. Dickie, Y. Wen, R. T. Paine, J. Gao, J. K. Grey, A. De Bettencourt-Dias, B. P. Hay, L. H. Delmau, *Inorg. Chem.*, **2013**, *52* (6), 3063–3083.
- [4] G. Chelucci, G. Orrù, G. a. Pinna, *Tetrahedron*, **2003**, *59*, 9471–9515.
- [5] H. Werner, *Angew. Chem.*, **2004**, *116*, 956–972; *Angew. Chem. Int. Ed.*, **2004**, *43*, 938–954.
- [6] F. Hung-Low, K. K. Klausmeyer, *Polyhedron*, **2010**, *29* (6), 1676–1686.
- [7] B. Shankar, P. Elumalai, R. Shanmugam, V. Singh, D. T. Masram, M. Sathiyendiran, *Inorg. Chem.*, **2013**, *52* (18), 10217–10219.

- [8] F. Leca, C. Lescop, E. Rodriguez-Sanz, K. Costuas, J. F. Halet, R. Réau, *Angew. Chem. Int. Ed.*, **2005**, *44* (28), 4362–4365.
- [9] D. A. Padron, K. K. Klausmeyer, *Polyhedron*, **2012**, *34* (1), 215–220.
- [10] M. P. Carroll, P. J. Guiry, *Chem. Soc. Rev.*, **2014**, *43* (3), 819–833.
- [11] K. N. Gavrilov, A. I. Polosukhin, *Russ. Chem. Rev.*, **2000**, *69* (8), 661–682.
- [12] J. C. Hierso, R. Smaliy, R. Amardeil, P. Meunier, *Chem. Soc. Rev.*, **2007**, *36* (11), 1754–1769.
- [13] P. Espinet, K. Soullantica, *Coord. Chem. Rev.*, **1999**, *193–195*, 499–556.
- [14] T. Gneuß, M. J. Leitzl, L. H. Finger, N. Rau, H. Yersin, J. Sundermeyer, *Dalton Trans.*, **2015**, *44* (18), 8506–8520.
- [15] M. J. Leitzl, D. M. Zink, A. Schinabeck, T. Baumann, D. Volz, H. Yersin, *Top. Curr. Chem.*, **2016**, *374* (3), 25.
- [16] M. J. Leitzl, F. R. Kuchle, H. A. Mayer, L. Wesemann, H. Yersin, *J. Phys. Chem. A*, **2013**, *117* (46), 11823–11836.
- [17] M. Elie, M. D. Weber, F. Di Meo, F. Sguerra, J. F. Lohier, R. B. Pansu, J. L. Renaud, M. Hamel, M. Linares, R. D. Costa, S. Gaillard, *Chem. - A Eur. J.*, **2017**, *23* (64), 16328–16337.
- [18] A. V. Artem'ev, E. P. Doronina, M. I. Rakhmanova, A. O. Sutyryna, I. Y. Bagryanskaya, P. M. Tolstoy, A. L. Gushchin, A. S. Mazur, N. K. Gusarova, B. A. Trofimov, *New J. Chem.*, **2016**, *40* (12), 10028–10040.
- [19] A. V. Artem'ev, M. R. Ryzhikov, I. V. Taidakov, M. I. Rakhmanova, E. A. Varaksina, I. Y. Bagryanskaya, S. F. Malysheva, N. A. Belogorlova, *Dalton Trans.*, **2018**, *47* (8), 2701–2710.
- [20] A. V. Artem'ev, A. Y. Baranov, M. I. Rakhmanova, S. F. Malysheva, D. G. Samsonenko, *New J. Chem.*, **2020**, *44* (17), 6916–6922.
- [21] A. V. Artem'ev, M. P. Davydova, A. S. Berezin, M. R. Ryzhikov, D. G. Samsonenko, *Inorg. Chem.*, **2020**, *59* (15), 10699–10706.
- [22] D. Joly, P.-A. Bouit, M. Hissler, *J. Mater. Chem. C*, **2016**, *4* (17), 3686–3698.
- [23] E. I. Musina, A. S. Balueva, A. A. Karasik, *Organophosphorus Chemistry*; **2019**, *48*, 1–63.
- [24] W. A. Munzeiwa, B. Omondi, V. O. Nyamori, *Beilstein J. Org. Chem.*, **2020**, *16*, 362–383.
- [25] A. Nojiri, N. Kumagai, M. Shibasaki, *J. Am. Chem. Soc.*, **2009**, *131* (10), 3779–3784.
- [26] D. E. Ryan, D. J. Cardin, F. Hartl, *Coord. Chem. Rev.*, **2017**, *335*, 103–149.
- [27] M. Reinmuth, P. Walter, M. Enders, E. Kaifer, H. J. Himmel, *Eur. J. Inorg. Chem.*, **2011**, *2011*, 83–90.
- [28] N. Kumagai, M. Shibasaki, *Angew. Chem.*, **2013**, *125* (1), 235–246; *Angew. Chem. Int. Ed.*, **2013**, *52* (1), 223–234.
- [29] G. Altenhoff, R. Goddard, C. W. Lehmann, F. Glorius, *J. Am. Chem. Soc.*, **2004**, *126* (46), 15195–15201.
- [30] G. G. Hammes, *Biochemistry*, **2002**, *41* (26), 8221–8228.
- [31] D. Herschlag, *Bioorg. Chem.*, **1988**, *16* (1), 62–96.
- [32] E. Katsoulakou, N. Lalioti, C. P. Raptopoulou, A. Terzis, E. Manessi-Zoupa, S. P. Perlepes, *Inorg. Chem. Commun.*, **2002**, *5* (9), 719–723.
- [33] J. Crawford, M. Sigman, *Synth.*, **2019**, *51* (05), 1021–1036.
- [34] D. C. Powers, T. Ritter, *Acc. Chem. Res.*, **2012**, *45* (6), 840–850.
- [35] Z. Xi, Y. Zhou, W. Chen, *J. Org. Chem.*, **2008**, *73* (21), 8497–8501.
- [36] R. Tagore, R. H. Crabtree, G. W. Brudvig, *Inorg. Chem.*, **2008**, *47* (6), 1815–1823.
- [37] M. Olaru, J. F. Kögel, R. Aoki, R. Sakamoto, H. Nishihara, E. Lork, S. Mebs, M. Vogt, J. Beckmann, *Chem. - A Eur. J.*, **2020**, *26* (1), 275–284.
- [38] M. J. Calhorda, C. Ceamanos, O. Crespo, M. C. Gimeno, A. Laguna, C. Larraz, P. D. Vaz, M. D. Villacampa, *Inorg. Chem.*, **2010**, *49* (18), 8255–8269.
- [39] F. Hung-Low, A. Renz, K. K. Klausmeyer, *Eur. J. Inorg. Chem.*, **2009**, 2994–3002.

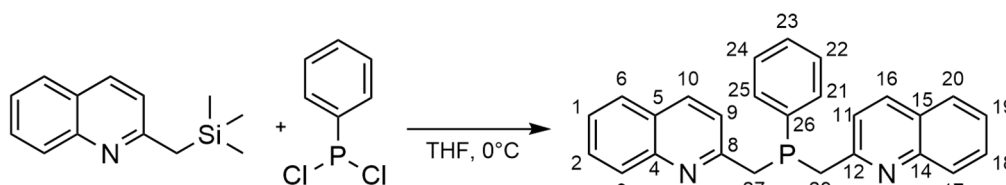
-
- [40] S. J. Berners-Price, R. K. Johnson, C. K. Mirabelli, L. F. Faucette, F. L. McCabe, P. J. Sadler, *Inorg. Chem.*, **1987**, *26* (20), 3383–3387.
- [41] N. Vijayashree, A. G. Samuelson, M. Nethaji, *Curr. Sci.*, **1993**, *65* (1), 57–67.
- [42] D. Saravanabharathi, M. Nethaji, A. G. Samuelson, *Polyhedron*, **2002**, *21* (27–28), 2793–2800.
- [43] S. Attar, W. H. Bearden, N. W. Alcock, E. C. Alyea, J. H. Nelson, *Inorg. Chem.*, **1990**, *29* (3), 425–433.
- [44] B. Mohr, E. E. Brooks, N. Rath, E. Deutsch, *Inorg. Chem.*, **1991**, *30* (24), 4541–4545.
- [45] S. Attar, N. W. Alcock, G. A. Bowmaker, J. S. Frye, W. H. Bearden, J. H. Nelson, *Inorg. Chem.*, **1991**, *30* (22), 4166–4176.
- [46] J. A. Davies, S. G. Dutremez, *Magn. Reson. Chem.*, **1993**, *31* (5), 439–443.
- [47] B. Mohr, J. Schmidt, E. E. Brooks, M. J. Heeg, D. M. Ho, E. Deutsch, *Inorg. Chem.*, **1993**, *32* (15), 3236–3240.
- [48] D. Rentsch, R. Hany, W. von Philipsborn, *Magn. Reson. Chem.*, **1997**, *35* (12), 832–838.
- [49] A. Parker, P. Lamata, F. Viguri, R. Rodríguez, J. A. López, F. J. Lahoz, P. García-Orduña, D. Carmona, *Dalton Trans.*, **2020**, *49* (39), 13601–13617.
- [50] D. Volz, M. Wallesch, S. L. Grage, J. Göttlicher, R. Steininger, D. Batchelor, T. Vitova, A. S. Ulrich, C. Heske, L. Weinhardt, T. Baumann, S. Bräse, *Inorg. Chem.*, **2014**, *53* (15), 7837–7847.
- [51] K. J. Cluff, N. Bhuvanesh, J. Blümel, *Chem. - A Eur. J.*, **2015**, *21* (28), 10138–10148.
- [52] M. Saigo, K. Miyata, H. Nakanotani, C. Adachi, K. Onda, **2020**, DOI:10.26434/chemrxiv.11798568.v2.
- [53] C. Hettstedt, P. Köstler, E. Ceylan, K. Karaghiosoff, *Tetrahedron*, **2016**, *72* (23), 3162–3170.
- [54] A. Kermagoret, F. Tomicki, P. Braunstein, *Dalton Trans.*, **2008**, *22*, 2945–2955.
- [55] Z. García-Hernández, A. Flores-Parra, J. M. Grevy, Á. Ramos-Organillo, R. Contreras, *Polyhedron*, **2006**, *25* (7), 1662–1672.
- [56] G. Venkatachalam, M. Heckenroth, A. Neels, M. Albrecht, *Helv. Chim. Acta*, **2009**, *92* (6), 1034–1045.
- [57] A. A. Fedorchuk, Y. I. Slyvka, V. Kinzhyballo, T. Lis, M. G. Mys'kiv, *Inorg. Chim. Acta*, **2019**, *484*, 79–86.
- [58] R. Meijboom, R. J. Bowen, S. J. Berners-Price, *Coord. Chem. Rev.*, **2009**, *253* (3–4), 325–342.
- [59] E. M. Njogu, B. Omondi, V. O. Nyamori, *J. Coord. Chem.*, **2015**, *68* (19), 3389–3431.
- [60] A. N. Khlobystov, A. J. Blake, N. R. Champness, D. A. Lemenovskii, A. G. Majouga, N. V. Zyk, M. Schröder, *Coord. Chem. Rev.*, **2001**, *222* (1), 155–192.
- [61] S. S. Batsanov, *Inorg. Mater.*, **2001**, *37* (9), 871–885.
- [62] H. Schmidbaur, A. Schier, *Angew. Chem.*, **2015**, *127* (3), 756–797; *Angew. Chem. Int. Ed.*, **2015**, *54* (3), 746–784.
- [63] A. Hazell, O. Mønsted, J. C. Rasmussen, H. Toftlund, *Acta Crystallogr. C*, **2008**, *64* (5), m185–m189.
- [64] S. Meghdadi, M. Amirnasr, S. B. H. Moein Sadat, K. Mereiter, A. Amiri, *Monatsh. Chem.*, **2014**, *145* (10), 1583–1594.
- [65] C. Janiak, *Dalton Trans.*, **2000**, *21*, 3885–3896.
- [66] W. B. Jennings, B. M. Farrell, J. F. Malone, *Acc. Chem. Res.*, **2001**, *34* (11), 885–894.
- [67] C. Hettstedt, M. Unglert, R. J. Mayer, A. Frank, K. Karaghiosoff, *Eur. J. Inorg. Chem.*, **2016**, *2016* (9), 1405–1414.
- [68] J. A. Rahn, D. J. O'Donnell, A. R. Palmer, J. H. Nelson, *Inorg. Chem.*, **1989**, *28* (13), 2631–2635.
- [69] J. A. Tang, B. D. Ellis, T. H. Warren, J. V. Hanna, C. L. B. Macdonald, R. W. Schurko, *J. Am. Chem. Soc.*, **2007**, *129* (43), 13049–13065.
- [70] M. Kügler, J. Scholz, A. Kronz, I. Siewert, *Dalton Trans.*, **2016**, *45* (16), 6974–6982.

2.3.5. Supporting information

2.3.5.1. Synthesis of 2-((trimethylsilyl)methyl)quinoline (**A**)

2-Methylquinoline (33.9 mL) was dissolved in 150 mL dry, degassed THF and cooled to $-78\text{ }^{\circ}\text{C}$. *n*-BuLi (2.4 M in *n*-hexane, 104.6 mL), was added dropwise to the solution while stirring. The reaction mixture turns dark red. After stirring for one hour, chloro(trimethyl)silane (32.2 mL, 376.4 mmol) was added quickly though dropwise at $-78\text{ }^{\circ}\text{C}$ to the mixture and the color changes to a light yellow.¹³ After stirring for another 14 hours while letting the mixture warm up to RT, the solvent is evaporated and the left-over liquid is distilled (bp. $65\text{ }^{\circ}\text{C}$ at $2.6 \cdot 10^{-2}$ mbar). A colorless to yellow liquid of **A** is received in 60 % yield (32.4 g, 150.4 mmol).

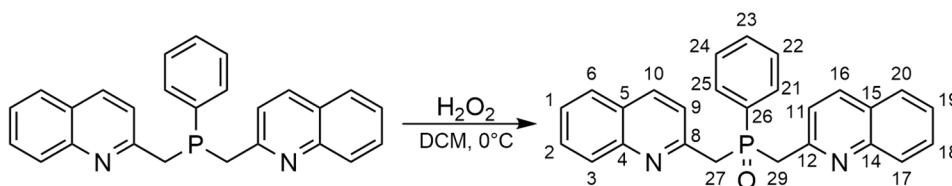
²⁹Si [CDCl₃, 79.495 MHz] $\delta = 2.6$ (¹*J*_{Si-C} = 25.6 Hz) ppm; ¹H [CDCl₃, 400.133 MHz] $\delta = 0.02$ (s, 9H, CH₃, ²*J*_{H-Si} = 58.9 Hz), 2.49 (s, 2H, CH₂), 6.92 (d, 1H, *J* = 6.92 Hz, *J* = 1.5 Hz), 7.26 (t, 1H, *J* = 8.0 Hz, *J* = 1.0 Hz), 7.51 (dq, 1H, *J* = 8.4 Hz, *J* = 1.5 Hz), 7.55 (d, 1H, *J* = 8.5 Hz, *J* = 1.2 Hz), 7.76 (d, 1H, *J* = 8.3 Hz), 8.02 (d, 1H, *J* = 8.4 Hz) ppm; ¹³C{¹H} [CDCl₃, 100.623 MHz] $\delta = -2.0$ (s, ¹*J*_{C-Si} = 25.3 Hz; CH₃), 30.9 (s, ¹*J*_{C-Si} = 21.4 Hz; CH₂), 121.0 (s), 124.3 (s), 125.3 (s), 126.9 (s), 128.0 (s), 128.5 (s), 134.9 (s, ²*J*_{C-Si} = 42.8 Hz), 147.7 (s), 161.2 (s, ³*J*_{C-Si} = 289.4 Hz) ppm; IR: $\tilde{\nu}_{\text{max}}$ (cm⁻¹) = 3057 (vw), 2954 (w), 2923 (w), 2852 (vw), 1618 (w), 1599 (m), 1560 (vw), 1501 (m), 1464 (w), 1424 (w), 1375 (vw), 1311 (w), 1248 (m), 1224 (w), 1141 (m), 1118 (w), 1092 (w), 1017 (vw), 950 (vw), 903 (w), 843 (s), 783 (m), 767 (m), 745 (s), 697 (m), 651 (w), 617 (w), 470 (m), 430 (vw).

2.3.5.2. Synthesis of bis(quinaldinyl)phenylphosphine (**1**)

To a solution of 2-((trimethylsilyl)methyl)quinoline (32 mmol) in 50 mL THF at $-10\text{ }^{\circ}\text{C}$, dichlorophenylphosphine (15 mmol) was added slowly, dropwise and further stirred for 18 hours. The color of the solution changes from yellow to orange. The reaction mixture was stripped off of its solvent under vacuum and heated to $80\text{ }^{\circ}\text{C}$ to remove excess 2-((trimethylsilyl)methyl)quinoline. **1** is received as a viscos, brown/orange oil in stoichiometric yields. Compound **1** is air and moisture sensitive and must be stored and handled under inert gas atmosphere. It is soluble in common organic solvents like tetrahydrofuran, dichloromethane, acetonitrile and toluene.

³¹P{¹H} [CDCl₃, 161.996 MHz] $\delta = -14.6$ (s) ppm; ³¹P [CDCl₃, 161.996 MHz] $\delta = -14.6$ (quin., ²*J*_{P-H} = 7.1 Hz) ppm; ¹H [CDCl₃, 400.182 MHz] $\delta =$ ABX spin system (A = B = H, X = P) 3.58 (m, 4H, ²*J*_{A-B} = 13.3 Hz, ²*J*_{A-X} = 1.1 Hz; H27, H29), 7.15 (d, 2H, ⁴*J*_{H-H} = 8.2 Hz; H9, H11), 7.28 (m, 3H; H26, H21, H25), 7.40 (m, 2 H, ³*J*_{H-H} = 8.1 Hz, ³*J*_{H-H} = 6.9 Hz, ⁴*J*_{H-H} = 1.2 Hz; H2, H18), 7.52 (m, 2H; H22, H24), 7.60 (m, 2H, ³*J*_{H-H} = 6.9 Hz, ⁴*J*_{H-H} = 1.5 Hz; H1, H19), 7.65 (d, 2H, ³*J*_{H-H} = 8.1 Hz; H3, H17), 7.84 (d, 2H, ³*J*_{H-H} = 8.5 Hz; H10, H16), 7.95 (d_d, 2H, ³*J*_{H-H} = 8.5 Hz; H6, H20) ppm; ¹³C{¹H} [CDCl₃, 100.636 MHz] $\delta = 38.6$ (d, ¹*J*_{C-P} = 19.3 Hz; C27, C29), 122.2 (d, ³*J*_{C-P} = 4.9 Hz; C9, C11), 125.7 (d, ⁶*J*_{C-P} = 0.7 Hz; C2, C18), 126.50 (d, ⁵*J*_{C-P} = 1.4 Hz; C5, C15), 127.4 (d, ⁵*J*_{C-P} = 0.7 Hz; C3, C17), 128.3 (d, ²*J*_{C-P} = 7.0 Hz; C21, C25), 128.8 (s; C6, C20), 129.2 (s; C1, C19), 132.8 (d, ³*J*_{C-P} = 19.9 Hz; C22, C24), 135.9 (s, C10, C16), 147.9 (d, ⁴*J*_{C-P} = 0.5 Hz; C4, C14), 158.6 (d, ²*J*_{C-P} = 5.9 Hz; C8, C12) ppm.

2.3.5.3. Synthesis of bis(quinaldinyl)phenylphosphine oxide (**2**)

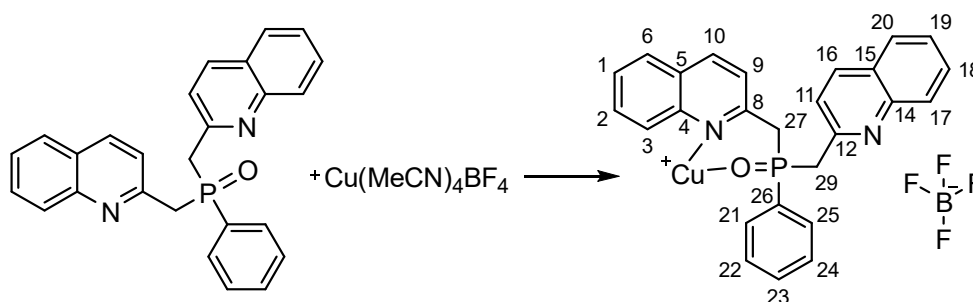


Bis(quinaldinyl)phenylphosphine **1** (5.89 g, 15.0 mmol) is dissolved in 50 mL dichloromethane. Hydrogen peroxide (30 %, 4 mL in 5 mL water) is added dropwise to the mixture while cooling with an ice-bath. After stirring for 4 hours, the solvent was removed and the left-over oil dissolved in ethyl acetate. After extracting the ethyl acetate mixture three times with water, the combined water phases were extracted again three times with ethyl acetate. The combined organic phases were reduced under pressure. The left over solid was dissolved in dry THF and stirred with 4 Å mol sieves in a tea bag to remove any leftover hydrogen peroxide and water. After removal of all volatiles, **2** is received as a white to beige powder. Crystals were received by recrystallization from dichloromethane. Yield: 81.6 %, 5.00 g, 12.2 mmol. The melting point of **2** is 168 °C, decomposition starts at 305 °C, determined from the DTA plot. Compound **2** is soluble in common organic solvents like tetrahydrofuran, dichloromethane and warm acetonitrile.

Elemental Anal. calcd. C₂₆H₂₁N₂OP, C: 76.46, H: 5.18, N: 6.86 %; found: C: 76.16, H: 4.80, N: 6.77 %; **ESI HRMS** (positive mode, CH₃CN/H₂O) m/z calcd for C₂₆H₂₁N₂OP [M+H]⁺: 409.1470 found 409.1461; ³¹P{¹H} [CDCl₃, 161.976 MHz] δ = 35.0 (s, ¹J_{P-C} = 28.6 Hz) ppm; ³¹P [CDCl₃, 161.976 MHz] δ = 35.0 (hept., ²J_{P-H} = 14.0 Hz) ppm; ³¹P{¹H} [CD₂Cl₂, 161.976 MHz] δ = 34.0 (¹J_{P-C} = 28.4 Hz) ppm; ³¹P [CD₂Cl₂, 161.976 MHz] δ = 34.0 (hept., ²J_{P-H} = 14.0 Hz) ppm; ³¹P{¹H} [CD₃CN, 161.976 MHz] δ = 33.7 (¹J_{P-C} = 28.8 Hz) ppm; ³¹P [CD₃CN, 161.976 MHz] δ = 33.7 (hept., ²J_{P-H} = 13.8 Hz) ppm; ¹⁵N [from ¹H¹⁵N HMBC, CDCl₃, 40.5387 MHz] δ = -91.9 (s) ppm; ¹H [CDCl₃, 400.133 MHz] δ = ABX spin system (A = B = H, X = P) 3.92 (d, 4H, ²J_{A-X} = 14.7 Hz; H27, H29), 7.34 (m, 2H, ³J_{H-H} = 7.6, ⁴J_{H-H} = 1.3 Hz; H21, H25), 7.42 (td, 2H, ³J_{H-H} = 8.4 Hz, ³J_{H-H} = 7.3 Hz, ⁴J_{H-H} = 1.6 Hz; H1, H19), 7.44 (m, 1H; H23), 7.47 (dd, 2H, ³J_{H-H} = 8.4 Hz, ⁴J_{H-P} = 1.3 Hz; H9, H11), 7.63 (ddd, 2H, ³J_{H-H} = 8.4 Hz, ³J_{H-H} = 6.9 Hz, ⁴J_{H-H} = 1.5 Hz; H2, H18), 7.69 (dd, ³J_{H-H} = 8.2 Hz, ⁴J_{H-H} = 1.4 Hz; 2H, H22, H24), 7.70 (dd, 2H, ³J_{H-H} = 8.3 Hz, ⁴J_{H-H} = 1.4 Hz; H6, H20), 7.90 (d, 2H, ³J_{H-H} = 8.5 Hz; H3, H17), 7.98 (d, 2H, ³J_{H-H} = 8.5 Hz; H10, H16) ppm; ¹H [CD₂Cl₂, 400.133 MHz] δ = ABX spin system (A = B = H, X = P) 3.93 (d, 4H, ²J_{A-B} = 14.2 Hz, ²J_{A-X} = 15.1 Hz; H27, H29), 7.41 – 7.35 (m, 2H; H21, H25), 7.40 (dd, 2H, ³J_{H-H} = 8.5 Hz, ⁴J_{H-H} = 1.3 Hz; H1, H19), 7.54 – 7.43 (m, 3H; H9, H11, H23), 7.72 – 7.62 (m, 4H; H22, H24, H2, H18), 7.77 (dd, 2H, ³J_{H-H} = 8.2 Hz, ⁴J_{H-H} = 1.4 Hz; H6, H20), 7.91 (dq, 2H, ³J_{H-H} = 8.5 Hz, ⁴J_{H-H} = 0.5 Hz; H3, H17), 8.02 (d, 2H, ³J_{H-H} = 8.5 Hz, H10, H16) ppm; ¹H [CD₃CN, 400.133 MHz] δ = ABX spin system (A = B = H, X = P) 3.97 (d, 4H, ²J_{A-B} = 15.6 Hz, ²J_{A-X} = 14.2 Hz, H27, H29), 7.36 (dd, 2H, ³J_{H-H} = 8.4, ⁴J_{H-H} = 1.3 Hz; H22, H24), 7.47 (dq, 2H, ³J_{H-H} = 6.7 Hz, ⁴J_{H-H} = 1.7 Hz; H1, H19), 7.44 (m, 1H; H23), 7.52 (ddt, 2H, ³J_{H-H} = 8.1 Hz, ⁴J_{PH} = 1.0 Hz; H9, H11), 7.71–7.63 (m, 4H; H22, H24, H2, H18), 7.83 (dd, 2H, ³J_{H-H} = 8.3 Hz, ⁴J_{H-H} = 1.4 Hz; H6, H20), 7.86 (ddd, 2H, ³J_{H-H} = 8.3 Hz, ⁴J_{H-H} = 1.4 Hz; H3, H17), 8.09 (d, 2H, ³J_{H-H} = 8.5 Hz, H10, H16) ppm; ¹³C{¹H} [CDCl₃, 100.623 MHz] δ = 41.9 (d, ¹J_{C-P} = 61.0 Hz; C27, C29), 122.9 (d, ³J_{C-P} = 2.9 Hz; C9, C11), 126.3 (d, ⁵J_{C-P} = 1.2 Hz; C1, C19), 127.0 (d, ⁵J_{C-P} = 1.8 Hz; C5, C15), 127.6 (d, ⁶J_{C-P} = 1.2 Hz; C6, C20), 128.4 (d, ³J_{C-P} = 11.9 Hz; C21, C25), 129.0 (d, ⁵J_{C-P} = 0.9 Hz; C3, C17), 129.6 (d, ⁶J_{C-P} = 0.9 Hz; C2, C18), 131.2 (d, ²J_{C-P} = 9.2 Hz; C22, C24), 131.5 (d, ¹J_{C-P} = 96.9 Hz; C26), 132.0 (d, ⁴J_{C-P} = 2.9 Hz; C23), 136.5 (d, ⁴J_{C-P} = 1.7 Hz; C10, C16), 148.1 (d, ⁴J_{C-P} = 1.9 Hz; C4, C14), 153.6 (d, ²J_{C-P} = 7.2 Hz; C8, C12) ppm; ¹³C{¹H} [CD₂Cl₂, 100.623 MHz] δ = 42.1 (d, ¹J_{C-P} = 60.9 Hz; C27, C29), 123.2 (d, ³J_{C-P} = 2.9 Hz; C9, C11), 126.5 (d, ⁵J_{C-P} = 1.3 Hz; C1, C19), 127.2 (d, ⁵J_{C-P} = 1.9 Hz; C5, C15), 128.0 (d, ⁶J_{C-P} = 1.4 Hz; C6, C20), 128.7 (d, ³J_{C-P} = 11.9 Hz; C21, C25), 129.2 (d, ⁵J_{C-P} = 0.8 Hz; C3, C17), 129.8 (d, ⁶J_{C-P} = 0.8 Hz; C2, C18), 131.4 (d, ²J_{C-P} = 8.9 Hz; C22, C24), 132.1 (d, ⁴J_{C-P} = 2.7 Hz; C23), 132.4 (d, ¹J_{C-P} = 96.3 Hz; C26), 136.5 (d, ⁴J_{C-P} = 1.6 Hz; C10, C16), 148.4 (d, ⁴J_{C-P} = 1.9 Hz; C4, C14), 154.2 (d, ²J_{C-P} = 7.6 Hz; C8,

C12) ppm; $^{13}\text{C}\{^1\text{H}\}$ [CD_3CN , 100.623 MHz] δ = 42.3 (d, $^1J_{\text{C-P}}$ = 61.2 Hz; C27, C29), 123.9 (d, $^3J_{\text{C-P}}$ = 3.1 Hz; C9, C11), 127.2 (d, $^5J_{\text{C-P}}$ = 1.3 Hz; C1, C19), 127.7 (d, $^5J_{\text{C-P}}$ = 1.9 Hz; C5, C15), 128.7 (d, $^6J_{\text{C-P}}$ = 1.2 Hz; C6, C20), 129.2 (d, $^3J_{\text{C-P}}$ = 11.6 Hz; C21, C25), 129.5 (d, $^5J_{\text{C-P}}$ = 1.1 Hz; C3, C17), 130.5 (d, $^6J_{\text{C-P}}$ = 1.1 Hz; C2, C18), 132.0 (d, $^2J_{\text{C-P}}$ = 8.9 Hz; C22, C24), 132.7 (d, $^4J_{\text{C-P}}$ = 2.8 Hz; C23), 133.4 (d, $^1J_{\text{C-P}}$ = 95.9 Hz; C26), 137.0 (d, $^4J_{\text{C-P}}$ = 1.6 Hz; C10, C16), 148.8 (d, $^4J_{\text{C-P}}$ = 2.3 Hz; C4, C14), 155.3 (d, $^2J_{\text{C-P}}$ = 7.9 Hz; C8, C12) ppm; IR: $\tilde{\nu}_{\text{max}}$ (cm^{-1}) = 3062 (vw), 2864 (w), 1617 (w), 1598 (m), 1558 (w), 1501 (m), 1425 (w), 1398 (w), 1311 (w); 1233 (w), 1205 (m), 1190 (s), 1017 (w), 1111 (m), 955 (w), 856 (s), 844 (s), 760 (s), 744 (vs), 725 (m), 693 (s), 659 (m), 639 (w), 616 (m), 555 (m), 542 (m), 497 (m), 477 (s), 467 (s), 444 (s).

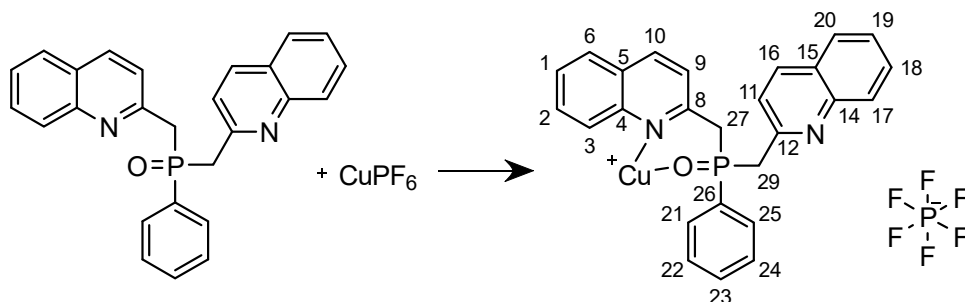
2.3.5.4. Synthesis of bis(quinaldinyl)phenylphosphine oxide copper(I) tetrafluoroborate (**3**)



A solution of bis(quinaldinyl)phenylphosphine oxide **2** (0.428 g, 1.05 mmol) in 20 mL dry, degassed acetonitrile was added to $\text{Cu}(\text{MeCN})_4\text{BF}_4$ (0.33 g, 1.05 mmol) and stirred for a few hours. Afterwards, the solvent was removed and the remaining solid dissolved in dry, degassed dichloromethane. After removal of all volatiles, **3** is received as a yellow powder (0.490 g, 0.877 mmol, 84 %). Yellow crystals were received by diffusion of diethylether into a solution of **3** in dichloromethane. MP: 195 °C. Compound **3** is soluble in DCM or MeCN. **3** is air and moisture sensitive and should be stored under protective gas.

Elemental Anal. calcd. $\text{C}_{26}\text{H}_{21}\text{BCuF}_4\text{N}_2\text{OP}$, C: 55.85, H: 3.79, N: 5.01 % found C: 53.81, H: 3.55, N: 5.12 %, C differs due to formation of phosphorus carbide; **ESI HRMS** (positive mode, $\text{CH}_3\text{CN}/\text{H}_2\text{O}$) m/z calcd for $\text{C}_{26}\text{H}_{21}\text{BCuF}_4\text{N}_2\text{OP} [\text{M}-\text{BF}_4]^-$: 471.0682 found 471.0683; $^{31}\text{P}\{^1\text{H}\}$ [CD_3CN , 161.996 MHz] δ = 36.0 (s) ppm; ^{31}P [CD_3CN , 161.996 MHz] δ = 36.0 (s) ppm; $^{31}\text{P}\{^1\text{H}\}$ [CD_2Cl_2 , 161.976 MHz] δ = 44.0 (s) ppm; ^{31}P [CD_2Cl_2 , 161.976 MHz] δ = 44.0 (s) ppm; $^{19}\text{F}\{^1\text{H}\}$ [CD_3CN , 376.508 MHz] δ = -152.58 (s) ppm; $^{19}\text{F}\{^1\text{H}\}$ [CD_2Cl_2 , 376.442 MHz] δ = -150.43 (s) ppm; $^{11}\text{B}\{^1\text{H}\}$ [CD_3CN , 128.394 MHz] δ = -2.01 (s) ppm; $^{11}\text{B}\{^1\text{H}\}$ [CD_2Cl_2 , 128.378 MHz] δ = -0.75 (s) ppm; ^1H [CD_3CN , 400.182 MHz] δ = 3.99 (d, 4H, 2J = 40.2 Hz; H27, H29), 7.36 (m, 3H, H23, H9, H11), 7.44 (m, 4H, H22, H24, H1, H19), 7.60 (m, 4H, H21, H25, H2, H18), 7.74 (s, 2H, H3, H17), 8.00 (m, 4H, H10, H16, H6, H20,) ppm; ^1H [CD_2Cl_2 , 400.133 MHz] δ = 4.25 (t, 2H, $^2J_{\text{H-H}}$ = 16.2 Hz, CH_2), 4.55 (t, 2H, $J_{\text{H-H}}$ = 13.3 Hz, CH_2), 7.26 (t, 2H, J = 7.7 Hz), 7.38 (t, 2H, J = 7.5 Hz), 7.49 (m, 1H), 7.60 (t, 1H, J = 7.5 Hz), 7.71 (d, 2H, J = 8.1 Hz), 7.83 (t, 2H, J = 7.8 Hz), 7.97 (d, 2H, J = 8.5 Hz), 8.08 (d, 2H, J = 8.7 Hz), 8.22 (d, 2H, J = 8.5 Hz) ppm; $^{13}\text{C}\{^1\text{H}\}$ [CD_3CN , 100.636 MHz] δ = 127.6 (d; C1, C19), 129.0 (s; C3, C17), 129.6 (s; C23), 130.9 (s; C2, C18), 131.8 (s; C21, C25), 133.3 (s; C22, C24), 137.8 (s; C10, C16), 148.3 (s; C4, C14), 155.0 (s; C8, C12) ppm; IR: $\tilde{\nu}_{\text{max}}$ (cm^{-1}) = 3059 (vw), 2964 (vw), 2912 (vw), 2286 (vw), 1619 (vw), 1598 (m), 1564 (vw), 1506 (m), 1432 (w), 1400 (vw), 1311 (vw), 1262 (w), 1238 (w), 1162 (w), , 1049 (vs), 1025 (vs), 910 (w), 844 (m), 799 (m), 747 (s), 716 (s), 693 (m), 659 (m), 642 (m), 618 (w), 556 (m), 540 (w), 520 (m), 501 (m), 488 (m), 427 (m).

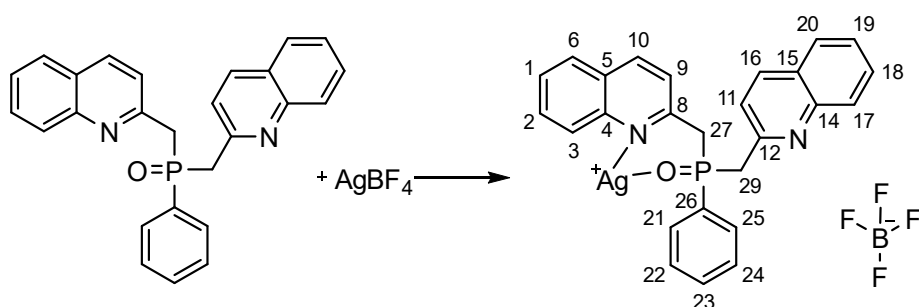
2.3.5.5. Synthesis of bis(quinaldinyl)phenylphosphine oxide copper(I) hexafluoro-phosphate (4)



A solution of bis(quinaldinyl)phenylphosphine oxide **2** (0.166 g, 0.406 mmol) in 20 mL dry, degassed acetonitrile was added to CuPF_6 (0.085 mg, 0.406 mmol) and stirred for a few hours. Afterwards, the solvent was removed and the remaining solid dissolved in dry, degassed dichloromethane. After removal of all volatiles, **4** is received as an orange powder (0.215 g, 0.350 mmol, 86 %). Orange crystals were received by diffusion of diethylether into a solution of **4** in dichloromethane. The so formed crystals do hardly dissolve in dichloromethane again. Compound **4** is air and moisture sensitive and should be stored under protective gas.

Elemental Anal. calcd. $\text{C}_{26}\text{H}_{21}\text{CuN}_2\text{F}_6\text{OP}_2$, C: 50.62, H: 3.25, N: 4.54 % found C: 50.56, H: 3.25, N: 4.41 %; **MALDI MS** (positive mode, sinapinic acid) m/z calcd for $\text{C}_{26}\text{H}_{21}\text{CuN}_2\text{F}_6\text{OP}_2$ $[\text{M}-\text{PF}_6^-]^+$: 471.07 found 471.58; $^{31}\text{P}\{^1\text{H}\}$ $[\text{CD}_3\text{CN}, 161.996 \text{ MHz}] \delta = 36.2$ (s), -141.8 (sept, $^1J_{\text{P-F}} = 710.0$ Hz) ppm; $^{19}\text{F}\{^1\text{H}\}$ $[\text{CD}_3\text{CN}, 376.489 \text{ MHz}] \delta = -72.9$ (d, $^1J_{\text{F-P}} = 706.4$ Hz) ppm; ^1H $[\text{CD}_3\text{CN}, 400.182 \text{ MHz}] \delta = 3.94$ (d, 4H, $^2J_{\text{P-H}} = 40.0$ Hz, CH_2), 7.35 (m, $J = 6.6$ Hz), 7.45 (m, $J = 7.3$ Hz), 7.61 (m), 7.78 (m), 7.89 (m), 8.04 (m) ppm; $^{13}\text{C}\{^1\text{H}\}$ $[\text{CD}_3\text{CN}, 100.636 \text{ MHz}] \delta = 127.6$ (s), 129.0 (s), 129.4 (d, $J = 8.5$ Hz), 130.8 (s), 131.9 (s), 133.1 (s), 137.7 (s), 148.3 (s), 155.0 (s) ppm; Due to the broadness of the signals, an assignment was not possible. **IR:** $\tilde{\nu}_{\text{max}}$ (cm^{-1}) = 3071 (vw), 2963.56 (vw), 2911 (vw), 1620 (vw), 1599 (w), 1566 (vw), 1509 (m), 1435 (w), 1402 (w), 1379 (vw), 1353 (vw), 1309 (w), 1269 (vw), 1243 (w), 1216 (vw), 1160 (m), 1123 (m), 1099 (m), 1072 (vw), 1026 (vw), 999 (vw), 956 (vw), 877 (m), 829 (vs), 780 (s), 748 (vs), 715 (s), 693 (s), 659 (m), 641 (w), 556 (vs), 494 (s), 472 (m), 457 (m), 436 (m).

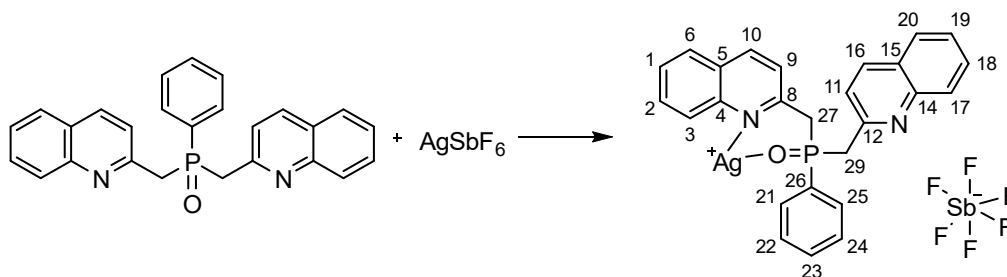
2.3.5.6. Synthesis of bis(quinaldinyl)phenylphosphine oxide silver(I) tetrafluoroborate (5)



A solution of bis(quinaldinyl)phenylphosphine oxide **2** (0.839 g, 2.05 mmol) in 20 mL dry, degassed acetonitrile was added to AgBF_4 (0.4 g, 2.05 mmol). A clear orange solution formed, and a colorless precipitate formed after a while of stirring. The solvent was concentrated in vacuo and left to crystallize (1.128 g, 1.870 mmol, 91 %). Colorless to beige crystals were received by diffusion of diethyl ether into a solution of **5** in acetonitrile. MP: 113 °C. Compound **5** is moisture sensitive and should be stored with the exclusion of light.

Elemental Anal. calcd. $C_{26}H_{21}BAgN_2F_4OP + CH_3CN$, C: 52.21, H: 3.76, N: 6.52 % found C: 52.32, H: 3.99, N: 6.47 %; **MALDI MS** (positive mode, sinapinic acid) m/z calcd for $C_{26}H_{21}BAgN_2F_4OP [M-BF_4]^-$: 515.0437 found 515.45; $^{31}P\{^1H\}$ [CD_3CN , 161.976 MHz] $\delta = 37.9$ (s) ppm; $^{31}P\{^1H\}$ [CD_3CN , 161.976 MHz] $\delta = 37.9$ (quint., $^2J_{P-H} = 13.4$ Hz) ppm; $^{31}P\{^1H\}$ [CD_2Cl_2 , 161.976 MHz] $\delta = 43.6$ (s) ppm; $^{19}F\{^1H\}$ [CD_3CN , 376.461 MHz] $\delta = -152.5$ (s) ppm; $^{19}F\{^1H\}$ [CD_2Cl_2 , 376.461 MHz] $\delta = -153.8$ (s) ppm; $^{11}B\{^1H\}$ [CD_3CN , 128.378 MHz] $\delta = -2.0$ (s) ppm; $^{11}B\{^1H\}$ [CD_2Cl_2 , 128.378 MHz] $\delta = -4.0$ (quint., $^1J_{B-F} = 1.3$ Hz) ppm; ^{15}N [CD_3CN *via* $^1H^{15}N$ HMBC, 40.5371 MHz] $\delta = -121.4$ (s) ppm; ^{15}N [CD_2Cl_2 *via* $^1H^{15}N$ HMBC, 40.5371 MHz] $\delta = -133.5$ (s), -137.0 (s) ppm; 1H [CD_3CN , 400.132 MHz] $\delta =$ ABX 4.23 (m, 4H, $^2J_{H-H} = 14.6$, $^2J_{H-P} = 5.2$ Hz; H27, H29), 7.33 (d_d, 2H, $^3J_{H-H} = 8.5$ Hz, $^4J_{H-H} = 1.0$ Hz; H9, H11), 7.49 (m, 6H, $^3J_{H-H} = 6.7$ Hz, $^4J_{H-H} = 1.7$ Hz; H1, H6, H19, H20, H22, H24), 7.60 (td, 1H, $^3J_{H-H} = 6.8$ Hz, $^4J_{H-H} = 1.4$ Hz; H23), 7.74 (dd, 2H, $^3J_{H-H} = 7.2$, $^4J_{H-H} = 1.4$ Hz; H21, H25), 7.81 (m, 2H, $^3J_{H-H} = 5.0$ Hz, $^4J_{H-H} = 1.7$ Hz; H2, H18), 7.95 (m, 2H, $^3J_{H-H} = 8.2$ Hz; H3, H17), 8.14 (d, 2H, $^3J_{H-H} = 8.5$ Hz; H10, H16) ppm; 1H [CD_2Cl_2 , 400.132 MHz] $\delta = 4.50$ (s, 2H, CH_2 ; H27, H29), 4.70 (t, 2H, $^3J_{H-H} = 14.1$ Hz; H27, H29), 7.32 (d_d, 2H, $^3J_{H-H} = 8.4$ Hz, H9, H11), 7.42 (t, 2H, $^3J_{H-H} = 7.5$ Hz; H10, H16), 7.69 (m, 9H, $^3J_{H-H} = 8.5$ Hz, H1, H3, H6, H17, H19, H20, H22, H23, H24), 8.10 (d, 2H, $^3J_{H-H} = 8.4$; H21, H25), 8.15 (m, 2H; H2, H18) ppm; 1H [CD_2Cl_2 , 400.132 MHz, $-80^\circ C$] $\delta =$ set 1: 8.13 (2H, H10, H16), 7.76 (2H, H6, H20), 7.57 (2H, H3, H17), 7.41 (2H, H1, H19), 7.28 (2H, H2, H18), 7.22 (2H, H9, H11), 4.78 (2H, H27, H29) ppm; set 2: 7.91 (2H, H10, H16), 7.65 (2H, H9, H11), 7.55 (2H, H3, H17), 7.50 (2H, H6, H20), 7.33 (2H, H1, H19), 7.15 (2H, H2, H18), 4.53 (1H, $^2J_{H-H} = 13.6$ Hz, H27 o. H29), 4.12 (1H, $^2J_{H-H} = 17.9$, $^2J_{H-P} = 24.1$ Hz, H27 o. H29) ppm; phenyl ring: 8.40 (2H, H21, H25), 7.74 (2H, H22, H24), 7.26 (1H, H23) ppm; $^{13}C\{^1H\}$ [CD_3CN , 100.623 MHz] $\delta = 43.0$ (d, $^1J_{C-P} = 58.9$ Hz; C27, C29), 124.8 (d, $^3J_{C-P} = 3.9$ Hz; C9, C11), 128.2 (d, $^5J_{C-P} = 1.9$ Hz; C5, C15), 128.3 (d, $^3J_{C-P} = 1.1$ Hz; C6, C20), 129.2 (d, $^6J_{C-P} = 1.3$ Hz; C2, C18), 129.6 (s; C3, C17), 129.9 (d, $^2J_{C-P} = 12.2$ Hz; C21, C25), 130.5 (d, $^1J_{C-P} = 99.0$ Hz; C26), 131.8 (d, $^3J_{C-P} = 9.6$ Hz; C22, C24), 131.9 (s; C1, C19), 134.0 (d, $^4J_{C-P} = 2.9$ Hz; C23), 139.8 (d, $^4J_{C-P} = 1.5$ Hz; C10, C16), 147.5 (d, $^4J_{C-P} = 2.2$ Hz; C4, C14), 155.8 (d, $^2J_{C-P} = 8.9$ Hz; C8, C12) ppm; $^{13}C\{^1H\}$ [CD_2Cl_2 , 100.623 MHz] $\delta = 43.5$ (d, $^1J_{C-P} = 58.5$ Hz; C27, C29), 125.0 (s; C9, C11), 128.0 (s; C5, C15), 127.9 (d, $^3J_{C-P} = 1.5$ Hz; C6, C20), 128.0 (s; C2, C18), 128.7 (s; C3, C17), 129.8 (d, $^2J_{C-P} = 12.7$ Hz; C21, C25), 131.7 (d, $^3J_{C-P} = 10.3$ Hz; C22, C24), 131.9 (s; C1, C19), 134.0 (d, $^4J_{C-P} = 2.9$ Hz; C23), 140.3 (s; C10, C16), 146.3 (s; C4, C14), 155.5 (d; C8, C12, $^2J_{C-P} = 8.1$ Hz); $^{13}C\{^1H\}$ [CD_2Cl_2 , 100.623 MHz, $-80^\circ C$] $\delta =$ set 1: 153.8 (d, $^2J_{C-P} = 10.1$ Hz), 145.2 (s), 139.4 (s), 130.8 (s), 129.0 (s), 128.0 (s), 127.0 (s), 123.0 (d, broad $^3J_{C-P}$ not resolved), 42.5 (s) ppm; set 2: 154.4 (d, $^2J_{C-P} = 8.9$ Hz), 144.4 (s), 139.0 (s), 131.2 (s), 127.4 (s), 127.0 (s), 127.0 (s), 126.2 (s), 123.9 (d, $^1J_{C-P} = 19.0$ Hz), 41.8 (d, $^2J_{C-P} = 41.9$ Hz), phenyl ring: 133.4 (C26), 133.4 (s), 130.8 (s), 130.6 (d) ppm; **IR:** $\tilde{\nu}_{max}$ (cm^{-1}) = 3118 (vw), 3061 (vw), 2964 (vw), 2899(vw), 2895 (vw), 2853 (vw), 1619 (vw), 1598 (w), 1567 (vw), 1509 (w), 1434 (w), 1403 (w), 1377 (vw), 1352 (vw), 1309 (w), 1237 (m), 1167 (m), 1125 (m), 1045 (s), 1033 (vs), 997 (s), 984 (m), 913 (w), 874 (m), 844 (m), 779 (w), 765 (m), 747 (vs), 714 (s), 693 (m), 658 (m), 636 (w), 558 (m), 520 (m), 497 (m), 483 (m), 472 (m), 454 (w), 434 (m).

2.3.5.7. Synthesis of bis(quinaldinyl)phenylphosphine oxide silver(I) hexafluoroantimonate (**6**)



A solution of bis(quinaldinyl)phenylphosphine oxide **2** (0.181 g, 0.443 mmol) in 20 mL dry dichloromethane was added to AgSbF_6 (0.152 g, 0.443 mmol). A clear beige solution formed, where a colorless precipitate appears after a while of stirring. The solvent was removed in vacuo and a beige solid was received (0.297 g, 0.394 mmol, 89 %). Crystals were received by a diffusion of diethylether into a solution of compound **6** in dichloromethane or acetonitrile. Compound **6** is moisture sensitive and should be stored with the exclusion of light.

Elemental Anal. was not possible due to Sb in the compound. **MALDI MS** (positive mode, sinapinic acid) m/z calcd for $\text{C}_{26}\text{H}_{21}\text{SbAgN}_2\text{F}_6\text{OP}$ $[\text{M}+\text{H}-\text{SbF}_6^-]^+$: 516.0515 found 516.08; $^{31}\text{P}\{^1\text{H}\}$ [CD_3CN , 161.976 MHz] $\delta = 41.4$ (s) ppm; $^{19}\text{F}\{^1\text{H}\}$ [CD_3CN , 376.461 MHz] $\delta = -124.1$ (m, $^1J_{\text{F-Sb}} = 1935$ Hz) ppm; ^{121}Sb [CD_3CN , 95.753 MHz] $\delta = 96.6$ (septett, $^1J_{\text{Sb-F}} = 1935$ Hz) ppm; ^{15}N [CD_3CN via $^1\text{H}^{15}\text{N}$ HMBC, 40.5371 MHz] $\delta = -127.2$ (s) ppm; ^1H [CD_3CN , 400.132 MHz] $\delta = \text{ABX } 4.25$ (m, 4H, $^3J_{\text{H-H}} = 14.2$; H27, H29), 7.36 (d, 2H, $^3J_{\text{H-H}} = 8.5$ Hz; H9, H11), 7.51–7.39 (m, 4H, $^3J_{\text{H-H}} = 6.7$ Hz; H1, H19, H6, H20), 7.54 (dd, 2H, $^3J_{\text{H-H}} = 7.6$, $^4J_{\text{H-H}} = 3.1$ Hz; H21, H25), 7.64 (t, 2H, $^3J_{\text{H-H}} = 7.0$; H23), 7.80 (d, 2H, $^3J_{\text{H-H}} = 8.2$ Hz; H2, H18), 7.88–7.83 (m, 2H; H22, H24), 7.91 (d, 2H, $^3J_{\text{H-H}} = 8.1$ Hz; H3, H17), 8.17 (d, 2H, $^3J_{\text{H-H}} = 8.5$ Hz; H10, H16) ppm; $^{13}\text{C}\{^1\text{H}\}$ [CD_3CN , 100.623 MHz] $\delta = 43.3$ (d, $^1J_{\text{C-P}} = 58.7$ Hz; C27, C29), 124.8 (d, $^3J_{\text{C-P}} = 4.3$ Hz; C9, C11), 128.3 (d, $^5J_{\text{C-P}} = 1.7$ Hz; C5, C15), 128.5 (s; C1, C19), 129.3 (s; C2, C18), 129.54 (s; C3, C17), 130.1 (d, $^2J_{\text{C-P}} = 12.2$ Hz; C21, C25), 130.2 (C26, second peak missing), 131.9 (d, $^3J_{\text{C-P}} = 9.8$ Hz; C22, C24), 132.3 (s; C6, C20), 134.2 (d, $^4J_{\text{C-P}} = 3.0$ Hz; C23), 140.4 (s; C10, C16), 147.2 (d, $^4J_{\text{C-P}} = 2.3$ Hz; C4, C14), 155.7 (d, $^2J_{\text{C-P}} = 9.2$ Hz; C8, C12) ppm.

2.3.5.8. Crystallographic and refinement data

Table 5. Crystallographic and refinement data for compounds 2–4.

	2	3	4
Formula	C ₂₆ H ₂₁ N ₂ OP	C ₅₂ H ₄₂ B ₂ Cu ₂ F ₈ N ₄ O ₂ P ₂	C _{59.09} H _{51.09} Cl _{2.30} Cu ₂ F ₁₂ N ₄ O ₂ P ₄
Formula weight	408.42	1117.53	1409.84
[g·mol ⁻¹]			
Colour	colorless	yellow	Colorless
Habit	rod	block	block
T [K]	113	129	123
λ [Å]	0.71073	0.71073	0.71073
Crystal system	monoclinic	monoclinic	monoclinic
Space group	<i>P</i> 2 ₁	<i>P</i> 2 ₁ / <i>c</i>	<i>P</i> 2 ₁ / <i>c</i>
<i>a</i> [Å]	10.3956(5)	9.1235(3)	11.0193(5)
<i>b</i> [Å]	5.7580(3)	10.7088(3)	9.1541(4)
<i>c</i> [Å]	17.4339(11)	23.9819(6)	29.122(2)
α [°]	90	90	90
β [°]	105.249(2)	95.620(3)	98.310(5)
γ [°]	90	90	90
<i>V</i> [Å ³]	1,006.81(10)	2,331.81(12)	2,906.7(3)
<i>Z</i>	2	2	2
ρ _{calc} [g·cm ⁻³]	1.347	1.592	1.611
μ [mm ⁻¹]	0.158	1.061	1.034
<i>F</i> (0 0 0)	428	1136	1429.6
Crystal size [mm]	0.10×0.02×0.02	0.25×0.25×0.20	0.25×0.20×0.10
θ range [°]	2.721–25.417	3.289–28.281	2.173–26.022
Index ranges	-11 ≤ <i>h</i> ≤ 12 -6 ≤ <i>k</i> ≤ 6 -21 ≤ <i>l</i> ≤ 19	-12 ≤ <i>h</i> ≤ 12 -7 ≤ <i>k</i> ≤ 14 -31 ≤ <i>l</i> ≤ 30	-13 ≤ <i>h</i> ≤ 13 -11 ≤ <i>k</i> ≤ 11 -32 ≤ <i>l</i> ≤ 35
reflns collected	9,090	20,435	22,121
Independent reflns	3,558 [<i>R</i> _{int} = 0.0532]	5,767 [<i>R</i> _{int} = 0.0619]	5,744 [<i>R</i> _{int} = 0.0538]
Completeness to theta	96.7 %	99.8 %	99.9 %
Refinement method	Full-matrix least-squares on <i>F</i> ²	Full-matrix least-squares on <i>F</i> ²	Full-matrix least-squares on <i>F</i> ²
Data/restraints/Parameters	3,558 / 1 / 271	5,767 / 0 / 325	5,742 / 5 / 405
Hydrogen atom treatment	constrained	constrained	constrained
<i>R</i> ₁ / <i>wR</i> ₂ (<i>I</i> > 2 σ (<i>I</i>))	0.0536/0.0965	0.0447/0.0875	0.0504/0.1168
<i>R</i> ₁ / <i>wR</i> ₂ (all data)	0.0786/0.1053	0.0697/0.0996	0.0739/0.1294
Goodness-of-fit on <i>F</i> ²	1.038	1.033	1.048
larg. diff peak/hole [e·Å ⁻³]	0.586/-0.295	0.628/-0.379	0.576/-0.446
CCDC No.	2042242	2042245	2042247

Table 6. Crystallographic and refinement data for compounds **5–6b**.

	5	6a	6b
Formula	C ₅₆ H ₄₈ Ag ₂ B ₂ F ₈ N ₆ O ₂ P ₂	C ₅₅ H ₄₈ Ag ₂ Cl ₆ F ₁₂ N ₄ O ₂ P ₂ Sb ₂	C ₅₆ H ₄₈ Ag ₂ F ₁₂ N ₆ O ₂ P ₂ Sb ₂
Formula weight [g·mol ⁻¹]	1,288.30	1,758.85	1,586.18
T [K]	130	123	123
λ [Å]	0.71073	0.71073	0.71073
Crystal system	triclinic	triclinic	triclinic
Space group	<i>P</i> -1	<i>P</i> -1	<i>P</i> -1
colour	colorless	brown-yellow	colorless
habit	block	block	block
<i>a</i> [Å]	9.9850(4)	10.6785(4)	10.0325(3)
<i>b</i> [Å]	11.3496(5)	12.9834(16)	11.2046(4)
<i>c</i> [Å]	12.7437(6)	24.0750(8)	13.4670(4)
α [°]	76.480(4)	74.980(4)	78.726(3)
β [°]	68.868(4)	82.951(3)	69.530(3)
γ [°]	84.189(4)	73.426(4)	86.217(3)
<i>V</i> [Å ³]	1309.51(11)	3085.6(2)	1390.87(8)
<i>Z</i>	1	2	1
ρ _{calc} [g·cm ⁻³]	1.634	1.893	1.894
μ [mm ⁻¹]	0.887	1.884	1.801
<i>F</i> (0 0 0)	648	1716	776
Crystal size [mm]	0.40×0.20×0.20	0.20×0.20×0.05	0.47×0.16×0.05
Θ range [°]	3.246–28.279	2.520–26.372	2.167–30.508
Index ranges	-13 ≤ <i>h</i> ≤ 13 -14 ≤ <i>k</i> ≤ 15 -15 ≤ <i>l</i> ≤ 16	-13 ≤ <i>h</i> ≤ 13 -16 ≤ <i>k</i> ≤ 14 -30 ≤ <i>l</i> ≤ 29	-14 ≤ <i>h</i> ≤ 14 -16 ≤ <i>k</i> ≤ 15 -19 ≤ <i>l</i> ≤ 19
Reflns collected	11,880	25,623	28,183
Independent reflns	6,477 [<i>R</i> _{int} = 0.0299]	12,611 [<i>R</i> _{int} = 0.0486]	8,503 [<i>R</i> _{int} = 0.0330]
Completeness to theta	99.8 %	99.9 %	99.9 %
Refinement method	Full-matrix least-squares on <i>F</i> ²	Full-matrix least-squares on <i>F</i> ²	Full-matrix least-squares on <i>F</i> ²
Data/restraints/ parameters	6,477 / 0 / 376	12,611 / 0 / 799	8,503 / 0 / 371
<i>R</i> ₁ / <i>wR</i> ₂ (<i>I</i> > 2 σ (<i>I</i>))	0.0345/0.0675	0.0509/0.1126	0.0287/0.0634
<i>R</i> ₁ / <i>wR</i> ₂ (all data)	0.0443/0.0732	0.0791/0.1272	0.0418/0.0694
Goodness-of-fit on <i>F</i> ²	1.057	1.031	1.056
larg. diff peak/hole [e·Å ⁻³]	0.635/-0.522	0.971/-1.558	1.201/-0.542
CCDC No.	2042243	2042244	2042246

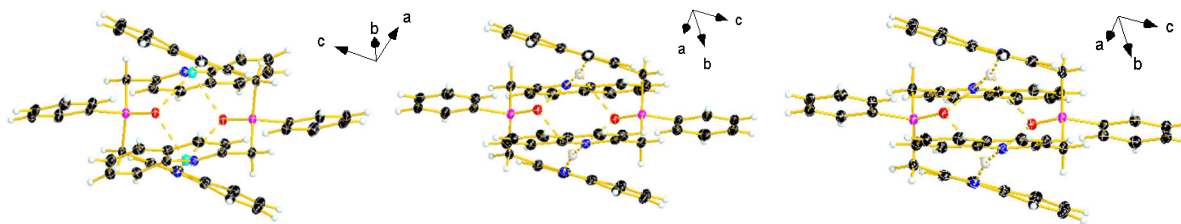


Figure 41. Visualization of the distorted/twisted quinaldiny rings in **3** (left), **5** (center) and **6b** (right). Thermal ellipsoids are drawn at 50 % probability level. Solvent molecules and anions are omitted.

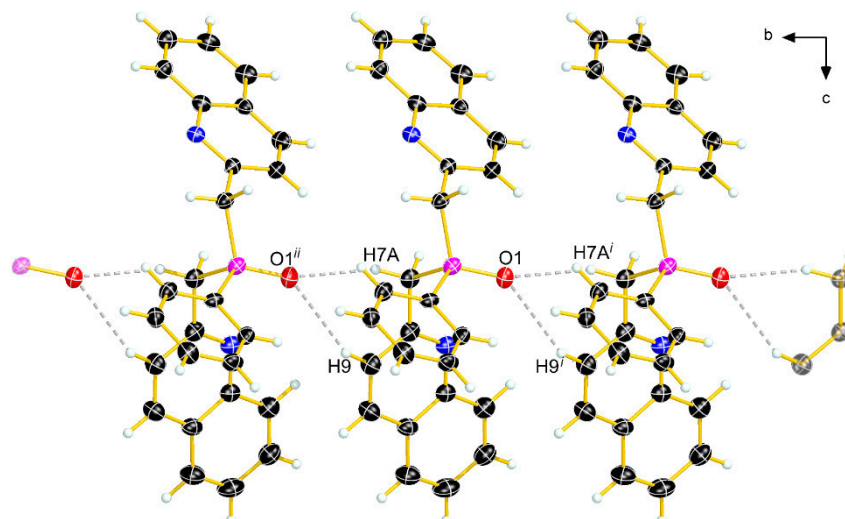


Figure 42. Non-classical hydrogen bonds in the crystal structure of phosphine oxide **2**: $H7A^i \cdots O1$ 2.437 Å, $H9^i \cdots O1$ 2.590 Å. Thermal ellipsoids are drawn at 50 % probability level. Symmetry code $i = x, 1+y, z$.

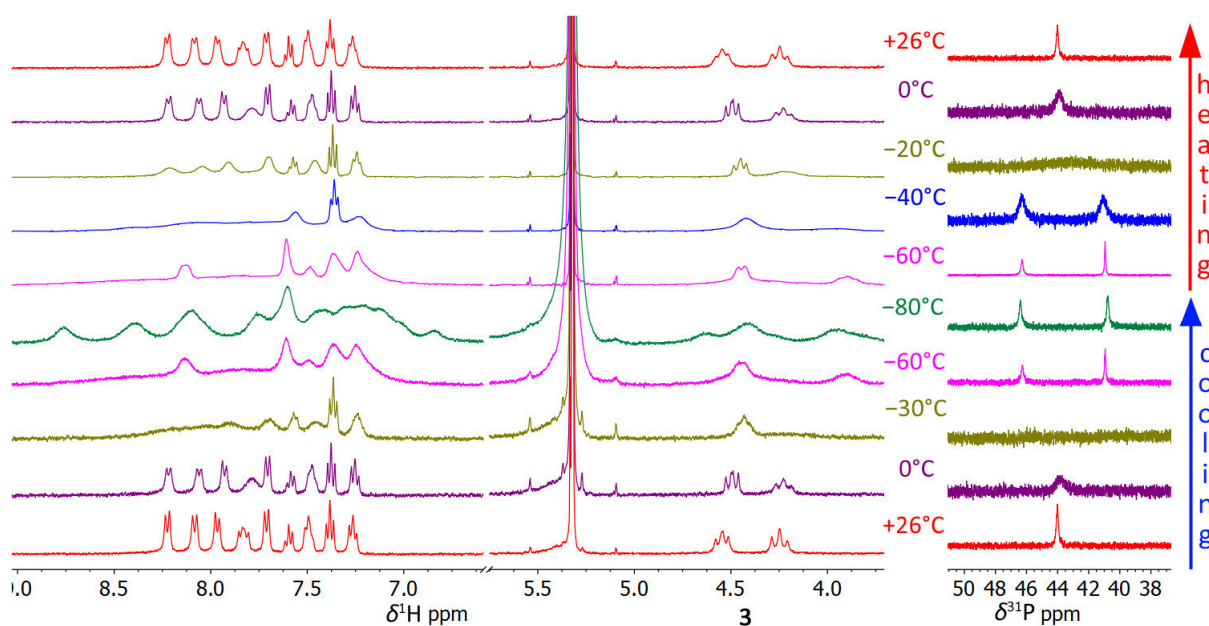


Figure 43. ^{31}P (right) and ^1H NMR (left) of compound **3** in CD_2Cl_2 at different temperatures.

2.3.5.9. Cyclic voltammetry

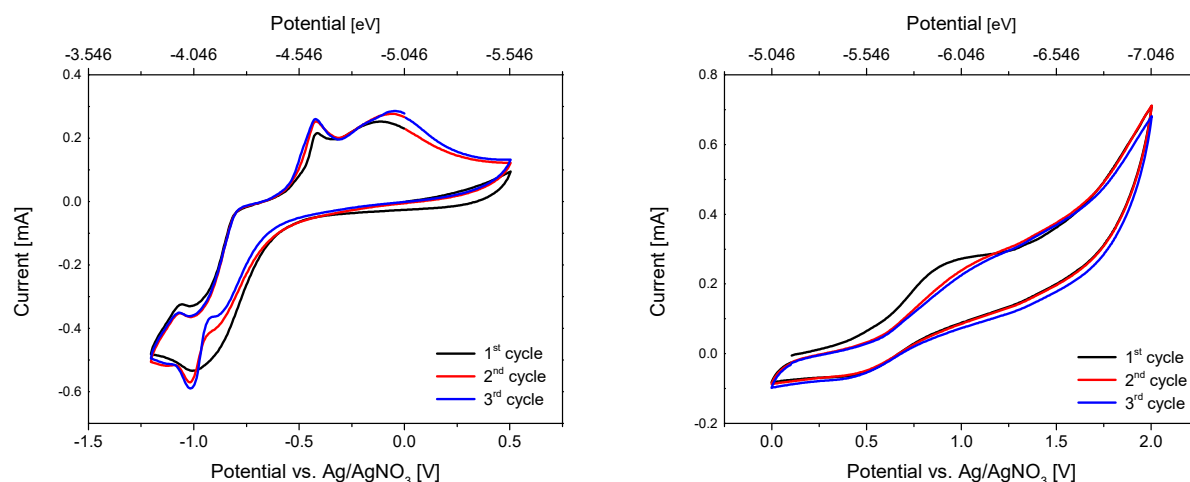


Figure 44. CV curves of complex 3 recorded between -1.2-0.5 V (left) and 0-2 V (right).

2.3.5.10. Hirshfeld surface analysis

To gain more insight into the intermolecular interactions of the presented compounds **2–6b** in the crystal, quantitative Hirshfeld surface analysis was conducted (Figure 45). In all structures of the complexes, attractive intermolecular (N \cdots H–C, F \cdots H–C) interactions (25.4–35.6%) and weak π - π -interactions (23–29.5%) are present to roughly the same extent (Figure 45). The only complex, that shows additional O \cdots H–C interactions (0.5%) is **6a** due to the different coordination geometry and the resulting more exposed oxygen atom. All complexes show strong intermolecular interactions with the fluorine containing counterion indicated by sharp spikes in the fingerprint plots. Contrary to the complexes, in the structure of the free ligand **2**, weak π - π -interactions (C \cdots C, C \cdots H–C) are predominant (38.6%). The shortest C \cdots H–C contacts originate from the CH₂ groups, as indicated by red dots in the d_{norm} maps.

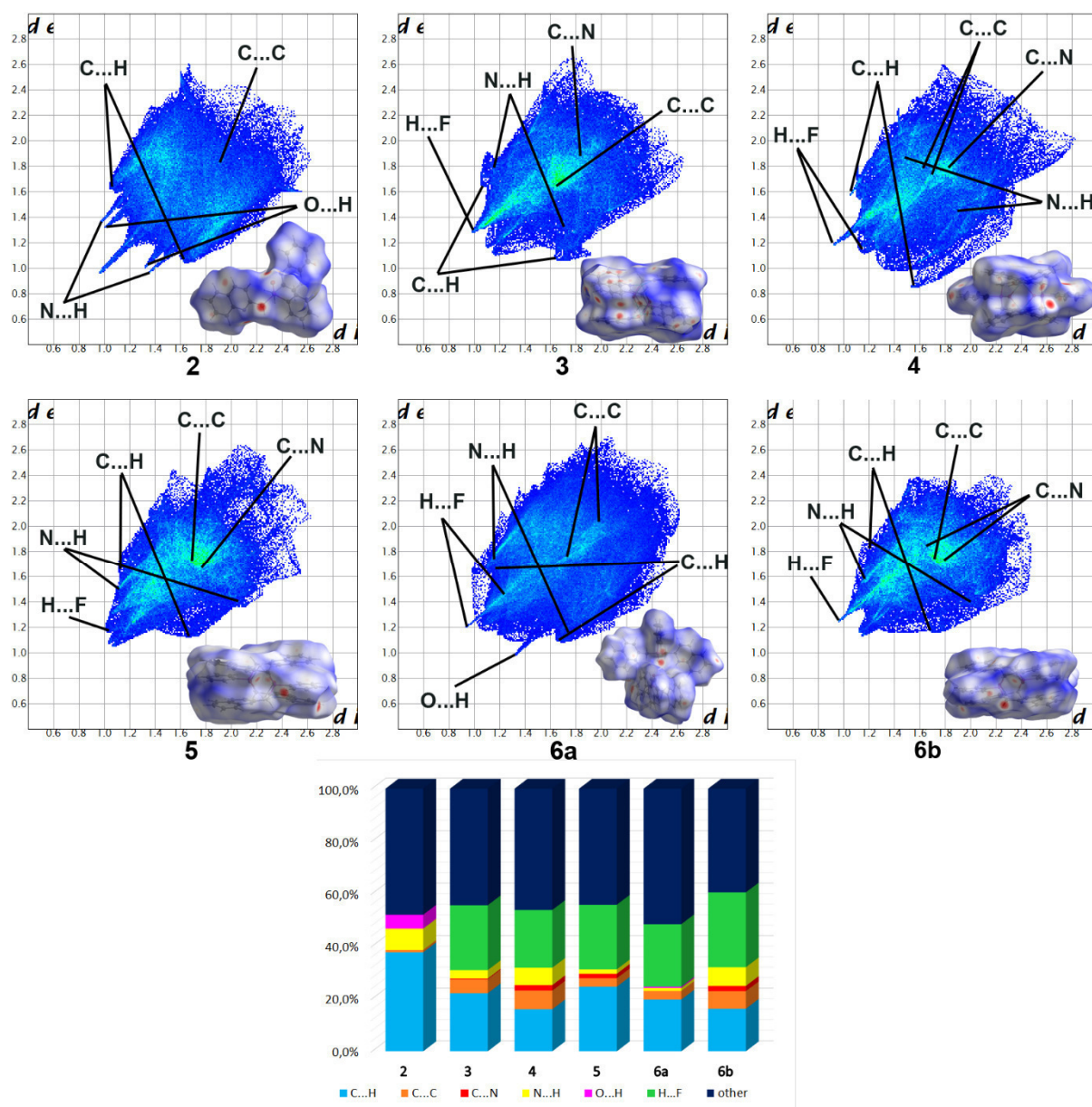


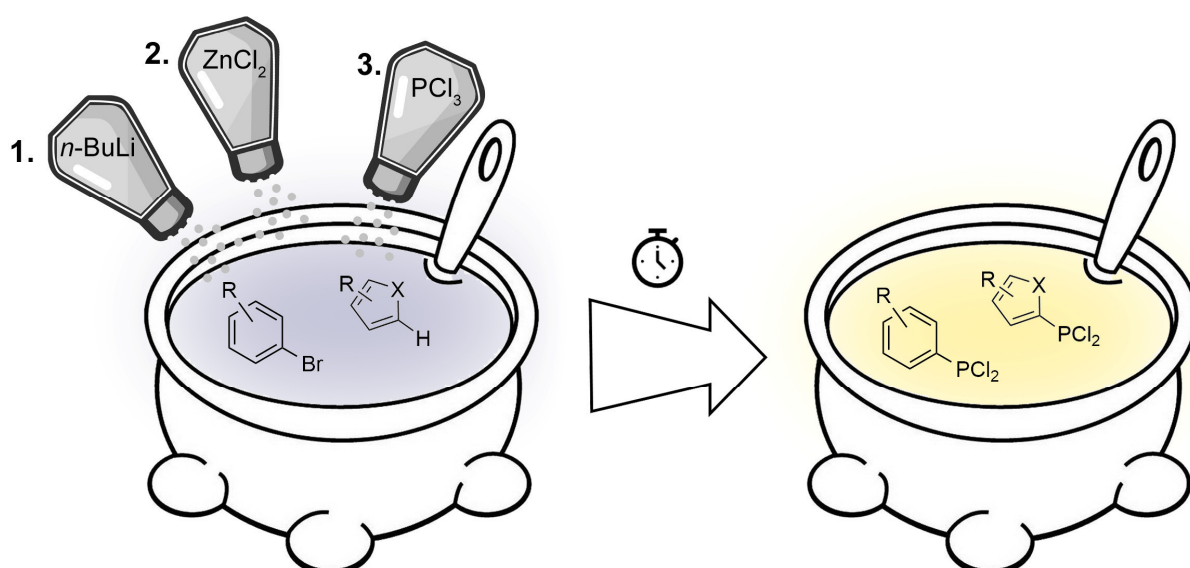
Figure 45. d_{norm} maps and fingerprint plots of compounds **2**–**6b**. The diagram on the bottom is showing the close contacts of compounds **2**–**6b** in the crystal packing.

2.4. The formation of P–C-bonds utilizing organozinc reagents for the synthesis of aryl- and heteroaryl-dichlorophosphines

Christin Kirst, Jonathan Tietze, Marian Ebeling, Lukas Horndasch, Konstantin Karaghiosoff

submitted to *Journal of Organic Chemistry*

Christin Kirst synthesized 10 of the 19 presented dichlorophosphines. She established the synthetic route and evaluated the corresponding NMR spectroscopy results in solution of these compounds. She further managed the project and wrote the original draft of the manuscript and designed the TOC graphic.



Abstract: Aryl- and heteroaryl-dichlorophosphines are mildly and selectively made in a one-pot synthesis in moderate to good yields starting from the respective aryl bromides or five-membered heterocycles, following lithiation with *n*BuLi, transmetalation with ZnCl₂ and subsequently the reaction with PCl₃. Selected aryl- and heteroaryl-dichlorophosphines were successfully synthesized using this reaction method and could easily be purified after isolation. The intermediate formation of the organozinc species is essential, as it prevents the formation of multiple substitution products. Important are also the reaction conditions: the usage of the proper solvent for the respective aromatic precursors and removal of the remaining salts by addition of a dioxane/pentane mixture. Depending on the solvent and steric demand of the substituent, mono- and bis-substitution products can be formed but formation also prevented. Hereby, different organozinc species might play an important role.

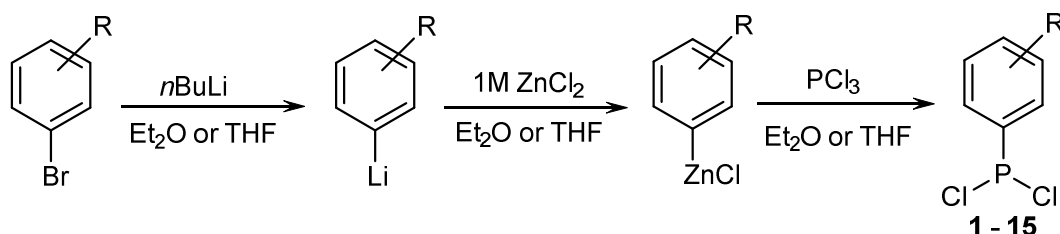
Remarkably, there are only few examples in the literature, which describe the synthesis of dichlorophosphines by reaction of an organozinc reagent with PCl_3 . Daugulis *et al.*^[22] and Wright *et al.*^[23] used an organozinc reagent for the selective preparation of 4-tolyldichlorophosphine, 4-(*tert*-butyl)phenyl)dichlorophosphine and 3,5-dimethylphenyldichlorophosphine and utilized these compounds *in situ* for the synthesis of other organophosphorus compounds. Bickelhaupt *et al.*^[24] described the synthesis of 2-(dichlorophosphino)-4,5-dimethylphosphinine using the organozinc derivative of the respective phosphinine. Ding *et al.*^[25] synthesized the alkyl dichlorophosphine (*n*-oct) PCl_2 starting from the organozinc compound. Last but not least, Zhu *et al.*^[26] prepared 2-pyridyldichlorophosphine utilizing the corresponding organozinc compound. Furthermore, organozinc compounds have been utilized for the synthesis of asymmetric monochlorophosphines in a few publications.^[27–29] Nevertheless, no systematic investigation of the formation of P–C-bonds starting from organozinc compounds is found in the literature.

During our systematic investigation on the synthesis of functionalized phosphines, we had a closer look into the formation of P–C-bonds with the aid of milder organozinc reagents. Our research is focused on the selective and scalable synthesis as well as the straight-forward isolation of clean products in high yields. In that regard, we have examined, as an example, the reaction of aryl- and heteroaryl-Zn compounds with PCl_3 and present herein our results on the synthesis of these dichlorophosphines.

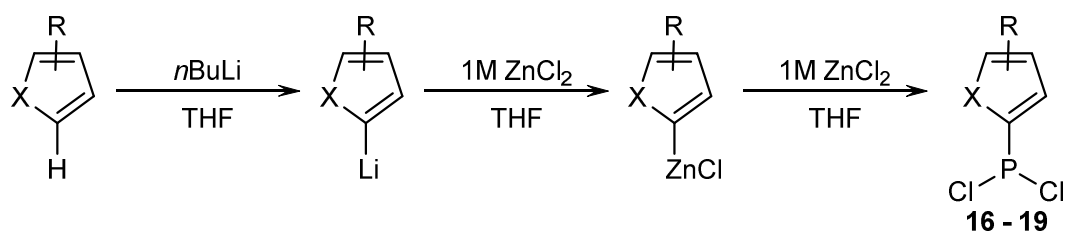
2.4.2. Results and discussion

The emphasis of our investigations is focused on the synthesis of functionalized aryl- or heteroaryl-dichlorophosphines starting from easily accessible aryl bromides or heteroaryl compounds. In the case of dichlorophosphines based on five-membered aromatic rings, the first step corresponds to a simple deprotonation. These dichlorophosphines are of special significance for the synthesis of a variety of organophosphorus compounds.^[30]

The aryl-bromides or heteroaryl compounds are first lithiated with *n*-butyllithium, according to well-known protocols, followed by transmetalation with dry zinc chloride ($-78/-100\text{ }^\circ\text{C}$ in THF, $-10\text{ }^\circ\text{C}$ in diethyl ether). THF and diethyl ether are used as a solvent for the reactions. During the lithiation, in part cloudy solutions are formed, which mostly clear up after the addition of the zinc chloride solution. After reaction of the resulting organozinc species with the equimolar amount of PCl_3 ($-78/-100\text{ }^\circ\text{C}$ in THF, $-10\text{ }^\circ\text{C}$ in diethyl ether), the dichlorophosphine is formed under mild conditions and can be isolated after purification in good yields (see Scheme 11 and Scheme 12). The order of the additions, e.g., if PCl_3 is added to the organozinc compound or the other way around, has no impact on the yields of the reaction products in most cases. Detailed reaction conditions are shown in Table 7 and in the experimental part. For almost all reactions, ^{31}P NMR spectra measured of samples taken straight from the reaction mixture show more than 80 % conversion of PCl_3 to the desired dichlorophosphine, with the exception being dichlorophosphine **11** (70 %).



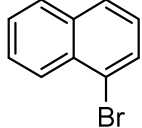
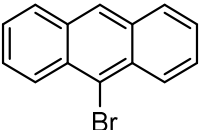
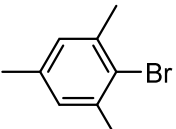
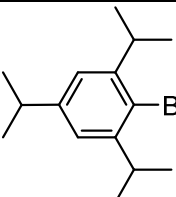
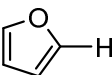
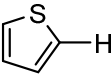
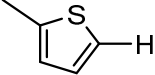
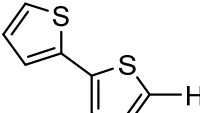
Scheme 11. Synthesis of aryl dichlorophosphines **1-15** *via* an organozinc species. For R see Table 7.



Scheme 12. Synthesis of heteroaryl dichlorophosphines **16-19** via an organozinc species. For R and X see Table 7.

Table 7. Reaction conditions of the syntheses of the different aryl- and heteroaryl dichlorophosphines **1-9**. Isolated yields are referenced to the used amount of starting material.

R-PCl ₂	Starting material	Reaction conditions	Isolated yield	Yield according to the literature
1		<i>n</i> BuLi/ $-78\text{ }^{\circ}\text{C}$ /THF, 2 h; ZnCl ₂ in THF (1 M)/ $-78\text{ }^{\circ}\text{C}$ →RT, 2 h; PCl ₃ / $-78\text{ }^{\circ}\text{C}$ →RT, 16 h	63 %	66 % ^[31] (method B)
2		<i>n</i> BuLi/ $-78\text{ }^{\circ}\text{C}$ /THF, 2 h; ZnCl ₂ in THF (1 M)/ $-78\text{ }^{\circ}\text{C}$ →RT, 2 h; PCl ₃ / $-78\text{ }^{\circ}\text{C}$ →RT, 16 h	55 %	68 % ^[31] (method B)
3		<i>n</i> BuLi/ $-78\text{ }^{\circ}\text{C}$ /THF, 2 h; ZnCl ₂ in THF (1 M)/ $-78\text{ }^{\circ}\text{C}$ →RT, 2 h; PCl ₃ / $-78\text{ }^{\circ}\text{C}$ →RT, 16 h	82 %	No yields reported ^[22,32]
4		<i>n</i> BuLi/ $-78\text{ }^{\circ}\text{C}$ /THF, 2 h; ZnCl ₂ in THF (1 M)/ $-78\text{ }^{\circ}\text{C}$ →RT, 2 h; PCl ₃ / $-78\text{ }^{\circ}\text{C}$ →RT, 16 h	87 %	70 % ^[33]
5		<i>n</i> BuLi/ $-78\text{ }^{\circ}\text{C}$ /THF, 0.5 h; ZnCl ₂ in THF (1 M)/ $-78\text{ }^{\circ}\text{C}$ →RT, 2 h; PCl ₃ / $-78\text{ }^{\circ}\text{C}$ →RT, 16 h	54 %	60 % ^[34] (method B)
6		<i>n</i> BuLi/ $-78\text{ }^{\circ}\text{C}$ /THF, 0.5 h; ZnCl ₂ in THF (1 M)/ $-78\text{ }^{\circ}\text{C}$ →RT, 2 h; PCl ₃ / $-78\text{ }^{\circ}\text{C}$ →RT, 16 h	49 %	26 % ^[35] (method B)
7		<i>n</i> BuLi/ $-78\text{ }^{\circ}\text{C}$ /THF, 2 h; ZnCl ₂ in THF (1 M)/ $-78\text{ }^{\circ}\text{C}$ →RT, 2 h; PCl ₃ / $-78\text{ }^{\circ}\text{C}$ →RT, 16 h	65 %	83 % ^[36] (method A)
8		<i>n</i> BuLi/ $-78\text{ }^{\circ}\text{C}$ /THF, 1 h; ZnCl ₂ in THF (1 M)/ $-78\text{ }^{\circ}\text{C}$ →RT, 2 h; PCl ₃ / $-78\text{ }^{\circ}\text{C}$ →RT, 16 h	61 %	89 % ^[36] (method A)
9		<i>n</i> BuLi/ $-78\text{ }^{\circ}\text{C}$ /THF, 1 h; ZnCl ₂ in THF (1 M)/ $-78\text{ }^{\circ}\text{C}$ →RT, 2 h; added to PCl ₃ in THF/ $-78\text{ }^{\circ}\text{C}$ →RT, 16 h	60 %	80 % ^[37]
10		<i>n</i> BuLi/ $-78\text{ }^{\circ}\text{C}$ /THF, 1 h; ZnCl ₂ in THF (1 M)/ $-78\text{ }^{\circ}\text{C}$ →RT, 2 h; added to PCl ₃ in THF/ $-78\text{ }^{\circ}\text{C}$ →RT, 16 h	61 %	New compound
11		<i>n</i> BuLi/ $-100\text{ }^{\circ}\text{C}$ /THF, 15 min; ZnCl ₂ in THF (1 M)/ $-100\text{ }^{\circ}\text{C}$, 30 min; PCl ₃ / $-100\text{ }^{\circ}\text{C}$ →RT, 16 h	42 %	44 % ^[38]

12		<i>n</i> BuLi/ $-78\text{ }^{\circ}\text{C}$ /THF, 2 h; ZnCl ₂ in THF (1 M)/ $-78\text{ }^{\circ}\text{C}$ →RT, 2 h; PCl ₃ / $-78\text{ }^{\circ}\text{C}$ →RT, 16 h	66 %	83 % ^[8] (method B)
13		<i>n</i> BuLi/ $-78\text{ }^{\circ}\text{C}$ /THF, 2 h; ZnCl ₂ in THF (1 M)/ $-78\text{ }^{\circ}\text{C}$ →RT, 2 h; PCl ₃ / $-78\text{ }^{\circ}\text{C}$ →RT, 16 h	62 %	61 % ^[39]
14		<i>n</i> BuLi/ $-10\text{ }^{\circ}\text{C}$ /Et ₂ O, 3 h → 30 °C; ZnCl ₂ in Et ₂ O (1 M)/ $-10\text{ }^{\circ}\text{C}$ → 30 °C, 2 h; PCl ₃ / $-10\text{ }^{\circ}\text{C}$ → RT, 16 h	63 %	79 % ^[40] (method B)
15		<i>n</i> BuLi/ $-10\text{ }^{\circ}\text{C}$ /Et ₂ O, 3 h → 30 °C; ZnCl ₂ in Et ₂ O (1 M)/ $-10\text{ }^{\circ}\text{C}$ → 30 °C, 2 h; PCl ₃ / $-10\text{ }^{\circ}\text{C}$ → RT, 16 h	67 %	76 % ^[41] (method A)
16		<i>n</i> BuLi/ $-78\text{ }^{\circ}\text{C}$ /THF, 2 h; ZnCl ₂ in THF (1 M)/ $-78\text{ }^{\circ}\text{C}$ →RT, 2 h; added to PCl ₃ in THF/ $-78\text{ }^{\circ}\text{C}$ →RT, 16 h	39 %	67 % ^[11] (method B)
17		<i>n</i> BuLi/ $-78\text{ }^{\circ}\text{C}$ /THF, 2 h; ZnCl ₂ in THF (1 M)/ $-78\text{ }^{\circ}\text{C}$ →RT, 2 h; PCl ₃ / $-78\text{ }^{\circ}\text{C}$ →RT, 16 h	52 %	40–50% ^[42]
18		<i>n</i> BuLi/ $-78\text{ }^{\circ}\text{C}$ → 0 °C/THF, 1 h; ZnCl ₂ in THF (1 M)/ $-78\text{ }^{\circ}\text{C}$ → RT, 2 h; PCl ₃ / $-78\text{ }^{\circ}\text{C}$ → RT, 16 h	68 %	No yields reported ^[43]
19		<i>n</i> BuLi/ $-78\text{ }^{\circ}\text{C}$ → RT/THF, 1 h; ZnCl ₂ in THF (1 M)/ $-78\text{ }^{\circ}\text{C}$ → RT, 2 h; PCl ₃ / $-78\text{ }^{\circ}\text{C}$ → RT, 16 h	47 %	Mixture of products ^[44]

The main problem when trying to isolate the dichlorophosphines, is the removal of the inorganic salts ZnCl₂ and LiCl left in the reaction mixture. When carrying out the reaction in THF as a solvent, it is necessary to add pentane and dioxane for the removal of the salts. If only pentane is used when trying to precipitate the salts, a viscous oil is obtained, which still contains ZnCl₂ and LiCl. A distillation to isolate and purify the dichlorophosphine is not successful in this case. Whereas, when using pentane together with dioxane, after filtration, a subsequent distillation or recrystallization of the products **1–17** is possible. The NMR data of the dichlorophosphines presented here have all been described before in the literature, except for dichlorophosphines **3**, **5**, **10**, **18** and **19** which are listed in the experimental section.

When synthesizing the halogen substituted dichlorophosphines **5** and **6** shorter reaction times after the lithiation step are needed to reduce homocoupling reactions. For the synthesis of dichlorophosphines **9**, **10** and **16**, the respective organozinc species has to be added to PCl₃ in THF to avoid multiple substitution. When synthesizing dichlorophosphine **11**, lower temperatures of $-100\text{ }^{\circ}\text{C}$ and below are needed to minimize the formation of side products resulting from nucleophilic additions to the electrophilic carbon atom. The ³¹P NMR spectra taken from a sample of the reaction mixture of **11** also shows the formation of the respective monochlorophosphine, while supposedly unreacted PCl₃ is also present. The integral ratio of dichlorophosphine to monochlorophosphine to PCl₃ is almost

exactly 5:1:1. When the organozinc species is added to PCl_3 in THF, the ^{31}P NMR spectra looks exactly the same. So, reactivity seems not to be the issue at hand. The observations rather indicate a disproportionation of the formed dichlorophosphine **11** in the reaction mixture. Compound **11** on its own has proven to be stable in THF. A complication in the synthesis of **16** is the removal of dioxane during work up and distillation without losing significant amounts of product. A distillation at a higher pressure of 10 mbar was performed, but complete separation could not be achieved. An issue in the synthesis of dichlorophosphine **19** is the separation of 2,2'-bithiophene from the final product. A ^{31}P NMR taken from the reaction mixture shows 90 % conversion of PCl_3 to the desired dichlorophosphine. However after distillation a ^1H NMR shows that roughly 20 % of 2,2'-bithiophene is present. The most probable cause for this is a disproportionation during distillation, where the respective monochlorophosphine stays in the distilling flask. This was not further investigated.

While for the synthesis of compounds **1–8**, **12**, **13**, and **17–19** no multiple substitution products were observed in THF, it is of great importance to stick to the right stoichiometry. Already a slight excess of ZnCl_2 in the reaction mixture can trigger the acid-catalyzed competing reaction of THF with PCl_3 , as has been described before in the literature.^[45,46] Both degradation products of THF, $[\text{Cl}(\text{CH}_2)_4\text{O}]\text{PCl}_2$ ($\delta = 178$ ppm) and $[\text{Cl}(\text{CH}_2)_4\text{O}]_2\text{PCl}$ ($\delta = 166$ ppm), are visible in the ^{31}P NMR spectrum of the reaction mixture. For instance, the usage of 1.5 eq of ZnCl_2 leads to the occurrence of at least 15 % of degradation products in total. In case of the dichlorophosphines **14** and **15**, performing the synthesis in diethyl ether leads to a selective reaction. The products are obtained without any multiple substitution side products or degradation products. The remaining salts can be removed easily by changing the solvent to pentane and the products **14** and **15** are purified by recrystallization.

When attempting the synthesis of dichlorophosphines **1–3** in diethyl ether, surprisingly the monochlorophosphines are formed almost exclusively, as indicated by the ^{31}P NMR spectrum of the reaction mixture. The influence of the solvent on the substitution at phosphorus is apparently dependent on the sterical demand of the organometallic reagent. Bulky substituents in *ortho*-position to the carbanionic carbon atom lead to the sole synthesis of the dichlorophosphines **14** and **15** in diethyl ether. This unanticipated disparity raises the question of the identity of the organozinc reagents in THF and diethyl ether.

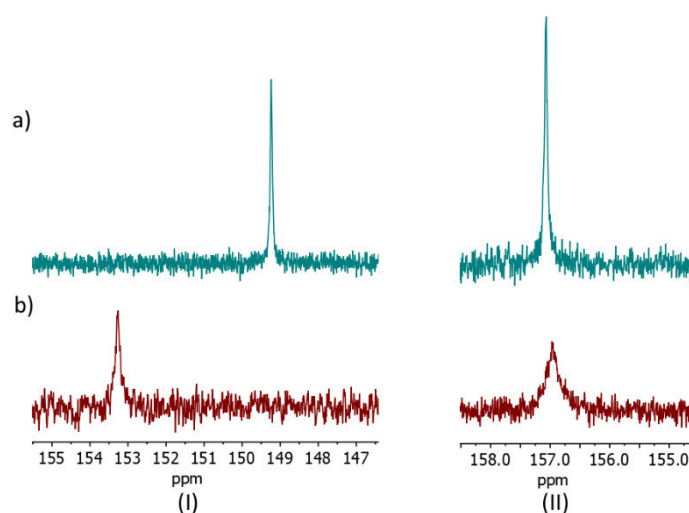


Figure 46. ^{13}C NMR spectra of *p*-tolyl–Li (I) and (2,4,6-triisopropylphenyl)–Li (II) after transmetallation with ZnCl_2 highlighting the zinc-bonded carbon atom. Reactions done in a) diethyl ether and b) in THF.

Therefore, NMR measurements of the reaction mixtures of the organozinc species resulting from *p*-tolyl–Li (I) and (2,4,6-triisopropylphenyl)–Li (II) after transmetallation with ZnCl_2 in THF or diethyl ether at RT were performed. The ^{13}C NMR spectra clearly show a difference depending on the solvent for

species (I), while no clear difference can be observed for species (II) (see Figure 46). The measured NMR spectra and a more detailed analysis can be found in the SI.

2.4.3. Conclusion

The synthesis of aryl- and heteroaryl-dichlorophosphines starting from the respective aryl-Li/heteroaryl-Li compound *via* transmetalation on to an organozinc intermediate to lower the reactivity is a convenient alternative to known synthetic procedures of the formation of P–C-bonds. This mild reaction can be done in one-pot and the resulting dichlorophosphines can easily be isolated *via* distillation or recrystallization. For the success of the reaction, it is essential to comply with the right conditions like the solvent used, stoichiometry and the subsequent work-up using dioxane/pentane. While in THF, the dichlorophosphines are obtained simply and successfully, the reaction in diethyl ether is dependent on the bulkiness of the substituent in *ortho*-position. First NMR spectroscopical investigations of the organozinc species show a divergence in the appearance depending on the aryl-substituent and solvent used, which could be the reason for the different reaction behavior. Future work will be done to further extend this synthetic approach to the synthesis of other dichlorophosphines and to examine the mechanism of their formation in more detail.

2.4.4. Experimental section

All reactions were performed using Schlenk techniques under dry argon. Unless otherwise specified, all reagents and solvents were purchased from commercial sources and used as received. The solvents THF and diethyl ether were dried over elemental sodium and freshly distilled prior to use. CDCl₃ was distilled and stored under Ar atmosphere over molecular sieves. NMR spectra were recorded on a Bruker Avance III spectrometer operating at 400.1 MHz (¹H), 161.9 MHz (³¹P) and 100.6 MHz (¹³C). As well as on a JEOL Eclipse 270+ instrument operating at 109.4 MHz (³¹P). Chemical shifts are referred to TMS (¹H, ¹³C) and 85 % H₃PO₄ (³¹P) as external standards. All NMR spectra were measured, if not mentioned otherwise, at 25 °C. The assignment of the signals for **3**, **5**, **10**, **18** and **19** are based on 2D (¹H,¹H–COSY, ¹H,¹³C–HSQC and ¹H,¹³C–HMBC) experiments. The multiplicity of each resonance observed in the NMR spectra is reported as s = singlet; d = doublet; t = triplet; q = quartet; m = multiplet.

Synthesis of aryl-dichlorophosphines **1–8**, **12** and **13** in THF. General procedure (for individual reaction times see Table 1): To a solution of the respective aryl-bromide (1.0 eq., 2 mL for liquids and 2 g/4 g for solids) in anhydrous THF (20 mL) the appropriate amount of *n*-butyllithium (1.0 eq., 2.4 M solution in hexane) was added dropwise at –78 °C and the reaction stirred for another hour. To the resulting suspension, a solution of anhydrous zinc(II) chloride (1.0 eq) in anhydrous THF (1 M), at –78 °C was added. The reaction was stirred (2 hrs) while warming up to RT to give a colorless/cloudy solution. Phosphorus trichloride (1.0 eq) was added dropwise at –78 °C and the resulting mixture was stirred for another 16 hours while warming to RT. Afterwards, the solvent was removed under reduced pressure. To precipitate the metal salts, 20 mL of pentane and 20 mL of dioxane were added and the mixture stirred for another hour. After removal of the solids via a Schlenk frit, the remaining solution is concentrated *in vacuo*. The left-over liquid is distilled to receive the purified aryl- and heteroaryl-dichlorophosphines **1–8** in moderate to good yields. Dichlorophosphines **12** and **13** are recrystallized from pentane in good yields.

p-tolylidichlorophosphine (**1**): 1.96 g, 63 %, colorless liquid, b.p. 57 °C at 1·10^{–3} mbar, ³¹P{¹H} NMR [CDCl₃, 109.365 MHz] δ = 162.4 ppm (s) (Ref.^[23] ³¹P NMR [C₆D₆, 161.98 MHz, +25 °C] δ = 162.8 (s) ppm, for ¹H and ¹³C NMR see Ref.^[23]).

4-(*tert*-butyl)phenyldichlorophosphine (**2**): 1.45 g, 55 %, colorless liquid, b.p. 72 °C at $1 \cdot 10^{-3}$ mbar, $^{31}\text{P}\{^1\text{H}\}$ NMR [CDCl_3 , 109.365 MHz] $\delta = 162.4$ (s) ppm (Ref.^[23] $^{31}\text{P}\{^1\text{H}\}$ NMR (161.98 MHz, C_6D_6 , +25 °C), $\delta = 162.8$ (s) ppm, for ^1H and ^{13}C NMR see Ref.^[23]).

3,5-dimethylphenyldichlorophosphine (**3**): 2.50 g, 82 %, colorless liquid, b.p. 53-57 °C at $1 \cdot 10^{-3}$ mbar, $^{31}\text{P}\{^1\text{H}\}$ NMR [CDCl_3 , 161.996 MHz] $\delta = 162.9$ ppm (s), ^1H NMR [CDCl_3 , 400.132 MHz] $\delta = 7.50$ (d, 2H, $^3J_{\text{H-P}} = 9.9$ Hz, $^4J_{\text{H-H}} = 0.7$ Hz), 7.18 (m, 1H), 2.39 (q, 6H, 2CH₃, $^4J_{\text{H-H}} = 0.7$ Hz) ppm; $^{13}\text{C}\{^1\text{H}\}$ NMR [CDCl_3 , 100.621 MHz] $\delta = 21.4$ (s, 2 CH₃), 127.8 (d, 2CH, $^2J_{\text{C-P}} = 32.0$ Hz), 134.7 (s, CH), 138.9 (d, Cq, $^3J_{\text{C-P}} = 8.5$ Hz), 140.3 (d, Cq, $^1J_{\text{C-P}} = 51.4$ Hz) ppm.

4-fluorophenyldichlorophosphine (**4**): 3.12 g, 87 %, colorless liquid, b.p. 62 °C at $1 \cdot 10^{-3}$ mbar, $^{31}\text{P}\{^1\text{H}\}$ NMR [CDCl_3 , 109.365 MHz] $\delta = 159.3$ (s) ppm; (Ref.^[33] $^{31}\text{P}\{^1\text{H}\}$ NMR [CDCl_3 , +25 °C], $\delta = 158.8$ ppm, for ^1H and ^{13}C NMR see Ref.^[47]).

4-chlorophenyldichlorophosphine (**5**): 1.20 g, 54 %, colorless liquid, b.p. 49 °C at $1 \cdot 10^{-3}$ mbar, $^{31}\text{P}\{^1\text{H}\}$ NMR [CDCl_3 , 109.365 MHz] $\delta = 159.5$ (s) ppm; ^1H NMR [CDCl_3 , 400.133 MHz] $\delta = 7.83$ (m, 2H), 7.50 (m, 2H) ppm; $^{13}\text{C}\{^1\text{H}\}$ NMR [CDCl_3 , 100.623 MHz] $\delta = 139.4$ (d, $^4J_{\text{C-P}} = 1.4$ Hz), 139.0 (d, $^1J_{\text{C-P}} = 53.2$ Hz), 131.7 (d, $^2J_{\text{C-P}} = 32.0$ Hz), 129.4 (d, $^3J_{\text{C-P}} = 8.2$ Hz) ppm; (Ref.^[5] $^{31}\text{P}\{^1\text{H}\}$ NMR $\delta = 158.3$ ppm).

4-bromophenyldichlorophosphine (**6**): 1.07 g, 49 %, colorless liquid, b.p. 60 °C at $1.2 \cdot 10^{-2}$ mbar, $^{31}\text{P}\{^1\text{H}\}$ NMR [CDCl_3 , 109.365 MHz] $\delta = 159.3$ (s) ppm; (Ref.^[35] $^{31}\text{P}\{^1\text{H}\}$ NMR [121 MHz, CDCl_3 , 293 K], $\delta = 158.6$ ppm, for ^1H and ^{13}C NMR see Ref.^[35]).

4-(trifluoromethyl)phenyldichlorophosphine (**7**): 2.08 g, 65 %, colorless liquid, b.p. 82 °C at $1 \cdot 10^{-3}$ mbar, $^{31}\text{P}\{^1\text{H}\}$ NMR [CDCl_3 , 109.365 MHz] $\delta = 160.0$ (s) ppm; (Ref.^[23] $^{31}\text{P}\{^1\text{H}\}$ NMR [121 MHz, C_6D_6 , +25 °C], $\delta = 157$ (s) ppm, for ^1H NMR see Ref.^[48]).

4-methoxyphenyldichlorophosphine (**8**): 1.36 g, 61 %, colorless liquid, b.p. 62 °C at $3 \cdot 10^{-3}$ mbar, $^{31}\text{P}\{^1\text{H}\}$ NMR [CDCl_3 , 109.365 MHz] $\delta = 164.0$ (s) ppm; (Ref.^[10] $^{31}\text{P}\{^1\text{H}\}$ NMR [161.98 MHz, CDCl_3 , +25 °C], $\delta = 162.4$ (s) ppm, for ^1H and ^{13}C NMR see Ref.^[10]).

1-naphthalenyldichlorophosphine (**12**): 2.93 g, 66 %, colorless, amorphous solid, $^{31}\text{P}\{^1\text{H}\}$ NMR [CDCl_3 , 109.365 MHz] $\delta = 163.6$ (s) ppm; (Ref.^[8] $^{31}\text{P}\{^1\text{H}\}$ NMR [CD_2Cl_2 , +25 °C], $\delta = 164.2$ (s) ppm, for ^1H and ^{13}C NMR see Ref.^[8]).

9-anthracenyldichlorophosphine (**13**): 2.70 g, 62 %, yellow colored, amorphous solid, $^{31}\text{P}\{^1\text{H}\}$ NMR [CDCl_3 , 109.365 MHz] $\delta = 160.0$ (s) ppm; (Ref.^[39] $^{31}\text{P}\{^1\text{H}\}$ NMR [121 MHz, C_6D_6 , +25 °C], $\delta = 159.5$ (s) ppm, for ^1H and ^{13}C NMR see Ref.^[49]).

Synthesis of aryl-dichlorophosphines **9** and **10** in THF. General procedure: To a solution of the respective aryl-bromide (2 g, 1.0 eq.) in anhydrous THF (20 mL) the appropriate amount of *n*-butyllithium (1.0 eq., 2.4 M solution in hexane) was added dropwise at -78 °C and the reaction stirred for another hour. To the resulting suspension, a solution of anhydrous zinc(II) chloride (1.0 eq) in anhydrous THF (1 M), at -78 °C was added. The reaction was stirred (2 hrs) while warming up to RT to give a turquoise/cloudy solution. Afterwards the solution containing the organozinc species was added dropwise to phosphorus trichloride (1.0 eq) in THF (10 mL) at -78 °C and the resulting mixture stirred for another 16 hours while warming to RT. Afterwards, the solvent was removed under reduced

pressure. To precipitate the metal salts, 20 mL of pentane and 20 mL of dioxane were added and the mixture stirred for another hour. After removal of the solids via a Schlenk frit, the remaining solution was concentrated *in vacuo*. The resulting solids were recrystallized from pentane to afford aryl-dichlorophosphines **9** and **10** in good yields.

4-(dimethylamino)phenyldichlorophosphine (**9**): 1.33 g, 60 %, colorless, amorphous solid, $^{31}\text{P}\{^1\text{H}\}$ NMR [CDCl_3 , 109.365 MHz] $\delta = 165.0$ (s) ppm; (Ref.^[36] $^{31}\text{P}\{^1\text{H}\}$ NMR [101.3 MHz, C_6D_6 , +25°C], $\delta = 165.3$ (s) ppm, for ^1H and ^{13}C NMR see Ref.^[37]).

4-(pyrrolidin-1-yl)phenyldichlorophosphine (**10**): *N*-(4-Bromophenyl)pyrrolidine was synthesized according to a literature procedure.^[50] 1.34 g, 61 %, colorless, amorphous solid, $^{31}\text{P}\{^1\text{H}\}$ NMR [CDCl_3 , 161.976 MHz] $\delta = 166.9$ (s) ppm; ^1H NMR [CDCl_3 , 400.133 MHz] $\delta = 7.76$ (m, 2H), 6.61 (m, 2H), 3.37 (m, 4H), 2.06 (m, 4H); $^{13}\text{C}\{^1\text{H}\}$ NMR [CDCl_3 , 100.636 MHz] $\delta = 150.9$ (s, Cq) 132.2 (d, 2CH, $^2J_{\text{C-P}} = 35.5$ Hz), 124.1 (d, Cq $^1J_{\text{C-P}} = 49.4$ Hz), 111.5 (d, 2CH, $^3J_{\text{C-P}} = 10.8$ Hz), 47.7 (s, 2CH₂), 25.5 (s, 2CH₂) ppm; ^{15}N NMR [*via* ^1H , ^{15}N -HMBC, CDCl_3] -313.8 ppm. EA could not be conducted due to air sensitivity. In HRMS (EI) measurements only the hydrolyzed product could be observed: HRMS (EI) m/z [M - H]⁺ calcd. for $\text{C}_{10}\text{H}_{13}\text{NO}_2\text{P}^+$ 210.0678, found 210.0635.

Synthesis of aryl-dichlorophosphine **11** in THF: To a solution of 4-bromobenzonitrile (2.0 g, 11.0 mmol, 1.0 eq.) in anhydrous THF (20 mL) *n*-butyllithium (11.0 mmol, 1.0 eq., 2.4 M solution in hexane) was added dropwise at -100 °C and the reaction stirred for 15 min. To the resulting mixture, a solution of anhydrous zinc(II) chloride (1.5 g, 11.0 mmol, 1.0 eq) in anhydrous THF (1 M), was added at -100 °C. The amber-colored solution was stirred for 30 min. Phosphorus trichloride (1.0 eq) was added dropwise to the mixture at -100 °C and stirred for another 16 hours while warming to RT. Afterwards, the solvent was removed under reduced pressure. To precipitate the metal salts, 20 mL of pentane and 20 mL of dioxane were added and the mixture stirred for another hour. After removal of the solids via a Schlenk frit, the remaining solution was concentrated *in vacuo*. The left-over liquid is distilled to receive the purified aryl-dichlorophosphine **11** in moderate yield.

p-cyanophenyldichlorophosphine (**11**): 0.94 g, 42 %, colorless liquid, b.p. 140 °C, $4.5 \cdot 10^{-2}$ mbar, $^{31}\text{P}\{^1\text{H}\}$ NMR [CDCl_3 , 161.835 MHz] $\delta = 155.6$ (s) ppm; (Ref.^[38] $^{31}\text{P}\{^1\text{H}\}$ NMR [CDCl_3] $\delta = 155.4$ ppm, for ^1H and ^{13}C NMR see Ref.^[38]).

Synthesis of aryl-dichlorophosphines **14** and **15** in diethyl ether. General procedure: To a solution of the respective aryl-bromide (5 mL, 1.0 eq.) in anhydrous diethyl ether (30 mL) was added the appropriate amount of *n*-butyllithium (1.0 eq., 2.4 M solution in hexane) dropwise at -10 °C and the reaction stirred for another 3 h at 30 °C. To the resulting suspension, a solution of anhydrous zinc(II) chloride (2 eq) in anhydrous diethyl ether (1 M), was added at -10 °C. The reaction was stirred further for 2 hrs at RT to give a colorless/cloudy solution. Phosphorus trichloride (1.1 eq) was added dropwise to the mixture at -10 °C and stirred for another 12 hours at RT. The solvent is removed *in vacuo* and the left over solid extracted two times with dry pentane. For further purification, product **14** can be distilled and **15** can be recrystallized from pentane. The aryl-dichlorophosphines **4** and **5** are received in good yields.

(2,4,6-trimethylphenyl)dichlorophosphine (**14**): 4.54 g, 63 %, colorless liquid, b.p. 64 °C at $1 \cdot 10^{-3}$ mbar, $^{31}\text{P}\{^1\text{H}\}$ NMR [CDCl_3 , 161.996 MHz] $\delta = 168.0$ ppm (s) with 6 % impurity of the PBrCl compound at 162.2 ppm (s). (Ref.^[40] $^{31}\text{P}\{^1\text{H}\}$ NMR [CD_2Cl_2] $\delta = 168.8$ (s) ppm, for ^1H see Ref.^[40]).

(2,4,6-triisopropylphenyl)dichlorophosphine (**15**): 3.84 g, 67 %, colorless, amorphous solid, $^{31}\text{P}\{^1\text{H}\}$ NMR [CDCl_3 , 161.996 MHz] $\delta = 166.6$ ppm (s) with 6 % impurity of the PBrCl compound at 160.5 ppm (s). (Ref.^[41] ^{31}P NMR [C_6D_6] $\delta = 165.2$ ppm, for ^1H and ^{13}C NMR see Ref.^[51]).

Synthesis of aryl-dichlorophosphines **16–19** in THF. General procedure (for individual reaction times and conditions see Table 1): To a solution of the respective heteroarene (2 mL, 1.0 eq.) in anhydrous THF (20 mL) the appropriate amount of *n*-butyllithium (1.0 eq., 2.4 M solution in hexane) was added dropwise at -78 °C and the reaction stirred for another hour. To the resulting suspension, a solution of anhydrous zinc(II) chloride (1.0 eq) in anhydrous THF (1 M), at -78 °C was added. The reaction was stirred (2 hrs) while warming up to RT to give a colorless/cloudy solution. Phosphorus trichloride (1.0 eq) was added dropwise to the mixture at -78 °C and stirred for another 16 hours. In the case of **16** the mixture containing the organozinc species is added dropwise to phosphorus trichloride (1.0 eq.) in anhydrous THF (10 mL) at -78 °C. Afterwards, the solvent was removed in vacuum. To precipitate the metal salts, 20 mL of pentane and 20 mL of dioxane were added and the mixture stirred for another hour. After removal of the solids via a Schlenk frit, the remaining solution is concentrated under vacuum. The left-over liquid is distilled to receive the purified aryl-dichlorophosphines **16–19** in moderate to good yields.

2-furanyldichlorophosphine (**16**): 1.82 g, 39 %, colorless liquid, b.p. 42 °C at 10 mbar, $^{31}\text{P}\{^1\text{H}\}$ NMR [CDCl_3 , 109.365 MHz] $\delta = 124.0$ (s) ppm; (Ref.^[11] $^{31}\text{P}\{^1\text{H}\}$ NMR [CD_2Cl_2] $\delta = 123.7$ (s) ppm, for ^1H and ^{13}C NMR see Ref.^[11]).

2-thienyldichlorophosphine (**17**): 2.40 g, 52 %, colorless liquid, b.p. 27 °C at $1 \cdot 10^{-3}$ mbar, $^{31}\text{P}\{^1\text{H}\}$ NMR [CDCl_3 , 161.976 MHz] $\delta = 146.5$ (s) ppm; (Ref.^[11] $^{31}\text{P}\{^1\text{H}\}$ NMR [CDCl_3] $\delta = 145.5$ (s) ppm, for ^1H and ^{13}C NMR see Ref.^[11]).

5-methylthien-2-ylidichlorophosphine (**18**): 2.81 g, 68 %, colorless liquid, b.p. 45 °C at $1 \cdot 10^{-3}$ mbar, ^1H NMR [CDCl_3 , 400.133 MHz] $\delta = 7.47$ (dd, 1H, $^3J_{\text{H-P}} = 7.5$ Hz, $^3J_{\text{H-H}} = 3.6$ Hz), 6.80 (ddq, 1H, $^3J_{\text{H-H}} = 3.9$ Hz, $^4J_{\text{H-P}} = 2.1$ Hz, $^4J_{\text{H-H}} = 1.0$ Hz), 2.59 (t, 3H, $^4J_{\text{H-H}} = 1.1$ Hz); $^{13}\text{C}\{^1\text{H}\}$ NMR [CDCl_3 , 100.636 MHz] $\delta = 152.42$ (d, Cq, $^4J_{\text{C-P}} = 1.2$ Hz), 140.26 (d, Cq, $^1J_{\text{C-P}} = 71.7$ Hz), 136.63 (d, CH, $^2J_{\text{C-P}} = 47.0$ Hz), 126.36 (d, CH, $^3J_{\text{C-P}} = 9.6$ Hz), 15.90 (s, CH_3) ppm; $^{31}\text{P}\{^1\text{H}\}$ NMR [CDCl_3 , 161.976 MHz] $\delta = 145.8$ (s) ppm.

2,2'-bithiophen-5-ylidichlorophosphine (**19**): 2,2'-Bithiophene was synthesized according to a literature procedure.^[52] 1.51 g, 47 %, colorless liquid, b.p. 120 - 130 °C at $8 \cdot 10^{-3}$ mbar, ^1H NMR [CDCl_3 , 400.133 MHz] $\delta = 7.52$ (dd, $^3J_{\text{H-P}} = 7.1$ Hz, $^3J_{\text{H-H}} = 3.8$ Hz, 1H), 7.34 (dd, $^3J_{\text{H-H}} = 5.1$ Hz, $^4J_{\text{H-H}} = 1.2$ Hz, 1H), 7.31 (dd, $^3J_{\text{H-H}} = 3.7$ Hz, $^4J_{\text{H-H}} = 1.2$ Hz, 1H), 7.15 (dd, $^3J_{\text{H-H}} = 3.8$ Hz, $^4J_{\text{H-P}} = 1.8$ Hz, 1H), 7.07 (dd, $^3J_{\text{H-H}} = 5.1$ Hz, $^3J_{\text{H-H}} = 3.7$ Hz, 1H) ppm; $^{13}\text{C}\{^1\text{H}\}$ NMR [CDCl_3 , 161.976 MHz] $\delta = 148.3$ (d, Cq, $^4J_{\text{C-P}} = 1.2$ Hz), 140.8 (d, Cq, $^1J_{\text{C-P}} = 70.4$ Hz), 136.8 (d, CH, $^2J_{\text{C-P}} = 46.2$ Hz), 135.8 (s, Cq), 128.3 (s, CH), 126.7 (CH), 125.8 (s, CH), 123.7 (d, CH, $^3J_{\text{C-P}} = 9.0$ Hz) ppm; $^{31}\text{P}\{^1\text{H}\}$ NMR [CDCl_3 , 161.976 MHz] $\delta = 144.8$ (s) ppm. (Ref.^[44] $^{31}\text{P}\{^1\text{H}\}$ NMR [CDCl_3] $\delta = 144.6$ (s) ppm).

Supporting Information

^1H NMR, ^{31}P NMR, $^{13}\text{C}\{^1\text{H}\}$ NMR, heteronuclear NMR and two-dimensional NMR spectra.

Acknowledgement:

This work was financially supported by the German Federal Ministry for Economic Affairs and Energy on the basis of a decision by the German Bundestag (ZIM, Grant ZF4477702SL7). We further gratefully acknowledge the financial support by the Department of Chemistry, Ludwig-Maximilian University of

Munich. Additionally, we are especially thankful to Prof. T. M. Klapötke for his constant support over the years. Konrad Schönleber is thanked for his participation in this project.

2.4.5. References

- [1] B. Wu, R. Chopra, N. Yoshikai, *Org. Lett.*, **2015**, *17* (22), 5666–5669.
- [2] Y. Fu, G. Hou, J. Xie, L. Xing, L. Wang, Q. Zhou, *J. Org. Chem.*, **2004**, *69* (23), 8157–8160.
- [3] T. Baumgartner, T. Neumann, B. Wirges, *Angew. Chem. Int. Ed.*, **2004**, *43* (45), 6197–6201.
- [4] B. Buchner, L. B. J. Lockhart, *J. Am. Chem. Soc.*, **1951**, *73*, 755–756.
- [5] A. Hinke, W. Kuchen, *Phosphorus Sulfur Relat. Elem.*, **1983**, *15* (1), 93–98.
- [6] P. Pellon, J. Hamelin, *Tetrahedron Lett.*, **1986**, *27* (46), 5611–5614.
- [7] J. A. Miles, M. T. Beeny, K. W. Ratts, *J. Org. Chem.*, **1975**, *40* (3), 343–347.
- [8] S. A. Reiter, S. D. Nogai, K. Karaghiosoff, H. Schmidbaur, *J. Am. Chem. Soc.*, **2004**, *126* (48), 15833–15843.
- [9] A. Karaçar, M. Freytag, H. Thönnessen, P. G. Jones, R. Bartsch, R. Schmutzler, *J. Organomet. Chem.*, **2002**, *643–644*, 68–80.
- [10] C. Hettstedt, M. Unglert, R. J. Mayer, A. Frank, K. Karaghiosoff, *Eur. J. Inorg. Chem.*, **2016**, *2016* (9), 1405–1414.
- [11] S. A. Reiter, S. D. Nogai, H. Schmidbaur, *Dalton Trans.*, **2005**, 247–255.
- [12] P. Knochel, G. A. Molander, *Comprehensive Organic Synthesis*, 2nd Editio., Knochel, P., Ed., Elsevier, **2014**.
- [13] P. Knochel, M. I. Calaza, E. Hupe, In *Metal-Catalyzed Cross-Coupling Reactions*; de Meijere, A., Diederich, F., Eds.; Wiley-VCH Verlag GmbH, Weinheim, Germany, **2008**; pp 619–670.
- [14] B. H. Lipshutz, A. R. Abela, Ž. V. Bošković, T. Nishikata, C. Duplais, A. Krasovskiy, *Top. Catal.*, **2010**, *53* (15–18), 985–990.
- [15] Y. H. Chen, M. Ellwart, V. Malakhov, P. Knochel, *Synth.*, **2017**, *49* (15), 3215–3223.
- [16] S. Enthaler, X. F. Wu, *Zinc Catalysis*, Enthaler, S., Wu, X.-F., Eds., Wiley-VCH Verlag GmbH & Co. KGaA, Weinheim, Germany, **2015**.
- [17] B. Verbelen, W. Dehaen, K. Binnemans, *Synth.*, **2018**, *50* (10), 2019–2026.
- [18] O. Dahl, U. Henriksen, C. Trebbien, G. E. Carlberg, O. Sterner, B. Wickberg, *Acta Chem. Scand.*, **1983**, *37b*, 639–642.
- [19] F. Langer, P. Knochel, *Tetrahedron Lett.*, **1995**, *36* (26), 4591–4594.
- [20] D. G. Yakhvarov, Y. S. Ganushevich, O. G. Sinyashin, *Mendeleev Commun.*, **2007**, *17* (4), 197–198.
- [21] F. Langer, K. Püntener, R. Stürmer, P. Knochel, *Tetrahedron Asymmetry*, **1997**, *8* (5), 715–738.
- [22] E. Vedejs, O. Daugulis, *J. Am. Chem. Soc.*, **2003**, *125* (14), 4166–4173.
- [23] S. A. Solomon, L. K. Allen, S. B. J. Dane, D. S. Wright, *Eur. J. Inorg. Chem.*, **2014**, No. 10, 1615–1619.
- [24] H. T. Teunissen, F. Bickelhaupt, *Organometallics*, **1996**, *15* (2), 802–808.
- [25] Z. Wang, N. Pu, Y. Tian, C. Xu, F. Wang, Y. Liu, L. Zhang, J. Chen, S. Ding, *Inorg. Chem.*, **2019**, *58* (9), 5457–5467.
- [26] X. Chen, H. Zhu, T. Wang, C. Li, L. Yan, M. Jiang, J. Liu, X. Sun, Z. Jiang, Y. Ding, *J. Mol. Catal. A Chem.*, **2016**, *414*, 37–46.
- [27] P. H. M. Budzelaar, J. H. G. Frijns, A. Guy Orpen, *Organometallics*, **1990**, *9* (4), 1222–1227.
- [28] H. Zhang, P. Ruiz-Castillo, S. L. Buchwald, *Org. Lett.*, **2018**, *20* (6), 1580–1583.
- [29] A. Fukazawa, J. Usuba, R. A. Adler, S. Yamaguchi, *Chem. Commun.*, **2017**, *53* (61), 8565–8568.
- [30] K. M. Błażewska, J. Drabowicz, J.-C. Fiaud, D. Gudat, E. Hey-Hawkins, A. A. Karasik, R. Karpowicz, B. A. Kashemirov, T. Kawashima, P. Kiełbasiński, N. L. Kilah, J. Kobayashi, D. Krasowska, J. Lacour, K. Lammertsma, J. Lewkowski, D. Linder, P. Łyżwa, A. Marinetti, C. E. McKenna, J. L. Methot, M. Mikołajczyk, K. M. Pietrusiewicz, J.-L. Pirat, W. R. Roush, J. C. Slootweg, M. Stankevič, C. V.

- Stevens, M. Toffano, S. Urgaonkar, J. G. Verkade, D. Virieux, J.-N. Volle, S. B. Wild, M. Yoshifuji, A. Zając, *Category 5, Compounds with One Saturated Carbon Heteroatom Bond*, Mathey, F., Trost, B. M., Eds., Georg Thieme Verlag, Stuttgart, **2009**.
- [31] N. D. Contrella, J. R. Sampson, R. F. Jordan, *Organometallics*, **2014**, *33* (13), 3546–3555.
- [32] D. Berthold, B. Breit, *Org. Lett.*, **2018**, *20* (3), 598–601.
- [33] R. C. Grabiak, J. A. Miles, G. M. Schwenzer, *Phosphorus Sulfur Relat. Elem.*, **1980**, *9* (2), 197–202.
- [34] W. G. Bentrude, J. L. Fu, P. E. Rogers, *J. Am. Chem. Soc.*, **1973**, *95* (11), 3625–3635.
- [35] R. den Heeten, E. Zuidema, M. Lutz, A. L. Spek, P. W. N. M. van Leeuwen, P. C. J. Kamer, *J. Organomet. Chem.*, **2011**, *696* (19), 3113–3120.
- [36] E. E. Coyle, B. J. Doonan, A. J. Holohan, K. A. Walsh, F. Lavigne, E. H. Krenske, C. J. O'Brien, *Angew. Chem. Int. Ed.*, **2014**, *53* (47), 12907–12911.
- [37] H. Jansen, M. C. Samuels, E. P. A. Couzijn, J. C. Slootweg, A. W. Ehlers, P. Chen, K. Lammertsma, *Chem. - A Eur. J.*, **2010**, *16* (5), 1454–1458.
- [38] J. Cui, F. Marankan, W. Fu, D. Crich, A. Mesecar, M. E. Johnson, *Bioorg. Med. Chem.*, **2002**, *10* (1), 41–46.
- [39] A. Tsurusaki, N. Nagahora, T. Sasamori, K. Matsuda, Y. Kanemitsu, Y. Watanabe, Y. Hosoi, Y. Furukawa, N. Tokitoh, *Bull. Chem. Soc. Jpn.*, **2010**, *83* (5), 456–478.
- [40] S. Freeman, M. J. P. Harger, *J. Chem. Soc. Perkin Trans. 1*, **1987**, 1399.
- [41] D. G. Yakhvarov, E. Hey-Hawkins, R. M. Kagiroy, Y. H. Budnikova, Y. S. Ganushevich, O. G. Sinyashin, *Russ. Chem. Bull.*, **2007**, *56* (5), 935–942.
- [42] M. Bentov, L. David, E. D. Bergmann, *J. Chem. Soc.*, **1964**, *11* (4750), 4750.
- [43] Z. S. Han, H. Wu, Y. Xu, Y. Zhang, B. Qu, Z. Li, D. R. Caldwell, K. R. Fandrick, L. Zhang, F. Roschangar, J. J. Song, C. H. Senanayake, *Org. Lett.*, **2017**, *19* (7), 1796–1799.
- [44] J. L. Freeman, Q. Zhao, Y. Zhang, J. Wang, C. M. Lawson, G. M. Gray, *Dalton Trans.*, **2013**, *42* (39), 14281.
- [45] T. Albers, P. G. Edwards, P. D. Newman, *Inorg. Chem. Commun.*, **2013**, *27*, 163–165.
- [46] P. Peringer, P. P. Winkler, *Inorg. Chim. Acta*, **1986**, *118* (1), 3–4.
- [47] A. Pedrini, F. Bertani, E. Dalcanale, *Molecules*, **2018**, *23* (10), 2670.
- [48] T. J. Clark, J. M. Rodezno, S. B. Clendenning, S. Aouba, P. M. Brodersen, A. J. Lough, H. E. Ruda, I. Manners, *Chem. - A Eur. J.*, **2005**, *11* (15), 4526–4534.
- [49] J. Wesemann, P. G. Jones, D. Schomburg, L. Heuer, R. Schmutzler, *Chem. Ber.*, **1992**, *125* (10), 2187–2197.
- [50] A. Noble, D. W. C. MacMillan, *J. Am. Chem. Soc.*, **2014**, *136* (33), 11602–11605.
- [51] H. Klöcker, J. C. Tendyck, L. Keweloh, A. Hepp, W. Uhl, *Chem. - A Eur. J.*, **2019**, *25* (18), 4793–4807.
- [52] B. Massoumi, N. Alipour, S. Fathalipour, M. Jaymand, *High Perform. Polym.*, **2015**, *27* (2), 161–170.

2.4.6. Supporting Information

The ^{13}C NMR spectrum of the organozinc species (**I**) in THF or diethyl ether at RT show clearly a shift of the metal-bonded carbon atom to lower frequencies of about 4 ppm, changing from THF to diethyl ether (see Figure 46). In contrast, the chemical shift of the metal-bonded carbon atom in the case of (**II**) is found to be constant at 157.0 ppm, independently of the solvent (THF or diethyl ether) used. This indicates the presence of different organozinc species in both cases, which would explain the observed different reaction behavior in these solvents. A reasonable assumption for this phenomenon might be that in general an equilibrium between mono-substituted and bis-substituted organozinc species is present in solution. However, in case of the (2,4,6-triisopropylphenyl) compound (**II**), independently of the solvent used, this equilibrium lies on the side of the mono-substituted compound due to steric

hindrance of the isopropyl substituents in *ortho*-position. Reaction of this species with PCl_3 leads to the monosubstituted product **15**. In case of the less sterically demanding *p*-tolyl substituent in (**1**), both compounds of the equilibrium might be present, though which side is predominant might be dependent on the solvent. The averaged signal of both compounds in equilibrium is then visible in solution NMR.

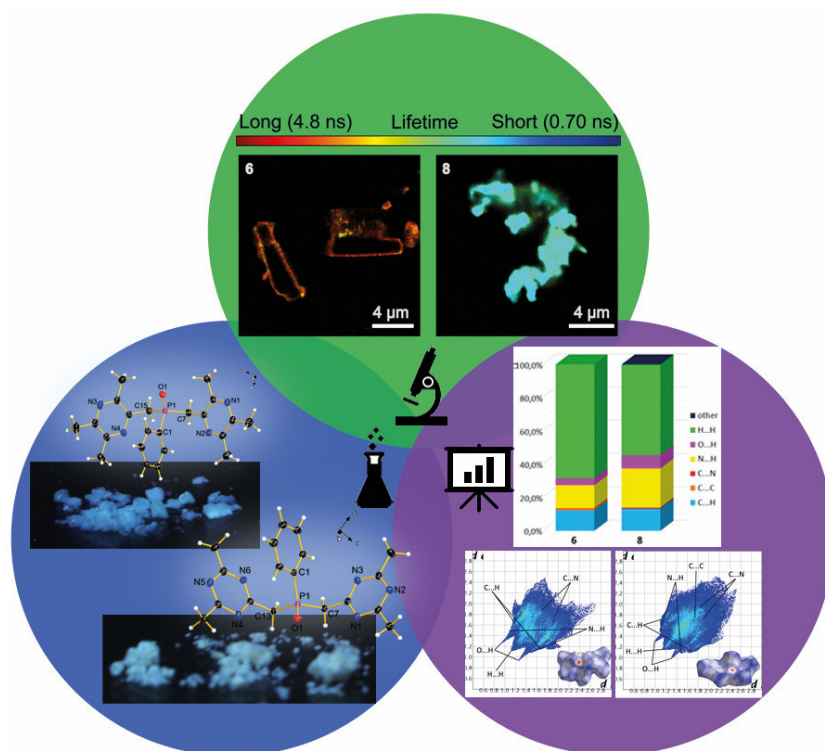
2.5. Methods for elucidating the structural-property relationship in luminescent materials

Christin Kirst, Nader A. Danaf, Fabian Knechtel, Tim Arcynski, Peter Mayer, Don C. Lamb and Konstantin L. Karaghiosoff

Published in *J. Mater. Chem. C* 2021

DOI: [10.1039/D1TC02634H](https://doi.org/10.1039/D1TC02634H)

Christin Kirst synthesized all the discussed compounds and performed the single crystal X-ray as well as UV-Vis absorption measurements and Hirshfeld surface analysis. She analyzed and evaluated the corresponding X-ray data and the NMR spectroscopy results in solution. She further managed the project and wrote the original draft of the manuscript, designed the TOC graphic and implemented the necessary corrections in the final version of the paper.



Abstract: The search for efficient and stable new blue luminescent compounds is still ongoing. In this respect, knowledge of the structure-property relationship is essential for the design and evaluation of blue emitting materials. However, several uncertainties still exist, such as crystal packing and intermolecular interactions, that can significantly complicate the design process. The application of fluorescence lifetime imaging microscopy in combination with Hirshfeld surface analysis for the characterization of luminescent materials are powerful tools that can be used to investigate the structure-property relationship in an emitting substance. However, they have been vastly underutilized in this field. Our results, based on exemplary, new, functionalized phosphine oxides, show that indeed general trends concerning the relationship between photoluminescence lifetimes, emitted light intensities, attractive intermolecular interactions and overall morphology of a compound can be derived through the combination of both analytical methods.

2.5.1. Introduction

Although knowledge regarding substituent effects and structural features, such as steric restrictions and hindrances, are considered in the design of light emitting materials, the basic design is still largely based on trial and error.^[1,2] Hence, additional tools are needed to provide more insights into the structure-property relationship. Here, we demonstrate the advantages of combining fluorescence lifetime imaging microscopy (FLIM) with the Hirshfeld surface (HS) analysis to provide additional insights and thereby reduce the amount of trial and error necessary.

We demonstrate the power of this approach on a new, promising class of luminescent materials: functionalized phosphines. In particular, we investigated picolyl derived phosphine compounds that are successively utilized as catalysts.^[3-9] Moreover, the group of A. Artem'ev and others have demonstrated luminescent properties of very similar pyridylphosphine derivatives and complexes thereof, as well as investigated their potential use as OLED materials.^[10-16] The compounds show promising results in regards to their photo- and electroluminescent properties. Additionally, their synthesis is quick and high yielding, use inexpensive starting materials and avoid rare metal catalysts. Another advantage of using such functionalized phosphines is that their optical properties can be easily adjusted *via* variations in the aromatic systems.^[10,17,18] By introduction of a methylene bridge between the nitrogen containing moiety and the phosphorus atom, an even more flexible ligand is obtained.^[19] This unique property allows the ligand to adapt to metals with different coordination geometries and sizes more easily (e.g. formation of polynuclear, mixed-metal complexes or coordination polymers), which has the possibility to improve catalytic properties, and generate interesting material properties such as high luminescence or porosity like in MOFs.^[17,20-27] Additionally, the normally rather labile P-C bond can be stabilized *via* complexation, which reduces its flexibility.^[28-30] The resulting, more rigid structure minimizes quenching and provides, in general, a more thermally-stable compound. A subsequent oxidation of the phosphine to the phosphine oxide results in air and moisture stable compounds. This stability is beneficial for applications utilizing luminescent materials such as long-lasting OLED devices, because it facilitates processing and enhances longevity.^[31-33]

The characterization of luminescent compounds is usually done in the solid state, in thin films or in solution by measuring the UV/Vis absorption and emission spectra. This is, in general, a convenient way to characterize the bulk material. However, these methods provide little information regarding the intermolecular interactions between the single molecules in the crystal or powder and the influence such structural features can have on the photophysical properties.

FLIM uses spatially resolved fluorescence lifetime decays to gain insight into the nanoscopic environment of a material, such as its defects and morphologies.^[34-37] FLIM is a fluorescence imaging technique where the contrast is based on the lifetime of individual fluorophores rather than their emission spectra. FLIM has been widely utilized during the last few years in different research fields such as medicine and biology, and has recently been applied to material sciences.^[38-40] Common implementations of FLIM allow nanoscopic investigations of a wealth of parameters in the vicinity of the sample of interest. This includes local environment sensing (pH, temperature, ion concentration, etc.), detection of molecular interactions and conformational changes in cellular biology.^[41-43] However, in the field of material science, the potential of FLIM has been underutilized.^[44,45] Although the characterization of luminescent materials utilizes time-correlated single photon counting (TCSPC) for lifetime measurements, the imaging technology of FLIM has not been exploited. Having both spatial imaging and lifetime information with FLIM is very useful for understanding important structure-property relationships of an emitting substance and to explain photophysical properties of the material, such as quantum yield, based on the observed structural motives or morphologies.

HS analysis can further aid in the interpretation of structural features and gives additional information based on the crystal structure data such as intermolecular interactions and, in particular, attractive hydrogen bonding.^[46] It is known that, after photoexcitation, a delocalization of the excitation through

hydrogen bond channels can occur and excimers can form.^[1,47–50] Normally, upon formation of the excimer, structural rearranges are necessary and the dimer becomes unstable upon deexcitation. This procedure consumes a lot of excited state energy and quenches the fluorescence. However, in the case of an excimer connected by hydrogen bonds, the structural changes with respect to the monomers are small, resulting in minimal energy loss when returning to the ground state. Consequently, the luminescence is enhanced.^[47,51,52] This knowledge can be beneficial when developing and evaluating the suitability of new luminescent materials for different applications such as OLEDs and should, therefore, become a standard characterization tool.

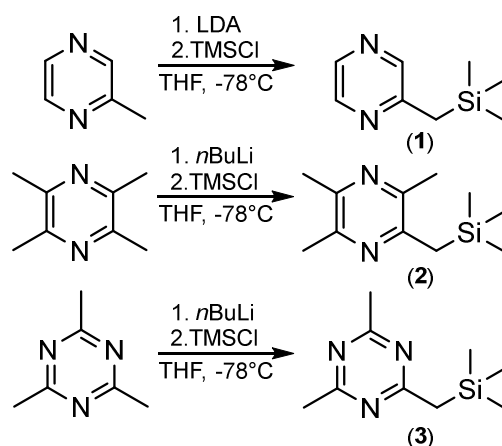
Herein, we present new functionalized phosphine oxides, which contain pyrazine and triazine derivatives in the heteroaromatic part, and their photophysical properties. The synthesized compounds were characterized *via* single crystal X-ray diffraction, multinuclear NMR, IR, MS and EA. Furthermore, their photophysical properties were measured either in solution or in the solid state. FLIM measurements were done to gain insight into the lifetime of the photoluminescence decay in the compounds. The combination of FLIM measurements together with quantitative HS analysis provided further insights into structural-property information, which can be broadly applied in the design and development of new luminescent materials.

2.5.2. Results and discussion

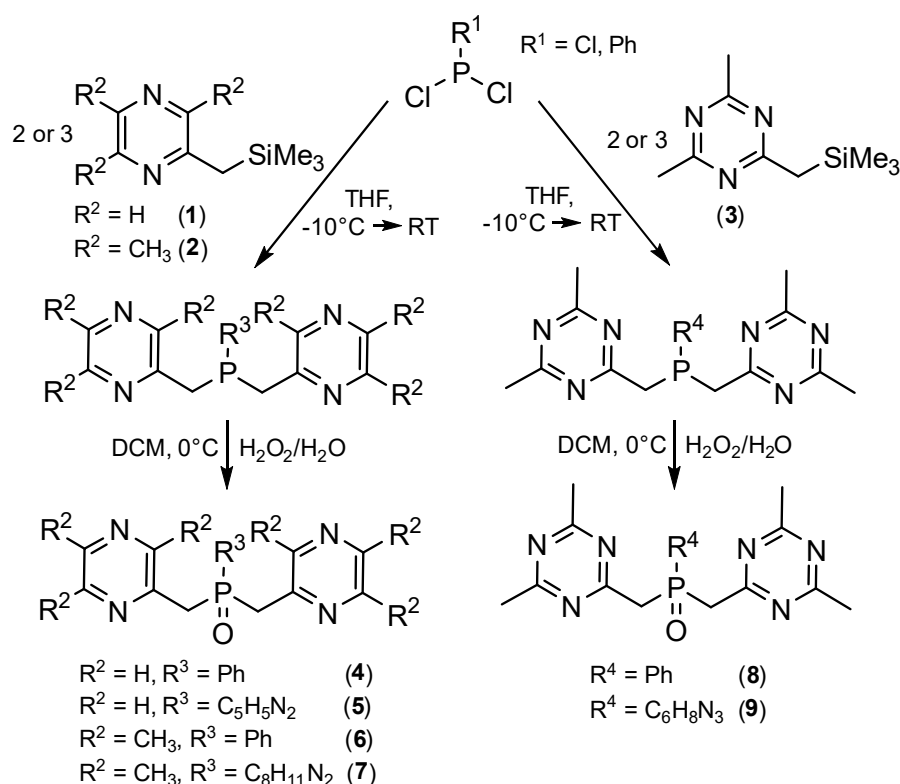
2.5.2.1. Synthesis

The synthesis of the trimethylsilyl (TMS) compounds used as precursors for the respective phosphines are shown in Scheme 13. Compound **1** has been mentioned and used before in the literature, but a synthesis procedure has not yet been described.^[53,54] Whereas compounds **2** and **3** could be synthesized with *n*-butyllithium (*n*BuLi), the milder lithiation reagent lithium diisopropylamine (LDA) has to be used for a successful reaction of compound **1**. The beginning substance for compound **3**, 2,4,6-trimethyl-1,3,5-triazine, was synthesized according to literature.^[55,56] The corresponding TMS compound **3** has a very characteristic smell, which is reminiscent of sweet popcorn. All TMS compounds synthesized are viscous colorless liquids and should be stored in sealed containers under protective gas.

Preparation of the phosphine oxides starting from their corresponding trimethylsilyl compounds is shown in Scheme 14. The synthesis is well established in our lab and was first described by Braunstein for bis(picolyl)phenylphosphine.^[57] This synthetic route is very advantageous when compared to the classic route, where the dichlorophosphine is allowed to react directly with the lithiated picolyl derivative. The so called “Braunstein-route” allows for synthesis of 5 g of ligands or more with quantitative yields and an easy workup. Any excess TMS compound can be easily removed under vacuum. All phosphine oxides are colorless powders when isolated. The compounds were further characterized by multinuclear NMR spectroscopy, high-resolution mass spectrometry, elemental analysis, infrared spectroscopy and thermogravimetry (for details, see ESI†).



Scheme 13. Synthesis of the TMS compounds **1–3**.



Scheme 14. Synthesis of the phosphine oxide ligands **4–9**.

2.5.2.2. Structural characterization

Next, we investigated the structure of the different compounds and their packing within the crystal using X-ray crystallography. Crystals of phosphine oxides **4–6** and **8** were obtained by slow diffusion of hexane into a solution of dichloromethane. Crystals of **7** and **9** were generated *via* slow evaporation of a solution of the compound in tetrahydrofuran. Crystallographic details and refinement data can be found in the Supporting Information (Table 8 and Table 9).

All compounds crystallize in monoclinic space groups (**4** and **8** in $P2_1/n$; **5** and **6** in $P2_1/c$, **9** in $C2/c$) with four or eight units in the unit cell (Figure 47), except for **7**, which crystallizes in the tetragonal space group $I4_1/a$ with 16 units in the unit cell. In all structures, the O–P–C angles are larger and the C–P–C angles are smaller than the ideal tetrahedron angle of 109.5° . Similar values have been reported for comparable phosphine oxides.^[8,19,58,59] Additionally, in all structures, weak, non-classical hydrogen bonds between the oxygen and methylene hydrogen atoms are observed.^[60] These interactions play

an important role in the formation of the structures in the crystal, which may influence their luminescence properties.

The molecules of **4** form antiparallel chains in the crystal, which are stacked along the *b* axis (Figure 51). Compound **5** forms zig-zag chains along the *c* axis in the crystal (Figure 52). Additional weak, face-to-face π - π interactions are present between two neighboring pyrazine rings with an average distance of 3.50 Å.^[61,62] Compound **6**, like **5**, forms zig-zag chains along the *c* axis (Figure 53). Weak, offset π - π interactions are present between neighboring trimethylpyrazine rings with an average distance of 3.50 Å.^[61,62] Compound **7** arranges in a helix along the *c* axis (Figure 54). Steric hinderance of the methyl groups prohibit possible close π - π interactions. The aromatic rings in the spiral are offset from each other with the closest distance being 3.73 Å. Solvent molecules tend to intercalate between the different helices causing structural disorders. However, an appropriate model to resolve the disorder could not be determined. Compound **8**, on the other hand, forms pairs of molecules in the crystal, which are arranged as H-bonded chains along the *b* axis (Figure 55). Compound **9** forms anti-parallel layers along the *b* axis in the crystal (Figure 56, left). The single molecules in these layers are arranged in chains along the *b* axis (Figure 56, right)

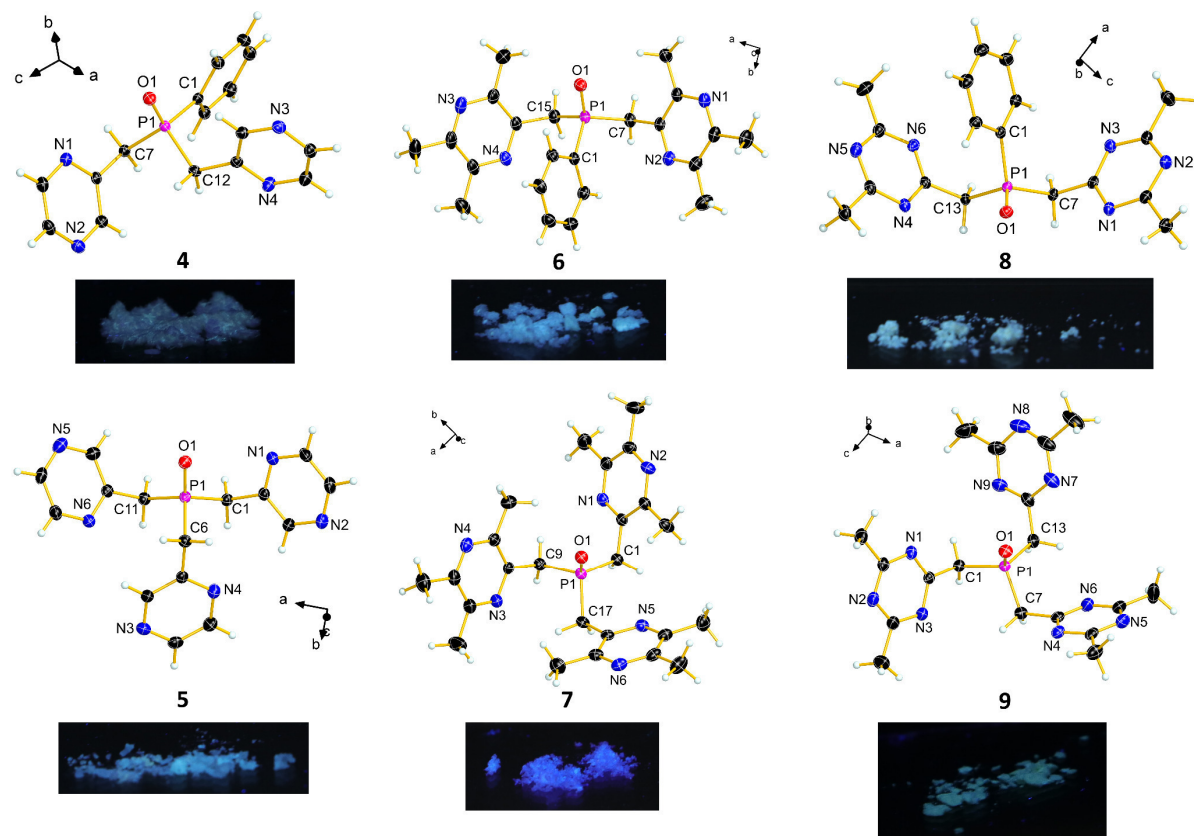


Figure 47. Molecular structure of the asymmetric unit of the phosphine oxides **4–9** in the crystal and a picture of the solid compounds under UV illumination (366 nm). Diamond 3 representation, thermal ellipsoids are drawn at 50 % probability level.

2.5.2.3. Photophysical characterization.

When the solid compounds **4–9** were irradiated with UV light (366 nm), a blue photoluminescence was observed (Figure 47). Further photophysical measurements were conducted to gain more insight into the luminescent properties of these compounds.

The UV-Vis absorption spectra recorded for the solid compounds **4–9** displayed maxima at 384 nm for **5**, **7** and **8**, 375 nm for **6** and 356 nm for **4** and **9** (Figure 57). The absorption spectra have a width of

around 100 nm and the tails even reach the region of the visible light. For compounds **4–6** and **8**, excitation and emission spectra were recorded in acetonitrile (Figure 58 and Figure 59). The photoluminescence maximum of the excitation scan was selected as λ_{exc} for the emission scan. Compounds **4** and **5** show the highest fluorescence emission when excited at 347 nm with a larger tail for **4**. Similarly, **6** shows the highest fluorescence emission when excited at 341 nm and **8** shows the highest hypsochromic shift with the highest emission for 336 nm excitation (Figure 58). Compounds **5** and **8** show an emission maximum at 430 nm and 425 nm, respectively. In agreement with the excitation spectra, **4** and **6** show the highest bathochromic shift with the highest emission at ~ 450 nm when excited at ~ 365 nm (Figure 59). The small spikes in the spectra result from Raman peaks of the solvent and can be seen in the solvent excitation and emission spectrum (Figure 58 and Figure 59, black spectra). These results show, that the functionalized phosphine oxides are promising candidates and may be used in the future as ligands for the possible development of luminescent metal complexes. When looking at the absorption and excitation/emission spectra, no clear trend with respect to structural properties of the compounds is discernable. The nitrogen content and/or the number of methyl groups on the heteroaromatic substituent has no apparent effect on the emission properties.

2.5.2.4. Lifetime characterization.

For further investigations, we focused on the photoluminescence and structural properties of the phosphine oxides **4–6** and **8**. Solvent molecules were observed within the crystal structures of compounds **7** and **9** and were therefore not further analyzed to avoid potential ambiguities in the FLIM data due to the presence of the solvent molecules. Compounds **4**, **5**, **6** and **8** were diluted in acetonitrile solution and investigated using FLIM. FLIM measurements showed the samples to consist of smaller microstructures with either distinct crystalline or amorphous morphology and different photoluminescence lifetimes (Figure 48a). Lifetimes between 1.8 and 4.05 ns were measured, indicative of single-single electronic transitions (i.e. fluorescence). Compound **4** shows a high homogeneity of rod-like crystals with a uniform fluorescence lifetime of ~ 1.80 ns (Figure 48a(i), blue), the shortest of the four compounds. Compound **5** displays an interesting morphology mainly comprised of quasi-spherically elongated and oval-like particles with a uniform fluorescence lifetime of ~ 2.35 ns (Figure 48a(ii), cyan, light green). Compound **6** shows distinct morphologies, mainly comprised of thick plate-like crystals. The fluorescence lifetime distribution is the most uniform between crystals and has the longest fluorescence lifetime decay of ~ 4.05 ns (Figure 48a(iii), orange). However, it displays a heterogeneous fluorescence intensity distribution with the majority of photons being emitted from the edges. In addition, the overall number of detected photons was very low even at maximum laser power (50 μ W, see ESI for more details) indicating that the emissive property of this compound is less efficient than compounds **4**, **5** and **8** (Figures 60–63, fluorescence intensity images). Compound **8**, in contrast to **4** or **6**, shows a more amorphous like morphology with a quite homogeneous fluorescence lifetime of ~ 2.75 ns (Figure 48a(iv), cyan). Figure 48b and Figure 48c show the FLIM data analysis by either analyzing the TCSPC data directly (Figure 48b) or via the phasor approach, which graphically translates the fluorescence lifetime from Figure 48b into Fourier space (Figure 48c).^[63,64] In the phasor plot, mono-exponential decays fall along an arc of radius 0.5 with long lifetime components located near the origin (0, 0) and short lifetime components near (1, 0). Multi-exponential decays comprise a weighted vector of the constituent phasors, meaning that all decay pathways in phasor space lie within the arc.^[63,65] For the different compounds investigated (**4–6** and **8**), the phasor space occupied by all crystals lies within the arc, indicating a multiexponential decay (biexponential in this case). A biexponential function was also sufficient to describe the fluorescence lifetime for the four different crystals of each compound (Figures 64–67, Table 11). The short lifetime component (~ 1 ns) is similar for all constructs whereas the longer lifetime component varies slightly between them ($\sim 3–5$ ns).

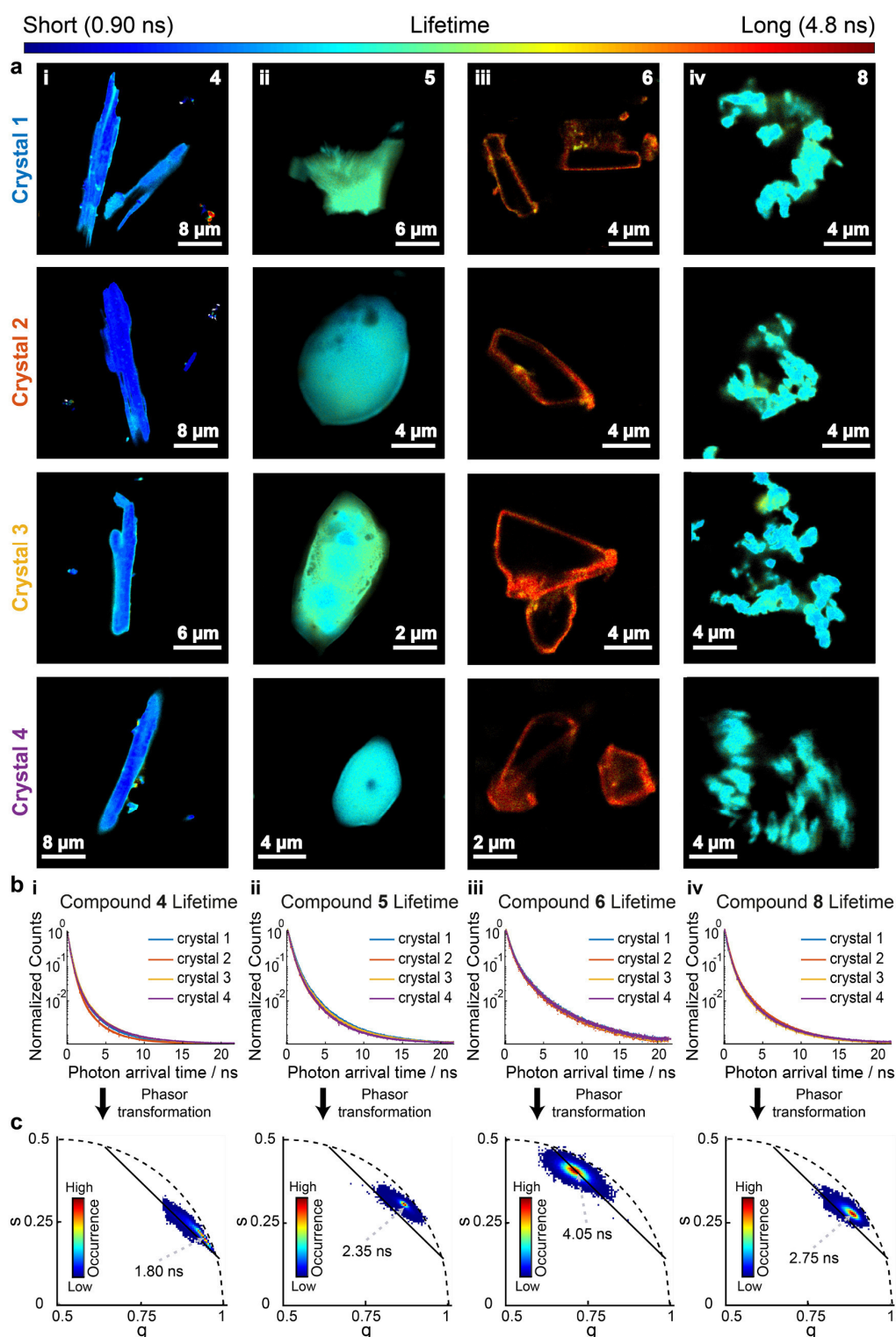


Figure 48. Fluorescence lifetime decays and FLIM images of the different compounds showing the diverse structural morphologies they possess. a) Representative FLIM images are shown for the four compounds i) 4, ii) 5, iii) 6 and iv) 8. The color-code corresponding to the fluorescence lifetime displayed on the FLIM images, goes from blue (indicating the shortest fluorescence lifetime) over green and yellow to orange and red (indicating the longest fluorescence lifetime), see the color bar for fluorescence lifetime. b) From the FLIM images, the fluorescence lifetime decay is plotted for the different compounds i) 4, ii) 5, iii) 6 and iv) 8. c) The corresponding phasor plot of the four FLIM images for each compound i) 4, ii) 5, iii) 6 and iv) 8 is shown, which is the Fourier transformation of the

lifetimes plotted in panel b. The dotted-grey arrows indicate the average phasor positions of the four FLIM images, with the indicated lifetime values. The color in the phasor plots corresponds to the number of pixels exhibiting the particular phasor value (blue indicating the lowest occurrence and red indicating the highest occurrence), see the occurrence color bar within the phasor plot. The black line in the phasor plots is used for generating the color table for the fluorescence lifetimes in the FLIM images in panel a. The pixel brightness corresponds to total counts, while the hue indicates the pixels' proximity to the black line.

Interestingly, the average fluorescence lifetime decreases with increasing brightness (Figure 68a). A detailed analysis of the FLIM data shows that the fluorescence brightness increases with the fraction of light coming from the short lifetime component (Figure 68b). This indicates that the inherent fluorescence properties of the compounds are different and not dominated by various quenching pathways. Here, the observed high brightness and short lifetime indicate an improved quantum yield in the shorter lifetime species, which also protects the substance against photodegradation typically occurring from the excited state.

The shortest average fluorescence lifetime populations obtained were for the crystalline rod-like compound **4**, followed by the oval-like particles of compound **5** and compound **8** with an amorphous like morphology. However, compound **4** displays spatial lifetime differences, where a longer lifetime is observed on the edges in comparison with the crystals' interior (Figure 60). The shorter lifetime component inside the crystals correlates with the higher brightness observed in the interior, which is in line with the improved quantum yield in the shorter lifetime species (Figure 60). On the other hand, **8** showed a more uniform lifetime distribution with minor differences between the internal and external parts of the amorphous structure (Figure 63). Compound **5**, similar to compound **8**, exhibits no significant lifetime differences between the internal and external parts of the structures (Figure 61).

2.5.2.5. Combining Hirshfeld surface analysis with the FLIM results

The FLIM results alone are insufficient for providing a direct correlation between structure-property relationship and normal crystal density packing (Table 8 and Table 9 of ESI). That is, the lifetime does not only depend on the density of the structures and the materials' morphology. Other factors that can also influence the fluorescence lifetime include strong intermolecular interactions such as π - π interactions and H-bonds, intra/intermolecular charge transfer processes, or excimer formation can be considered as contributing factors for lifetime changes.

Here, we applied the Hirshfeld surface analysis for a quantitative comparison of intermolecular interactions between molecules in the crystal based on the crystallographic output file (.cif) obtained from single crystal X-ray diffraction.^[46,66] Short contacts are visualized by red dots in the d_{norm} maps and by sharp spikes in the fingerprint plots (Figure 49a-d). These data can aid in the interpretation of the FLIM results and overall luminescent properties, and enable the possibility of investigating correlating effects.

The HS analysis of compound **4** reveals a high percentage of attractive C-H \cdots N (26.2 %) and C-H \cdots O (7.7 %) interactions (see Figure 49).^[5,50,51] For compound **5**, a slightly higher percentage of attractive C-H \cdots N (29.4 %) and C-H \cdots O (9.5 %) interactions are observed. Compound **6** has the highest number of C-H \cdots H (68.5 %) interactions and the lowest number of attractive C-H \cdots N (13.9 %) and C-H \cdots O (4.1 %) interactions of the investigated compounds limiting excimer formation between the single molecules in the structure.^[1,48,49] Compound **8** has a similar amount of attractive interactions to compounds **4** and **5** with C-H \cdots N content of 23.6 % and C-H \cdots O content of 7.8 %. Weak π - π -interactions, present in all compounds, are visible as C \cdots H, C \cdots N and C \cdots C contacts in the fingerprint plots (27.3 % for **4**, 18.8 % for **5**, 13.9 % for **8** and 13.6 % for **6**; Figure 49), with the C \cdots H interactions

being the major contributor. All π - π -interactions are below the values for face-to-face (<3.8 Å), offset (<3.4 Å) and/or T-shaped (<4.9 Å) π - π -interactions of pyridine, which indicates that these π - π contacts count as attractive interactions and influence the structural geometry.^[61,62]

By combining the HS analysis and the FLIM information, we can investigate whether there is a correlation between the intermolecular bonding interactions and the fluorescence properties. With increasing attractive C-H \cdots N and C-H \cdots O interactions within the crystals, we observe an increase in the fluorescence brightness (Figure 48f) and an overall trend of decreasing average lifetimes (Figure 68a). We attribute this to an increase in the fraction of light emitted from the short lifetime component (Figure 68b). This suggests that the short lifetime component is coming from the excimer state, indicating that there is a relationship between the material properties, morphology and crystal packing. Alongside the structural parameters, these interactions are crucial in understanding the differences in the emissive properties of the different compounds and the way these particles interact with each other under different structural conditions in the crystals. Hence, the FLIM measurements combined with the Hirschfeld surface analysis reinforce our understanding of the morphology and its role for the observed photophysical differences among the diverse compounds. For example, the FLIM images of compound **6**, which has the longest fluorescence lifetime decay of the four investigated compounds, reveal quenching in the middle of the crystal and weak luminescent properties of the compound. In addition, the HS analysis discloses that this compound has the lowest amounts of π - π -interactions and attractive C-H \cdots N and C-H \cdots O interactions in the crystal, in addition to the loose packing of its structure (Table 8 and Table 9). On the other hand, compound **5** seems to possess the best overall properties of the four compounds that were more closely investigated. Its fairly high emissive properties with a maximum at 425 nm is in the ideal wavelength region for a blue emitter. The fluorescence lifetime decay is short (2.35 ns), but uniformly spread over the spherical structure, which suggests a homogenous emission throughout the structure. Additionally, **5** exhibits the highest intensity of emitted light, which is supported by the HS analysis showing the highest percentage of attractive C-H \cdots N and C-H \cdots O interactions.

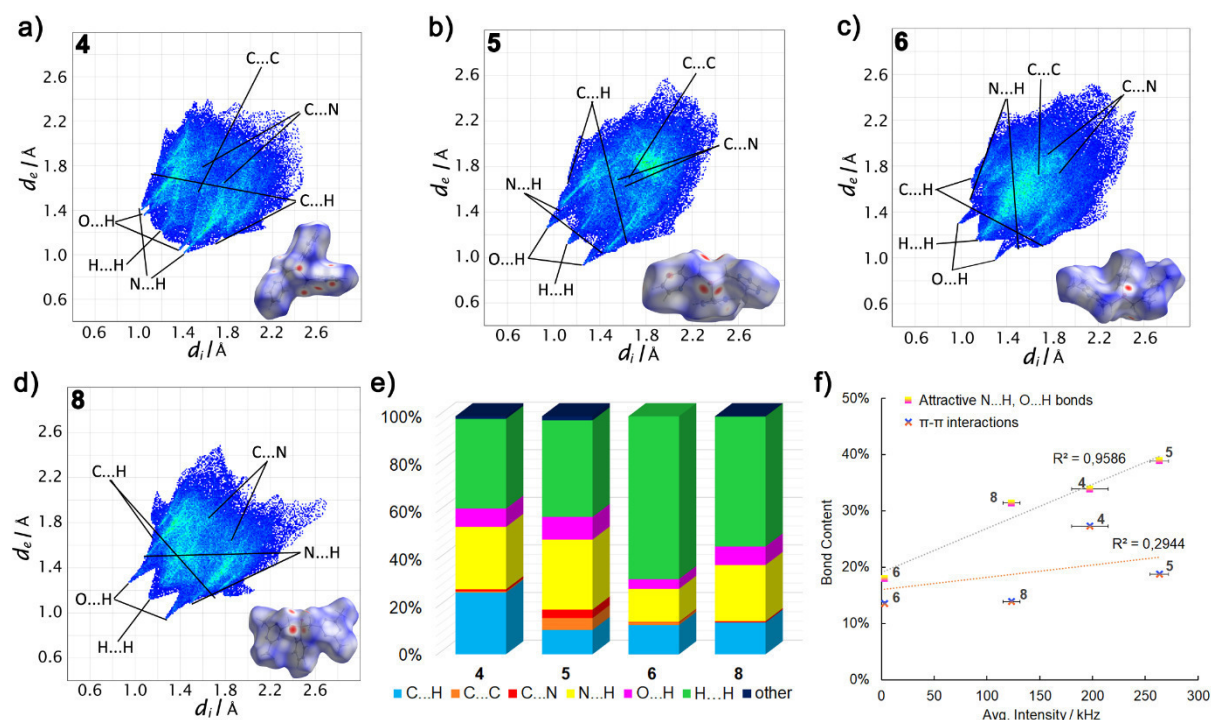


Figure 49. d_{norm} maps and fingerprint plots of compounds **4–6** and **8** (a–d). e) Diagram showing the percentages of the close contacts in the crystal packing of the selected compounds. f) correlation of intermolecular interactions in the crystal versus average intensity.

2.5.3. Conclusion

The synthesis of six multidentate phosphine oxides was reported. The compounds were characterized using NMR, MS, IR spectroscopy, EA and X-ray crystallography. The solid compounds show fluorescence when irradiated with UV light (366 nm). A closer characterization of the photophysical properties of these compounds was done by absorption and fluorescence excitation/emission spectroscopy. The preliminary results show that the developed phosphine oxides are promising candidates for blue emitters.

The combination of FLIM measurements and the quantitative Hirshfeld surface analysis made it possible to elucidate structural-property-relationships of the synthesized luminescent phosphine oxide ligands. The data suggests that knowledge about morphology, crystal packing and nature of intermolecular interactions is important for interpreting the uniformity and decay of the fluorescence lifetime, as well as the observed differences in the emitted light intensities. With increasing attractive C–H...N and C–H...O interactions within the crystals, an increase in the fluorescence brightness and a decrease in the average lifetime are observed. Although these types of hydrogen bond acceptors (C–H...N and C–H...O) are of a relatively weak nature, they still seem to have an impact on the luminescent properties of the compounds.

Our results also provide a basis for more in depth investigations using quantum-chemical simulations. These could provide additional insights into how phenomena such as quenching, charge-transfer or morphology can influence the photoluminescent properties of the materials.

In general, novel insights can be obtained by combining FLIM information with a quantitative Hirshfeld surface analysis and should be taken into account when designing and investigating future luminescent materials for e.g. OLED applications. In this particular case, the FLIM and HS analysis combination provides an important preselection tool for choosing potential compounds based on their photoluminescence properties. Additionally, the introduction of weak and/or strong hydrogen bond acceptors is an option that can be employed as means to improve the luminescence lifetime and intensity of the compounds.

Author Contributions

Author 1 and Author 2 contributed equally to this work.

Conflicts of interest

There are no conflicts to declare.

Acknowledgements

The German Federal Ministry for Economic Affairs and Energy on the basis of a decision by the German Bundestag (ZIM, Grant ZF4477702SL7) supported this work financially as well as by the Deutsche Forschungsgemeinschaft (DFG, German Research Foundation) – Project-ID 201269156 – SFB 1032 Project B03. The financial support of Ludwig-Maximilian University of Munich via the Department of Chemistry, the Center for NanoScience (CeNS) and the LMUinnovativ initiative BioImaging Network (BIN) is also gratefully acknowledged. Additionally, we are particularly grateful to Prof. Dr. T. M. Klapötke for his continuous support over the years.

Keywords: phosphine oxide ligands • luminescence • pyrazine • triazine • FLIM

2.5.4. References

- [1] J. Gierschner, S. Y. Park, *J. Mater. Chem. C*, **2013**, *1* (37), 5818–5832.
- [2] C. Poriel, J. Rault-Berthelot, *Adv. Funct. Mater.*, **2021**, *2010547*, 1–43.

- [3] L. A. Adrio, K. K. Hii, *Organometallic Chemistry*, Fairlamb, I. J. S., Lynam, J. M., Eds., *Organometallic Chemistry*, Royal Society of Chemistry, Cambridge, **2009**, Vol. 35.
- [4] M. P. Carroll, P. J. Guiry, *Chem. Soc. Rev.*, **2014**, 43 (3), 819–833.
- [5] W. Tang, X. Zhang, *Chem. Rev.*, **2003**, 103 (8), 3029–3070.
- [6] E. I. Musina, A. S. Balueva, A. A. Karasik, In *Organophosphorus Chemistry*; **2019**; Vol. 48, pp 1–63.
- [7] C. Hettstedt, M. Unglert, R. J. Mayer, A. Frank, K. Karaghiosoff, *Eur. J. Inorg. Chem.*, **2016**, 2016 (9), 1405–1414.
- [8] C. Hettstedt, P. Köstler, E. Ceylan, K. Karaghiosoff, *Tetrahedron*, **2016**, 72 (23), 3162–3170.
- [9] K. N. Gavrilov, A. I. Polosukhin, *Russ. Chem. Rev.*, **2000**, 69 (8), 661–682.
- [10] A. V. Artem'ev, M. R. Ryzhikov, I. V. Taidakov, M. I. Rakhmanova, E. A. Varaksina, I. Y. Bagryanskaya, S. F. Malysheva, N. A. Belogorlova, *Dalton Trans.*, **2018**, 47 (8), 2701–2710.
- [11] A. Y. Baranov, A. S. Berezin, D. G. Samsonenko, A. S. Mazur, P. M. Tolstoy, V. F. Plyusnin, I. E. Kolesnikov, A. V. Artem'ev, *Dalton Trans.*, **2020**, 49 (10), 3155–3163.
- [12] A. V. Artem'ev, E. P. Doronina, M. I. Rakhmanova, A. O. Sutyryna, I. Y. Bagryanskaya, P. M. Tolstoy, A. L. Gushchin, A. S. Mazur, N. K. Gusarova, B. A. Trofimov, *New J. Chem.*, **2016**, 40 (12), 10028–10040.
- [13] A. S. Berezin, A. V. Artem'ev, V. Y. Komarov, A. Y. Baranov, *New J. Chem.*, **2020**, 44 (23), 9858–9862.
- [14] A. V. Artem'ev, A. Y. Baranov, M. I. Rakhmanova, S. F. Malysheva, D. G. Samsonenko, *New J. Chem.*, **2020**, 44 (17), 6916–6922.
- [15] M. A. Shameem, A. Orthaber, *Chem. - A Eur. J.*, **2016**, 22 (31), 10718–10735.
- [16] S. Bestgen, C. Schoo, B. L. Neumeier, T. J. Feuerstein, C. Zovko, R. Köppe, C. Feldmann, P. W. Roesky, *Angew. Chem. Int. Ed.*, **2018**, 57 (43), 14265–14269.
- [17] M. I. Rogovoy, M. P. Davydova, I. Y. Bagryanskaya, A. V. Artem'ev, *Mendeleev Commun.*, **2020**, 30 (3), 305–307.
- [18] D. Joly, P.-A. Bouit, M. Hissler, *J. Mater. Chem. C*, **2016**, 4 (17), 3686–3698.
- [19] C. Kirst, F. Zoller, T. Bräuniger, P. Mayer, D. Fattakhova-Rohlfing, K. Karaghiosoff, *Inorg. Chem.*, **2021**, 60 (4), 2437–2445.
- [20] A. Nojiri, N. Kumagai, M. Shibasaki, *J. Am. Chem. Soc.*, **2009**, 131 (10), 3779–3784.
- [21] J. Crawford, M. Sigman, *Synth.*, **2019**, 51 (05), 1021–1036.
- [22] S. Schäfer, M. T. Gamer, S. Lebedkin, F. Weigend, M. M. Kappes, P. W. Roesky, *Chem. - A Eur. J.*, **2017**, 23 (50), 12198–12209.
- [23] C. G. J. Tazelaar, J. C. Slootweg, K. Lammertsma, *Coord. Chem. Rev.*, **2018**, 356, 115–126.
- [24] R. Robson, *Dalton Trans.*, **2008**, No. 38, 5113.
- [25] S.-Q. Bai, D. J. Young, T. S. A. Hor, *Chem. - An Asian J.*, **2011**, 6 (2), 292–304.
- [26] A. G. Blackman, *Eur. J. Inorg. Chem.*, **2008**, 2008 (17), 2633–2647.
- [27] M. I. Rogovoy, A. S. Berezin, D. G. Samsonenko, A. V. Artem'ev, *Inorg. Chem.*, **2021**, 60 (9), 6680–6687.
- [28] N. Lin, J. Qiao, L. Duan, H. Li, L. Wang, Y. Qiu, *J. Phys. Chem. C*, **2012**, 116 (36), 19451–19457.
- [29] K. Katagiri, Y. Yamamoto, Y. Takahata, R. Kishibe, N. Fujimoto, *Tetrahedron Lett.*, **2019**, 60 (30), 2026–2029.
- [30] H. Li, M. Hong, A. Scarpaci, X. He, C. Risko, J. S. Sears, S. Barlow, P. Winget, S. R. Marder, D. Kim, J.-L. Brédas, *Chem. Mater.*, **2019**, 31 (5), 1507–1519.
- [31] M. M. Azrain, M. R. Mansor, S. H. S. M. Fadzullah, G. Omar, D. Sivakumar, L. M. Lim, M. N. A. Nordin, *Synth. Met.*, **2018**, 235 (December 2017), 160–175.
- [32] S. Schmidbauer, A. Hohenleutner, B. König, *Adv. Mater.*, **2013**, 25 (15), 2114–2129.
- [33] L.-L. Chen, W.-Y. Tan, X.-H. Zhu, *Sci. Bull.*, **2020**, 65 (24), 2033–2035.

-
- [34] W. Becker, *J. Microsc.*, **2012**, *247* (2), 119–136.
- [35] W. Schrimpf, G. Ossato, P. Hirschle, S. Wuttke, D. C. Lamb, *Small*, **2016**, *12* (27), 3651–3657.
- [36] B. M. Connolly, M. Aragonés-Anglada, J. Gandara-Loe, N. A. Danaf, D. C. Lamb, J. P. Mehta, D. Vulpe, S. Wuttke, J. Silvestre-Albero, P. Z. Moghadam, A. E. H. Wheatley, D. Fairen-Jimenez, *Nat. Commun.*, **2019**, *10* (1), 2345.
- [37] N. Al Danaf, W. Schrimpf, P. Hirschle, D. C. Lamb, Z. Ji, S. Wuttke, *J. Am. Chem. Soc.*, **2021**, *143* (28), 10541–10546.
- [38] A. Periasamy, R. M. Clegg, *FLIM Microscopy in Biology and Medicine*, 1st ed., Periasamy, A., Clegg, R. M., Eds., Chapman and Hall/CRC, **2009**.
- [39] C. Giansante, G. Raffy, C. Schäfer, H. Rahma, M.-T. Kao, A. G. L. Olive, A. Del Guerso, *J. Am. Chem. Soc.*, **2011**, *133* (2), 316–325.
- [40] J.-H. Huang, F.-C. Chien, P. Chen, K.-C. Ho, C.-W. Chu, *Anal. Chem.*, **2010**, *82* (5), 1669–1673.
- [41] H.-J. Lin, P. Herman, J. R. Lakowicz, *Cytometry*, **2003**, *52A* (2), 77–89.
- [42] M. A. Bennet, P. R. Richardson, J. Arlt, A. McCarthy, G. S. Buller, A. C. Jones, *Lab Chip*, **2011**, *11* (22), 3821.
- [43] M. Lahn, C. Dosche, C. Hille, *Am. J. Physiol. Physiol.*, **2011**, *300* (6), C1323–C1336.
- [44] Y. Y. Liao, S. T. A. G. Melissen, J. F. Audibert, T. T. Vu, G. Clavier, R. Méallet-Renault, P. Retailleau, J. P. Lemaistre, V. Génot, R. Pansu, *ChemPhotoChem*, **2018**, *2* (2), 72–80.
- [45] V. M. Korshunov, T. N. Chmovzh, I. S. Golovanov, E. A. Knyazeva, L. V. Mikhalchenko, R. S. Saifutyarov, I. C. Avetisov, J. D. Woollins, I. V. Taydakov, O. A. Rakitin, *Dye. Pigment.*, **2021**, *185*, 108917.
- [46] M. A. Spackman, D. Jayatilaka, *CrystEngComm*, **2009**, *11* (1), 19–32.
- [47] Y. Liu, X. Tao, F. Wang, J. Shi, J. Sun, W. Yu, Y. Ren, D. Zou, M. Jiang, *J. Phys. Chem. C*, **2007**, *111* (17), 6544–6549.
- [48] G.-J. Zhao, K.-L. Han, *Acc. Chem. Res.*, **2012**, *45* (3), 404–413.
- [49] S.-J. Yoon, J. W. Chung, J. Gierschner, K. S. Kim, M.-G. Choi, D. Kim, S. Y. Park, *J. Am. Chem. Soc.*, **2010**, *132* (39), 13675–13683.
- [50] K. Zhang, J. Liu, Y. Zhang, J. Fan, C.-K. Wang, L. Lin, *J. Phys. Chem. C*, **2019**, *123* (40), 24705–24713.
- [51] M. Sims, D. D. C. Bradley, M. Ariu, M. Koeberg, A. Asimakis, M. Grell, D. G. Lidzey, *Adv. Funct. Mater.*, **2004**, *14* (8), 765–781.
- [52] J. B. Birks, *Photophysics of aromatic molecules*, Wiley, London, **1970**.
- [53] T. Konakahara, T. Murayama, K. Sano, S. Kubota, *ChemInform*, **2010**, *27* (32).
- [54] P. H. Olesen, J. B. Hansen, H. C. Hansen, Novel Substituted Azacyclic or Azabicyclic compounds. WO 97/11072, 1996.
- [55] F. C. Schaefer, G. A. Peters, *J. Org. Chem.*, **1961**, *26* (8), 2778–2784.
- [56] F. C. Schaefer, G. A. Peters, *J. Org. Chem.*, **1961**, *26* (8), 2784–2786.
- [57] A. Kermagoret, F. Tomicki, P. Braunstein, *Dalton Trans.*, **2008**, *22*, 2945–2955.
- [58] S. Malysheva, N. Gusarova, N. Belogorlova, A. Sutyrina, Y. Litvintsev, A. Albanov, I. Sterkhova, A. Artem'ev, *Synlett*, **2016**, *27* (17), 2451–2454.
- [59] S. F. Malysheva, N. A. Belogorlova, V. A. Kuimov, Y. I. Litvintsev, I. V. Sterkhova, A. I. Albanov, N. K. Gusarova, B. A. Trofimov, *Tetrahedron Lett.*, **2018**, *59* (8), 723–726.
- [60] T. Steiner, *Angew. Chem. Int. Ed.*, **2002**, *41*, 48–76.
- [61] C. Janiak, *Dalton Trans.*, **2000**, No. 21, 3885–3896.
- [62] W. B. Jennings, B. M. Farrell, J. F. Malone, *Acc. Chem. Res.*, **2001**, *34* (11), 885–894.
- [63] M. A. Digman, V. R. Caiolfa, M. Zamai, E. Gratton, *Biophys. J.*, **2008**, *94* (2), L14–L16.
- [64] G. I. Redford, R. M. Clegg, *J. Fluoresc.*, **2005**, *15* (5), 805–815.

- [65] W. Schrimpf, J. Jiang, Z. Ji, P. Hirschle, D. C. Lamb, O. M. Yaghi, S. Wuttke, *Nat. Commun.*, **2018**, 9 (1), 1647.
- [66] M. J. Turner, J. J. McKinnon, S. K. Wolff, D. J. Grimwood, P. R. Spackman, D. Jayatilaka, M. A. Spackman, *CrystalExplorer17*, University of Western Australia, Australia, **2017**.

2.5.5. Supporting information

2.5.5.1. Synthesis

2-((trimethylsilyl)methyl)pyrazine (1): 2-Methylpyrazine (20 mL, 219 mmol) was dissolved in 40 mL tetrahydrofuran and cooled down to $-78\text{ }^{\circ}\text{C}$. Freshly prepared lithium diisopropylamine (1 eq., 153 mL, 219 mmol) was added dropwise while stirring. The yellow solution turned orange and, after stirring for another hour, trimethylsilyl chloride (2 eq., 56 mL, 438 mmol) was added dropwise to the mixture at $-78\text{ }^{\circ}\text{C}$. The color of the mixture turned clear red and was allowed to warm up to RT overnight. The solvent was removed under vacuum. After distillation (10^{-3} bar, $28\text{ }^{\circ}\text{C}$, $60\text{ }^{\circ}\text{C}$ oil bath), **1** was received as a yellow oil. Yield: 10 g (27.5 %).

^1H (CDCl_3 , 400 MHz): δ [ppm] = 8.31 (s, 1 H, CH_{Ar}), 8.22 (s, $^2J_{\text{H,Si}}$ = 8.6 Hz, 1 H, CH_{Ar}), 8.18 (d, $^1J_{\text{H,H}}$ = 2.5 Hz, 1 H, CH_{Ar}), 2.27 (s, 2 H, CH_2), -0.04 (s, $^2J_{\text{H,Si}}$ = 58.7 Hz, 9 H, Si- CH_3). $^{13}\text{C}\{^1\text{H}\}$ (CDCl_3 , 100 MHz): δ [ppm] = 157.6 (s, Cq), 143.9 (s, CH_{Ar}), 143.7 (s, CH_{Ar}), 140.2 (s, CH_{Ar}), 27.4 (s, $^1J_{\text{C,Si}}$ = 21.2 Hz, CH_2), -1.7 (s, $^1J_{\text{C,Si}}$ = 25.8 Hz, Si- CH_3). ^{29}Si INEPT (CDCl_3 , 80 MHz): δ [ppm] = 3.2 (s). Elemental analysis calculated (%) for $[\text{C}_8\text{H}_{14}\text{N}_2\text{Si}]$: C 57.78, H 8.49, N 16.85; found C 57.86, H 8.19, N 17.07. GC/EI MS (positive mode) m/z calculated for $[\text{C}_8\text{H}_{14}\text{N}_2\text{Si}]$ $[\text{M}]^+$: 166.0926, found 166.0918. IR: $\tilde{\nu}$ [cm^{-1}] = 3054 (vw), 2956 (w), 2901 (vw), 1575 (vw), 1521 (w), 1472 (m), 1409 (m), 1393 (m), 1304 (w), 1248 (s), 1169 (w), 1145 (m), 1070 (w), 1014 (m), 848 (vs), 749 (m), 695 (m), 636 (w), 405 (s).

2,3,5-trimethyl-6-((trimethylsilyl)methyl)pyrazine (2): 2,3,5,6-tetra-methylpyrazine (15.0 g, 110 mmol) was dissolved in 50 mL tetrahydrofuran and cooled down to $-78\text{ }^{\circ}\text{C}$. *n*-Butyllithium (0.95 eq., 43.6 mL, 105 mmol, 2.40 M in hexane) was added dropwise while stirring. The solution turns deep red and, after stirring for another hour, trimethylsilyl chloride (1.5 eq, 21.0 mL, 165 mmol) was added dropwise to the mixture at $-78\text{ }^{\circ}\text{C}$. The color of the mixture turned colorless and was allowed to warm up to RT overnight. The solvent was removed under vacuum. After distillation (10^{-3} bar, $50\text{ }^{\circ}\text{C}$, $80\text{ }^{\circ}\text{C}$ oil bath), **2** was received as a colorless, viscos oil. Yield: 19.9 g (86.7 %).

^1H (CDCl_3 , 400 MHz): δ [ppm] = 2.40 (s, 9 H, CH_3), 2.26 (s, 2 H, CH_2), 0.01 (s, $^2J_{\text{H,Si}}$ = 3.0 Hz, $^1J_{\text{H,C}}$ = 58.7 Hz, 9 H, Si- CH_3). $^{13}\text{C}\{^1\text{H}\}$ (CDCl_3 , 100 MHz): δ [ppm] = 151.7 (s), 148.1 (s), 146.7 (s), 146.2 (s), 25.7 (s), 22.0 (s), 21.5 (s), 21.4 (s), -1.0 (s, $^1J_{\text{C,Si}}$ = 25.8 Hz, Si- CH_3). ^{29}Si INEPT (CDCl_3 , 80 MHz): δ [ppm] = 3.3 (s, $^2J_{\text{Si,C}}$ = 25.3 Hz). Elemental analysis calculated (%) for $[\text{C}_{11}\text{H}_{20}\text{N}_2\text{Si}]$: C 63.40, H 9.67, N 13.44; found C 62.92, H 9.32, N 13.26. GC/EI MS (positive mode) m/z calculated for $[\text{C}_9\text{H}_{17}\text{N}_3\text{Si}]$ $[\text{M}]^+$: 208.1396, found 208.1389. IR: $\tilde{\nu}$ [cm^{-1}] = 2952 (w), 2918 (vw), 1546 (vw), 1444 (w), 1412 (m), 1393 (m), 1372 (w), 1357 (vw), 1284 (vw), 1247 (m), 1222 (m), 1188 (w), 1151 (w), 1126 (vw), 1077 (w), 1021 (vw), 987 (m), 841 (vs), 819 (s), 779 (w), 749 (w), 722 (w), 693 (m), 666 (w).

2,4-dimethyl-6-((trimethylsilyl)methyl)-1,3,5-triazine (3): 2,4,6-Trimethyl-1,3,5-triazine was synthesized according to adapted literature procedures.^[10] A 300 mL *Erlenmeyer*-flask was charged with potassium carbonate (34.6 g, 250 mmol, 1.04 eq.) in 120 mL H_2O and 60 mL dichloromethane. Ethyl acetimidate hydrochloride (29.7 g, 240 mmol, 1.00 eq.) was added at RT and the resulting solution was stirred for 15 min. After separation of the organic phase, the aqueous layer was extracted with dichloromethane (2 x 60 mL). The combined organic layers were dried over K_2CO_3 and stored overnight in the fridge. The reaction mixture was filtered and the residue was extracted with dichloromethane (2 x 20 mL). Dichloromethane was removed carefully from the resulting filtrate *via* distillation at $37\text{ }^{\circ}\text{C}$. Glacial acetic acid (1.00 mL, 17.5 mmol, 0.07 eq.) was added to the remaining solution over 20 min at RT. After 1.5 h of stirring, the resulting cloudy solution was allowed to stand overnight. The remaining acid was neutralized with a $\text{K}_2\text{CO}_3/\text{H}_2\text{O}$ -mixture. The organic layer was separated and dried over K_2CO_3 . and the resulting precipitate was filtered off. The organic solvent is carefully removed *in vacuo* and the remaining solid was dissolved in Et_2O (30 mL). After separating any

resulting precipitate, the crude product was concentrated *in vacuo* to obtain 2,4,6-trimethyl-1,3,5-triazine (4.90 g, 39.8 mmol, 50 % yield) as colorless crystals. For the synthesis of the trimethylsilyl-compound, 2,4,6-trimethyl-1,3,5-triazine (4.90 g, 39.8 mmol) was dissolved in 40 mL tetrahydrofuran and cooled down to $-78\text{ }^{\circ}\text{C}$. *n*-Butyllithium (0.97 eq., 16.0 mL, 38.4 mmol, 2.40 M in hexane) was added dropwise while stirring. The solution turned yellow and, after stirring for another hour, trimethylsilyl chloride (1.2 eq, 6.10 mL, 47.9 mmol) was added dropwise to the mixture at $-78\text{ }^{\circ}\text{C}$. The color of the mixture turned colorless and was allowed to warm up to RT overnight. The solvent was removed under vacuum. After distillation (10^{-3} bar, $33\text{ }^{\circ}\text{C}$, $50\text{ }^{\circ}\text{C}$ oil bath), **3** was received as a colorless liquid. Yield: 2.68 g (34.0 %).

^1H (CDCl_3 , 400 MHz): δ [ppm] = 2.40 (s, 6 H, CH_3), 2.29 (s, 2 H, CH_2), -0.07 (s, $^1J_{\text{H,Si}} = 8.3$ Hz, 9 H, $\text{Si}-\text{CH}_3$); $^{13}\text{C}\{^1\text{H}\}$ (CDCl_3 , 100 MHz): δ [ppm] = 178.9 (s, Cq), 175.2 (s, Cq), 31.9 (s, $^1J_{\text{C,Si}} = 38.2$ Hz, CH_2), 25.5 (s, CH_3), -1.6 (s, $^1J_{\text{C,Si}} = 52.5$ Hz, $\text{Si}-\text{CH}_3$). ^{29}Si INEPT (CDCl_3 , 80 MHz): δ [ppm] = 4.5 (s). ^{15}N *via* ^1H , ^{15}N -HMBC (CDCl_3 , 41 MHz): δ [ppm] = -136.3 (s). Elemental analysis calculated (%) for $[\text{C}_9\text{H}_{17}\text{N}_3\text{Si}]$: C 55.34, H 8.77, N 21.51, found: C 55.15, H 8.53, N 21.55. GC/EI MS (positive mode) m/z calculated for $[\text{C}_9\text{H}_{17}\text{N}_3\text{Si}]$ $[\text{M}]^+$: 195.1192, found 195.1184. IR: $\tilde{\nu}$ [cm^{-1}] = 2957 (w), 2897 (vw), 1530 (vs), 1434 (m), 1391 (m), 1349 (m), 1250 (m), 1136 (m), 1036 (w), 960 (w), 938 (w), 845 (vs), 697 (m), 566 (m).

bis(pyrazin-2-ylmethyl)phenylphosphine oxide (4): Compound **1** (3 eq., 7.48 g, 45.0 mmol) was dissolved in 30 mL of dry, degassed tetrahydrofuran and cooled to $-10\text{ }^{\circ}\text{C}$. Dichlorophenylphosphine (2.04 mL, 15.0 mmol) was added dropwise while stirring. The solution turned from bright yellow to pale yellow, to orange and a colorless precipitate was formed. The reaction mixture was warmed up to RT overnight. The volatiles were removed *in vacuo* and bis(pyrazin-2-ylmethyl)phenylphosphine was obtained as an orange viscos oil (^{31}P NMR $\delta = -12.8$ ppm). The freshly synthesized phosphine (15.0 mmol, 4.41 g) was dissolved in 30 mL dichloromethane. A water/ H_2O_2 mixture (2 mL 30 % H_2O_2 in 5 mL water) was added dropwise to the mixture at $-10\text{ }^{\circ}\text{C}$ and stirred for 5 h. The solvent was removed under reduced pressure. The left-over mixture was dissolved in dichloromethane and extracted with water three times. The dichloromethane fractions were combined and all volatiles were removed. **4** was received as a colorless solid. Crystalline yield: 3.11 g (66.8 %), m.p. $170\text{ }^{\circ}\text{C}$.

^1H (CDCl_3 , 400 MHz): δ [ppm] = 8.49 (d, $^2J_{\text{H,H}} = 1.7$ Hz, 2 H, CH_{pyr}), 8.42 (dt, $J_{\text{H,P}} = 11.9$ Hz, $J_{\text{H,H}} = 2.0$ Hz, 2 H, CH_{pyr}), 7.56 (m, 2 H, $\text{CH}_{\text{phenyl}}$), 7.49 (tq, $^3J_{\text{H,H}} = 6.5$, $J_{\text{H,H}} = 1.4$ Hz, 1 H, $\text{CH}_{\text{phenyl}}$), 7.39 (m, 2 H, $\text{CH}_{\text{phenyl}}$), ABX spin system (A = B = H, X = P) 3.76 (dd, $^2J_{\text{A,B}} = 14.5$, $^2J_{\text{X,B}} = 15.0$ Hz, 2 H, CH_2), 3.73 (dd, $^2J_{\text{A,B}} = 14.5$, $^2J_{\text{A,X}} = 14.4$ Hz, 2 H, CH_2). $^{13}\text{C}\{^1\text{H}\}$ (CDCl_3 , 100 MHz): δ [ppm] = 149.0 (d, $^2J_{\text{C,P}} = 7.9$ Hz, Cq), 146.1 (d, $^3J_{\text{C,P}} = 4.6$ Hz, C_{Ar}), 144.2 (d, $^3J_{\text{C,P}} = 2.3$ Hz, C_{Ar}), 143.1 (d, $^4J_{\text{C,P}} = 3.0$ Hz, C_{Ar}), 132.5 (d, $^3J_{\text{C,P}} = 2.8$ Hz, C_{Ar}), 130.4 (d, $^1J_{\text{C,P}} = 98.1$ Hz, Cq), 130.7 (d, $^2J_{\text{C,P}} = 9.2$ Hz, C_{Ar}), 128.8 (d, $^1J_{\text{C,P}} = 11.9$ Hz, C_{Ar}), 38.1 (d, $^1J_{\text{C,P}} = 61.4$ Hz, CH_2). ^{31}P (CDCl_3 , 162 MHz): δ [ppm] = 35.1 (hept, $^2J_{\text{P,H}} = 14.3$ Hz). ^{15}N *via* ^1H , ^{15}N -HMBC (CDCl_3 , 41 MHz): δ [ppm] = -68.0 (s). Elemental analysis calculated (%) for $[\text{C}_{16}\text{H}_{15}\text{N}_4\text{PO}]$: C 61.93, H 4.87, N 18.06; found: C 61.98, H 5.03 N 17.85. ESI MS (positive mode) m/z calculated for $[\text{C}_{16}\text{H}_{15}\text{N}_4\text{PO}]$ $[\text{M}+\text{H}]^+$: 311.1017, found 311.1059. IR: $\tilde{\nu}$ [cm^{-1}] = 3077 (vw), 2965 (w), 2933 (w), 2880 (w), 1606 (vs), 1577 (w), 1524 (w), 1471 (m), 1402 (m), 1318 (w), 1258 (m), 1199 (s), 1157 (m), 1115 (s), 1057 (m), 1018 (s), 867 (s), 756 (m), 731 (vs), 694 (s), 609 (w), 498 (vs), 434 (s), 408 (vs).

tris(pyrazin-2-ylmethyl)phosphine oxide (5): Compound **1** (3.5 eq, 9.98 g, 60.0 mmol) was dissolved in 30 mL of dry, degassed tetrahydrofuran and cooled to $-10\text{ }^{\circ}\text{C}$. PCl_3 (1.31 mL, 15.0 mmol) was added dropwise while stirring. The reaction mixture was warmed up to RT overnight. The volatiles were removed *in vacuo* and tris(pyrazin-2-ylmethyl)phosphine was obtained as an orange viscos oil (^{31}P NMR $\delta = -12.6$ ppm). The freshly synthesized phosphine (15.0 mmol, 4.66 g) was dissolved in 30 mL dichloromethane. A water/ H_2O_2 mixture (2 mL 30 % H_2O_2 in 5 mL water) was added dropwise to the mixture at $-10\text{ }^{\circ}\text{C}$ and stirred for 5 h. The solvent was removed under reduced pressure. The left-over mixture was dissolved in dichloromethane and extracted with water three times. The dichloromethane

fractions were combined and all volatiles were removed. **5** was received as a colorless solid. Crystalline yield: 2.98 g (60.9 %), m.p. 130 °C.

^1H (CDCl_3 , 400 MHz): δ [ppm] = 8.62 (t, $^4J = 1.5$ Hz, 3 H, CH_{pyr}), 8.50 (dd, $^3J = 1.5$ Hz, 3 H, CH_{pyr}), 8.47 (dd, $^3J_{\text{H,H}} = 1.9$ Hz, 3 H, CH_{pyr}), 3.59 (d, $^2J_{\text{H,P}} = 14.9$ Hz, 6 H, CH_2). $^{13}\text{C}\{^1\text{H}\}$ (CDCl_3 , 100 MHz): δ [ppm] = 149.1 (d, $^2J_{\text{C,P}} = 7.9$ Hz, Cq), 146.3 (d, $^3J_{\text{C,P}} = 5.4$ Hz, CH_{pyr}), 144.2 (d, $^5J_{\text{C,P}} = 2.3$ Hz), 143.3 (d, $^4J_{\text{C,P}} = 2.7$ Hz, CH_{pyr}), 36.1 (d, $^1J_{\text{C,P}} = 60.1$ Hz, CH_2). $^{31}\text{P}\{^1\text{H}\}$ (CDCl_3 , 162 MHz): δ [ppm] = 42.2 (s). ^{31}P (CDCl_3 , 162 MHz): δ [ppm] = 42.2 (sept, $^2J_{\text{P,H}} = 15.2$ Hz). ^{15}N *via* ^1H , ^{15}N -HMBC (CDCl_3 , 41 MHz): δ [ppm] = -69.1 (s). Elemental analysis calculated (%) for $[\text{C}_{15}\text{H}_{15}\text{N}_6\text{PO}]$: C 55.21, H 4.63, N 25.76 found: C 55.11, H 4.62, N 25.75. ESI MS (positive mode) m/z calculated for $[\text{C}_{15}\text{H}_{15}\text{N}_6\text{PO}]$ $[\text{M}+\text{H}]^+$: 327.1097, found 327.1119. IR: $\tilde{\nu}$ [cm^{-1}] = 3136 (w), 3060 (w), 2951 (w), 2908 (w), 2841 (w), 1582 (w), 1524 (w), 1504 (m), 1475 (m), 1401 (m), 1315 (w), 1257 (m), 1198 (m), 1160 (m), 1090 (m), 1058 (m), 1018 (s), 932 (w), 865 (s), 844 (m), 762 (w), 732 (m), 671 (w), 610 (w), 490 (m), 405 (vs).

bis((3,5,6-trimethylpyrazin-2-yl)methyl)phenylphosphine oxide (6): Compound **2** (2.1 eq, 6.56 g, 31.5 mmol) was dissolved in 30 mL of dry, degassed tetrahydrofuran and cooled to -10 °C. Dichlorophenylphosphine (2.04 mL, 15.0 mmol) was added dropwise while stirring. The solution stays colorless. The reaction mixture was warmed up to RT overnight. The volatiles were removed *in vacuo* and phenylbis((3,5,6-trimethylpyrazin-2-yl)methyl)phosphine was obtained as a yellow viscos oil (^{31}P NMR $\delta = -23.7$ ppm). The freshly synthesized phosphine (15.0 mmol, 5.68 g) was dissolved in 30 mL dichloromethane. A water/ H_2O_2 mixture (2 mL 30 % H_2O_2 in 5 mL water) was added dropwise to the mixture at -10 °C and stirred for 5 h. The solvent was removed under reduced pressure. The left-over mixture was dissolved in dichloromethane and extracted with water three times. The dichloromethane fractions were combined and all volatiles were removed. **6** was received as a colorless solid. Crystalline yield: 5.10 g (86.2 %), m.p. 140 °C.

^1H (CDCl_3 , 400 MHz): δ [ppm] = 7.60 (dd, $^3J_{\text{H,H}} = 7.0$ Hz, $^4J_{\text{H,H}} = 1.3$ Hz, 2 H, $\text{CH}_{\text{phenyl}}$), 7.74 (t, $^3J_{\text{H,H}} = 7.4$ Hz, $^4J_{\text{H,H}} = 1.1$ Hz, 1 H, $\text{CH}_{\text{phenyl}}$), 7.36 (t, $^3J_{\text{H,H}} = 7.5$ Hz, $^3J_{\text{H-H}} = 1.3$ Hz, 2 H, $\text{CH}_{\text{phenyl}}$), ABX spin system (A = B = H, X = P) 3.77 (dd, $^2J_{\text{A,B}} = 14.8$, $^2J_{\text{X,B}} = 15.1$ Hz, 2 H, CH_2), 3.73 (dd, $^2J_{\text{A,B}} = 14.6$, $^2J_{\text{X,B}} = 14.1$ Hz, 2 H, CH_2), 2.42 (d, $^2J_{\text{H,P}} = 2.2$ Hz, 6 H, CH_3), 2.36 (s, 12 H, CH_3). $^{13}\text{C}\{^1\text{H}\}$ (CDCl_3 , 100 MHz): δ [ppm] = 149.9 (d, $^3J_{\text{C,P}} = 5.1$ Hz, Cq- CH_3), 148.7 (d, $^4J_{\text{C,P}} = 2.4$ Hz, Cq- CH_3), 148.3 (s, Cq- CH_3), 143.4 (d, $^2J_{\text{C,P}} = 8.8$ Hz, Cq), 132.1 (d, $^4J_{\text{C,P}} = 2.6$ Hz, $\text{CH}_{\text{phenyl}}$), 132.0 (s, second peak missing, Cq, $\text{CH}_{\text{phenyl}}$), 131.0 (d, $^3J_{\text{C,P}} = 9.6$ Hz, $\text{CH}_{\text{phenyl}}$), 128.3 (d, $^2J_{\text{C,P}} = 11.7$ Hz, $\text{CH}_{\text{phenyl}}$), 37.2 (d, $^1J_{\text{C,P}} = 62.4$ Hz, CH_2), 21.5 (t, $^4J_{\text{C,P}} = 1.0$ Hz, CH_3), 21.2 (s, CH_3). $^{31}\text{P}\{^1\text{H}\}$ (CDCl_3 , 162 MHz): δ [ppm] = 37.9 (s). ^{31}P (CDCl_3 , 162 MHz): δ [ppm] = 37.9 (quintet, $^2J_{\text{P,H}} = 14.6$ Hz). ^{15}N *via* ^1H , ^{15}N -HMBC (CDCl_3 , 41 MHz): δ [ppm] = -69.7 (s), -71.6 (s). Elemental analysis calculated (%) for $[\text{C}_{22}\text{H}_{27}\text{N}_4\text{PO}]$: C 66.99, H 6.90, N 14.20, found: C 66.73, H 6.77, N 14.20. ESI MS (positive mode) m/z calculated for $[\text{C}_{22}\text{H}_{27}\text{N}_4\text{PO}]$ $[\text{M}+\text{H}]^+$: 395.1956 found 395.1994. IR: $\tilde{\nu}$ [cm^{-1}] = 2988 (vw), 2962 (w), 2919 (w), 1592 (vw), 1432 (m), 1406 (vs), 1221 (m), 1195 (vs), 1114 (m), 1069 (w), 989 (m), 863 (w), 803 (m), 726 (s), 697 (m), 631 (s), 515 (m), 437 (vs), 415 (s).

tris((3,5,6-trimethylpyrazin-2-yl)methyl)phosphine oxide (7): Compound **2** (3.5 eq, 9.98 g, 47.9 mmol) was dissolved in 30 mL of dry, degassed tetrahydrofuran and cooled to -10 °C. PCl_3 (1.31 mL, 13.7 mmol) was added dropwise while stirring. The reaction mixture was warmed up to RT overnight. The volatiles were removed *in vacuo* and tris((3,5,6-trimethylpyrazin-2-yl)methyl)phosphine was obtained as an orange viscos oil, which hardens after a while (^{31}P NMR $\delta = -25.9$ ppm). The freshly synthesized phosphine (15.0 mmol, 4.66 g) was dissolved in 30 mL dichloromethane. A water/ H_2O_2 mixture (2 mL 30 % H_2O_2 in 5 mL water) was added dropwise to the mixture at -10 °C and stirred for 1 h. Leftover tetramethylpyrazin crystallizes at -10 °C and can be filtered off. The solvent was removed under reduced pressure and **7** was received as a colorless solid. Yield: 5.12 g (82.7 %), m.p. 190 °C.

^1H (CDCl_3 , 400 MHz): δ [ppm] = 3.66 (d, $^3J_{\text{H,P}} = 14.6$ Hz, 6 H, CH_2), 2.44 (s, 18 H, CH_3). $^{13}\text{C}\{^1\text{H}\}$ (CDCl_3 , 101 MHz): δ [ppm] = 149.7 (d, $^3J_{\text{C,P}} = 5.8$ Hz, Cq- CH_3), 149.3 (d, $^4J_{\text{C,P}} = 3.2$ Hz, Cq- CH_3), 148.5 (d, $^5J_{\text{C,P}} = 1.9$ Hz, Cq- CH_3), 144.3 (d, $^2J_{\text{C,P}} = 8.5$ Hz, Cq), 36.7 (d, $^1J_{\text{C,P}} = 60.4$ Hz, CH_2), 21.7 (d, $^4J_{\text{C,P}} = 0.9$ Hz, CH_3), 21.6 (d, $^5J_{\text{C,P}} = 0.9$ Hz, CH_3), 21.6 (s, CH_3). $^{31}\text{P}\{^1\text{H}\}$ (CDCl_3 , 162 MHz): δ [ppm] = 44.4 (s). ^{31}P (CDCl_3 , 162 MHz): δ [ppm] = 44.4 (septet, $^2J_{\text{P,H}} = 14.8$ Hz). ^{15}N *via* ^1H , ^{15}N -HMBC (CDCl_3 , 41 MHz): δ [ppm] = -68.8 (s). ESI MS (negative mode) m/z calculated for $[\text{C}_{24}\text{H}_{33}\text{N}_6\text{PO}] [\text{M}-\text{H}]^-$: 451.23752, found 451.2380. IR: $\tilde{\nu}_{\text{max}}$ (cm^{-1}) = 2988 (vw), 2920 (w), 1442 (m), 1412 (vs), 1397 (s), 1286 (vw), 1244 (w), 1234 (w), 1190 (m), 1168 (vs), 1127 (w), 1089 (w), 1029 (w), 1010 (w), 988 (s), 875 (m), 803 (m), 782 (w), 743 (w), 711 (w), 690 (w).

bis((4,6-dimethyl-1,3,5-triazin-2-yl)methyl)phenylphosphine oxide (8): Compound **3** (2.10 eq., 2.38 g, 12.2 mmol) was dissolved in 40 mL of dry, degassed tetrahydrofuran and cooled to -10 °C. Dichlorophenylphosphine (1.00 eq, 0.79 mL, 5.83 mmol) was added dropwise while stirring. The solution stays colorless. The reaction mixture was warmed up to RT overnight. The volatiles were removed *in vacuo* and bis((4,6-dimethyl-1,3,5-triazin-2-yl)methyl)phenyl-phosphine was obtained as a yellow viscos oil (^{31}P NMR $\delta = -13.8$ ppm). The freshly synthesized phosphine (5.83 mmol) was dissolved in 50 mL dichloromethane. A water/ H_2O_2 mixture (1 mL 30 % H_2O_2 in 5 mL water) was added dropwise to the mixture at -10 °C and stirred for 5 h. The solvent was removed under reduced pressure. The left-over mixture was dissolved in dichloromethane and extracted with water three times. The dichloromethane fractions were combined and all volatiles were removed. **8** was received as a colorless solid. Crystalline yield: 0.50 g (23.0 %) m.p. 148 °C.

^1H (CDCl_3 , 400 MHz): δ [ppm] = 7.70 (ddt, $^3J_{\text{H,P}} = 12.1$ Hz, $^3J_{\text{H,H}} = 7.0$ Hz, $^4J_{\text{H,H}} = 1.1$ Hz, 2 H, $\text{CH}_{\text{Phenyl}}$), 7.50 (tq, $^3J_{\text{H,H}} = 7.4$ Hz, $^4J_{\text{H,H}} = 1.4$ Hz, $^5J_{\text{H,P}} = 1.3$ Hz, 1H, $\text{CH}_{\text{Phenyl}}$), 7.42 (tdd, $^3J_{\text{H,H}} = 7.3$ Hz, $^4J_{\text{H,P}} = 3.3$ Hz, $^4J_{\text{H,H}} = 1.2$ Hz, 2 H, $\text{CH}_{\text{Phenyl}}$), ABX spin system (A = B = H, X = P) 3.94 (dd, $^2J_{\text{A,B}} = 13.9$, $^2J_{\text{X,B}} = 15.6$ Hz, 2 H, CH_2), 3.92 (dd, $^2J_{\text{A,B}} = 13.9$, $^2J_{\text{X,B}} = 15.5$ Hz, 2 H, CH_2), 2.52 (s, $^1J_{\text{H,C}} = 128.7$ Hz, 12 H, CH_3). $^{13}\text{C}\{^1\text{H}\}$ (CDCl_3 , 101 MHz): δ [ppm] = 176.5 (d, $^4J_{\text{C,P}} = 1.2$ Hz, Cq- CH_3), 171.6 (d, $^2J_{\text{C,P}} = 7.1$ Hz, Cq), 132.3 (d, $^4J_{\text{C,P}} = 3.0$ Hz, $\text{CH}_{\text{Phenyl}}$), 131.5 (d, $^1J_{\text{C,P}} = 101.0$ Hz, Cq, $_{\text{Phenyl}}$), 130.9 (d, $^3J_{\text{C,P}} = 9.5$ Hz, $\text{CH}_{\text{Phenyl}}$), 128.4 (d, $^2J_{\text{C,P}} = 12.2$ Hz, $\text{CH}_{\text{Phenyl}}$), 42.0 (d, $^1J_{\text{C,P}} = 60.7$ Hz, CH_2), 25.6 (s, CH_3). ^{31}P (CDCl_3 , 162 MHz): δ [ppm] = 34.2 (quintet, $^2J_{\text{P,H}} = 15.3$ Hz). ^{15}N *via* ^1H , ^{15}N -HMBC (CDCl_3 , 41 MHz): δ [ppm] = -129.2 (s), -131.3 (s). EI MS (positive mode) m/z calculated for $[\text{C}_{18}\text{H}_{21}\text{N}_6\text{PO}] [\text{M}+\text{H}]^+$: 369.1592, found 369.1591. IR: $\tilde{\nu}$ [cm^{-1}] = 3058 (vw), 3012 (vw), 2975 (w), 2926 (w), 2513 (vw), 1527 (vs), 1434 (s), 1390 (m), 1352 (s), 1284 (w), 1231 (w), 1206 (s), 1192 (s), 1161 (m), 1114 (m), 1074 (w), 1033 (m), 992 (w), 968 (w), 935 (m), 865 (m), 841 (m), 750 (w), 728 (s), 695 (s), 676 (m), 593 (w), 581 (vw), 564 (m), 550 (s), 501 (s), 432 (s), 401 (m).

tris((4,6-dimethyl-1,3,5-triazin-2-yl)methyl)phosphine oxide (9): Compound **3** (3.5 eq., 9.98 g, 51.1 mmol) was dissolved in 30 mL of dry, degassed tetrahydrofuran and cooled to -10 °C. PCl_3 (1.31 mL, 14.6 mmol) was added dropwise while stirring. The reaction mixture was warmed up to RT overnight. The volatiles were removed *in vacuo* and tris((4,6-dimethyl-1,3,5-triazin-2-yl)methyl)-phosphine was obtained as a yellow viscos oil, which hardens after a while (^{31}P NMR $\delta = -16.8$ ppm). The freshly synthesized phosphine (15.0 mmol, 4.66 g) was dissolved in 30 mL dichloromethane. A water/ H_2O_2 mixture (2 mL 30 % H_2O_2 in 5 mL water) was added dropwise to the mixture at -10 °C and stirred for 1 h. The solvent was removed under reduced pressure and **9** was received as a colorless solid. Crystalline yield: 4.88 g (80.9 %) m.p. 143 °C.

^1H (CDCl_3 , 400 MHz): δ [ppm] = 3.91 (d, $^2J_{\text{H,P}} = 16.1$ Hz, 6 H, CH_2), 2.57 (s, 18 H, CH_3); $^{13}\text{C}\{^1\text{H}\}$ (CDCl_3 , 101 MHz): δ [ppm] = 176.6 (d, $^4J_{\text{C,P}} = 0.7$ Hz, Cq- CH_3), 171.7 (d, $^2J_{\text{C,P}} = 6.4$ Hz, Cq), 40.8 (d, $^1J_{\text{C,P}} = 61.5$ Hz, CH_2), 25.7 (s, CH_3). $^{31}\text{P}\{^1\text{H}\}$ (CDCl_3 , 162 MHz): δ [ppm] = 40.3 (s). ^{31}P (CDCl_3 , 162 MHz): δ [ppm] = 40.3 (septet, $^2J_{\text{P,H}} = 16.0$ Hz). ^{15}N *via* ^1H , ^{15}N HMBC (CDCl_3 , 41 MHz): δ [ppm] = -130.3 (s). EI MS (positive mode) m/z calculated for $\text{C}_{18}\text{H}_{24}\text{N}_9\text{PO} [\text{M}-\text{H}]^-$: 412.1763, found 412.1768. IR: $\tilde{\nu}_{\text{max}}$ (cm^{-1}) = 2976 (vw), 2926 (w), 1623 (vw), 1527 (vs), 1427 (s), 1390 (s), 1353 (s), 1216 (m), 1192 (s), 1171 (m), 1103 (w), 1033

(m), 967 (m), 940 (m), 854 (m), 824 (w), 801 (w), 740 (m), 690 (vw), 666 (w), 591 (vw), 567 (s), 487 (vw), 459 (vw).

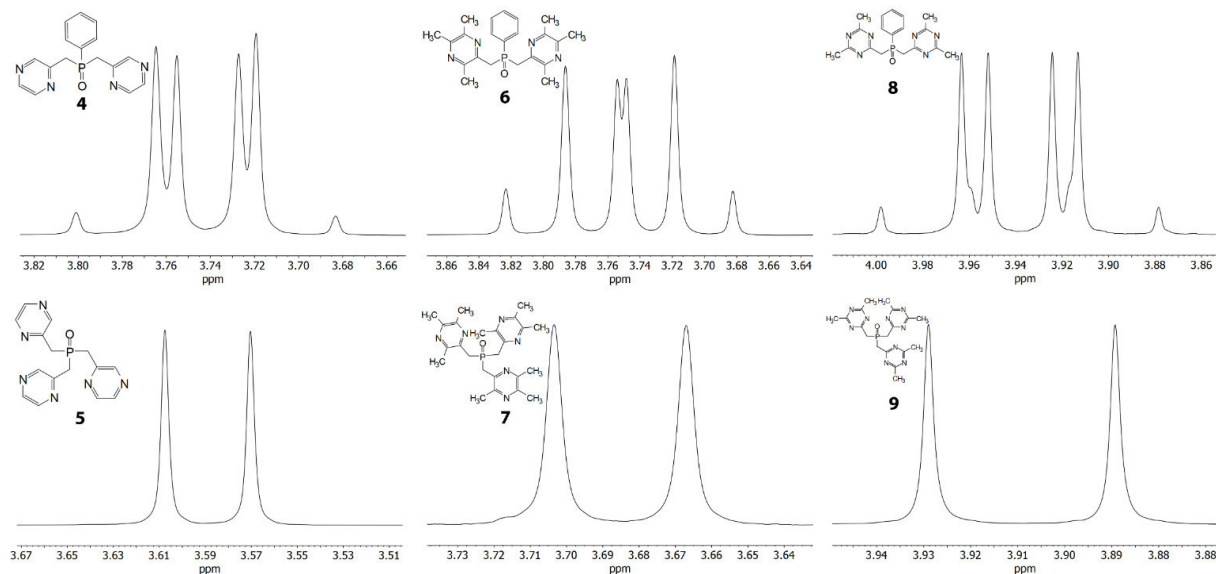


Figure 50. ^1H NMR signal of the methylene groups of the phosphine oxides in CDCl_3 . The bis-substituted phosphine oxides (**2**, **5**, **8**) show the typical AB part of an ABX spectrum. The tris-substituted phosphine oxides (**3**, **6**, **9**) show a normal doublet.

2.5.5.2. Crystallographic data and figures

Table 8. Crystallographic and refinement data for compounds 4-6.

	4	5	6
Formula	C ₁₆ H ₁₅ N ₄ PO	C ₁₅ H ₁₅ N ₆ PO	C ₂₂ H ₂₇ N ₄ PO
Formula weight [g·mol ⁻¹]	310.29	326.30	394.44
Color	colorless	yellow	colorless
Habit	block	prism	Block
<i>T</i> [K]	110	130	123
λ [Å]	0.71073	0.71073	0.71073
Crystal system	monoclinic	monoclinic	monoclinic
Space group	<i>P</i> 2 ₁ / <i>n</i>	<i>P</i> 2 ₁ / <i>c</i>	<i>P</i> 2 ₁ / <i>c</i>
<i>a</i> [Å]	12.2538(6)	18.8494(8)	14.1437(4)
<i>b</i> [Å]	5.6173(3)	10.2782(4)	17.3752(7)
<i>c</i> [Å]	20.9600(11)	7.9072(3)	8.7363(3)
α [°]	90	90	90
β [°]	96.397(2)	91.332(4)	97.662(3)
γ [°]	90	90	90
<i>V</i> [Å ³]	1,433.76(13)	1,531.51(11)	2,127.77(13)
<i>Z</i>	4	4	4
ρ_{calc} [g·cm ⁻³]	1.437	1.415	1.231
μ [mm ⁻¹]	0.199	0.194	0.149
<i>F</i> (0 0 0)	648	680	840
Crystal size [mm]	0.07×0.03×0.02	0.45×0.20×0.10	0.40×0.35×0.08
θ range [°]	3.211–26.373	3.407–29.570	3.322–28.277
Index ranges	–15 ≤ <i>h</i> ≤ 15 –7 ≤ <i>k</i> ≤ 7 –25 ≤ <i>l</i> ≤ 26	–26 ≤ <i>h</i> ≤ 23 –14 ≤ <i>k</i> ≤ 14 –10 ≤ <i>l</i> ≤ 10	–18 ≤ <i>h</i> ≤ 18 –23 ≤ <i>k</i> ≤ 22 –11 ≤ <i>l</i> ≤ 11
reflns collected	21,161	15,018	21,576
Independent reflns	2,910 [<i>R</i> _{int} = 0.0588]	4,273 [<i>R</i> _{int} = 0.0502]	5,250 [<i>R</i> _{int} = 0.0493]
Completeness to theta	99.7 %	99.7 %	99.6 %
Refinement method	Full-matrix least-squares on <i>F</i> ²	Full-matrix least-squares on <i>F</i> ²	Full-matrix least-squares on <i>F</i> ²
Data/restraints/ Parameters	2,910 / 0 / 199	4,273 / 0 / 208	5,250 / 0 / 259
Hydrogen atom treatment	constrained	constrained	constrained
<i>R</i> ₁ / <i>wR</i> ₂ (<i>I</i> > 2 σ (<i>I</i>))	0.0327/0.0758	0.0463/0.0959	0.0447/0.1035
<i>R</i> ₁ / <i>wR</i> ₂ (all data)	0.0433/0.0828	0.0737/0.1104	0.0685/0.1175
Goodness-of-fit on <i>F</i> ²	1.021	1.029	1.019
larg. diff peak/hole [e·Å ⁻³]	0.328/–0.347	0.387/–0.352	0.326/–0.290
CCDC No.	2072432	2072408	2072409

Table 9. Crystallographic and refinement data for compounds **7-9**.

	7		8		9	
Formula	C ₂₄ H ₃₃ N ₆ OP		C ₁₈ H ₂₁ N ₆ OP		C ₁₈ H _{25.13} N ₉ O _{1.56} P	
Formula weight [g·mol ⁻¹]	452.53		368.38		423.59	
Colour	colorless		colorless		colorless	
Habit	Rod		Rod		block	
T [K]	123		123		102	
λ [Å]	0.71073		0.71073		0.71073	
Crystal system	tetragonal		monoclinic		monoclinic	
Space group	I4 ₁ /a		P2 ₁ /n		C2/c	
a [Å]	23.6498(4)		13.1900(7)		33.2658(19)	
b [Å]	23.6498(4)		5.2949(3)		4.8664(3)	
c [Å]	19.4811(7)		25.7235(13)		27.5320(15)	
α [°]	90		90		90	
β [°]	90		97.212(5)		105.702(2)	
γ [°]	90		90		90	
V [Å ³]	10,896.0(5)		1,782.31(17)		4,290.7(4)	
Z	16		4		8	
ρ _{calc} [g·cm ⁻³]	1.103		1.373		1.311	
μ [mm ⁻¹]	0.126		0.175		0.160	
F(0 0 0)	3872		776		1789	
Crystal size [mm]	0.40×0.10×0.10		0.456×0.133×0.064		0.06×0.05×0.04	
θ range [°]	2.191–26.021		2.687–28.280		2.992–26.733	
Index ranges	-29 ≤ h ≤ 29		-14 ≤ h ≤ 17		-42 ≤ h ≤ 39	
	-29 ≤ k ≤ 29		-7 ≤ k ≤ 6		0 ≤ k ≤ 6	
	-24 ≤ l ≤ 24		-28 ≤ l ≤ 34		0 ≤ l ≤ 34	
reflns collected	72,022		8,533		4,419	
Independent reflns	5,359 [R _{int} = 0.0964]		4,406 [R _{int} = 0.0425]		4,419 [R _{int} = 0.0683]	
Completeness to theta	99.9 %		99.8 %		98.4 %	
Refinement method	Full-matrix	least-	Full-matrix	least-	Full-matrix	least-
	squares on F ²		squares on F ²		squares on F ²	
Data/restraints/ Parameters	5,359 / 0 / 298		4,406 / 0 / 239		4,419 / 0 / 279	
Hydrogen atom treatment	constrained		constrained		constrained	
R ₁ /wR ₂ (I > 2 σ (I))	0.0501/0.1166		0.0505/0.0975		0.0556/0.1143	
R ₁ /wR ₂ (all data)	0.0775/0.1303		0.0847/0.1110		0.0752/0.1235	
Goodness-of-fit on F ²	1.027		1.018		1.118	
larg. diff peak/hole [e·Å ⁻³]	0.414/-0.273		0.427/-0.402		0.322/-0.297	
CCDC No.	2072410		2072407		2069784	

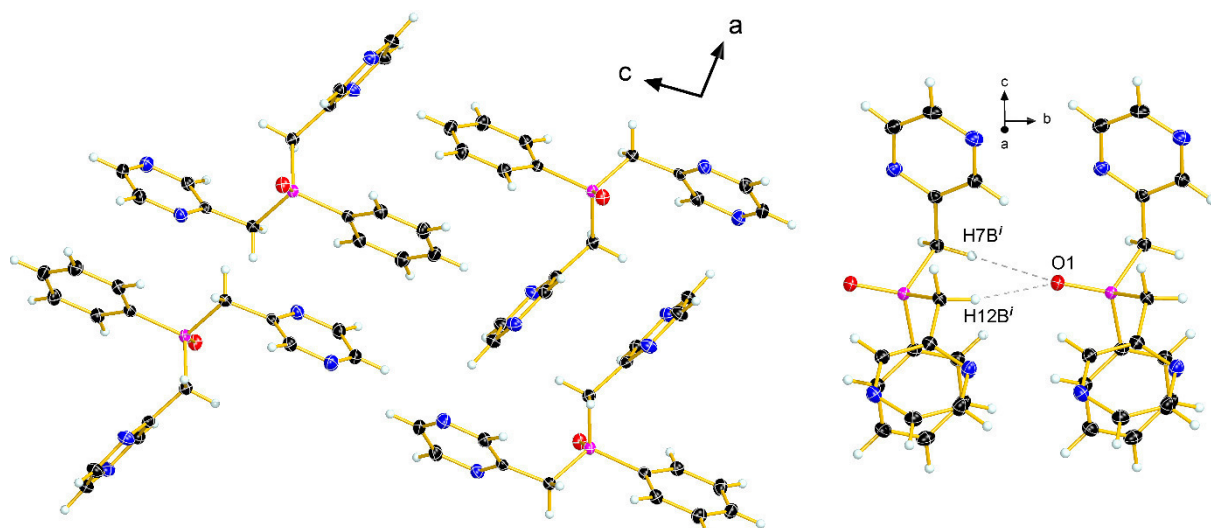


Figure 51. Arrangement of the molecules of **4** in the crystal (left) and visualization of the non-classical hydrogen bonds (right). Diamond representation, thermal ellipsoids are drawn at 50 % probability level. Bond lengths of hydrogen bonds [Å]: O1...H7B'ⁱ 2.732, O1...H12B'ⁱ 2.512. Symmetry code: $i = x, 1+y, z$.

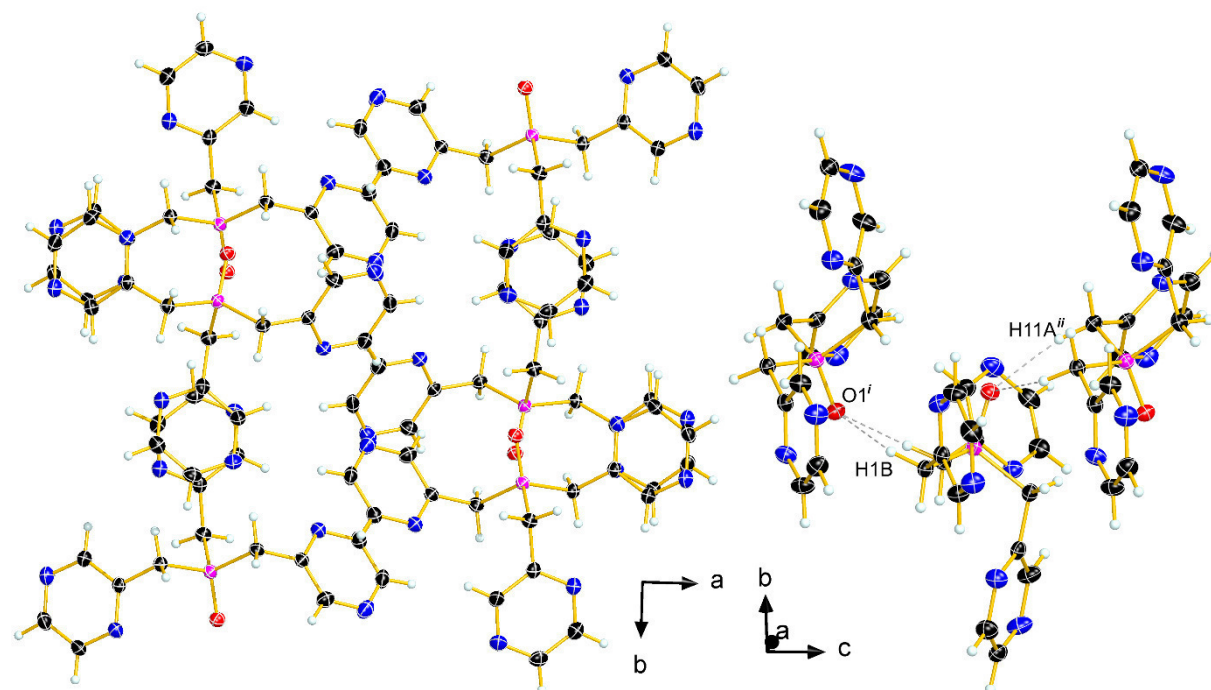


Figure 52. Arrangement of the molecules of **5** in the crystal (left) and visualization of the non-classical hydrogen bonds (right). Diamond representation, thermal ellipsoids are drawn at 50 % probability level. Bond lengths of hydrogen bonds [Å]: O1'...H1Bⁱ 2.336, O1'...H11A''ⁱ 2.279. Symmetry code: $i = x, 0.5-y, 0.5+z$.

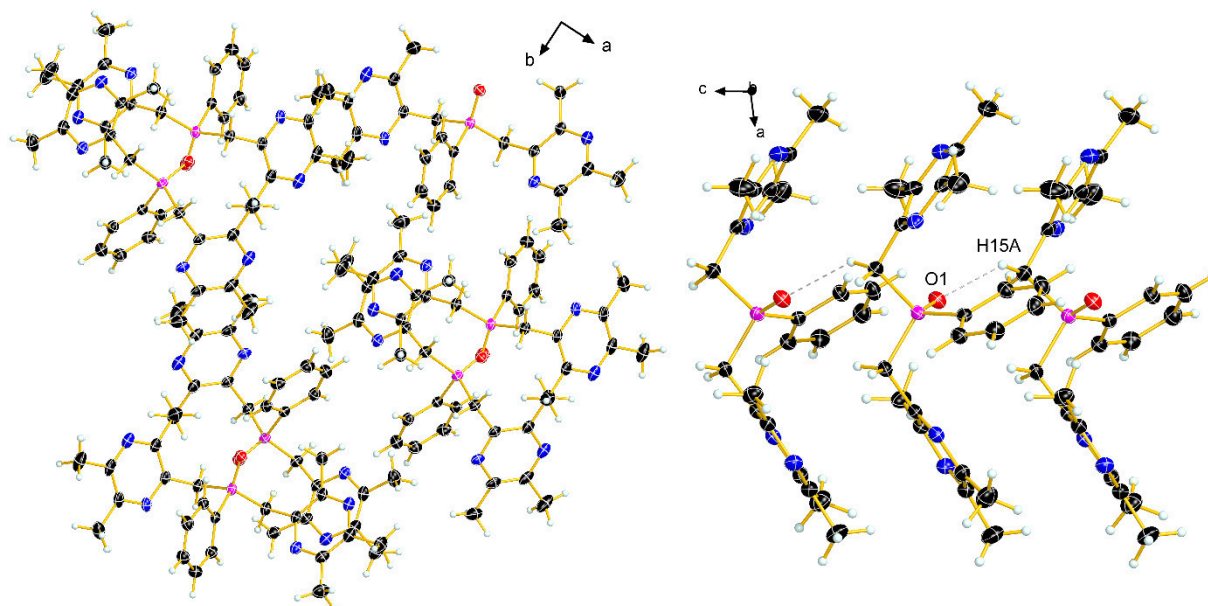


Figure 53. Arrangement of the molecules of **6** in the crystal (left) and visualization of the non-classical hydrogen bonds (right). Diamond representation, thermal ellipsoids are drawn at 50 % probability level. Bond lengths of hydrogen bonds [Å]: O1...H15Aⁱ 2.859, O1...H7B'ⁱ 2.375. Symmetry code: $i = x, 0.5-y, 0.5+z$.

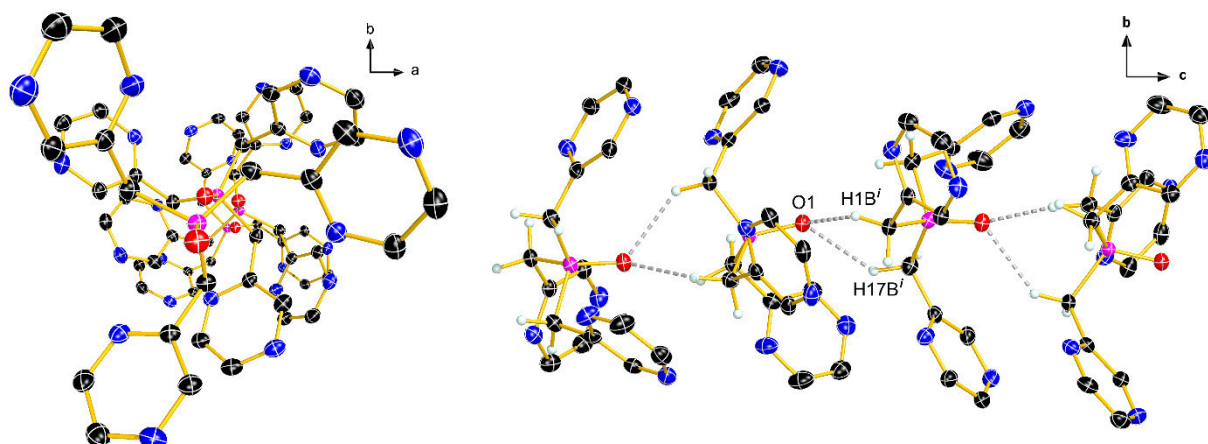


Figure 54. Spiral arrangement of the molecules of **7** in the crystal along the *c* axis (left) and visualization of the non-classical hydrogen bonds (right). Diamond representation, thermal ellipsoids are drawn at 50 % probability level. Methyl groups and some hydrogen atoms are omitted for clarity. Bond lengths of hydrogen bonds [Å]: O1...H1B'ⁱ 2.358, O1...H17B'ⁱ 2.411. Symmetry code: $i = -0.25+x, 1.25-y, -0.25+z$.

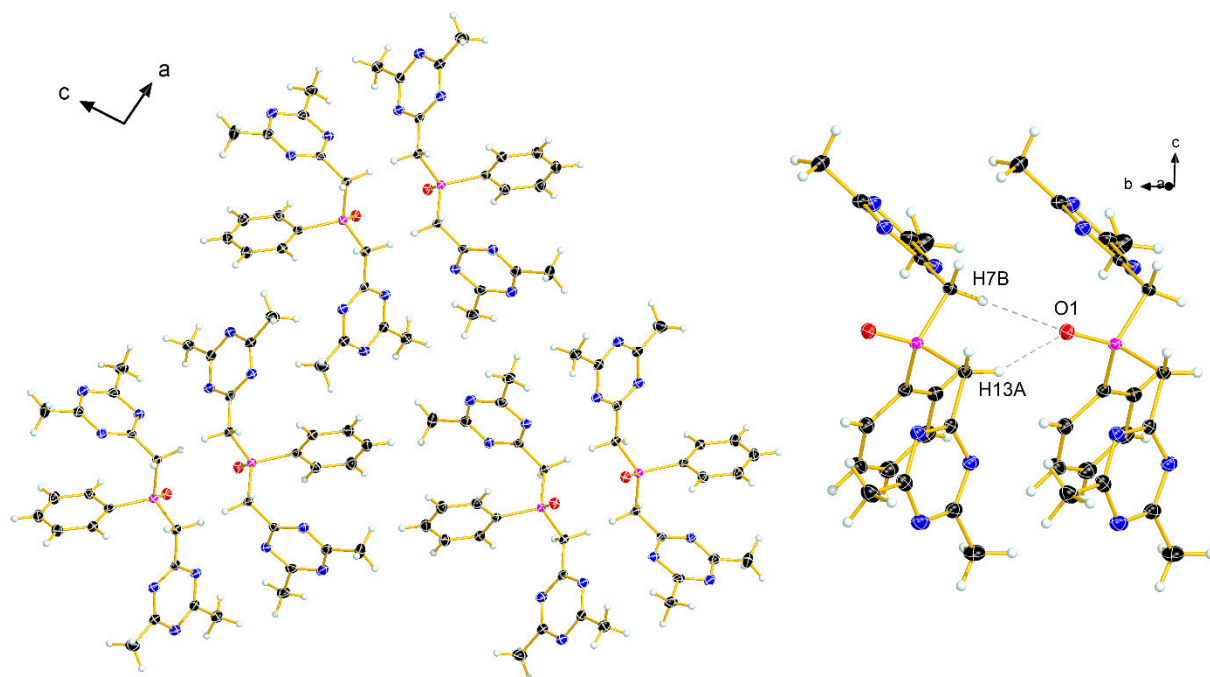


Figure 55. Arrangement of the molecules of **8** in the crystal (left) and visualization of the non-classical hydrogen bonds (right). Diamond representation, thermal ellipsoids are drawn at 50 % probability level. Bond lengths of hydrogen bonds [Å]: O1...H7Aⁱ 2.619, O1...H13Bⁱ 2.400. Symmetry code: $i = 1.5-x, 0.5+y, 1.5-z$.

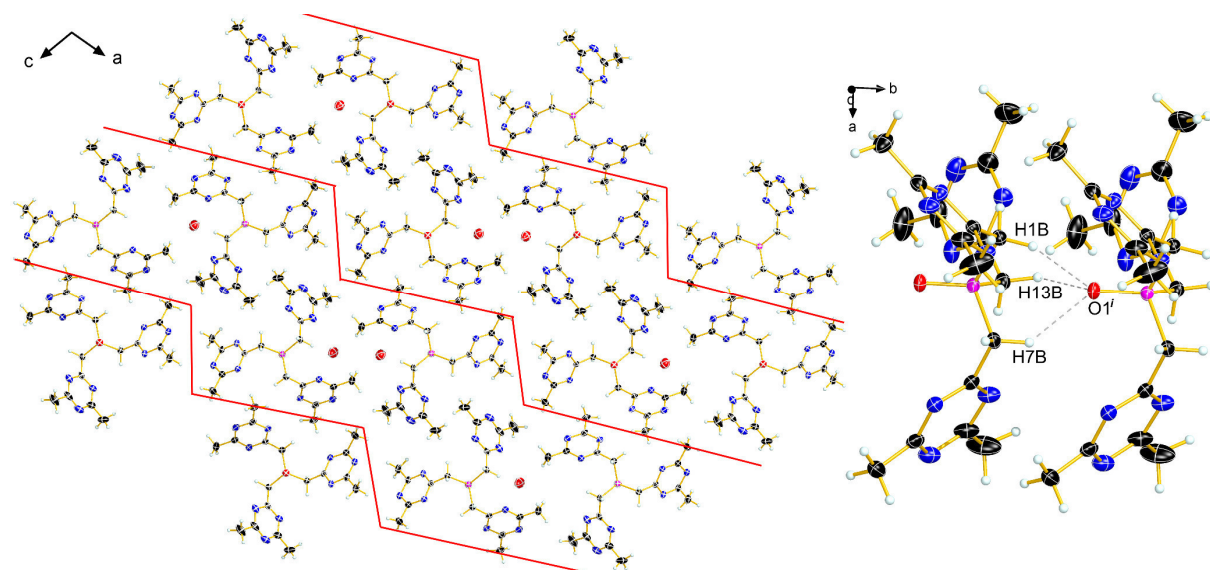


Figure 56. Arrangement of the molecules of **9** in the crystal (left) and visualization of the non-classical hydrogen bonds (right). Diamond representation, thermal ellipsoids are drawn at 50 % probability level. Bond lengths of hydrogen bonds [Å]: O1...H1Bⁱ 2.328, O1...H7Bⁱ 2.368, O1...H13Bⁱ 2.343. Symmetry code: $i = x, -1+y, z$.

Table 10. Selected bond lengths [Å] and angles [°].

4			
P1–O1	1.488(2)	O1–P1–C7	115.2(7)
P1–C1	1.804(2)	O1–P1–C12	114.6(7)
P1–C7	1.817(2)	C1–P1–C7	105.8(7)
P1–C12	1.815(2)	C1–P1–C12	106.0(7)
O1–P1–C1	112.4(7)	C7–P1–C12	102.0(7)
5			
P1–O1	1.484(2)	O1–P1–C6	111.5(8)
P1–C1	1.816(2)	O1–P1–C11	112.6(8)
P1–C6	1.822(2)	C1–P1–C6	106.3(8)
P1–C11	1.806(2)	C1–P1–C11	105.2(8)
O1–P1–C1	113.1(7)	C6–P1–C11	107.6(8)
6			
P1–O1	1.489(2)	O1–P1–C7	113.3(7)
P1–C1	1.797(2)	O1–P1–C15	113.4(7)
P1–C7	1.819(2)	C1–P1–C7	109.5(8)
P1–C15	1.825(2)	C1–P1–C15	104.1(8)
O1–P1–C1	111.3(7)	C7–P1–C15	104.7(7)
7			
P1–O1	1.489(2)	O1–P1–C9	112.0(9)
P1–C1	1.813(2)	O1–P1–C17	113.7(9)
P1–C9	1.822(2)	C1–P1–C9	106.1(1)
P1–C17	1.825(2)	C1–P1–C17	107.0(1)
O1–P1–C1	113.0(9)	C9–P1–C17	104.4(1)
8			
P1–O1	1.481(2)	O1–P1–C9	114.6(9)
P1–C1	1.804(2)	O1–P1–C17	113.6(9)
P1–C9	1.811(2)	C1–P1–C9	109.8(9)
P1–C17	1.821(2)	C1–P1–C17	104.4(9)
O1–P1–C1	111.0(9)	C9–P1–C17	102.7(9)
9			
P1–O1	1.486(2)	O1–P1–C9	112.7(7)
P1–C1	1.809(2)	O1–P1–C17	113.1(7)
P1–C9	1.814(2)	C1–P1–C9	106.6(7)
P1–C17	1.814(2)	C1–P1–C17	104.9(7)
O1–P1–C1	113.3(7)	C9–P1–C17	105.6(7)

2.5.5.3. Photophysical spectra

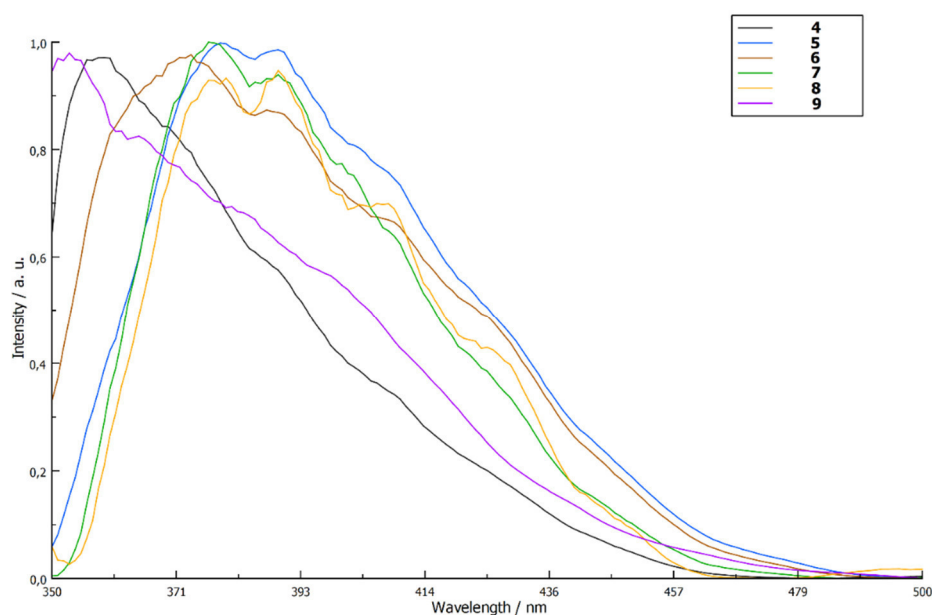


Figure 57. UV Vis spectra of the solid compounds **4–9**. Normalized to 1 in the region from 500–350 nm. Data were smoothed using a linear moving average (interval = five data points).

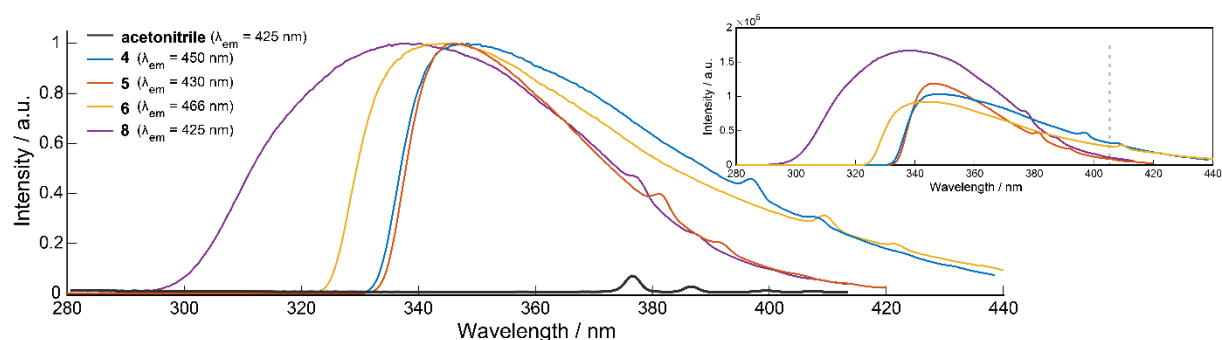


Figure 58. Excitation spectra of compounds **4–6** and **8** (a concentration of ~ 10 mM was used) normalized to the maximum, with a spectrum of the acetonitrile solvent (black) plotted to show the position of the Raman peaks at 425 nm emission. The inset shows the unnormalized excitation spectra, where the dotted line shows the wavelength of excitation used for the FLIM measurements and the differences in absorption ratio were calculated for the compounds **5** and **8** and were scaled relative to compounds **4** and **6** (factors of 3.6 and 2.9, respectively).

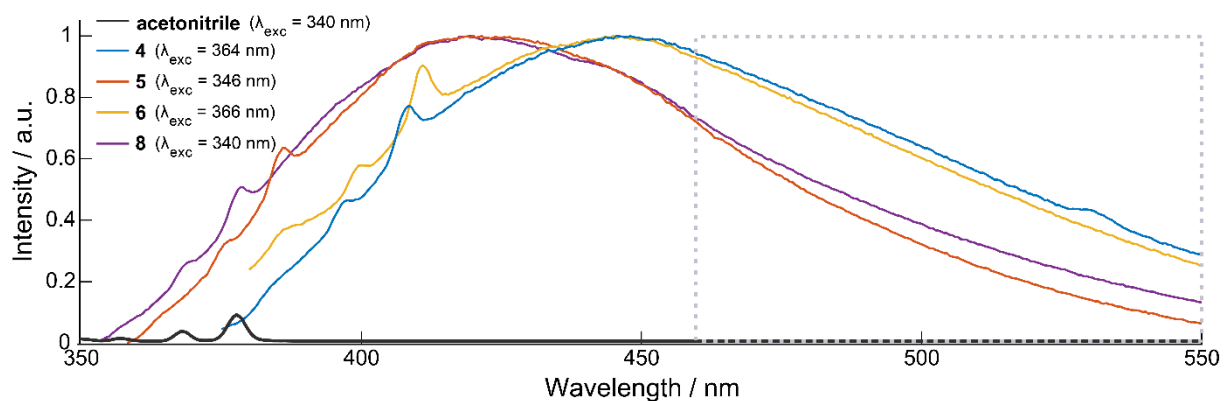


Figure 59. Emission spectra of compounds **4–6** and **8** (a concentration of ~ 10 mM was used) normalized to the maximum, with a spectrum of the acetonitrile solvent (black) plotted to show the position of the Raman peaks at 340 nm excitation. For the FLIM measurements, the detected photons must pass of a long pass filter that transmits above 460 nm. The rectangular box indicates the region of the spectrum that is detected by the instrument. To compensate for the relative differences between compounds **5**, **6** and **8**, relative to compound **4**, an additional factor of ~ 1.5 was applied for compounds **5** and **8**, where a correction factor of 1.2 was applied for compound **6**.

2.5.5.4. Fluorescence lifetime and FLIM images

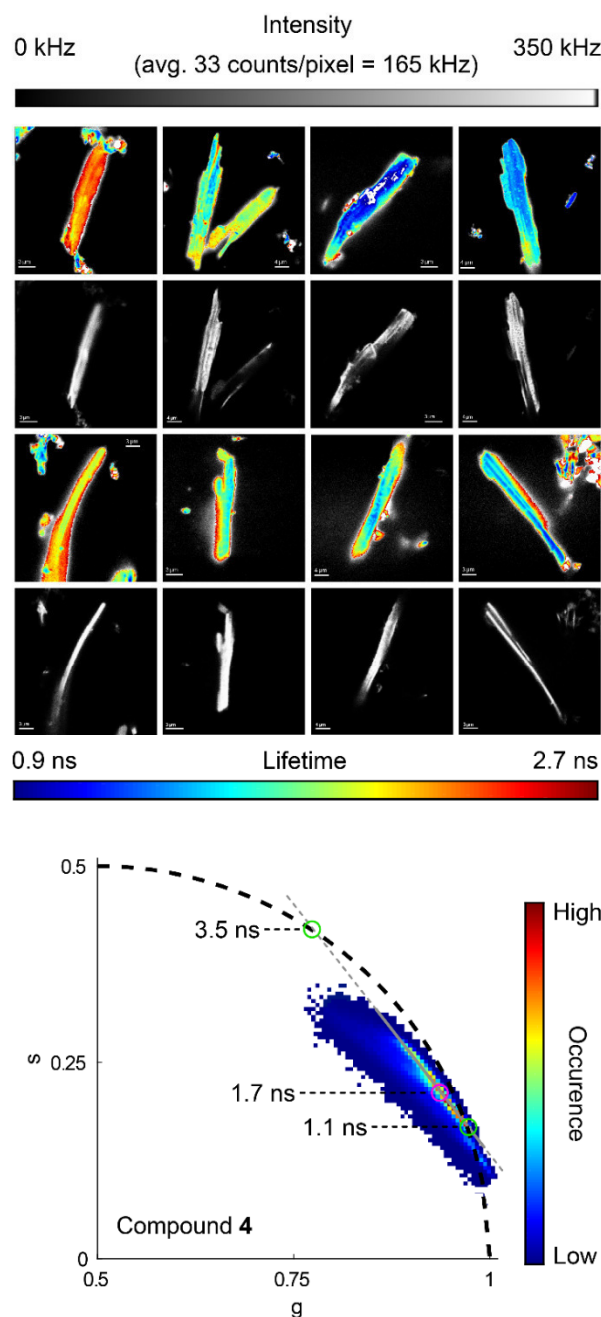


Figure 60. Fluorescence intensity and FLIM images of compound **4** showing its rod-like crystal structure. The intensity images show the photon counts per pixel for the different crystals, see upper intensity color bar. The last panel shows the corresponding phasor plot of the different FLIM images. The color in the phasor plot corresponds to the number of pixels exhibiting the particular phasor value (blue indicating the lowest occurrence and red indicating the highest occurrence, see occurrence on the color bar). The black line in the phasor plots is used for the color coding of the fluorescence lifetimes in the FLIM images, where the pixel brightness corresponds to counts, while the hue indicates the pixels' proximity to the black line. The color-code corresponding to the fluorescence lifetime displayed on the FLIM images, goes from blue (indicating the shortest fluorescence lifetime) over green and yellow to orange and red (indicating the longest fluorescence lifetime), see lifetime color bar.

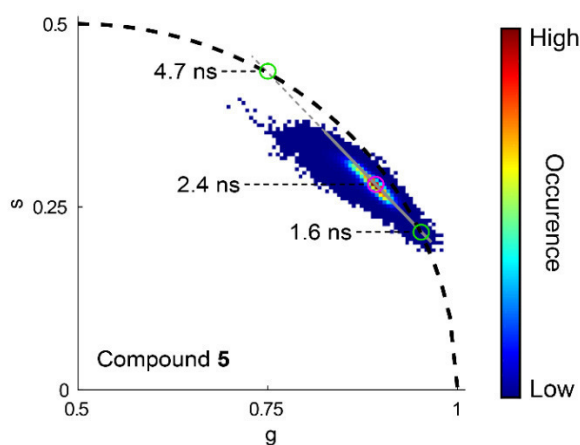
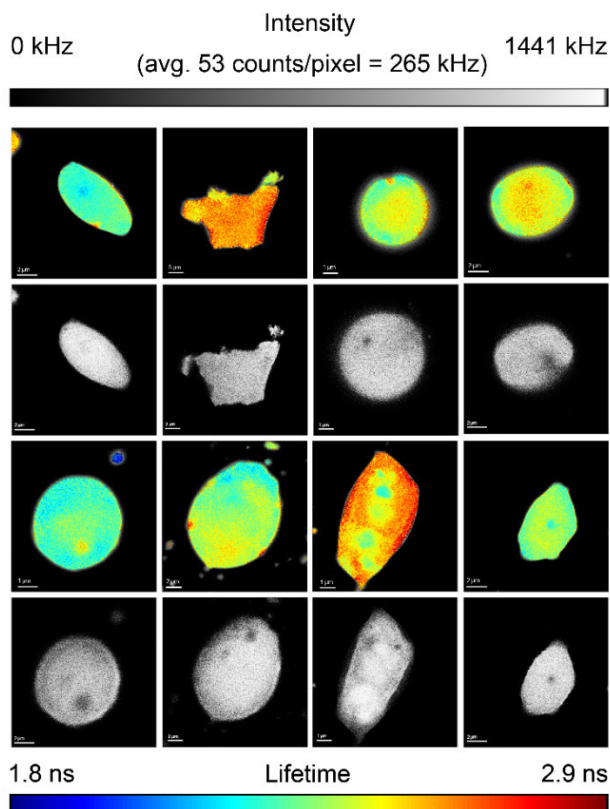


Figure 61. Fluorescence intensity and FLIM images of **5** showing its quasi-spherically elongated and oval-like structure. The intensity images show the photon counts per pixel for the different crystals, see upper intensity color bar. The intensity values were adjusted based on the excitation and emission correction factors (check the FLIM section, SI for the correction factor details). The last panel shows the corresponding phasor plot of the different FLIM images. The color in the phasor plot corresponds to the number of pixels exhibiting the particular phasor value (blue indicating the lowest occurrence and red indicating the highest occurrence, see occurrence on the color bar). The black line in the phasor plots is used for the color coding of the fluorescence lifetimes in the FLIM images, where the pixel brightness corresponds to counts, while the hue indicates the pixels' proximity to the black line. The color-code corresponding to the fluorescence lifetime displayed on the FLIM images, goes from blue (indicating the shortest fluorescence lifetime) over green and yellow to orange and red (indicating the longest fluorescence lifetime), see color bar.

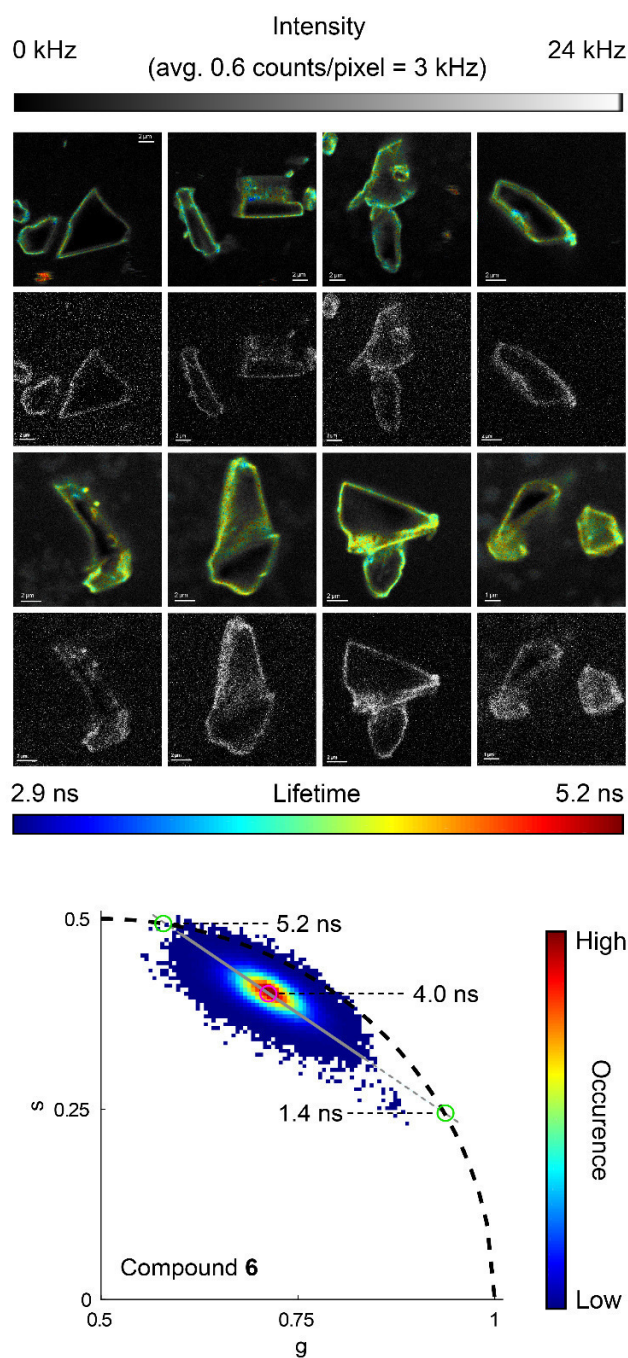


Figure 62. Fluorescence intensity and FLIM images of **6** showing its diversely shaped structures. The intensity images show the photon counts per pixel for the different crystals, see upper intensity color bar. The intensity values were adjusted based on the emission correction factors (check the FLIM section, SI for the correction factor details). The last panel shows the corresponding phasor plot of the different FLIM images. The color in the phasor plot corresponds to the number of pixels exhibiting the particular phasor value (blue indicating the lowest occurrence and red indicating the highest occurrence, see occurrence on the color bar). The black line in the phasor plots is used for the color coding of the fluorescence lifetimes in the FLIM images, where the pixel brightness corresponds to counts, while the hue indicates the pixels' proximity to the black line. The color-code corresponding to the fluorescence lifetime displayed on the FLIM images, goes from blue (indicating the shortest fluorescence lifetime) over green and yellow to orange and red (indicating the longest fluorescence lifetime), see color bar.

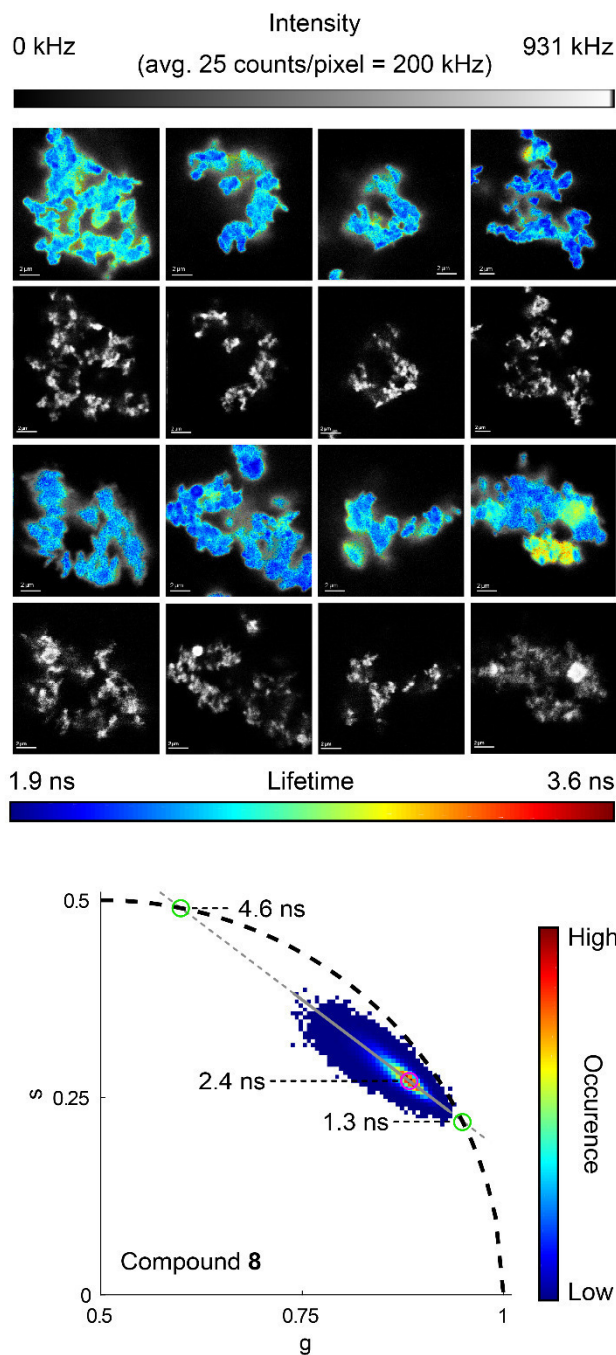


Figure 63. Fluorescence intensity and FLIM images of **8** showing its amorphous-like structure. The intensity images show the photon counts per pixel for the different crystals, see upper intensity color bar. The intensity values were adjusted based on the excitation and emission correction factors (check the FLIM section, SI for the correction factor details). The last panel shows the corresponding phasor plot of the different FLIM images. The color in the phasor plot corresponds to the number of pixels exhibiting the particular phasor value (blue indicating the lowest occurrence and red indicating the highest occurrence, see occurrence on the color bar). The black line in the phasor plots is used for the color coding of the fluorescence lifetimes in the FLIM images, where the pixel brightness corresponds to counts, while the hue indicates the pixels' proximity to the black line. The color-code corresponding to the fluorescence lifetime displayed on the FLIM images, goes from blue (indicating the shortest fluorescence lifetime) over green and yellow to orange and red (indicating the longest fluorescence lifetime), see color bar.

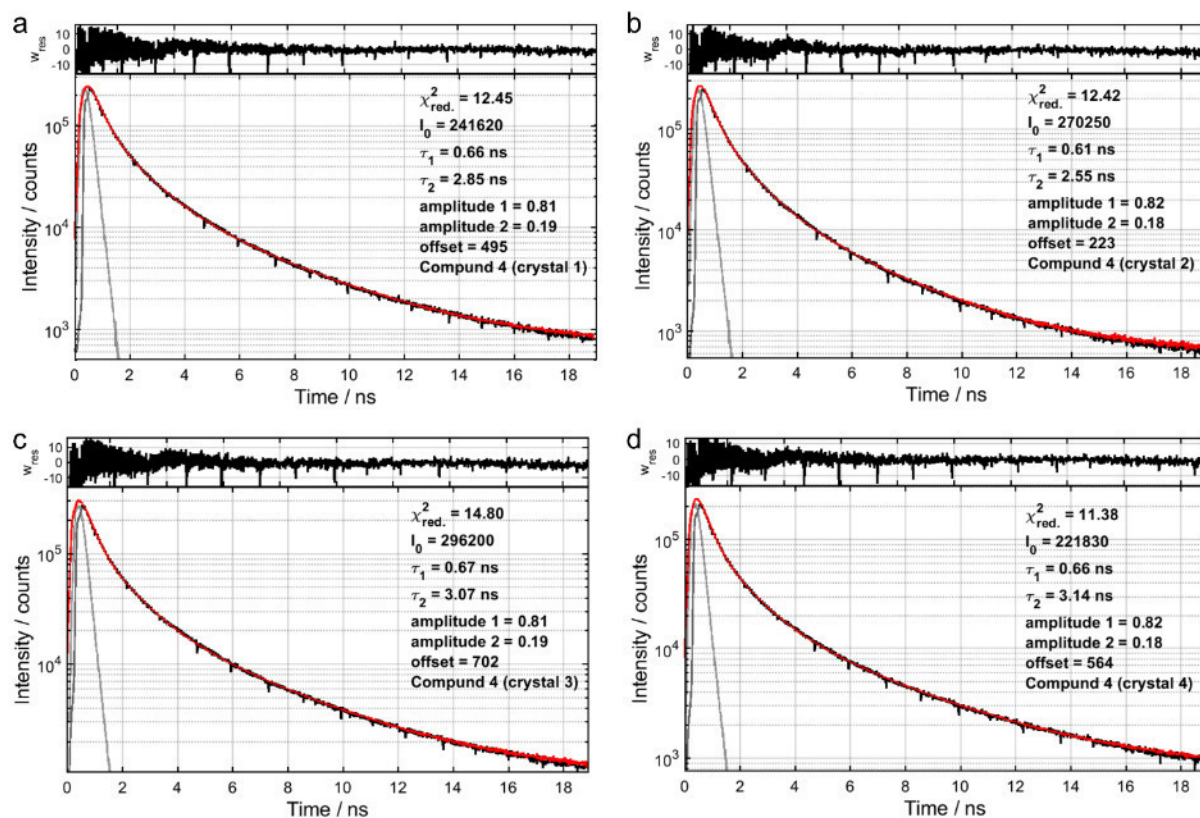


Figure 64. Fluorescence lifetime decay data and fits obtained for the four crystals (i) of compound 4 imaged in Figure 48, which shows a bi-exponential fluorescence lifetime decay.

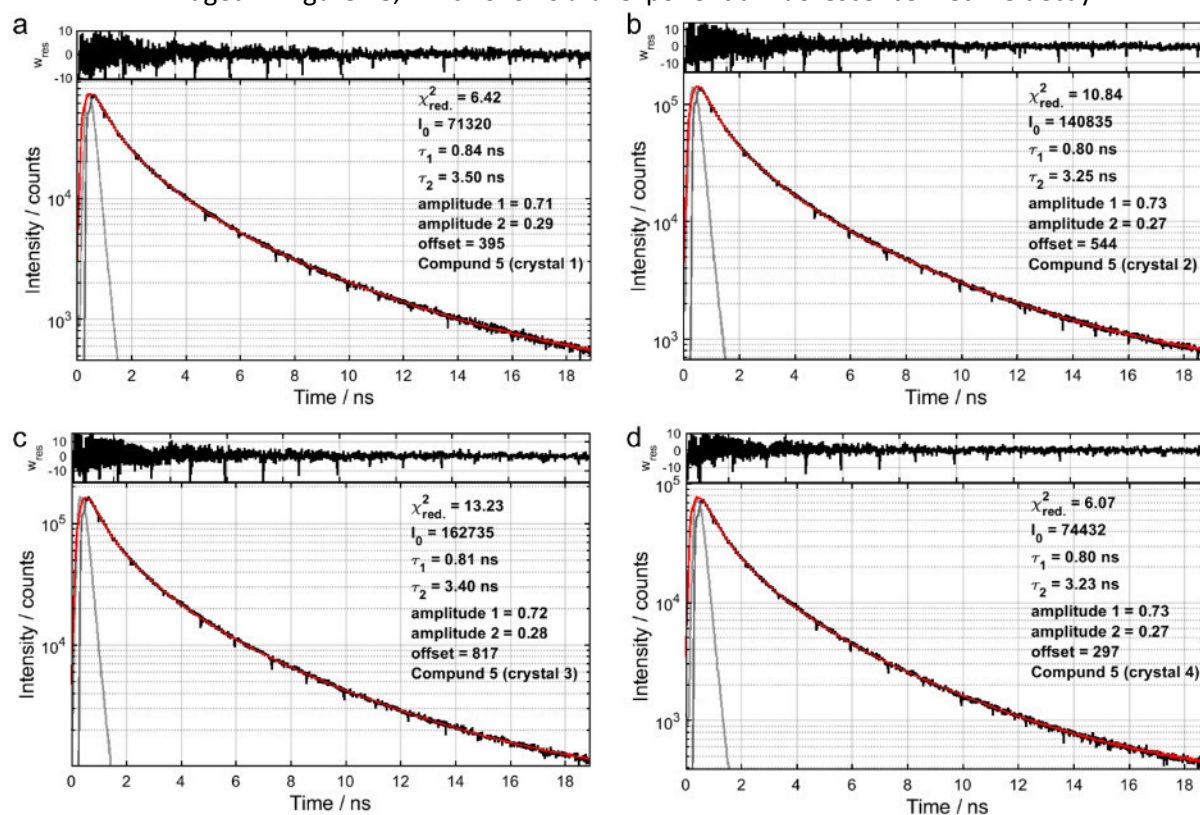


Figure 65. Fluorescence lifetime decay data and fits obtained for the four crystals (ii) of compound 5 imaged in Figure 48, which shows a bi-exponential fluorescence lifetime decay.

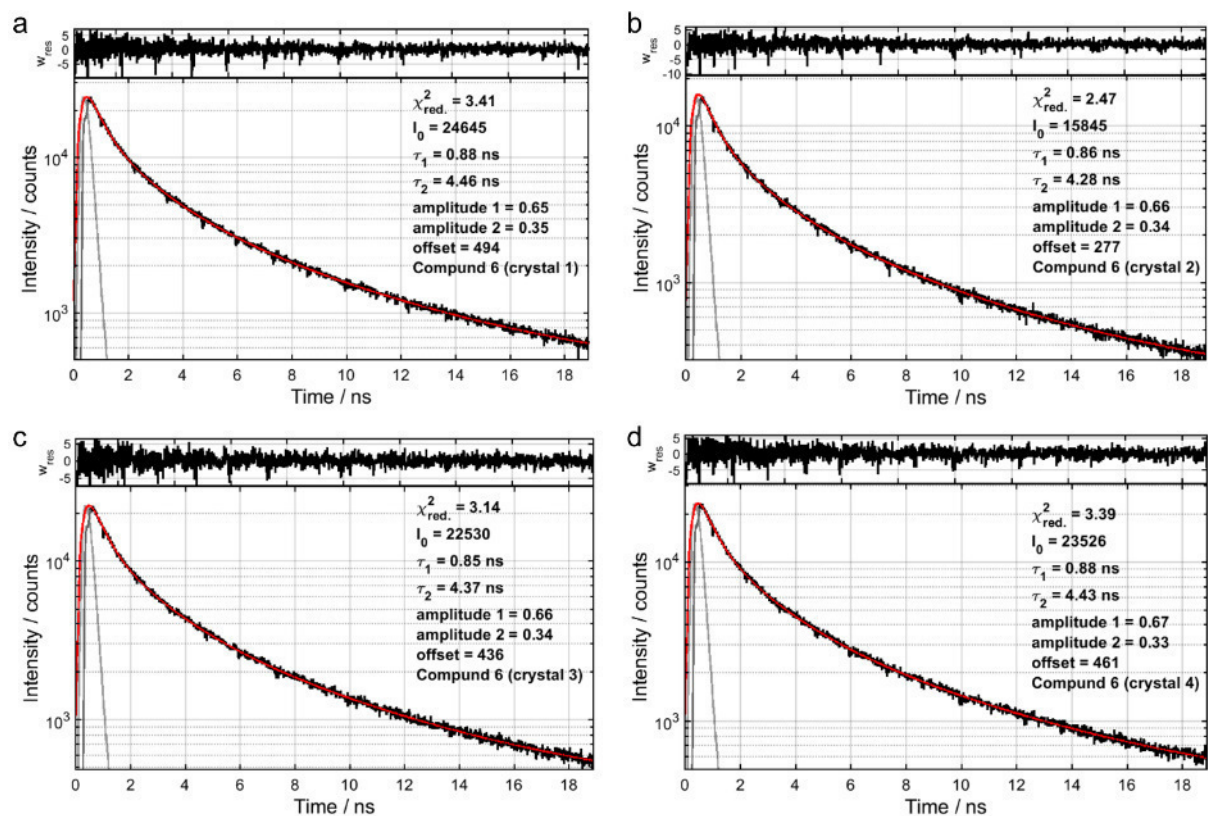


Figure 66. Fluorescence lifetime decay data and fits obtained for the four crystals (iii) of compound 6 imaged in Figure 48, which shows a bi-exponential fluorescence lifetime decay.

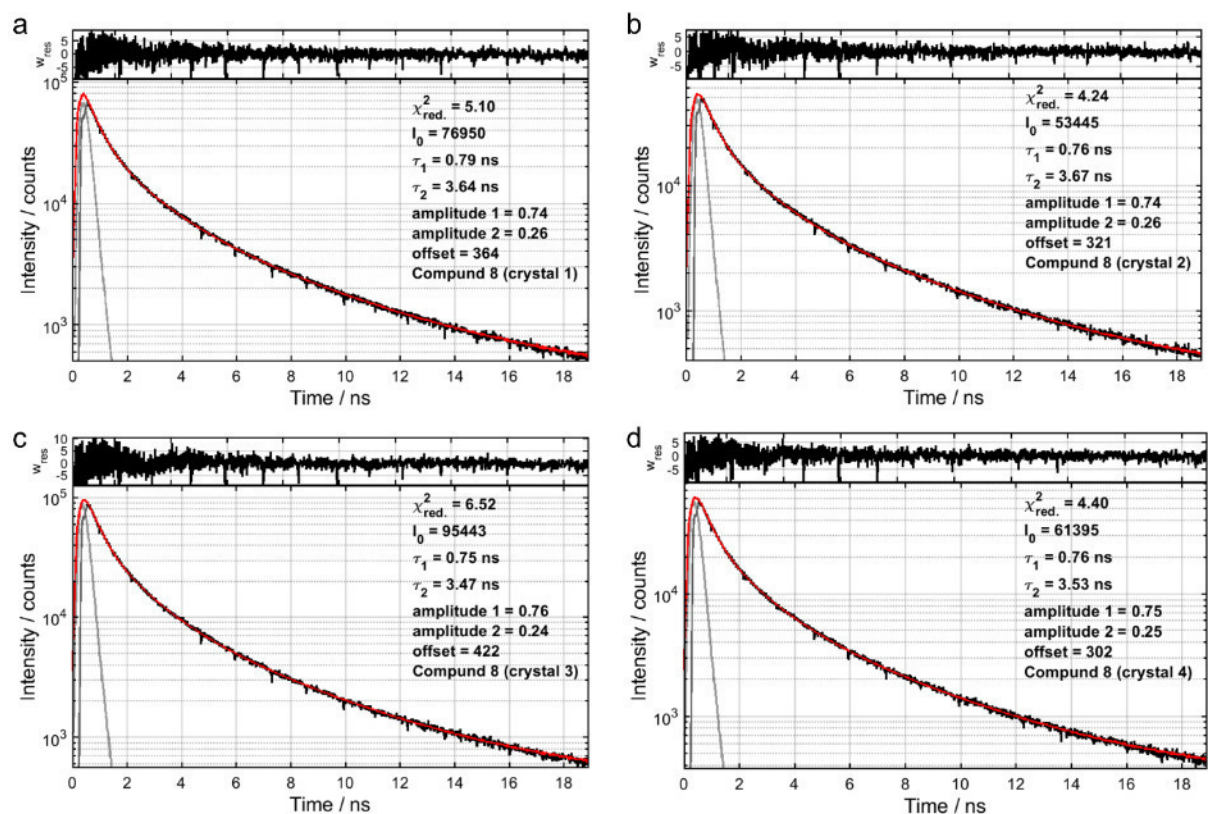


Figure 67. Fluorescence lifetime decay data and fits obtained for the four crystals (iv) of compound 8 imaged in Figure 48, which shows a bi-exponential fluorescence lifetime decay.

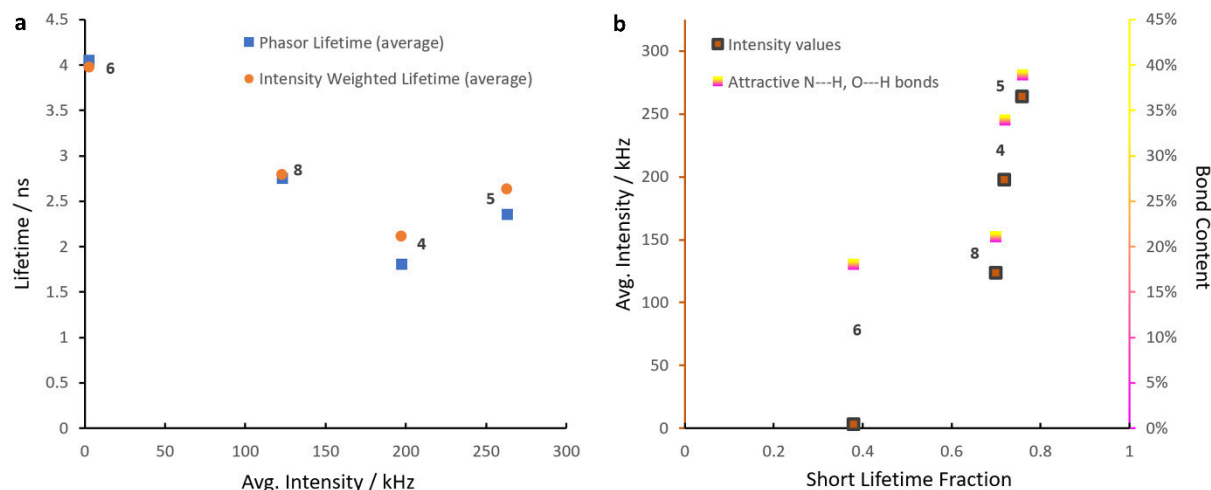


Figure 68. The relation between the fluorescence lifetime and intensity relative to the attractive bond contents for the four crystals of the different compounds imaged in Figure 48. a) Average fluorescence lifetimes obtained from the phasor and tail fits to the TCSPC data showing an increase of fluorescence intensity with decrease in the lifetime average. b) The increase in the short lifetime fraction correlates with the increase in fluorescence intensity and attractive bond contents within the investigated crystals.

Table 11. Fluorescence lifetime decay values obtained for the different four crystals measured in Figure 48 for each of the compounds.

	Compound 4		Compound 5		Compound 6		Compound 8	
	τ_1 /ns (A_1) ^a	τ_2 /ns (A_2) ^b	τ_1 /ns (A_1) ^a	τ_2 /ns (A_2) ^b		τ_1 /ns (A_1) ^a	τ_2 /ns (A_2) ^b	τ_1 /ns (A_1) ^a
Crystal 1	0.66 (81%)	2.85 (19%)	0.84 (71%)	3.50 (29%)	Crystal 1	0.66 (81%)	2.85 (19%)	0.84 (71%)
Crystal 2	0.61 (82%)	2.55 (18%)	0.80 (73%)	3.25 (27%)	Crystal 2	0.61 (82%)	2.55 (18%)	0.80 (73%)
Crystal 3	0.67 (81%)	3.07 (19%)	0.81 (72%)	3.40 (28%)	Crystal 3	0.67 (81%)	3.07 (19%)	0.81 (72%)
Crystal 4	0.66 (82%)	3.14 (18%)	0.80 (73%)	3.23 (27%)	Crystal 4	0.66 (82%)	3.14 (18%)	0.80 (73%)
Crystals^c average	0.65±0.02 (0.82)	2.90±0.19 (0.18)	0.81±0.02 (0.72)	3.35±0.11 (0.28)	Crystals^c average	0.65±0.02 (0.82)	2.90±0.19 (0.18)	0.81±0.02 (0.72)
Intensity weighted lifetime^d	1.79 ± 0.16		2.36 ± 0.11		3.41 ± 0.06		2.49 ± 0.09	
Phasor lifetimes	0.90^e (0.72)	2.75^f (0.28)	1.56^e (0.76)	3.95^f (0.24)	Phasor lifetimes	0.90^e (0.72)	2.75^f (0.28)	1.56^e (0.76)
Phasor lifetimes average^g	1.80		2.35		4.05		2.75	

^aShort lifetime component and its relative population (A_1) from a biexponential fit to the cumulative TCSPC data coming from the crystals. ^bLong lifetime component and its relative population (A_2) from a biexponential fit to the cumulative TCSPC data coming from the crystals. ^cAverage lifetime values (mean) and standard deviation of the individual components for the four different crystals. ^dThe average fluorescence lifetime (τ_{avg}) values were obtained by using the following equation: $\tau_{avg} = (\sum_{i=1}^n A_i \tau_i^2) / (\sum_{i=1}^n A_i \tau_i)$; where τ_i is the individual lifetime with corresponding amplitude A_i

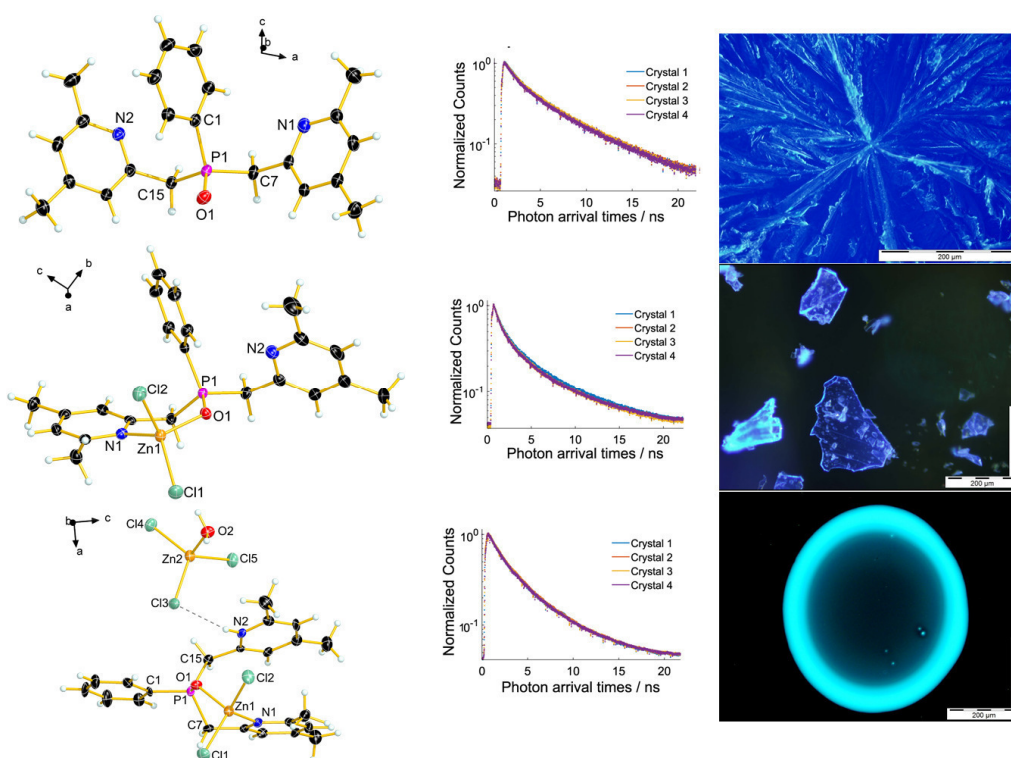
^eShort lifetime component taken from its position on the phasor semicircle. ^fLong lifetime component taken from its position on the phasor semicircle. ^gThe intensity values are obtained by performing a mask to select for the pixels with the crystals, where the average counts for each compound (averaging over the four crystals) is shown.

2.6. Aggregation induced emission in a flexible phosphine oxide and its Zn(II) complexes – a simple approach to blue luminescent materials

Christin Kirst, Manuel Gensler, David Fischermeier, , Fabian Knechtel, Nader A. Danaf, Jens Petersen, Armin Wedel,* Don C. Lamb,* Roland Mitrić,* Konstantin Karaghiosoff*

to be submitted to *Advanced Functional Materials*

Christin Kirst synthesized all the discussed compounds and performed the single crystal X-ray measurements and Hirshfeld surface analysis. She analyzed and evaluated the corresponding X-ray data and the NMR spectroscopy results in solution. She further managed the project and wrote the original draft of the manuscript, designed the TOC graphic and implemented the necessary corrections in the final version of the paper.



Abstract: The design and development of novel organic luminescent materials is still attracting the attention of many researchers due to their promising application e.g. in lighting, flat panel displays and optical communication. Especially blue emitting materials are in the focus of ongoing research, as they still lack in efficiency and lifetime as compared to red and green.

The new multidentate phosphine oxide and its two ZnCl_2 complexes (one neutral and one cationic) presented here combine a straightforward synthesis with high yields and show interesting luminescent properties. The phosphine oxide ligand alone as well as its neutral ZnCl_2 complex show blue luminescence in the crystalline state, but not in amorphous films or solution. On the contrary, the cationic Zn(II) complex shows high blue luminescence in the crystalline state and also in amorphous thin films and in solution. Variable temperature NMR provides a possible explanation for this deviation. Fluorescence lifetime imaging microscopy measurements show luminescence lifetime of 3–6 ns indicative of fluorescence. According to quantum chemical calculations, we propose a model, in which the crystal environment or the steric fixation by the coordinating central atom blocks the thermal relaxation into the ground state. All in all, the results show that these are promising compounds for possible use as emitters in OLED application.

2.6.1. Introduction

The search for novel organic solid-state luminescent materials is still attracting many researchers due to their promising application in lighting, flat panel displays, optical communication, etc. Currently used materials are based on rather expensive and rare metals such as Ir(III), Pt(II) and Os(II) or large organic molecules.^[1–10] Their synthesis is often tedious, low yielding and hardly scalable. Especially blue emitting materials are still a challenge due to their lacking efficiency and limited lifetime comparing to red and green emitting materials.^[11,12] The use of phosphines or phosphine oxides as hosts, emitters or ligands in luminescent metal complexes for organic light-emitting diode (OLED) applications are investigated extensively.^[13–24] Used as hosts, particularly in blue phosphorescent (2nd generation) and thermally activated delayed fluorescence (TADF) (3rd generation) OLEDs, phosphine oxides stand out due to their high T_1 energy and charge mobility and can improve device properties and performances.^[15,25] The drawback of phosphines and phosphine oxides is their rather labile P–C bond.^[26,27] Finding ways to stabilize this bond is crucial for the development of highly performing and longtime-stable OLEDs. Possible options for reaching a stabilization might be *via* complexation (limiting the degrees of freedom) and/or *via* exploitation of favorable packing effects in the crystal or aggregated solution. These effects, in the end, could also lead to aggregation-induced emission (AIE) and thus enhance luminescence.^[28,29]

Our research focus lies on picolyl substituted phosphines and phosphine oxides and derivatives thereof. Many research groups have reported luminescent complexes of related P,N-ligands before, which show promising results with regard to their luminescence.^[30–39] By introduction of a methylene group between the pyridine unit and phosphorus, our ligands gain in flexibility while at the same time sufficient stability is provided when coordinated to a metal. This produces ligands and complexes, which show interesting structural, chemical and physical properties.^[40,41]

In the following, we present a picolyl derived phosphine oxide ligand and its neutral and ionic zinc-based complexes, which show a blue luminescence. Materials based on these compounds could be a practicable, cheap and “green” alternative for currently used heavy metal-based emitters.

The synthesized ligand and complexes were characterized *via* single crystal X-ray diffraction, multinuclear NMR, IR, MS and EA. Moreover, their photophysical properties were measured in solution, solid state and thin film. Fluorescence lifetime imaging microscopy (FLIM) measurements were conducted to gain insight into the time scale of the photoluminescence decay in the compounds. Quantitative Hirshfeld surface (HS) analysis was done to provide knowledge about structural-property relationships, when combining the results with FLIM. Lastly, quantum chemical calculations were done both in the gas phase and in the crystal, to investigate the origin of the luminescence.

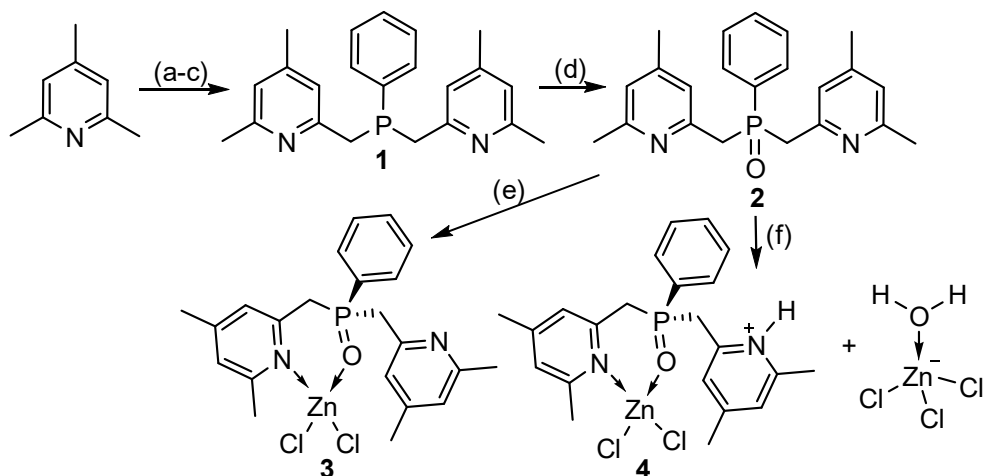
2.6.2. Results and Discussion

2.6.2.1. Synthesis and NMR characterization

The synthesis of all compounds is shown in Scheme 15, detailed procedures can be found in the Supporting Information. The compounds are easily synthesized in high yields. ZnCl₂ complexes of the phosphine oxide ligand were prepared, to investigate a possible stabilization of the compounds and the influence of coordination on the luminescence properties. All compounds are obtained as colorless powders and can be purified by recrystallization.

In the ³¹P NMR spectra measured in CDCl₃, compound **1** shows a signal at –13.3 ppm, **2** at 36.7 ppm, **3** at 50.6 ppm and **4** at 49.5 ppm. The change in chemical shift is as expected for such compounds. As is known from similar picolylphosphine oxide complexes, the presented ligands are fairly flexible in solution.^[40] To investigate possible structural changes of the complexes, variable temperature NMR was conducted of compound **3** and **4** in CD₂Cl₂ (Figure 78 and 79 of SI). The results show that at room

temperature, a fast dynamics is present for compound **3**, where the zinc(II) atom stays coordinated to oxygen but the N-coordination switches between one collidinyl substituent and the other (Figure 78 of SI). This rapid exchange is drastically slowed down at low temperature. The signals for both collidinyl substituents (coordinating and non-coordinating to Zn(II)) are then visible in the ^1H NMR spectrum of compound **3** at -80°C . For compound **4**, a dynamical behavior in solution is also observed, displaying only one set of signals for the collidinyl substituents. However, when lowering the temperature to -60°C , the dynamics is slowed down and signals for the four different methyl groups become visible in the ^1H NMR spectrum. Additionally, an aggregation of the molecules of **4** at -80°C occurs, visible by a broadening of the signals in the ^1H NMR spectrum (Figure 79 of SI).



Scheme 15. Synthesis of compounds **1–4**. a) $n\text{BuLi}$, tetrahydrofuran, -78°C , 1 h, b) TMSCl 2 eq, -78°C to RT, 12 h, c) PhPCl_2 0.5 eq, tetrahydrofuran, -10°C to RT, 12 h, quantitative, d) H_2O_2 , H_2O , dichloromethane, -10°C to RT, 5 h, 93 %, e) ZnCl_2 , acetonitrile, 4 h, 97 %, f) ZnCl_2 , H_2O , HCl , acetonitrile, 4 h, 83 %

2.6.2.2. Structural characterization

The molecular structures in the solid-state of the synthesized compounds were investigated by single crystal X-ray crystallography. Crystals of **2**, **3** and **4** are obtained by slow diffusion of cyclohexane into a solution of **2** in DCM or slow evaporation of acetonitrile for **3** and **4** and are analyzed by single-crystal X-ray diffraction. The crystallographic data and structure refinement details as well as selected bond lengths and angles for all compounds are listed in the Supporting Information. Compound **2** is forming pairs of molecules in the crystal, which are arranged as chains along the b axis (Figure 75 of SI). In the crystal packing, **2** shows weak attractive hydrogen interactions between oxygen and CH_2 hydrogen atoms.^[42] The crystal structure of compound **3** is shown in Figure 76 of SI. The Zn(II) atom is coordinated in a distorted tetrahedral environment by oxygen and nitrogen atoms of the phosphine oxide ligand. The phenyl ring is almost perpendicular to the coordinated trimethylpyridine ring ($77.9(8)^\circ$). In the crystal packing of **3**, there are attractive π – π stacking interactions present between the non-coordinated trimethylpyridine rings of neighboring molecules. Figure 77 of SI depicts the crystal structure of compound **4** containing a protonated phosphine oxide ligand coordinating to ZnCl_2 and a $[\text{Zn}(\text{H}_2\text{O})\text{Cl}_3]^-$ anion. Both Zn(II) atoms display a distorted tetrahedral environment, formed by oxygen and nitrogen atoms in the case of the cation and by three chlorine atoms and a water molecule in the case of the anion.

2.6.2.3. Photophysical characterization

As observed in pre-experiments, the solid compounds **2–4** show luminescence when illuminated with UV-light (366 nm). On the other hand, neither the ligand nor the complexes show a strong luminescence in diluted solution. However, the ligand as well as the complexes show a luminescence in very concentrated solutions under these conditions, which could implicate AIE. To gain more insights into the luminescent properties of the compounds, a thorough photophysical characterization was performed.

The luminescent properties of compounds **2–4** are investigated in solution (acetonitrile), in powder form (small crystals), and spin-coated thin films (amorphous). Solutions and thin films are measured by UV-Vis spectroscopy in transmission mode and luminescence spectroscopy in reflective mode using quartz glass cuvettes and substrates. Powder samples are encapsulated in borosilicate cavity glass and measured in an Ulbricht sphere with tunable excitation wavelength and luminescence detector attached. Compound **2** exhibits the same absorbance behavior in solution and thin film with two maxima at 265-266 nm and 272 nm (Figure 69). Illumination at 265 nm or 270 nm yields a luminescence maximum for the concentrated solution at 367 nm and for freshly crystallized powder at 389 nm. The luminance in powder state is decaying over the course of several days in samples stored under air in the dark. No significant emission is measured for freshly prepared thin films. Interestingly, thin films of compound **2** are crystallizing within some days, yielding luminescent crystals (inset in Figure 69).

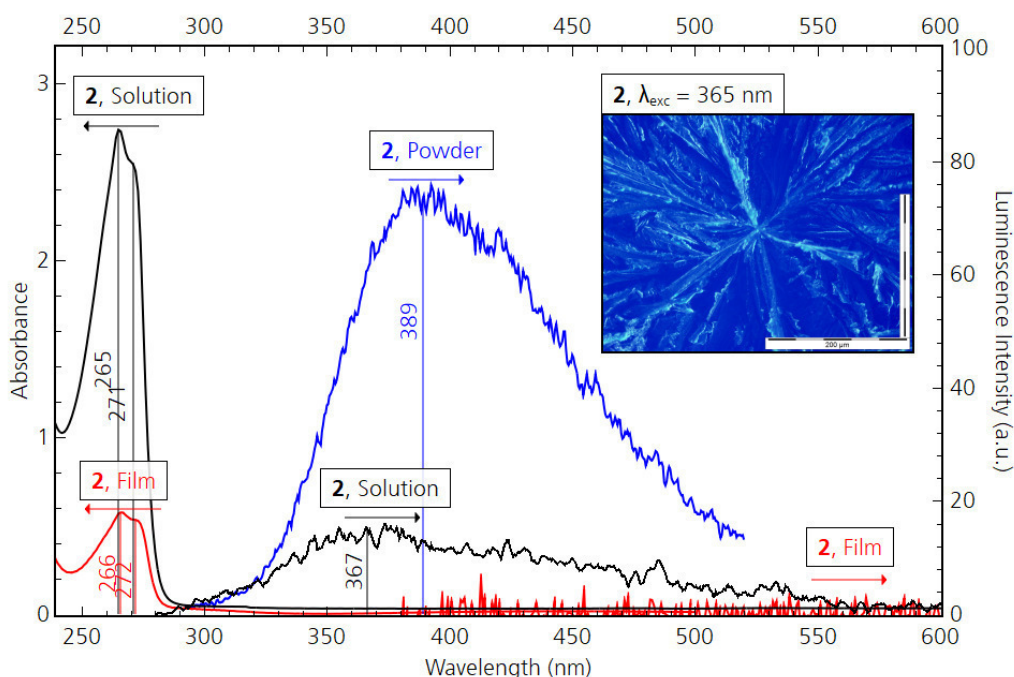


Figure 69. Luminescence properties of compound **2**. The absorbance spectra are recorded from a thin solution in MeCN (0.1 g/L) and from a thin film on quartz glass. Emission spectra are recorded from a higher concentrated solution (10 g/L), the same thin film and a thin layer of crystals on quartz glass at an excitation wavelength of 265 nm (solution) or 270 nm (powder and film). The inset shows a luminescence microscopic picture of the crystallized thin film with illumination at 365 nm. Luminescent crystals (cyan) are visible in front of a blue background of scattered light (scale bars: 200 μm).

Complex **3** exhibits similar absorbance maxima as compound **2** (Figure 70). Illumination at 265 nm yields a broad luminescence for the concentrated solution. The luminescence of the powder sample is

measured at an illumination of 350 nm instead of 270 nm due to the sample holder being non-transparent in the UV-range (borosilicate glass). This most likely induced a fluorescence band shift to higher wavelengths from 303 nm in thin film and 310 nm in solution to 414 nm in the solid-state.^[43–45] The enclosed sample holder is required, because in contrast to compound **2**, compound **3** does not crystallize on a quartz slide with good adhesion. Although the absorbance at 350 nm is weak, a photoluminescence quantum yield (PLQY) of $36 \pm 5 \%$ is measured using an Ulbricht sphere setup and a luminescence can be seen in the luminescence microscope (inset in Figure 70). In contrast to compound **2**, the thin film exhibits some luminance signal with a maximum at 303 nm, strong tailing to higher wavelengths, and a poor PLQY of $3 \pm 1 \%$.

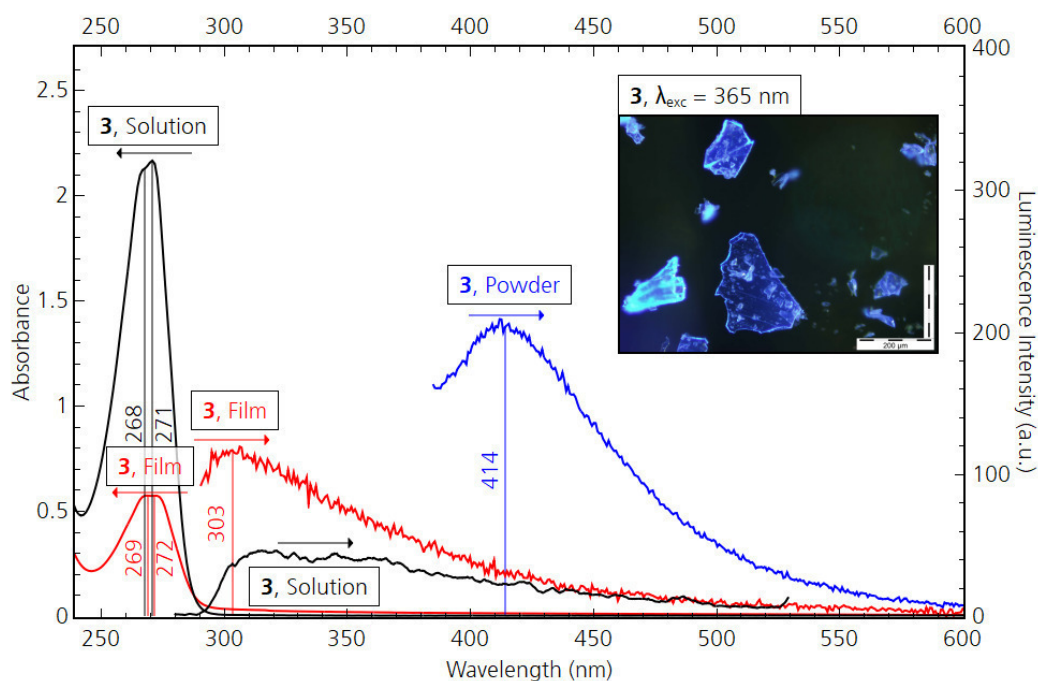


Figure 70. Luminescence properties of compound **3**. The absorbance spectra are recorded from a thin solution in MeCN (0.1 g/L) and a thin film on quartz glass. Emission spectra are recorded from a higher concentrated solution (10 g/L), the same film on quartz glass at and from a powder sample inside a borosilicate cavity glass at excitation wavelengths of 265 nm, 270 nm and 350 nm. The inset shows a luminescence microscopic picture of the powder sample with illumination at 365 nm (scale bars: 200 μm).

Compound **4** exhibits the same absorbance maximum as compounds **2** and **3** (Figure 71). In contrast to compounds **2** and **3**, all three states (solution, crystals, film) luminesce around 400 nm. Illumination at 265 nm yields luminescence at 404 nm for the concentrated solution. The luminescence of the powder sample is at 406 nm, its PLQY slightly higher than for compound **3** ($42 \pm 1 \%$). The thin film exhibits a luminescence at 393 nm with much lower PLQY ($7.6 \pm 1 \%$).

Interestingly, the luminescence of all three compounds in concentrated solution (10 g/L) is increased when excitation is not done at the main absorbance around 270 nm, but in the shoulder region at 300–350 nm (see Figures 80–83 of SI). There are only a few reports in the literature discussing this phenomenon. When exciting a compound in solution at the red edge of the absorption band the emission is red shifted, which is most probably due to the excitation of only certain configurations.^[44]

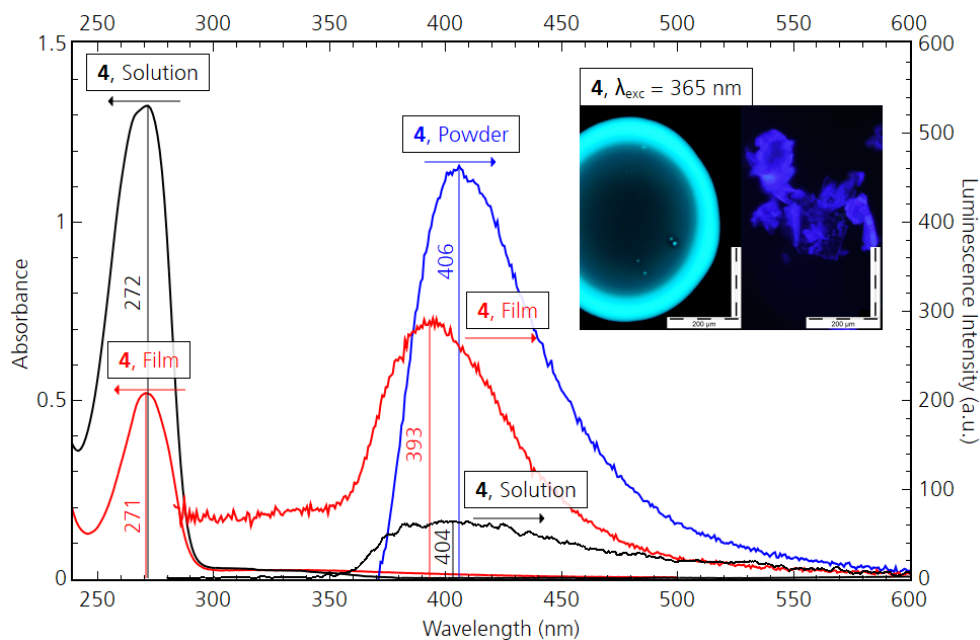


Figure 71. Luminescence properties of compound **4**. The absorbance spectra are recorded from a thin solution in MeCN (0.1 g/L) and from a thin film on quartz glass. Emission spectra are recorded from a higher concentrated solution (10 g/L), the same thin film on quartz glass and from a powder sample inside a borosilicate cavity glass at excitation wavelengths of 265 nm, 270 nm, and 350 nm. The inset shows light microscopic pictures of an amorphous droplet (left) and crystals at 365 nm illumination (scale bars: 200 μm , different colors are due to different white balance settings of the camera).

2.6.2.4. Lifetime characterization

Fluorescence-lifetime imaging microscopy (FLIM) was used to measure the autofluorescence lifetime decay of compounds **2**, **3** and **4**. For the measurement, compounds **2** and **3** were dissolved in acetonitrile and compound **4** was dissolved in ethyl acetate, due to its high solubility in acetonitrile causing an increased luminescent background. The evaluation of the FLIM images shows, that the samples consist of smaller microstructures with crystalline morphology and different photoluminescence lifetimes (Figure 72, see SI for more details). Lifetimes in the range of 3.5 and 5.9 ns were measured, which are indicative of fluorescence. Compound **2** shows spherical shaped aggregates, with an average autofluorescence lifetime of ~ 5.9 ns. Compound **3** forms homogeneous needle-like crystals with differing lifetimes in the center (3–4 ns) and the edges (4–5 ns) of the crystals. Compound **4** displays plates with a rectangular shape with homogeneous lifetime distribution of 3.5 ns. Figure 72b and Figure 72c show the FLIM data analysis by fitting of the time-correlated single photon counting (TCSPC) data and the phasor approach. The phasor approach graphically transforms the lifetime into Fourier space.^[46,47] Mono-exponential lifetime decays lie along a semi-circle with a radius of 0.5. Long lifetime species are located close to the origin (0, 0) and short lifetime species near (1, 0). Multi-exponential decays are depicted by the weighted vector of the single species phasors. As a result, the decays fall inside the semi-circle.^[47,49] The phasors of crystals **3** and **4** lie inside the arc, indicating a multi-exponential decay. As for compound **2** the larger portion of the pixels (higher occurrence) exhibit a lifetime located close to the semicircle line of the phasor. A smaller portion of the pixels is located inside the semicircle, and indicates a bi-exponential decay (Figure 85–87 of SI, tail fit). Comparing the autofluorescence lifetime decays, the lifetime is reduced by coordination to ZnCl_2 (from 5.9 ns in **2** to ~ 3.6 ns in **3** and **4**). In contrast, the fluorescence intensity is raised via complexation (from 332 kHz in **2** to 590 kHz in **4**).

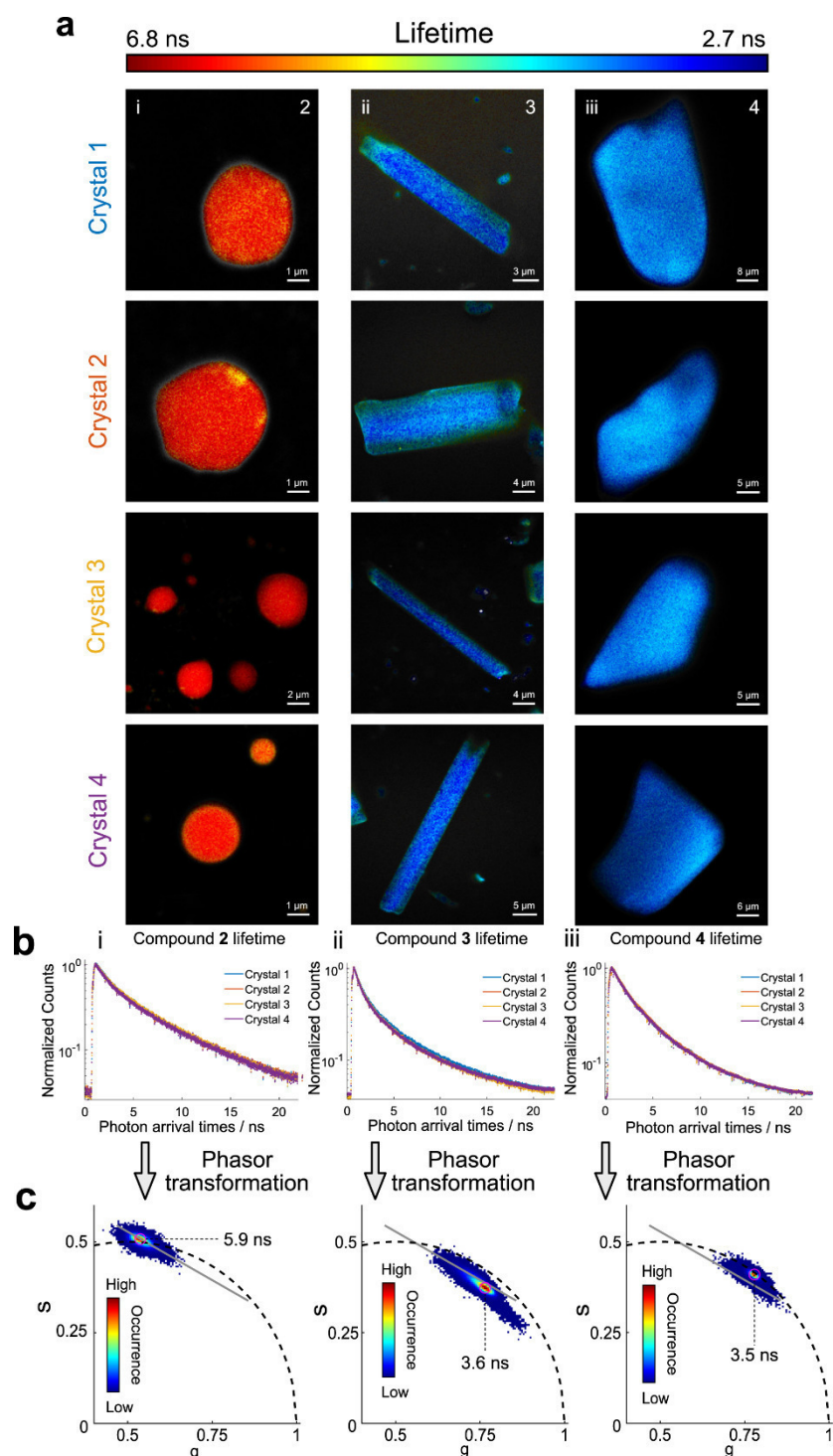


Figure 72. FLIM images and fluorescence lifetime decays of the compounds **2** (left column), **3** (middle column) and **4** (right column), highlighting their diverse structural morphologies. a) FLIM images of representative crystals for the three compounds. The color code indicates the fluorescence lifetime as a function of the spatial position on the crystal. b) Temporal evolution of the total fluorescence intensity for each crystal shown in a). c) Phasor plot of the four FLIM images per compound as shown in a), determined by phasor transformation of the individual lifetimes for each spatial pixel on the crystals. The dotted-grey lines indicate the average phasor coordinates of the four FLIM images. In addition, the corresponding lifetime is given. The color bar in the phasor plots represents the number of pixels exhibiting the particular phasor value (blue indicating the lowest and red indicating the highest occurrence).

2.6.2.5. Combination of Hirshfeld surface analysis with the FLIM results

As is known from previous results, morphology, crystal packing as well as intermolecular interactions play an important role in the length and uniformity of the autofluorescence lifetime decay as well as the overall fluorescence intensity.^[49] Hirshfeld surface (HS) analysis quantifies intermolecular interactions between molecules or predefined units in the crystal based on the crystallographic output file (.cif) obtained from single crystal X-ray diffraction using the software CrystalExplorer17 (see Figure 88 of SI).^[50,51] By combining FLIM results with HS analysis, correlating effects between intermolecular bonding interactions and fluorescence properties can be identified. Major contributors to the total HS are C–H···H–C and C–H···C contacts, which make up the majority of all interactions in all investigated compounds (**2**: 86.3 %, **3**: 67.1 %, **4**: 50.4 %). The π – π stacking interactions are almost non-existent in **2** (C···C: 0 % and C···N: 0.6 %) and **4** (C···C: 0.3 % and C···N: 0 %), and only increase slightly in **3** (C···C: 1.3 % and C···N: 0.9 %). The C–H···N, C–H···Cl and C–H···O contacts represent the attractive, non-classical hydrogen bonds and contribute with 13.2 % to the HS of **2**, 30.4 % in **3** and 48.2 % in **4**. The C–H···N and C–H···O contact contributions decrease with coordination, as expected. By combination of the FLIM results with HS analysis, we indicated in previous investigations, that the increase in the attractive hydrogen bond interactions within the crystal can result in an increase in the fluorescence brightness.^[49] Here, a correlation of the fluorescence intensity and the attractive hydrogen bonds is observed as well, however, it is in compounds **2–4** not as straightforward. In an aggregated structure a multitude of quenching effects compete with emissive effects, which explains why compound **2** deviates from the clear trend shown in Figure 73a. Additional effects apart from the types of hydrogen bonds and crystal density influence the intensity values in these compounds. Additionally, the error bar for **2** is rather large compared to the one of **3** and **4** indicating a higher uncertainty in the intensity values. In case of the π – π stacking interactions, the compounds follow a clear trend: the higher the content of π – π stacking interactions the lower the intensity. Compound **4** has the least amount of π – π stacking interactions and also shows the highest intensity of the three compounds. The same is observed for the lifetime, which decreases with the increase in attractive hydrogen bond content (Figure 73b).

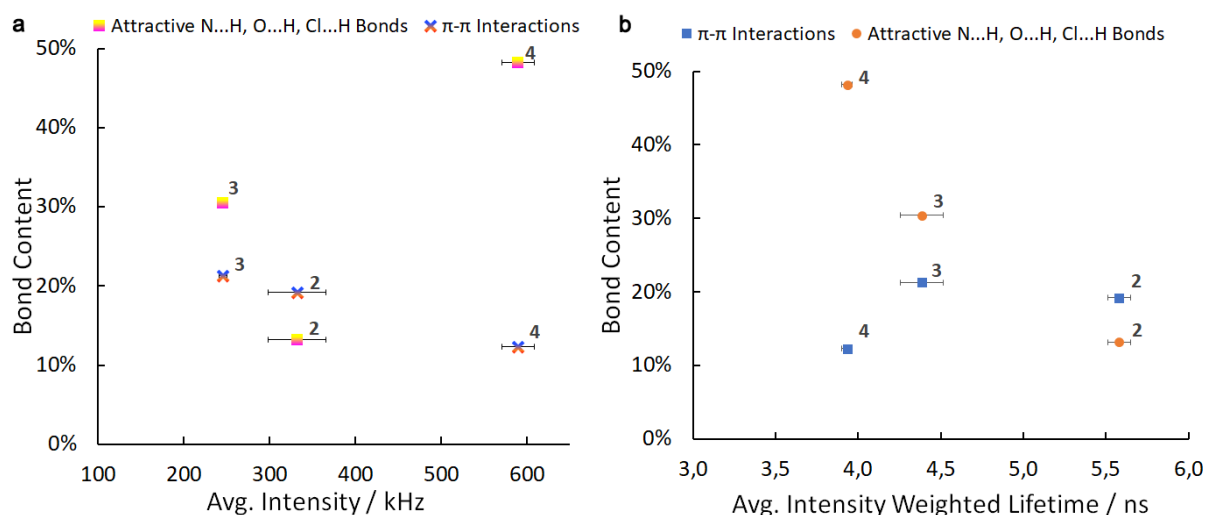


Figure 73. The relation between fluorescence lifetime and intensity relative to the attractive bond contents for the three compounds imaged in Figure 72. a) Correlation of the averaged fluorescence intensity and attractive bond contents within the investigated solid-state molecular structures of the respective compounds. b) Average intensity weighted fluorescence lifetimes in correlation to the bond content.

2.6.2.6. Quantum chemical calculations

To shed light on the different fluorescence behaviors and explaining the origin of luminescence, quantum chemical calculations and nonadiabatic surface-hopping simulations were performed. A detailed description of the employed methods can be found in the Supporting Information.

Compound **2** in isolated form as well as in the crystal environment was propagated starting in the first excited singlet state. Of the ten gas-phase trajectories propagated at 300 K, four decayed to the electronic ground state within 2.5 ps via a conical intersection (CI). In most of these cases, the involved CI was characterized by an increased C–P bond length (up to 2.8 Å), as illustrated in Figure 74.

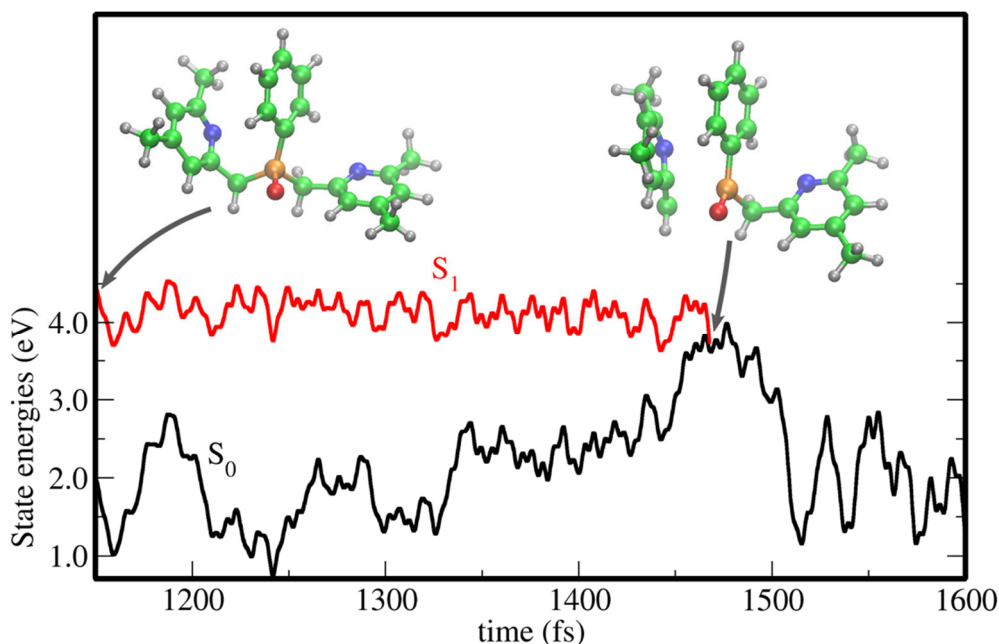


Figure 74. Temporal evolution of the electronic state energies of species **2** along a simulated surface-hopping trajectory, which was initiated in the S_1 state. At $t = 1468$ fs, the transition to the ground state occurs *via* a conical intersection characterized by an elongated C–P bond.

This configuration seems to be stabilized by a π – π interaction of the collidine and benzene ring, which exhibit a more pronounced stacking pattern while reaching the CI. The access to the CI seems to be limited by an energetic barrier that can be overcome thermally. This is further confirmed by trajectories propagated at an elevated temperature of 400 K, where three trajectories out of five decay via elongation of the C–P bond. This process cannot be possible in the solid state due to steric hindrance owing to neighboring molecules. To obtain insight into the initial steps of molecular relaxation in the solid phase, nonadiabatic trajectories have been propagated for 3 ps in two crystal models of compound **2** based on the quantum mechanical-molecular mechanical (QM/MM) approach. The models have been constructed by describing a single molecule quantum mechanically (QM part) and representing the crystal environment of several 100 molecules by a classical force field (MM part). Specifically, six trajectories were run with all MM molecules subjected to rigidifying constraints, while additional 11 were propagated with the inner layer of 14 molecules allowed to move unconstrained (for further details see the SI). Relaxation to the ground state was not observed in these cases, indicating that the frustrated and densely packed crystal environment hinders the access to conical intersections. To elucidate the nature of luminescence, adiabatic excitation energies, vibrationally resolved fluorescence and phosphorescence spectra as well as radiative lifetimes were calculated for compound **2** in the gas phase. As described in detail in the SI, an excited state of np^* character (similar to isolated pyridine) as well as one involving excitation from an oxygen lone pair p-orbital to p^* orbitals

of ring systems were found, corresponding to vertical emission energies of 3.76 and 2.15 eV, respectively. For the np^* state as well as for the lowest triplet state emission spectra and lifetimes could be calculated. Overall, the obtained intensity for fluorescence is about nine orders of magnitude higher than for phosphorescence (see SI, Figure 90 and 91), which is paralleled by lifetimes of about 2 ns for fluorescence vs. 1.6 s for phosphorescence (see the rate constants in the SI, Table 17). The calculated emission maximum of the fluorescence is situated at 320 nm, which fits well to the experimentally known fluorescence of the isolated pyridine chromophore. However, for compound **2** itself, the experimental data indicate that another state should be responsible for emission. While the theoretically found lone pair- p^* state has too low an energy in the gas phase, it might be a candidate for emission in the condensed phase where the more rigid environment prevents a strong structural relaxation that would lower the excitation energy. To substantiate this hypothesis, the excited state character and approximated fluorescence intensities were calculated for the geometries along the crystal trajectories. Indeed, the excited state involves large contributions of lone pair- p^* excitation, and the fluorescence spectrum shown in Figure 92 of the SI exhibits a maximum around 430 nm, which is in fair agreement with the experimental spectrum shown in Figure 69. Although the calculated phosphorescence also maximizes in the same wavelength range, the presence of a singlet state in the same range as well as the very long calculated phosphorescence lifetime contrasting with the ns time scale obtained in the FLIM experiments supports the conclusion that the experimentally observed emission is indeed due to fluorescence.

For compound **3**, no fluorescence spectrum could be computed due to too strongly deviating geometries in the ground and excited states. However, the energy difference between the lowest vibrational levels of these states corresponds to 332 nm (3.74 eV, Table 16 of SI), which matches the onset of the experimental spectrum for the amorphous phase with a luminescence maximum at 303 nm quite well. The phosphorescence spectrum, by contrast, is peaked at 430 nm (Figure 93 of SI) and appears to match the measured luminescence maximum at 414 nm for the crystalline compound (Figure 70). However, as for compound **2**, a small intensity and long time-constant (0.6 s, Table S2 of SI) are calculated, while the FLIM measurements yield a ns time scale for emission. This indicates that by a similar reasoning as for compound **2**, fluorescence emission should be more likely than phosphorescence also for compound **3**.

2.6.3. Conclusion

We presented a novel, functionalized phosphine oxide ligand and its $ZnCl_2$ complexes, which show an unexpected but interesting and fascinating blue luminescence. The synthesis of these compounds is straight-forward, efficient and scalable starting from commercially available and inexpensive educts. The resulting compounds were characterized using NMR, MS, IR spectroscopy, EA and X-ray crystallography. Variable temperature NMR reveals that both complexes show a dynamic behavior in solution. However, the dynamics is minimized in compound **4**, where the nitrogen atom of the second collidiny ring is protonated. The characterization of the physical properties of the compounds in solid/crystalline-state, solution and thin film was performed by absorption and fluorescence excitation/emission spectroscopy. The emission maxima of all compounds are around 400 nm, indicating a possible use as blue emitters. Compounds **3** and **4** form stable thin films, however, only compound **4** is luminescent in thin film. The PLQY for powdered samples of compounds **3** and **4** is around 40 %, both when excited at 350 nm, and comparable to other known, blue luminescent Zn(II) complexes. FLIM measurements reveal luminescent lifetimes of 3.5-5.9 ns, with compound **2** having the longest lifetime, but compound **4** displaying the highest luminescence intensity. Combining these results with Hirshfeld surface analysis, we can further conclude that the higher the content of π - π stacking interactions is, the lower is the luminescence intensity. The same is observed for the lifetime. Quantum chemical calculations were used to elucidate the nature of luminescence exhibited in the

solid state as well as the non-radiative relaxation pathways in the gas phase. We propose a model, in which the crystal environment and/or the steric fixation by the coordinating central atoms blocks the thermal relaxation into the ground state. This is further facilitated by aggregation of the molecules in concentrated solution or solid state.

All in all, these findings are not only beneficial to the proposed ligand but are also important for similar compounds. The results can open the door for a targeted refinement of these phosphine ligands to obtain suitable luminescent materials for all possible uses in the future. A further modification of the substituents on phosphorus can induce a red shift of the emission maximum and improve photophysical properties.

CCDC ##### contains the supplementary crystallographic data for this paper. These data can be obtained free of charge from The Cambridge Crystallographic Data Centre via www.ccdc.cam.ac.uk/data_request/cif.

Supporting Information

Supporting Information is available from the Wiley Online Library or from the author.

Acknowledgements

C. K., M. G., D. F. and N. D. contributed equally to this work.

Financial support by the German Federal Ministry for Economic Affairs and Energy on the basis of a decision by the German Bundestag (ZIM, Grant ZF4477702SL7, ZF4065408SL7) is gratefully acknowledged. Furthermore, this work is financially supported by the Department of Chemistry, Ludwig-Maximilian University of Munich. For his continuous support over the years Prof. Dr. T. M. Klapötke is thanked. Furthermore, we thank Nathalie Robel und Jiyong Kim for their support in performing luminescence measurements.

Conflict of Interest

The authors declare no conflict of interest.

2.6.4. References

- [1] H. Yersin, *Highly efficient OLEDs with phosphorescent materials*, Wiley-VCH, **2007**.
- [2] H. Yersin, A. F. Rausch, R. Czerwieniec, T. Hofbeck, T. Fischer, *Coord. Chem. Rev.*, **2011**, 255 (21–22), 2622–2652.
- [3] C. Adachi, M. A. Baldo, M. E. Thompson, S. R. Forrest, *J. Appl. Phys.*, **2001**, 90 (10), 5048–5051.
- [4] D. F. O'Brien, M. a. Baldo, M. E. Thompson, S. R. Forrest, *Appl. Phys. Lett.*, **1999**, 74 (3), 442.
- [5] C.-M. Che, C.-C. Kwok, S.-W. Lai, A. F. Rausch, W. J. Finkenzeller, N. Zhu, H. Yersin, *Chem. - A Eur. J.*, **2010**, 16 (1), 233–247.
- [6] J. Zhao, F. Dang, Z. Feng, B. Liu, X. Yang, Y. Wu, G. Zhou, Z. Wu, W.-Y. Wong, *Chem. Commun.*, **2017**, 53 (54), 7581–7584.
- [7] C. Cebrián, M. Mauro, *Beilstein J. Org. Chem.*, **2018**, 14 (li), 1459–1481.
- [8] T. C. Lee, J. Y. Hung, Y. Chi, Y. M. Cheng, G. H. Lee, P. T. Chou, C. C. Chen, C. H. Chang, C. C. Wu, *Adv. Funct. Mater.*, **2009**, 19 (16), 2639–2647.
- [9] W.-C. Chen, C.-S. Lee, Q.-X. Tong, *J. Mater. Chem. C*, **2015**, 3 (42), 10957–10963.
- [10] C. Y. Chan, M. Tanaka, Y. T. Lee, Y. W. Wong, H. Nakanotani, T. Hatakeyama, C. Adachi, *Nat. Photonics*, **2021**, 15 (3), 203–207.
- [11] J. H. Lee, C. H. Chen, P. H. Lee, H. Y. Lin, M. K. Leung, T. L. Chiu, C. F. Lin, *J. Mater. Chem. C*, **2019**, 7 (20), 5874–5888.

- [12] G. Hong, X. Gan, C. Leonhardt, Z. Zhang, J. Seibert, J. M. Busch, S. Bräse, *Adv. Mater.*, **2021**, *33* (9), 2005630.
- [13] C. Han, Y. Zhao, H. Xu, J. Chen, Z. Deng, D. Ma, Q. Li, P. Yan, *Chem. - A Eur. J.*, **2011**, *17* (21), 5800–5803.
- [14] J. Uk Kim, Y. M. Wong, S. Kumar, O. G. Hayes, F. Duncan, C.-Y. Chan, B. Y.-W. Wong, H. Ye, L.-S. Cui, H. Nakanotani, E. Zysman-Colman, C. Adachi, *Chem. Lett.*, **2019**, *48*, 1225–1228.
- [15] G. Mallesham, C. Swetha, S. Niveditha, M. E. Mohanty, N. J. Babu, A. Kumar, K. Bhanuprakash, V. J. Rao, *J. Mater. Chem. C*, **2015**, *3* (6), 1208–1224.
- [16] K. Duan, D. Wang, M. Yang, Z. Liu, C. Wang, T. Tsuboi, C. Deng, Q. Zhang, *ACS Appl. Mater. Interfaces*, **2020**, *12* (27), acsami.0c02800.
- [17] C. Kerzig, X. Guo, O. S. Wenger, *J. Am. Chem. Soc.*, **2019**, *141* (5), 2122–2127.
- [18] X. Song, H. Xu, *J. Inf. Disp.*, **2020**, *0* (0), 1–24.
- [19] C. Han, H. Xu, *Chinese Sci. Bull.*, **2019**, *64* (7), 663–681.
- [20] D. Joly, P.-A. Bouit, M. Hissler, *J. Mater. Chem. C*, **2016**, *4* (17), 3686–3698.
- [21] K. Katagiri, Y. Yamamoto, Y. Takahata, R. Kishibe, N. Fujimoto, *Tetrahedron Lett.*, **2019**, *60* (30), 2026–2029.
- [22] M. K. Rong, F. Holtrop, J. C. Slootweg, K. Lammertsma, *Coord. Chem. Rev.*, **2019**, *382*, 57–68.
- [23] A. V. Artem'ev, M. Z. Shafikov, A. Schinabeck, O. V. Antonova, A. S. Berezin, I. Y. Bagryanskaya, P. E. Plusnin, H. Yersin, *Inorg. Chem. Front.*, **2019**, *6* (11), 3168–3176.
- [24] C. Poriel, J. Rault-Berthelot, *Adv. Funct. Mater.*, **2021**, 2010547, 1–43.
- [25] J. Zhang, D. Ding, Y. Wei, H. Xu, *Chem. Sci.*, **2016**, *7* (4), 2870–2882.
- [26] N. Lin, J. Qiao, L. Duan, H. Li, L. Wang, Y. Qiu, *J. Phys. Chem. C*, **2012**, *116* (36), 19451–19457.
- [27] H. Li, M. Hong, A. Scarpaci, X. He, C. Risko, J. S. Sears, S. Barlow, P. Winget, S. R. Marder, D. Kim, J.-L. Brédas, *Chem. Mater.*, **2019**, *31* (5), 1507–1519.
- [28] F. Würthner, *Angew. Chem.*, **2020**, *132* (34), 14296–14301; *Angew. Chem. Int. Ed.*, **2020**, *59* (34), 14192–14196.
- [29]
- [30] Z. He, C. Ke, B. Z. Tang, *ACS Omega*, **2018**, *3* (3), 3267–3277.
- [30] L. Bergmann, J. Friedrichs, M. Mydlak, T. Baumann, M. Nieger, S. Bräse, *Chem. Commun.*, **2013**, *49* (58), 6501–6503.
- [31] A. V. Artem'ev, M. R. Ryzhikov, I. V. Taidakov, M. I. Rakhmanova, E. A. Varaksina, I. Y. Bagryanskaya, S. F. Malysheva, N. A. Belogorlova, *Dalton Trans.*, **2018**, *47* (8), 2701–2710.
- [32] A. V. Artem'ev, E. P. Doronina, M. I. Rakhmanova, A. O. Sutyryna, I. Y. Bagryanskaya, P. M. Tolstoy, A. L. Gushchin, A. S. Mazur, N. K. Gusarova, B. A. Trofimov, *New J. Chem.*, **2016**, *40* (12), 10028–10040.
- [33] L. Douce, L. Charbonnière, M. Cesario, R. Ziesel, *New J. Chem.*, **2001**, *25* (8), 1024–1030.
- [34] A. V. Artem'ev, A. Y. Baranov, M. I. Rakhmanova, S. F. Malysheva, D. G. Samsonenko, *New J. Chem.*, **2020**, *44* (17), 6916–6922.
- [35] G. A. Bowmaker, J. V. Hanna, S. P. King, F. Marchetti, C. Pettinari, A. Pizzabiocca, B. W. Skelton, A. N. Sobolev, A. Tăbăcaru, A. H. White, *Eur. J. Inorg. Chem.*, **2014**, *2014* (35), 6104–6116.
- [36] O. Crespo, M. C. Gimeno, A. Laguna, C. Larraz, *Z. Naturforsch.*, **2009**, *64* (11–12), 1525–1534.
- [37] S. Bestgen, C. Schoo, B. L. Neumeier, T. J. Feuerstein, C. Zovko, R. Köppe, C. Feldmann, P. W. Roesky, *Angew. Chem.*, **2018**, *130* (43), 14461–14465; *Angew. Chem. Int. Ed.*, **2018**, *57* (43), 14265–14269.
- [38] I. M. Dixon, E. Lebon, P. Sutra, A. Igau, *Chem. Soc. Rev.*, **2009**, *38*, 1621–1634.
- [39] M. I. Rogovoy, A. S. Berezin, D. G. Samsonenko, A. V. Artem'ev, *Inorg. Chem.*, **2021**, *60* (9), 6680–6687.

- [40] C. Kirst, F. Zoller, T. Bräuniger, P. Mayer, D. Fattakhova-Rohlfing, K. Karaghiosoff, *Inorg. Chem.*, **2021**, *60* (4), 2437–2445.
- [41] K. Groutchik, K. Jaiswal, R. Dobrovetsky, *Org. Biomol. Chem.*, **2021**, *19* (25), 5544–5550.
- [42] T. Steiner, *Angew. Chem.*, **2002**, *114*, 50–80; *Angew. Chem. Int. Ed.*, **2002**, *41*, 48–76.
- [43] A. N. Fletcher, *J. Phys. Chem.*, **1968**, *72* (8), 2742–2749.
- [44] K. Itoh, T. Azumi, *Chem. Phys. Lett.*, **1973**, *22* (2), 395–399.
- [45] R. M. Adhikari, D. C. Neckers, *J. Phys. Chem. A*, **2009**, *113* (2), 417–422.
- [46] M. A. Digman, V. R. Caiolfa, M. Zamai, E. Gratton, *Biophys. J.*, **2008**, *94* (2), L14–L16.
- [47] G. I. Redford, R. M. Clegg, *J. Fluoresc.*, **2005**, *15* (5), 805–815.
- [48] W. Schrimpf, J. Jiang, Z. Ji, P. Hirschle, D. C. Lamb, O. M. Yaghi, S. Wuttke, *Nat. Commun.*, **2018**, *9* (1), 1647.
- [49] C. Kirst, N. A. Danaf, F. Knechtel, T. Arczynski, P. Mayer, D. C. Lamb, K. Karaghiosoff, *submitted to publication*.
- [50] M. A. Spackman, D. Jayatilaka, *CrystEngComm*, **2009**, *11* (1), 19–32.
- [51] M. J. Turner, J. J. McKinnon, S. K. Wolff, D. J. Grimwood, P. R. Spackman, D. Jayatilaka, M. A. Spackman, CrystalExplorer17, University of Western Australia, Australia, **2017**.

2.6.5. Supporting information

2.6.5.1. Synthesis and Characterization

Synthesis of 2,4-dimethyl-6-((trimethylsilyl)methyl)pyridine A: 2,4,6-trimethylpyridine (1 eq, 0.1 mol, 13.2 mL) is dissolved in 100 mL dry THF and cooled down to $-78\text{ }^{\circ}\text{C}$. *n*BuLi (1 eq, 74.6 mL, 1.34 M in Hexane) is added drop wise while stirring. After stirring for another hour, TMSCl (1.1 eq, 12.8 mL) is added dropwise to the mixture at $-78\text{ }^{\circ}\text{C}$. The mixture is allowed to warm up to RT overnight. The solvent is removed under vacuum and filtered (optional), the left-over liquid is distilled under reduced pressure (10^{-3} mbar, $36\text{ }^{\circ}\text{C}$, oil bath at $45\text{--}50\text{ }^{\circ}\text{C}$) to receive 2,4-dimethyl-6-((trimethylsilyl)methyl)pyridine **A** as a colorless oil (14.0 g, 72.4 mmol, 72.4 %). ^1H NMR (400 MHz, CDCl_3 , δ): 6.59 (s, 1H, Pyridyl-H), 6.51 (s, 1H, Pyridyl-H), 2.36 (s, 3H, CH_3), 2.20 (s, 2H, CH_2), 2.14 (s, 3H, CH_3), -0.06 (s, 9H, Si- CH_3); $^{13}\text{C}\{^1\text{H}\}$ NMR (100 MHz, CDCl_3 , δ): 160.3 (s, Cq- CH_3), 157.1 (s, Cq- CH_2), 146.7 (s, Cq- CH_3), 119.9 (s, Pyridyl-C), 119.7 (s, Pyridyl-C), 29.9 (s, $^1J_{\text{C-Si}} = 22.0$ Hz, CH_2), 24.3 (s, CH_3), 20.8 (s, CH_3), -1.67 (s, $^1J_{\text{C-Si}} = 25.6$ Hz, Si- CH_3); ^{29}Si INEPT NMR (162 MHz, CDCl_3 , δ): 1.9 (s, $^1J_{\text{Si-C}} = 25.4$ Hz) ppm.

Synthesis of bis((4,6-dimethylpyridin-2-yl)methyl)(phenyl)phosphine 1: A (2 eq, 2.0 g, 30.3 mmol) is dissolved in 60 mL of dry, degassed THF and cooled to $-10\text{ }^{\circ}\text{C}$. Dichlorophenylphosphine (0.68 mL, 15 mmol) is added dropwise while stirring. The reaction mixture is warmed up to RT overnight. The solvent is removed in vacuo and **1** is obtained as an orange viscos oil (stoichiometric yields). $^{31}\text{P}\{^1\text{H}\}$ NMR (162 MHz, reaction mixture, δ): -14.1 (s); ^1H NMR (400 MHz, CDCl_3 , δ): 7.47 (m, 2H; Phenyl-H), 7.29 (m, 3H, Phenyl-H), 6.70 (s, 2H, Pyridyl-H), 6.62 (s, 2H, Pyridyl-H), 3.28 (dd, $J_{\text{H-P}} = 12.8$ Hz, 4H, CH_2), 2.42 (s, 6H, CH_3), 2.14 (s, 6H, CH_3); $^{13}\text{C}\{^1\text{H}\}$ NMR (100 MHz, CDCl_3 , δ): 157.4 (s, Cq- CH_3), 157.2 (d, $J_{\text{C-P}} = 6.0$ Hz, Cq- CH_2), 147.1 (s, Cq- CH_3), 137.5 (d, $J_{\text{C-P}} = 18.8$ Hz, Cq), 132.8 (d, $J_{\text{C-P}} = 17.8$ Hz, Phenyl-C), 128.9 (s, Phenyl-C), 128.0 (d, $J_{\text{C-P}} = 7.4$ Hz, Phenyl-C), 121.6 (d, $J_{\text{C-P}} = 5.5$ Hz, Pyridyl-C), 121.4 (d, $J_{\text{C-P}} = 2.5$ Hz, Pyridyl-C), 119.4 (d, $J_{\text{C-P}} = 142.6$ Hz, Phenyl-Cq), 37.7 (d, $J_{\text{C-P}} = 17.5$ Hz, CH_2), 24.3 (s, CH_3), 20.7 (s, CH_3); $^{31}\text{P}\{^1\text{H}\}$ NMR (162 MHz, CDCl_3 , δ): -13.3 (s); ^{31}P NMR (162 MHz CDCl_3 , δ): -13.3 (t, $^2J_{\text{P-H}} = 14.6$ Hz) ppm.

Synthesis of bis((4,6-dimethylpyridin-2-yl)methyl)(phenyl)phosphine oxide 2: Compound **1** is taken without further purification and dissolved in 60 mL DCM. A water/H₂O₂ mixture (4 mL 30 % H₂O₂ in 11 mL water) is added dropwise to the mixture at -10 °C and stirred for 5 h. The solvent is removed under reduced pressure. The left-over mixture is dissolved in DCM and extracted with water three times. After removal of all volatiles, **2** is received as a colorless solid (4.87 g, 13.36 mmol, 93.12 %). m.p. 105 °C; ¹H NMR (400 MHz, CDCl₃, δ): 7.63 (m, 2H, Phenyl-H), 7.44 (m, 1H; Phenyl-H), 7.36 (m, 2H, Phenyl-H), 6.96 (s, 2H, Pyridyl-H), 6.77 (s, 2H, Pyridyl-H), 3.58 (d, ²J_{H-P} = 14.6 Hz, 4H, CH₂), 2.37 (s, 6H, CH₃), 2.20 (s, 6H, CH₃); ¹³C{¹H} NMR (100 MHz, CDCl₃, δ): 157.8 (d, ⁴J_{C-P} = 1.9 Hz, Cq-CH₃), 151.9 (d, ²J_{C-P} = 7.3 Hz, Cq-CH₂), 147.8 (d, ⁴J_{C-P} = 2.5 Hz, Cq-CH₃), 131.8 (d, ¹J_{C-P} = 96.4 Hz, Cq), 131.6 (d, ⁴J_{C-P} = 2.8 Hz, Phenyl-C), 131.3 (d, ³J_{C-P} = 9.2 Hz, Phenyl-C), 128.1 (d, ²J_{C-P} = 11.6 Hz, Phenyl-C), 122.9 (d, ³J_{C-P} = 4.2 Hz, Pyridyl-C), 122.4 (d, ⁵J_{C-P} = 2.7 Hz, Pyridyl-C), 40.5 (d, ¹J_{C-P} = 62.0 Hz, CH₂), 24.3 (s, CH₃), 20.9 (s, CH₃); ³¹P{¹H} NMR (162 MHz, CDCl₃, δ): 36.8 (s); ³¹P NMR (162 MHz CDCl₃, δ): 36.8 (sept, ²J_{P-H} = 13.7 Hz); ¹⁵N (*via* ¹H, ¹⁵N-HMBC) NMR (40 MHz, CDCl₃, δ): -94.7 (s) ppm; IR: ν = 2907 (vw), 1605 (s), 1566 (m), 1435 (m), 1317 (w), 1222 (m), 1183 (vs), 1113 (m), 1029 (w), 931 (w), 852 (m), 737 (m), 723 (vs), 693 (s), 643 (m), 571 (w), 533 (w), 502 (vs), 462 (vw), 435 cm⁻¹ (vs); HRMS (ESI) *m/z*: [M + H]⁺ calcd for C₂₂H₂₅N₂OP, 365.1738; found, 365.1777. Anal. calcd for C₂₂H₂₅N₂OP: C 72.51, H 6.91, N 7.69; found: C 72.52, H 6.90, N 7.50.

Synthesis of the zinc(II) chloride complex of bis((4,6-dimethylpyridin-2-yl)methyl)(phenyl)phosphine oxide (3): Dry ZnCl₂ (0.80 g, 5.50 mmol) and **2** (2.00 g, 5.50 mmol) are mixed together in a Schlenk flask and dissolved in dry, degassed acetonitrile. After removing the solvent, **3** is received as a colorless solid (2.67 g, 5.20 mmol, 97.16 %). m.p. 205 °C; ¹H NMR (400 MHz, CDCl₃, δ): 7.79 (dd, ³J_{H-H} = 8.3 Hz, ⁴J_{H-H} = 1.4 Hz, 2H, Phenyl-H), 7.58 (t, ³J_{H-H} = 7.3 Hz, ⁴J_{H-H} = 1.5 Hz, 1H; Phenyl-H), 7.48 (t, ³J_{H-H} = 7.2 Hz, ⁴J_{H-H} = 2.9 Hz, 2H, Phenyl-H), 6.91 (s, 4H, Pyridyl-H), 3.86 (d, ²J_{H-P} = 15.1 Hz, 4H, CH₂), 2.70 (s, 6H, CH₃), 2.25 (s, 6H, CH₃); ¹³C{¹H} NMR (100 MHz, CDCl₃, δ): 159.2 (s, Cq-CH₃), 151.1 (s, Cq-CH₂), 150.1 (d, ⁴J_{C-P} = 7.7 Hz, Cq-CH₃), 133.7 (d, ¹J_{C-P} = 3.0 Hz, Cq), 131.1 (d, ⁴J_{C-P} = 10.3 Hz, Phenyl-C), 129.3 (d, ³J_{C-P} = 12.8 Hz, Phenyl-C), 127.0 (s, ¹J_{C-P} = 101.9 Hz, Phenyl-C), 124.9 (d, ³J_{C-P} = 5.6 Hz, Pyridyl-C), 124.6 (d, ⁵J_{C-P} = 1.7 Hz, Pyridyl-C), 38.0 (d, ¹J_{C-P} = 60.7 Hz, CH₂), 25.0 (s, CH₃), 21.1 (s, CH₃); ³¹P{¹H} NMR (162 MHz, CDCl₃, δ): 50.6 (s); ³¹P NMR (162 MHz CDCl₃, δ): 50.6 (sept, ²J_{P-H} = 13.3 Hz); ¹⁵N (*via* ¹H, ¹⁵N HMBC) NMR (40 MHz, CDCl₃, δ): -208.3 (s) ppm; ¹H NMR (400 MHz, CD₂Cl₂, δ): 7.73 (m, 2H, Phenyl-H), 7.61 (tq, ³J_{H-H} = 7.4 Hz, ⁴J_{H-H} = 1.6 Hz, 1H; Phenyl-H), 7.48 (m, 2H, Phenyl-H), 6.95 (s, 2H, Pyridyl-H), 6.86 (s, 2H, Pyridyl-H), 3.87 (m, ²J_{H-P} = 15.6 Hz, 4H, CH₂), 2.67 (s, 6H, CH₃), 2.25 (s, 6H, CH₃); ¹³C{¹H} NMR (100 MHz, CD₂Cl₂, δ): 159.6 (s, Cq-CH₃), 151.3 (s, Cq-CH₂), 150.6 (s, Cq-CH₃), 133.9 (d, ¹J_{C-P} = 2.7 Hz, Cq), 131.2 (d, ⁴J_{C-P} = 9.9 Hz, Phenyl-C), 129.4 (d, ³J_{C-P} = 12.5 Hz, Phenyl-C), 128.1 (s), 124.9 (s, ¹J_{C-P} = 31.9 Hz, Phenyl-C), 124.9 (d, ³J_{C-P} = 5.6 Hz, Pyridyl-C), 124.6 (d, ⁵J_{C-P} = 1.7 Hz, Pyridyl-C), 38.3 (d, ¹J_{C-P} = 66.3 Hz, CH₂), 25.0 (s, CH₃), 21.0 (s, CH₃); ³¹P{¹H} NMR (162 MHz, CD₂Cl₂, δ): 50.7 (s); ³¹P NMR (162 MHz, CD₂Cl₂, δ): 50.7 (quin, ²J_{P-H} = 14.4 Hz); ¹H NMR (400 MHz, CD₂Cl₂, -80 °C, δ): 7.66 (m, 2H, Phenyl-H), 7.55 (t, ³J_{H-H} = 8.2 Hz, 1H; Phenyl-H), 7.48 (t, ³J_{H-H} = 7.2 Hz, ⁴J_{H-H} = 2.9 Hz, 2H, Phenyl-H), 6.95 (s, 1H, Pyridyl-H), 6.87 (s, 1H, Pyridyl-H), 6.81 (s, 1H, Pyridyl-H), 6.75 (s, 1H, Pyridyl-H), 3.73 (m, 4H, CH₂), 2.69 (s, 3H, CH₃), 2.40 (s, 3H, CH₃), 2.24 (s, 3H, CH₃), 2.09 (s, 3H, CH₃); ¹³C{¹H} NMR (100 MHz, CD₂Cl₂, -80 °C, δ): 158.4 (s, Cq-CH₃), 157.4 (s, Cq-CH₃), 152.6 (s, Cq-CH₃), 149.9 (s, Cq-CH₂), 148.2 (s, Cq-CH₃), 133.3 (s, Cq), 130.1 (s, Phenyl-C), 128.7 (s, Phenyl-C), 128.6 (s, Phenyl-C), 125.5 (s, Pyridyl-C), 124.6 (s, Pyridyl-C), 122.8 (s), 122.5 (s), 37.9 (s, CH₂), 35.4 (s, CH₂), 25.0 (s, CH₃), 23.6 (s, CH₃), 20.6 (s, CH₃), 20.1 (s, CH₃); ³¹P{¹H} NMR (162 MHz, CD₂Cl₂, -80 °C, δ): 51.4 (s); ¹⁵N (*via* ¹H, ¹⁵N-HMBC) NMR (40 MHz, CD₂Cl₂, -80 °C, δ): -155.0 (s) ppm; IR: ν = 2944 (vw), 2886 (vw), 1614 (s), 1559 (m), 1439 (s), 1400 (w), 1372 (w), 1323 (vw), 1272 (w), 1219 (m), 1172 (s), 1131 (s), 1097 (s), 1074 (w), 1038 (w), 1014 (w), 996 (vw), 963 (vw), 936 (w), 875 (vw), 868 (s), 838 (w), 768 (m), 750 (s), 724 (vw), 693 (s), 648 (s), 543 (w), 539 (w), 507 (vs), 478 (w), 444 (s), 423 cm⁻¹ (vs);

LRMS (MALDI) m/z : $[M + H - 2Cl]^+$ calcd for $C_{22}H_{25}N_2OPZnCl_2$, 429.1069; found, 429.49. Anal. calcd for $C_{22}H_{25}N_2OPZnCl_2$: C 52.77, H 5.03, N 5.59; found: C 52.67, H 5.03, N 5.68.

Synthesis of zinc(II) chloride complex of 2-(((4,6-dimethylpyridin-2-yl)methyl)(phenyl)phosphoryl)methyl)-4,6-dimethylpyridin-1-ium aqua trichloro zincate 4: $ZnCl_2$ (0.80 g, 5.50 mmol) and **2** (2.00 g, 5.50 mmol) are mixed together in a Schlenk flask and dissolved in acetonitrile. A few drops of a water/HCl (conc.) mixture is added to the solution and vigorously stirred for 2 hours. After removing the solvents, **4** is received as a colorless solid (2.27 g, 4.53 mmol, 82.61 %). mp 150-160 °C; 1H NMR (400 MHz, $CDCl_3$, δ): 8.01 (dd, $J = 7.1$ Hz, 1.0 Hz, 2H, Phenyl-H), 7.59 (m, 1H; Phenyl-H), 7.52 (ddd, $J = 7.0$ Hz, 2.8 Hz, 2H, Phenyl-H), 7.33 (s, 2H, Pyridyl-H), 7.06 (s, 2H, Pyridyl-H), 4.27 (t, $J = 13.9$ Hz, 2H, CH_2), 4.11 (m, 2H, $J = 15.6, 8.1, 7.2$ Hz, CH_2), 2.80 (s, 6H, CH_3), 2.35 (s, 6H, CH_3); $^{13}C\{^1H\}$ NMR (100 MHz, $CDCl_3$, δ): 158.1 (s, Cq- CH_3), 154.5 (s, Cq- CH_2), 148.5 (s, Cq- CH_3), 134.2 (d, $J = 3.1$ Hz, Cq), 131.5 (d, $J = 10.9$ Hz, Phenyl-C), 129.6 (d, $J = 13.1$ Hz, Phenyl-C), 126.5 (d, $J = 6.2$ Hz, Pyridyl-C), 125.9 (s, Pyridyl-C), 124.9 (s), 36.7 (d, $J = 60.8$ Hz, CH_2), 23.8 (s, CH_3), 21.6 (s, CH_3); $^{31}P\{^1H\}$ NMR (162 MHz, $CDCl_3$, δ): 49.5 (s); ^{31}P NMR (162 MHz $CDCl_3$, δ): 49.5 (quin, $^2J_{P-H} = 12.3$ Hz); 1H NMR (400 MHz, CD_2Cl_2 , δ): 8.02 (m, 2H, Phenyl-H), 7.59 (tq, $^3J_{H-H} = 5.6$ Hz, $^4J_{H-H} = 1.9$ Hz, 1H; Phenyl-H), 7.58 (m, 2H, Phenyl-H), 7.38 (s, 2H; Pyridyl-H), 7.11 (s, 2H; Pyridyl-H), 4.32 (t, $^2J_{H-H} = 14.1$ Hz, 2H; CH_2), 4.16 (t, $^2J_{H-H} = 15.5$ Hz, 2H; CH_2), 2.79 (s, 6H; CH_3), 2.37 (s, 6H, CH_3); $^{13}C\{^1H\}$ NMR (100 MHz, CD_2Cl_2 , δ): 158.0 (s, Cq- CH_3), 155.9 (s, Cq- CH_2), 148.3 (s, Cq- CH_3), 134.5 (d, $^6J_{C-P} = 2.6$ Hz, Cq), 131.7 (d, $^4J_{C-P} = 10.7$ Hz, Phenyl-C), 129.9 (d, $^3J_{C-P} = 13.8$ Hz, Phenyl-C), 126.3 (d, $^5J_{C-P} = 5.8$ Hz, Pyridyl-C), 125.5 (d, $^1J_{C-P} = 104.5$ Hz, Phenyl-Cq), 36.6 (d, $^1J_{C-P} = 60.4$ Hz, CH_2), 23.7 (s, CH_3), 21.7 (s, CH_3); $^{31}P\{^1H\}$ NMR (162 MHz, CD_2Cl_2 , δ): 50.0 (s) ppm.

2.6.5.2. Crystallographic data

Table 12. Crystallographic and refinement data for compounds **2–4**.

	2	3	4
Formula	C ₂₂ H ₂₅ N ₂ OP	C ₂₂ H ₂₅ N ₂ OPZnCl ₂	C ₂₂ H ₂₈ N ₂ O ₂ PZn ₂ Cl ₅
Formula weight [g·mol ⁻¹]	364.41	500.68	691.42
Colour	colorless	colorless	colorless
Habit	rod	prism	platelet
T [K]	133	133	123
λ [Å]	0.71073	0.71073	0.71073
Crystal system	monoclinic	orthorhombic	orthorhombic
Space group	<i>P2₁/n</i>	<i>Pbca</i>	<i>P2₁2₁2₁</i>
<i>a</i> [Å]	13.9463(4)	8.2785(6)	12.0891(6)
<i>b</i> [Å]	5.3806(2)	20.1973(16)	14.1717(8)
<i>c</i> [Å]	25.6746(9)	26.8491(17)	16.9956(8)
α [°]	90	90	90
β [°]	97.973(3)	90	90
γ [°]	90	90	90
<i>V</i> [Å ³]	1,907.98(11)	4,489.3(6)	2,911.7(3)
<i>Z</i>	4	8	4
ρ _{calc} [g·cm ⁻³]	1.269	1.482	1.577
μ [mm ⁻¹]	0.157	1.420	2.184
<i>F</i> (0 0 0)	776	2,064	1,400
Crystal size [mm]	0.40×0.15×0.05	0.30×0.15×0.08	0.10×0.10×0.05
θ range [°]	3.547–28.281	2.524–26.369	2.067–26.371
Index ranges	-18 ≤ <i>h</i> ≤ 17 -7 ≤ <i>k</i> ≤ 7 -34 ≤ <i>l</i> ≤ 34	-10 ≤ <i>h</i> ≤ 10 -25 ≤ <i>k</i> ≤ 25 -33 ≤ <i>l</i> ≤ 27	-14 ≤ <i>h</i> ≤ 15 -17 ≤ <i>k</i> ≤ 17 -21 ≤ <i>l</i> ≤ 21
reflns collected	18,208	34,121	21,848
Independent reflns	4,709 [<i>R</i> _{int} = 0.0364]	4,591 [<i>R</i> _{int} = 0.0853]	5,950 [<i>R</i> _{int} = 0.1105]
Completeness to theta	99.4 %	99.8 %	100.0 %
Refinement method	Full-matrix least- squares on <i>F</i> ²	Full-matrix least- squares on <i>F</i> ²	Full-matrix least- squares on <i>F</i> ²
Data/ restraints/ Parameters	4,709 / 0 / 239	4,591 / 0 / 266	5,950 / 0 / 324
Hydrogen atom treatment	constrained	constrained	constrained
<i>R</i> ₁ / <i>wR</i> ₂ (<i>I</i> > 2 σ (<i>I</i>))	0.0435/0.1026	0.0406/0.0832	0.0592/0.0826
<i>R</i> ₁ / <i>wR</i> ₂ (all data)	0.0567/0.1109	0.0665/0.0935	0.0938/0.0932
Goodness-of-fit on <i>F</i> ²	1.029	1.021	1.009
larg. diff peak/hole [e·Å ⁻³]	0.397/-0.269	0.435/-0.321	0.794/-0.523
CCDC No.			

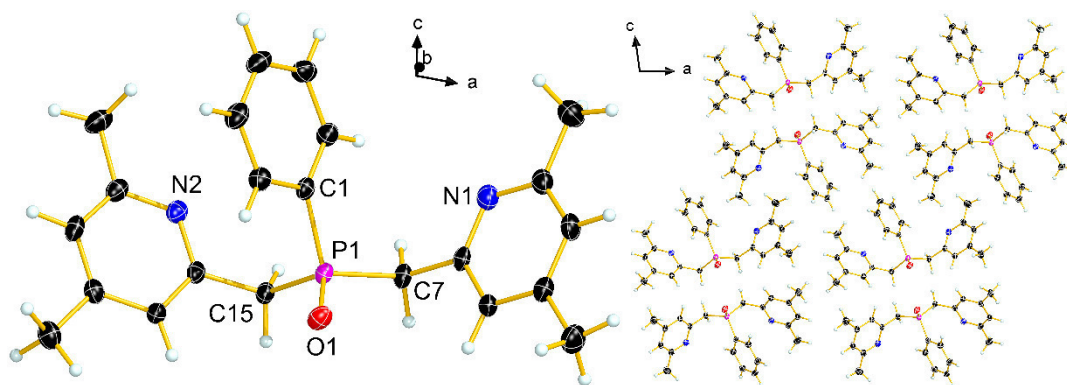


Figure 75. Molecular structure of the asymmetric unit of **2** in the crystal (left). Arrangement of the molecules of **2** in the crystal (right). Diamond representation, thermal ellipsoids are drawn at 50 % probability level.

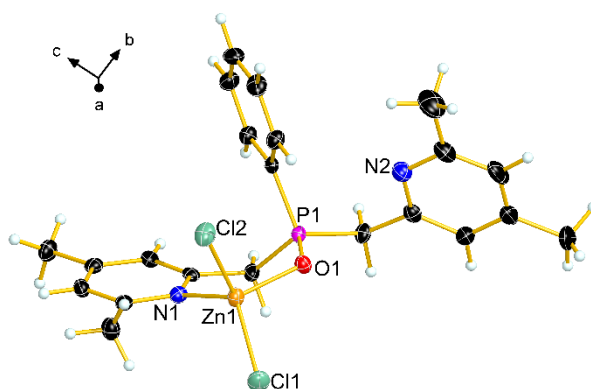


Figure 76. Molecular structure of the asymmetric unit of **3** in the crystal. Diamond representation, thermal ellipsoids are drawn at 50 % probability level.

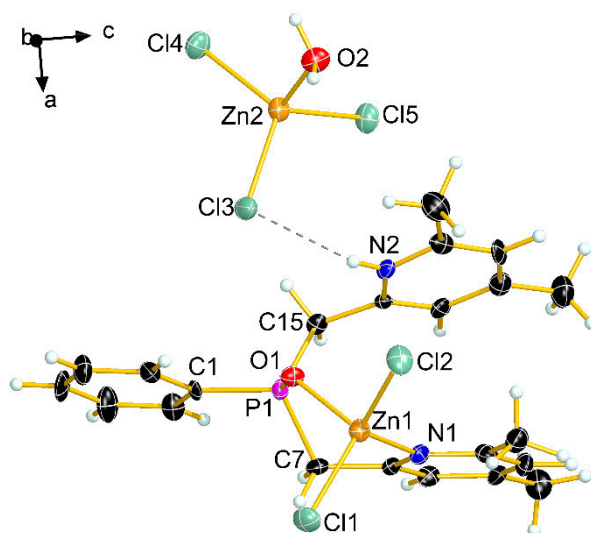
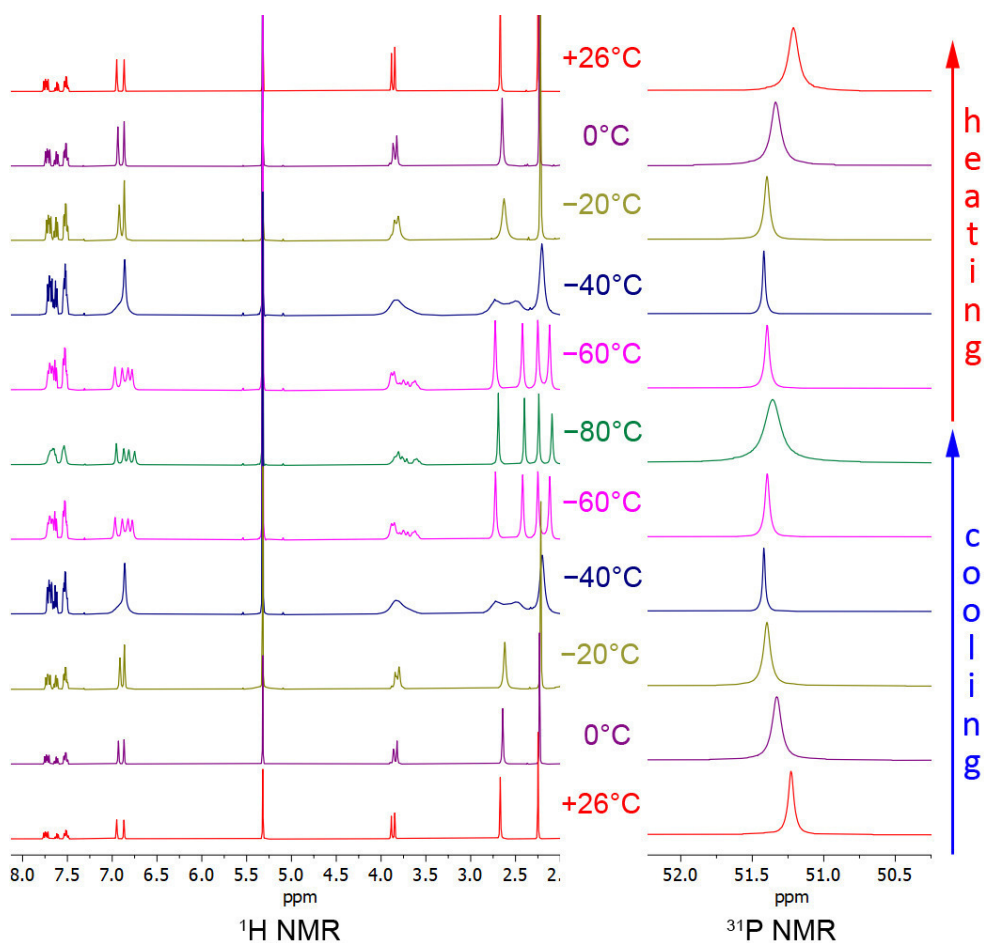
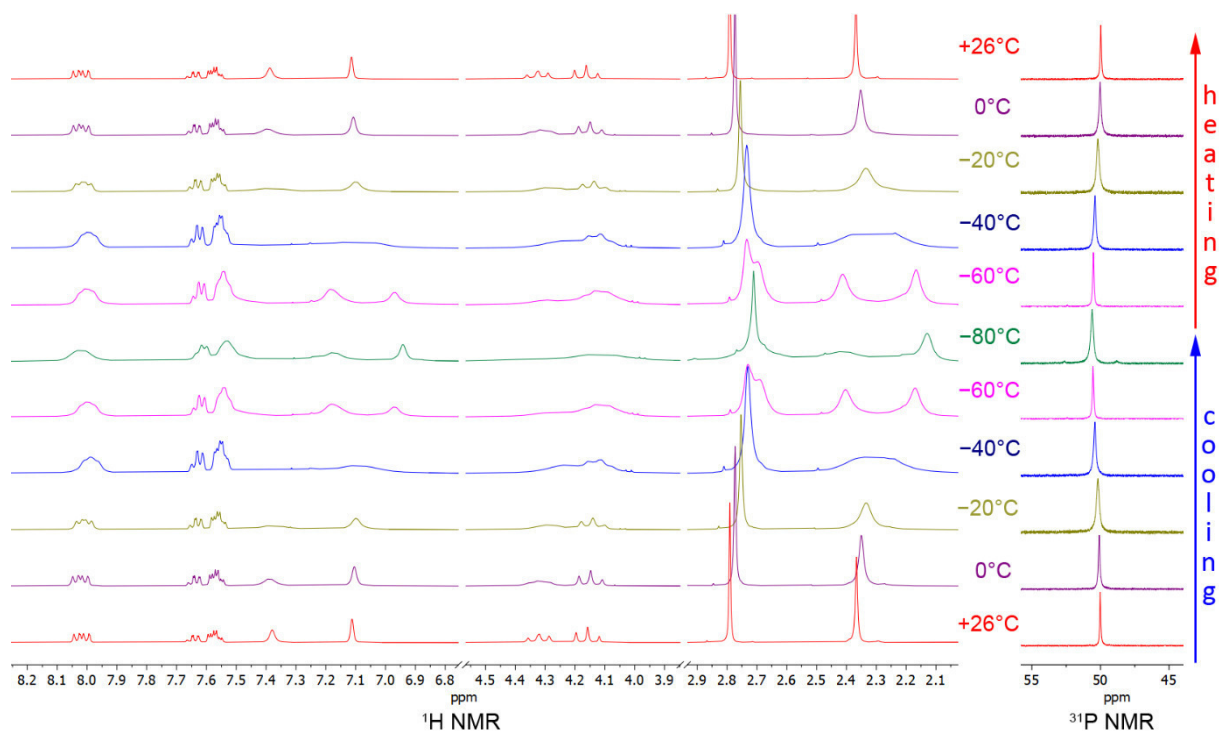


Figure 77. Molecular structure of the asymmetric unit of **4** in the crystal. Diamond representation, thermal ellipsoids are drawn at 50 % probability level.

2.6.5.3. Variable Temperature NMR spectra

Figure 78. ¹H NMR (left) and ³¹P NMR (right) of compound **3** in CD₂Cl₂ at varying temperatures.Figure 79. ¹H NMR (left) and ³¹P NMR (right) of compound **4** in CD₂Cl₂ at varying temperatures.

2.6.5.4. UV/Vis and luminescence images

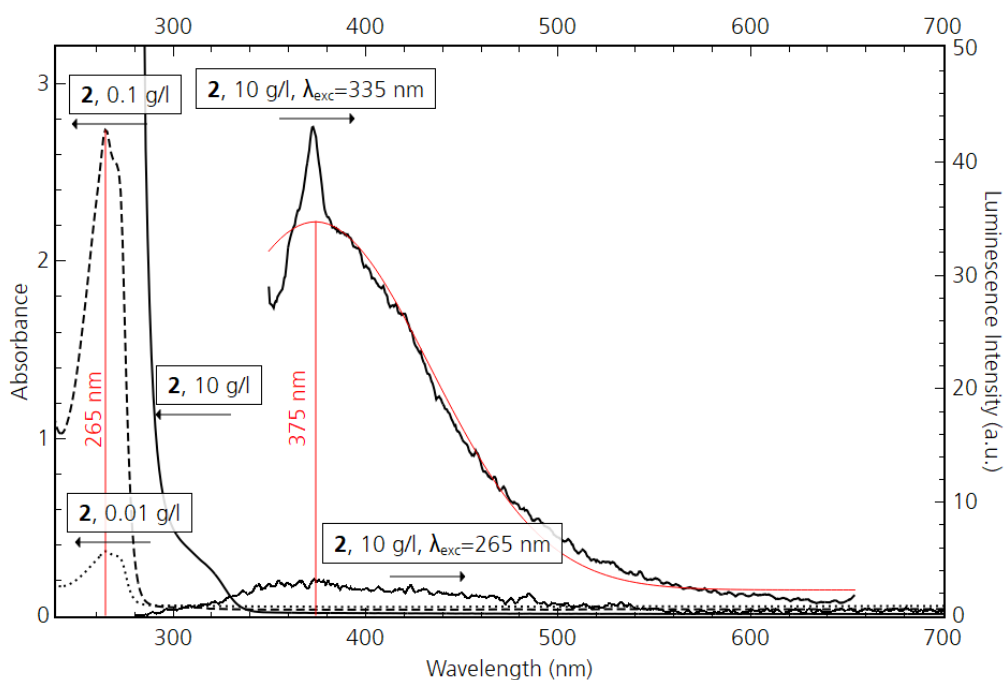


Figure 80. UV/Vis absorption and luminescence spectroscopy of compound **2** in MeCN. Increasing the analyte concentration from 0.01 to 10 g/L exposes a shoulder around 320 nm. The signal at 265 nm yields only a small luminescence. Excitation at 335 nm yields a much higher intensity peak at 375 nm (estimated using a Gaussian fit due to the Raman Stokes signal of MeCN).

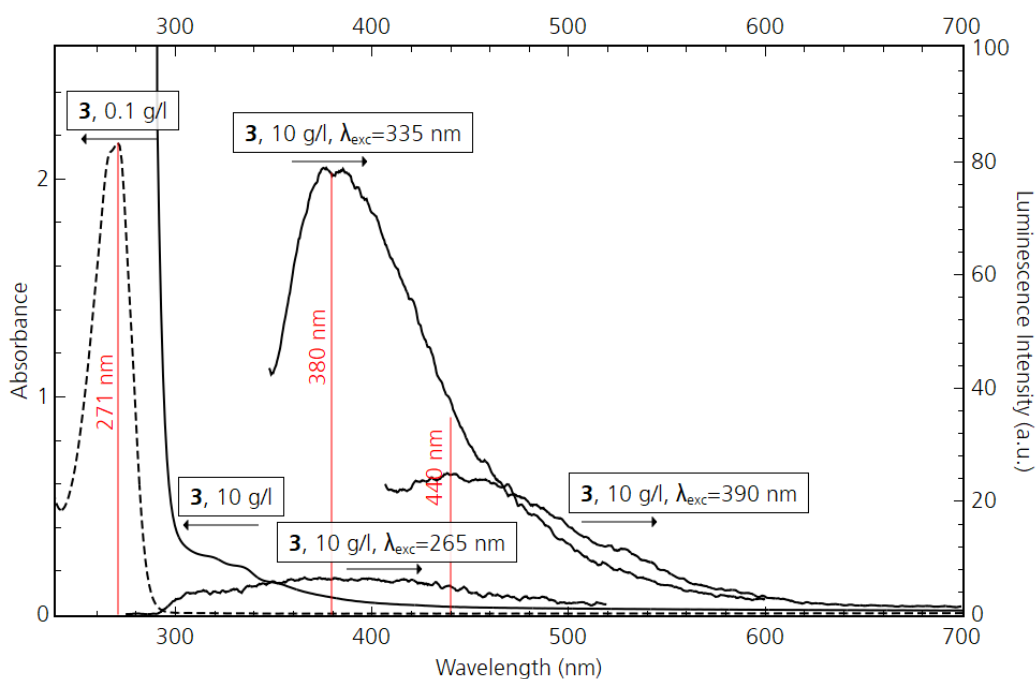


Figure 81. UV/Vis absorption and luminescence spectroscopy of compound **3** in MeCN. Increasing the analyte concentration from 0.1 to 10 g/L exposes a shoulder around 320 nm. The signal at 271 nm (excited at 265 nm) yields only a small luminescence. Excitation at 335 nm yields a much higher intensity peak at 380 nm.

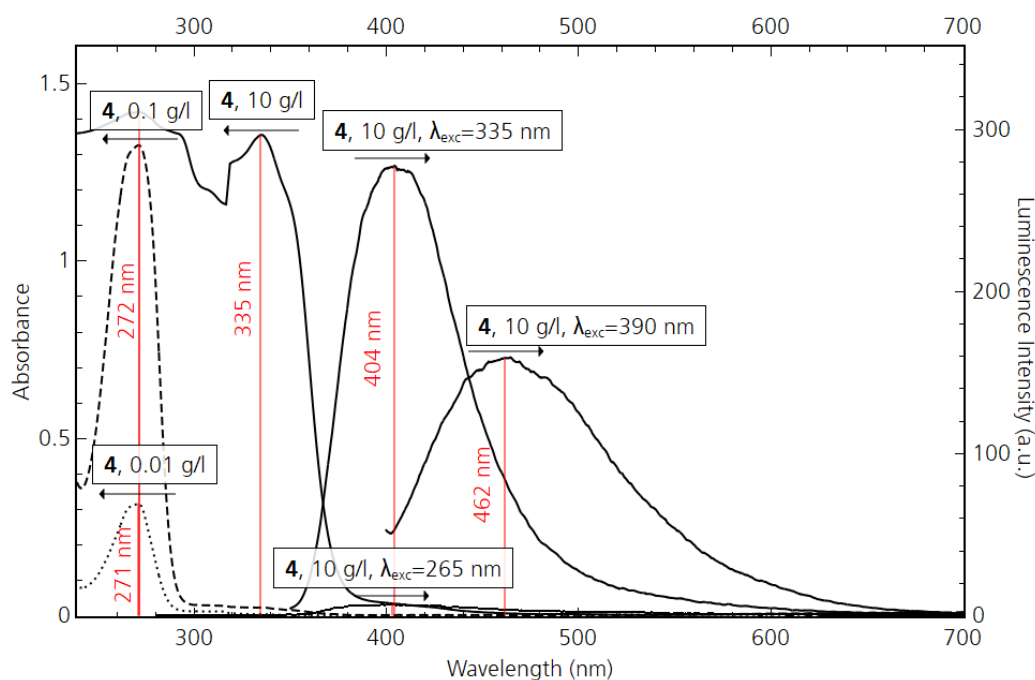


Figure 82. UV/Vis absorption and luminescence spectroscopy of compound **4** in MeCN. Increasing the analyte concentration from 0.01 to 10 g/L exposes a peak at 335 nm. Both, the signal at 272 nm (excited at 265 nm to compare with **2**) and the shoulder at 335 nm luminesce at 404 nm, but the latter one much stronger. Being excited at 335 nm, the luminescence is also much stronger compared to the luminescence spectra of **2** and **3** above. Excitation at even longer wavelengths (390 nm) also yields a significant luminescence signal at 462 nm, despite the low absorption.

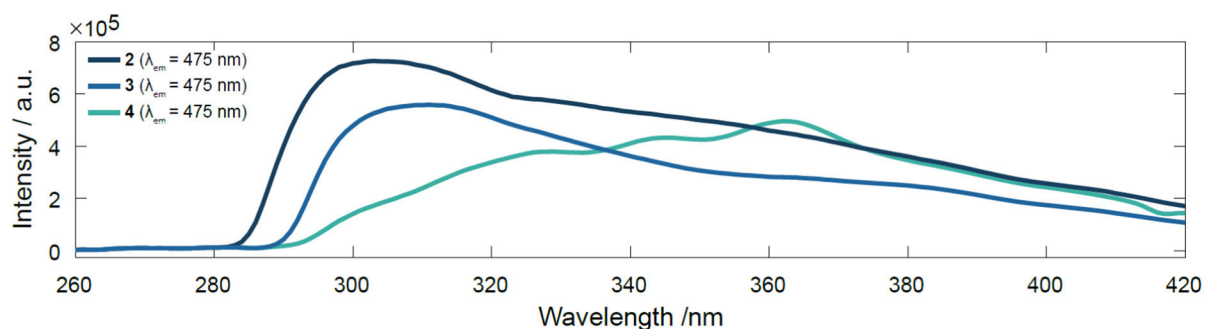


Figure 83. Excitation spectra of compounds **2-4** in MeCN ($c = 10$ g/L) in direct comparison. The spectra of compounds **2** and **3** are similar with a maximum around 300 nm and strong tailing. Compound **3** has a lower intensity. The spectrum of compound **4** exhibits a maximum around 360 nm.

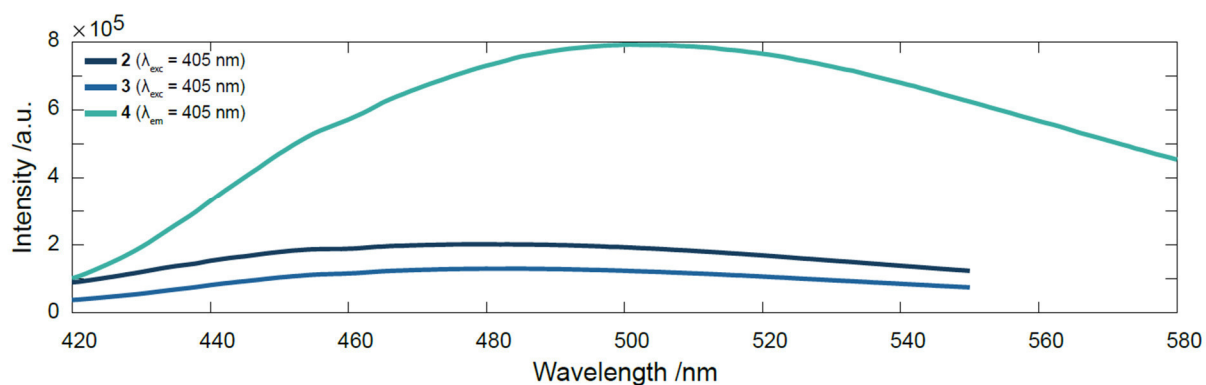


Figure 84. Emission spectra of compounds **2-4** in MeCN ($c = 10 \text{ g/L}$) when excited with 405 nm in direct comparison. The luminance of complex **3** is slightly lower than that of pure ligand **2**. Complex **4** exhibits a much higher intensity.

2.6.5.5. Additional FLIM data

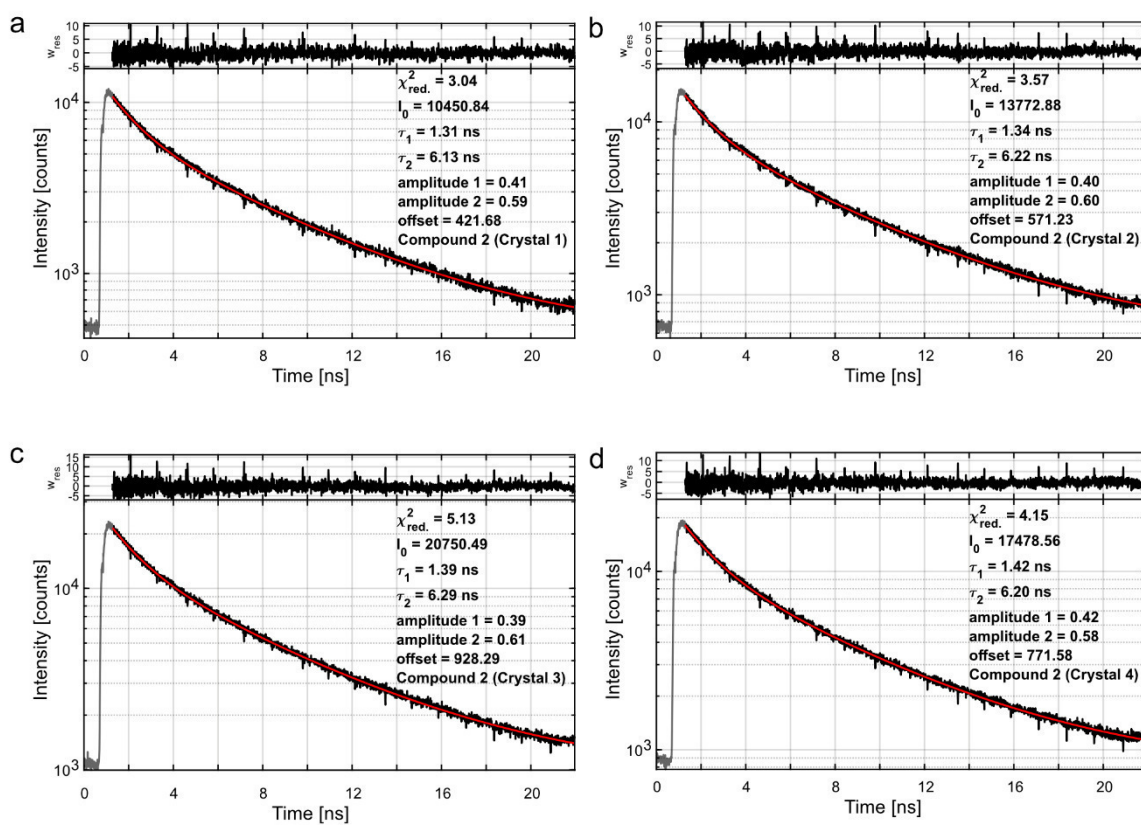


Figure 85. Fluorescence lifetime decay data and fits obtained for the four crystals of compound **2** imaged in Figure 72, which shows a bi-exponential fluorescence lifetime decay.

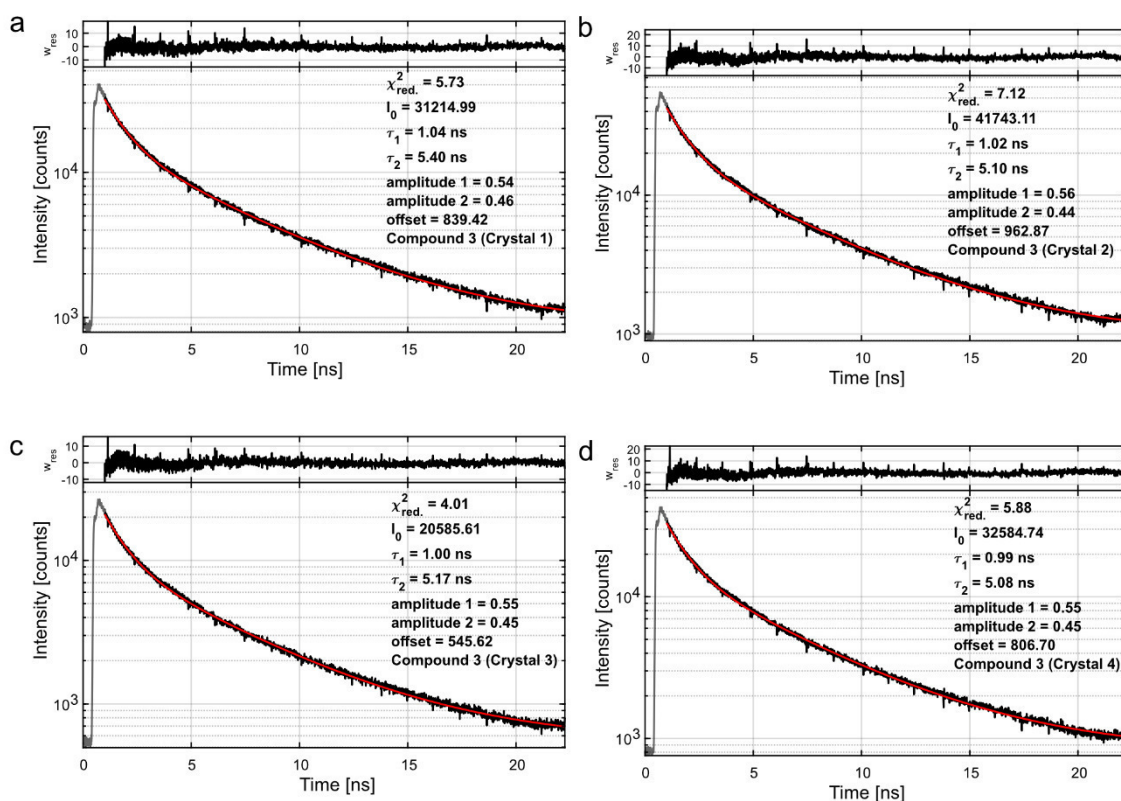


Figure 86. Fluorescence lifetime decay data and fits obtained for the four crystals of compound **3** imaged in Figure 72, which shows a bi-exponential fluorescence lifetime decay.

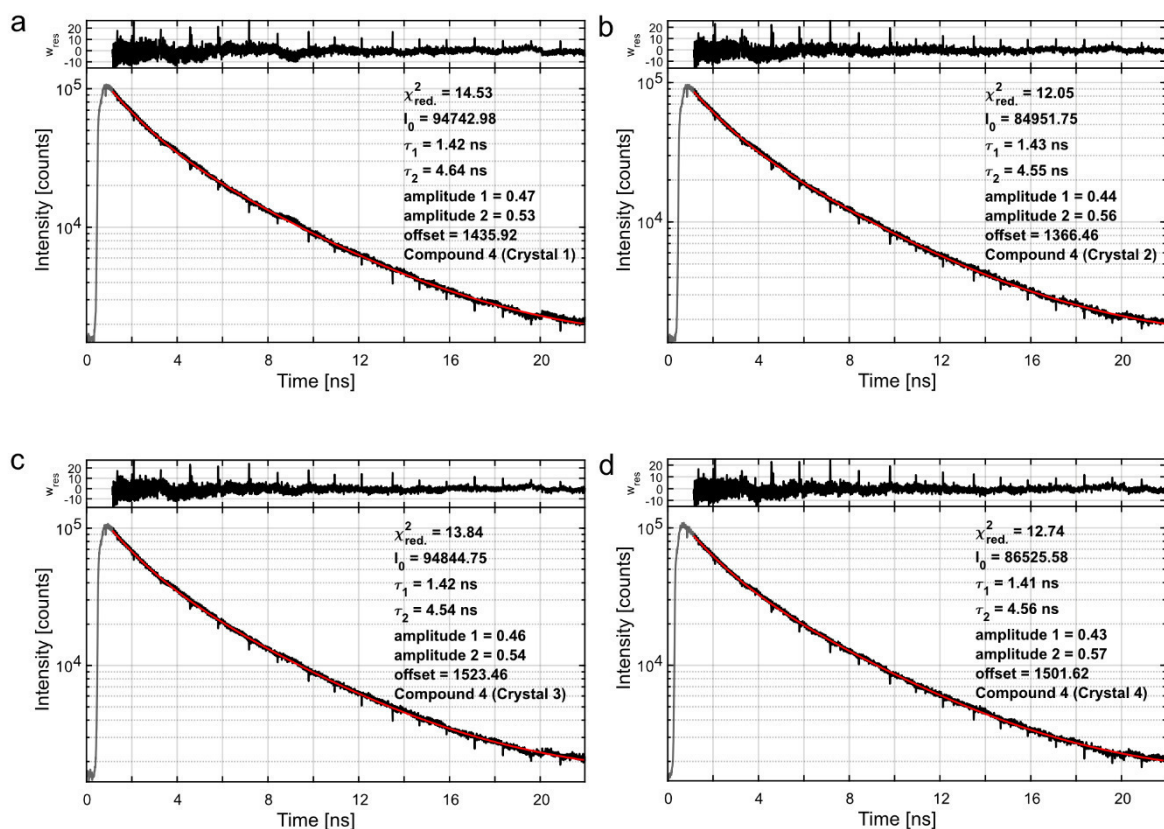


Figure 87. Fluorescence lifetime decay data and fits obtained for the four crystals of compound **4** imaged in Figure 72, which shows a bi-exponential fluorescence lifetime decay.

2.6.5.6. Hirshfeld surface analysis

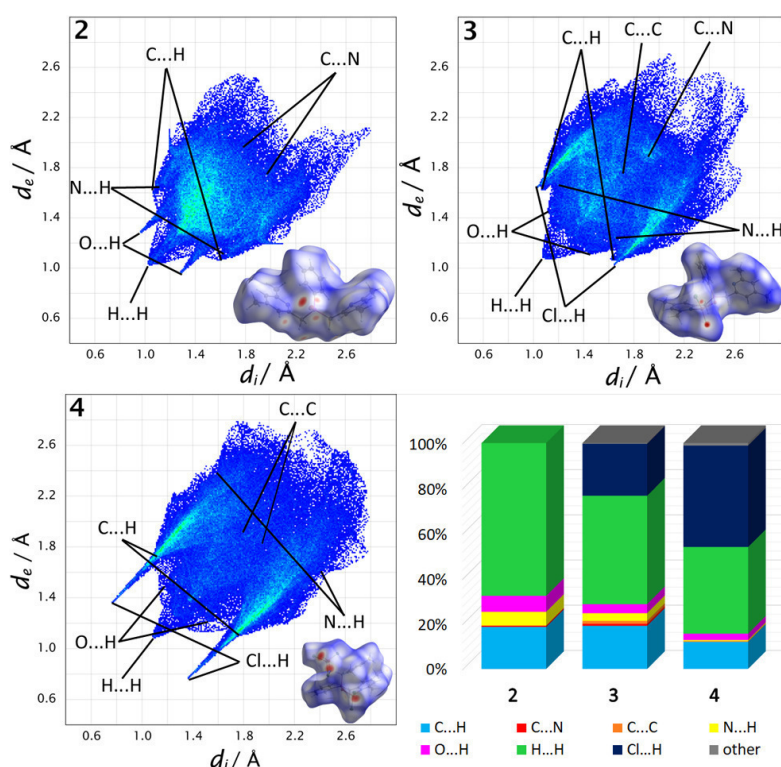


Figure 88. Fingerprint plots and d_{norm} maps including a summary of the close contacts of crystalline **2-4**.

2.6.5.7. Additional computational data

1) Critical evaluation of the employed TDDFT methodology for the excited states

The low-lying excited states are dominated by localized excitations of the collidine moieties. Within TDDFT, both using the B3LYP and CAM-B3LYP functionals, the two lowest states of compound **2** are predicted to exhibit collidine $n\pi^*$ character, which is similar to the well-studied situation in the parent chromophore pyridine. In the present case, a pair of nearly degenerate states is obtained due to the presence of two collidine moieties in an almost symmetrical configuration. However, the presence of multiple chromophores in the molecule also gives rise to various additional states that bear charge-transfer character. For these, too low energies are obtained by employing density functionals lacking a long-range correction such as B3LYP. A qualitatively correct treatment of these states in the frame of TDDFT is only possible using range-separated functionals such as CAM-B3LYP, which appropriately shifts them to higher energies. Therefore, we consider the sequence of excited states obtained using CAM-B3LYP qualitatively correct, which predicts a bright collidine pp^* excited state as the third excited state. From comparison with experimental and theoretical data on pyridine, it can be assumed that it is this state that makes the dominant contribution to the lowest absorption band centered around 270 nm (4.59 eV) in the experiment. The np^* state is only weakly allowed and should only marginally contribute to the absorption intensity in the low energy part of the spectrum. However, the energetic positions of the excited states obtained with CAM-B3LYP are shifted towards higher energies, such that the bright state of compound **2** lies at 5.4 eV compared to the experimental absorption maximum at 4.6 eV.

In order to critically assess this energetic shift due to the CAM-B3LYP functional, a comparison can be made to benchmark data on pyridine, which are collected in Table 13 and make clear, that while the

CAM-B3LYP state ordering agrees with higher-level methods such as CAS-PT2 or EOM-CCSD(T) as well as with experimental findings, the bright $\pi\pi^*$ state is shifted towards higher energies by about 0.7-0.8 eV. For the $\pi\pi^*$ state, the shift is less pronounced and amounts to ~ 0.25 eV, while for the triplet states no shift is present. The same is true for the adiabatic excitation energy to the lowest-lying $\pi\pi^*$ state.

Table 13. Benchmark data on excited electronic states of pyridine. Electronic state energies are given in eV.

	Vertical energies at S_0 geometry				Adiabatic excitation energy to 1B_1 ($n\pi^*$)	Vertical emission energy at 1B_1 geometry
	Singlet		Triplet			
	1B_1 ($n\pi^*$)	1B_2 ($\pi\pi^*$)	3A_1 ($\pi\pi^*$)	3B_1 ($n\pi^*$)		
Experiment	4.78 ^a	4.99 ^a	3.86 ^a	4.12 ^a	4.47 ^b	3.76 ^c
CASPT2/ aug-cc-pVDZ ^b	4.93	4.88	4.06	4.31	4.43	
EOM- CCSD(T)/Sadlej ^d	4.80	4.81				
EOM-CCSD/aug-cc- pVDZ ^b	5.19	5.19	4.04	4.58	4.68	
TD-B3LYP/ cc-pVDZ ^b	4.83	5.58	3.90	4.06	4.40	
TD-CAM-B3LYP/ SVP ^e	5.04	5.74	3.74	4.19	4.54	3.76

References: ^a I. Linert, M. Zubek, Eur. Phys. J. D 70, 74 (2016), ^b Z.-L. Cai, J. R. Reimers, J. Phys. Chem. A 104, 8389 (2000), ^c I. Yamazaki, K. Sushida, H. Baba, J. Chem. Phys. 71, 381 (1979), ^d J. E. Del Bene, J. D. Watts, R. J. Bartlett, J. Chem. Phys. 106, 6051 (1997), ^e this work.

2) Vertical and adiabatic excitation energies of compounds **2** and **3**

The excitation energies of compound **2** and **3** both at the optimized ground state geometry and at two excited state geometries are presented in Tables S7 and S8.

At the ground state geometry, the highest oscillator strength is exhibited by a collidine $\pi\pi^*$ state. Based on a harmonic Wigner distribution of the vibrational normal modes of the ground state, ensemble-broadened absorption spectra have been simulated for both compound, which are shown in Figure S17. In line with the discussion in Section XX (Assessment of methods), the spectra have been adjusted to account for the energy shift due to the CAM-B3LYP functional by shifting the excitation energies by -0.6 eV. The resulting spectra, which are dominated by the $\pi\pi^*$ state, match well the experimentally observed absorption maxima, strongly indicating that the lowest absorption band is mainly caused by the collidine $\pi\pi^*$ state.

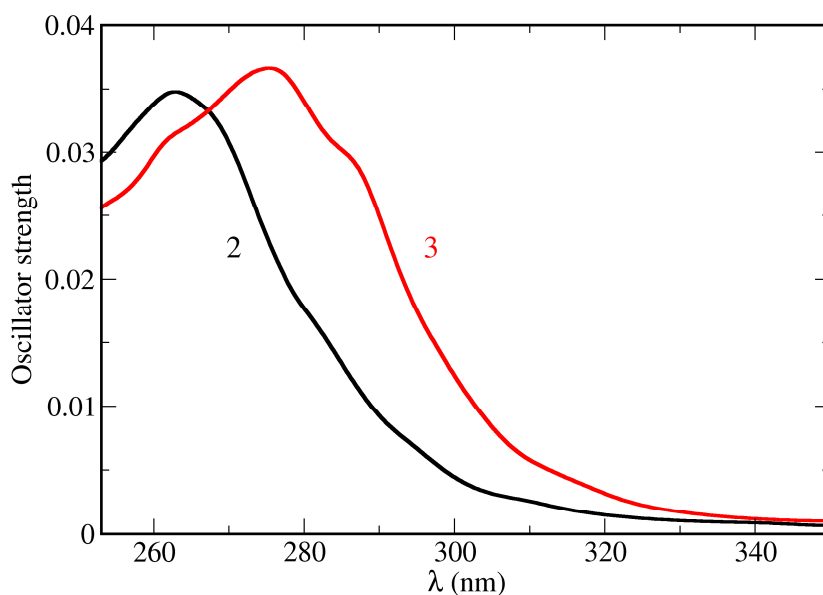


Figure 89. Simulated UV absorption spectra of compounds **2** and **3** obtained from 100 molecular geometries sampled from a harmonic Wigner distribution function of the vibrational normal modes. The excitation energies and transition dipole moments were computed at the TDDFT/CAM-B3LYP/SVP level. The final spectrum was obtained by shifting the excitation energies by -0.6 eV, calculating the oscillator strength from these energies and the transition dipole moments and finally convolving the individual transitions by a Lorentzian with a width of 0.15 eV.

To gain an insight into the nature of the observed emission spectra, we attempted to optimize the geometries at the excited states, which allows for the calculation of adiabatic excitation and vertical emission energies. It should be noted that since these optimizations have been carried out for gas-phase molecules, a full agreement with the experimental data obtained in the condensed phase cannot be expected. However, for both molecules **2** and **3**, two different excited state minima have been found, one pertaining to the $n\pi^*$ state and another characterized by excitation from a nonbonding p orbital at oxygen (compound **2**) or chlorine (compound **3**) to the π^* orbitals of the chromophores. The $n\pi^*$ state is analogous to the respective 1B_1 state of pyridine (see Table 13) and thus localized on a collidine group. Its adiabatic excitation energy lies at 4.6 – 4.7 eV in both molecules, while the energy difference to the ground state at the excited state geometry, which can be roughly connected to the peak position of fluorescence emission, amounts to ~ 3.8 eV (326 nm). This value matches roughly the experimentally observed emission maximum at 303 nm obtained for compound **3** after excitation at 270 nm (see Figure 70 of the main paper).

The second type of excited states has no pyridine analog as the excitation is distributed over a larger part of the molecules. Characteristically, both in compound **2** and **3**, the vertical energies at the excited state geometry are relatively low, 2.15 eV for compound **2** and only 1.14 eV for compound **3**. These energies are significantly smaller than those of the experimental emission maxima at 389 nm (3.19 eV) and 414 nm (3.00 eV). However, for compound **2** a state of the same character is seen to be populated during the simulated excited state dynamics in the crystal environment. Since the structural optimization in the gas phase allows for stronger structural deformations, it may well be that in the condensed phase the emission energy of states of similar character are distinctly higher, and thus these $p\text{-}\pi^*$ excited states can be considered candidates for the emissive states of compound **2** and **3**.

Table 14. Electronic states of compound **2** computed at the TDDFT/CAM-B3LYP/SVP level. For the state character, “c” represents a shorthand notation for an excitation localized at the collidine moieties of the molecule, while p(O) and p(Cl) denote p-Orbitals situated at oxygen and chlorine atoms, respectively. Vertical energy differences at optimized excited state geometries, corresponding to emission energies, are given as italic numbers.

State	Optimized structure								
	S ₀			np*-c			p(O)-π*		
	E (eV)	f	Char.	E (eV)	f	Char.	E (eV)	f	Char.
S ₀	0.0	-		0.87 <i>(0.0)</i>	-		2.79 <i>(0.0)</i>	-	
S ₁	5.25 (B3LYP: 4.92)	0.009	np*-c	4.63 <i>(3.76)</i>	0.002	np*-c	4.94 <i>(2.15)</i>	0.015	p(O)p*
S ₂	5.26 (B3LYP: 4.93)	0.007	np*-c	5.60	0.003	np*-c	5.76	0.027	p(O)p*
S ₃	5.41	0.156	pp*-c	6.11	0.097	pp*/np*-c	7.03	0.305	pp*

Table 15. Electronic states of compound **3** computed at the TDDFT/CAM-B3LYP/SVP level.

State	Optimized structure								
	S ₀			np*-c			pp*-c		
	E (eV)	f	Char.	E (eV)	f	Char.	E (eV)	f	Char.
S ₀	0.0	-		0.79 <i>(0.0)</i>	-		2.68 <i>(0.0)</i>	-	
S ₁	5.15	0.106	pp*-c	4.67 <i>(3.88)</i>	0.002	np*-c	3.82 <i>(1.14)</i>	0.0001	p(Cl)p*-c
S ₂	5.29	0.006	np*-c	5.56	0.002	np*-c	5.12	0.0000	p(Cl)p*-c

3) Vibrationally broadened fluorescence and phosphorescence spectra and radiative lifetimes of compounds **2** and **3**

Table 16. Energy differences in eV between the lowest vibrational levels of the S₀ and S₁ or T₁ states (vibronic 0-0 transitions) for compounds **2** and **3**.

Method	Compound 2		Compound 3	
	S ₁	T ₁	S ₁	T ₁
B3LYP/def2-SVP	4.14	3.45	-	3.31
CAM-B3LYP/def2-SVP	4.51	3.38	3.74	3.35

Table 17. Emission rate constants in s⁻¹ for the indicated singlet and triplet states of compounds **2** and **3**. The respective radiative lifetimes are given in brackets.

Method	Compound 2		Compound 3
	S ₁	T ₁	T ₁
B3LYP/def2-SVP	4.10×10 ⁸ (2.4 ns)	6.23×10 ⁻¹ (1.61 s)	2.31×10 ³ (433 μs)
CAM-B3LYP/def2-SVP	2.51×10 ⁹ (398 ps)	1.61×10 ⁻¹ (6.21 s)	1.81 (552 ms)

2.6.5.8. Calculated fluorescence and phosphorescence spectra

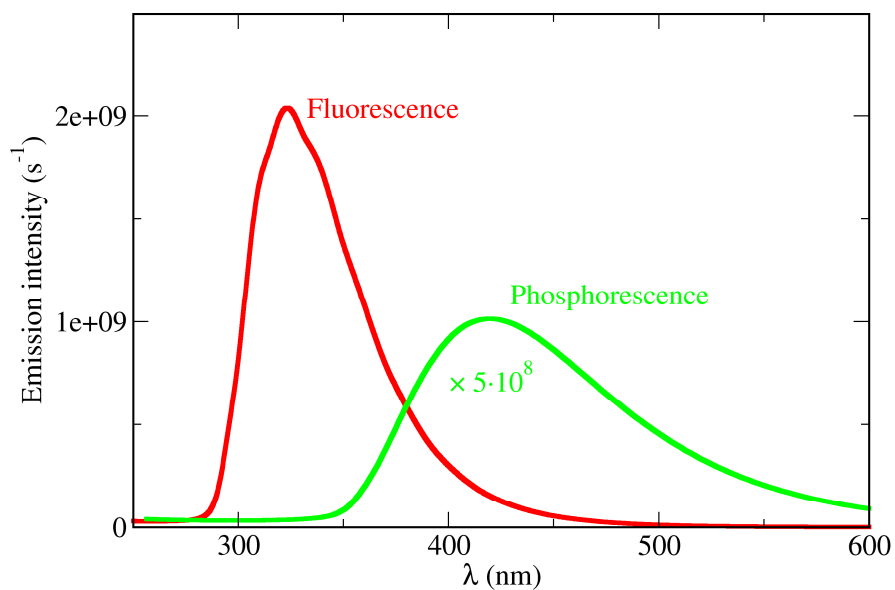


Figure 90. Fluorescence and phosphorescence spectrum of compound **2**, obtained by TDDFT/B3LYP/def2-SVP. The emission rate constant k from Table S2 is related to the shown emission intensity $I(\omega)$ by $k = \int \frac{I(\omega)}{\omega} d\omega$.

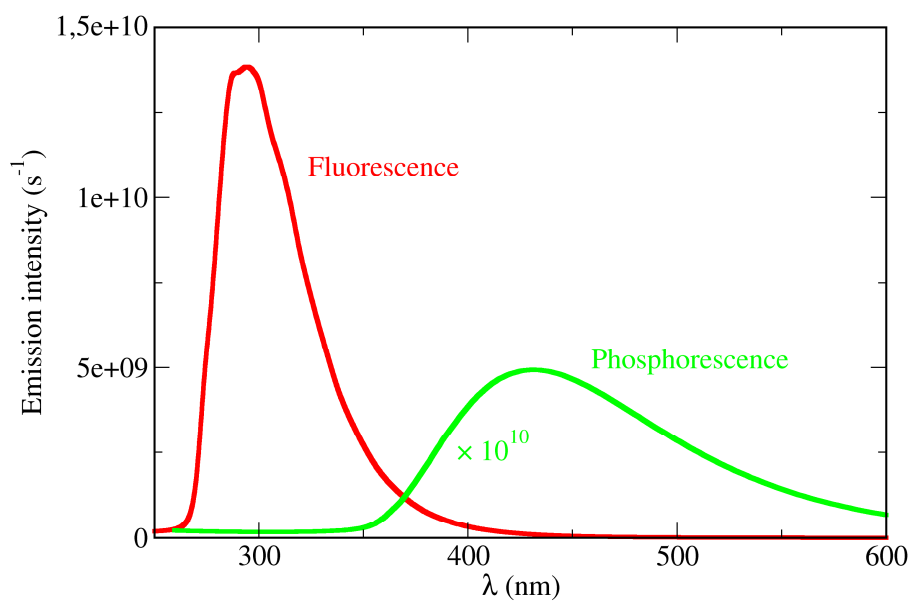


Figure 91. Fluorescence and phosphorescence spectrum of compound **2**, obtained by TDDFT/CAM-B3LYP/def2-SVP.

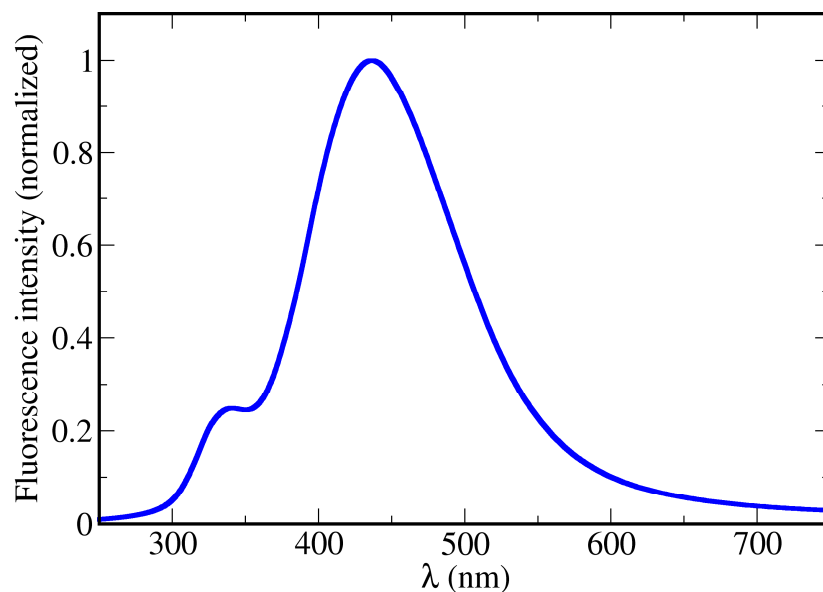


Figure 92. Approximate fluorescence of compound **2** in crystal environment. The data has been obtained from the TDDFT/B3LYP/def2-SVP dynamics simulations in the S_1 state by calculating the spectral power density for emission, $I \propto (E_{S_1} - E_{S_0})^4 |\mu_{01}|^2$, for the structures along 10 trajectories of 3 ps duration, starting with $t > 1000$ fs to account for initial relaxation, and convolving the result by a Lorentzian function.

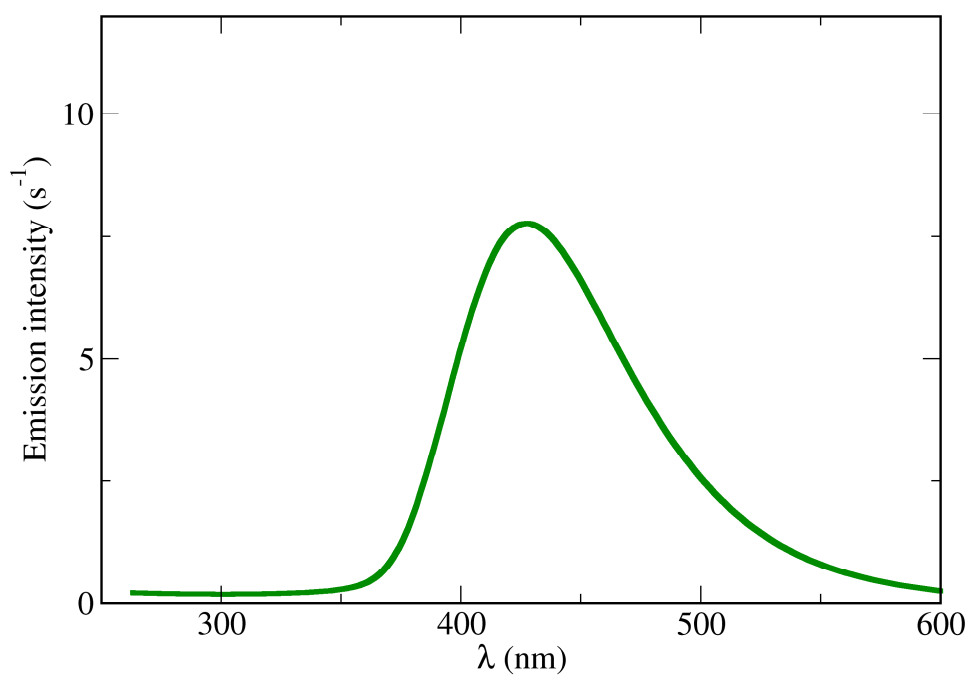


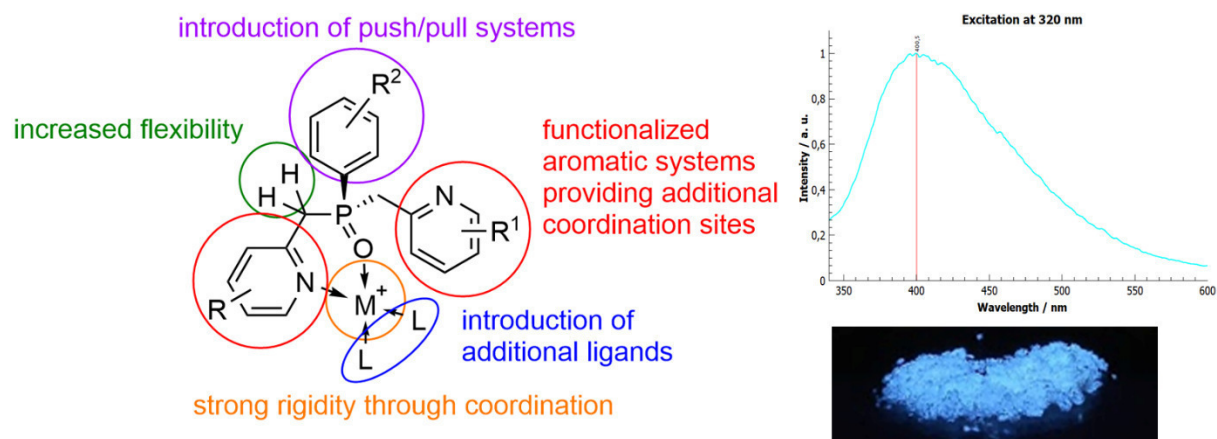
Figure 93. Phosphorescence spectrum of compound **3**, obtained by TDDFT/CAM-B3LYP/def2-SVP.

2.7. Coordination behavior of multidentate phosphine and phosphine oxide ligands towards Zn(II) and their luminescence properties

Christin Kirst, Manuel Gensler, Florian Zoller, Peter Mayer, Dina Fattakhova-Rohlfing, Armin Wedel, Konstantin Karaghiosoff

to be submitted

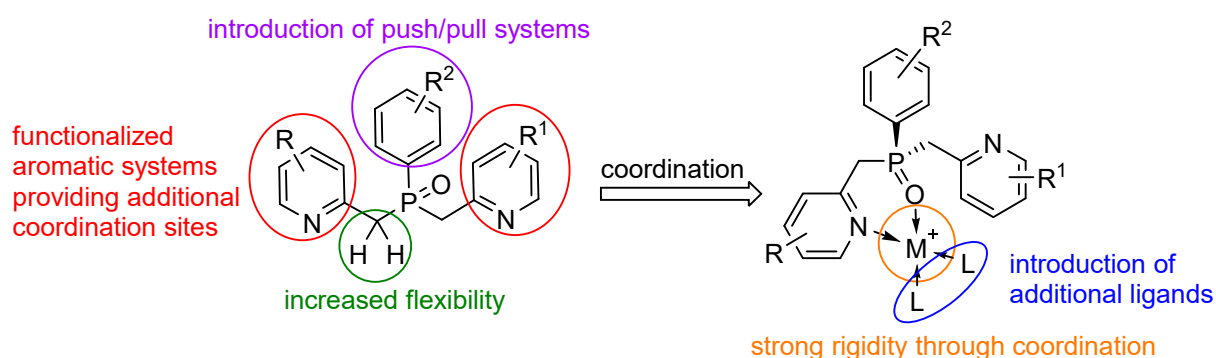
Christin Kirst synthesized all the discussed compounds and performed the single crystal X-ray, UV-Vis absorption measurements and Hirshfeld surface analysis. She analyzed and evaluated the corresponding X-ray data and the NMR spectroscopy results in solution. She further managed the project and wrote the original draft of the manuscript, designed the TOC graphic and implemented the necessary corrections in the final version of the paper.



Abstract: The coordination behavior of phenylbis(pyridin-2-ylmethyl)phosphine, phenylbis(quinaldin-2-ylmethyl)phosphine and their oxides with $ZnCl_2$ are described. The ligands and complexes thereof are synthesized in high yields (>80 %). VT-NMR disclose a dynamic of the complexes in solution, where the zinc(II) atom in the phosphine complexes switches from N,N to P,N coordination at low temperature. The crystal structures show an unusual P,N coordination of Zn(II) when expanding the π -system in the nitrogen containing substituents on phosphorus. Through Hirshfeld analysis important information could be gathered about intermolecular interactions in the crystal of each complex. Photophysical data show a luminescence of the ligands and complexes in the solid state. Quantumchemical calculations reveal the location of the HOMO and LUMO in the different compounds. The CV of the Zn(II) complex of the phosphine oxide shows no obvious redox activity.

2.7.1. Introduction

The research and development of novel, flexible tertiary phosphine ligands with tunable coordination properties towards a variety of metal ions is a cornerstone of phosphorus chemistry and crucial for applications in science and industry utilizing transition metal catalysis.^[1–5] Especially of interest are tertiary phosphines containing functionalized substituents, which are able to provide additional coordination sites. This can be realized, for example, by the introduction of nitrogen containing substituents forming N,P,N-ligands. These additional coordination sites enlarge the potential use of such phosphines in catalytic reactions.^[6–11] The presence of a methylene group between phosphorus and the aromatic N-containing system, like picolyl substituents and derivatives thereof, can drastically increase the flexibility of the ligand. Indeed, a multitude of picolyl phosphines and derivatives thereof are known and their use in catalytic reactions has been assessed.^[8,12] These kind of phosphines are not only of interest for catalysis but also for other applications like OLEDs.^[13–19] The advantages of these phosphines are their ambivalent (N/P) Lewis base properties, their steric demand (prevention of geometric changes of the complex in the excited state), adjustable binding abilities and their easy synthesis or even commercial availability. Through variation of the aromatic systems, the optical properties of the phosphines can easily be adjusted.^[17,20] The disadvantage of phosphines is their easy oxidation initiated by even traces of oxygen or moisture, making phosphine oxides superior due to their improved stability. Nevertheless, research on phosphine oxide complexes is scarce.^[21,22,31,23–30] The use of phosphine and phosphine oxides in OLED materials has the drawback of the rather labile P–C bond.^[32,33] However, through coordination to a metal atom, the P–C bond can be stabilized significantly. This stabilization can in return raise the melting and degradation point of the resulting compound (see Scheme 16). Additionally, by complexation the flexibility of the functionalized substituents attached to phosphorus are lowered and possible vibration and geometric changes after excitation of the molecule are reduced. Another benefit of this concept would be the metal center itself, which can not only take over the role of the stabilizer of the molecular system but also take part in the luminescence process (MLCT or LMCT). A further benefit of a metal center is the provision of extra coordination sites which can be covered by other ligands with extensive π -systems and as such finetune the luminescence. Extensive research covering these areas has not been done so far for metal complexes of phosphines and phosphine oxides.



Scheme 16. General research concept based on phosphine oxide ligands as new OLED materials and the possible variation thereof to influence the luminescent properties.

In general, there is still a great demand for new materials for OLED application, especially for blue emitters due to their limited lifetime spans. Moreover, a replacement for the currently used expensive and rare metal complexes (e.g. Iridium) has to be found.^[34–36] The currently used fabrication of OLED materials is based on vacuum deposition techniques; however, solution-processed devices prepared *via* spin coating, screen printing, and inkjet printing are of increasing interest. The focus in the design of novel OLED materials is therefore also on solubility and stability in solution.^[37,38]

Our proposed concept is centered around cheap, commercially available starting materials, the facile, scalable and high yielding synthesis of the ligands and an easy work-up for purification of the products. The proposed class of ligands can have a wide range of application as they are easily modified. Firstly, we focused on the coordination of such ligands towards Zn(II) and on the question, whether the resulting complexes show luminescent properties.

In general, the interest in Zn(II) complexes is rising due to their possible use as emitters, hosts or electron transport layer in OLEDs. In principle, they are a cheap, low-toxic alternative towards currently used iridium and osmium complexes.^[34–36] So far, not many zinc complexes of P,N-ligands have been prepared and investigated for their potential use in OLEDs.^[39–41] The main focus of current research are nitrogen and oxygen containing heterocycles as ligands for the preparation of emitting Zn(II) complexes.^[34,42,43] The zinc(II) atom in these complexes is in general electronically inactive due to the filled d-shell. The purpose of Zn(II) is to fixate the ligand to improve luminescence and the stability of the system by complexation. Most of the photophysical data published of these complexes have been acquired of solids or solutions thereof. Some zinc(II) complexes form polymers or aggregates and show luminescence in thin film or even in devices.^[44–48] The emission wavelength of these compounds ranges from UV to blue light. In the following, we present our first results based on the proposed concept shown in Scheme 15, which, to our opinion, opens a wide and promising field for future studies.

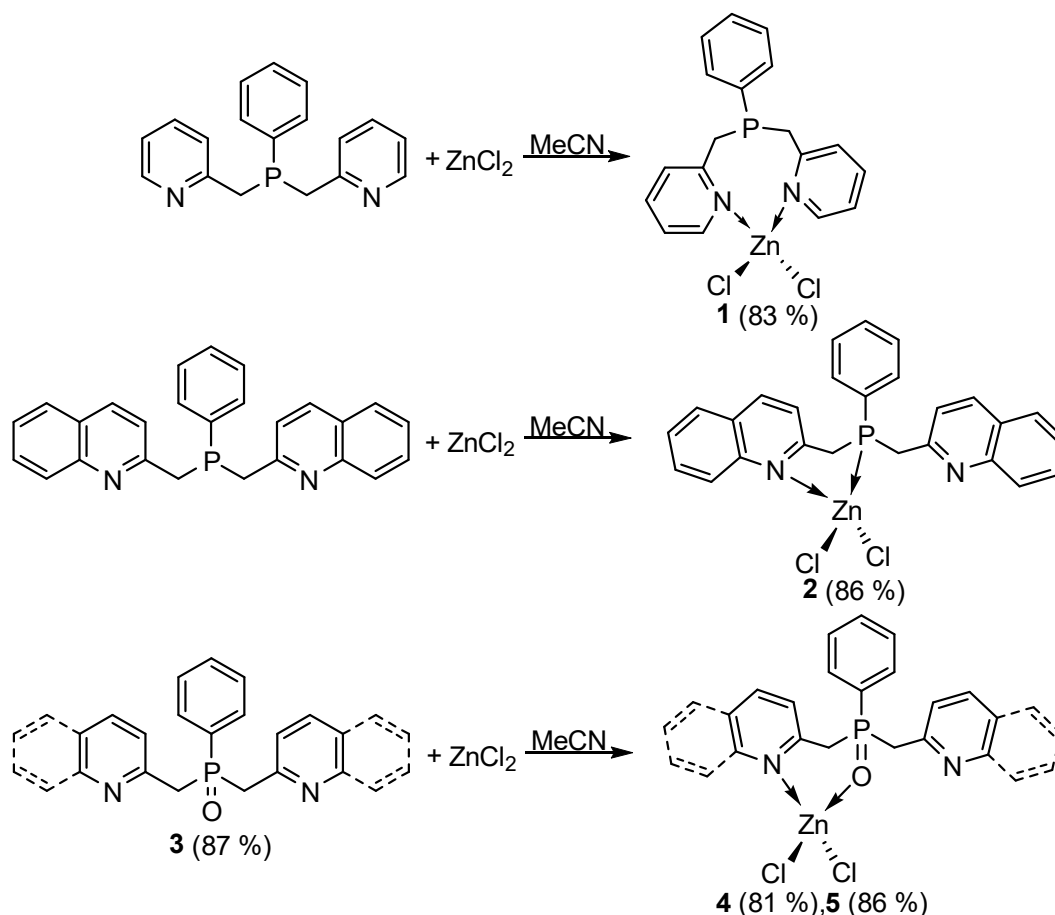
2.7.2. Results and discussion

2.7.2.1. Design and synthesis of the ligands and complexes

Phenylbis(pyridin-2-ylmethyl)phosphine, phenylbis(quinaldin-2-ylmethyl)phosphine and their corresponding oxides are the focus of our primary investigations, as they are already known and well-established ligands in our lab. Their preparation was published previously by Braunstein *et al.* and our group.^[31,49,50] It is a very convenient synthesis which can be varied easily by adaptation of the starting materials. Almost any (trimethylsilyl)methyl compound and R₂PCl, RPCl₂ or PCl₃ can be used for the synthesis of the phosphine.

The preparation of the zinc chloride complexes **1**, **2**, **4** and **5** is straight forward and shown in Scheme 17. The phosphines or the corresponding phosphine oxides are dissolved in dry, degassed acetonitrile and the resulting solution is transferred *via* a cannula to the corresponding amount of dry, solid zinc chloride under inert gas in a separate Schlenk flask to exclude possible contamination by water. The zinc(II) chloride dissolves in course of the reaction. After stirring for a few hours and removal of the solvent, compound **1** is obtained as a colorless powder and recrystallized by diffusion of diethyl ether into a solution of **1** in acetonitrile or dichloromethane yielding 83 %. Compounds **2** and **5** are obtained as light beige powders and recrystallized by diffusion of diethyl ether into a solution of compound **2** or **5** in warm acetonitrile or dichloromethane yielding 86 % in both cases. Compound **4** is obtained similarly as a white powder in 81 % yield.

Due to the easy access of the phosphines, cheap starting materials and straight forward preparation of the zinc complexes, the synthesis can easily be done on a higher gram scale (>5 g). The Zn(II) complexes containing phosphine oxides are air insensitive, but moisture and water sensitive due to a possible coordination of water to zinc. All complexes are soluble in solvents like dichloromethane and acetonitrile. The IR spectra of **3**, **4** and **5** show bands at 1186 cm⁻¹ (**3**), 1161–1105 cm⁻¹ (**4**) and 1161–1094 cm⁻¹ (**5**) for the $\nu(\text{PO})$ vibration.

Scheme 17. Synthesis of zinc(II) complexes **1**, **2**, **4** and **5**.

2.7.2.2. Molecular and crystal structures

The asymmetric unit of compounds **1–3** and **5** in the crystal are shown in Figure 94. Crystallographic refinement data can be found in the Supporting Information (Table 20 and Table 21). Selected atom distances and bond angles are listed in Table 18.

Compound **1a** crystallizes in the triclinic space group $P\bar{1}$ with two formula units in the unit cell. The asymmetric unit consists of one molecule of **1a** (Figure 94). Compound **1b** crystallizes in the triclinic space group $P\bar{1}$ with four formula units in the unit cell (Figure 102). Structure **1a** and **1b** are polymorphs.^[51] The zinc(II) is coordinated in both structures in a for zinc(II) typical distorted tetrahedral-geometry by both nitrogen atoms of the phosphine ligand and both chlorine atoms. This is not surprising, as zinc(II) usually prefers N over P coordination. The phosphorus atom in both structures **1a** and **1b** is trigonal pyramidal surrounded by the two pyridyl rings and the phenyl ring. All C–P–C angles (100–102°) are within the typical range, leaving room for the lone pair on phosphorus. In the crystal, the single units of **1a** are interconnected *via* weak, non-classical hydrogen bonds between the chlorine atoms and the hydrogen atoms of neighboring units, as well as the co-crystallized acetonitrile with a H⋯Cl distance of >2.9 Å.^[52] Face-to-face π - π interactions are present between offset, neighboring phenyl rings (H-to-ring-center distance of 4.232(3) Å) and between neighboring pyridyl rings with an average distance of 3.46 Å and an angle of 0.1(2)° between both pyridyl rings (Figure 103 of SI).^[53,54]

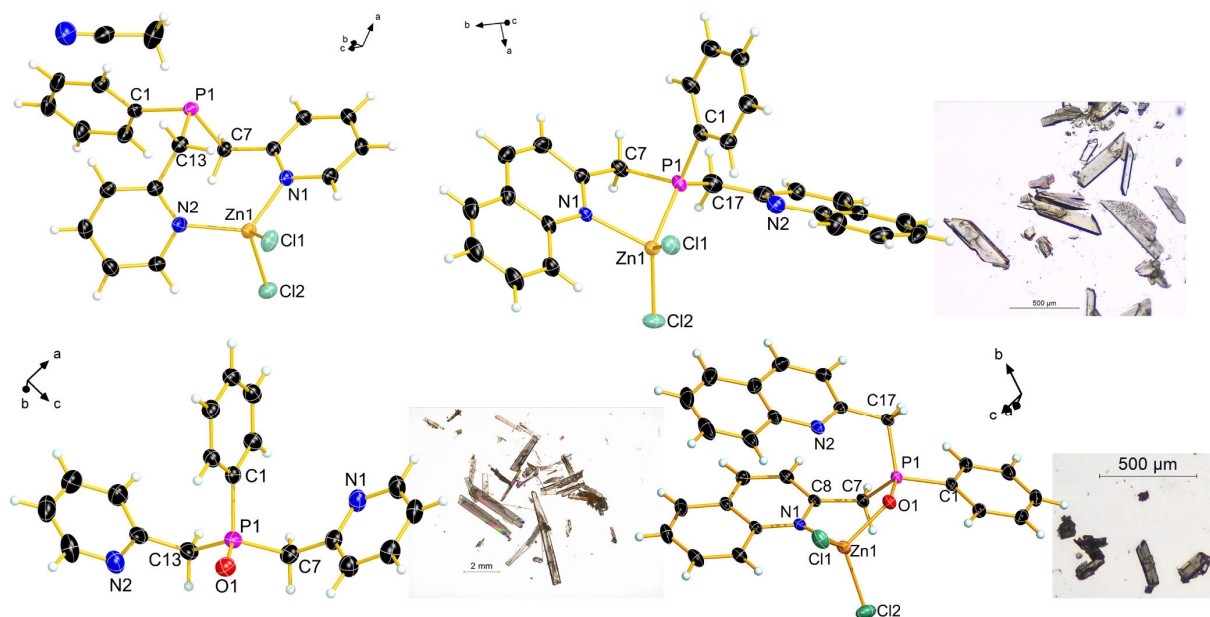


Figure 94. Molecular structure of the asymmetric unit of **1a** (top left), **2** (top right), **3** (bottom left) and **5** (bottom right) in the crystal. Thermal ellipsoids are drawn at 50 % probability level.

Compound **2** crystallizes in the triclinic space group $P\bar{1}$ with two formula units in the unit cell (Figure 94). Unlike in **1**, the zinc(II) atom in **2** is coordinated to phosphorus and one nitrogen atom of the phosphine ligand. The phosphorus atom in **2** is distorted tetrahedrally surrounded by zinc, the two quinaldinyl rings and the phenyl ring. The direct coordination to phosphorus is very unlikely for zinc(II), as it mostly prefers other hard atoms (N or O). There are only about 200 coordination compounds known in the CCDC data bank, where zinc is directly coordinating to phosphorus of a phosphine. However, in none of these compounds the zinc(II) atom has the choice to coordinate to a more favorable atom. This is the first case, to our knowledge, where Zn(II) indeed has the choice and prefers P,N over N,N coordination. Most probably this is due to the size of the quinaldinyl rings, which makes N,N and P,N coordination energetically similar. Additionally, other factors, like steric and packing effects, overweigh and result in the preferred P,N coordination of Zn(II) in the crystal. The non-coordinating nitrogen atom in **2** faces towards the zinc atom in the crystal. The phenyl ring and the Zn-coordinating quinaldinyl ring are almost perpendicular to each other (85.6°). There are weak, non-classical hydrogen bonds present between the chlorine atoms and hydrogen atoms of the phosphine ligand with distances between 2.655 \AA and 3.030 \AA .^[52] In the packing of **2**, there are face-to-face π - π interactions present between almost parallel, neighboring quinaldinyl rings (average distance of 3.354 \AA , angle of 0.1° between rings, Figure 104 of SI).^[53,54]

The synthesis of compound **3** is already known in the literature^[21], though the crystal structure has not been reported yet and is shown in Figure 1. Compound **3** crystallizes in the monoclinic space group $P2_1/n$ with four formula units in the unit cell. The phosphorus atom is distorted tetrahedrally surrounded by oxygen, the two pyridyl substituents and the phenyl ring. The O–P–C angles ($111\text{--}115^\circ$) are slightly larger and the C–P–C angles ($102\text{--}107^\circ$) are slightly smaller than the standard tetrahedron angle of 109° . In the crystal packing, compound **3** is forming antiparallel pairs of molecules, which are arranged as chains along the *b* axis (Figure 105). The single units are interconnected *via* weak non-classical hydrogen bonds (N \cdots H–C and O \cdots H–C).^[52] The shortest N \cdots H distances are between 2.606 \AA and 2.827 \AA , the O \cdots H distances between 2.404 \AA and 2.777 \AA . The shortest non-classical hydrogen bonds originate from the CH₂ groups.

Despite multiple crystallization attempts, single crystals of compound **4** suitable for x-ray diffraction could not be attained. Compound **5** crystallizes in the triclinic space group $P\bar{1}$ with two formula units in the unit cell (Figure 94). The phosphorus atom in **5** is again distorted tetrahedrally surrounded by

oxygen, the two quinaldinyl rings and the phenyl ring. The O–P–C (108–114°) are larger and the C–P–C angles (105–110°) are smaller than the standard tetrahedron angle of 109°. The P1–O1 bond length in **5** (1.501 Å) is a little bit longer than in the free phosphine oxide (1.484 Å). The distance between two quinaldinyl rings of one molecule is on average 3.390 Å. They are close to being parallel and span an acute angle of 11.2°. The phenyl ring is twisted away from the non-coordinating quinaldinyl ring and together they span an angle of 11.4°. The zinc chloride molecules in the packing of **5** are alternating when looking along the *a* axis, though form a chain when looking along the *c* axis (Figure 106). There are weak, non-classical hydrogen bonds present between the chlorine and the hydrogen atoms of the phosphine oxide ligand in the packing of **5**.^[52] There are different face-to-face π - π -interactions present in the 3D structure of **5**, between two parallel, neighboring phenyl rings (average distance of 3.368 Å), phenyl rings and neighboring quinaldinyl rings (average distance of 3.519 Å, angle of 11.4(6)°) as well as between two parallel, neighboring quinaldinyl rings (average distance of 3.552 Å).^[53,54]

Table 18. Selected bond lengths [Å] and angles [°] of complexes **1a–3** and **5**.

1a	<i>i</i> = - <i>x</i> , -1- <i>y</i> , - <i>z</i> ; <i>ii</i> = - <i>x</i> , - <i>y</i> , 1- <i>z</i> ; <i>iii</i> = - <i>x</i> , - <i>y</i> , - <i>z</i> ; <i>iv</i> = -1+ <i>x</i> , -1+ <i>y</i> , <i>z</i> .		
P1–C1	1.829(1)	Cl1...H11 ^{<i>i</i>}	2.957(4)
P1–C7	1.852(1)	Cl1...H12 ^{<i>i</i>}	2.911(3)
P1–C13	1.874(1)	Cl1...H16 ^{<i>ii</i>}	2.841(3)
N1–Zn1	2.052(1)	Cl1...H20B ^{<i>iii</i>}	2.961(7)
N2–Zn1	2.047(2)	Cl2...H8 ^{<i>iii</i>}	2.705(3)
Zn1–Cl1	2.224(1)	Cl2...H9 ^{<i>iii</i>}	2.965(4)
Zn1–Cl2	2.251(2)	Cl2...H20A ^{<i>iv</i>}	2.888(8)
C1–P1–C7	102.1(4)	Cl1–Zn1–Cl2	112.8(4)
C1–P1–C13	101.2(6)	N1–Zn1–Cl1	107.0(5)
C7–P1–C13	100.8(4)	N1–Zn1–Cl2	104.7(6)
C8–N1–Zn1	126.2(8)	N2–Zn1–Cl1	110.5(5)
C14–N2–Zn1	125.5(5)	N2–Zn1–Cl2	105.7(3)
1b			
P1–C1	1.823(3)	N3–Zn2	2.054(3)
P2–C19	1.820(3)	N2–Zn1	2.056(2)
P1–C7	1.847(3)	N4–Zn2	2.048(2)
P2–C25	1.848(3)	Zn1–Cl1	2.228(8)
P1–C13	1.877(3)	Zn2–Cl3	2.233(8)
P2–C31	1.867(3)	Zn1–Cl2	2.241(8)
N1–Zn1	2.056(2)	Zn2–Cl4	2.229(9)
C1–P1–C7	102.7(2)	N1–Zn1–Cl1	104.8(8)
C19–P2–C25	102.2(2)	N3–Zn2–Cl3	106.0(7)
C1–P1–C13	102.5(2)	N1–Zn1–Cl2	104.0(7)
C19–P2–C31	102.5(2)	N3–Zn2–Cl4	105.6(7)
C7–P1–C13	101.3(2)	N2–Zn1–Cl1	110.1(7)
C25–P2–C31	101.0(2)	N4–Zn2–Cl3	105.3(7)
Cl1–Zn1–Cl2	115.8(3)	N2–Zn1–Cl2	105.4(7)
Cl3–Zn2–Cl4	116.8(3)	N4–Zn2–Cl4	106.9(7)
2	<i>i</i> = 1- <i>x</i> , 1- <i>y</i> , - <i>z</i> ; <i>ii</i> = 1+ <i>x</i> , <i>y</i> , <i>z</i> ; <i>iii</i> = 1- <i>x</i> , 1- <i>y</i> , 1- <i>z</i> .		
P1–C1	1.816(1)	Zn1–Cl2	2.219(1)
P1–C7	1.841(1)	Cl1...H3 ^{<i>iv</i>}	2.873(1)
P1–C17	1.845(1)	Cl1...H5 ^{<i>ii</i>}	2.881(1)
P1–Zn1	2.379(1)	Cl1...H14 ^{<i>i</i>}	2.870(1)
N1–Zn1	2.111(1)	Cl2...H17A ^{<i>iii</i>}	2.668(1)

Zn1–Cl1	2.228(1)		
C1–P1–C7	107.4(3)	C8–N1–Zn1	118.6(5)
C1–P1–C17	106.6(2)	P1–C7–C8	112.4(4)
C7–P1–C17	99.2(2)	Cl1–Zn1–Cl2	114.6(2)
C1–P1–Zn1	115.1(4)	P1–Zn1–Cl1	115.3(2)
C7–P1–Zn1	94.5(3)	P1–Zn1–Cl2	118.8(4)
C17–P1–Zn1	129.5(3)	N1–Zn1–Cl1	105.3(3)
P1–Zn1–N1	83.9(3)	N1–Zn1–Cl2	114.0(3)
3	$i = x, 1+y, z, ii = -x, 1-y, 1-z$		
P1–O1	1.485(2)	O1…H13B ⁱ	2.404(2)
P1–C1	1.808(2)	O1…H6 ⁱ	2.777(2)
P1–C7	1.813(2)	N1 ⁱ …H10	2.780(2)
P1–C13	1.814(2)	N2…H7A ⁱⁱ	2.606(2)
O1…H13A ⁱ	2.530(2)	N2…H9 ⁱⁱ	2.827(2)
O1–P1–C1	111.3(8)	C1–P1–C7	107.2(9)
O1–P1–C7	114.0(8)	C1–P1–C13	106.4(9)
O1–P1–C13	115.0(9)	C7–P1–C13	102.2(9)
5	$i = -1+x, y, z; ii = -x, -y, -z; iii = 1+x, y, z; iv = 1-x, -y, -z.$		
P1–O1	1.506(1)	Zn1–Cl2	2.223(6)
P1–C1	1.795(2)	Cl1…H2 ⁱⁱⁱ	2.751(2)
P1–C7	1.814(2)	Cl1…H7B ⁱⁱⁱ	2.760(3)
P1–C17	1.803(2)	Cl1…H9 ⁱⁱⁱ	2.958(2)
O1–Zn1	1.983(1)	Cl1…H17B ⁱⁱⁱ	2.939(3)
N1–Zn1	2.093(2)	Cl1…H19 ⁱⁱⁱ	2.953(3)
Zn1–Cl1	2.225(5)	Cl2…H5 ^{iv}	2.897(3)
O1–P1–C1	110.7(8)	Cl1–Zn1–Cl2	120.9(2)
O1–P1–C7	108.7(8)	O1–Zn1–N1	100.1(3)
O1–P1–C17	114.6(8)	O1–Zn1–Cl1	102.5(4)
C1–P1–C7	106.0(8)	O1–Zn1–Cl2	112.8(4)
C1–P1–C17	106.5(8)	N1–Zn1–Cl1	113.1(4)
C7–P1–C17	110.0(9)	N1–Zn1–Cl2	105.6(4)
Zn1–O1–P1	121.4(7)	Zn1–N1–C8	119.0(2)

2.7.2.3. Hirshfeld surface analysis

Hirshfeld surface (HS) and two-dimensional (2D) fingerprint analyses visualize the packing motifs and intermolecular hydrogen bonding interaction in the crystalline compounds using the crystallographic output file (.cif) obtained from single crystal X-ray diffraction. They were plotted using the software CrystalExplorer version 17.5.^[55]

The investigation of the 2D-fingerprint plots for compounds **1a**, **2** and **5** indicate the presence of attractive intermolecular interactions and weak π - π -interactions in the crystal (Figure 95). The C–H…H–C and C–H…C contacts are the major contributor to the total HS. The π - π stacking interactions (C…C and C…N) contribute to the total HS only to a small extend. By enlarging the π -system of the ligand, an increase of C…C interactions is observed in **2** and **5**, which is represented by an increase in planar, aromatic π -stacking arrangements. Non-classical hydrogen bonds are represented by C–H…N, C–H…O and C–H…Cl contacts and are visible by the spherical red colored areas in the d_{norm} maps. All

complexes show strong intermolecular interactions with the chlorine atoms as indicated by sharp spikes in the fingerprint plots.

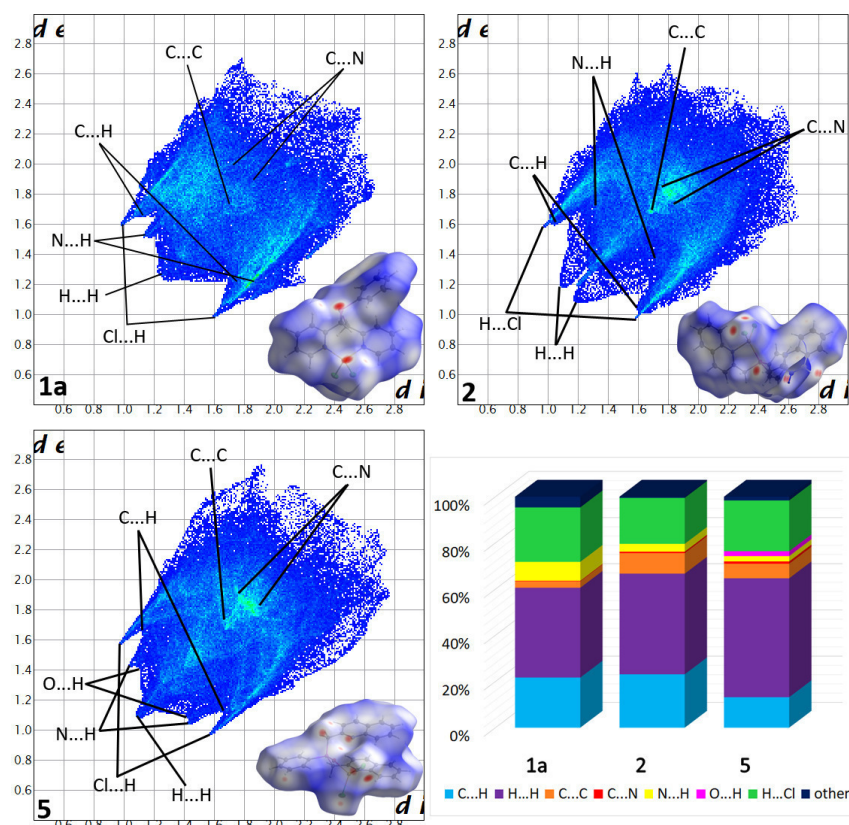


Figure 95. Visualization of the 2D-dimensional fingerprint plots including the d_{norm} maps obtained from HS analysis and a summary of the close contacts of crystalline **1a**, **2** and **5**.

2.7.2.4. NMR data

Selected NMR data of compounds **1–5** are listed in Table 19. The chemical shift of compound **1** in the ^{31}P NMR spectrum is slightly shifted to higher frequencies when compared to the free ligand ($\Delta\delta = 4$ ppm). This indicates that most probably phosphorus does not participate in the coordination to zinc(II) and is further confirmed by the resulting single crystal X-ray structure (Figure 94). On the other hand, in the ^{31}P NMR spectrum of compound **2**, the signal for **2** appears at lower frequencies when compared to the free ligand ($\Delta\delta = 10$ ppm), suggesting a possible coordination of phosphorus to zinc(II). In the ^{31}P NMR spectrum for compounds **4** and **5** the signals are shifted to higher frequencies when compared to the respective free ligand ($\Delta\delta = 14$ ppm), indicating the coordination of P=O to zinc(II). In the ^1H NMR spectra of all compounds only one set of signals for the CH_2 protons is visible, which are typical for the AB part of an ABX spectrum ($A = B = \text{H}$, $X = \text{P}$) (Figure 96).

Table 19. Selected NMR properties of the compounds **1**, **2**, **4** and **5**. Chemical shifts δ in ppm in reference to CD_2Cl_2 .

	1	2	4	5
$^{31}\text{P}\{^1\text{H}\}$	-9.3	-23.2	48.3	49.9
ABX spin system ($A = B = \text{H}$, $X = \text{P}$)				
^1H CH_2	3.42 (d, 2H, $^2J_{\text{A-B}} = 13.5$ Hz), 3.32 (dd, 2H, $^2J_{\text{A-B}} = 14.0$ Hz, $^2J_{\text{A-X}} = 4.1$ Hz)	4.11 (dd, 2H, $^2J_{\text{A-B}} = 15.4$ Hz), 3.92 (dd, 2H, $^2J_{\text{A-B}} = 15.4$ Hz, $^2J_{\text{B-X}} = 6.3$ Hz)	4.08 (t, 2H, $^2J_{\text{H-H}} = 12.3$ Hz), 3.89 (t, 2H, $^2J_{\text{H-H}} = 15.8$ Hz)	4.37–4.21 (m, 4H, $^2J_{\text{H-H}} = 15.0$ Hz, $^2J_{\text{H-H}} = 15.8$ Hz, $^2J_{\text{H-P}} = 5.0$ Hz)

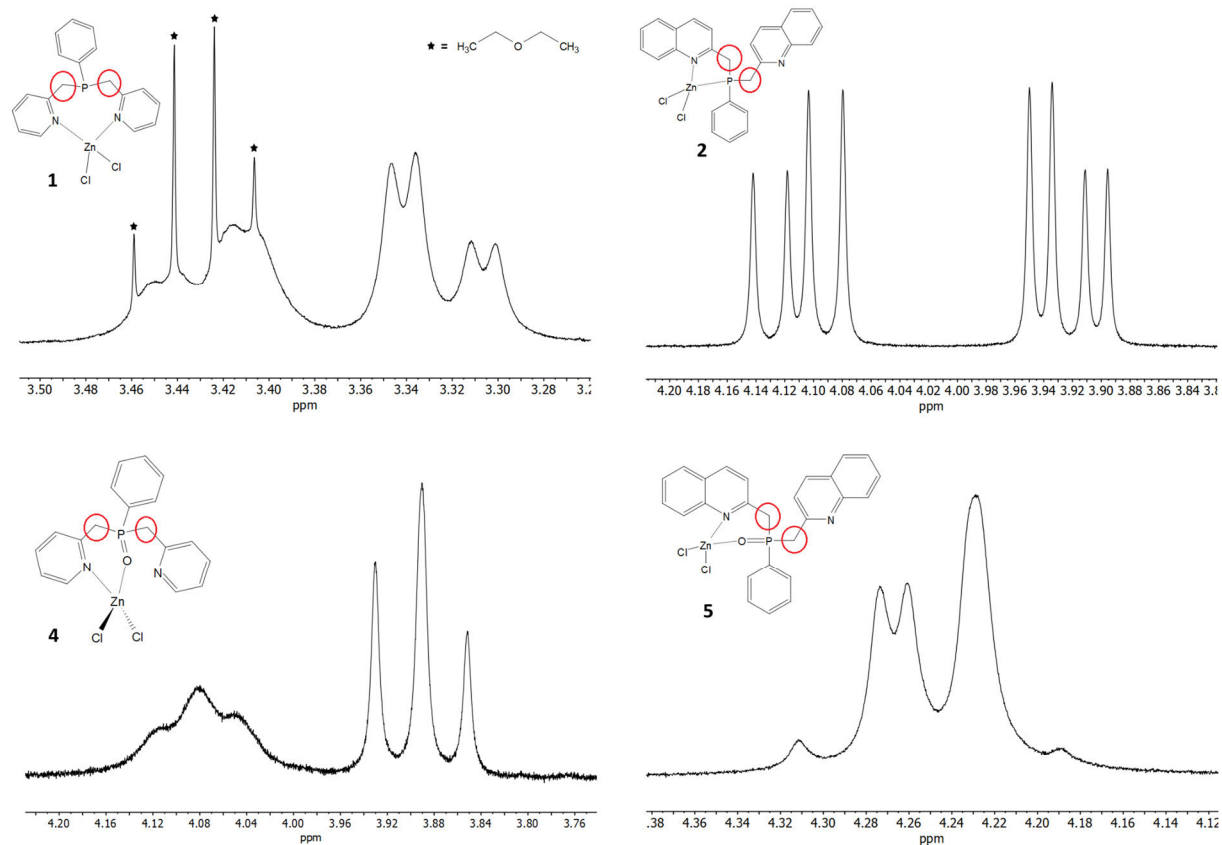


Figure 96. Signals of the CH₂ protons in the ¹H NMR spectrum of compounds **1**, **2**, **4** and **5**.

The observation of only one set of signals for both CH₂ groups indicates a dynamic behavior of the complexes **2**, **4** and **5** in solution. In order to study this behavior, NMR spectra at low temperatures are collected.

2.7.2.5. Variable temperature NMR

Variable-temperature NMR spectroscopy was performed on all complexes in the non-coordinating solvent CD₂Cl₂ to further investigate the structural behavior of the zinc(II) complexes **1**, **2**, **4** and **5** in solution. This is especially of interest for solution processed OLED materials as it is important to know how the molecules behave in solution or an ink formulation at different temperatures. A change in coordination in solution could influence the optical properties of the so processed OLEDs.

In general, all observed changes in the spectra are completely reversible. At RT, the ³¹P NMR spectrum of compound **1** shows a signal at -9.3 ppm (Figure 97). At -80 °C, the signal is shifted to lower frequencies ($\delta^{31}\text{P} = -12.1$ ppm, $\Delta\delta = 3.0$ ppm). As mentioned before, in the ¹H NMR spectrum at RT, there is only one set of signals visible typical for the diastereotopic methylene protons. After cooling down to -80 °C, the signals for the methylene group are split into two different sets. In the aromatic region additional signals appear when lowering the temperature, which suggest the presence of two different pyridyl rings. This is also confirmed by the presence of two ¹⁵N NMR signals ($\delta^{15}\text{N}$ (CD₂Cl₂, -80 °C) = -144.4 ppm, -147.6 ppm) in the ¹H¹⁵N-HMBC spectrum at -80 °C (Figure 98), as well as the change of the signal correlations in the ¹H¹H-COSY NMR spectrum. These NMR results can be explained by the change of Zn(II) from N,N to N,P coordination at low temperature. This explains the signals of two different pyridyl rings in the ¹H NMR spectrum at -80 °C and accounts for the large shift towards lower frequencies in the ³¹P NMR spectrum (Scheme 18).

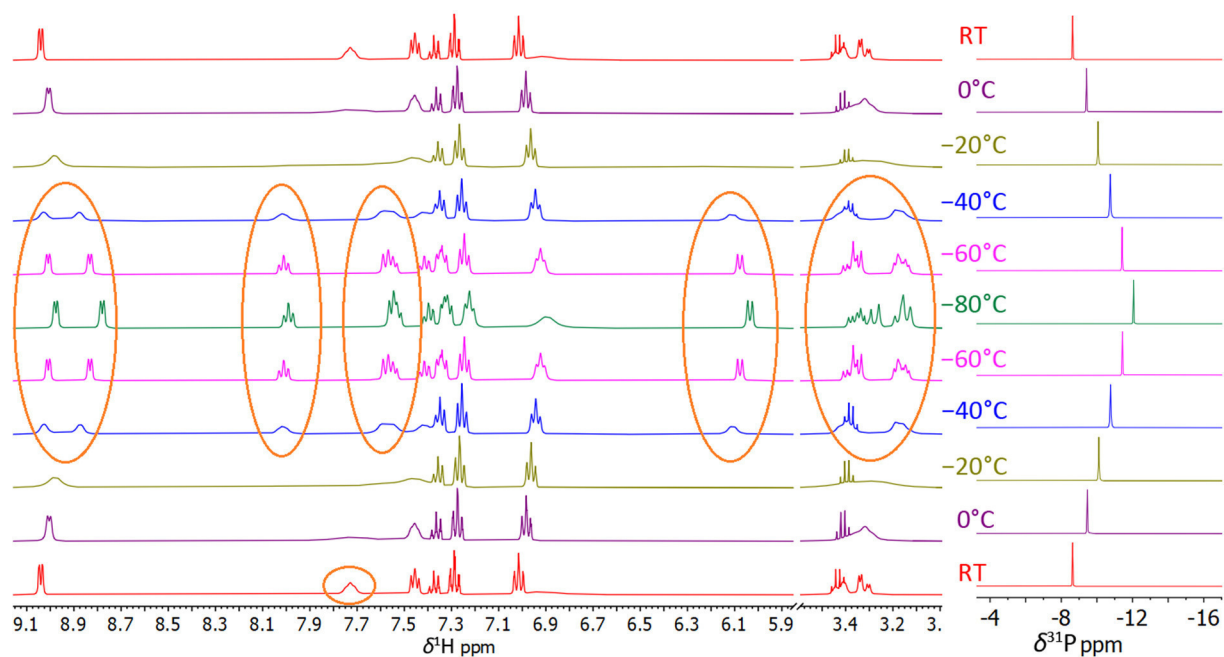


Figure 97. Variable temperature ^1H and ^{31}P NMR spectra of compound **1** in CD_2Cl_2 .

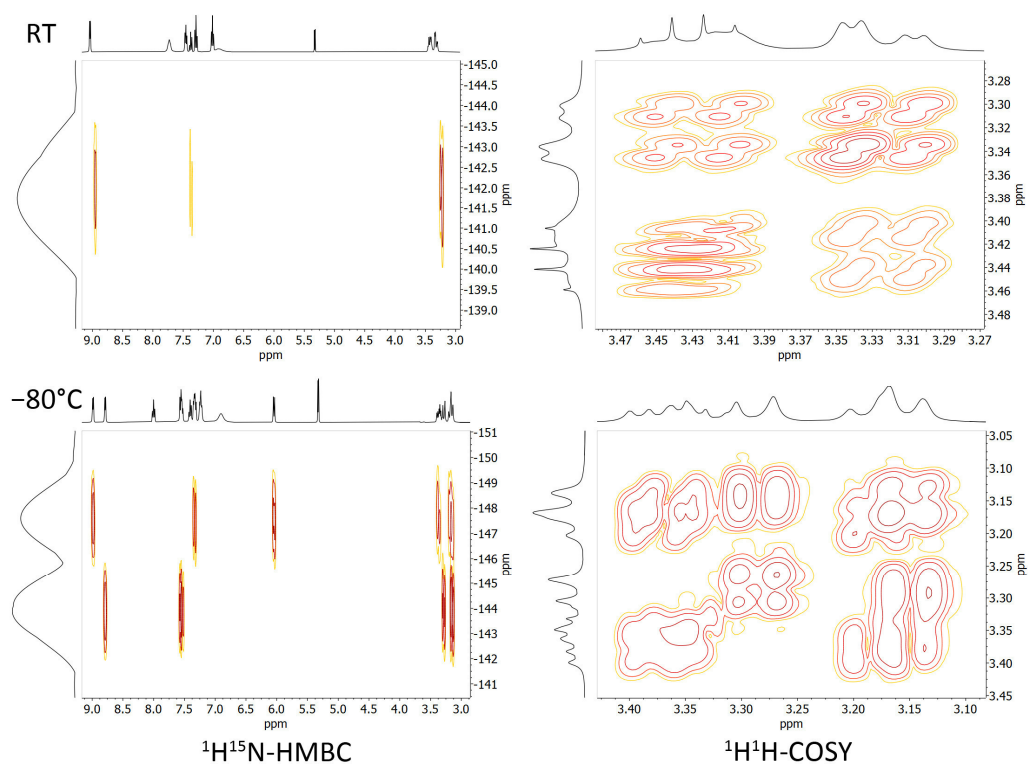
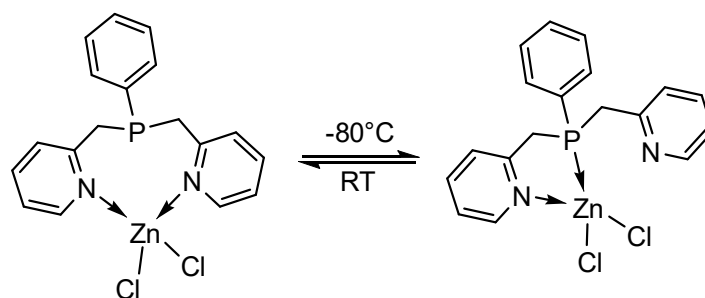


Figure 98. $^1\text{H}^{15}\text{N}$ -HMBC (left) and $^1\text{H}^1\text{H}$ -COSY (right) NMR spectra of compound **1** in CD_2Cl_2 at RT (top) and at -80°C (bottom).



Scheme 18. Transition from N,N to N,P coordination in Zn(II) complex **1** at low temperature in solution.

Continuing with compound **2**, there are some small changes visible in the low temperature ^1H and ^{31}P NMR spectra for compound **2** (Figure 107 of SI). In the ^1H NMR spectrum at RT, the signals for only one set of quinaldinyl rings are observed. When cooling the sample down to $-80\text{ }^\circ\text{C}$, the signals for the quinaldinyl rings and in particular those for the methylene protons in the ^1H NMR spectrum are broadened, which is indicative for a beginning of a signal splitting. Most probably at even lower temperatures the situation would be similar to that of compound **1**. At RT in solution, the zinc(II) atom in **2** is N,N coordinating, contrary to the P,N coordination visible in the crystal, resulting in two chemically equivalent quinaldinyl substituents in the ^1H NMR spectrum. When lowering the temperature, the dynamic of the system becomes visible. However, the activation energy of the dynamic seems to be lower for compound **2** than **1** and thus the complete splitting of the CH_2 signals is not fully reached at $-80\text{ }^\circ\text{C}$. Apparently, the structure observed in the crystal of the complexes is also influenced by packing effects depending on the substituent and can differ from the structure present in solution.

Moving to the variable temperature ^1H NMR and ^{31}P NMR spectra for compound **4** (Figure 99), multiple new signals appear in the ^{31}P NMR spectrum at lower temperatures with one in the region where the chemical shift of the free ligand in CD_2Cl_2 is located ($\delta^{31}\text{P} = 35.3\text{ ppm}$, $\delta^{31}\text{P}$ (free ligand) = 34.6 ppm). The ^1H NMR and $^1\text{H}^1\text{H}$ -COSY NMR spectra indicate the presence of at least four to five different sets of CH_2 groups at $-80\text{ }^\circ\text{C}$ (Figure 100). Accordingly, the ^{31}P NMR spectra at low temperature also show the presence of multiple different species belonging most probably to different coordination geometries, which are in equilibrium at RT. This is further indicated by the broad signal in the ^{31}P NMR spectrum at RT (see Figure 99).

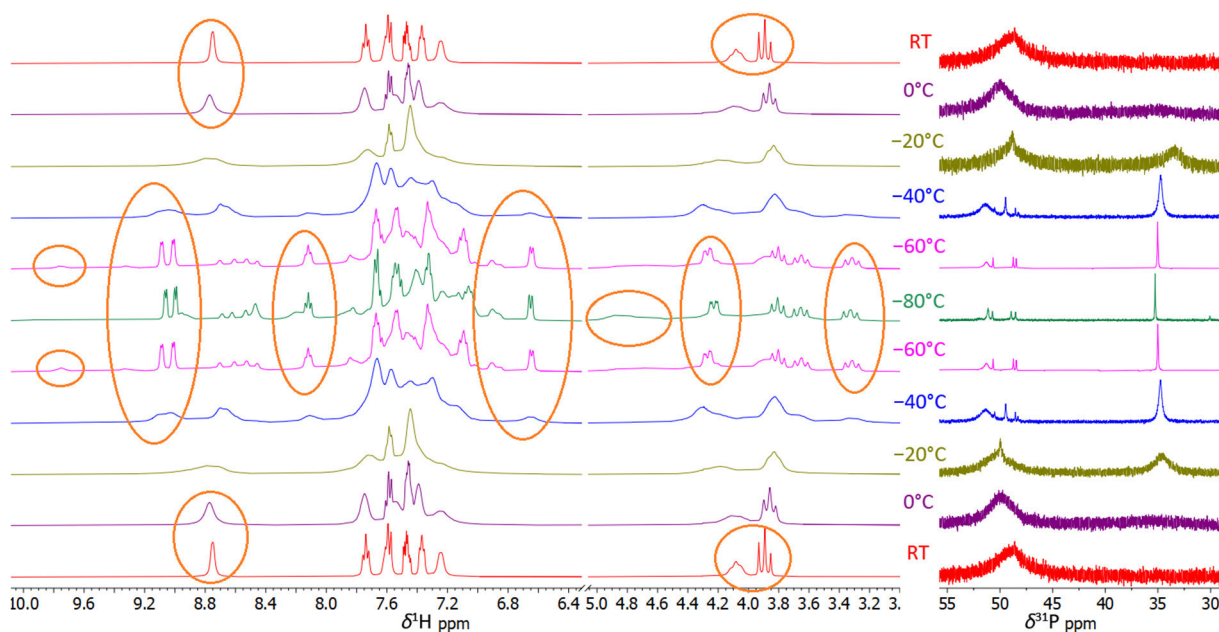


Figure 99. Variable temperature ^1H and ^{31}P NMR spectra of compound **4** in CD_2Cl_2 .

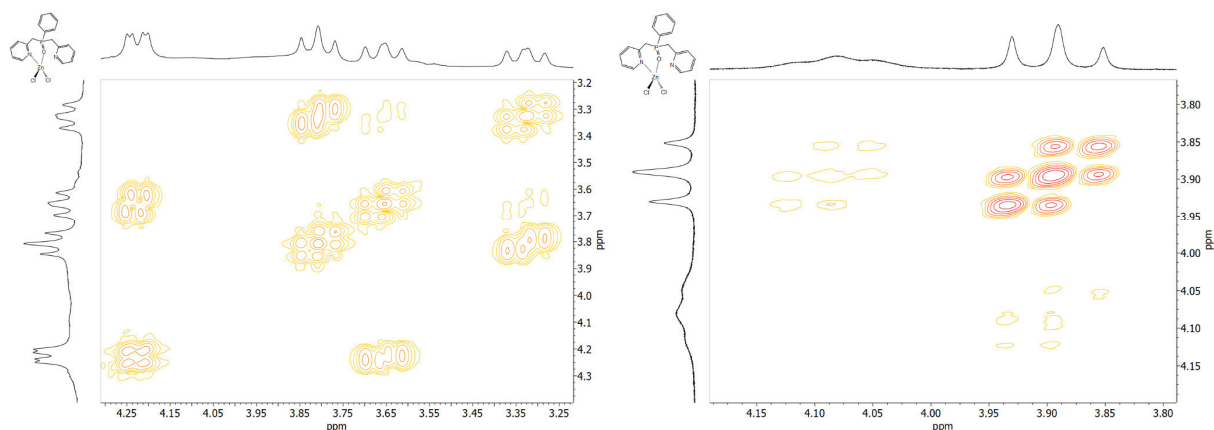


Figure 100. Region of the CH₂ signals in the ¹H-¹H-COSY NMR spectra of compound **4** at RT (right) and at -80 °C (left) in CD₂Cl₂.

Last but not least, compound **5** shows changes in the ¹H NMR spectrum with the appearance of new signals at low temperature (see Figure 108 of SI). Unfortunately, the signals at low temperature also get very broad making further analysis by 2D NMR impossible. In the ³¹P NMR spectrum at low temperatures the signal for compound **5** is observed at 50.9 ppm with a minor shift of $\Delta\delta = 1.0$ ppm to higher frequencies when comparing to the shift at RT. A dynamic is suspected similar to the other compounds. At RT the complex experiences a fast dynamic/exchange, where the Zn(II) stays coordinated to oxygen but switches the N-coordination between one quinaldinyl ring and the other. At low temperatures, this exchange is slowed down resulting in different signals for the coordinated and non-coordinated quinaldinyl substituent in the ¹H NMR spectrum.

2.7.2.6. Electrochemical properties

The stability of complex **5** in solution was studied by cyclic voltammetry in a potential window of 2 V to -1.2 V. The measurements were performed in a three-electrode cell using a Pt coil as working electrode, a glassy carbon counter electrode and an Ag wire as pseudo reference electrode (Figure 109 of SI). The complex showed no redox activity in the studied potential window indicating a good stability under those conditions.

2.7.2.7. Photophysical properties

When illuminating the solid compounds **1–5** with UV light (366 nm), they show blue/green luminescence (Figure 101). The absorption spectrum shows for all compounds a strong absorption in the UV region with additional maxima in the blue to green region of the spectrum (Figure 110 of SI). The emission spectrum of the ligand of **5** shows a maximum at 400 nm (Figure 111 of SI).

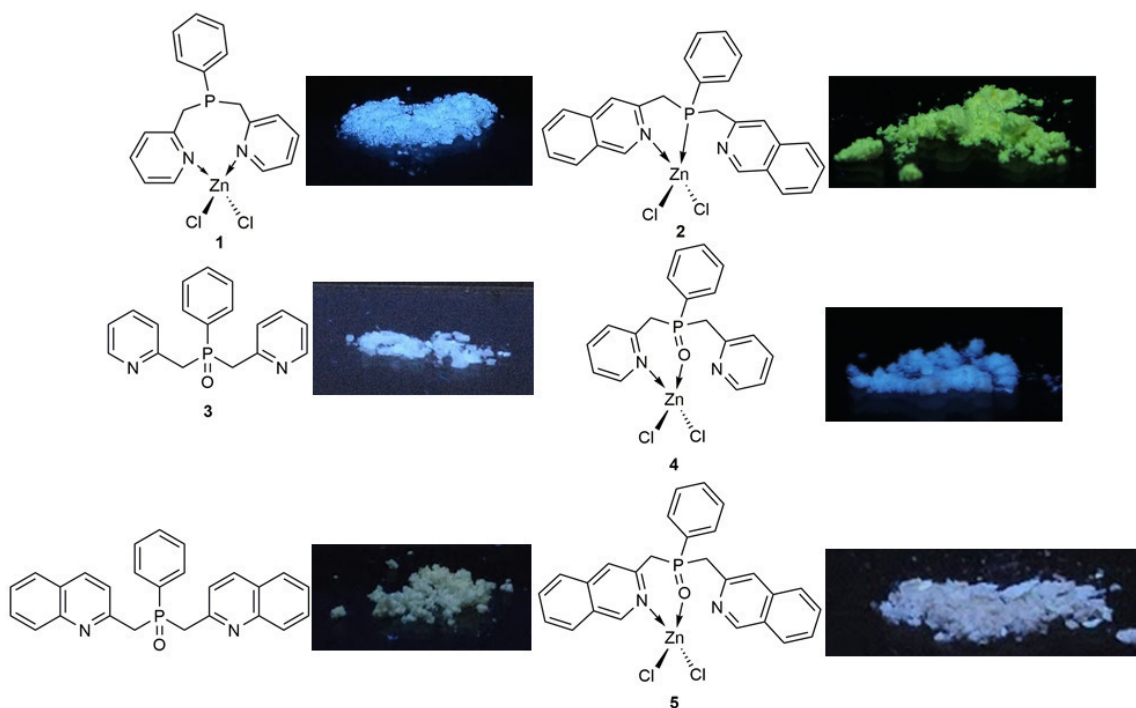


Figure 101. Solid compounds when illuminated with UV light (366 nm).

2.7.2.8. Theoretical calculations

To gain insight into the electronic properties of the compounds, density functional theory (DFT) calculations are performed using the ground state geometry optimized at the B3LYP/6-31+G(d,p) level. The molecular orbital distributions of compounds **1**–**5** are shown in Figure 112 of the SI. As there is no crystal structure available for compound **4**, we did not guess and optimize a structure as it is unclear which coordination the zinc(II) will prefer in this compound (N,N or N,PO).

In the zinc(II) complexes, the highest occupied molecular orbital (HOMO) is mostly localized on the chlorine atoms, whereas the lowest unoccupied molecular orbital (LUMO) is localized on the nitrogen containing substituent coordinating to the zinc(II). The zinc(II) atom is not taking part in the orbitals contributing to the HOMO or LUMO. An excitation would implicate the presence of a ligand-to-ligand charge transfer. In the phosphine oxide ligand **3**, the HOMO is localized on both pyridyl rings and the LUMO is located orthogonal to these, on the phenyl ring. In the phosphine oxide ligand of **5**, the HOMO and LUMO are located on both opposite quinaldinyl rings respectively. When comparing the energy levels for **1** and **2**, the HOMO energy rises by 0.24 eV whereas the LUMO energy gets lower by almost double the amount (0.42 eV). A similar trend is observed when comparing the free ligand **3** and the ligand of **5**. In general, by expanding the π -system a change in the HOMO and LUMO energies is achieved, but the energy gap thereof remains untouched. Remarkably, an oxidation of the ligand has no drastic changes on the energy levels of the HOMO and LUMO.

2.7.3. Conclusion

Two phosphines, two phosphine oxides and the Zn(II)Cl₂ complexes thereof were prepared in high yields (>80 %) and characterized. The crystal structure of the phenylbis(pyridin-2-ylmethyl)phosphine Zn(II) complex shows the expected N,N coordination. In contrast, Zn(II) is unexpectedly P,N coordinated using the phenylbis(quinaldin-2-ylmethyl)phosphine ligand, probably due to steric and packing effects. The complexes show a high dynamic in solution, indicating the presence of divergent structures in solution and in the crystal, as revealed by VT-NMR. In case of the phosphine complexes,

when lowering the temperature, a shift from N,N coordination to P,N coordination in solution is observed. The ligands as well as the Zn(II) complexes show luminescent properties when illuminated with UV light. Collected absorption and emission spectra confirm the observed colors under UV light. Quantum chemical calculations reveal the location of the HOMOs and LUMOs in the ligands and Zn(II) complexes. An excitation of the ligands would imply in an intraligand charge transfer. When exciting the complexes, a ligand-to-ligand charge transfer would take place. Electrochemical measurements of complex **5** shows no redox activity in solution.

In future studies, a change of the chlorine ligands on the zinc(II) to a ligand with an extensive π -system or similar, could change the orbital energies resulting in a smaller HOMO-LUMO gap and influence the emission wavelength.

Associated Content

Supporting Information.

Experimental, crystallographic and spectroscopic data are available free of charge online at <http://pubs.acs.org>.

Author Information

Corresponding Author.

† klk@cup.uni-muenchen.de

Notes.

There are no conflicts of interest.

Acknowledgment

The German Federal Ministry for Economic Affairs and Energy on the basis of a decision by the German Bundestag (ZIM, Grant ZF4065408SL7, ZF4477702SL7) financially supported this work. We further gratefully acknowledge the financial support by the Department of Chemistry, Ludwig-Maximilian University of Munich. Prof. Dr. T. M. Klapötke is thanked for his continuous support over the years. The entire NMR team at the Ludwig-Maximilian University of Munich are thanked for the time consuming multi-nuclear and variable temperature NMR measurements.

2.7.4. References

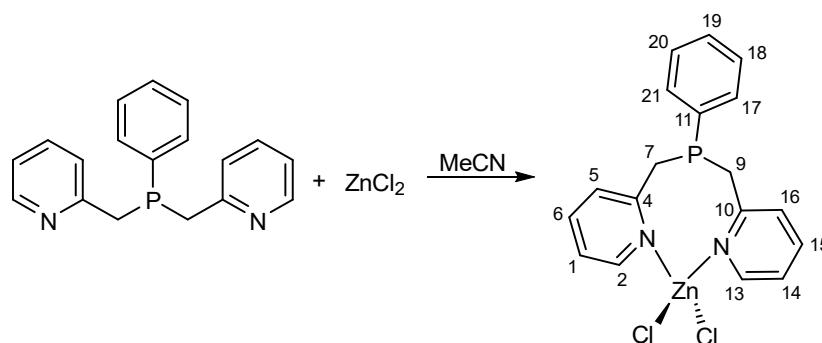
- [1] Y. Xiao, Z. Sun, H. Guo, O. Kwon, *Beilstein J. Org. Chem.* **2014**, *10*, 2089–2121.
- [2] C. G. J. Tazelaar, J. C. Slootweg, K. Lammertsma, *Coord. Chem. Rev.* **2018**, *356*, 115–126.
- [3] C. A. Tolman, *Chem. Rev.* **1977**, *77*, 313–348.
- [4] E. I. Musina, A. S. Balueva, A. A. Karasik, *Organophosphorus Chem.*, **2019**, 1–63.
- [5] J. T. Fleming, L. J. Higham, *Coord. Chem. Rev.* **2015**, *297–298*, 127–145.
- [6] K. N. Gavrilov, A. I. Polosukhin, *Russ. Chem. Rev.* **2000**, *69*, 661–682.
- [7] M. P. Carroll, P. J. Guiry, *Chem. Soc. Rev.* **2014**, *43*, 819–833.
- [8] L. Fanfoni, A. Meduri, E. Zangrando, S. Castillon, F. Felluga, B. Milani, *Molecules* **2011**, *16*, 1804–1824.
- [9] H. Jaafar, H. Li, L. C. Misal Castro, J. Zheng, T. Roisnel, V. Dorcet, J.-B. Sortais, C. Darcel, *Eur. J. Inorg. Chem.* **2012**, *2012*, 3546–3550.
- [10] G. Chelucci, G. Orrù, G. a. Pinna, *Tetrahedron* **2003**, *59*, 9471–9515.
- [11] P. Braunstein, *J. Organomet. Chem.* **2004**, *689*, 3953–3967.
- [12] S. Liu, R. Pattacini, P. Braunstein, *Organometallics* **2011**, *30*, 3549–3558.

-
- [13] L. Bergmann, J. Friedrichs, M. Mydlak, T. Baumann, M. Nieger, S. Bräse, *Chem. Commun.* **2013**, 49, 6501–3.
- [14] O. Crespo, M. C. Gimeno, A. Laguna, C. Larraz, *Z. Naturforsch.* **2009**, 64, 1525–1534.
- [15] A. Eichhöfer, G. Buth, S. Lebedkin, M. Kühn, F. Weigend, *Inorg. Chem.* **2015**, 54, 9413–9422.
- [16] I. D. Strel'nik, V. V. Sizov, V. V. Gurzhiy, A. S. Melnikov, I. E. Kolesnikov, E. I. Musina, A. A. Karasik, E. V. Grachova, *Inorg. Chem.* **2020**, 59, 244–253.
- [17] A. V. Artem'ev, M. R. Ryzhikov, I. V. Taidakov, M. I. M. I. Rakhmanova, E. A. Varaksina, I. Y. Bagryanskaya, S. F. Malysheva, N. A. N. Belogorlova, *Dalton Trans.* **2018**, 2, 2701–2710.
- [18] C. Han, H. Xu, *Chinese Sci. Bull.* **2019**, 64, 663–681.
- [19] D. Joly, P. A. Bouit, M. Hissler, *J. Mater. Chem. C* **2016**, 4, 3686–3698.
- [20] A. V. Artem'ev, A. Y. Baranov, M. I. Rakhmanova, S. F. Malysheva, D. G. Samsonenko, *New J. Chem.* **2020**, 44, 6916–6922.
- [21] F. Hung-Low, K. K. Klausmeyer, *Polyhedron* **2010**, 29, 1676–1686.
- [22] D. A. Padron, K. K. Klausmeyer, *Polyhedron* **2012**, 34, 215–220.
- [23] G. Minghetti, S. Stoccoro, M. A. Cinellu, A. Zucca, M. Manassero, M. Sansoni, *Dalton Trans.* **1998**, 4119–4126.
- [24] L. Douce, L. Charbonnière, M. Cesario, R. Ziessel, *New J. Chem.* **2001**, 25, 1024–1030.
- [25] F. Hung-Low, A. Renz, K. K. Klausmeyer, *Eur. J. Inorg. Chem.* **2009**, 2994–3002.
- [26] B. M. Rapko, E. N. Duesler, P. H. Smith, R. T. Paine, R. R. Ryan, *Inorg. Chem.* **1993**, 32, 2164–2174.
- [27] G. Pilloni, B. Corain, M. Degano, B. Longato, G. Zanotti, *Dalton Trans.* **1993**, 2, 1777–1778.
- [28] G. Mallesham, C. Swetha, S. Niveditha, M. E. Mohanty, N. J. Babu, A. Kumar, K. Bhanuprakash, V. J. Rao, *J. Mater. Chem. C* **2015**, 3, 1208–1224.
- [29] K. Duan, D. Wang, M. Yang, Z. Liu, C. Wang, T. Tsuboi, C. Deng, Q. Zhang, *ACS Appl. Mater. Interfaces* **2020**, 12, acsami.0c02800.
- [30] J. Uk Kim, Y. M. Wong, S. Kumar, O. G. Hayes, F. Duncan, C.-Y. Chan, B. Y.-W. Wong, H. Ye, L.-S. Cui, H. Nakanotani, E. Zysman-Colman, C. Adachi, *Chem. Lett.* **2019**, 48, 1225–1228.
- [31] C. Kirst, F. Zoller, T. Bräuniger, P. Mayer, D. Fattakhova-Rohlfing, K. Karaghiosoff, *Inorg. Chem.* **2021**, 60 (4), 2437–2445.
- [32] N. Lin, J. Qiao, L. Duan, H. Li, L. Wang, Y. Qiu, *J. Phys. Chem. C* **2012**, 116, 19451–19457.
- [33] K. Katagiri, Y. Yamamoto, Y. Takahata, R. Kishibe, N. Fujimoto, *Tetrahedron Lett.* **2019**, 60, 2026–2029.
- [34] F. Dumur, *Synth. Met.* **2014**, 195, 241–251.
- [35] M. G. Kaplunov, S. S. Krasnikova, S. L. Nikitenko, I. K. Yakushchenko, *Mol. Cryst. Liq. Cryst.* **2014**, 589, 48–55.
- [36] C. Bizzarri, E. Spuling, D. M. Knoll, D. Volz, S. Bräse, *Coord. Chem. Rev.* **2018**, 373, 49–82.
- [37] Y. Zou, S. Gong, G. Xie, C. Yang, *Adv. Opt. Mater.* **2018**, 6, 1800568.
- [38] D. Volz, M. Wallesch, S. L. Grage, J. Göttlicher, R. Steininger, D. Batchelor, T. Vitova, A. S. Ulrich, C. Heske, L. Weinhardt, T. Baumann, S. Bräse, *Inorg. Chem.* **2014**, 53, 7837–7847.
- [39] T. Tsukuda, C. Nishigata, K. Arai, T. Tsubomura, *Polyhedron* **2009**, 28, 7–12.
- [40] R. Mondal, P. K. Giesbrecht, D. E. Herbert, *Polyhedron* **2016**, 108, 156–162.
- [41] S. Bestgen, C. Schoo, B. L. Neumeier, T. J. Feuerstein, C. Zovko, R. Köppe, C. Feldmann, P. W. Roesky, *Angew. Chem.*, **2018**, 130 (43), 14461–14465; *Angew. Chem. Int. Ed.*, **2018**, 57 (43), 14265–14269.
- [42] A. Gusev, E. Braga, V. Shul'gin, K. Lyssenko, I. Eremenko, L. Samsonova, K. Degtyarenko, T. Kopylova, W. Linert, *Materials*, **2017**, 10, 897.
- [43] I. E. Mikhailov, L. D. Popov, V. V. Tkachev, S. M. Aldoshin, G. A. Dushenko, Y. V. Revinskii, V. I. Minkin, *J. Mol. Struct.* **2018**, 1157, 374–380.
- [44] S.-C. Yu, C.-C. Kwok, W.-K. Chan, C.-M. Che, *Adv. Mater.* **2003**, 15, 1643–1647.

- [45] K. G. Vladimirova, A. Y. Freidzon, O. V. Kotova, A. A. Vaschenko, L. S. Lepnev, A. A. Bagatur'yants, A. G. Vitukhnovskiy, N. F. Stepanov, M. V. Alfimov, *Inorg. Chem.* **2009**, *48*, 11123–11130.
- [46] S. F. Liu, Q. Wu, H. L. Schmider, H. Aziz, N. X. Hu, Z. Popović, S. Wang, *J. Am. Chem. Soc.* **2000**, *122*, 3671–3678.
- [47] K. Singh, A. Kumar, R. Srivastava, P. S. Kadyan, M. N. Kamalasanan, I. Singh, *Opt. Mater.* **2011**, *34*, 221–227.
- [48] H.-J. Son, W.-S. Han, J.-Y. Chun, B.-K. Kang, S.-N. Kwon, J. Ko, S. J. Han, C. Lee, S. J. Kim, S. O. Kang, *Inorg. Chem.* **2008**, *47*, 5666–5676.
- [49] A. Kermagoret, F. Tomicki, P. Braunstein, *Dalton Trans.* **2008**, *22*, 2945–2955.
- [50] C. Hettstedt, P. Köstler, E. Ceylan, K. Karaghiosoff, *Tetrahedron* **2016**, *72*, 3162–3170.
- [51] S. M. E. Linert, Functionalised Phosphines - Fascinating Multidentate Ligands for Luminescent Zn(II) and Cu(I) Complexes, Ludwig-Maximilians University Munich, **2020**.
- [52] T. Steiner, *Angew. Chem.*, **2002**, *114*, 50–80; *Angew. Chem. Int. Ed.*, **2002**, *41*, 48–76.
- [53] C. Janiak, *Dalton Trans.* **2000**, 3885–3896.
- [54] W. B. Jennings, B. M. Farrell, J. F. Malone, *Acc. Chem. Res.* **2001**, *34*, 885–894.
- [55] M. J. Turner, J. J. McKinnon, S. K. Wolff, D. J. Grimwood, P. R. Spackman, D. Jayatilaka, M. A. Spackman, *CrystalExplorer17*, University of Western Australia, Australia, **2017**.

2.7.5. Supporting information

2.7.5.1. Synthesis of bis(picoyl)phenylphosphine zinc(II) chloride (**1**)

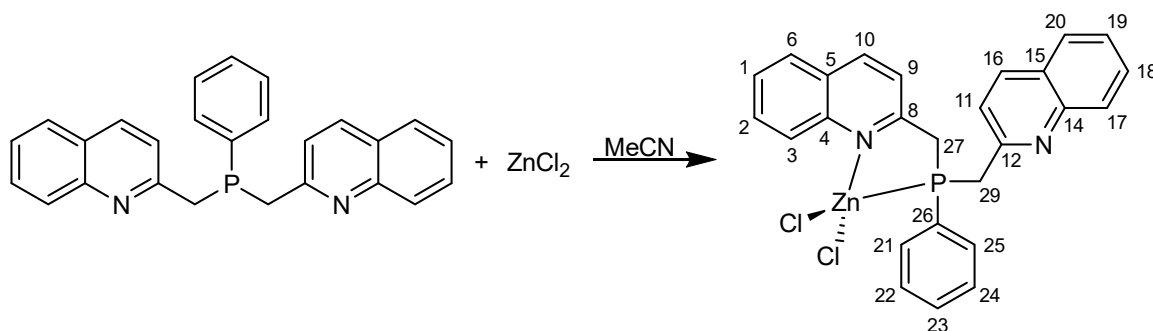


Bis(picoyl)phenylphosphine was synthesized according to the literature. The phosphine (15.0 mmol, 4.38 g) was dissolved in dry, degassed acetonitrile and added *via* a cannula to the stoichiometric amount of dry ZnCl₂ (15.0 mmol, 2.04 g). After stirring for 12 h at RT, all volatiles were removed under vacuum and compound **1** was received as a colorless solid (5.34g, 12.5 mmol, 83%). Crystals of **1** were received by diffusion of diethyl ether into a solution of **1** in acetonitrile. m.p.: 217°C

Elemental Anal. calcd. C₁₈H₁₇Cl₂N₂PZn, C: 50.44, H: 4.00, N: 6.54 %; found: C: 48.54, H: 3.79 N: 6.45 % (carbon differs due to (P₂O₅)_x(H₂O)_yC-formation); ³¹P{¹H} [CDCl₃, 161.976 MHz] δ = -9.1 (s) ppm; ³¹P [CDCl₃, 161.976 MHz] δ = -9.1 (q, ²J_{P-H} = 6.3 Hz) ppm; ³¹P{¹H} [CD₂Cl₂, 161.976 MHz] δ = -9.3 (s) ppm; ³¹P [CD₂Cl₂, 161.976 MHz] δ = -9.3 (s) ppm; ¹⁵N [CDCl₃, *via* ¹H¹⁵N HMBC, 40.5371 MHz] = -141.7 (s) ppm; ¹⁵N [CD₂Cl₂, *via* ¹H¹⁵N HMBC, 40.5371 MHz] = -141.0 (s) ppm; ¹H [CDCl₃, 400.133 MHz] δ = ABX spin system (A = B = H, X = P) 3.30 (d, ²J_{A-B} = 10.9 Hz, ²J_{A-X} = 2.9 Hz; 2H, H7, H9), 3.41 (d, ²J_{A-B} = 10.9 Hz, 2H, H7, H9), 6.87 (s, 2H; H5, H16), 6.98 (t, 2 H, ³J_{H-H} = 7.3; H17, H21), 7.26 (m, 2 H, ³J_{H-H} = 6.7, 5.0 Hz; H18, H20), 7.35 (t, ³J_{H-H} = 7.2; 1H, H19), 7.42 (t, ³J_{H-H} = 6.5 Hz; 2 H, H1, H14), 7.69 (s, 2H, H6, H15), 9.10 (d, ³J_{H-H} = 5.0 Hz, 2 H, H2, H13) ppm; ¹H [CD₂Cl₂, 400.133 MHz] δ = ABX spin system (A = B = H, X = P) 3.32 (d, ²J_{A-B} = 13.7 Hz, ²J_{A-X} = 4.2 Hz; 2H, H7, H9), 3.42 (d, ²J_{A-B} = 10.9 Hz, 2H, H7, H9), 6.91 (s, 2H; H5, H16), 7.02 (t, 2 H, ³J_{H-H} = 7.05, ³J_{H-H} = 1.3 Hz; H17, H21), 7.29 (tq, 2 H, ³J_{H-H} = 7.1, ³J_{H-H} = 1.4 Hz; H18,

H20), 7.38 (tq, $^3J_{\text{H-H}} = 6.6$, $^3J_{\text{H-H}} = 1.2$ Hz; 1H, H19), 7.45 (t, $^3J_{\text{H-H}} = 6.6$ Hz; 2 H, H1, H14), 7.73 (t, $^3J_{\text{H-H}} = 6.8$ Hz, 2H, H6, H15), 9.04 (d, $^3J_{\text{H-H}} = 5.6$ Hz, $^3J_{\text{H-H}} = 0.9$ Hz, 2H, H2, H13) ppm; ^1H [CD₂Cl₂, 400.133 MHz, -80°C] $\delta =$ ABX spin system (A = B = H, X = P) 3.22 (dd, $^2J_{\text{A-B}} = 10.8$ Hz, $^2J_{\text{A-X}} = 3.1$ Hz; 2H, H7', H9'), 3.34 (m, $^2J_{\text{A-B}} = 13.2$ Hz, $^2J_{\text{B-X}} = 6.6$ Hz, 2H, H7, H9), 6.05 (d, $^3J_{\text{H-H}} = 7.8$; 2H; H5, H16), 6.90 (s; 2 H, H5', H15'), 7.24 (t, $^3J_{\text{H-H}} = 7.5$; 2H, H18, H20), 7.34 (dd, $^3J_{\text{H-H}} = 6.9$, $^3J_{\text{H-H}} = 5.2$ Hz; 1H, H1, H14), 7.41 (td, $^3J_{\text{H-H}} = 7.7$ Hz; 2H, H6, H15), 7.55 (dd, $^3J_{\text{H-H}} = 7.3$ Hz, $^3J_{\text{H-H}} = 6.8$ Hz; 2H, H1', H14'), 8.00 (t, $^3J_{\text{H-H}} = 7.8$ Hz; 2H, H6', H15'), 8.79 (d, $^3J_{\text{H-H}} = 5.7$ Hz, 2H, H2', H13'), 8.99 (d, $^3J_{\text{H-H}} = 5.6$ Hz, 2H, H2, H13) ppm; $^{13}\text{C}\{^1\text{H}\}$ [CDCl₃, 100.623 MHz] $\delta =$ 32.5 (d, $^1J_{\text{C-P}} = 26.1$ Hz, C7, C9), 123.0 (s; C1, C14), 126.5 (d, $^2J_{\text{C-P}} = 2.7$ Hz, C5, C16), 129.0 (d, $^4J_{\text{C-P}} = 6.9$ Hz, C18, C20), 130.4 (s; C19), 132.2 (d, $^3J_{\text{C-P}} = 20.4$ Hz, C17, C21), 132.8 (d, $^1J_{\text{C-P}} = 17.4$ Hz, C11), 140.2 (s, C6, C15), 149.8 (s, C2, C13), 156.8 (s, C4, C10) ppm; $^{13}\text{C}\{^1\text{H}\}$ [CD₂Cl₂, 100.623 MHz] $\delta =$ 32.7 (d, $^1J_{\text{C-P}} = 26.4$ Hz, C7, C9), 123.3 (d, $^2J_{\text{C-P}} = 1.1$ Hz; C1, C14), 126.8 (d, $^2J_{\text{C-P}} = 2.7$ Hz, C5, C16), 129.2 (d, $^4J_{\text{C-P}} = 6.9$ Hz, C18, C20), 130.5 (s, C19), 132.2 (d, $^3J_{\text{C-P}} = 20.4$ Hz, C17, C21), 133.4 (s; C11), 140.6 (s, C6, C15), 149.7 (s, C2, C13), 157.2 (s, C4, C10) ppm, $^{13}\text{C}\{^1\text{H}\}$ [CD₂Cl₂, 100.623 MHz, -80°C] $\delta =$ 29.7 (d, $^4J_{\text{C-P}} = 19.8$ Hz, C7, C9), 32.5 (d, $^1J_{\text{C-P}} = 32.1$ Hz, C7', C9'), 122.1 (s, C11), 123.1 (s, C1, C14), 125.7 (s; C5, C16), 126.3 (d, $^4J_{\text{C-P}} = 3.6$ Hz, C19), 128.2 (d, $^3J_{\text{C-P}} = 8.2$ Hz, C18, C20), 129.6 (s, C1', C14'), 131.2 (d, $^4J_{\text{C-P}} = 17.0$ Hz, C5', C16'), 131.8 (d, $^2J_{\text{C-P}} = 17.8$ Hz, C17, C21), 139.3 (s, C6, C15), 141.0 (s, C6', C15'), 148.0 (s, C2, C13), 148.6 (s, C2', C13'), 154.2 (d, $^4J_{\text{C-P}} = 6.0$ Hz, C4, C10), 157.0 (d, $^4J_{\text{C-P}} = 13.4$ Hz, C4', C10') ppm; **IR**: $\tilde{\nu}_{\text{max}}$ (cm⁻¹) = 3075 (vw), 3032 (vw), 1606 (vs), 1569 (m), 1482 (vs), 1435 (vs), 1313 (m), 1242 (m), 1185 (w), 1163 (s), 1130 (m), 1070 (m), 1060 (m), 1025 (s), 998 (w), 864 (m), 825 (m), 799 (vs), 776 (s), 760 (m), 744 (vs), 694 (vs), 648 (m), 591 (m), 501 (m), 489 (m), 479 (m), 420 (m).

2.7.5.2. Synthesis of bis(quinaldinyl)phenylphosphine zinc(II) chloride (**2**)

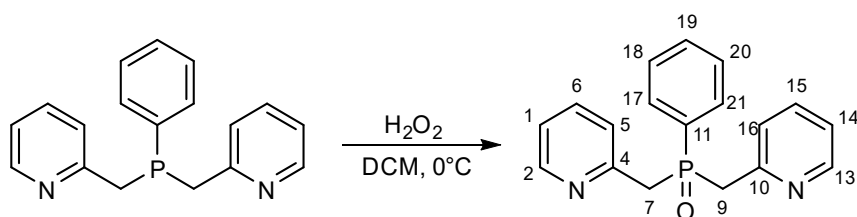


To a solution of 2-((trimethylsilyl)methyl)quinoline (32.0 mmol) in dry THF at 0 °C, dichlorophenylphosphine (15.0 mmol) was added dropwise and further stirred for 18 hours. The color of the solution changes from yellow to orange. The reaction mixture was stripped off of its solvent under vacuum and heated to 80 °C to remove excess 2-((trimethylsilyl)methyl)quinoline. The resulting bis(quinaldinyl)phenylphosphine (^{31}P NMR at -13.9 ppm) was taken as is and dissolved in dry, degassed acetonitrile. The solution was transferred *via* cannula to a stoichiometric amount of ZnCl₂ (15.0 mmol, 2.04 g) in an extra flask and further stirred for eight hours. Crystals were received by diffusion of diethyl ether into a solution of **2** in acetonitrile. After removal of all volatiles, a light-yellow powder of **2** remained (12.9 mmol, 6.65 g, 86%).

Elemental Anal. calcd. C₂₆H₂₁Cl₂N₂PZn, C: 59.06, H: 4.00; N: 5.30 % found: C: 58.81, H: 3.75, N: 5.38 %; $^{31}\text{P}\{^1\text{H}\}$ [CDCl₃, 161.976 MHz] $\delta = -22.3$ (s) ppm; $^{31}\text{P}\{^1\text{H}\}$ [CD₂Cl₂, 161.976 MHz] $\delta = -23.2$ (s) ppm; ^1H [CDCl₃, 400.133 MHz] $\delta =$ 8.32 (d, 2H, $J = 8.6$ Hz), 7.93 (dd, 2H), 7.82 (d, 2H, $^3J_{\text{H-H}} = 8.4$ Hz), 7.75 (ddd, 2H, $^3J_{\text{H-H}} = 8.5$ Hz, $^3J_{\text{H-H}} = 6.8$ Hz, $^4J_{\text{H-H}} = 1.6$ Hz), 7.58 (dd, 2H, $^3J_{\text{H-H}} = 7.9$ Hz), 7.55-7.40 (m, 5H), 7.29 (d, 2H, $^3J_{\text{H-H}} = 8.5$ Hz), ABX spin system (A = B = H, X = P) 4.09 (dd, 2H, $^2J_{\text{A-X}} = 9.9$ Hz, $^2J_{\text{A-B}} = 15.2$ Hz), 3.90 (dd, 2H, $^2J_{\text{A-B}} = 15.1$, $^2J_{\text{B-X}} = 5.6$ Hz) ppm; ^1H [CD₂Cl₂, 400.133 MHz] $\delta =$ 8.27 (d, 2H, H3, H17, $^3J_{\text{H-H}} = 8.6$ Hz), 7.95 (d, 2H, H10, H16, $^3J_{\text{H-H}} = 8.5$ Hz), 7.91 (d, 2H, H9, H11, $^3J_{\text{H-H}} = 7.2$ Hz), 7.75 (ddd, 2H, H2, H18, $^3J_{\text{H-H}} = 8.5$ Hz, $^3J_{\text{H-H}} = 6.9$ Hz, $^4J_{\text{H-H}} = 1.5$ Hz), 7.68 (dd, 2H, H6, H20, $^3J_{\text{H-H}} = 8.1$ Hz), 7.53-7.41 (m, 5H, H1,

H19, H22, H24, H23), 7.32 (d, 2H, H10, H16, $^3J_{\text{H-H}} = 8.4$ Hz), ABX spin system (A = B = H, X = P) 4.11 (dd, 2H, H27, H29, $^2J_{\text{A-X}} = 9.5$ Hz, $^2J_{\text{A-B}} = 15.4$ Hz), 3.92 (dd, 2H, H27, H29, $^1J_{\text{A-B}} = 15.4$, $^2J_{\text{B-X}} = 6.3$ Hz) ppm; ^1H [CD_2Cl_2 , 400.133 MHz, -80°C] $\delta = 8.01$ (d, 2H, H3, H17, $^3J_{\text{H-H}} = 8.5$ Hz), 7.90 (m, 2H, H21, H25, $^3J_{\text{H-H}} = 8.5$ Hz), 7.64 (t, 2H, H2, H18, $^3J_{\text{H-H}} = 7.4$ Hz), 7.58 (d, 2H, H6, H16, $^3J_{\text{H-H}} = 8.1$ Hz), 7.53 (d, 1H, H23, $^3J_{\text{H-H}} = 7.4$ Hz), 7.48 (t, 2H, H22, H24, $^3J_{\text{H-H}} = 7.5$ Hz), 7.41 (t, 2H, H1, H19, $^3J_{\text{H-H}} = 7.7$ Hz), 7.22 (d, 2H, H9, H11, $^3J_{\text{H-H}} = 8.4$ Hz) ABX spin system (A = B = H, X = P) 4.08 (dd, 2H, H27, H29, $^2J_{\text{A-X}} = 2.9$ Hz, $^2J_{\text{A-B}} = 14.9$ Hz), 3.87 (dd, 2H, H27, H29, $^2J_{\text{A-B}} = 15.7$, $^2J_{\text{B-X}} = 6.1$ Hz) ppm; $^{13}\text{C}\{^1\text{H}\}$ [CDCl_3 , 100.623 MHz] $\delta = 155.1$ (s), 146.4 (s), 138.7 (s), 133.7 (d, $J_{\text{C-P}} = 14.3$ Hz), 132.4 (d, $J_{\text{C-P}} = 2.3$ Hz), 131.1 (s), 129.7 (d, $J_{\text{C-P}} = 10.8$ Hz), 128.2 (s), 127.8 (s), 127.3 (s), 127.2 (d, $J_{\text{C-P}} = 1.9$ Hz), 122.8 (d, $J_{\text{C-P}} = 3.9$ Hz), 34.3 (d, $J_{\text{C-P}} = 12.7$ Hz) ppm; $^{13}\text{C}\{^1\text{H}\}$ [CD_2Cl_2 , 100.623 MHz] $\delta = 155.7$ (s, C8, C12), 146.6 (s, C4, C15), 139.1 (s, C10, C16), 133.9 (d, C21, C25, $^2J_{\text{C-P}} = 13.9$ Hz), 132.5 (d, C23, $^4J_{\text{C-P}} = 2.3$ Hz), 131.2 (s, C2, C18), 129.7 (d, C22, C24, $^3J_{\text{C-P}} = 10.4$ Hz), 128.2 (s, C6, C20), 128.2 (s, C3, C17), 127.6 (d, C5, C15, $^5J_{\text{C-P}} = 2.3$ Hz), 127.5 (s, C1, C19), 126.2 (s, C26), 123.1 (d, C9, C11, $^3J_{\text{C-P}} = 3.9$ Hz), 34.5 (d, C27, C29, $^1J_{\text{C-P}} = 16.6$ Hz) ppm; $^{13}\text{C}\{^1\text{H}\}$ [CD_2Cl_2 , 100.623 MHz, -80°C] $\delta = 154.6$ (s, C8, C12), 144.8 (s, C4, C15), 138.2 (s, C10, C16), 133.9 (d, C21, C25, $^2J_{\text{C-P}} = 12.7$ Hz), 131.8 (s, C23), 130.3 (s, C2, C18), 128.8 (d, C22, C24, $^2J_{\text{C-P}} = 9.4$ Hz), 127.3 (s, C6, C20), 126.6 (s, C1, C19), 126.5 (s, C3, C17), 126.0 (d, C5, C15, $^2J_{\text{C-P}} = 2.2$ Hz), 124.5 (d, C26, $^1J_{\text{C-P}} = 36.1$ Hz), 122.2 (d, C9, C11, $^3J_{\text{C-P}} = 2.2$ Hz), 33.1 (d, C27, C29, $^1J_{\text{C-P}} = 19.4$ Hz) ppm; **IR**: $\tilde{\nu}_{\text{max}}$ (cm^{-1}) = 3056 (vw), 2954 (vw), 2912 (vw), 2880 (vw), 1619 (w), 1597 (m), 1566 (w), 1504 (m), 1431 (m), 1379 (w), 1354 (m), 1315 (m), 1281 (vw), 1246 (w), 1162 (w), 1136 (m), 1101 (m), 1027 (vw), 999 (vw), 972 (vw), 961 (w), 873 (m), 862 (m), 845 (s), 822 (m), 782 (m), 742 (vs), 713 (m), 694 (s), 633 (w), 618 (w), 559 (w), 536 (m), 504 (m), 479 (m), 422 (w).

2.7.5.3. Synthesis of bis(picoly)phenylphosphine oxide (3)

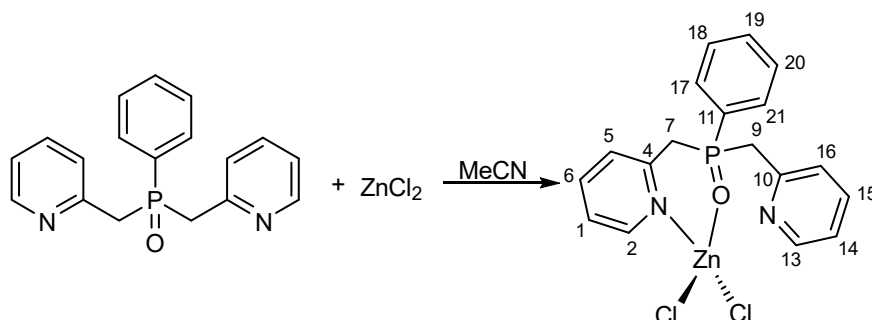


Bis(picoly)phenylphosphine (4.38 g, 15.0 mmol) is dissolved in 50 mL dichloromethane. Hydrogen peroxide (30 %, 4 mL in 5 mL water) is added dropwise to the mixture while cooling with an ice-bath. After stirring for four hours, the solvent was removed and the left-over oil dissolved in ethyl acetate. After extracting the ethyl acetate mixture three times with water, the combined water phases were extracted again three times with ethyl acetate. The combined organic phases were reduced under pressure. The left over solid was dissolved in dry THF and stirred with 4 Å mol sieves in a tea bag to remove any leftover hydrogen peroxide and water. Crystals were received by recrystallization from dichloromethane yielding 4.03 g (13.07 mmol, 87 %). m.p.: 117 °C.

Elemental Anal. calcd. $\text{C}_{18}\text{H}_{17}\text{Cl}_2\text{N}_2\text{OP}$, C: 70.12, H: 5.56, N: 9.09 %; found: C: 69.91, H: 5.32, N: 8.91 %; **ESI MS** (positive mode, $\text{MeCN}/\text{H}_2\text{O}$) m/z calcd for $\text{C}_{18}\text{H}_{17}\text{N}_2\text{OP}$ $[\text{M}+\text{H}]^+$: 309.1112 found 309.1149; $^{31}\text{P}\{^1\text{H}\}$ [CDCl_3 , 161.976 MHz] $\delta = 36.4$ (s) ppm; ^{31}P [CDCl_3 , 161.976 MHz] $\delta = 36.4$ (hept, $^3J_{\text{P-H}} = 14.1$ Hz) ppm; ^{15}N [CDCl_3 , *via* $^1\text{H}^{15}\text{N}$ HMBC, 40.5371 MHz] $\delta = -86.4$ (s) ppm; ^1H [CDCl_3 , 400.133 MHz] $\delta = 8.44$ (d, 2H, H2, H13, $^3J_{\text{H-H}} = 4.9, 0.9$ Hz), 7.57 (dd, 2H, H18, H20, $^3J_{\text{H-H}} = 7.8, 1.6$ Hz), 7.53 (t, 2H, H1, H14, $^3J_{\text{H-H}} = 7.5$ Hz), 7.43 (tq, 1H, H19, $^3J_{\text{H-H}} = 6.7, 1.4$ Hz), 7.33 (m, 2H, H17, H21, $^3J_{\text{H-H}} = 7.2, 1.0$ Hz), 7.28 (dd, 2H, H5, H16, $^3J_{\text{H-H}} = 7.9, 1.0$ Hz), 7.09 (tdd, 2H, H6, H15, $^3J_{\text{H-H}} = 7.7, 4.9, 1.2$ Hz), ABX spin system (A = B = H, X = P) 3.70 (dd, 2H, $^2J_{\text{A-B}} = 14.4$ Hz, $^2J_{\text{A-X}} = 2.1$ Hz) 3.69 (dd, 2H, $^2J_{\text{A-B}} = 15.1$ Hz, $^2J_{\text{B-X}} = 2.9$ Hz, H7, H9) ppm; $^{13}\text{C}\{^1\text{H}\}$ [CDCl_3 , 100.623 MHz] $\delta = 152.9$ (d, C4, C10, $^2J_{\text{C-P}} = 7.3$ Hz), 149.6 (d, C2, C13, $^4J_{\text{C-P}} = 2.0$ Hz), 136.6 (d, C1, C14, $^5J_{\text{C-P}} = 2.3$ Hz), 131.9 (d, C19, $^4J_{\text{C-P}} = 2.8$ Hz), 131.1 (d, C11, $^1J_{\text{C-P}} = 96.7$ Hz), 131.0 (d, C18, C20, $^3J_{\text{C-P}} = 8.9$ Hz), 128.4 (d, C17, C21, $^2J_{\text{C-P}} = 11.9$ Hz), 125.0 (d, C5, C16, $^3J_{\text{C-P}} = 4.2$ Hz), 121.9

(d, C6, C15, $^4J_{C-P} = 2.7$ Hz), 40.7 (d, C7, C9, $^1J_{C-P} = 61.7$ Hz) ppm; **IR**: $\tilde{\nu}_{\max}$ (cm $^{-1}$) = 3050 (w), 3006 (vw), 2955 (w), 2907 (vw), 1587 (m), 1568 (m), 1474 (m), 1435 (s), 1404 (m), 1315 (w), 1258 (m), 1186 (s), 1160 (m), 1139 (m), 1111 (m), 1089 (m), 1069 (m), 1048 (m), 1029 (w), 993 (m), 919 (w), 866 (m), 839 (s), 795 (s), 744 (s), 716 (s), 691 (vs), 628 (m), 604 (m), 590 (w), 508 (s), 497 (vs), 435 (m), 415 (w), 405 (w).

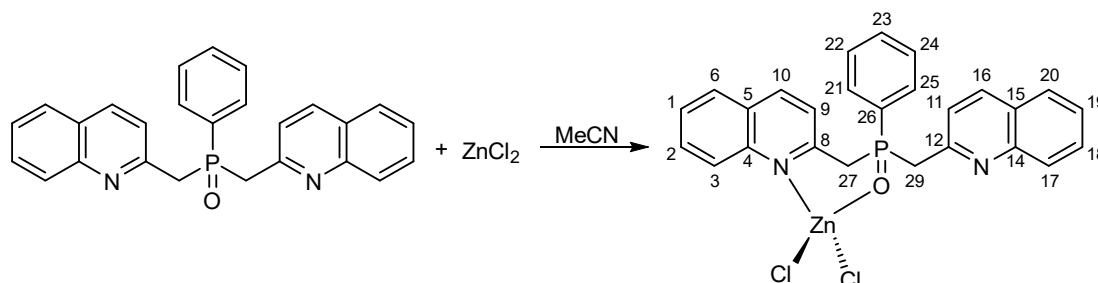
2.7.5.4. Synthesis of bis(picoly)phenylphosphine oxide zinc(II) chloride (**4**)



Bis(picoly)phenylphosphine oxide (0.802 g, 2.60 mmol) was dissolved in dry, degassed acetonitrile and transferred *via* a cannula to dry, solid ZnCl $_2$ (0.354 g, 2.60 mmol) in an extra Schlenk flask. The mixture was stirred for 12 hours at RT. After removal of all volatiles, **3** is received as a grey powder in high yields (0.940 g, 2.11 mmol, 81 %).

Elemental Anal. calcd. C $_{18}$ H $_{17}$ Cl $_2$ N $_2$ OPZn, C: 48.63, H: 3.85, N: 6.30 %; found: C: 47.42, H: 3.72, N: 6.07 % (carbon differs due to (P $_2$ O $_5$) $_x$ (H $_2$ O) $_y$ C-formation); **MALDI MS** (positive mode, sinapic acid) *m/z* calcd for C $_{18}$ H $_{17}$ Cl $_2$ N $_2$ OPZn [M-Cl $^-$] $^+$: 407.0058 found 407.57; $^{31}\text{P}\{^1\text{H}\}$ [CD $_2$ Cl $_2$, 161.976 MHz] $\delta = 48.3$ (s) ppm; ^1H [CD $_2$ Cl $_2$, 400.133 MHz] $\delta = 8.75$ (s, 2H, H2, H13), 7.74 (t, 2H, H1, H14, $^3J_{H-H} = 7.5$ Hz), 7.59 (m, 3H, H18, H19, H20), 7.47 (td, 2H, H17, H21, $^3J_{H-H} = 7.9$ Hz), 7.37 (t, 2H, H6, H14, $^3J_{H-H} = 6.2$ Hz), 7.25 (d, 2H, H5, H16, $^3J_{H-H} = 4.2$ Hz), ABX spin system (A = B = H, X = P) 4.08 (t, 2H, H7, H9, $^2J_{A-B} = 12.3$ Hz), 3.89 (t, 2H, H7, H9, $^2J_{A-B} = 15.8$ Hz) ppm; $^{13}\text{C}\{^1\text{H}\}$ [CD $_2$ Cl $_2$, 100.623 MHz] $\delta = 151.6$ (d, C4, C10, $^2J_{C-P} = 8.0$ Hz), 150.2 (d, C2, C13, $^4J_{C-P} = 2.0$ Hz), 139.8 (s, C1, C14), 133.9 (d, C19, $^4J_{C-P} = 3.1$ Hz), 131.0 (d, C18, C20, $^3J_{C-P} = 10.0$ Hz), 129.5 (d, C17, C21, $^2J_{C-P} = 12.6$ Hz), 128.3 (s, C11), 127.3 (s, C5, C16), 123.9 (d, C6, C15, $^4J_{C-P} = 2.2$ Hz), 38.4 (d, C7, C9, $^1J_{C-P} = 62.3$ Hz) ppm; **IR**: $\tilde{\nu}_{\max}$ (cm $^{-1}$) = 3065 (vw), 2952 (vw), 2896 (vw), 1606 (m), 1591 (m), 1570 (m), 1481 (m), 1436 (s), 1395 (w), 1318 (m), 1256 (w), 1202 (w), 1162 (m), 1129 (s), 1105 (s), 1085 (s), 1026 (w), 997 (w), 903 (vw), 844 (s), 817 (m), 748 (s), 723 (s), 692 (s), 646 (w), 614 (w), 597 (w), 508 (vs), 498 (vs), 455 (w), 421 (m).

2.7.5.5. Synthesis of bis(quinaldiny)phenylphosphine oxide zinc(II) chloride (**5**)



Bis(quinaldiny)phenylphosphine oxide (1.09 g, 2.67 mmol) was dissolved in dry, degassed acetonitrile and transferred *via* a cannula to dry, solid ZnCl $_2$ (0.364 g, 2.67 mmol) in an extra Schlenk flask. The mixture was stirred for 12 hours at RT. Crystals were received by diffusion of hexane into a solution of **4** in acetonitrile. After removal of all volatiles, **4** is received as a light beige powder in high yields (0.940 g, 2.30 mmol, 86 %). Compound **4** melts and decomposes starting at 220 °C.

Elemental Anal. calcd. C₂₆H₂₁Cl₂N₂OPZn, C: 57.33, H: 3.89, N: 5.14 %; found: C: 57.09, H: 3.65, N: 5.16 %; **MALDI MS** (positive mode, sinapic acid) m/z calcd for C₂₆H₂₁Cl₂N₂OPZn [M-Cl]⁺: 509.0340 found 509.66; ³¹P{¹H} [CD₂Cl₂, 161.976 MHz] δ = 46.9 (s) ppm; ¹H [CD₂Cl₂, 400.133 MHz] δ = 8.43 (d, 2H, H3, H17, ³J_{H-H} = 8.1 Hz), 7.95 (d, 2H, H10, H16, ³J_{H-H} = 8.4 Hz), 7.86 (dd, 2H, H21, H25, ³J_{H-H} = 12.1 Hz, ³J_{H-H} = 7.4 Hz), 7.79 (t, 2H, H2, H18, ³J_{H-H} = 7.3 Hz), 7.67 (d, 2H, H6, H20, ³J_{H-H} = 7.4 Hz), 7.62 (t, 1H, H23, ³J_{H-H} = 7.2 Hz), 7.54 (t, 2H, H1, H19), 7.52 (m, 2H, H21, H25, ³J_{H-H} = 7.3 Hz), 7.32 (d, 2H, H9, H11, ³J_{H-H} = 8.3 Hz), ABX spin system (A = B = H, X = P) 4.25 (dddd, 4H, H27, H29, ²J_{A-B} = 15.2 Hz, ²J_{A-B} = 15.9 Hz, ²J_{A-X} = 5.1 Hz) ppm; ¹³C{¹H} [CD₂Cl₂, 100.623 MHz] δ = 152.9 (d, C8, C12, ²J_{C-P} = 9.9 Hz), 147.0 (s, C4, C14), 139.3 (s, C10, C16), 134.1 (d, C23, ⁴J_{C-P} = 3.0 Hz), 131.4 (s, C2, C18), 131.3 (d, C22, C24, ³J_{C-P} = 10.4 Hz), 129.6 (d, C21, C25, ²J_{C-P} = 12.8 Hz), 128.3 (s, C6, C20, ⁶J_{C-P} = 0.7 Hz), 128.2 (s, C3, C17), 127.8 (s, C1, C19), 127.6 (d, C5, C15, ⁵J_{C-P} = 1.5 Hz), 127.2 (s, C26), 124.0 (d, C9, C11, ³J_{C-P} = 4.9 Hz), 39.7 (d, C27, C29, ¹J_{C-P} = 62.3 Hz) ppm; **IR:** $\tilde{\nu}_{\max}$ (cm⁻¹) = 3056 (vw), 2957 (vw), 2879 (vw), 1620 (w), 1598 (m), 1564 (w), 1502 (m), 1430 (m), 1420 (vw), 1378 (vw), 1356 (vw), 1314 (m); 1280 (w), 1263 (vw), 1246 (m), 1207 (w), 1185 (m), 1161 (m), 1125 (m), 1094 (s), 1027 (vw), 999 (vw), 958 (w), 957 (w), 868 (m), 844 (vs), 812 (w), 785 (w), 749 (vs), 712 (s), 693 (s), 656 (w), 639 (w), 617 (m), 559 (vs), 507 (m), 497 (m), 474 (s), 459 (m), 432 (m), 420 (m).

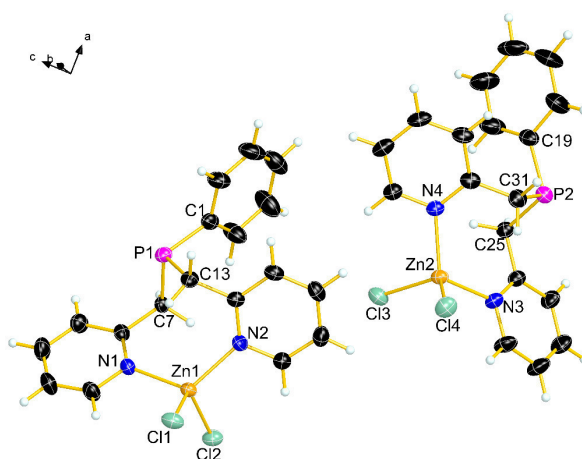


Figure 102. Molecular structure of the asymmetric unit of **1b** in the crystal. Thermal ellipsoids are drawn at 50 % probability level.

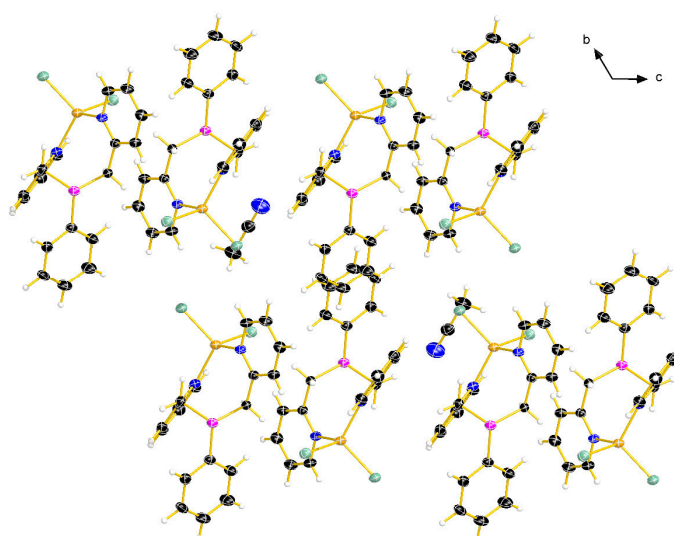


Figure 103. Packing of **1a** along the *a* axis visualizing the different π -stacking motifs in the 3D-structure. Thermal ellipsoids are drawn at 50 % probability level.

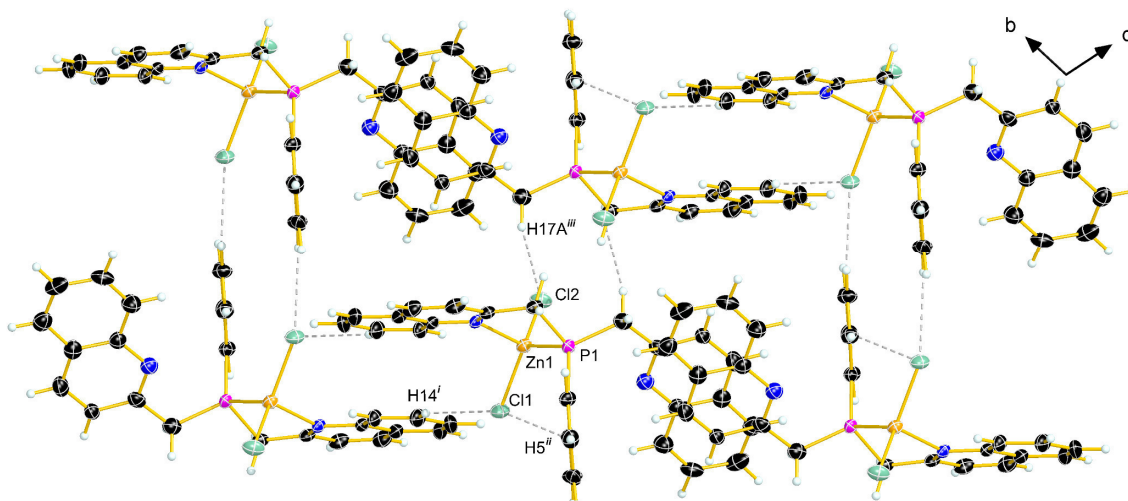


Figure 104. Packing of **2** along the *a* axis visualizing the alternating ZnCl_2 -molecules coordinating to the phosphine ligand, the non-classical hydrogen bonds and the π -stacking of the quinaldinyl rings. Thermal ellipsoids are drawn at 50 % probability level. Symmetry code: *i* = $-x, 1-y, -z$, *ii* = $1+x, y, z$, *iii* = $1-x, 1-y, 1-z$.

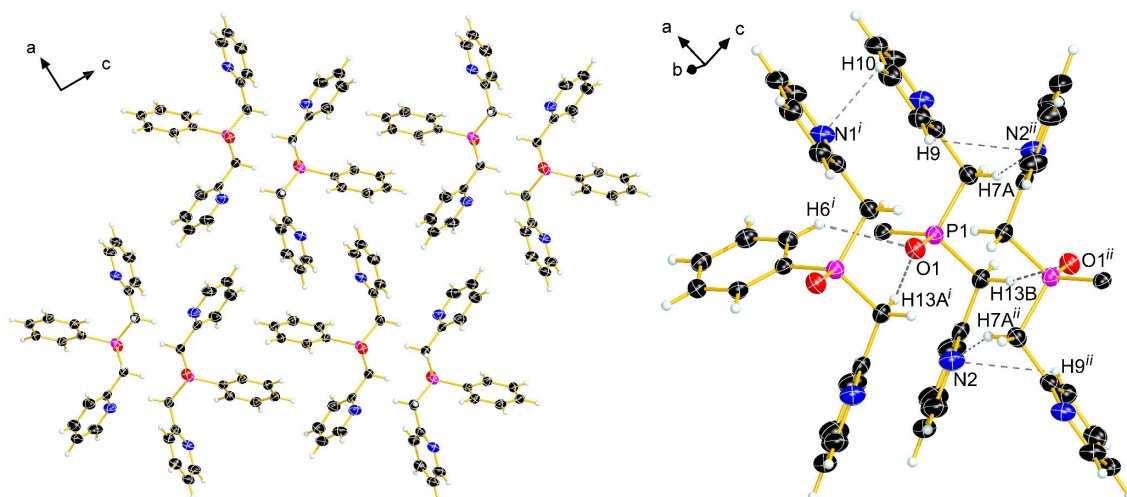


Figure 105. Visualization of the non-classical hydrogen bonds in the packing of **3**. Thermal ellipsoids are drawn at 50 % probability level. Symmetry code: (*i*) $x, 1+y, z$, (*ii*) $-x, 1-y, 1-z$.

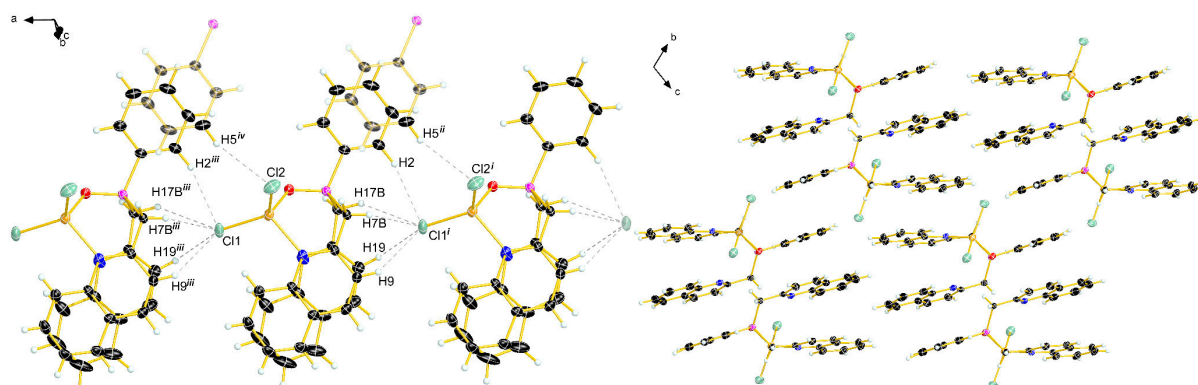


Figure 106. Visualization of the non-classical hydrogen bonds in the packing of **5** and the chainlike structure along the *c* axis (left). Packing of **5** along the *a* axis visualizing the alternating ZnCl_2 -molecules coordinating to the phosphine oxide ligand and the π -stacking of the aromatic rings (right). Thermal ellipsoids are drawn at 50 % probability level. Symmetry code: (*i*) $-1+x, y, z$; (*ii*) $-x, -y, -z$; (*iii*) $1+x, y, z$; (*iv*) $1-x, -y, -z$.

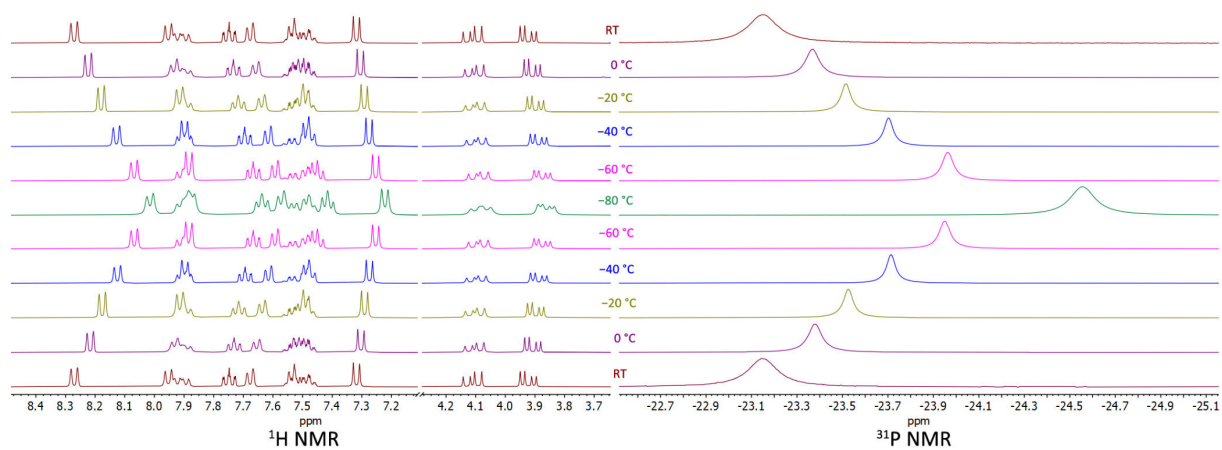


Figure 107. Variable temperature ^1H and ^{31}P NMR spectra of compound **2** in CD_2Cl_2 .

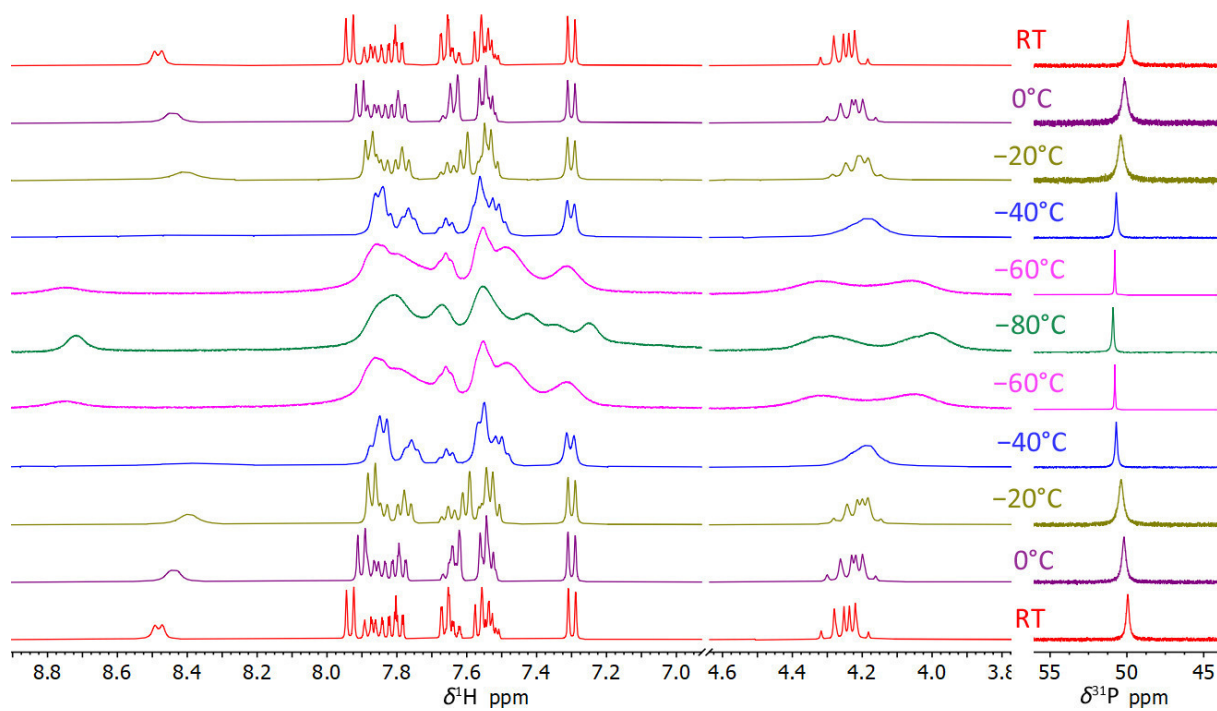


Figure 108. Variable temperature ^1H and ^{31}P NMR of compound **5** in CD_2Cl_2 .

2.7.5.6. Crystallographic data

Table 20. Crystallographic and refinement data for compounds **1a–2**.

	1a		1b		2
Formula	C ₂₀ H ₂₀ Cl ₂ N ₃ PZn		C ₁₈ H ₁₇ Cl ₂ N ₂ PZn		C ₂₆ H ₂₁ Cl ₂ N ₂ PZn
Formula weight	469.63		428.57		528.69
[g·mol ⁻¹]					
Color	colorless		colorless		colorless
Habit	block		block		block
<i>T</i> [K]	143		143		108
λ [Å]	0.71073		0.71073		0.71073
Crystal system	triclinic		triclinic		monoclinic
Space group	<i>P</i> -1		<i>P</i> -1		<i>P</i> -1
<i>a</i> [Å]	8.6426(6)		11.9745(4)		8.2394(4)
<i>b</i> [Å]	12.0128(7)		14.0085(6)		11.5981(6)
<i>c</i> [Å]	12.3376(8)		15.0123(6)		13.1577(7)
α [°]	117.731(6)		62.197(4)		101.470(4)
β [°]	100.957(6)		89.218(3)		103.047(4)
γ [°]	100.529(6)		73.498(3)		98.287(4)
<i>V</i> [Å ³]	1,057.53(13)		2,114.71(16)		1,176.68(11)
<i>Z</i>	2		4		2
ρ_{calc} [g·cm ⁻³]	1.475		1.346		1.492
μ [mm ⁻¹]	1.499		1.491		1.356
<i>F</i> (0 0 0)	480		872		540
Crystal size [mm]	0.20×0.20×0.15		0.39×0.33×0.20		0.30×0.10×0.05
θ range [°]	4.564–30.506		4.372–27.481		3.412–32.179
Index ranges	-12 ≤ <i>h</i> ≤ 10		-15 ≤ <i>h</i> ≤ 15		-12 ≤ <i>h</i> ≤ 12
	-17 ≤ <i>k</i> ≤ 17		-18 ≤ <i>k</i> ≤ 18		-17 ≤ <i>k</i> ≤ 16
	-17 ≤ <i>l</i> ≤ 17		-11 ≤ <i>l</i> ≤ 19		-19 ≤ <i>l</i> ≤ 19
reflns collected	11,207		18,591		13,518
Independent reflns	6,432 [<i>R</i> _{int} = 0.0355]		9,633 [<i>R</i> _{int} = 0.0279]		7,590 [<i>R</i> _{int} = 0.0517]
Completeness to theta	99.3 %		98.9 %		98.9 %
Refinement method	full-matrix	least-squares on <i>F</i> ²	full-matrix	least-squares on <i>F</i> ²	full-matrix least-squares on <i>F</i> ²
Data/restraints/Parameters	6,432 / 0 / 313		9,633 / 0 / 433		7,590 / 0 / 290
Hydrogen atom treatment	constrained		constrained		constrained
<i>R</i> ₁ / <i>wR</i> ₂ (<i>I</i> > 2 σ (<i>I</i>))	0.0440/0.0835		0.0423/0.1058		0.0696/0.1360
<i>R</i> ₁ / <i>wR</i> ₂ (all data)	0.0698/0.0978		0.0605/0.1167		0.1214/0.1624
Goodness-of-fit on <i>F</i> ²	1.033		1.045		1.045
larg. diff peak/hole [e·Å ⁻³]	0.694/-0.402		0.706/-0.458		1.337/-0.611
CCDC No.					

Table 21. Crystallographic and refinement data for compounds **3** and **4**.

	3	4
Formula	C ₁₈ H ₁₇ N ₂ OP	C ₂₆ H ₂₁ Cl ₂ N ₂ OPZn
Formula weight [g·mol ⁻¹]	308.30	544.69
Color	colorless	colorless
Habit	block	block
<i>T</i> [K]	143	143
λ [Å]	0.71073	0.71073
Crystal system	monoclinic	triclinic
Space group	<i>P</i> 2 ₁ / <i>n</i>	<i>P</i> -1
<i>a</i> [Å]	12.8032(14)	8.2177(4)
<i>b</i> [Å]	5.6866(6)	12.0807(6)
<i>c</i> [Å]	21.115(3)	13.2372(7)
α [°]	90	107.770(5)
β [°]	91.976(10)	94.562(4)
γ [°]	90	104.660(4)
<i>V</i> [Å ³]	1,536.4(3)	1,193.03(11)
<i>Z</i>	4	2
ρ_{calc} [g·cm ⁻³]	1.333	1.516
μ [mm ⁻¹]	0.182	1.343
<i>F</i> (0 0 0)	648	556
Crystal size [mm]	0.25×0.10×0.05	0.50×0.45×0.10
Θ range [°]	4.347–28.282	4.278–30.507
Index ranges	-16 ≤ <i>h</i> ≤ 17 -7 ≤ <i>k</i> ≤ 7 -28 ≤ <i>l</i> ≤ 26	-11 ≤ <i>h</i> ≤ 11 -17 ≤ <i>k</i> ≤ 17 -18 ≤ <i>l</i> ≤ 18
reflns collected	12,372	13,623
Independent reflns	3,799 [<i>R</i> _{int} = 0.0659]	7,244 [<i>R</i> _{int} = 0.0251]
Completeness to theta	99.2 %	99.3 %
Refinement method	full-matrix least-squares on <i>F</i> ²	full-matrix least-squares on <i>F</i> ²
Data/ restraints/ Parameters	3,799 / 0 / 199	7,244 / 0 / 382
Hydrogen atom treatment	constrained	constrained
<i>R</i> ₁ / <i>wR</i> ₂ (<i>I</i> > 2 σ (<i>I</i>))	0.0521/0.1173	0.0365/0.0778
<i>R</i> ₁ / <i>wR</i> ₂ (all data)	0.0788/0.1416	0.0510/0.0867
Goodness-of-fit on <i>F</i> ²	1.039	1.033
larg. diff peak/hole [e·Å ⁻³]	0.497/-0.358	0.527/-0.420
CCDC No.		

2.7.5.7. Electrochemical data

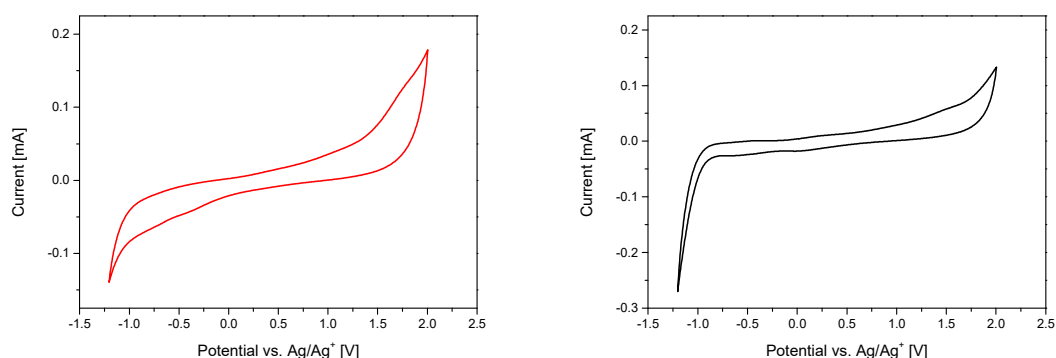


Figure 109. Cyclic voltammograms of complex **5** (red curve) and the ligand of **5** (black curves) recorded between 2 and (-1.2) V. The measurements were performed in a three-electrode cell using a Pt coil as working electrode, a glassy carbon counter electrode and an Ag wire as pseudo reference electrode at a scan rate of 50 mV s^{-1} .

2.7.5.8. Photophysical spectra

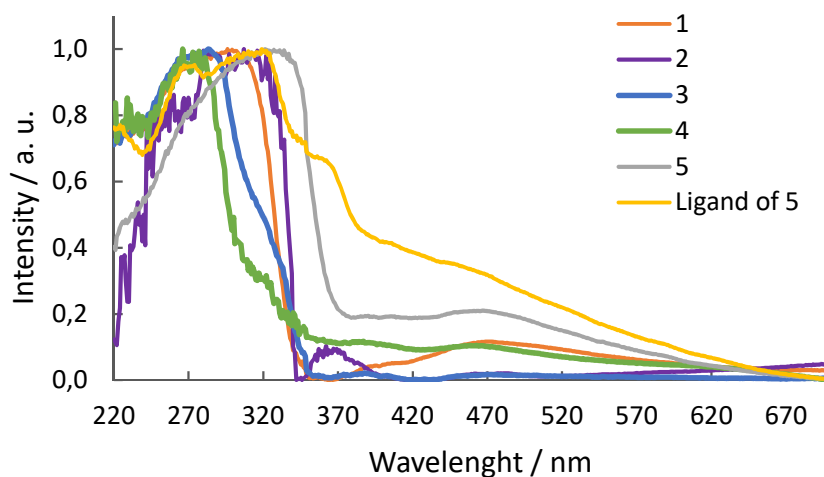


Figure 110. Solid-state UV Vis spectra of compounds **1-5** as well as the Ligand of **5**.

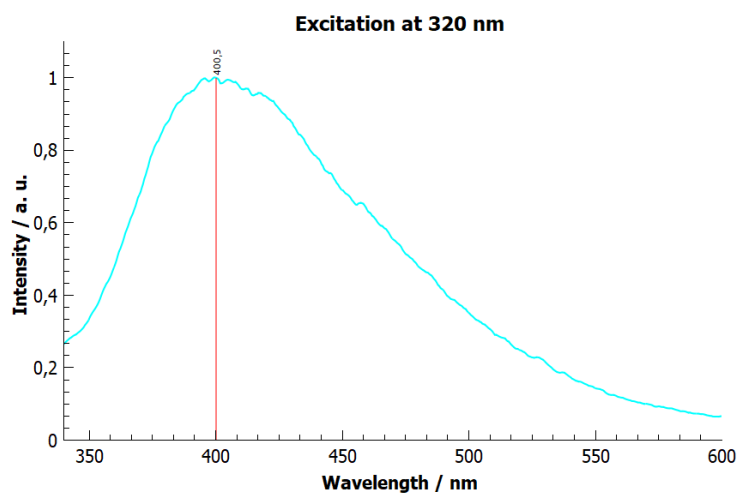


Figure 111. Emission spectrum of the ligand of **5**. The intensity is normalized to 1.

2.7.5.9. Computational details

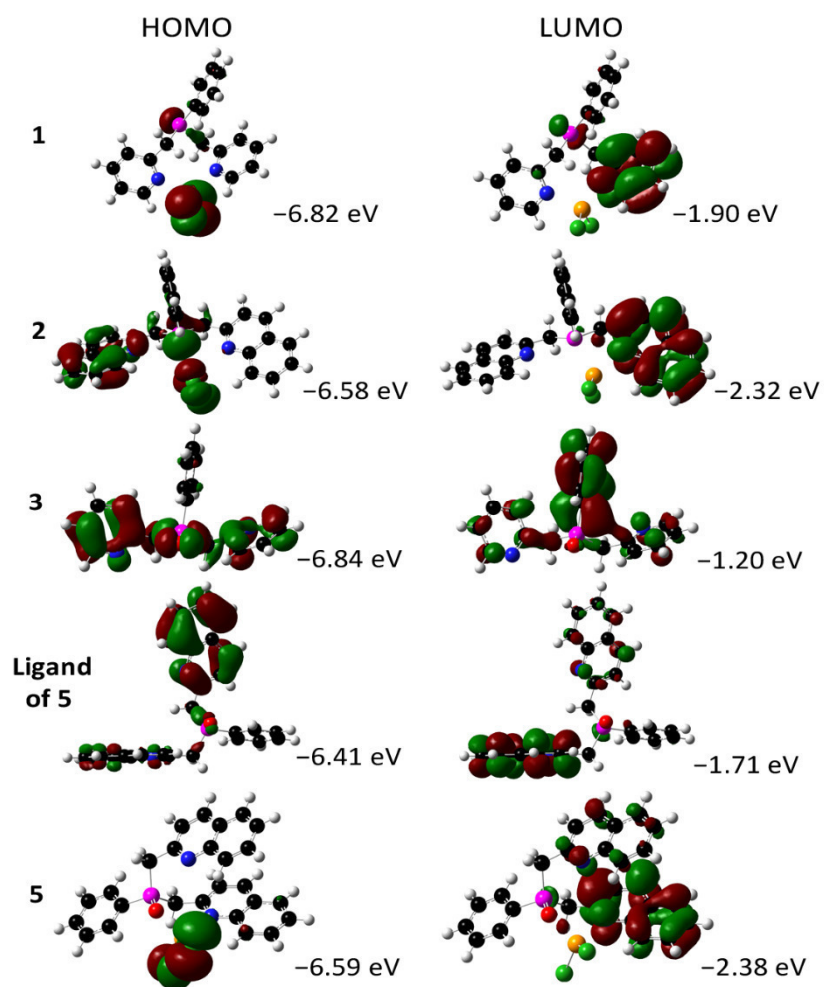


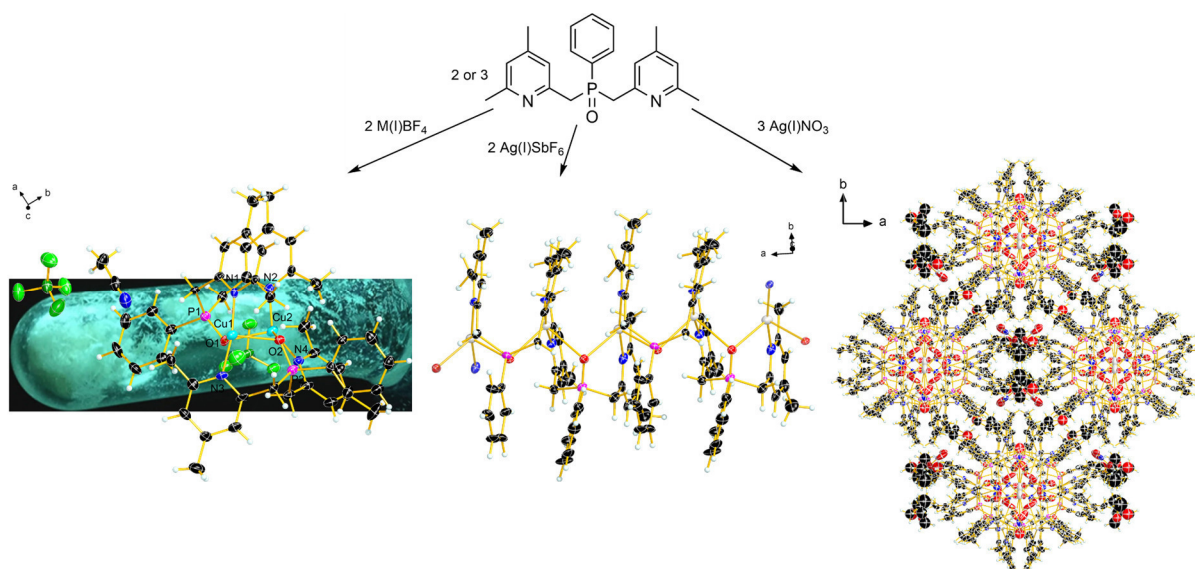
Figure 112. Visualization of the HOMO and LUMO of the optimized structures of compounds 1–5.

2.8. Structural diversity of a flexible, multidentate phosphine oxide ligand in Cu(I) and Ag(I) complexes

Christin Kirst, Jonathan Tietze, Manuel Gensler, Peter Mayer, Armin Wedel and Konstantin Karaghiosoff

to be submitted to *Dalton Transactions*

Christin Kirst synthesized the copper(I) compound and performed the single crystal X-ray measurements. She analyzed and evaluated the corresponding X-ray data and the NMR spectroscopy results in solution for this compound. She further managed the project and wrote the original draft of the manuscript, designed the TOC graphic and implemented the necessary corrections in the final version of the paper.



Abstract: Cu(I) and Ag(I) complexes with different anions of a sterically demanding though flexible bis(collidinyl)phenylphosphine oxide ligand have been synthesized and characterized. By changing the anion of the silver(I) salt, diverse coordination complexes are formed, as revealed by their single-crystal X-ray structures in the solid state. Structures ranging from dimers comparable to the copper(I) complex using the BF_4 anion, over 1D-coordination polymers utilizing the SbF_6 anion, to a remarkable cyclic hexamer when using the coordinating NO_3 anion are observed. The silver(I) complexes do not display any luminescent properties in the solid-state or solution when irradiated with UV light (366 nm). The copper(I) complex on the other hand shows a cyan luminescence at 492 nm in the solid state with a high photoluminescence quantum yield of 94 % under 350 nm illumination.

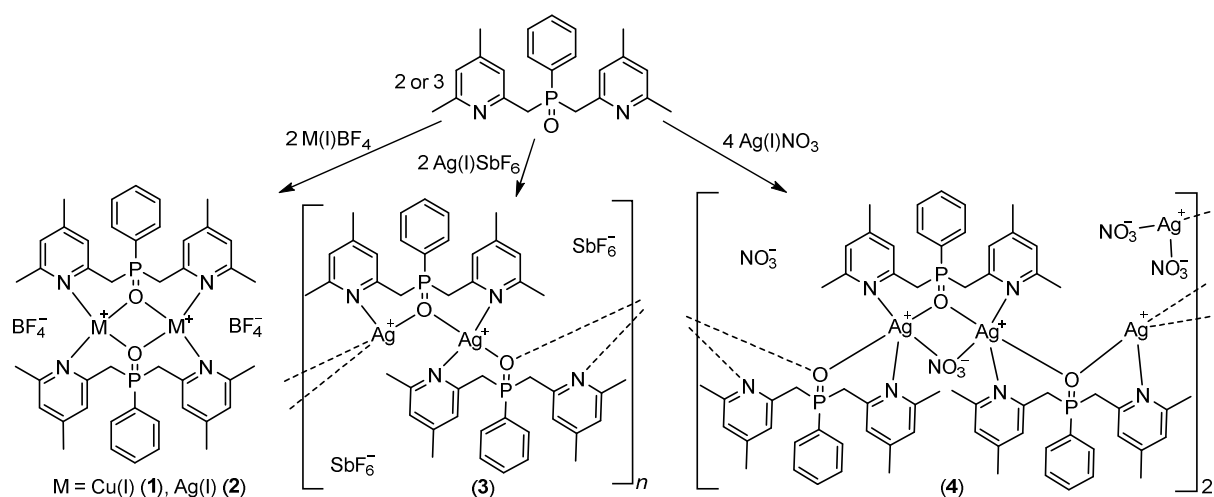
2.8.1. Introduction

The research field around functionalized phosphines substituted with nitrogen-containing aromatic systems is very competitive and still offers a lot of room for new possibilities. Ligands based on such phosphines are multidentate and thus offer multiple coordination sites for a wide range of metal atoms. Even the synthesis of coordination polymers is possible.^[1,2] Their application ranges from catalysis to functional materials, such as MOFs or possible emitters in OLEDs.^[3–9] By introduction of a methylene group between phosphorus and the nitrogen-containing heterocycle, the flexibility of the ligand is increased and unusual coordination geometries around the used metal ions are reached.^[10,11] We recently reported on the luminescent properties of bis(collidinyl)phenylphosphine oxide and zinc(II) complexes thereof. Now, we extended the used metal centre to other d^{10} metal ions, like copper(I) and silver(I). The group of A. Artem'ev have already published numerous results on copper(I) and silver(I) complexes of similar phosphine and phosphine oxide ligands in the past few years, including their luminescent properties.^[12–17] Consequently, we were curious, if we could observe similar properties for our ligand system with selected copper(I) and silver(I) salts and these results will be presented in the following.

2.8.2. Results and discussion

2.8.2.1. Synthesis.

The synthesis of the ligand is carried out according to our published procedure. For the synthesis of the copper(I) and silver(I) complexes, bis(collidinyl)phenylphosphine oxide is dissolved in dry, degassed acetonitrile and the resulting mixture transferred *via* a cannula to the respective amount of solid $\text{Cu}[\text{BF}_4]$, $\text{Ag}[\text{BF}_4]$, $\text{Ag}[\text{SbF}_6]$ or AgNO_3 under inert gas (Scheme 19). The complexes are isolated in high yields (>80 %) as colorless to light green powders. Compounds **1–4** are air-stable but not moisture-stable and should be stored under inert gas. The complexes are highly soluble in MeCN and THF, but only slightly soluble in CH_2Cl_2 and CHCl_3 .



Scheme 19. Synthesis of the complexes **1–4** including a visualization of the coordination modes in the products.

2.8.2.2. Crystal structures.

All crystal structures of the complexes **1–4** were determined *via* single-crystal x-ray diffraction and are shown in Figure 113–116 together with their respective bond lengths and angles. Crystallographic refinement data can be found in the ESI† (Table 23 and 24). In complexes **1** and **2**, the binuclear metal (Cu(I) and Ag(I)) unit is bridged by two bis(collidinyl)phenylphosphine oxide ligands. Complex **1a** crystallizes in the orthorhombic space group $Pca2_1$. One copper(I) atom (Cu1) is coordinated in a distorted disphenoidal geometry (see-saw geometry) by both oxygen (equatorial) and nitrogen atoms (axial) of the two ligands in the unit. The Cu2 atom is coordinated by both oxygen atoms and the nitrogen atoms of two opposite ligands in a distorted tetrahedral geometry. The four-membered Cu–O–Cu–O ring is not planar. The collidinyl-rings of one ligand are facing towards each other, indicating the presence of attractive, weak face-to-face π - π -interactions.^[18,19]

The collidinyl-rings of the other ligand in the unit are perpendicular to each other. Another polymorph of **1** is observed in crystals obtained by slow evaporation of **1** in MeCN. The polymorph **1b** crystallizes in the monoclinic space group $P2_1/c$ with four units in the unit cell. This structure also contains MeCN as co-crystallized solvent. The asymmetric unit shows little divergence when compared to **1a**, though the packing in the crystal is different (see Figure 119 and 120 of ESI†).

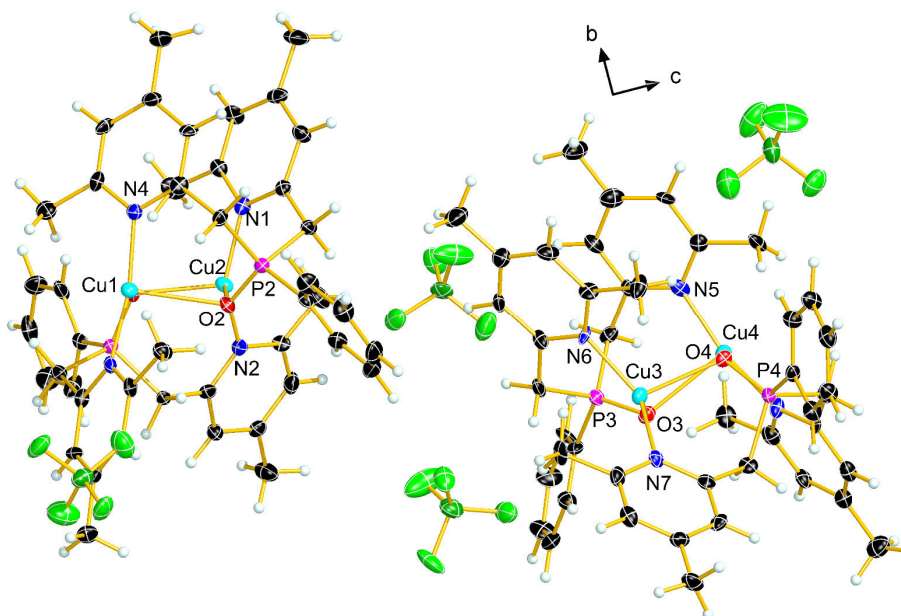


Figure 113. Solid-state molecular structure of complex **1a** in the crystal. Thermal ellipsoids are set to 50 % probability. Selected bond lengths [Å] and angles [°]: P1–O1 1.506(8), P1–C1 1.794(2), P1–C7 1.802(2), P1–C15 1.804(2), Cu1–O1 2.296(8), Cu2–O2 2.236(7), Cu1–N3 1.955(9), Cu1–N4 1.926(9), O1–P1–C1 112.2(5), O1–P1–C7 110.9(5), O1–P1–C15 111.5(5), O1–Cu1–O2 78.9(2), Cu1–O1–Cu2 98.5(3), N3–Cu1–N4 161.9(4), O1–Cu1–N3 101.1(3).

Complex **2** crystallizes in the triclinic space group $P-1$. The molecular structure of the asymmetric unit of **2** is shown in Figure 114; the packing of **2** in the crystal is visualized in the ESI† (Figure 121). Compound **2** forms, just like **1**, dimeric units in the crystal, but now both silver(I) ions are coordinated in a distorted disphenoidal geometry (see-saw geometry) by both oxygen (equatorial) and nitrogen atoms (axial) of two ligands. The four-membered Ag–O–Ag–O ring is planar, in contrast to **1**. The collidinyl-rings of one ligand are in both cases facing towards each other, indicating the presence of attractive, weak face-to-face π - π -interactions.^[18,19] In the crystal packing, the dimeric units of **2** form pillars along the *b* axis.

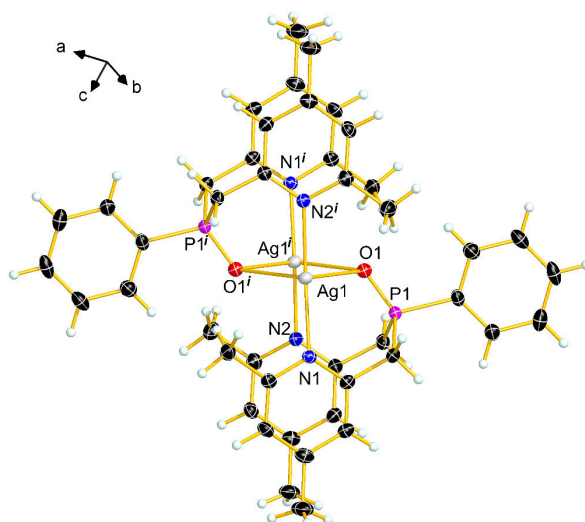


Figure 114. Solid-state molecular structure of complex **2** in the crystal. Thermal ellipsoids are set to 50 % probability. Anions are omitted for clarity. Selected bond lengths [Å] and angles [°]: P1–O1 1.498(2), P1–C1 1.806(3), P1–C7 1.818(3), P1–C15 1.816(3), Ag1–O1 2.565(2), Ag1–N1 2.222(2), O1–P1–C1 112.6(2), O1–P1–C7 112.6(2), O1–P1–C15 112.7(2), O1–Ag1–O1' 88.7(7), Ag1–O1–Ag1' 91.3(7), N1–Ag1–N2' 172.3(9), O1–Ag1–N1 90.1(8). Symmetry code: $i = 2-x, -y, -z$.

Complex **3** does not show a dimeric unit in the crystal like **1** and **2**, but forms a 1D-coordination polymer along the a axis. The complex crystallizes in the orthorhombic space group $P2_12_12_1$ with four units in the unit cell. The repeating unit is the asymmetric unit shown in Figure 115. The silver(I) atom is again coordinated in a distorted disphenoidal geometry (see-saw geometry) by both oxygen (equatorial) and nitrogen atoms (axial). It is noteworthy, that the Ag–N bond lengths (2.190 Å) are shorter than in **2** (2.222 Å), but the Ag–O bond lengths are similar to the ones in **2**. In the crystal packing, the collidinyl-rings of one ligand are facing towards each other with a slight offset, indicating the presence of attractive, weak face-to-face π - π -interactions (see also Figure 122 of ESI⁺).^[18,19] The phenyl rings of two neighboring ligands on the same side of the chain are π -stacking although slightly displaced with respect to each other.^[19] The size of the non-coordinating anion shows an influence on the coordination behavior and packing in the crystal. This effect is clearly visible in the crystal structures of complexes **2** and **3**.

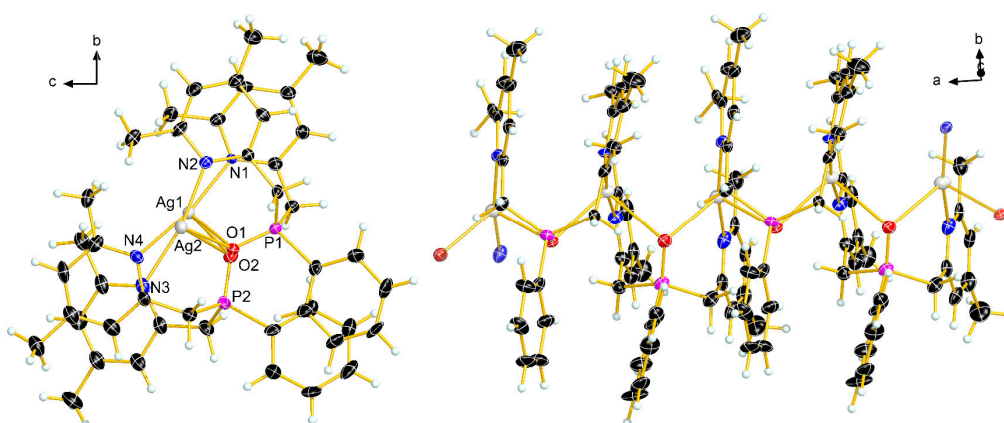


Figure 115. Solid state molecular structure of complex **3** in the crystal. Thermal ellipsoids are set to 50 % probability. Anions are omitted for clarity. Selected bond lengths [Å] and angles [°]: P1–O1 1.499(6), P1–C1 1.802(9), P1–C7 1.805(9), P1–C15 1.823(9), Ag1–O1 2.590(6), Ag1–N1 2.190(6), O1–P1–C1 111.5(4), O1–P1–C7 111.1(4), O1–P1–C15 111.7(4), O1–Ag1–O2 88.2(2), Ag1–O1–Ag2 92.0(2), N1–Ag1–N4 167.0(3), O1–Ag1–N1 91.9(2).

In contrast, using the NO_3^- anion, which more easily coordinates to silver(I), a new and unexpected structure of the respective complex **4** is obtained. Complex **4** crystallizes in the monoclinic space group $C2/c$ with four units in the unit cell. The structure of **4** in the crystal is shown in Figure 116. Compound **4** forms a hexamer that contains a 12-membered ring consisting of alternating silver and oxygen atoms. The ligands bridge each two silver atoms *via* oxygen of the phosphine oxide moiety and are arranged alternating above and below the 12-membered ring. Additional coordination of nitrogen of the collidinyl rings results in the formation of nearly spherical units. The cavity inside these units has a diameter of 6 Å and contains two nitrate anions. The six silver(I) atoms forming the hexamer are penta-coordinated by oxygen and nitrogen atoms of two neighboring ligands and the oxygen atom of one nitrate ion positioned inside the cavity. The Ag–O distances vary between 2.55 and 2.80 Å. The seventh silver(I) atom is coordinated by the oxygen atoms of three nitrate ions in a trigonal-planar arrangement and occupies the bottom of the hexamer (see Figure 116, middle). The observed structure is very rare and a similar arrangement has only been described for silver fulminate, where the 12-membered ring consists of alternating silver and carbon atoms.^[20]

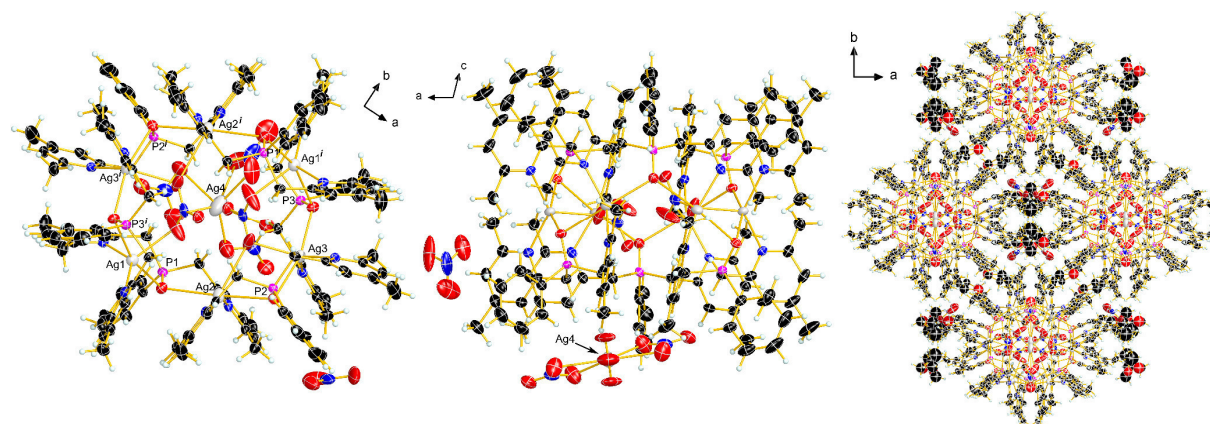


Figure 116. Solid-state molecular structure of complex **4** in the crystal. Thermal ellipsoids set to 50 % probability. Selected bond lengths [Å] and angles [°]: P1–O1 1.491(3), P1–C1 1.795(4), P1–C7 1.808(4), P1–C15 1.821(4), Ag1–O1 2.617(3), Ag1–N1 2.280(3), O1–P1–C1 111.8(2), O1–P1–C7 113.2(2), O1–P1–C15 114.5(2), O1–Ag1–O3^{*i*} 163.1(8), Ag1–O1–Ag2 108.4(9), Ag2–O6–Ag3 103.4(9), N1–Ag1–N6^{*i*} 133.3(2), O1–Ag1–N6^{*i*} 106.6(2). Symmetry code: $i = -x, 1-y, 1-z$.

2.8.2.3. Solution NMR.

Selected NMR data of the complexes are listed in Table 22. The chemical shifts in the ^{31}P NMR spectra of the complexes **1–4** show a shift to higher frequencies, when compared to the free ligand ($\delta^{31}\text{P} = 36.8$ ppm). The ^1H and ^{31}P NMR spectra of the silver complexes in CD_2Cl_2 show very broad signals. In $\text{MeCN-}d_3$ however, the ^1H NMR signals are sharp and easily distinguishable. The copper(I) complex **1** only shows a broad signal in the ^{31}P NMR, the signals in the ^1H NMR are reasonably sharp, nevertheless indicating possible dynamics in solution. In the ^1H NMR of all complexes, the typical AB part of an ABX spin system is visible for the diastereotopic methylene protons (see Figure 117 for an example). Variable temperature NMR of the silver(I) complexes **2** and **3** in CD_2Cl_2 suggest a possible dynamic behaviour in solution. When lowering the temperature to -80°C , the signal in the ^{31}P NMR of **2** is split into three major signals with a ratio of 2:2:1. In the case of **3**, three main signals together with other signals with low intensity are observed at -80°C . Moreover, in the ^1H NMR of **2** and **3**, new signals appear in the methylene and aromatic region. This phenomenon is completely reversed when raising the temperature to RT again in all cases. We suggest this phenomenon to be similar to the dynamics observed for copper(I) and silver(I) complexes of bis(quinaldinyl)phenyl phosphine oxide.^[11] Due to the

flexibility of the ligand, different coordination motifs are in equilibrium at RT in solution. When lowering the temperature and slowing down all movements, certain motifs are preferred and selected phosphorus environments are formed, which results in different chemical shifts in the ^{31}P NMR.

Table 22. Selected NMR details of the complexes **1–4** at RT. Chemical shifts δ in ppm and in reference to CDCl_3 for **1** and $\text{MeCN-}d_3$ for **2–4**, coupling constants are in Hz.

	1	2	3	4
$^{31}\text{P}\{^1\text{H}\}$	44.4	38.6	37.7	38.5
^1H (CH_2)	4.23 (dd, $^2J_{\text{HH}} = ^2J_{\text{HP}} = 13.1$), 3.74 (dd, $^2J_{\text{HH}} = ^2J_{\text{HP}} = 16.2$)	3.91 (dd, $^2J_{\text{HH}} = ^2J_{\text{HP}} = 14.4$), 3.88 (dd, $^2J_{\text{HH}} = ^2J_{\text{HP}} = 14.3$)	3.86 (dd, $^2J_{\text{HH}} = ^2J_{\text{HP}} = 14.4$), 3.85 (dd, $^2J_{\text{HH}} = ^2J_{\text{HP}} = 14.5$)	3.96 (dd, $^2J_{\text{HH}} = ^2J_{\text{HP}} = 14.5$), 3.94 (dd, $^2J_{\text{HH}} = ^2J_{\text{HP}} = 14.3$)

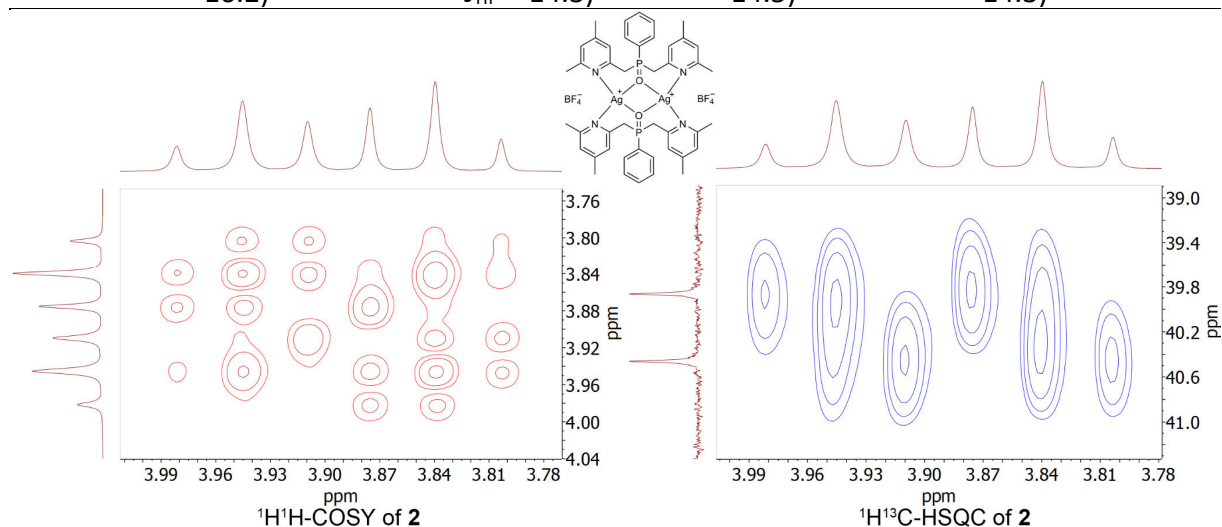


Figure 117. $^1\text{H}^1\text{H}$ -COSY and $^1\text{H}^{13}\text{C}$ -HSQC of complex **2** in $\text{MeCN-}d_3$ highlighting the methylene group and the resulting AB part of an ABX spin system.

2.8.2.4. Photophysical data

Compound **1** exhibits a bright cyan photoluminescence at 492 nm with a Full Width at Half Maximum (FWHM) of 103 nm (Figure 118). The photoluminescence quantum yield (PLQY) is 94 %. For the silver complexes **2–4**, no luminescence was observed under these conditions.

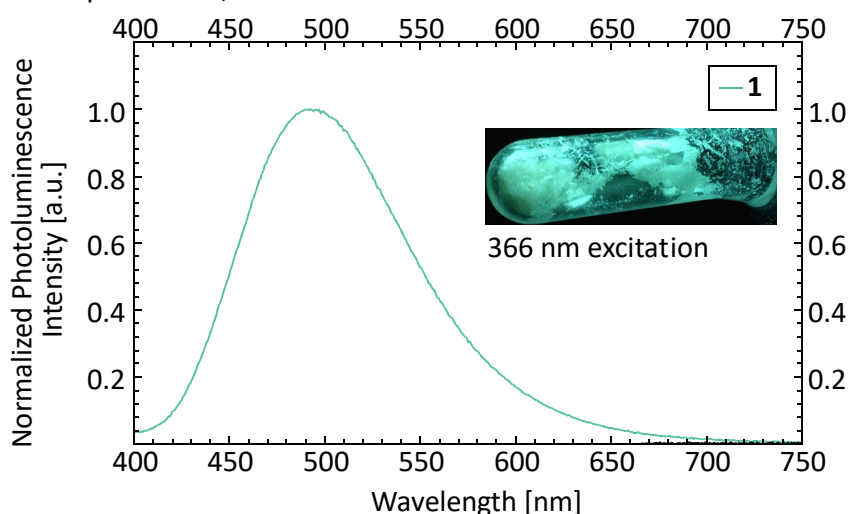


Figure 118. Photoluminescence spectrum of **1** at 350 nm illumination, normalized to 1, and a photo of the powder under 366 nm UV illumination.

2.8.3. Conclusions

Bis(collidinyl)phenylphosphine oxide is a versatile ligand, which is shown by the different solid-state crystal structures of the silver(I) complexes with two different non-coordinating (BF_4^- , SbF_6^-) and one coordinating anion (NO_3^-). The copper(I) complex shows a slightly different coordination motif when compared to the silver(I) complexes. All complexes show dynamic behaviour in solution, which is most likely comparable to previously published results from our group concerning copper(I) and silver(I) complexes of bis(quinaldinyl)phenyl phosphine oxide.

The copper(I) complex shows luminescence at 492 nm in solid-state when irradiated with UV light (350 nm) with high quantum yield (94 %). The combined results show that phosphine oxides with functionalized substituents can be promising building blocks of luminescent materials in copper(I) complexes.

2.8.4. Experimental

2.8.4.1. General information

All compounds were handled using Schlenk techniques under dry Ar. Unless stated otherwise, all reagents and solvents were bought from commercial sources and used as received. The solvents dichloromethane, acetonitrile and diethyl ether were dried, freshly distilled and degassed prior to use. Calcium hydride was used as drying agent for dichloromethane, SICAPENT[®] was used for acetonitrile, and sodium for diethyl ether. The deuterated solvents CDCl_3 and $\text{MeCN-}d_3$ were distilled and stored under Ar atmosphere over molecular sieves. NMR spectra were recorded with a Bruker Avance III spectrometer. Chemical shifts are referred to TMS (^1H , ^{13}C), 85% H_3PO_4 (^{31}P), MeNO_2 (^{15}N), CCl_3F (^{19}F) and $\text{BF}_3 \cdot \text{Et}_2\text{O}$ (^{11}B) as external standards. The assignment of the signals is based on 2D (^1H , ^1H -COSY, ^1H , ^{13}C -HSQC and ^1H , ^{13}C -HMBC) experiments. Values of coupling constants (J) are given in Hertz (Hz). The multiplicity of each resonance observed in the NMR spectra is reported as s = singlet; d = doublet; t = triplet; q = quartet; m = multiplet. Infrared spectroscopy data was collected using a Smith DuraSampLIR II ATR device equipped with a Perkin Elmer BX II FT-IR System spectrometer. MALDI measurements were done on a Bruker Daltonics Autoflex II mass spectrometer using a nitrogen-cartridge-laser with 337 nm and sinapinic acid as matrix. ESI measurements were performed on a Thermo Finnigan LTQ FT Ultra Fourier Transform Ion Cyclotron Resonance mass spectrometer. The spray capillary voltage at the IonMax ESI-head was 4 kV, the heating capillary temperature was 250 °C, the nitrogen heat gas flow 20 and the sweep gas flow were five units. An Elementar vario micro cube instrument or an Elementar vario EL instrument was used for elemental analysis.

Photoluminescence spectra and absolute quantum yields of powder samples of **1** were recorded on a Hamamatsu C9920-02 spectrometer, equipped with a 150 W Xenon lamp, monochromatized to 350 nm excitation wavelength (FWHM = 7.4 nm), an integrating sphere, and a photonic multichannel analyzer.

2.8.4.2. General synthesis of bis((4,6-dimethylpyridin-2-yl)methyl)phenylphosphine oxide complexes **1–4**.

Bis((4,6-dimethylpyridin-2-yl)methyl)phenylphosphine oxide (1 eq, 0.36 g, 1.00 mmol for synthesis of **1**; 0.03 g, 146 μmol for **2**; 0.09 g, 257 μmol for **3**; 0.05 g, 294 μmol for **4**) is dissolved in dry, degassed MeCN (10 mL) and added dropwise while stirring to a solution of the respective metal salt (1 eq) in dry, degassed MeCN. Evaporation of the solvent under vacuum gave the respective complexes **1–4** as light green to colourless powders.

Bis((4,6-dimethylpyridin-2-yl)methyl)phenylphosphine oxide CuBF₄ complex (1). Yield: 0.470 g, (91.3 %). Anal. calcd for C₂₂H₂₅N₂POCuBF₄: C, 51.33; H, 4.90; N, 5.44. Found: C, 51.07; H, 4.74; N, 5.59. ¹H NMR (400 MHz, CDCl₃): δ 8.00 (dd, ³J_{HP} = 12.1 Hz, ³J_{HH} = 7.3 Hz, 2 H, phenyl-H), 7.59 (m, 5 H, phenyl-H, pyridyl-H), 6.91 (s, 2 H, pyridyl-H), 4.23 (dd, ²J_{HH} = ²J_{HP} = 13.1 Hz, 2 H, CH₂), 3.74 (dd, ²J_{HH} = ²J_{HP} = 16.2 Hz, 2 H, CH₂), 2.50 (s, 6 H, N-C-CH₃), 2.34 (s, 6 H, CH₃). ¹³C{¹H} NMR (101 MHz, CDCl₃): δ 157.4 (s, Cq), 151.8 (s, Cq-CH₃), 151.7 (s, Cq-CH₃), 133.6 (s, Cq_{phenyl}, second peak is missing), 131.1 (d, ³J_{CP} = 10.1 Hz, C_{phenyl}), 129.6 (d, ²J_{CP} = 12.1 Hz, C_{phenyl}), 128.5 (s, C_{phenyl}), 127.2 (s, C_{pyridyl}), 124.5 (d, ³J_{CP} = 1.4 Hz, C_{pyridyl}), 39.7 (d, ¹J_{CP} = 61.9 Hz, CH₂), 26.3 (s, N-C-CH₃), 21.1 (s, CH₃). ³¹P{¹H} NMR (162 MHz, CDCl₃): δ 44.4 (s). ¹⁹F{¹H} NMR (376 MHz, CDCl₃): δ -151.0 (s). ¹¹B{¹H} NMR (128 MHz, CDCl₃): δ -0.7 (s). ¹⁵N NMR (41 MHz, CDCl₃, *via* ¹H, ¹⁵N HMBC): δ -149.8 (s).

Bis((4,6-dimethylpyridin-2-yl)methyl)phenylphosphine oxide AgBF₄ complex (2). Yield: 0.123 g, (85.5 %). Anal. calcd for C₂₂H₂₅N₂POAgBF₄: C, 47.26; H, 4.51; N, 5.01. Found: C, 47.26; H, 4.56; N, 5.13. ¹H NMR (400 MHz, MeCN-*d*₃): δ (ppm) 7.70 (m, 2 H, phenyl-H), 7.62 (m, 1 H, phenyl-H), 7.53 (m, 2 H, phenyl-H), 7.07 (s, 2 H, pyridyl-H), 6.88 (s, 2 H, pyridyl-H), 3.91 (dd, ²J_{HH} = ²J_{HP} = 14.4 Hz, 2 H, CH₂), 3.88 (dd, ²J_{HH} = ²J_{HP} = 14.3 Hz, 2 H, CH₂), 2.54 (s, 6 H, N-C-CH₃), 2.19 (s, 6 H, CH₃). ¹³C{¹H} NMR (101 MHz, MeCN-*d*₃): δ (ppm) 159.2 (d, ⁴J_{CP} = 2.3 Hz, Cq-CH₃), 153.0 (d, ²J_{CP} = 9.2 Hz, Cq), 152.0 (d, ⁴J_{CP} = 2.0 Hz, Cq-CH₃), 133.8 (d, ⁴J_{CP} = 3.0 Hz, C_{phenyl}), 131.8 (d, ³J_{CP} = 9.4 Hz, C_{phenyl}), 130.9 (s, Cq_{phenyl}), 129.8 (d, ²J_{CP} = 12.1 Hz, C_{phenyl}), 125.5 (d, ³J_{CP} = 5.4 Hz, C_{pyridyl}), 124.7 (d, ⁴J_{CP} = 2.6 Hz, C_{pyridyl}), 42.0 (d, ¹J_{CP} = 60.2 Hz, CH₂), 27.1 (s, N-C-CH₃), 21.0 (s, CH₃). ³¹P{¹H} NMR (162 MHz, MeCN-*d*₃): δ (ppm) 38.6 (s). ¹⁹F{¹H} NMR (376 MHz, MeCN-*d*₃): δ (ppm) -152.5 (s). ¹¹B{¹H} NMR (128 MHz, MeCN-*d*₃): δ (ppm) -2.0 (s). ¹⁵N NMR (41 MHz, MeCN-*d*₃, *via* ¹H, ¹⁵N HMBC): δ (ppm) -127.7 (s). HR ESI-MS (positive ion): 471.0765, [M-BF₄]⁺ (calcd 471.0750) *m/z*. IR: ν (cm⁻¹) 476 (w), 488 (m), 701 (w), 725 (w), 753 (w), 762 (w), 1041 (s), 1061 (s), 1103 (w), 1622 (w).

Bis((4,6-dimethylpyridin-2-yl)methyl)phenylphosphine oxide AgSbF₆ complex (3). Yield: 0.093 g, (90.5 %). ¹H NMR (400 MHz, MeCN-*d*₃): δ (ppm) 7.63 (m, 3 H, phenyl-H), 7.52 (m, 2 H, phenyl-H), 7.11 (s, 2 H, pyridyl-H), 6.86 (s, 2 H, pyridyl-H), 3.86 (dd, ²J_{HH} = ²J_{HP} = 14.4 Hz, 2 H, CH₂), 3.85 (dd, ²J_{HH} = ²J_{HP} = 14.5 Hz, 2 H, CH₂), 2.57 (s, 6 H, N-C-CH₃), 2.21 (s, 6 H, CH₃). ¹³C{¹H} NMR (101 MHz, MeCN-*d*₃): δ (ppm) 157.2 (d, ⁴J_{CP} = 2.3 Hz, Cq-CH₃), 150.9 (d, ²J_{CP} = 9.2 Hz, Cq), 150.6 (s, Cq-CH₃), 132.0 (d, ⁴J_{CP} = 2.9 Hz, C_{phenyl}), 129.9 (d, ³J_{CP} = 9.3 Hz, C_{phenyl}), 129.0 (s, Cq_{phenyl}), 127.9 (d, ²J_{CP} = 12.0 Hz, C_{phenyl}), 123.8 (d, ³J_{CP} = 5.4 Hz, C_{pyridyl}), 123.0 (d, ⁴J_{CP} = 2.6 Hz, C_{pyridyl}), 39.7 (d, ¹J_{CP} = 59.3 Hz, CH₂), 24.8 (s, N-C-CH₃), 19.1 (s, CH₃). ³¹P{¹H} NMR (162 MHz, MeCN-*d*₃): δ (ppm) 37.7 (s). ¹⁹F{¹H} NMR (376 MHz, MeCN-*d*₃): δ (ppm) -124.4 (sextet, ¹J_{Fsb} = 1935 Hz coupling to ¹²¹Sb, octet, ¹J_{Fsb} = 1055 Hz coupling to ¹²³Sb). ¹⁵N NMR (41 MHz, MeCN-*d*₃, *via* ¹H, ¹⁵N HMBC): δ (ppm) -130.5 (s). HR ESI-MS (positive ion): 471.0762, [M-SbF₆]⁺ (calcd 471.0750) *m/z*. IR: ν (cm⁻¹) 477 (m), 487 (m), 545 (w), 641 (s), 654 (s), 727 (w), 737 (w), 750 (w), 1140 (w), 1177 (w), 1439 (w), 1618 (m).

Bis((4,6-dimethylpyridin-2-yl)methyl)phenylphosphine oxide AgNO₃ complex (4). Yield: 0.143 g, (87.6 %). ¹H NMR (400 MHz, MeCN-*d*₃): δ (ppm) 7.72 (m, 2 H, phenyl-H), 7.60 (m, 1 H, phenyl-H), 7.51 (m, 2 H, phenyl-H), 7.07 (s, 2 H, pyridyl-H), 6.89 (s, 2 H, pyridyl-H), 3.96 (dd, ²J_{HH} = ²J_{HP} = 14.5 Hz, 2 H, CH₂), 3.94 (dd, ²J_{HH} = ²J_{HP} = 14.3 Hz, 2 H, CH₂), 2.55 (s, 6 H, N-C-CH₃), 2.19 (s, 6H, CH₃). ¹³C{¹H} NMR (101 MHz, MeCN-*d*₃): δ (ppm) 159.2 (d, ⁴J_{CP} = 2.3 Hz, Cq-CH₃), 153.1 (d, ²J_{CP} = 9.2 Hz, Cq), 152.0 (d, ⁴J_{CP} = 2.0 Hz, Cq-CH₃), 133.7 (d, ⁴J_{CP} = 2.8 Hz, C_{phenyl}), 131.9 (d, ³J_{CP} = 9.5 Hz, C_{phenyl}), 130.5 (d, ¹J_{CP} = 97.3 Hz, Cq_{phenyl}), 129.8 (d, ²J_{CP} = 12.1 Hz, C_{phenyl}), 125.6 (d, ³J_{CP} = 5.4 Hz, C_{pyridyl}), 124.7 (d, ⁴J_{CP} = 2.5 Hz, C_{pyridyl}), 42.1 (d, ¹J_{CP} = 59.9 Hz, CH₂), 27.1 (s, N-C-CH₃), 21.0 (s, CH₃). ³¹P{¹H} NMR (162 MHz, MeCN-*d*₃): δ (ppm) 38.5 (s). ¹⁵N NMR (41 MHz, MeCN-*d*₃, *via* ¹H, ¹⁵N HMBC): δ (ppm) -128.5 (s).

HR ESI-MS (positive ion): 471.0772, $[M-\text{NO}_3]^+$ (calcd 471.0750) m/z . IR: ν (cm^{-1}) 424 (s), 498 (s), 533 (w), 697 (m), 728 (s), 859 (w), 1174 (m), 1321 (s), 1374 (m), 1411 (w), 1438 (w), 1617 (m).

Conflicts of interest

There are no conflicts of interest to declare.

Acknowledgements

The German Federal Ministry for Economic Affairs and Energy on the basis of a decision by the German Bundestag (ZIM, Grant ZF4065408SL7, ZF4477702SL7) financially supported this research. We further gratefully acknowledge the monetary support by the Department of Chemistry, Ludwig-Maximilian University of Munich. Additionally, we are particularly grateful to Prof. Dr. T. M. Klapötke for his continuous support over the years. The entire NMR team at the Ludwig-Maximilian University of Munich is thanked for the multi-nuclear and variable temperature NMR measurements.

2.8.5. References

- [1] S. K. Petrovskii, A. V. Paderina, A. A. Sizova, A. Y. Baranov, A. A. Artem'ev, V. V. Sizov, E. V. Grachova, *Dalton Trans.*, **2020**, 49 (38), 13430–13439.
- [2] A. Y. Baranov, M. I. Rakhmanova, D. G. Samsonenko, S. F. Malysheva, N. A. Belogorlova, I. Y. Bagryanskaya, V. P. Fedin, A. V. Artem'ev, *Inorg. Chim. Acta*, **2019**, 494, 78–83.
- [3] L. A. Adrio, K. K. Hii, *Organometallic Chemistry*, Fairlamb, I. J. S., Lynam, J. M., Eds., *Organometallic Chemistry*, Royal Society of Chemistry, Cambridge, **2009**, Vol. 35.
- [4] M. K. Rong, F. Holtrop, J. C. Sloopweg, K. Lammertsma, *Coord. Chem. Rev.*, **2019**, 382, 57–68.
- [5] M. P. Carroll, P. J. Guiry, *Chem. Soc. Rev.*, **2014**, 43 (3), 819–833.
- [6] D. M. Zink, M. Bächle, T. Baumann, M. Nieger, M. Kühn, C. Wang, W. Klopfer, U. Monkowius, T. Hofbeck, H. Yersin, S. Bräse, *Inorg. Chem.*, **2013**, 52 (5), 2292–2305.
- [7] S. Bestgen, C. Schoo, B. L. Neumeier, T. J. Feuerstein, C. Zovko, R. Köppe, C. Feldmann and P. W. Roesky, *Angew. Chem.*, **2018**, 130 (43), 14461–14465; *Angew. Chem. Int. Ed.*, **2018**, 57 (43), 14265–14269.
- [8] X. Tan, L. Li, J. Zhang, X. Han, L. Jiang, F. Li, C. Y. Su, *Chem. Mater.*, **2012**, 24 (3), 480–485.
- [9] S. N. Arbutova, P. A. Volkov, N. I. Ivanova, N. K. Gusarova, L. I. Larina, O. N. Kazheva, G. G. Alexandrov, O. A. Dyachenko, B. A. Trofimov, *J. Organomet. Chem.*, **2011**, 696 (10), 2053–2058.
- [10] F. Hung-Low, A. Renz, K. K. Klausmeyer, *Eur. J. Inorg. Chem.*, **2009**, 2994–3002.
- [11] C. Kirst, F. Zoller, T. Bräuniger, P. Mayer, D. Fattakhova-Rohlfing, K. Karaghiosoff, *Inorg. Chem.*, **2021**, 60 (4), 2437–2445.
- [12] A. V. Artem'ev, M. R. Ryzhikov, I. V. Taidakov, M. I. Rakhmanova, E. A. Varaksina, I. Y. Bagryanskaya, S. F. Malysheva, N. A. Belogorlova, *Dalton Trans.*, **2018**, 47 (8), 2701–2710.
- [13] A. V. Artem'ev, E. P. Doronina, M. I. Rakhmanova, A. O. Sutyryna, I. Y. Bagryanskaya, P. M. Tolstoy, A. L. Gushchin, A. S. Mazur, N. K. Gusarova, B. A. Trofimov, *New J. Chem.*, **2016**, 40 (12), 10028–10040.
- [14] A. V. Artem'ev, E. P. Doronina, M. I. Rakhmanova, O. A. Tarasova, I. Y. Bagryanskaya, N. A. Nedolya, *Inorg. Chem. Front.*, **2019**, 6 (3), 671–679.
- [15] A. S. Berezin, A. V. Artem'ev, V. Y. Komarov, A. Y. Baranov, *New J. Chem.*, **2020**, 44 (23), 9858–9862.
- [16] M. I. Rogovoy, M. P. Davydova, I. Y. Bagryanskaya, A. V. Artem'ev, *Mendeleev Commun.*, **2020**, 30 (3), 305–307.

- [17] A. V. Artem'ev, M. I. Rogovoy, D. G. Samsonenko, M. I. Rakhmanova, *Inorg. Chem. Commun.*, **2020**, *115* (February), 27–30.
- [18] C. Janiak, *Dalton Trans.*, **2000**, No. 21, 3885–3896.
- [19] W. B. Jennings, B. M. Farrell, J. F. Malone, *Acc. Chem. Res.*, **2001**, *34* (11), 885–894.
- [20] D. Britton, J. D. Dunitz, *Acta Crystallogr.*, **1965**, *19* (4), 662–668.

2.8.6. Supporting information

2.8.6.1. Additional figures

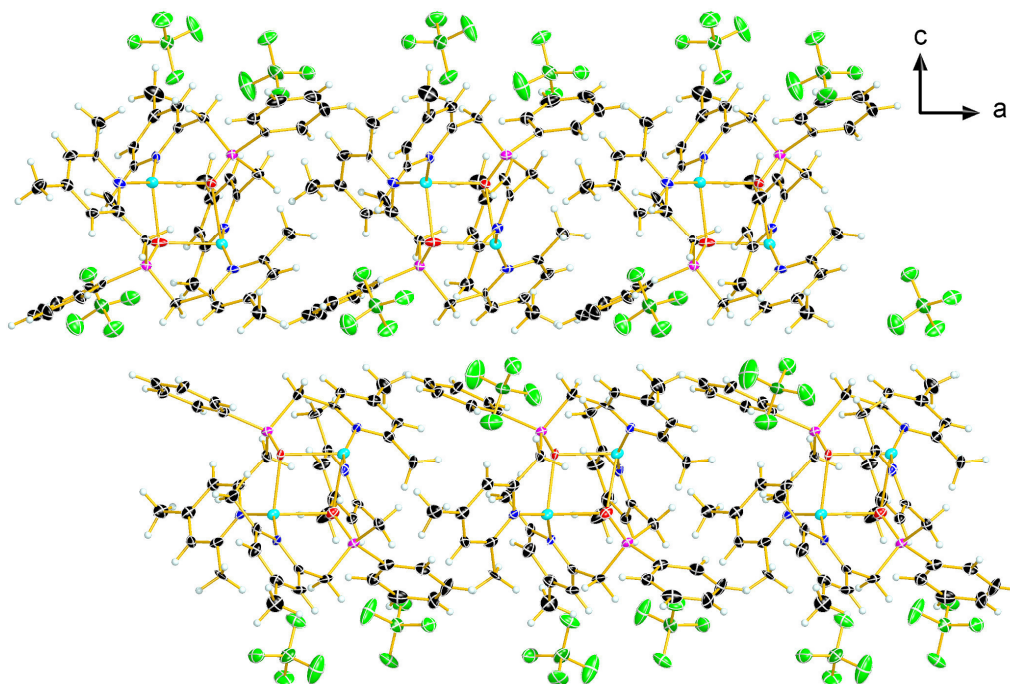


Figure 119. Packing of **1a** in the crystal. Thermal ellipsoids are set to 50 % probability.

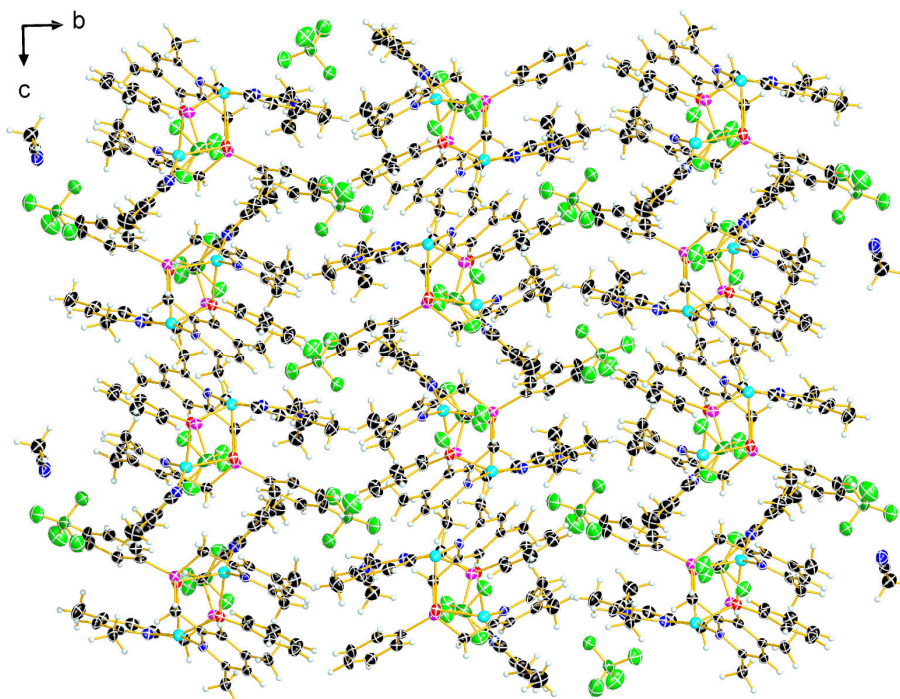


Figure 120. Packing of **1b** in the crystal. Thermal ellipsoids are set to 50 % probability.

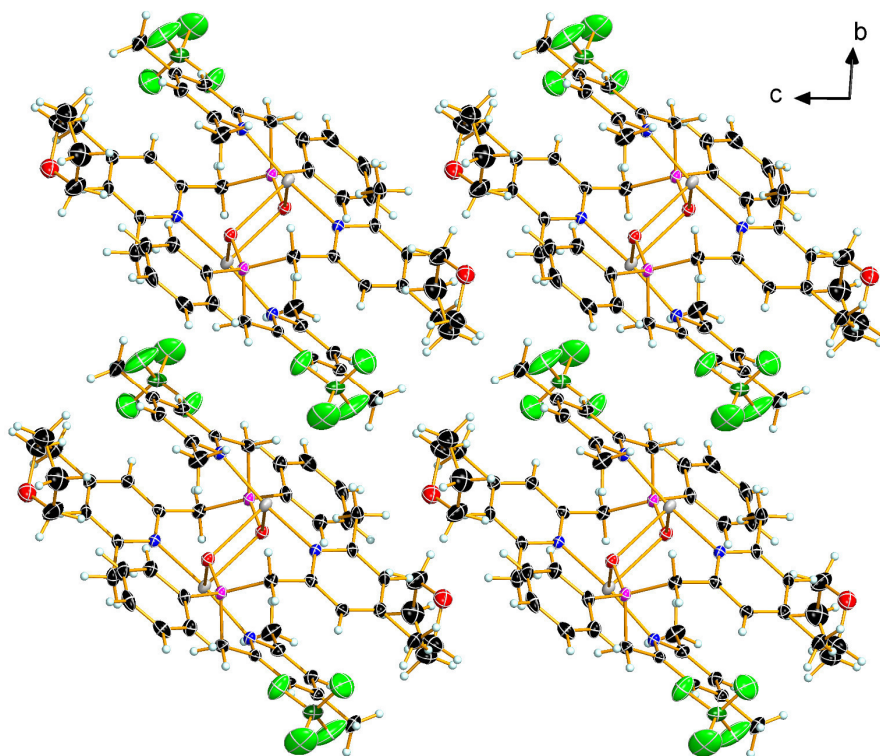


Figure 121. Packing of **2** in the crystal. Thermal ellipsoids are set to 50% probability.

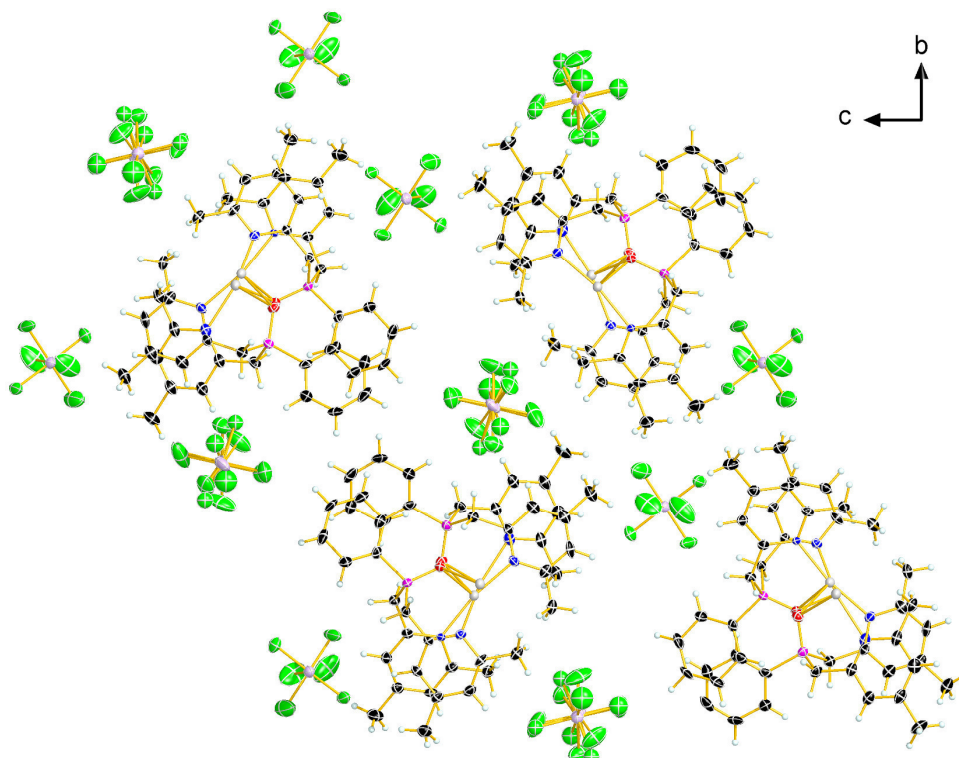


Figure 122. Packing of **3** in the crystal. Thermal ellipsoids are set to 50% probability.

2.8.6.2. Crystallographic data

Table 23. Crystallographic and refinement data for compounds **1** and **2**.

	1a	1b	2
Formula	C ₄₄ H ₅₀ N ₄ P ₂ O ₂ Cu ₂ B ₂ F ₈	C ₄₆ H ₅₃ N ₅ P ₂ O ₂ Cu ₂ B ₂ F ₈	C ₅₂ H ₆₆ N ₄ P ₂ O ₄ Ag ₂ B ₂ F ₈
Formula weight	1029.52	1070.57	1262.38
[g·mol ⁻¹]			
Colour	colorless	Colorless	colorless
Habit	Rod	Platelet	Block
T [K]	111	143	223
λ [Å]	0.71073	0.71073	0.71073
Crystal system	monoclinic	monoclinic	triclinic
Space group	<i>Pca</i> 2 ₁	<i>P</i> 2 ₁ / <i>c</i>	<i>P</i> -1
<i>a</i> [Å]	20.0999(19)	14.4334(12)	10.2955(4)
<i>b</i> [Å]	10.4761(10)	23.252(3)	11.0662(5)
<i>c</i> [Å]	42.751(4)	14.0284(12)	12.7270(5)
α [°]	90	90	92.848(4)
β [°]	90	90.624(8)	91.618(3)
γ [°]	90	90	112.232(4)
<i>V</i> [Å ³]	9,002.0(15)	4,707.7(8)	1,338.82(10)
<i>Z</i>	8	4	1
ρ _{calc} [g·cm ⁻³]	1.519	1.510	1.566
μ [mm ⁻¹]	1.092	1.048	0.867
<i>F</i> (0 0 0)	4224	2200	644
Crystal size [mm]	0.10×0.03×0.02	0.40×0.10×0.05	0.20×0.10×0.05
θ range [°]	2.723–26.020	4.112–26.371	1.992–26.372
Index ranges	-24 ≤ <i>h</i> ≤ 22 -12 ≤ <i>k</i> ≤ 12 -52 ≤ <i>l</i> ≤ 52	-18 ≤ <i>h</i> ≤ 18 -29 ≤ <i>k</i> ≤ 24 -17 ≤ <i>l</i> ≤ 16	-10 ≤ <i>h</i> ≤ 12 -13 ≤ <i>k</i> ≤ 13 -14 ≤ <i>l</i> ≤ 15
reflins collected	69,876	38,994	10,678
Independent reflns	17,597 [<i>R</i> _{int} = 0.0943]	9,579 [<i>R</i> _{int} = 0.1824]	5,456 [<i>R</i> _{int} = 0.0297]
Completeness to theta	99.7 %	99.5 %	99.8 %
Refinement method	Full-matrix least-squares on <i>F</i> ²	Full-matrix least-squares on <i>F</i> ²	Full-matrix least-squares on <i>F</i> ²
Data/restraints/Parameters	17,597 / 1 / 1,170	9,579 / 0 / 613	5,456 / 0 / 338
Hydrogen atom treatment	Constrained	Constrained	Constrained
<i>R</i> ₁ / <i>wR</i> ₂ (<i>I</i> > 2 σ (<i>I</i>))	0.0688/0.1301	0.0777/0.1123	0.0351/0.0811
<i>R</i> ₁ / <i>wR</i> ₂ (all data)	0.1083/0.1468	0.1902/0.1485	0.0449/0.0860
Goodness-of-fit on <i>F</i> ²	1.031	0.962	1.037
larg. diff peak/hole [e·Å ⁻³]	1.456/-0.619	0.802/-0.502	1.050/-0.662
CCDC No.			

Table 24. Crystallographic and refinement data for compounds **3** and **4**.

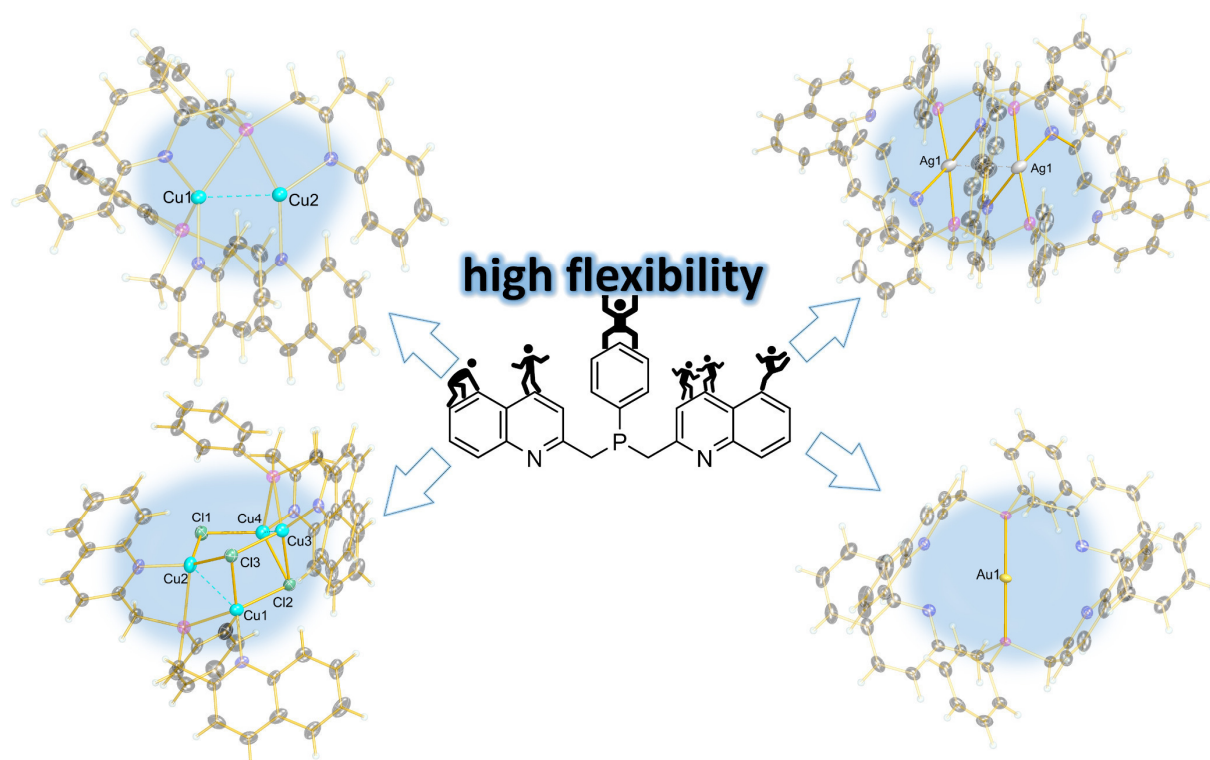
	3	4
Formula	C ₄₄ H ₅₀ N ₄ P ₂ O ₂ Ag ₂ Sb ₂ F ₁₂	C ₁₄₈ H ₁₈₂ N ₁₉ P ₆ O ₃₁ Ag ₇
Formula weight [g·mol ⁻¹]	1416.06	3664.03
Colour	colorless	colorless
Habit	Rod	Block
T [K]	102	102
λ [Å]	0.71073	0.71073
Crystal system	orthorhombic	monoclinic
Space group	<i>P</i> 2 ₁ 2 ₁ 2 ₁	<i>C</i> 2/ <i>c</i>
<i>a</i> [Å]	7.2037(3)	20.7558(9)
<i>b</i> [Å]	25.5028(9)	26.3784(11)
<i>c</i> [Å]	29.3863(12)	29.1593(12)
α [°]	90	90
β [°]	90	104.4800(10)
γ [°]	90	90
<i>V</i> [Å ³]	5,398.7(4)	15,457.7(11)
<i>Z</i>	4	4
ρ _{calc} [g·cm ⁻³]	1.742	1.574
μ [mm ⁻¹]	1.843	1.009
<i>F</i> (0 0 0)	2768	7480
Crystal size [mm]	0.10×0.01×0.01	0.07×0.03×0.02
Θ range [°]	3.019–26.372	2.506–26.373
Index ranges	–8 ≤ <i>h</i> ≤ 9 –31 ≤ <i>k</i> ≤ 31 –36 ≤ <i>l</i> ≤ 36	–25 ≤ <i>h</i> ≤ 25 –32 ≤ <i>k</i> ≤ 32 –36 ≤ <i>l</i> ≤ 36
reflns collected	62,557	129,906
Independent reflns	10,975 [<i>R</i> _{int} = 0.0858]	15,743 [<i>R</i> _{int} = 0.0550]
Completeness to theta	99.5 %	99.6 %
Refinement method	Full-matrix least-squares on <i>F</i> ²	Full-matrix least-squares on <i>F</i> ²
Data/ restraints/ Parameters	10,975 / 90 / 650	15,743 / 44 / 935
Hydrogen atom treatment	Constrained	Constrained
<i>R</i> ₁ / <i>wR</i> ₂ (<i>I</i> > 2 σ (<i>I</i>))	0.0494/0.0831	0.0445/0.1027
<i>R</i> ₁ / <i>wR</i> ₂ (all data)	0.0700/0.0884	0.0582/0.1105
Goodness-of-fit on <i>F</i> ²	1.064	1.034
larg. diff peak/hole [e·Å ⁻³]	0.659/–0.758	3.228/–2.284
CCDC No.		

2.9. Coinage metal complexes of bis(quinaldinyl)phenylphosphine – simple reactions can lead to unprecedented results

Christin Kirst, Jonathan Tietze, Peter Mayer, Hans-Christian Böttcher and Konstantin Karaghiosoff

submitted to *ChemistryOpen*

Christin Kirst synthesized all the discussed compounds and performed the single crystal X-ray measurements. She analyzed and evaluated the corresponding X-ray data and the NMR spectroscopy results in solution. She further managed the project and wrote the original draft of the manuscript, designed the TOC graphic and implemented the necessary corrections in the final version of the paper.



Abstract: The different coordination behavior of the flexible yet sterically demanding, hemilabile P,N ligand bis(quinaldinyl)phenylphosphine towards selected Cu(I), Ag(I) and Au(I) species is described. The resulting X-ray crystal structures reveal interesting coordination geometries. With $[\text{Cu}(\text{MeCN})_4]\text{BF}_4$ compound **1** $[\text{Cu}_2(\text{C}_{26}\text{H}_{21}\text{N}_2\text{P})_2](\text{BF}_4)_2$ is obtained, wherein the copper(I) atoms display a distorted tetrahedron and a trigonal planar arrangement. The steric demand and π -stacking of the ligand allow for a short $\text{Cu}\cdots\text{Cu}$ distance (2.588(9) Å). Cu(I) complex **2** contains a rarely observed Cu_4Cl_3 cluster, probably enabled by left-over chloride from the synthesis of the phosphine. In the cluster, even shorter $\text{Cu}\cdots\text{Cu}$ distances (2.447(1) Å) are present. The reaction of $\text{Ag}[\text{SbF}_6]$ with the ligand leads to a dinuclear compound (**3**) in solution, as is confirmed by $^{31}\text{P}\{^1\text{H}\}$ NMR. During crystallization, instead of the expected phosphine complex **3**, a diphosphine compound $[\text{Ag}_2(\text{C}_{42}\text{H}_{33}\text{N}_3\text{P})_2](\text{SbF}_6)_2$ **4** is formed by elimination of quinaldine. The Au(I) compound $[\text{Au}_2(\text{C}_{26}\text{H}_{21}\text{N}_2\text{P})_2]\text{PF}_6$ (**5**) is prepared as expected and shows a linear arrangement of two phosphine ligands around Au(I).

2.9.1. Introduction

Multidentate P,N ligands stand out due to their hemilability, as they contain two electronically different coordination atoms (soft phosphorus and hard nitrogen). This versatile coordination behavior is very beneficial and needed in catalysis, for the preparation of MOFs or even luminescent materials.^[1-7] Hemilabile, tertiary phosphines are preferably used due to their outstanding flexibility which can be modified by changing the substituents accordingly. The modification of the substituents can result in the adaptation of their steric and electronic properties, their bite angle and solubility, and even chiral phosphine ligands can be formed. These features can be used for the complexation of a wide range of metal ions, even the bridging of metal ions is possible with tertiary phosphines. As the bridging capabilities of phosphines are nowadays widely known in literature, they became popular only about 20 years ago.^[8-10] In the meantime, further complexes have been synthesized, wherein the tertiary phosphine adapts a bridging position between two metal centers.^[11-14]

In particular coinage metals ions in combination with P,N ligands are prone to the formation of polynuclear complexes which can even support metallophilic interactions. These short metal-metal contacts can strongly influence the properties of the resulting complexes.^[15-20] Nevertheless, conformation and composition of the complexes of coinage metals with P,N ligands are rather unpredictable due to the reactivity and diverse coordination capabilities of such ligands.^[21,22] The newly synthesized Cu(I), Ag(I) and Au(I) complexes of bis(quinaldinyl)phenylphosphine, presented in the following, complement the great variety of complexes of coinage metals and impressively demonstrate the unique coordination behavior of P,N ligands. The new complexes have been characterized by multinuclear (¹H, ¹³C, ³¹P, ¹¹B, ¹⁹F) 1D and 2D NMR spectroscopy as well as single-crystal X-ray diffraction, elemental analysis and mass spectrometry.

2.9.2. Results and discussion

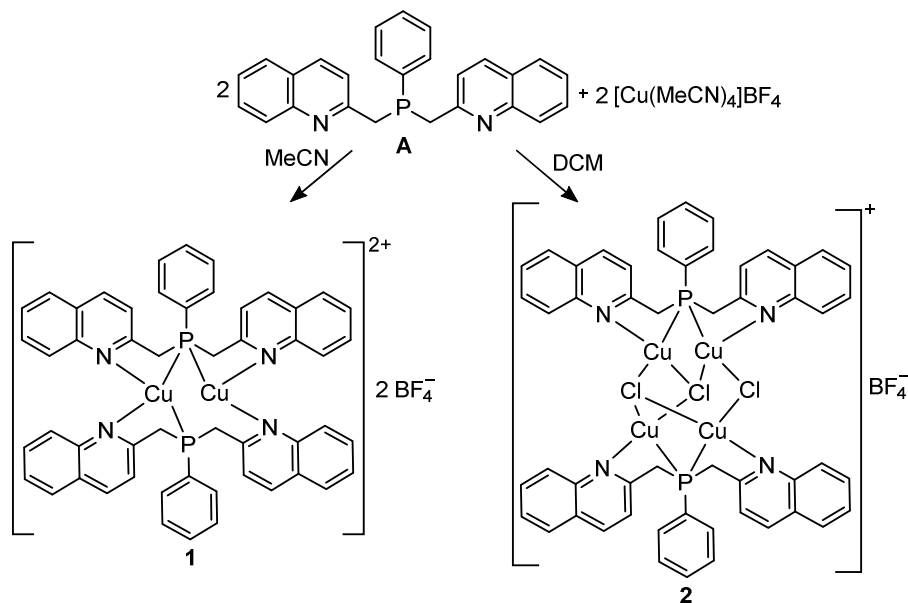
2.9.2.1. Synthesis and crystal structures

The synthesis of bis(quinaldinyl)phenylphosphine (**A**) has been previously published by our group.^[23] The crystal structure of **A** is now provided in the Supporting Information (Figure 129). For the synthesis of the copper(I) complex, **A** is dissolved in dry, degassed acetonitrile and the resulting mixture transferred *via* cannula to the equivalent amount of [Cu(MeCN)₄]BF₄ dissolved in MeCN under inert gas. After stirring for 12 h at room temperature, the Cu(I) compound **1** is obtained from the orange reaction solution after work-up (see experimental part) as an orange powder (Scheme 20). The compound is recrystallized by diffusion of diethyl ether into a solution of compound **1** in acetonitrile or dichloromethane at room temperature yielding 74 % of orange crystals. The compound should be stored under inert gas in a sealed container to prevent any oxidation.

The copper(I) complex **1** crystallizes in the monoclinic space group *P*2₁/*c* and a view of the molecular structure in the crystal is shown in Figure 123. Selected bond lengths and angles of compound **1** are listed in Table 25, crystal and structure refinement data can be found in the Supporting Information. In the cationic complex **1**, two phosphine ligands bridge two copper(I) ions, similar to the silver(I) hexafluoroantimonate compound of the respective phosphine oxide previously published by our group, where oxygen takes over the coordination task of phosphorus.^[23]

Similar to the previously published phosphine oxide ligand, the structure of the ligand in **1** can be compared to a bird, where one ligand spreads both quinaldinyl substituents in an open-wing arrangement, whereas the other ligand displays a closed-wing arrangement with a N3...N4 distance of 3.082(5) Å. The Cu1 atom exhibits a distorted tetrahedral geometry with angles ranging from 83.3(1)–134.4(1)°. The second copper(I) atom is tricoordinated by one nitrogen atom of one ligand and one nitrogen and phosphorus atom of the other ligand. Both copper atoms are very close to each other

(2.588(9) Å), regardless, the shortest Cu...Cu distance in a phosphine complex was reported for a copper(I) hexafluorophosphate complex salt of bis(picoly)phenylphosphine with 2.488(12) Å.^[24] The close proximity and the resulting π -stacking interaction of the quinaldinyl rings of the closed-wings ligand probably allow for such close copper contacts. Furthermore, the Cu1–P1 (2.527(2) Å) and Cu2–P1 distances are not equidistant and differ by 0.281 Å. The Cu2–P2 distance of 3.333(1) Å is beyond a bonding distance. The Cu2–P1 distance of 2.246(1) Å is typical for this type of bond, the same accounts for the Cu–N distances of 1.982(4)–2.133(4) Å.



Scheme 20. Synthesis of the Cu(I) compound **1** and **2** including the visualization of the binding mode in the crystal structures of the products.

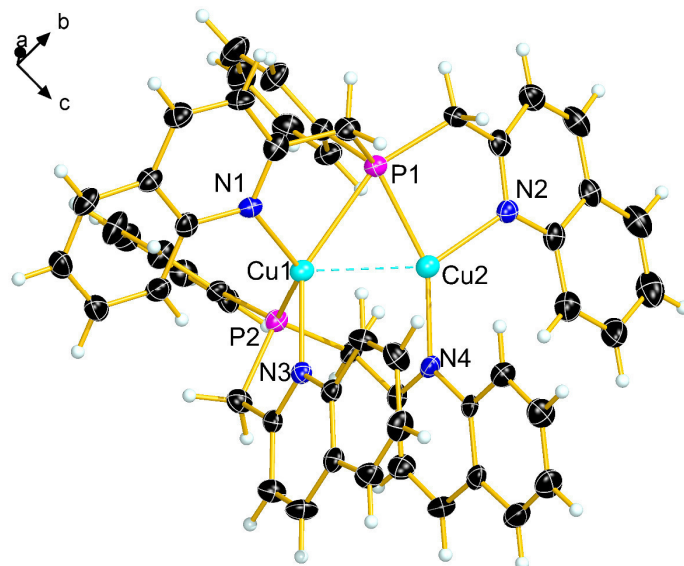


Figure 123. Molecular structure of the dinuclear complex cation of compound **1** in the crystal; view of the asymmetric unit. Thermal ellipsoids are drawn at 50 % probability level. Solvent molecules and anions are omitted for clarity.

During the crystallization attempt of the latter copper(I) compound in DCM, another compound (**2**) is formed with a different molecular structure. It crystallizes in the monoclinic space group $P2_1/n$. A view of the molecular structure of **2** in the crystal is shown in Figure 124. How the formation of **2** occurred, is still unclear. A possible source for chloride atoms might be the solvent dichloromethane. In fact, in

the crystal structure of **2** additional electron density is observed, indicating the presence of disordered dichloromethane molecules. However, the disorder could not be resolved by an appropriate model (see Supporting Information). Selected bond lengths and angles of compound **2** are listed in Table 25, crystal and structure refinement data can be found in the Supporting Information.

All copper(I) atoms in the crystal structure of **2** have a distorted tetrahedral geometry with angles ranging from 86.2(2)–128.5(2)°. The metal–metal distances (Cu1···Cu2 2.451(1) Å and Cu3···Cu4 2.447(1) Å) in **2** are very short, even shorter than in the previously mentioned copper(I) hexafluorophosphate complex salt of bis(picoly)phenylphosphine.^[24] The coordination of both ligands in **2** occurs in an open-wing manner. The Cu1–P1 and Cu2–P1 distances are very similar and only differ by 0.016 Å, whereas the Cu3–P2 and Cu4–P2 distances differ by 0.138 Å. The Cu–N distances with an average value of 2.020 Å are very similar to each other, with the exception of Cu1–N1 (2.005 Å).

The highlight of this structure is the Cu₄Cl₃ distorted triangular prism with an additional vertex on one edge (Cl1 atom). Such Cu₄Cl₃ clusters are very rare, and a similar structure as observed in **2** has not been reported so far in the literature.^[25] The distortion of the triangular prism results from the incorporation of chloride into the framework leading to diverse Cu–Cl and Cu···Cu distances. The Cu–Cl distances (2.279(2)–2.424(2) Å) are within the typical range for such distances. The different units of **2** are connected *via* attractive π -interactions between the quinaldinyl rings of neighboring molecules in the crystal (see Figure 130 of Supporting Information).^[26,27]

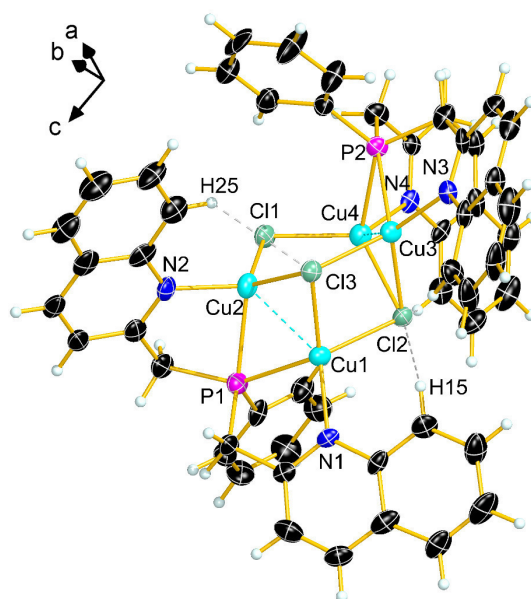


Figure 124. Molecular structure of cluster complex cation **2** in the crystal, view of the asymmetric unit. Thermal ellipsoids are drawn at 50 % probability level. Solvent molecules and anions are omitted for clarity.

Table 25. Selected bond lengths [Å] and angles [°] for compounds **1** and **2**.

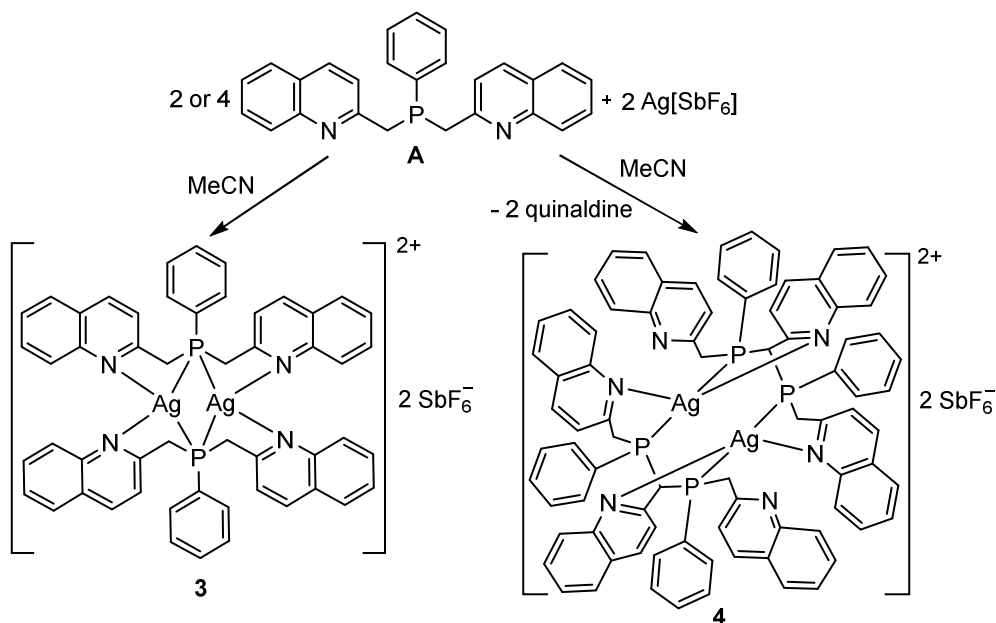
1			
P1–Cu1	2.527(2)	P2–C33	1.841(5)
P1–Cu2	2.246(1)	P2–C43	1.848(5)
P2–Cu1	2.256(1)	Cu1–N1	2.038(4)
P1–C1	1.814(5)	Cu1–N3	2.133(4)
P1–C7	1.815(5)	Cu2–N2	2.101(4)
P1–C17	1.839(5)	Cu2–N4	1.982(4)
P2–C27	1.809(5)	Cu1···Cu2	2.588(9)
C1–P1–C7	107.0(2)	P1–Cu2–N2	88.5(1)

C1–P1–C17	102.8(2)	P2–Cu1–N3	83.3(1)
C7–P1–C17	98.0(2)	P2–Cu1–N1	134.4(1)
C27–P2–C33	105.7(2)	Cu1–P1–Cu2	65.4(4)
C27–P2–C43	103.7(2)	N1–Cu1–N3	110.9(2)
C33–P2–C43	101.8(2)	N2–Cu2–N4	115.9(2)
P1–Cu1–N1	83.6(1)		
2			
P1–Cu1	2.377(2)	Cu2–Cl1	2.294(2)
P1–Cu2	2.393(2)	Cu3–N3	2.020(5)
P2–Cu3	2.314(2)	Cu3–Cl2	2.382(2)
P2–Cu4	2.452(2)	Cu3–Cl3	2.380(2)
P1–C1	1.815(8)	Cu4–N4	2.019(5)
P1–C7	1.828(6)	Cu4–Cl1	2.279(2)
P1–C17	1.843(6)	Cu4–Cl2	2.415(2)
Cu1–N1	2.005(5)	Cl2...H15	2.849(1)
Cu1–Cl2	2.435(2)	Cl3...H25	2.850(2)
Cu1–Cl3	2.383(2)	Cl2...H51	2.801(2)
Cu2–N2	2.021(5)	Cu1...Cu2	2.451(1)
Cu2–Cl3	2.424(2)	Cu3...Cu4	2.447(1)
C1–P1–C7	104.6(4)	Cu1–P1–Cu2	61.9(5)
C1–P1–C17	100.9(3)	Cu3–P2–Cu4	61.7(5)
C7–P1–C17	100.0(3)	Cu1–Cl3–Cu2	61.3(5)
C27–P2–C33	102.3(3)	Cu3–Cl2–Cu4	61.3(5)
C27–P2–C43	103.2(3)	Cu2–Cl1–Cu4	93.7(6)
C33–P2–C43	99.7(3)	N1–Cu1–Cl2	114.1(2)
P1–Cu1–N1	87.4(2)	N2–Cu2–Cl1	117.5(2)
P1–Cu2–N2	87.6(2)	N3–Cu3–Cl2	128.5(2)
P2–Cu3–N3	88.4(2)	N4–Cu4–Cl1	117.9(4)
P2–Cu4–N4	86.2(2)		

The silver(I) compound **3** is synthesized by dissolving **A** in dry, degassed dichloromethane and transferring the resulting mixture *via* a cannula to the equivalent amount of Ag[SbF₆] dissolved in acetonitrile. After stirring for 12 h at room temperature, the Ag(I) compound **3** is obtained after removal of all volatiles as an orange oil. Crystallization attempts to obtain a suitable single-crystal of **3** for X-ray diffraction were so far unsuccessful. However, during the attempts, where diethyl ether was diffused into a solution of compound **3** in acetonitrile revealed the crystal structure to compose of a diphosphine as the ligand (see Scheme 21 and Figure 125). Apparently, Ag[SbF₆] can react with the phosphine in a side reaction whereby compound **4** containing silver(I) coordinating to a diphosphine is obtained. The formation of a diphosphine is very uncommon and a similar reaction behavior was not to be found in the literature. The formation of the diphosphine ligand involves the elimination of quinaldine, which is confirmed by NMR spectroscopy (see Supporting Information). Compound **4** is air sensitive and should be stored under inert gas.

The silver(I) compound **4** crystallizes in the triclinic space group *P*-1 and its molecular structure in the crystal is shown in Figure 125. Selected bond lengths and angles of compound **4** are listed in Table 26, crystal and structure refinement data can be found in the Supporting Information. The dinuclear cationic complex possesses an inversion center which lies in the middle of the Ag1–Ag1' vector. The silver(I) atom Ag1 has a distorted tetrahedral geometry with angles ranging from 69.8(3)–131.4(2)°. The distance between both Ag atoms (3.221(2) Å) is shorter than the sum of van der Waals radii (3.44 Å),^[28] but rather long compared to standard Ag–Ag distances, which are around 3.0 Å. In contrast, the Ag–N bonds are within the normal range (Ag1–N1 2.676(2) Å, Ag1–N2 2.635(1) Å). The Ag1–P1 and

Ag1–P2 distances are very similar and only differ by 0.027 Å. The Ag1⋯N3ⁱ distance of 3.871(8) Å and Ag1⋯P1ⁱ distance of 3.671(4) Å are beyond a bonding distance. The different units of **4** are connected *via* attractive π -interactions between the quinaldinyl rings of neighboring molecules in the crystal with an averaged distance of 3.4 Å (Figure 131).^[26,27]



Scheme 21. Suggested synthesis of the Ag(I) compounds **3** and **4**. Visualization of the suspected binding mode in the potential crystal structure of **3** (left) and the actual binding mode in the crystal structure of **4** (right).

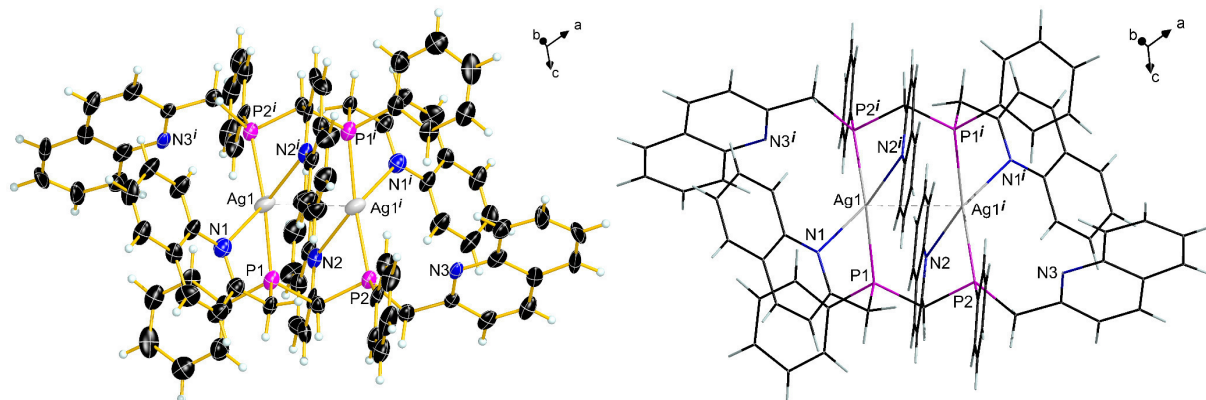
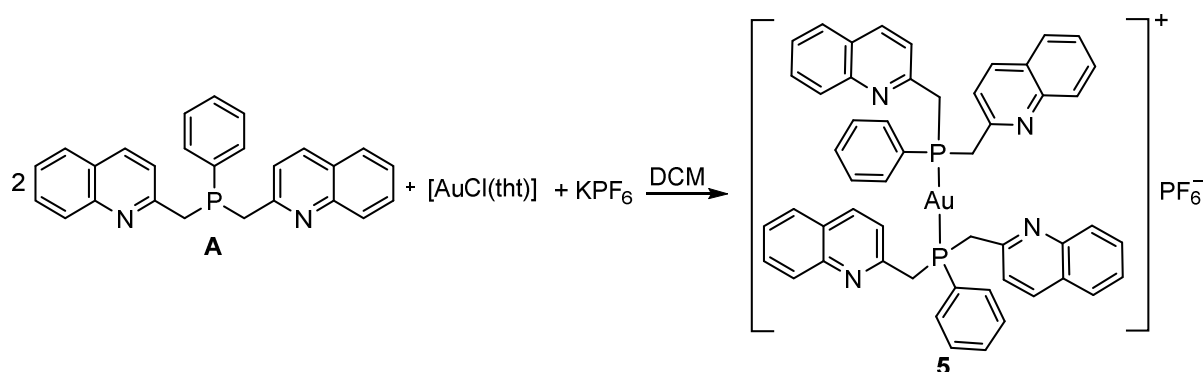


Figure 125. Molecular structure of the cationic complex of **4** in the crystal, view of the asymmetric unit. Ellipsoid representation (left) and stick representation (right). Thermal ellipsoids are drawn at 50 % probability level. Anions are omitted for clarity. Symmetry code: $i = 2-x, 2-y, 1-z$.

For the synthesis of the gold(I) complex **5**, bis(quinaldinyl)phenylphosphine **A** is dissolved in dry, degassed dichloromethane and the resulting mixture transferred *via* a cannula to the equimolar amount of solid [AuCl(tht)] (tht = tetrahydrothiophene) under inert gas. Solid potassium hexafluorophosphate is added to the mixture to remove chloride and to form the gold(I) compound **5** containing the non-coordinating hexafluorophosphate anion (see Scheme 22 for details). After filtration, the remaining solvent is removed and the Au(I) complex **5** is obtained as a yellow powder. Compound **5** can be recrystallized by diffusion of diethyl ether into a solution of compound **5** in dichloromethane yielding 80 % of crystalline **5**. Compound **5** should be stored under inert gas and with the exclusion of light.

The gold(I) compound **5** crystallizes in the triclinic space group $P\bar{1}$ with one formula unit in the unit cell (Figure 126). Selected bond lengths and angles of compound **5** are listed in Table 26, crystal and structure refinement data can be found in the Supporting Information. The cationic complex of **5** possesses an inversion center at Au1. The gold(I) atom is coordinated by the two phosphine ligands in a linear arrangement. The Au1–P1 distance 2.306(5) Å is within the normal range. The Au1⋯N distances of 3.481(2) Å and 3.610(2) Å are beyond a bonding distance. The different units of **5** are connected *via* attractive π -interactions between the quinaldinyl rings of neighboring molecules in the crystal with an averaged distance of 3.7 Å (Figure 132).^[26,27]



Scheme 22. Synthesis of the Au(I) compound **5** and visualization of the binding mode in the crystal structure of the product.

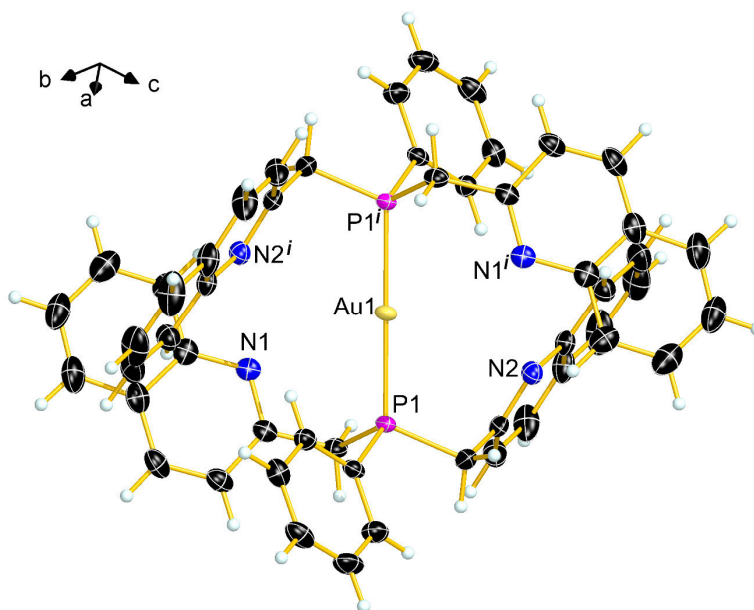


Figure 126. Molecular structure of the complex cation of compound **5** in the crystal, view of the asymmetric unit. Thermal ellipsoids are drawn at 50 % probability level. Anions are omitted for clarity. Symmetry code: $i = -x, 1-y, -z$.

Table 26. Selected bond lengths [Å] and angles [°] for compounds **4** and **5**.

4		symmetry code: $i = 2-x, 2-y, 1-z$	
P1–Ag1	2.410(4)	P2–C27	1.818(1)
P2–Ag1	2.437(3)	P2–C33	1.835(1)
P1–C1	1.845(1)	Ag1–N1	2.676(2)
P1–C7	1.821(1)	Ag1–N2	2.635(1)
P1–C17	1.865(1)	Ag1⋯N3	3.871(8)
P2–C17	1.861(1)	Ag1⋯Ag1 ⁱ	3.221(2)

Ag1–P1–C1	114.7(4)	P1–Ag1–N1	69.8(3)
Ag1–P1–C7	106.3(4)	P1–Ag1–N2	131.4(2)
Ag1–P1–C17	123.5(4)	N1–Ag1–N2	96.1(4)
C1–P1–C7	100.5(6)	P1–Ag1–Ag1 ⁱ	79.9(9)
C1–P1–C17	103.6(6)	N1–Ag1–Ag1 ⁱ	139.4(3)
C7–P1–C17	105.7(5)	P2–Ag1–Ag1 ⁱ	91.8(9)
P1–Ag1–P2	152.4(1)		
5		symmetry code: $i = -x, 1-y, -z$	
P1–C1	1.808(2)	P1–Au1	2.306(5)
P1–C7	1.830(2)	Au1...N1	3.481(2)
P1–C17	1.831(2)	Au1...N2	3.610(2)
C1–P1–C7	105.5(1)	C7–P1–Au1	113.0(7)
C1–P1–C17	106.1(1)	C17–P1–Au1	114.8(8)
C7–P1–C17	104.1(1)	P1–Au1–P1 ⁱ	180.0
C1–P1–Au1	112.6(7)		

2.9.2.2. Characterization of the compounds by NMR spectroscopy

Due to different solubilities, the NMR spectra of the complexes were measured in different solvents. The $^{31}\text{P}\{^1\text{H}\}$ NMR spectrum of **1** in CD_3CN shows only one signal at -14.0 ppm. The coordination of the ligand seems not to affect $\delta^{31}\text{P}$ of the latter ($\delta^{31}\text{P} = -14.0$ ppm) and results only in a strong broadening of the signal ($\Delta\nu_{1/2} = 300$ Hz). Coordination of the ligand to Cu(I) becomes evident in the splitting pattern of the diastereotopic protons of the CH_2 groups in the ^1H NMR spectrum (Figure 127). The CH_2 group in **1** shows larger $^2J_{\text{PH}}$ couplings (6 and 8 Hz), which is in accordance with the increased coordination number of phosphorus.

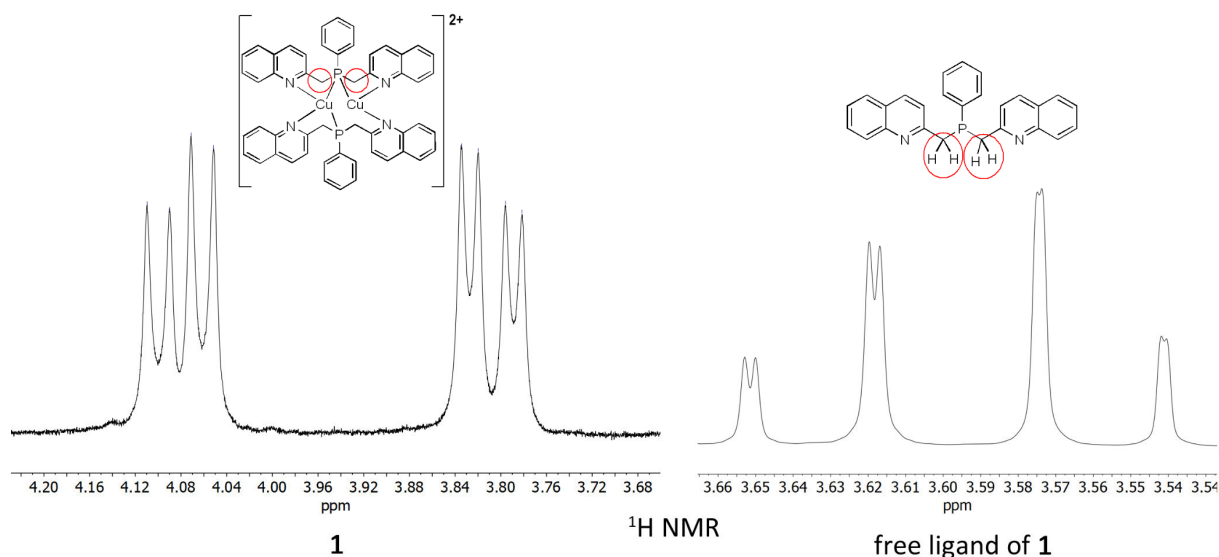


Figure 127. Comparison of the signals for the CH_2 group in the ^1H NMR spectra of **1** (left) in CD_3CN and the free ligand (right) in CDCl_3 .

The $^{31}\text{P}\{^1\text{H}\}$ NMR spectrum of **3** in CD_3CN shows a phosphorus resonance at 12.2 ppm ($\Delta\nu_{1/2} = 60$ Hz) and is shifted to higher frequencies when compared to the free ligand ($\Delta\delta = 22.8$ ppm). However, the $^{31}\text{P}\{^1\text{H}\}$ NMR spectrum of **3** in CD_2Cl_2 shows a phosphorus resonance at 6.8 ppm ($\Delta\nu_{1/2} = 400$ Hz; shifted to higher frequencies when compared to the free ligand by $\Delta\delta = 17.4$ ppm). When lowering the temperature to -80 °C, the signal of the Ag(I) complex in the $^{31}\text{P}\{^1\text{H}\}$ NMR in CD_2Cl_2 is split into a triplet

(Figure 128, left). The splitting of the signal becomes already visible at RT (see Supporting Information), and is caused by the coupling of phosphorus to silver(I) with a coupling constant of $^1J_{P-Ag} = 250$ Hz at -80 °C. This silver-phosphorus coupling constant indicates a tetracoordinated silver(I) cation in solution, a possible structure of **3** is shown in Figure 128.^[29–31]

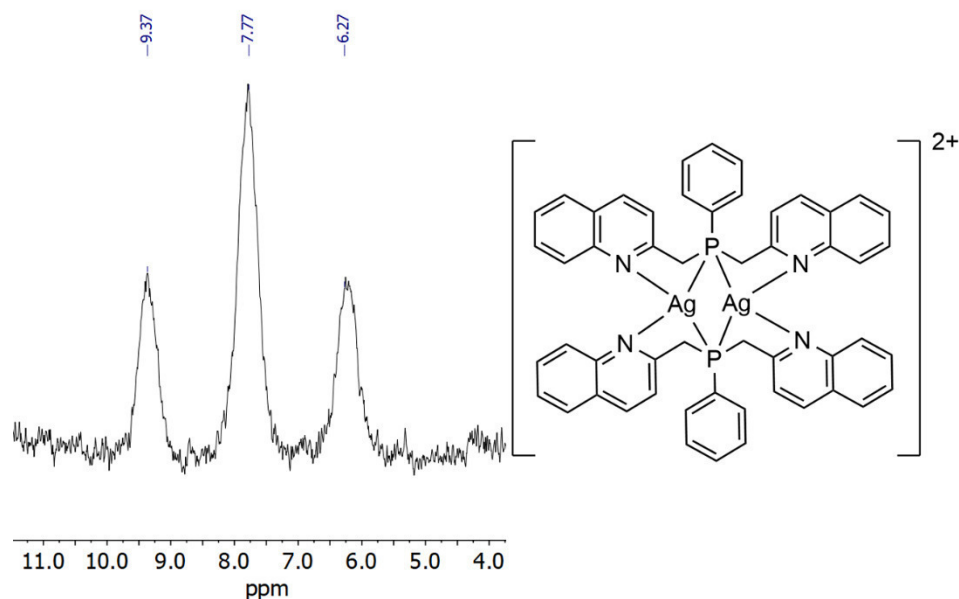


Figure 128. ^{31}P NMR spectrum of **3** in CD_2Cl_2 at -80 °C visualizing the coupling of phosphorus to both silver(I) atoms and a possible molecular structure of **3** in solution.

The $^{31}\text{P}\{^1\text{H}\}$ NMR spectrum of **4** in CD_3CN shows a phosphorus resonance at 11.4 ppm ($\Delta\nu_{1/2} = 66$ Hz; $\Delta\delta = 22.8$ ppm compared to the free ligand). For the gold(I) compound **5** in CD_2Cl_2 , the $^{31}\text{P}\{^1\text{H}\}$ NMR spectrum displays a phosphorus resonance at 36.4 ppm ($\Delta\nu_{1/2} = 45$ Hz). Compared to the free ligand, the signal is shifted to higher frequencies ($\Delta\delta = 50.4$ ppm). This change in chemical shift is common for gold(I) complexes of phosphines.^[32]

All complexes show a broad phosphorus resonance in the ^{31}P NMR spectrum at room temperature indicating a dynamic behavior in solution, similar to the complexes of the respective phosphine oxide published previously by our group.^[23] The corresponding variable temperature NMR spectra of compounds **1**, **3** and **5** are shown in the Supporting Information.

2.9.3. Conclusion

The new compounds **1–5** formed utilizing Cu(I), Ag(I) and Au(I) salts demonstrate the coordination versatility of the bis(quinaldinyl)phenylphosphine ligand towards coinage metals. With this ligand very short Cu...Cu distances in the copper(I) complexes are supported. The steric demand and the possibility of π -stacking of the quinaldinyl rings facilitate the existence of these short contacts. Compound **2** contains a rarely observed Cu_4Cl_3 cluster unit with a distorted trigonal prism, in which one edge is capped by a chloride atom. The formation of **2** is probably induced by the presence of DCM as solvent. The unexpected formation of a diphosphine ligand during the synthesis of the Ag(I) compound **4** impressively shows the manifold reaction possibilities offered by the bis(quinaldinyl)phenylphosphine ligand. In **4**, a weak argentophilic interaction is observed between the two silver(I) ions. The Au(I) compound **5** completes the series of coinage group one complexes with bis(quinaldinyl)phenylphosphine and shows the usually expected composition and molecular geometry of similar constituted gold(I) complexes.

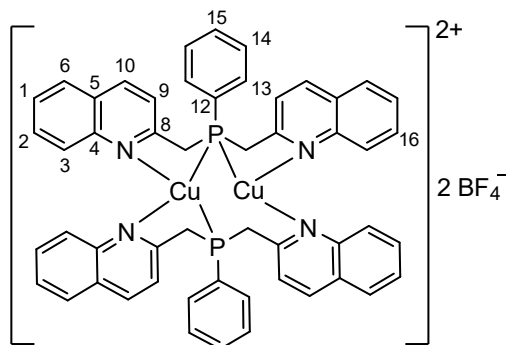
2.9.4. Experimental Section

2.9.4.1. General procedures

All compounds were handled under exclusion of moisture and oxygen in a protecting argon atmosphere using Schlenk techniques. Unless otherwise specified, all reagents and solvents were purchased from commercial sources and used as received. Complex $[\text{AuCl}(\text{tht})]^{[33]}$ and ligand $\text{C}_{26}\text{H}_{21}\text{N}_2\text{P}^{[23]}$ were prepared according to literature procedures. The solvents used were dried, freshly distilled and degassed prior to use. As drying agents SICAPENT[®] was used for acetonitrile, and sodium for diethyl ether. DCM was distilled under nitrogen atmosphere from CaH_2 . The deuterated solvents CD_2Cl_2 and CD_3CN were distilled and stored under argon atmosphere over molecular sieves. NMR spectra were recorded with a Bruker Avance III spectrometer operating at 400.1 MHz (^1H), 376.4 MHz (^{19}F), 161.9 MHz (^{31}P), 128.4 MHz (^{11}B) and 100.6 MHz (^{13}C). Chemical shifts are referenced to TMS (^1H , ^{13}C), 85 % H_3PO_4 (^{31}P), CCl_3F (^{19}F) and BF_3 in Et_2O (^{11}B) as external standards. All spectra were measured, if not mentioned otherwise, at 25 °C. The assignment of the signals is based on 2D ($^1\text{H}^1\text{H}$ -COSY, $^1\text{H}^{13}\text{C}$ -HSQC and $^1\text{H}^{13}\text{C}$ -HMBC) NMR experiments. Coupling constant (J) values are given in Hertz (Hz). The multiplicity of each resonance observed in the NMR spectra is reported as s = singlet; d = doublet; t = triplet; q = quartet; m = multiplet. ESI measurements were conducted using a Thermo Finnigan LTQ FT Ultra Fourier Transform Ion Cyclotron Resonance Mass Spectrometer. MALDI measurements were performed on a Bruker Daltonics Autoflex II Mass Spectrometer using a nitrogen-cartridge-laser with $\lambda = 337$ nm and sinapinic acid as matrix.

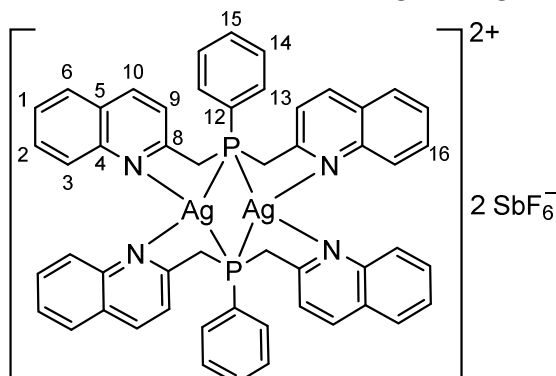
2.9.4.2. Synthesis

Bis(quinaldinyl)phenylphosphine copper(I) tetrafluoroborate $[\text{Cu}_2(\text{C}_{26}\text{H}_{21}\text{N}_2\text{P})_2](\text{BF}_4)_2$ (1**):** A solution of bis(quinaldinyl)phenylphosphine (**A**) (0.286 g, 0.728 mmol) in dry acetonitrile was added to $[\text{Cu}(\text{MeCN})_4]\text{BF}_4$ (0.229 g, 0.728 mmol) and stirred for 12 h. The solution turns orange. The solvent is removed and the remaining residue dissolved in dry, degassed dichloromethane. After removal of all volatiles, **1** is obtained as an orange powder. Crystallization from DCM yields an orange microcrystalline solid: 0.291 g, 74 %.



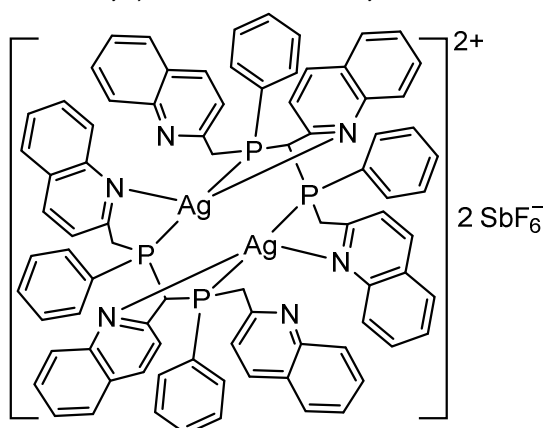
^1H NMR (CD_3CN , 400 MHz): δ [ppm] = ABX spin system (A = B = H, X = P) 3.81 (dd, 2H, $^2J_{\text{BX}} = 5.8$ Hz, $^2J_{\text{AB}} = 15.3$ Hz; H11), 4.08 (dd, 2H, $^2J_{\text{AX}} = 8.0$ Hz, $^2J_{\text{AB}} = 15.4$ Hz; H11), 7.32 (d, 2H, $^3J_{\text{HH}} = 8.5$ Hz, H9), 7.37 (t, 2H, $^3J_{\text{HH}} = 7.4$ Hz, H2 or H16), 7.45 (m, 3H, H23, H2 or H16), 7.52 (t, 2H, $^3J_{\text{HH}} = 7.5$ Hz, H1), 7.64 (t, 2H, $^3J_{\text{HH}} = 8.7$ Hz, H13), 7.75 (dd, 2H, $^3J_{\text{HH}} = 8.1$ Hz, $^4J_{\text{HH}} = 1.6$ Hz, H3), 7.78 (d, 2H, $^3J_{\text{HH}} = 8.5$ Hz, H6), 8.07 (d, 2H, $^3J_{\text{HH}} = 8.4$ Hz, H10). $^{13}\text{C}\{^1\text{H}\}$ (CD_3CN , 101 MHz) δ [ppm] = 38.5 (d, $^1J_{\text{CP}} = 15.4$ Hz, C11), 123.7 (d, $^3J_{\text{CP}} = 3.7$ Hz; C9), 127.5 (s; C2), 127.9 (d, $^2J_{\text{CP}} = 1.3$ Hz; C8), 128.9 (s; C3), 129.1 (s; C6), 129.9 (d, $^3J_{\text{CP}} = 9.1$ Hz; C14), 131.1 (s; C1), 131.5 (d, $^4J_{\text{CP}} = 1.0$ Hz; C15), 133.3 (d, $^2J_{\text{CP}} = 15.6$ Hz; C13), 138.5 (s; C10), 147.5 (s; C5), 159.0 (s; C4). $^{31}\text{P}\{^1\text{H}\}$ (CD_3CN , 162 MHz) δ [ppm] = -14.0 (s). $^{11}\text{B}\{^1\text{H}\}$ (CD_3CN , 128 MHz) δ [ppm] = -1.4 (s). +ESI HRMS ($\text{CH}_3\text{CN}/\text{H}_2\text{O}$) for $[\text{C}_{26}\text{H}_{21}\text{CuN}_2\text{P}]^+$: calcd. 455.0738 m/z ; found 455.0733 m/z .

Bis(quinaldinyl)phenylphosphine silver(I) hexafluoroantimonate $[\text{Ag}_2(\text{C}_{26}\text{H}_{22}\text{N}_2\text{P})_2](\text{SbF}_6)_2$ (**3**): A solution of bis(quinaldinyl)phenylphosphine (0.224 g, 0.570 mmol) in dry acetonitrile was added to AgSbF_6 (0.098 g, 0.285 mmol) and the resulting mixture was stirred for 12 h. The solution turns orange and cloudy. After removal of all volatiles, **3** is obtained as a light orange oil.

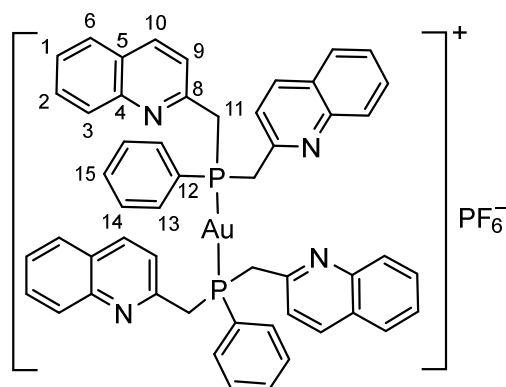


^1H NMR (CD_3CN , 400 MHz): δ [ppm] = ABX spin system (A = B = H, X = P) 4.17 (dd, 2H, $^2J_{\text{BX}} = 8.8$ Hz, $^2J_{\text{AB}} = 14.4$ Hz; H11), 4.26 (dd, 2H, $^2J_{\text{AX}} = 7.9$ Hz, $^2J_{\text{AB}} = 14.4$ Hz; H11), 7.21 (t, 2H, $^3J_{\text{HH}} = 7.4$ Hz, H1), 7.35 (t, 2H, $^3J_{\text{HH}} = 7.2$ Hz, H2), 7.48 (m, 3H, H14, H9), 7.55 (d, 3H, $^3J_{\text{HH}} = 7.8$ Hz, H6, H15), 7.73 (d, 2H, $^3J_{\text{HH}} = 8.2$ Hz, $^4J_{\text{HH}} = 1.1$ Hz, H3), 7.82 (m, 2H, H13), 8.21 (d, 2H, $^3J_{\text{HH}} = 8.4$ Hz, H10). $^{13}\text{C}\{^1\text{H}\}$ (CD_3CN , 101 MHz) δ [ppm] = 38.7 (d, $^1J_{\text{CP}} = 14.8$ Hz, C11), 124.3 (d, $^3J_{\text{CP}} = 3.3$ Hz; C9), 128.0 (s, $^6J_{\text{CP}} = 0.8$ Hz; C2), 128.2 (d, $^2J_{\text{CP}} = 2.6$ Hz; C8), 128.6 (d, $^6J_{\text{CP}} = 0.6$ Hz; C6), 129.0 (d, $^1J_{\text{CP}} = 68.1$ Hz; C12), 129.1 (d, $^5J_{\text{CP}} = 0.8$ Hz; C3), 130.4 (d, $^3J_{\text{CP}} = 10.1$ Hz; C14), 131.6 (s; C1), 133.0 (d, $^4J_{\text{CP}} = 1.9$ Hz; C15), 134.1 (d, $^2J_{\text{CP}} = 16.3$ Hz; C13), 140.0 (s; C10), 147.5 (s; C5), 158.1 (d, $^4J_{\text{CP}} = 1.2$ Hz; C4). $^{31}\text{P}\{^1\text{H}\}$ (CD_3CN , 162 MHz) δ [ppm] = 12.2 (s). $^{19}\text{F}\{^1\text{H}\}$ (CD_3CN , 376 MHz) δ [ppm] = -125.6 (m, $^1J_{\text{Fsb}} = 1935$ Hz). +ESI HRMS ($\text{CH}_3\text{CN}/\text{H}_2\text{O}$) for $[\text{C}_{26}\text{H}_{22}^{109}\text{AgN}_2\text{P}]^+$: calcd. 501.0490 m/z ; found 501.0486 m/z .

$[\text{Ag}_2(\text{C}_{42}\text{H}_{33}\text{N}_3\text{P}_2)](\text{SbF}_6)_2$ (4**):** $^{31}\text{P}\{^1\text{H}\}$ (CD_3CN , 162 MHz) δ [ppm] = 11.4 (s). +ESI HRMS ($\text{CH}_3\text{CN}/\text{H}_2\text{O}$) for $[\text{C}_{42}\text{H}_{33}^{107}\text{AgN}_3\text{P}_2]^+$: calcd. 748.1201 m/z ; found 748.1685 m/z .



Bis(quinaldinyl)phenylphosphine gold(I) hexafluorophosphate $[\text{Au}_2(\text{C}_{26}\text{H}_{21}\text{N}_2\text{P})_2]\text{PF}_6$ (**4**): $[\text{AuCl}(\text{tht})]$ was prepared according to literature procedures.^[33] A solution of bis(quinaldinyl)phenylphosphine (0.100 g, 0.250 mmol) in dry dichloromethane was added to $[\text{AuCl}(\text{tht})]$ (0.040 g, 0.125 mmol) dissolved in dichloromethane. After stirring for 20 min, $\text{K}[\text{PF}_6]$ (0.023 g, 0.125 mmol) is added to the solution to precipitate KCl. The reaction mixture was filtered and the solvent was removed in vacuo. A yellow solid is obtained. Crystallization from DCM yields a yellow microcrystalline solid: 0.146 g, 80 %.



^1H NMR (CD_2Cl_2 , 400 MHz): δ [ppm] = ABX spin system (A = B = H, X = P) 3.97 (d, 2H, $^2J_{\text{AB}} = 15.1$ Hz; H11), 4.26 (d, 2H, $^2J_{\text{AB}} = 15.1$ Hz; H11), 7.09 (s, 2H, H9), 7.29 (t, 2H, $^3J_{\text{HH}} = 7.5$ Hz, H2 or H16), 7.44 (m, 2H, H1), 7.49 (m, 2H, H13), 7.52 (s, 2H, H3), 7.67 (m, 2H, H6), 7.83 (d, 2H, $^3J_{\text{HH}} = 8.3$ Hz, H10). $^{13}\text{C}\{^1\text{H}\}$ (CD_2Cl_2 , 101 MHz) δ [ppm] = 37.4 (s; C11), 122.4 (s; C9), 127.1 (d, $^2J_{\text{CP}} = 8.5$ Hz; C8), 128.1 (s; C6), 129.5 (s; C14), 130.3 (s; C1), 132.6 (s; C15), 133.7 (s; C13), 137.2 (s; C10), 147.5 (s; C5), 154.7 (s; C4). $^{31}\text{P}\{^1\text{H}\}$ (CD_2Cl_2 , 162 MHz) δ [ppm] = 36.4 (s), -143.8 (sept, $^1J_{\text{PF}} = 710$ Hz, PF_6^-). $^{19}\text{F}\{^1\text{H}\}$ (CD_2Cl_2 , 376 MHz) δ [ppm] = -73.6 (d, $^1J_{\text{PF}} = 710$ Hz). +ESI HRMS ($\text{CH}_3\text{CN}/\text{H}_2\text{O}$) for $[\text{C}_{26}\text{H}_{21}\text{AuN}_2\text{P}]^+$: calcd. 981.2550 m/z ; found 981.2567 m/z .

X-ray crystallographic studies: Detailed crystal and structure refinement data are provided in the Supporting Information.

Associated Content: Structure refinement data, NMR spectra of compounds **1**, **3**, **4** and **5**.

Deposition numbers 2072266-2072269 and 2084633 contain the supplementary crystallographic data for this paper. These data are provided free of charge by the joint Cambridge Crystallographic Data Centre.

Acknowledgements

Financial support by the German Federal Ministry for Economic Affairs and Energy on the basis of a decision by the German Bundestag (ZIM, Grant ZF4477702SL7) is gratefully acknowledged. Prof. Dr. T. M. Klapötke is thanked for his uninterrupted support over the years.

2.9.5. References

- [1] L. Fanfoni, A. Meduri, E. Zangrando, S. Castillon, F. Felluga, B. Milani, *Molecules* **2011**, *16*, 1804–1824.
- [2] H. Jaafar, H. Li, L. C. Misal Castro, J. Zheng, T. Roisnel, V. Dorcet, J.-B. Sortais, C. Darcel, *Eur. J. Inorg. Chem.* **2012**, *2012*, 3546–3550.
- [3] D. Rosario-Amorin, S. Ouizem, D. A. Dickie, Y. Wen, R. T. Paine, J. Gao, J. K. Grey, A. De Bettencourt-Dias, B. P. Hay, L. H. Delmau, *Inorg. Chem.* **2013**, *52*, 3063–3083.
- [4] G. Chelucci, G. Orrù, G. a. Pinna, *Tetrahedron* **2003**, *59*, 9471–9515.
- [5] F. Hung-Low, K. K. Klausmeyer, *Polyhedron* **2010**, *29*, 1676–1686.
- [6] B. Shankar, P. Elumalai, R. Shanmugam, V. Singh, D. T. Masram, M. Sathiyendiran, *Inorg. Chem.* **2013**, *52*, 10217–10219.
- [7] F. Leca, C. Lescop, E. Rodriguez-Sanz, K. Costuas, J. F. Halet, R. Réau, *Angew. Chem.* **2005**, *117*, 4436–4439; *Angew. Chemie Int. Ed.* **2005**, *44*, 4362–4365.
- [8] T. Pechmann, C. D. Brandt, H. Werner, *Angew. Chem.* **2000**, *112*, 4069–4072; *Angew. Chem. Int. Ed.* **2000**, *39*, 3909–3911.
- [9] T. Pechmann, C. D. Brandt, C. Röger, H. Werner, *Angew. Chem.* **2002**, *114*, 2398–2401; *Angew. Chem. Int. Ed.* **2002**, *41*, 2301–2303.

- [10] H. Werner, *Angew. Chem.* **2004**, *116*, 956–972; *Angew. Chem. Int. Ed.* **2004**, *43*, 938–954.
- [11] S. Schinzel, R. Müller, S. Riedel, H. Werner, M. Kaupp, *Chem. - A Eur. J.* **2011**, *17*, 7228–7235.
- [12] M. B. Smith, *Platin. Met. Rev.* **2008**, *52*, 215–221.
- [13] B. Nohra, R. Reau, C. Lescop, *Eur. J. Inorg. Chem.* **2014**, *2*, 1788–1796.
- [14] B. Attenberger, M. El Sayed Moussa, T. Brietzke, V. Vreshch, H.-J. Holdt, C. Lescop, M. Scheer, *Eur. J. Inorg. Chem.* **2015**, *2015*, 2934–2938.
- [15] H. Schmidbaur, A. Schier, *Angew. Chem.* **2015**, *127*, 756–797; *Angew. Chem. Int. Ed.* **2015**, *54*, 746–784.
- [16] F. Scherbaum, A. Grohmann, B. Huber, C. Krüger, H. Schmidbaur, *Angew. Chem.* **1988**, *100*, 1602–1604; *Angew. Chem. Int. Ed. Engl.* **1988**, *27*, 1544–1546.
- [17] S. Dinda, A. G. Samuelson, *Chem. - A Eur. J.* **2012**, *18*, 3032–3042.
- [18] Z.-W. Ruan, X. Zhang, A.-Y. Pang, F.-R. Dai, Z.-N. Chen, *Inorg. Chem. Commun.* **2020**, *116*, 107916.
- [19] M. J. Calhorda, C. Ceamanos, O. Crespo, M. C. Gimeno, A. Laguna, C. Larraz, P. D. Vaz, M. D. Villacampa, *Inorg. Chem.* **2010**, *49*, 8255–8269.
- [20] M. K. Rong, F. Holtrop, J. C. Slootweg, K. Lammertsma, *Coord. Chem. Rev.* **2019**, *382*, 57–68.
- [21] S. K. Gibbons, R. P. Hughes, D. S. Glueck, A. T. Royappa, A. L. Rheingold, R. B. Arthur, A. D. Nicholas, H. H. Patterson, *Inorg. Chem.* **2017**, *56*, 12809–12820.
- [22] S. Schäfer, M. T. Gamer, S. Lebedkin, F. Weigend, M. M. Kappes, P. W. Roesky, *Chem. - A Eur. J.* **2017**, *23*, 12198–12209.
- [23] C. Kirst, F. Zoller, T. Bräuniger, P. Mayer, D. Fattakhova-Rohlfing, K. Karaghiosoff, *Inorg. Chem.* **2021**, *60*, 2437–2445.
- [24] F. Hung-Low, A. Renz, K. K. Klausmeyer, *Eur. J. Inorg. Chem.* **2009**, 2994–3002.
- [25] R. Peng, M. Li, D. Li, *Coord. Chem. Rev.* **2010**, *254*, 1–18.
- [26] C. Janiak, *Dalton Trans.* **2000**, 3885–3896.
- [27] W. B. Jennings, B. M. Farrell, J. F. Malone, *Acc. Chem. Res.* **2001**, *34*, 885–894.
- [28] S. S. Batsanov, *Inorg. Mater.* **2001**, *37*, 871–885.
- [29] S. M. Socol, J. G. Verkade, *Inorg. Chem.* **1984**, *23*, 3487–3493.
- [30] S. Attar, N. W. Alcock, G. A. Bowmaker, J. S. Frye, W. H. Bearden, J. H. Nelson, *Inorg. Chem.* **1991**, *30*, 4166–4176.
- [31] R. E. Bachman, D. F. Andretta, *Inorg. Chem.* **1998**, *37*, 5657–5663.
- [32] R. Narayanaswamy, M. A. Young, E. Parkhurst, M. Ouellette, M. E. Kerr, D. M. Ho, R. C. Elder, A. E. Bruce, M. R. M. Bruce, *Inorg. Chem.* **1993**, *32*, 2506–2517.
- [33] R. Uson, A. Laguna, J. Vicente, *J. Organomet. Chem.* **1977**, *131*, 471–475.

2.9.6. Supporting information

2.9.6.1. Crystallographic and refinement data

Table 27. Crystallographic and refinement data for compounds **A**, **1** and **2**.

	A		1		2	
Formula	C ₂₆ H ₂₁ N ₂ P		C ₅₃ H ₄₄ N ₄ P ₂ Cl ₂ Cu ₂ B ₂ F ₈		C ₅₃ H ₄₄ N ₄ P ₂ Cl ₅ Cu ₄ BF ₄	
Formula weight [g·mol ⁻¹]	392.42		1170.46		1317.08	
Colour	colorless		orange		yellow	
Habit	rod		prism		block	
T [K]	123		113		123	
λ [Å]	0.71073		0.71073		0.71073	
Crystal system	monoclinic		monoclinic		monoclinic	
Space group	P2 ₁		P2 ₁ /c		P2 ₁ /n	
a [Å]	10.5191(14)		10.5369(4)		14.3093(6)	
b [Å]	5.8020(7)		21.1437(8)		28.4914(7)	
c [Å]	17.3511(19)		22.6528(10)		16.1829(6)	
α [°]	90		90		90	
β [°]	105.475(12)		100.495(4)		101.001(3)	
γ [°]	90		90		90	
V [Å ³]	1020.6(2)		4962.4(4)		6476.4(4)	
Z	2		4		4	
ρ _{calc} [g·cm ⁻³]	1.277		1.567		1.351	
μ [mm ⁻¹]	0.149		1.102		1.597	
F(0 0 0)	412		2376		2648	
Crystal size [mm]	0.20×0.05×0.05		0.25×0.10×0.05		0.20×0.20×0.05	
θ range [°]	2.053–26.017		1.966–26.022		1.883–26.022	
Index ranges	-12 ≤ h ≤ 12 -7 ≤ k ≤ 7 -21 ≤ l ≤ 21		-13 ≤ h ≤ 12 -24 ≤ k ≤ 26 -27 ≤ l ≤ 20		-17 ≤ h ≤ 17 -29 ≤ k ≤ 35 -19 ≤ l ≤ 19	
reflns collected	12954		36165		45617	
Independent reflns	4006 [R _{int} = 0.0886]		9745 [R _{int} = 0.1036]		12748 [R _{int} = 0.1343]	
Completeness to theta	99.9 %		100.0 %		100.0 %	
Refinement method	full-matrix	least-	full-matrix	least-	full-matrix	least-
	squares on F ²		squares on F ²		squares on F ²	
Data/restraints/Parameters	4006 / 0 / 262		9745 / 0 / 668		12748 / 0 / 658	
Hydrogen atom treatment	constrained		constrained		constrained	
R ₁ /wR ₂ (I > 2 σ (I))	0.0766/0.1759		0.0630/0.1342		0.0716/0.1524	
R ₁ /wR ₂ (all data)	0.1003/0.1946		0.1205/0.1616		0.1444/0.1887	
Goodness-of-fit on F ²	1.055		1.020		0.955	
larg. diff peak/hole [e·Å ⁻³]	0.832/-0.236		0.849/-0.622		1.115/-0.799	
CCDC No.	2084633		2072267		2072269	

Table 28. Crystallographic and refinement data for compounds **4** and **5**.

	4	5
Formula	C ₈₄ H ₆₆ N ₆ P ₄ Ag ₂ Sb ₂ F ₁₂	C ₅₂ H ₄₂ Au ₂ F ₆ N ₄ P ₃
Formula weight [g·mol ⁻¹]	1970.54	1126.77
Colour	colorless	colorless
Habit	block	block
<i>T</i> [K]	101	102
λ [Å]	0.71073	0.71073
Crystal system	triclinic	triclinic
Space group	<i>P</i> -1	<i>P</i> -1
<i>a</i> [Å]	12.8552(17)	8.8417(4)
<i>b</i> [Å]	13.8150(18)	10.9684(5)
<i>c</i> [Å]	14.0363(18)	12.3120(6)
α [°]	66.451(4)	99.888(2)
β [°]	89.656(4)	104.447(2)
γ [°]	63.092(4)	98.692(2)
<i>V</i> [Å ³]	1990.6(5)	1115.28(9)
<i>Z</i>	1	1
ρ_{calc} [g·cm ⁻³]	1.644	1.678
μ [mm ⁻¹]	1.313	3.474
<i>F</i> (0 0 0)	976	560
Crystal size [mm]	0.02×0.02×0.02	0.03×0.03×0.01
Θ range [°]	2.682–25.135	3.138–28.282
Index ranges	-15 ≤ <i>h</i> ≤ 15 -16 ≤ <i>k</i> ≤ 16 -16 ≤ <i>l</i> ≤ 16	-11 ≤ <i>h</i> ≤ 11 -14 ≤ <i>k</i> ≤ 14 -16 ≤ <i>l</i> ≤ 16
reflns collected	19074	20123
Independent reflns	6969 [<i>R</i> _{int} = 0.1323]	5525 [<i>R</i> _{int} = 0.0373]
Completeness to theta	97.7 %	99.7 %
Refinement method	full-matrix least-squares on <i>F</i> ²	full-matrix least-squares on <i>F</i> ²
Data/ restraints/ Parameters	6969 / 0 / 496	5525 / 0 / 301
Hydrogen atom treatment	constrained	constrained
<i>R</i> ₁ / <i>wR</i> ₂ (<i>I</i> > 2 σ (<i>I</i>))	0.0911/0.1798	0.0215/0.0476
<i>R</i> ₁ / <i>wR</i> ₂ (all data)	0.1919/0.2179	0.0217/0.0477
Goodness-of-fit on <i>F</i> ²	1.011	1.042
larg. diff peak/hole [e·Å ⁻³]	1.909/-0.990	0.672/-0.535
CCDC No.	2072268	2072266

2.9.6.2. Additional figures

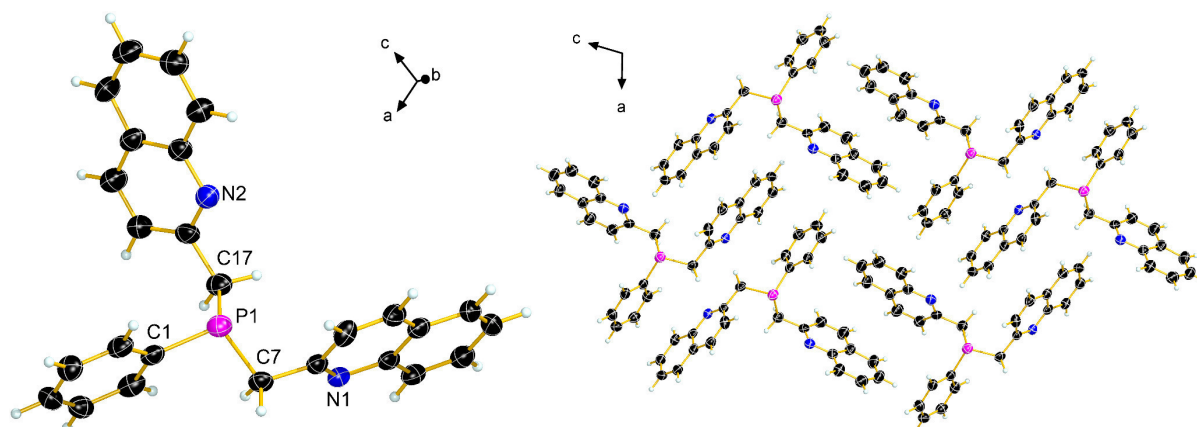


Figure 129. Molecular structure of compound **A** in the crystal; view of the asymmetric unit (left). Crystal Packing of **A** along the *b* axis (right). Thermal ellipsoids are drawn at 50 % probability level.

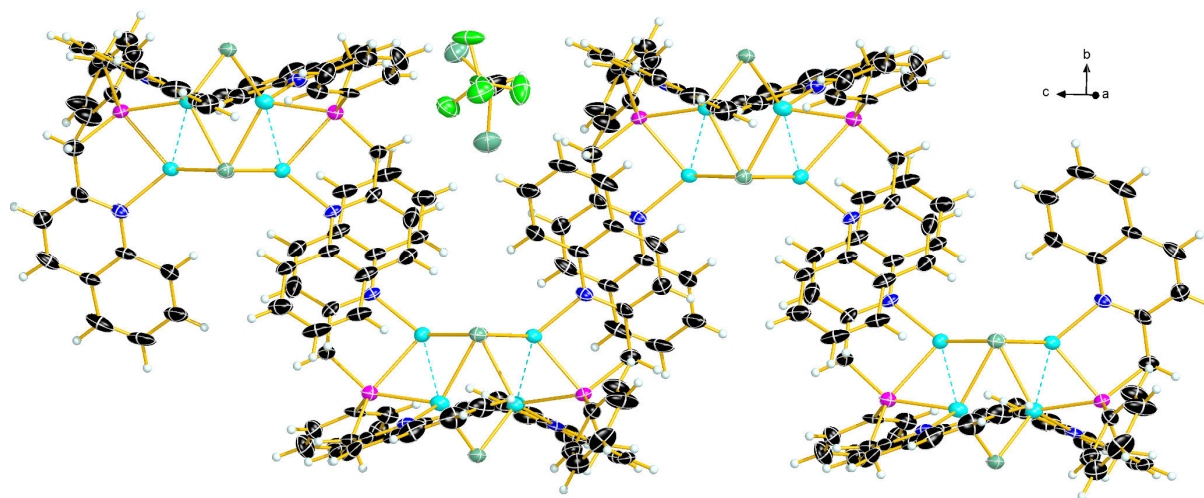


Figure 130. Packing of **2** visualizing the π -stacking of the quinaldinyll rings in the 3D-structure of the crystal. Thermal ellipsoids are drawn at 50 % probability level.

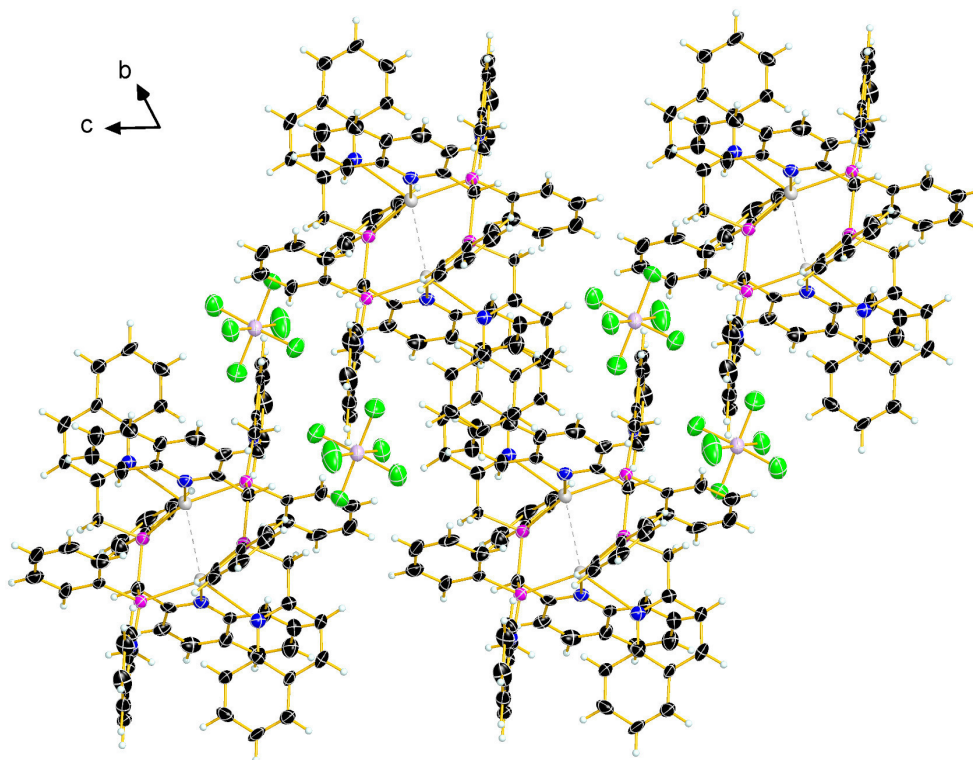


Figure 131. Packing of **4** along the a axis visualizing the π -stacking motifs in the 3D-structure of the crystal. Thermal ellipsoids are drawn at 50 % probability level.

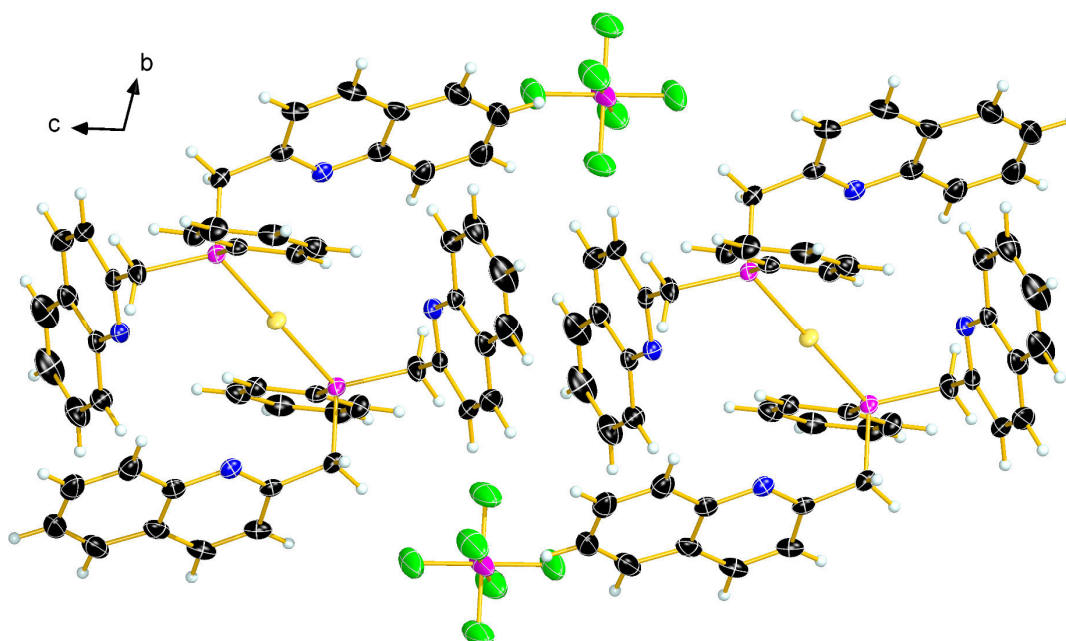
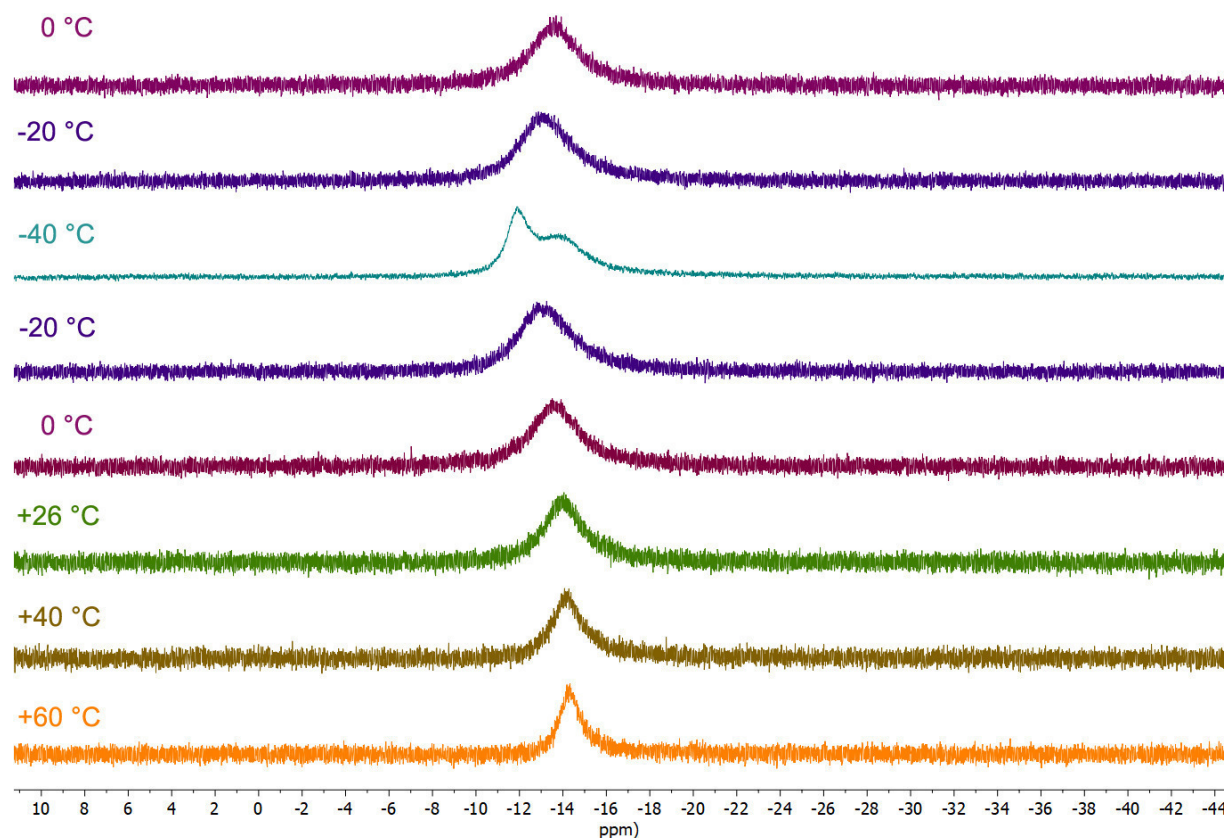
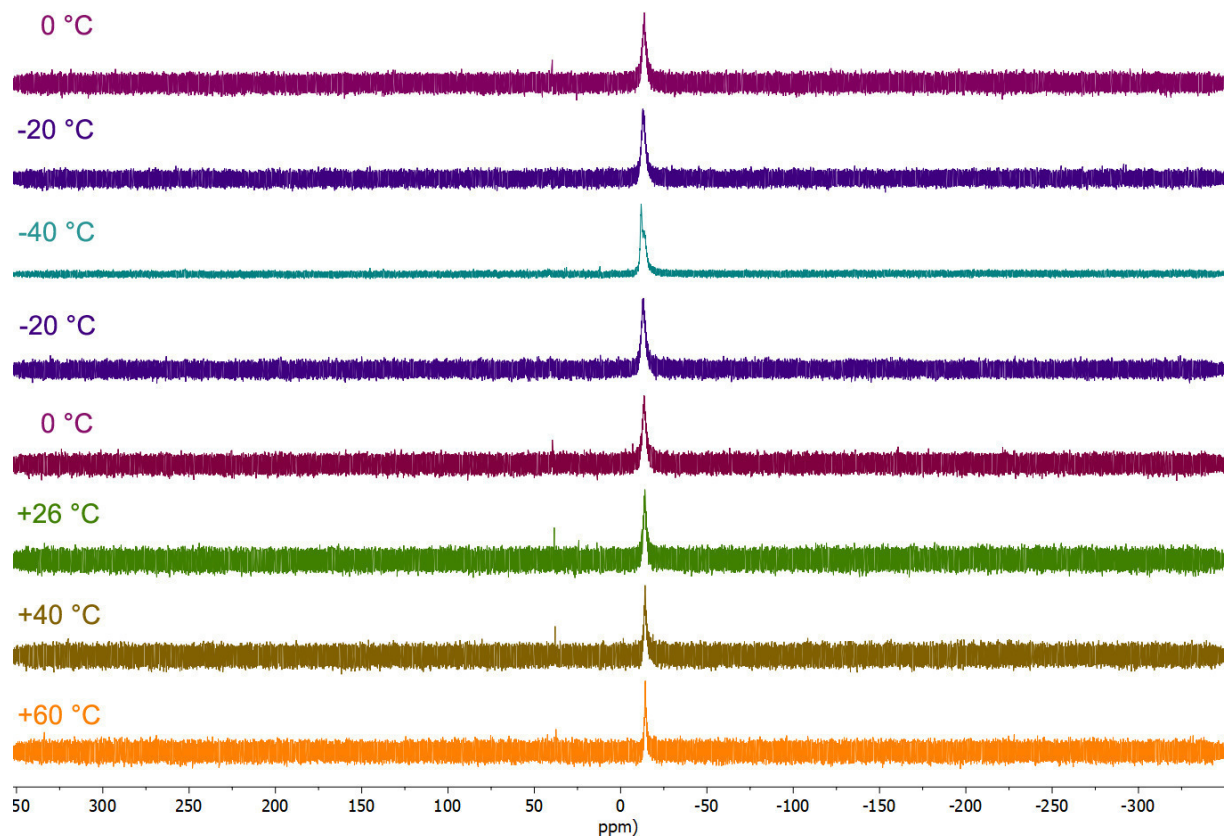


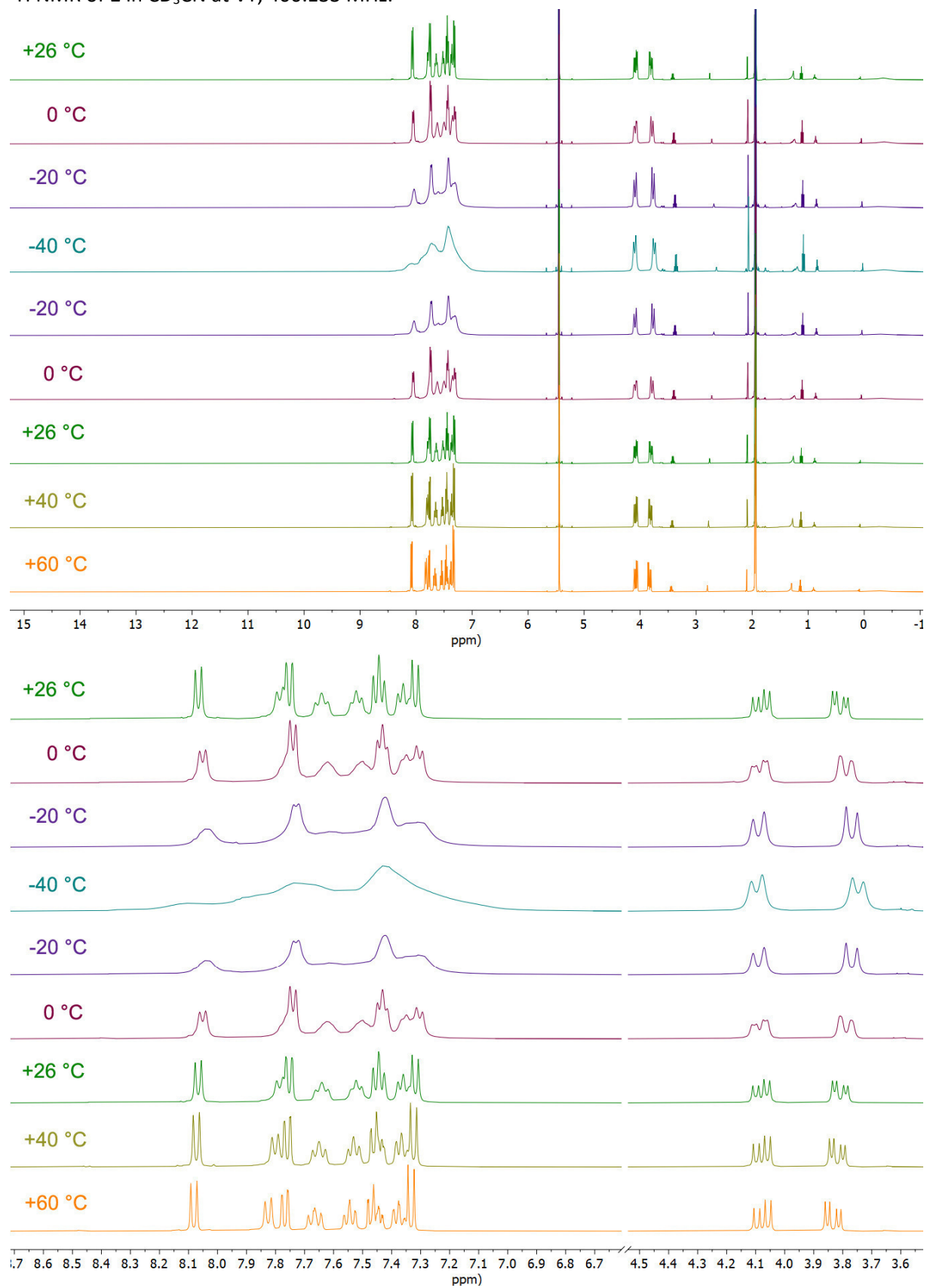
Figure 132. Packing of **5** along the a axis visualizing the π -stacking of the quinaldinyl rings in the 3D-structure of the crystal. Thermal ellipsoids are drawn at 50 % probability level.

2.9.6.3. VT NMR Spectra

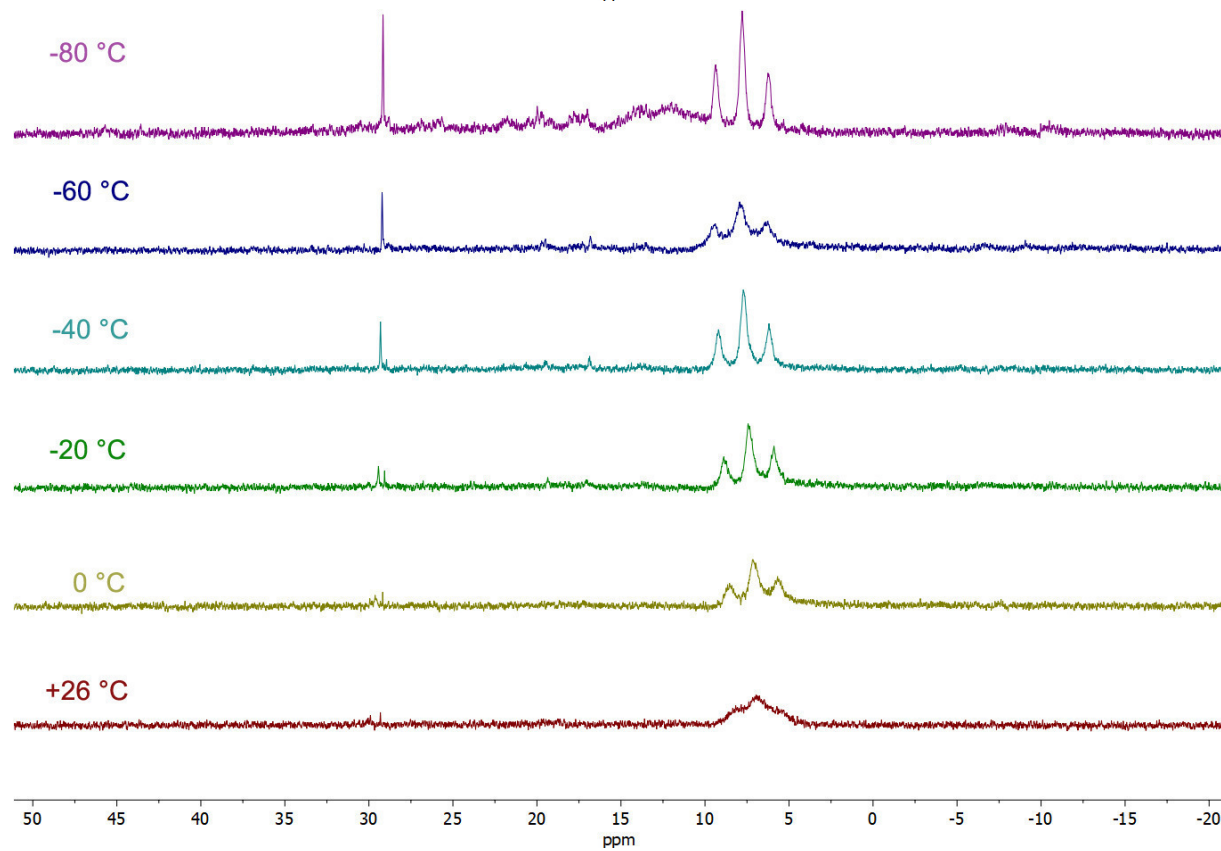
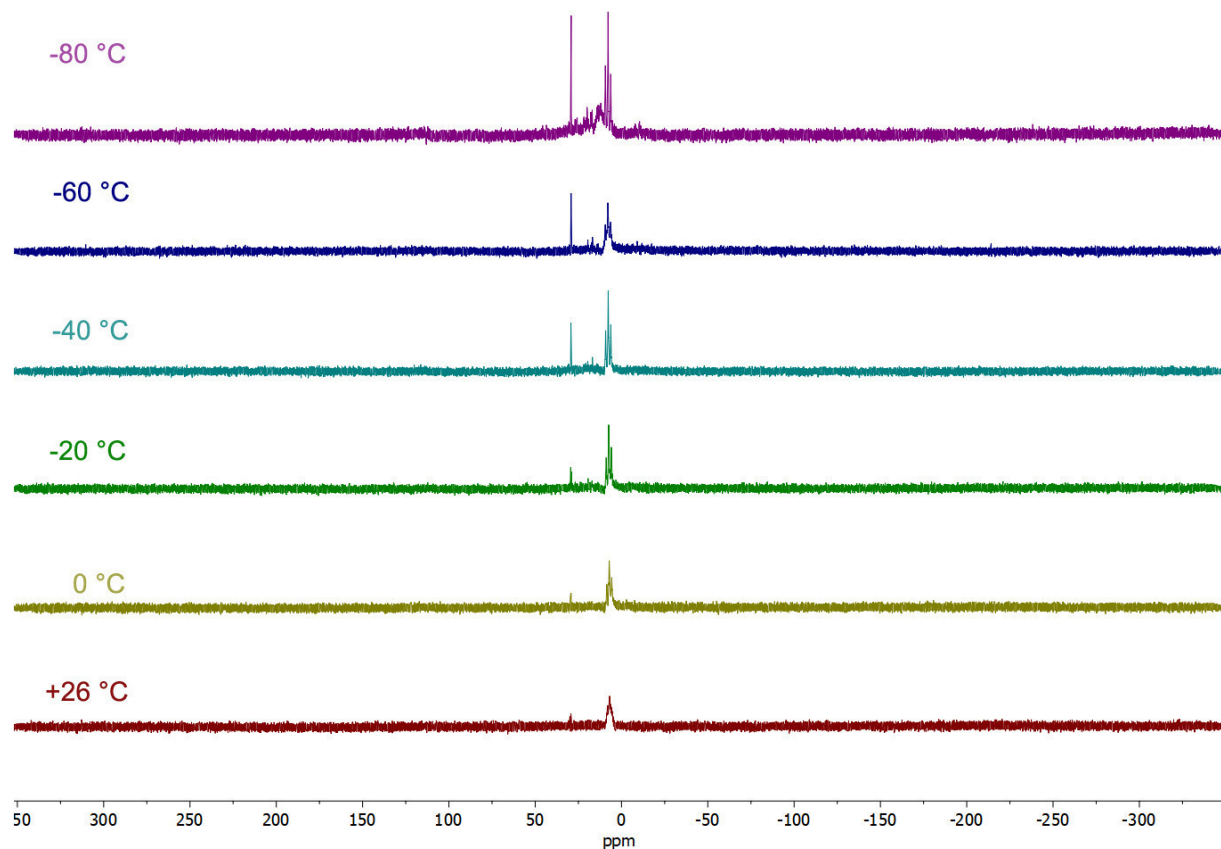
$^{31}\text{P}\{^1\text{H}\}$ NMR of **1** in CD_3CN at VT, 161.976 MHz.



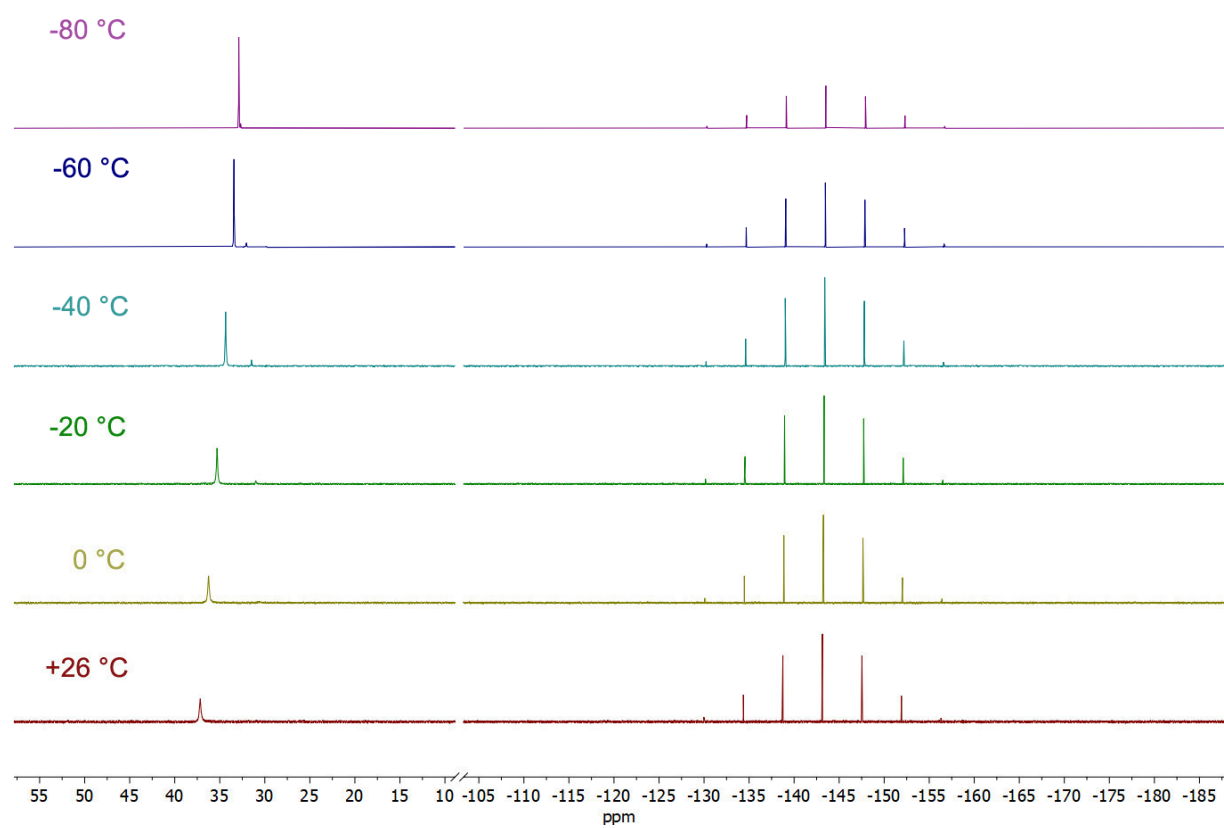
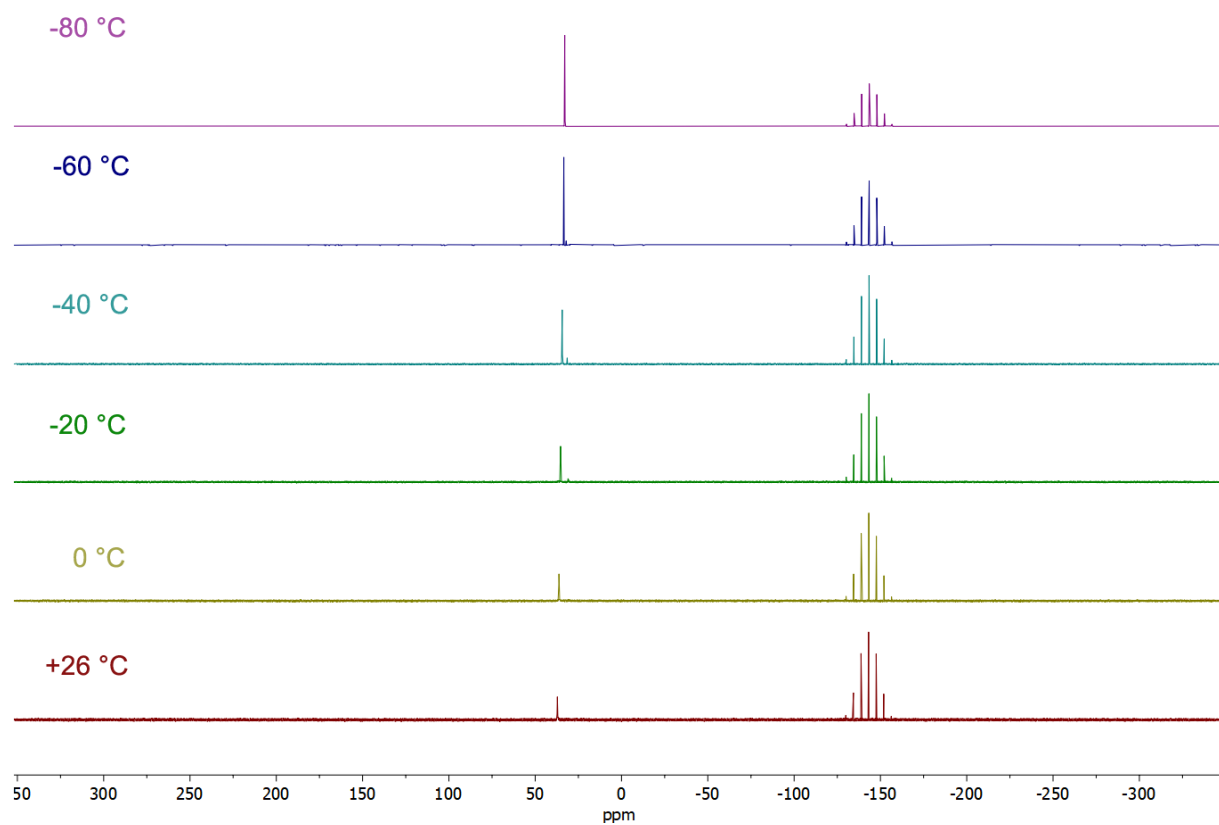
^1H NMR of **1** in CD_3CN at VT, 400.133 MHz.



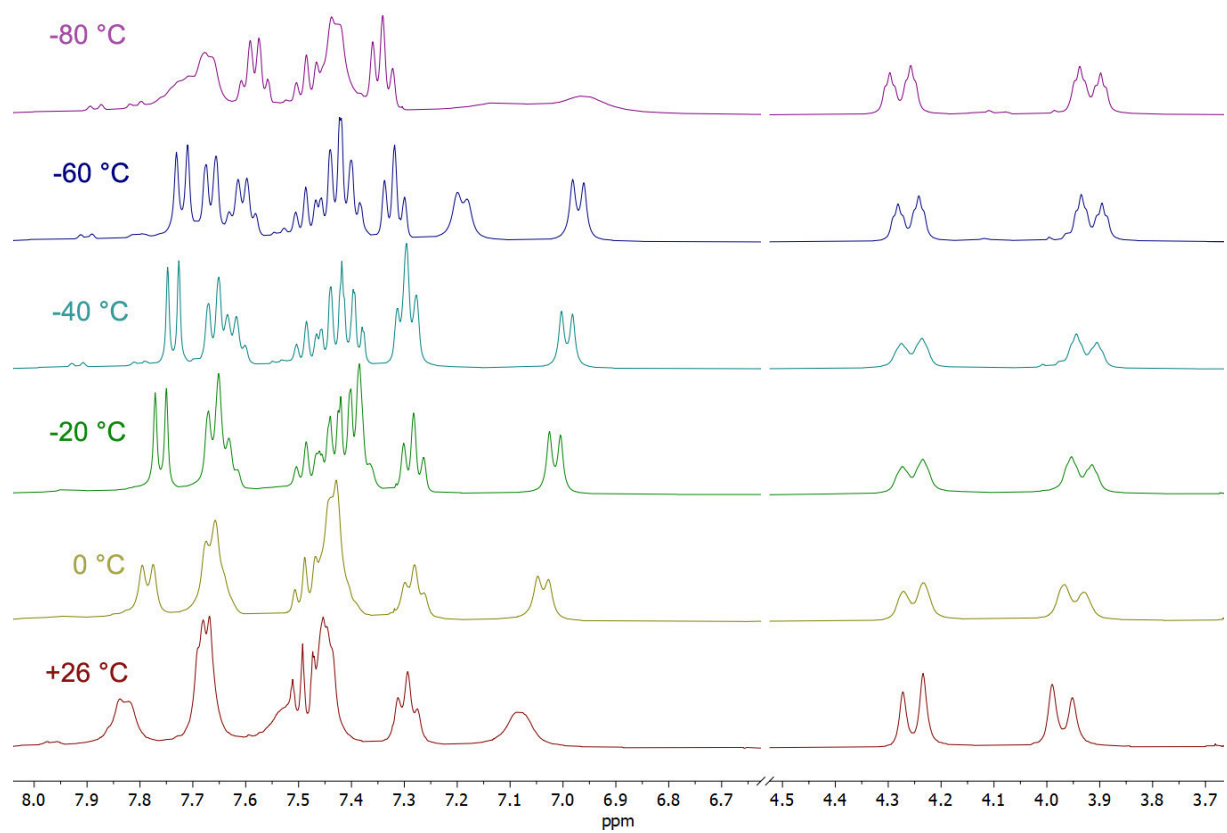
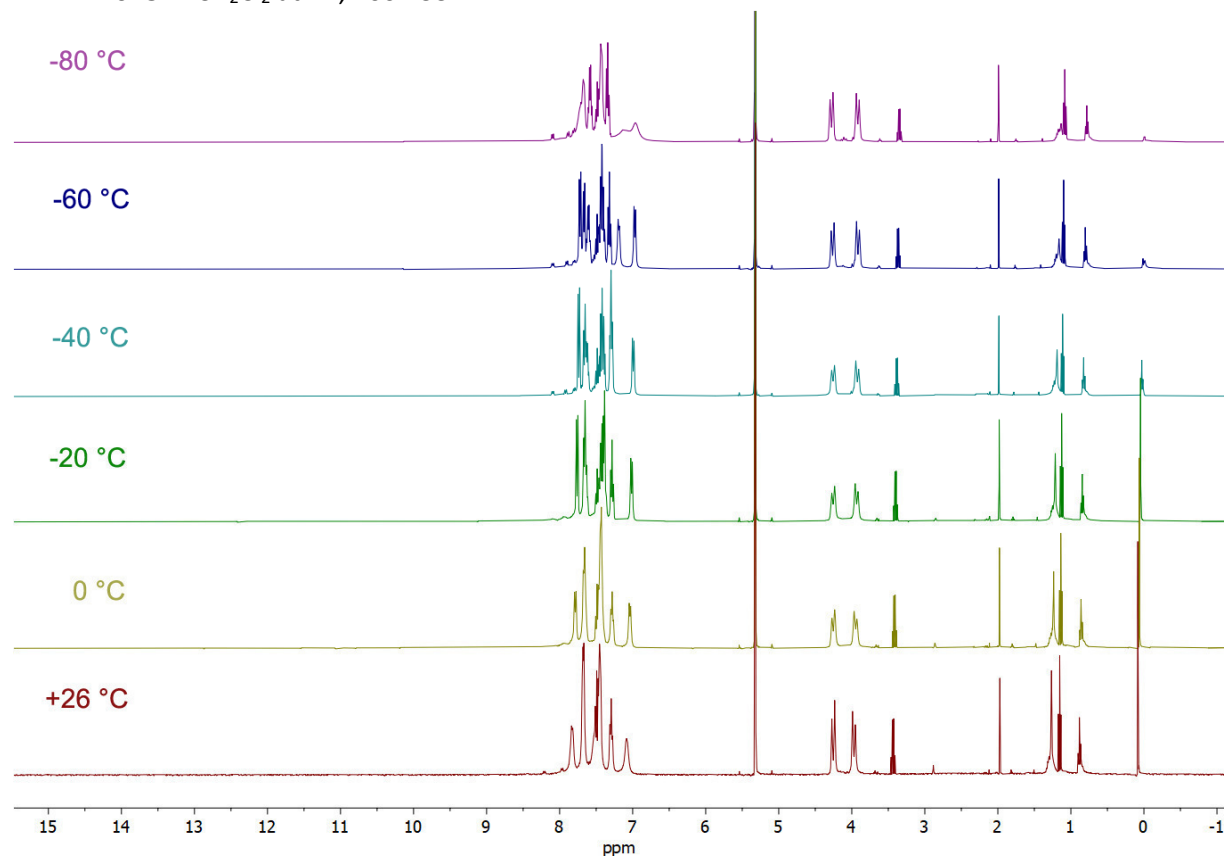
$^{31}\text{P}\{^1\text{H}\}$ NMR of **3** in CD_2Cl_2 at VT, 161.976 MHz.



$^{31}\text{P}\{^1\text{H}\}$ NMR of **5** in CD_2Cl_2 at VT, 161.976 MHz.



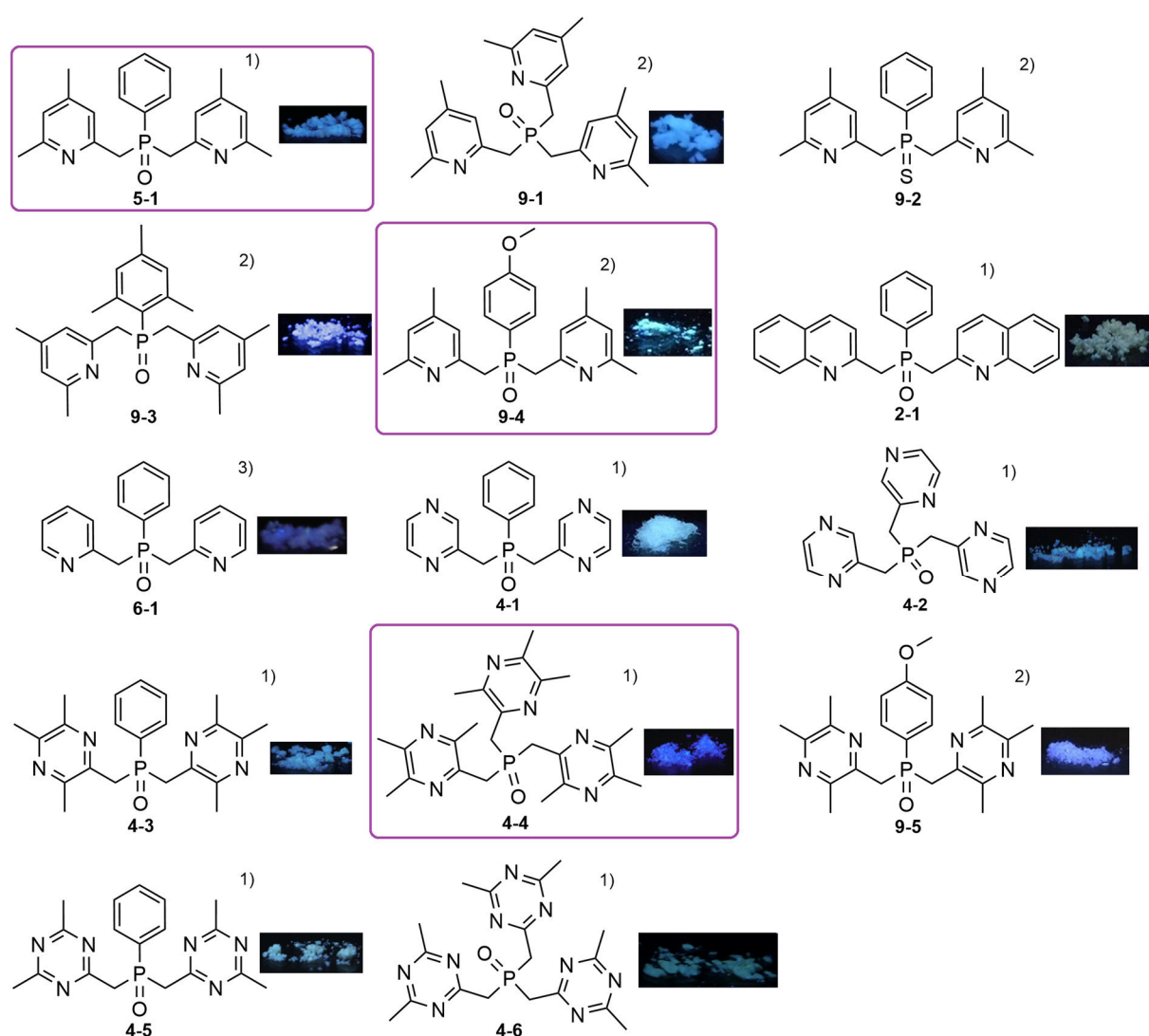
^1H NMR of **5** in CD_2Cl_2 at VT, 400.133 MHz.



3. Summary and conclusion – key findings

3.1. Functionalized P,N-ligands – small changes, big impacts

A library containing fourteen P,N-ligands with two or three picolyl-derived substituents and their corresponding phosphine oxides was successfully prepared. The synthesis of the phosphines follows the Braunstein route and starts from the respective organic trimethylsilyl-derivatives involving the reaction with dichlorophosphines or PCl_3 (Scheme 22). The electron content of the aromatic ligands was varied by introducing different numbers of nitrogen atoms. To further increase the solubility of the compounds methyl groups were added to the aromatic systems. The trimethylsilyl-compounds of the pyrazine- and triazine-derivatives were synthesized for the first time. In case of ligands with two picolyl-derived substituents, the third group at phosphorus was varied by using phenyl-, methoxyphenyl- or mesityl dichlorophosphine in the synthesis.



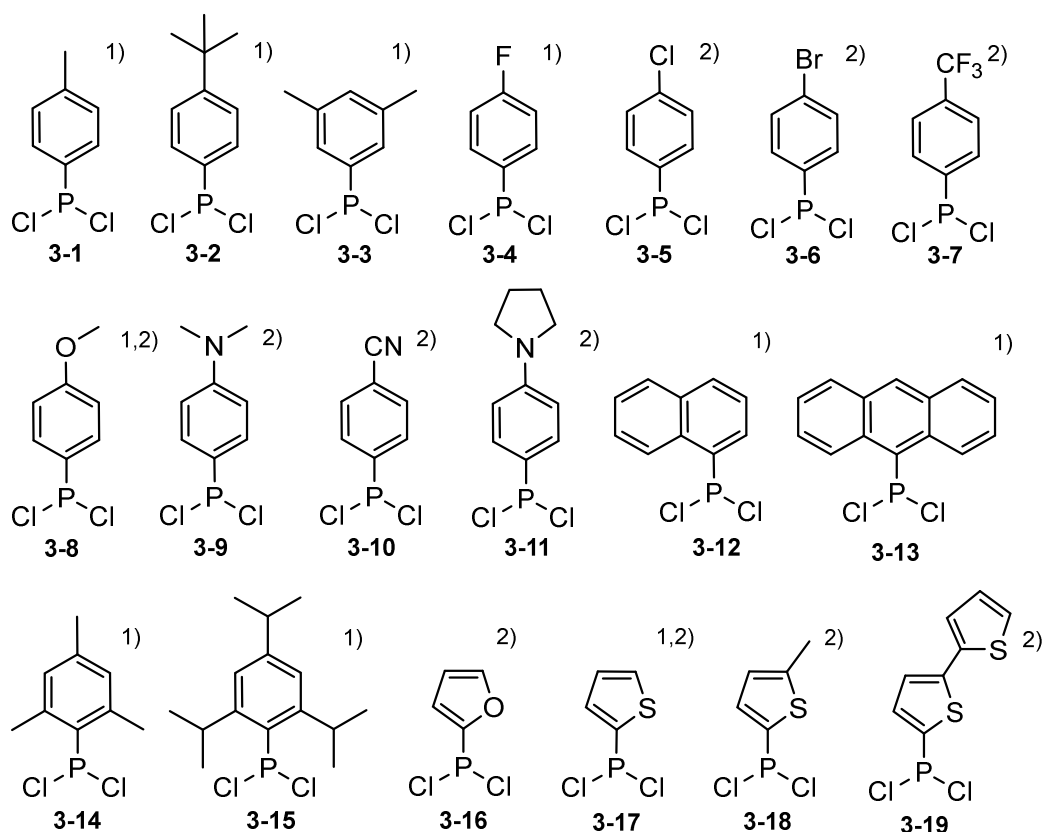
Scheme 23. Synthesized P,N-ligands during the course of this thesis and pictures of the solids when irradiated with UV light (366 nm). The compounds with the most interesting optical appearances are highlighted in purple.

After oxidation of the phosphines in solution with hydrogen peroxide, a hydrogen peroxide molecule oftentimes coordinates to bis-substituted phosphine oxides, which is visible in the crystal structures as well as in the ^1H NMR spectra. The coordinating hydrogen peroxide, however, can be removed by the use of molecular sieves.

The ligands show luminescence in the solid state when illuminated with UV light (366 nm) mostly in the blue light region. The lifetime of the autofluorescence decay of compounds **4-1–4-6** and **5-1** was measured using FLIM and is in the region of 3–6 ns (fluorescence). FLIM combined with Hirshfeld surface analysis revealed that the morphology, crystal packing and the quantity and nature of intermolecular interactions play an important role in the manifestation of luminescent properties. The higher the amount of attractive hydrogen bonds, the higher the intensity and the lower the average fluorescence lifetime. Compounds containing functional groups such as cyano-, methoxy- or dialkylamino groups should be synthesized to further verify this trend.

3.2. A general approach to dichlorophosphines – an easy and mild route for P-C-bond formation

An alternative, one-pot synthesis for literature-known and new dichlorophosphines utilizing an organozinc intermediate was found. This synthesis was successfully applied to the dichlorophosphines shown in Scheme 23. The compounds were isolated in medium to high yields (41–82 %). The developed procedure is executed under mild conditions and offers the opportunity for the synthesis of other, new dichlorophosphines, such as compound **3-11**.



1) this thesis

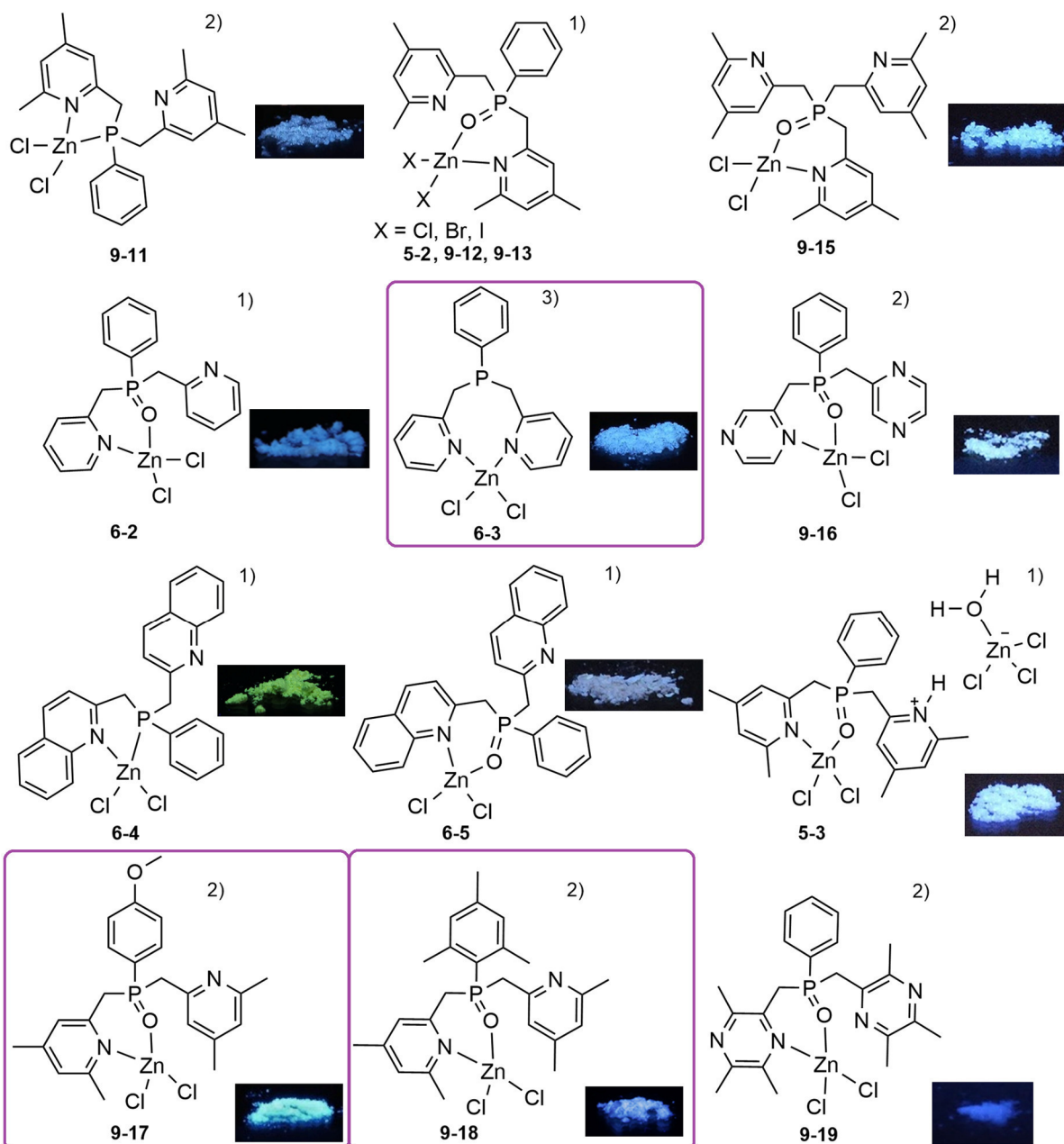
2) additional results of Jonathan Tietze, M.Sc.

Scheme 24. Dichlorophosphines synthesized utilizing organozinc intermediates.

3.3. Zinc and phosphorus – a luminescent combination

Fourteen Zn(II) complexes were synthesized (Scheme 24) using some of the phosphine and phosphine oxide ligands presented in Scheme 22. They all show luminescence in the UV/blue to green-blue region and in one case in the green-yellow region of the visible spectrum when illuminated with UV light (366 nm). The powdered compounds **5-2** and **5-3** show emission maxima at around 400 nm and a PLQY of 36-42 %, which is comparable to other known, blue-emitting Zn(II) complexes. The autofluorescence lifetimes of compounds **5-2** and **5-3** were further investigated using FLIM and lifetimes of 3.5-5.9 ns were measured. Again, these lifetimes are indicative of single-single electron transitions. The combination of these results with Hirshfeld surface analysis further show: the higher the content of π - π stacking interactions, the lower the fluorescence intensity. A similar trend is observed for the fluorescence lifetime, which decreases the higher the amount of attractive hydrogen bond interactions.

To investigate the influence of different anions on the properties of the resulting complexes ZnCl₂, ZnBr₂ and ZnI₂ were used in the complexation of one ligand. They show a red shift of the emission maximum in going from Cl⁻ to Br⁻ to I⁻. In the same order the melting points decrease with the zinc(II) iodide complex having the lowest. Non-coordinating ions might also have an influence on the optical and thermal properties of the corresponding Zn(II) complexes, which should be further investigated. In general, the complexes show a dynamic behavior in solution, where Zn(II) stays coordinated to oxygen but switches from coordinating to one nitrogen atom or the other. This movement can be slowed down by lowering the temperature, which is observable *via* variable-temperature NMR spectroscopy. The salt **3-2**, is the only compound of the investigated complexes, which is emissive in thin film. This compound does not display strong dynamics in solution as the second nitrogen atom is blocked, which probably also facilitates the emission in thin film. Blocking free coordination sites of the ligand with other metals or *via* protonation might result in improved optical properties and behavior in thin films.



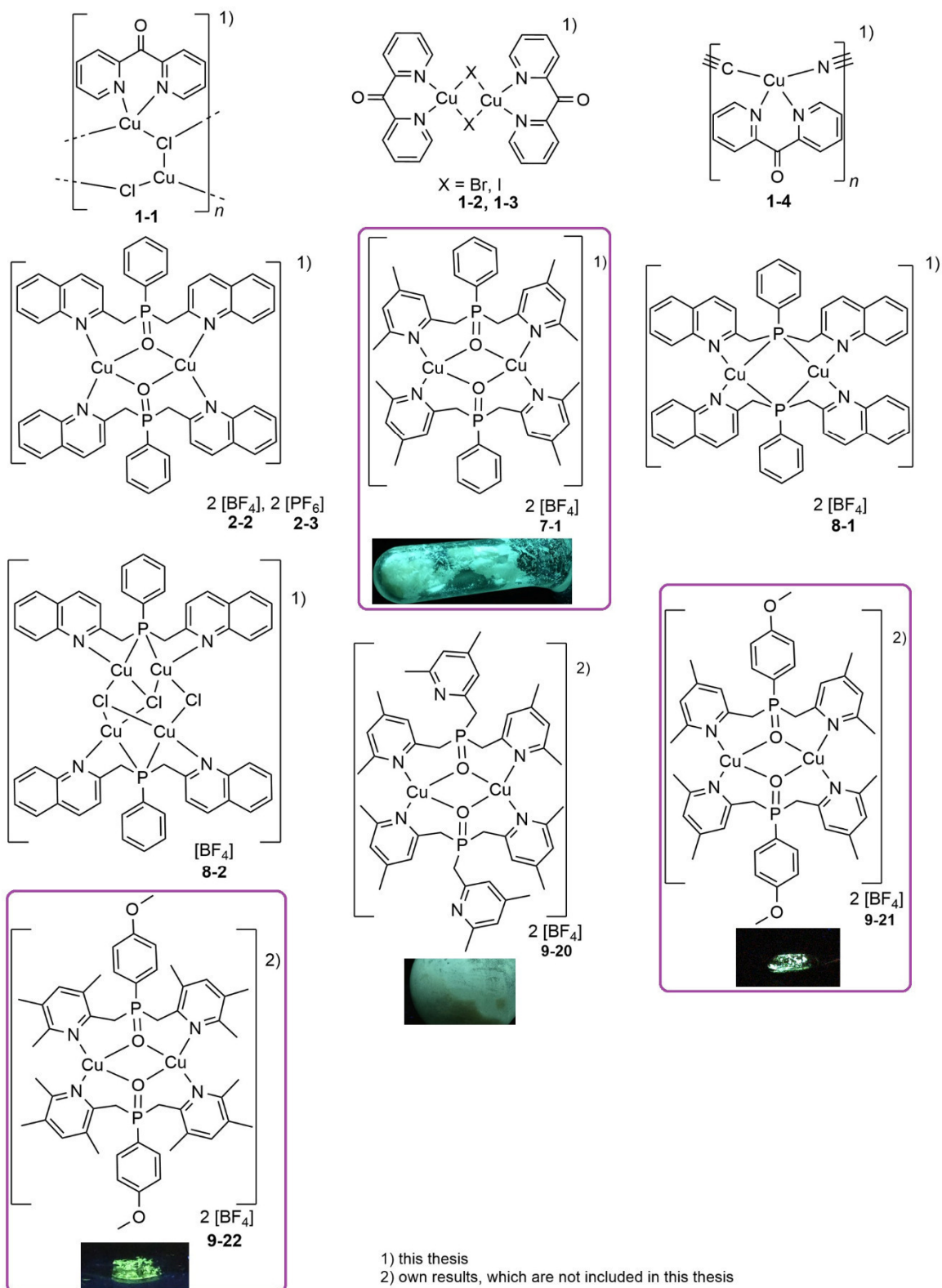
- 1) this thesis
 2) own results, which are not included in this thesis
 3) known compound, crystal structure is new

Scheme 25. Zn(II) complexes of selected phosphine and phosphine oxide ligands and pictures of the solids when irradiated with UV light (366 nm). The compounds with the most interesting optical properties are highlighted in purple.

3.4. Copper(I) complexes – from blue to green

Five copper(I) complexes of phosphine oxides and one complex using bisquinaldinyl phenylphosphine were prepared (Scheme 25). The complexes containing bisquinaldinyl phenylphosphine and its oxide do not show luminescent properties when irradiated with UV light (366 nm). However, the other four Cu(I) phosphine oxide complexes show luminescence in the blue/green region of the visible spectrum when irradiated with UV light (366 nm). Electrochemical measurements reveal, that complex **2-2** is redox active and its oxidation and reduction are reversible.

In addition to phosphine oxides, also di(2-pyridyl)ketone (dpk) was used as a ligand for the complexation of copper(I). In contrast to dpk complexes with other metals described in the literature, the Cu(I) complexes of dpk prepared in this thesis do not emit in the visible light region. Remarkably, the Cu(I) dpk complexes can be prepared mechanochemically without using a solvent, which is clearly observable by a rapid color change from colorless to dark red/black or orange.

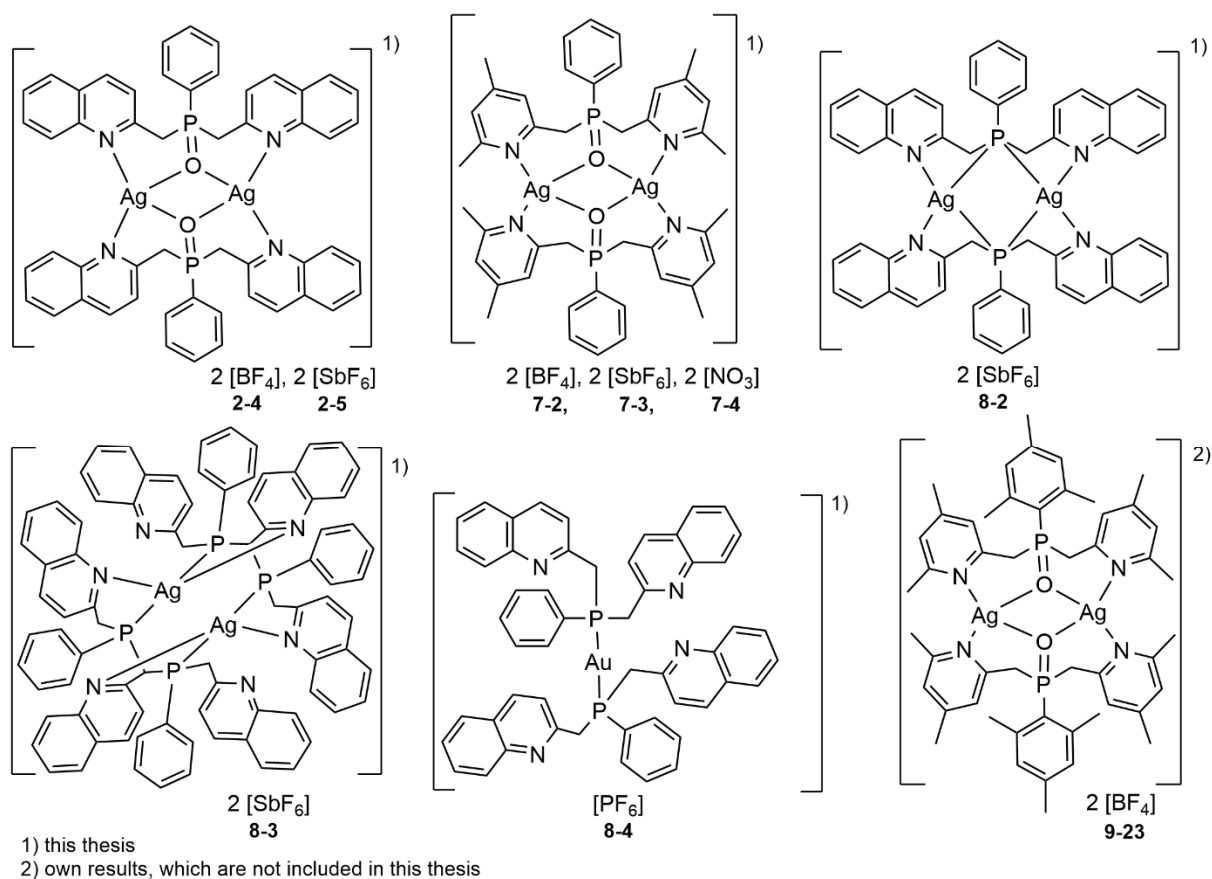


Scheme 26. Copper(I) complexes of selected phosphines, phosphine oxides and dpk and pictures of the solids when irradiated with UV light (366 nm). The compounds with the most interesting optical properties are highlighted in purple.

3.5. Silver(I) and gold(I) – noble but non-emissive complexes

Over the course of this thesis, six silver(I) complexes and one gold(I) complex of selected phosphines and phosphine oxides with non-coordinating counterions were prepared and characterized (Scheme 26). Contrary to the copper(I) and zinc(II) complexes, none of these silver(I) or gold(I) complexes show luminescence in the visible light spectrum in the solid state, even when using the more electron donating phosphine instead of phosphine oxide (compound **2-1**). Stronger donating phosphine ligands have to be designed to reduce quenching in the solid state.

Surprisingly, when Ag(I)SbF₆ was allowed to react with phosphine (**2-1**), complex **8-3** containing silver(I) coordinating to a diphosphine was obtained during the crystallization attempt instead of the expected phosphine complex **8-2**. The formation of the diphosphine during the complex-preparation is, to the best of my knowledge, quite unusual. The ³¹P NMR spectrum of complex **8-2** shows a triplet, caused by the coupling of phosphorus to two silver(I) atoms with a coupling constant of $J_{P-Ag} = 250$ Hz at -80 °C. With Ag(I), the multidentate phosphine oxide ligands impressively demonstrate their versatile coordination behavior, especially shown in the crystal structures of compounds **7-2–7-4**. The coordination motifs in general range from dimers, over 1D-coordination polymers to an impressive cyclic hexamer (see Figure 133). Similar to the zinc(II) complexes, the silver(I) complexes show a dynamic behavior in solution.



Scheme 27. Silver(I) and gold(I)-complexes of selected phosphine and phosphine oxide ligands.

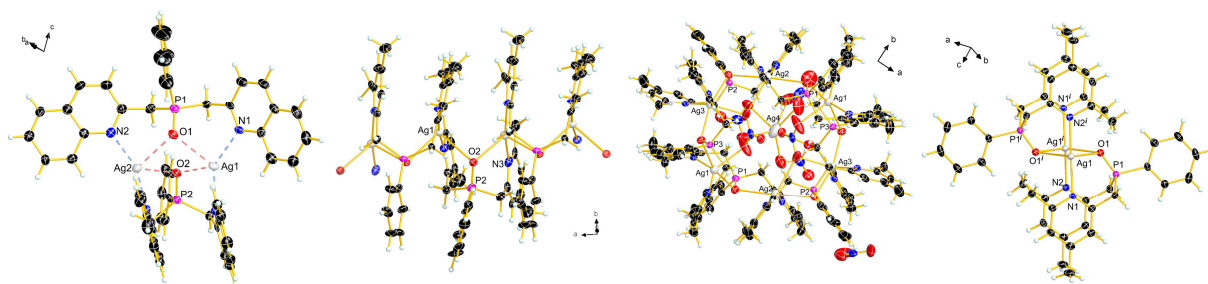


Figure 133. Crystal structures of the silver(I) complexes highlighting the different coordination motifs.

3.6. Unique ligand properties – first insights into luminescence mechanism

First quantum chemical calculations of the bis-substituted phosphine oxides indicate that the nitrogen containing substituent on phosphorus influences the energy of the HOMO and the substituent introduced by the dichlorophosphine influences the energy of the LUMO. The ligand itself is non-emissive in thin film, however, when crystallized, the ligands are emissive, probably due to what is commonly called aggregation induced emission (AIE) (Figure 134). This AIE is also observed experimentally in concentrated solutions of the ligands as well as the complexes. The aggregation apparently blocks certain vibrational movements of the molecule and thus making fluorescence possible. Interestingly, when measuring the luminescence of some compounds in concentrated solution (10 g/L) the emission maxima are red-shifted when excitation is not done at the main absorbance around 270 nm, but in the red edge of the absorption band at 300–350 nm.

Initial experiments show, that with the ligands, as well as the Zn(II) complexes, promising OLED devices can be prepared (Figure 135). The compounds show electroluminescence when voltage is applied. In case of **9-19**, the color of the electroluminescence is different than the color of the luminescence of the solid, when illuminated with UV light (366 nm) (Figure 135 vs. Scheme 24).

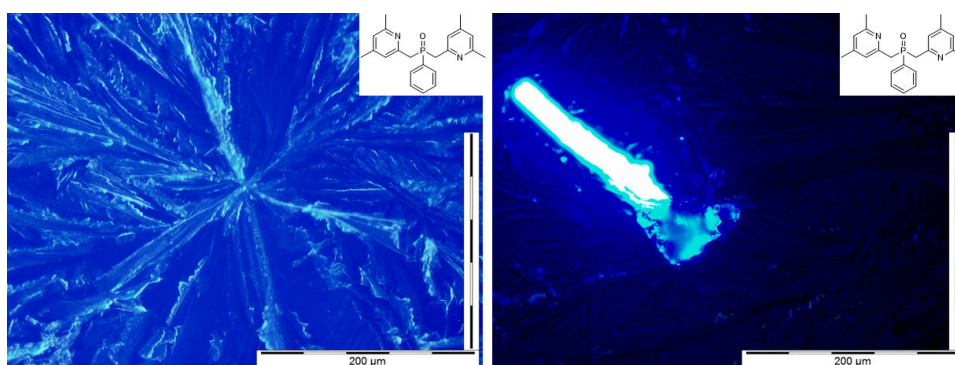


Figure 134. Crystallized thin films of compound **5-1** under UV light (365 nm). Thin films were prepared by Fraunhofer IAP via spin-coating. Pictures provided by the Fraunhofer IAP.

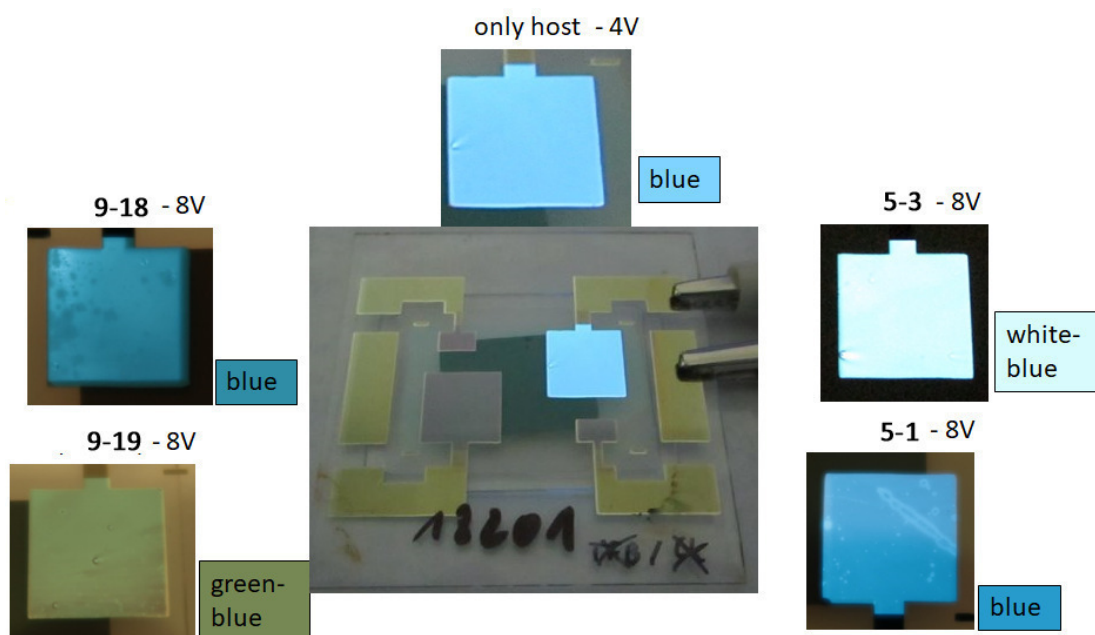


Figure 135. Simple OLED devices prepared by Fraunhofer IAP containing selected ligands and zinc(II) complexes in the emissive layer.

3.7. Primary results of M(III) complexes – an outlook.

Due to the easy synthesis of the ligands described in this thesis and their emitting properties on excitation with UV light, they can also be of interest for application in sensor technology. Preliminary experiments using the ligand **9-1** show, that the phosphine oxides can in principle coordinate to rare earth metals, as demonstrated by the complex of lanthanum(III) nitrate with said phosphine oxide as an example (Figure 136, right).

In an attempt to prepare an aluminum(III) complex of the same phosphine oxide ligand by reaction with aluminium(III) nitrate in ethanol, the nitrate salt of the protonated phosphine oxide was obtained (Figure 136, left).

Especially the formation of the La(III)-complex highlights the versatility and the potential of the ligands developed in this thesis.

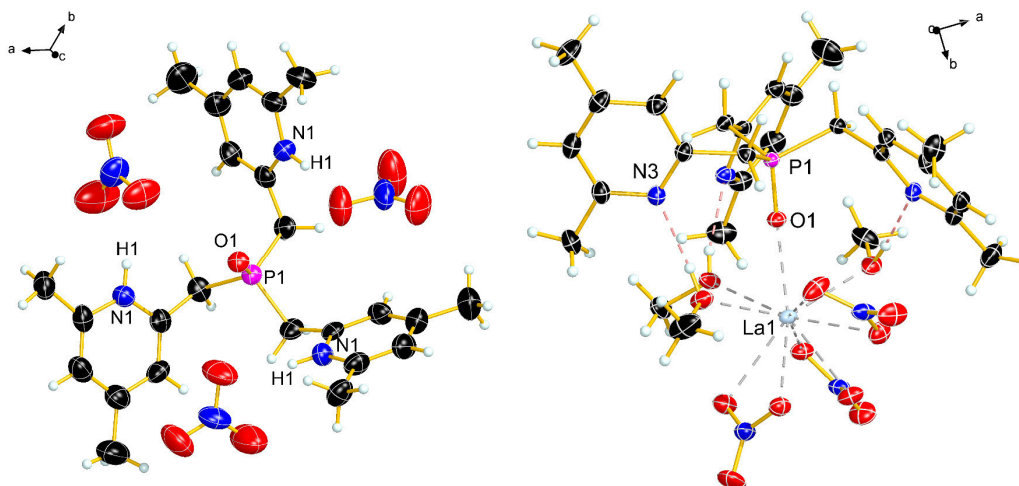


Figure 136. Product of the reaction of trimethylpyridinylphosphine oxide with aluminium(III) nitrate in ethanol (left) and the lanthanum(III) nitrate complex of the same ligand in methanol (right).

4. Appendix

4.1. List of symbols and abbreviations

%	percent	HS	Hirshfeld surface
°C	degree Celsius	i.e.	<i>id est</i> , that means
1D	one dimensional	InGaN	Indiumgallium nitride
1 st	first	IR	infrared spectroscopy
2D	two dimensional	J	coupling constant
2 nd	second	L	liter
3 rd	third	LCD	liquid crystal display
Å	Angstrom	LED	light emitting diode
AIE	aggregation induced emission	LiCl	lithium chloride
B3LYP	hybrid functional, Becke, 3-parameter, Lee–Yang–Parr	LMCT	ligand to metal charge transfer
bpy	bipyridine	LUMO	lowest unoccupied molecular orbital
br	broad	m	medium (IR spectroscopy), multiplet (NMR spectroscopy)
calcd.	calculated	m.p.	melting point
CAM	Coulomb-attenuating method	MeCN	acetonitrile
cm	centimeter	MLCT	metal to ligand charge transfer
Cu(I)Br	copper(I)bromide	MOF	metal organic framework
Cu(I)Cl	copper(I)chloride	mq	2-methyl-8-hydroxyquinoline
Cu(I)I	copper(I)iodide	MS	mass spectrometry
d	doublet	nm	nanometer
DCM	dichloromethane	NMR	nuclear magnetic resonance
DDCzTrz	9,9',9'',9'''-(6-phenyl-1,3,5-triazine-2,4-diyl)bis(benzene-5,3,1-triyl))tetrakis(9 <i>H</i> -carbazole)	ns	nanoseconds
dpk	di(2-pyridyl)ketone	OLED	organic light emitting diode
δ	chemical shift	p	p-orbital
EA	elemental analysis	PPI	2-(1-phenyl-1 <i>H</i> -phenanthro[9,10- <i>d</i>]imidazol-2-yl)phenol
eq.	equivalent	ppm	parts per million
ESI	electrospray ionization	ppy	polypyrrol
eV	electron volt	ps	pico seconds
FLIM	fluorescence lifetime imaging microscopy	q	hydroxyquinoline, quartet (NMR spectroscopy)
FRET	Förster resonance energy transfer	s	strong (IR spectroscopy), singlet (NMR spectroscopy)
fs	femto seconds	S ₀	singlet state
g	gram	SVP	shortest vector problem
GaAs	Gallium arsenide	T ₁	triplet state
GaN	Gallium nitride	TADF	thermally activated delayed fluorescence
GmbH	Gesellschaft mit beschränkter Haftung	TDDFT	time-dependent density-functional theory
h	hour	thpy	2-(2-thienyl)pyridine
H ₂ O	water	TMS	trimethylsilyl
HLCT	hybridized local charge transfers		
HOMO	highest occupied molecular orbital		
hpb	(2-(2-hydroxyphenyl)benzoxazolot)		

TPM	4-[2-[4-(diphenylamino)phenyl]-1 <i>H</i> -phenanthro[9,10- <i>d</i>]imidazol-1-yl]benzotrile
™	trademark
UV	ultra violet
$\tilde{\nu}$	wavenumber
Vis	visible
vs	very strong (IR spectroscopy)
vw	very weak (IR spectroscopy)
w	weak (IR spectroscopy)
X-ray	roentgen radiation
α	alpha
λ	lambda
π	pi

4.2. List of tables

Table 1.	Crystallographic and refinement data for complexes 1–4	23
Table 2.	Selected bond lengths [Å] and angles [°] of complexes 1–4	31
Table 3.	Selected IR spectroscopy bands (cm ⁻¹) for free dpk and complexes 1–4	32
Table 4.	Selected NMR details of the synthesized phosphorus containing compounds 1–6b . Chemical shifts δ in ppm and in reference to CD ₂ Cl ₂ , if not otherwise stated.	51
Table 5.	Crystallographic and refinement data for compounds 2–4	64
Table 6.	Crystallographic and refinement data for compounds 5–6b	65
Table 7.	Reaction conditions of the syntheses of the different aryl- and heteroaryl dichlorophosphines 1–9 Isolated yields are referenced to the used amount of starting material.	72
Table 8.	Crystallographic and refinement data for compounds 4–6	100
Table 9.	Crystallographic and refinement data for compounds 7–9	101
Table 10.	Selected bond lengths [Å] and angles [°].	105
Table 11.	Fluorescence lifetime decay values obtained for the different four crystals measured in Figure 48 for each of the compounds.	114
Table 12.	Crystallographic and refinement data for compounds 2–4	130
Table 13.	Benchmark data on excited electronic states of pyridine. Electronic state energies are given in eV.	138
Table 14.	Electronic states of compound 2 computed at the TDDFT/CAM-B3LYP/SVP level. For the state character, “c” represents a shorthand notation for an excitation localized at the collidine moieties of the molecule, while p(O) and p(Cl) denote p-Orbitals situated at oxygen and chlorine atoms, respectively. Vertical energy differences at optimized excited state geometries, corresponding to emission energies, are given as italic numbers.	140
Table 15.	Electronic states of compound 3 computed at the TDDFT/CAM-B3LYP/SVP level. ...	140
Table 16.	Energy differences in eV between the lowest vibrational levels of the S ₀ and S ₁ or T ₁ states (vibronic 0-0 transitions) for compounds 2 and 3	140
Table 17.	Emission rate constants in s ⁻¹ for the indicated singlet and triplet states of compounds 2 and 3 . The respective radiative lifetimes are given in brackets.	140
Table 18.	Selected bond lengths [Å] and angles [°] of complexes 1a–3 and 5	148
Table 19.	Selected NMR properties of the compounds 1, 2, 4 and 5 . Chemical shifts δ in ppm in reference to CD ₂ Cl ₂	150
Table 20.	Crystallographic and refinement data for compounds 1a–2	165
Table 21.	Crystallographic and refinement data for compounds 3 and 4	166
Table 22.	Selected NMR details of the complexes 1–4 at RT. Chemical shifts δ in ppm and in reference to CDCl ₃ for 1 and MeCN- <i>d</i> ₃ for 2–4 , coupling constants are in Hz.	174
Table 23.	Crystallographic and refinement data for compounds 1 and 2	180
Table 24.	Crystallographic and refinement data for compounds 3 and 4	181
Table 25.	Selected bond lengths [Å] and angles [°] for compounds 1 and 2	185
Table 26.	Selected bond lengths [Å] and angles [°] for compounds 4 and 5	188

Table 27.	Crystallographic and refinement data for compounds A , 1 and 2 .	195
Table 28.	Crystallographic and refinement data for compounds 4 and 5 .	196

4.3. List of schemes

Scheme 1.	General research concept containing phosphine oxide ligands as new OLED materials and possible variation thereof to influence and control the luminescent properties.	13
Scheme 2.	General synthesis of mono-, bis- and tris-substituted phosphines according to P. Braunstein <i>et al.</i>	14
Scheme 3.	Two most common routes for the synthesis of dichlorophosphines.	14
Scheme 4.	Synthesis of the copper(I) complexes 1–4 in solution.	22
Scheme 5.	Synthesis of the novel phosphine oxide ligand 3 starting from 2-methylquinoline.	40
Scheme 6.	Synthesis of copper(I) tetrafluoroborate complex 4 , silver(I) tetrafluoroborate complex 5 and silver(I) hexafluorophosphate complex 6 of the phosphine oxide 3 showing the coordination mode of the ligand to the respective metal ions.	41
Scheme 7.	Synthesis of bis(quinaldinyl)phenylphosphine (1), bis(quinaldinyl)phenylphosphine oxide (2) and copper(I) tetrafluoroborate complex (3), copper(I) hexafluorophosphate complex (4), silver(I) tetrafluoroborate complex (5) and silver(I) hexafluoroantimonate complex (6) of the phosphine oxide (2) showing the coordination mode of the ligand to the respective metal ions.	48
Scheme 8.	General use of dichlorophosphines in organic chemistry.	70
Scheme 9.	Conventional synthesis of dichlorophosphines <i>via</i> method A and B.	70
Scheme 10.	Synthesis of dichlorophosphines <i>via</i> an organozinc reagent.	70
Scheme 11.	Synthesis of aryl dichlorophosphines 1–15 <i>via</i> an organozinc species. For R see Table 7.	71
Scheme 12.	Synthesis of heteroaryl dichlorophosphines 16–19 <i>via</i> an organozinc species. For R and X see Table 7.	72
Scheme 13.	Synthesis of the TMS compounds 1–3 .	85
Scheme 14.	Synthesis of the phosphine oxide ligands 4–9 .	85
Scheme 15.	Synthesis of compounds 1–4 . a) <i>n</i> BuLi, tetrahydrofuran, $-78\text{ }^{\circ}\text{C}$, 1 h, b) TMSCl 2 eq, $-78\text{ }^{\circ}\text{C}$ to RT, 12 h, c) PhPCl ₂ 0.5 eq, tetrahydrofuran, $-10\text{ }^{\circ}\text{C}$ to RT, 12 h, quantitative, d) H ₂ O ₂ , H ₂ O, dichloromethane, $-10\text{ }^{\circ}\text{C}$ to RT, 5 h, 93 %, e), ZnCl ₂ , acetonitrile, 4 h, 97 %, f) ZnCl ₂ , H ₂ O, HCl, acetonitrile, 4 h, 83 %.	117
Scheme 16.	General research concept based on phosphine oxide ligands as new OLED materials and the possible variation thereof to influence the luminescent properties.	144
Scheme 17.	Synthesis of zinc(II) complexes 1 , 2 , 4 and 5 .	146
Scheme 18.	Transition from N,N to N,P coordination in Zn(II) complex 1 at low temperature in solution.	153

Scheme 19.	Synthesis of the complexes 1–4 including a visualization of the coordination modes in the products.....	170
Scheme 20.	Synthesis of the Cu(I) compound 1 and 2 including the visualization of the binding mode in the crystal structures of the products.....	184
Scheme 21.	Suggested synthesis of the Ag(I) compounds 3 and 4 . Visualization of the suspected binding mode in the potential crystal structure of 3 (left) and the actual binding mode in the crystal structure of 4 (right).	187
Scheme 22.	Synthesis of the Au(I) compound 5 and visualization of the binding mode in the crystal structure of the product.....	188
Scheme 23.	Synthesized P,N-ligands during the course of this thesis and pictures of the solids when irradiated with UV light (366 nm). The compounds with the most interesting optical appearances are highlighted in purple.....	204
Scheme 24.	Dichlorophosphines synthesized utilizing organozinc intermediates.	205
Scheme 25.	Zn(II) complexes of selected phosphine and phosphine oxide ligands and pictures of the solids when irradiated with UV light (366 nm). The compounds with the most interesting optical properties are highlighted in purple.	207
Scheme 26.	Copper(I) complexes of selected phosphines, phosphine oxides and dpk and pictures of the solids when irradiated with UV light (366 nm). The compounds with the most interesting optical properties are highlighted in purple.....	209
Scheme 27.	Silver(I) and gold(I)-complexes of selected phosphine and phosphine oxide ligands.....	210

4.4. List of figures

Figure 1.	Simplistic scheme of an OLED stack. Layers are not drawn for scale.....	7
Figure 2.	Evolution of OLED emission mechanisms over time. ^[6]	8
Figure 3.	Schematic presentation of Hyperfluorescence™. ^[7]	8
Figure 4.	Examples for currently used fluorescence emitters based on heavy metal complexes.....	9
Figure 5.	Examples for currently used blue TADF emitters based on large organic molecules. ^[20]	9
Figure 6.	Crustal abundance and price for selected elements based on data from 2013. Picture was modified and taken from ref. ^[25]	10
Figure 7.	Luminescent Zn(II) complexes known in the literature and Alq ₃ on the left in comparison.....	10
Figure 8.	Luminescent Zn(II) complexes containing P,N-ligands.....	11
Figure 9.	Structures of currently available, efficiently luminescent Cu(I) and Ag(I) complexes.....	12
Figure 10.	Examples of luminescent complexes published by Artem'ev <i>et al.</i>	12
Figure 11.	Solid-state molecular structure of 1 . Thermal ellipsoids are set at 50 % probability. Symmetry code: (i) = x, 1+y, z; (ii) -0.5+x, 1.5-y, -0.5+z.....	25
Figure 12.	Visualization of the chain-like structure of the Cu ₃ Cl ₃ -units in 1 . Thermal ellipsoids are set at 50 % probability. Symmetry code: (i) = x, 1+y, z; (ii) -0.5+x, 1.5-y, -0.5+z.	26

Figure 13.	Visualization of the packing arrangement of 1 along the <i>b</i> axis. Thermal ellipsoids are set at 50 % probability. Symmetry code: (ii) = $-0.5+x, 1.5-y, -0.5+z$; (iii) $1-x, -y, 2-z$	26
Figure 14.	Solid-state molecular structure of 2 . Thermal ellipsoids are set at 50 % probability. Symmetry code: (i) = $1-x, -y, 1-z$, (ii) = $2-x, 1-y, -z$	27
Figure 15.	Visualization of the packing arrangement of 2 along the <i>a</i> axis. Thermal ellipsoids are set at 50 % probability.....	27
Figure 16.	Visualization of the H-bonds of a section in the crystal structure of 2 . Thermal ellipsoids are set at 50 % probability. Symmetry code: (i) = $1-x, -y, 1-z$, (ii) = $2-x, -y, 1-z$, (iii) = $x, -1+y, z$, (iv) = $-1+x, y, z$, (v) = $1-x, -y, 1-z$	28
Figure 17.	Solid-state molecular structure of 3 . Thermal ellipsoids are set at 50 % probability. Symmetry code: (i) = $0.5+x, 1.5-y, 1-z$, (ii) = $-0.5+x, 1.5-y, 1-z$	29
Figure 18.	Packing of 3 along the <i>c</i> axis showing the <i>syndiotactic</i> form. Thermal ellipsoids are set at 50 % probability.....	29
Figure 19.	Visualization of the packing arrangement of 3 along the <i>c</i> axis. Thermal ellipsoids are set at 50 % probability.....	29
Figure 20.	Solid-state molecular structure of 4 (left) and picture of the crystals of 4 under the microscope showing the different crystal shapes (right). Thermal ellipsoids are set at 50 % probability. Symmetry code: (i) = $-x, -y, 1-z$	30
Figure 21.	Packing of 4 (left) and the previously published structure (right) visualizing the differently layered structure when comparing both polymorphs. Thermal ellipsoids are set at 50 % probability.....	31
Figure 22.	Visualization of the mixtures after combining solid Cu(I)X and dpk.	32
Figure 23.	UV Vis spectra of the solid compounds 1–4 and dpk of the reactions in solution.....	33
Figure 24.	Generated d_{norm} maps (top) and fingerprint plots (bottom) of the chain structures of compound 1 (left) and 3 (right).....	34
Figure 25.	Generated d_{norm} maps (top) and fingerprint plots (bottom) of the dimeric compounds 2 (left) and 4 (right).....	35
Figure 26.	Molecular structure of 3 in the crystal, view of the asymmetric unit (left). Pictures of the needle-like crystals of 3 under the microscope (right). Thermal ellipsoids are drawn at 50 % probability level for all structures. Selected bond lengths [Å] and angles [°]: P1–O1: 1.482(2), O1–P1–C1: 111.6(2), O1–P1–C7: 114.5(2), O1–P1–C17: 113.6(2).	40
Figure 27.	^1H NMR spectra of 3 in a) CDCl_3 (blue), b) CD_2Cl_2 (green) and c) CD_3CN (red) showing the signals of the CH_2 -group.	41
Figure 28.	Non-classical hydrogen bonding in the crystal structure of phosphine oxide 3 : $\text{H7A}^i \cdots \text{O1}$ 2.437(2) Å, $\text{H9}^i \cdots \text{O1}$ 2.590(2) Å. Symmetry code $i = x, 1+y, z$	41
Figure 29.	Molecular structure of complex 4 in the crystal; view of the asymmetric unit (left). BF_4 anions were omitted for clarity. View of the crystals of 4 under the microscope through polarization filter (right). Selected bond lengths [Å] and angles [°]: Cu1–N1: 1.941(2), Cu1–O1: 2.305(2), Cu1 i –N2: 1.946(2), Cu1 i –Cu1 i : 3.607(4), O1 i –O1 i : 2.853(2), Cu1–O1–Cu1 i : 103.3(6). Symmetry code: $i = 2-x, -y, 1-z$	42

Figure 30.	Molecular structure of complex 5 in the crystal; view of the asymmetric unit (left). Solvent molecules and BF ₄ anions were omitted for clarity. Pictures of crystals of 5 under the microscope (right). Selected bond lengths [Å] and angles [°]: Ag1–O1: 2.491(2), Ag1–N1: 2.230(2), Ag1–N2 ⁱ : 2.228(2), Ag1···Ag1 ⁱ : 3.673(4), O1···O1 ⁱ : 3.349(2), Ag1–O1–Ag1 ⁱ : 95.3(3). Symmetry code: <i>i</i> = – <i>x</i> , 1– <i>y</i> , – <i>z</i>	42
Figure 31.	Molecular structure of complex 6a in the crystal; view of the asymmetric unit (left). Solvent molecules and SbF ₆ anions were omitted for clarity. Pictures of the crystals of 6a under the microscope (right). Selected bond lengths [Å] and angles [°]: O1–Ag1: 2.685(5), O1–Ag2: 2.605(4), Ag1–N1: 2.228(4), Ag1···Ag2: 3.792(7), O1···O2: 3.199(5), O1–Ag1–N1: 83.1(3), O1–Ag2–N2: 88.5(3), O1–Ag1–O2: 76.0(3), Ag1–O1–Ag2: 91.6(3), Ag1–O2–Ag2: 96.1(3), O1–Ag1–O2–Ag2: –33.5(3)....	43
Figure 32.	Molecular structure of complex 6b in the crystal; view of the asymmetric unit (left). Solvent molecules and SbF ₆ anions were omitted for clarity. Pictures of the crystals of 6b under the microscope (right). Selected bond lengths [Å] and angles [°]: O1–Ag1: 2.510(2), Ag1–N1: 2.240(2), Ag1···Ag1 ⁱ : 3.630(4), O1···O1 ⁱ : 3.464(2), Ag1–O1–Ag1 ⁱ : 92.7(5). Symmetry code: <i>i</i> = – <i>x</i> , 1– <i>y</i> , – <i>z</i>	43
Figure 33.	View of the free coordination sides of the metal ions in complex 4 . Selected bond lengths in [Å]: Cu1···F4 ⁱⁱ : 4.061(1), C9···C19: 3.055(1). Symmetry code: <i>ii</i> = <i>x</i> , –1+ <i>y</i> , <i>z</i>	44
Figure 34.	View of the free coordination sides of the metal ions in complex 5 . Selected bond lengths in [Å]: Ag1···H12 ⁱⁱ : 3.273(2), C9···C19: 3.237(1). Symmetry code: <i>ii</i> = 1– <i>x</i> , 1– <i>y</i> , – <i>z</i>	44
Figure 35.	¹ H (left) and ³¹ P (right) NMR spectra of complex 4 in CD ₃ CN at different temperatures.	44
Figure 36.	Molecular structures of the asymmetric unit in the crystal of bis(quinaldinyl)phenyl-phosphine oxide 2 , copper(I) tetrafluoroborate complex 3 , copper(I) hexafluorophosphate complex 4 , silver(I) tetrafluoroborate complex 5 and silver(I) hexafluoroantimonate complexes 6a and 6b in addition to a schematic representation of the conformation of the double closed-wing (X), open-wing/closed-wing (Y) and double open-wing (Z) arrangement of the ligand in the complexes. Thermal ellipsoids are drawn at 50 % probability level. Solvent molecules and anions are omitted.	49
Figure 37.	¹ H NMR spectra (left) of phosphine oxide 2 in a) CDCl ₃ (blue), b) CD ₂ Cl ₂ (green) and c) CD ₃ CN (red) showing the signals of the CH ₂ -group. ¹ H NMR spectrum of phosphine 1 in CDCl ₃ (right) highlighting the diastereotopy of the CH ₂ -protons. X and O highlight the different AB sub spectra.	50
Figure 38.	³¹ P NMR and ¹ H NMR of compounds 5 (left) and 6 (middle) in CD ₂ Cl ₂ at different temperatures. ¹ H ¹ H-NOESY and ¹ H ¹³ C-HSQC NMR of the CH ₂ group of 5 at –80 °C (right).	52
Figure 39.	Solid-state ³¹ P MAS NMR [20 kHz] of 2 , 3 and 5 and ⁶³ Cu MAS NMR [20 kHz] of 3 . Spinning side bands are marked with an asterisk.	53
Figure 40.	Cyclic voltammograms of complex 3 (red curves) and ligand 2 (black curves) recorded between 0.5– (–1.2) V (left) and 0–2 V (right). The measurements are performed in a three-electrode cell using a Pt coil as working electrode, a glassy carbon counter electrode and an Ag/AgNO ₃ (0.01 M) reference electrode at a scan rate of 50 mV s ^{–1}	54

Figure 41.	Visualization of the distorted/twisted quinaldinyl rings in 3 (left), 5 (center) and 6b (right). Thermal ellipsoids are drawn at 50 % probability level. Solvent molecules and anions are omitted.	66
Figure 42.	Non-classical hydrogen bonds in the crystal structure of phosphine oxide 2 : H7A ⁱ ...O1 2.437 Å, H9 ⁱ ...O1 2.590 Å. Thermal ellipsoids are drawn at 50 % probability level. Symmetry code $i = x, 1+y, z$	66
Figure 43.	³¹ P (right) and ¹ H NMR (left) of compound 3 in CD ₂ Cl ₂ at different temperatures.	66
Figure 44.	CV curves of complex 3 recorded between -1.2-0.5 V (left) and 0-2 V (right).	67
Figure 45.	d _{norm} maps and fingerprint plots of compounds 2–6b . The diagram on the bottom is showing the close contacts of compounds 2–6b in the crystal packing.	68
Figure 46.	¹³ C NMR spectra of <i>p</i> -tolyl-Li (I) and (2,4,6-triisopropylphenyl)-Li (II) after transmetalation with ZnCl ₂ highlighting the zinc-bonded carbon atom. Reactions done in a) diethyl ether and b) in THF.	74
Figure 47.	Molecular structure of the asymmetric unit of the phosphine oxides 4–9 in the crystal and a picture of the solid compounds under UV illumination (366 nm). Diamond 3 representation, thermal ellipsoids are drawn at 50 % probability level.	86
Figure 48.	Fluorescence lifetime decays and FLIM images of the different compounds showing the diverse structural morphologies they possess. a) Representative FLIM images are shown for the four compounds i) 4 , ii) 5 , iii) 6 and iv) 8 . The color-code corresponding to the fluorescence lifetime displayed on the FLIM images, goes from blue (indicating the shortest fluorescence lifetime) over green and yellow to orange and red (indicating the longest fluorescence lifetime), see the color bar for fluorescence lifetime. b) From the FLIM images, the fluorescence lifetime decay is plotted for the different compounds i) 4 , ii) 5 , iii) 6 and iv) 8 . c) The corresponding phasor plot of the four FLIM images for each compound i) 4 , ii) 5 , iii) 6 and iv) 8 is shown, which is the Fourier transformation of the lifetimes plotted in panel b. The dotted-grey arrows indicate the average phasor positions of the four FLIM images, with the indicated lifetime values. The color in the phasor plots corresponds to the number of pixels exhibiting the particular phasor value (blue indicating the lowest occurrence and red indicating the highest occurrence), see the occurrence color bar within the phasor plot. The black line in the phasor plots is used for generating the color table for the fluorescence lifetimes in the FLIM images in panel a. The pixel brightness corresponds to total counts, while the hue indicates the pixels' proximity to the black line.	88
Figure 49.	d _{norm} maps and fingerprint plots of compounds 4–6 and 8 (a–d). e) Diagram showing the percentages of the close contacts in the crystal packing of the selected compounds. f) correlation of intermolecular interactions in the crystal versus average intensity.	90
Figure 50.	¹ H NMR signal of the methylene groups of the phosphine oxides in CDCl ₃ . The bis-substituted phosphine oxides (2 , 5 , 8) show the typical AB part of an ABX spectrum. The tris-substituted phosphine oxides (3 , 6 , 9) show a normal doublet.	99

Figure 51.	Arrangement of the molecules of 4 in the crystal (left) and visualization of the non-classical hydrogen bonds (right). Diamond representation, thermal ellipsoids are drawn at 50 % probability level. Bond lengths of hydrogen bonds [Å]: O1...H7B ⁱ 2.732, O1...H12B ⁱ 2.512. Symmetry code: $i = x, 1+y, z$	102
Figure 52.	Arrangement of the molecules of 5 in the crystal (left) and visualization of the non-classical hydrogen bonds (right). Diamond representation, thermal ellipsoids are drawn at 50 % probability level. Bond lengths of hydrogen bonds [Å]: O1...H1B ⁱ 2.336, O1...H11A ⁱ 2.279. Symmetry code: $i = x, 0.5-y, 0.5+z$	102
Figure 53.	Arrangement of the molecules of 6 in the crystal (left) and visualization of the non-classical hydrogen bonds (right). Diamond representation, thermal ellipsoids are drawn at 50 % probability level. Bond lengths of hydrogen bonds [Å]: O1...H15A ⁱ 2.859, O1...H7B ⁱ 2.375. Symmetry code: $i = x, 0.5-y, 0.5+z$	103
Figure 54.	Spiral arrangement of the molecules of 7 in the crystal along the <i>c</i> axis (left) and visualization of the non-classical hydrogen bonds (right). Diamond representation, thermal ellipsoids are drawn at 50 % probability level. Methyl groups and some hydrogen atoms are omitted for clarity. Bond lengths of hydrogen bonds [Å]: O1...H1B ⁱ 2.358, O1...H17B ⁱ 2.411. Symmetry code: $i = -0.25+x, 1.25-y, -0.25+z$	103
Figure 55.	Arrangement of the molecules of 8 in the crystal (left) and visualization of the non-classical hydrogen bonds (right). Diamond representation, thermal ellipsoids are drawn at 50 % probability level. Bond lengths of hydrogen bonds [Å]: O1...H7A ⁱ 2.619, O1...H13B ⁱ 2.400. Symmetry code: $i = 1.5-x, 0.5+y, 1.5-z$	104
Figure 56.	Arrangement of the molecules of 9 in the crystal (left) and visualization of the non-classical hydrogen bonds (right). Diamond representation, thermal ellipsoids are drawn at 50 % probability level. Bond lengths of hydrogen bonds [Å]: O1...H1B ⁱ 2.328, O1...H7B ⁱ 2.368, O1...H13B ⁱ 2.343. Symmetry code: $i = x, -1+y, z$..	104
Figure 57.	UV Vis spectra of the solid compounds 4–9 . Normalized to 1 in the region from 500–350 nm. Data were smoothed using a linear moving average (interval = five data points).....	106
Figure 58.	Excitation spectra of compounds 4–6 and 8 (a concentration of ~ 10 mM was used) normalized to the maximum, with a spectrum of the acetonitrile solvent (black) plotted to show the position of the Raman peaks at 425 nm emission. The inset shows the unnormalized excitation spectra, where the dotted line shows the wavelength of excitation used for the FLIM measurements and the differences in absorption ratio were calculated for the compounds 5 and 8 and were scaled relative to compounds 4 and 6 (factors of 3.6 and 2.9, respectively)...	106
Figure 59.	Emission spectra of compounds 4–6 and 8 (a concentration of ~10 mM was used) normalized to the maximum, with a spectrum of the acetonitrile solvent (black) plotted to show the position of the Raman peaks at 340 nm excitation. For the FLIM measurements, the detected photons must pass of a long pass filter that transmits above 460 nm. The rectangular box indicates the region of the spectrum that is detected by the instrument. To compensate for the relative differences between compounds 5 , 6 and 8 , relative to compound 4 , an additional factor of ~1.5 was applied for compounds 5 and 8 , where a correction factor of 1.2 was applied for compound 6	107

- Figure 60. Fluorescence intensity and FLIM images of compound **4** showing its rod-like crystal structure. The intensity images show the photon counts per pixel for the different crystals, see upper intensity color bar. The last panel shows the corresponding phasor plot of the different FLIM images. The color in the phasor plot corresponds to the number of pixels exhibiting the particular phasor value (blue indicating the lowest occurrence and red indicating the highest occurrence, see occurrence on the color bar. The black line in the phasor plots is used for the color coding of the fluorescence lifetimes in the FLIM images, where the pixel brightness corresponds to counts, while the hue indicates the pixels' proximity to the black line. The color-code corresponding to the fluorescence lifetime displayed on the FLIM images, goes from blue (indicating the shortest fluorescence lifetime) over green and yellow to orange and red (indicating the longest fluorescence lifetime), see lifetime color bar. 108
- Figure 61. Fluorescence intensity and FLIM images of **5** showing its quasi-spherically elongated and oval-like structure. The intensity images show the photon counts per pixel for the different crystals, see upper intensity color bar. The intensity values were adjusted based on the excitation and emission correction factors (check the FLIM section, SI for the correction factor details). The last panel shows the corresponding phasor plot of the different FLIM images. The color in the phasor plot corresponds to the number of pixels exhibiting the particular phasor value (blue indicating the lowest occurrence and red indicating the highest occurrence, see occurrence on the color bar. The black line in the phasor plots is used for the color coding of the fluorescence lifetimes in the FLIM images, where the pixel brightness corresponds to counts, while the hue indicates the pixels' proximity to the black line. The color-code corresponding to the fluorescence lifetime displayed on the FLIM images, goes from blue (indicating the shortest fluorescence lifetime) over green and yellow to orange and red (indicating the longest fluorescence lifetime), see color bar. 109
- Figure 62. Fluorescence intensity and FLIM images of **6** showing its diversely shaped structures. The intensity images show the photon counts per pixel for the different crystals, see upper intensity color bar. The intensity values were adjusted based on the emission correction factors (check the FLIM section, SI for the correction factor details). The last panel shows the corresponding phasor plot of the different FLIM images. The color in the phasor plot corresponds to the number of pixels exhibiting the particular phasor value (blue indicating the lowest occurrence and red indicating the highest occurrence, see occurrence on the color bar. The black line in the phasor plots is used for the color coding of the fluorescence lifetimes in the FLIM images, where the pixel brightness corresponds to counts, while the hue indicates the pixels' proximity to the black line. The color-code corresponding to the fluorescence lifetime displayed on the FLIM images, goes from blue (indicating the shortest fluorescence lifetime) over green and yellow to orange and red (indicating the longest fluorescence lifetime), see color bar. 110

Figure 63.	Fluorescence intensity and FLIM images of 8 showing its amorphous-like structure. The intensity images show the photon counts per pixel for the different crystals, see upper intensity color bar. The intensity values were adjusted based on the excitation and emission correction factors (check the FLIM section, SI for the correction factor details). The last panel shows the corresponding phasor plot of the different FLIM images. The color in the phasor plot corresponds to the number of pixels exhibiting the particular phasor value (blue indicating the lowest occurrence and red indicating the highest occurrence, see occurrence on the color bar. The black line in the phasor plots is used for the color coding of the fluorescence lifetimes in the FLIM images, where the pixel brightness corresponds to counts, while the hue indicates the pixels' proximity to the black line. The color-code corresponding to the fluorescence lifetime displayed on the FLIM images, goes from blue (indicating the shortest fluorescence lifetime) over green and yellow to orange and red (indicating the longest fluorescence lifetime), see color bar.	111
Figure 64.	Fluorescence lifetime decay data and fits obtained for the four crystals (i) of compound 4 imaged in Figure 48, which shows a bi-exponential fluorescence lifetime decay.	112
Figure 65.	Fluorescence lifetime decay data and fits obtained for the four crystals (ii) of compound 5 imaged in Figure 48, which shows a bi-exponential fluorescence lifetime decay.	112
Figure 66.	Fluorescence lifetime decay data and fits obtained for the four crystals (iii) of compound 6 imaged in Figure 48, which shows a bi-exponential fluorescence lifetime decay.	113
Figure 67.	Fluorescence lifetime decay data and fits obtained for the four crystals (iv) of compound 8 imaged in Figure 48, which shows a bi-exponential fluorescence lifetime decay.	113
Figure 68.	The relation between the fluorescence lifetime and intensity relative to the attractive bond contents for the four crystals of the different compounds imaged in Figure 48. a) Average fluorescence lifetimes obtained from the phasor and tail fits to the TCSPC data showing an increase of fluorescence intensity with decrease in the lifetime average. b) The increase in the short lifetime fraction correlates with the increase in fluorescence intensity and attractive bond contents within the investigated crystals.	114
Figure 69.	Luminescence properties of compound 2 . The absorbance spectra are recorded from a thin solution in MeCN (0.1 g/L) and from a thin film on quartz glass. Emission spectra are recorded from a higher concentrated solution (10 g/L), the same thin film and a thin layer of crystals on quartz glass at an excitation wavelength of 265 nm (solution) or 270 nm (powder and film). The inset shows a luminescence microscopic picture of the crystallized thin film with illumination at 365 nm. Luminescent crystals (cyan) are visible in front of a blue background of scattered light (scale bars: 200 μ m).	118

Figure 70.	Luminescence properties of compound 3 . The absorbance spectra are recorded from a thin solution in MeCN (0.1 g/L) and a thin film on quartz glass. Emission spectra are recorded from a higher concentrated solution (10 g/L), the same film on quartz glass at and from a powder sample inside a borosilicate cavity glass at excitation wavelengths of 265 nm, 270 nm and 350 nm. The inset shows a luminescence microscopic picture of the powder sample with illumination at 365 nm (scale bars: 200 μ m).	119
Figure 71.	Luminescence properties of compound 4 . The absorbance spectra are recorded from a thin solution in MeCN (0.1 g/L) and from a thin film on quartz glass. Emission spectra are recorded from a higher concentrated solution (10 g/L), the same thin film on quartz glass and from a powder sample inside a borosilicate cavity glass at excitation wavelengths of 265 nm, 270 nm, and 350 nm. The inset shows light microscopic pictures of an amorphous droplet (left) and crystals at 365 nm illumination (scale bars: 200 μ m, different colors are due to different white balance settings of the camera).	120
Figure 72.	FLIM images and fluorescence lifetime decays of the compounds 2 (left column), 3 (middle column) and 4 (right column), highlighting their diverse structural morphologies. a) FLIM images of representative crystals for the three compounds. The color code indicates the fluorescence lifetime as a function of the spatial position on the crystal. b) Temporal evolution of the total fluorescence intensity for each crystal shown in a). c) Phasor plot of the four FLIM images per compound as shown in a), determined by phasor transformation of the individual lifetimes for each spatial pixel on the crystals. The dotted-grey lines indicate the average phasor coordinates of the four FLIM images. In addition, the corresponding lifetime is given. The color bar in the phasor plots represents the number of pixels exhibiting the particular phasor value (blue indicating the lowest and red indicating the highest occurrence).	121
Figure 73.	The relation between fluorescence lifetime and intensity relative to the attractive bond contents for the three compounds imaged in Figure 72. a) Correlation of the averaged fluorescence intensity and attractive bond contents within the investigated solid-state molecular structures of the respective compounds. b) Average intensity weighted fluorescence lifetimes in correlation to the bond content.	122
Figure 74.	Temporal evolution of the electronic state energies of species 2 along a simulated surface-hopping trajectory, which was initiated in the S_1 state. At $t = 1468$ fs, the transition to the ground state occurs <i>via</i> a conical intersection characterized by an elongated C–P bond.	123
Figure 75.	Molecular structure of the asymmetric unit of 2 in the crystal (left). Arrangement of the molecules of 2 in the crystal (right). Diamond representation, thermal ellipsoids are drawn at 50 % probability level.	131
Figure 76.	Molecular structure of the asymmetric unit of 3 in the crystal. Diamond representation, thermal ellipsoids are drawn at 50 % probability level.	131
Figure 77.	Molecular structure of the asymmetric unit of 4 in the crystal. Diamond representation, thermal ellipsoids are drawn at 50 % probability level.	131
Figure 78.	^1H NMR (left) and ^{31}P NMR (right) of compound 3 in CD_2Cl_2 at varying temperatures.	132

Figure 79.	^1H NMR (left) and ^{31}P NMR (right) of compound 4 in CD_2Cl_2 at varying temperatures.....	132
Figure 80.	UV/Vis absorption and luminescence spectroscopy of compound 2 in MeCN. Increasing the analyte concentration from 0.01 to 10 g/L exposes a shoulder around 320 nm. The signal at 265 nm yields only a small luminescence. Excitation at 335 nm yields a much higher intensity peak at 375 nm (estimated using a Gaussian fit due to the Raman Stokes signal of MeCN).	133
Figure 81.	UV/Vis absorption and luminescence spectroscopy of compound 3 in MeCN. Increasing the analyte concentration from 0.1 to 10 g/L exposes a shoulder around 320 nm. The signal at 271 nm (excited at 265 nm) yields only a small luminescence. Excitation at 335 nm yields a much higher intensity peak at 380 nm.....	133
Figure 82.	UV/Vis absorption and luminescence spectroscopy of compound 4 in MeCN. Increasing the analyte concentration from 0.01 to 10 g/L exposes a peak at 335 nm. Both, the signal at 272 nm (excited at 265 nm to compare with 2) and the shoulder at 335 nm luminesce at 404 nm, but the latter one much stronger. Being excited at 335 nm, the luminescence is also much stronger compared to the luminescence spectra of 2 and 3 above. Excitation at even longer wavelengths (390 nm) also yields a significant luminescence signal at 462 nm, despite the low absorption.....	134
Figure 83.	Excitation spectra of compounds 2-4 in MeCN ($c = 10$ g/L) in direct comparison. The spectra of compounds 2 and 3 are similar with a maximum around 300 nm and strong tailing. Compound 3 has a lower intensity. The spectrum of compound 4 exhibits a maximum around 360 nm.....	134
Figure 84.	Emission spectra of compounds 2-4 in MeCN ($c = 10$ g/L) when excited with 405 nm in direct comparison. The luminance of complex 3 is slightly lower than that of pure ligand 2 . Complex 4 exhibits a much higher intensity.....	135
Figure 85.	Fluorescence lifetime decay data and fits obtained for the four crystals of compound 2 imaged in Figure 72, which shows a bi-exponential fluorescence lifetime decay.	135
Figure 86.	Fluorescence lifetime decay data and fits obtained for the four crystals of compound 3 imaged in Figure 72, which shows a bi-exponential fluorescence lifetime decay.	136
Figure 87.	Fluorescence lifetime decay data and fits obtained for the four crystals of compound 4 imaged in Figure 72, which shows a bi-exponential fluorescence lifetime decay.	136
Figure 88.	Fingerprint plots and d_{norm} maps including a summary of the close contacts of crystalline 2-4	137
Figure 89.	Simulated UV absorption spectra of compounds 2 and 3 obtained from 100 molecular geometries sampled from a harmonic Wigner distribution function of the vibrational normal modes. The excitation energies and transition dipole moments were computed at the TDDFT/CAM-B3LYP/SVP level. The final spectrum was obtained by shifting the excitation energies by -0.6 eV, calculating the oscillator strength from these energies and the transition dipole moments and finally convolving the individual transitions by a Lorentzian with a width of 0.15 eV.....	139

Figure 90.	Fluorescence and phosphorescence spectrum of compound 2 , obtained by TDDFT/B3LYP/def2-SVP. The emission rate constant k from Table S2 is related to the shown emission intensity $I(\omega)$ by $k = I(\omega)\omega d\omega$	141
Figure 91.	Fluorescence and phosphorescence spectrum of compound 2 , obtained by TDDFT/CAM-B3LYP/def2-SVP.....	141
Figure 92.	Approximate fluorescence of compound 2 in crystal environment. The data has been obtained from the TDDFT/B3LYP/def2-SVP dynamics simulations in the S_1 state by calculating the spectral power density for emission, $I \propto ES1 - ES04\mu012$, for the structures along 10 trajectories of 3 ps duration, starting with $t > 1000$ fs to account for initial relaxation, and convolving the result by a Lorentzian function.....	142
Figure 93.	Phosphorescence spectrum of compound 3 , obtained by TDDFT/CAM-B3LYP/def2-SVP.....	142
Figure 94.	Molecular structure of the asymmetric unit of 1a (top left), 2 (top right), 3 (bottom left) and 5 (bottom right) in the crystal. Thermal ellipsoids are drawn at 50 % probability level.	147
Figure 95.	Visualization of the 2D-dimensional fingerprint plots including the d_{norm} maps obtained from HS analysis and a summary of the close contacts of crystalline 1a , 2 and 5	150
Figure 96.	Signals of the CH ₂ protons in the ¹ H NMR spectrum of compounds 1 , 2 , 4 and 5	151
Figure 97.	Variable temperature ¹ H and ³¹ P NMR spectra of compound 1 in CD ₂ Cl ₂	152
Figure 98.	¹ H ¹⁵ N-HMBC (left) and ¹ H ¹ H-COSY (right) NMR spectra of compound 1 in CD ₂ Cl ₂ at RT (top) and at -80 °C (bottom).	152
Figure 99.	Variable temperature ¹ H and ³¹ P NMR spectra of compound 4 in CD ₂ Cl ₂	153
Figure 100.	Region of the CH ₂ signals in the ¹ H ¹ H-COSY NMR spectra of compound 4 at RT (right) and at -80 °C (left) in CD ₂ Cl ₂	154
Figure 101.	Solid compounds when illuminated with UV light (366 nm).....	155
Figure 102.	Molecular structure of the asymmetric unit of 1b in the crystal. Thermal ellipsoids are drawn at 50 % probability level.....	162
Figure 103.	Packing of 1a along the a axis visualizing the different π -stacking motifs in the 3D-structure. Thermal ellipsoids are drawn at 50 % probability level.	162
Figure 104.	Packing of 2 along the a axis visualizing the alternating ZnCl ₂ -molecules coordinating to the phosphine ligand, the non-classical hydrogen bonds and the π -stacking of the quinaldiny rings. Thermal ellipsoids are drawn at 50 % probability level. Symmetry code: $i = -x, 1-y, -z$, $ii = 1+x, y, z$, $iii = 1-x, 1-y, 1-z$	163
Figure 105.	Visualization of the non-classical hydrogen bonds in the packing of 3 . Thermal ellipsoids are drawn at 50 % probability level. Symmetry code: $(i) x, 1+y, z$, $(ii) -x, 1-y, 1-z$	163
Figure 106.	Visualization of the non-classical hydrogen bonds in the packing of 5 and the chainlike structure along the c axis (left). Packing of 5 along the a axis visualizing the alternating ZnCl ₂ -molecules coordinating to the phosphine oxide ligand and the π -stacking of the aromatic rings (right). Thermal ellipsoids are drawn at 50 % probability level. Symmetry code: $(i) -1+x, y, z$; $(ii) -x, -y, -z$; $(iii) 1+x, y, z$; $(iv) 1-x, -y, -z$	163
Figure 107.	Variable temperature ¹ H and ³¹ P NMR spectra of compound 2 in CD ₂ Cl ₂	164

Figure 108.	Variable temperature ^1H and ^{31}P NMR of compound 5 in CD_2Cl_2	164
Figure 109.	Cyclic voltammograms of complex 5 (red curve) and the ligand of 5 (black curves) recorded between 2 and (-1.2) V. The measurements were performed in a three-electrode cell using a Pt coil as working electrode, a glassy carbon counter electrode and an Ag wire as pseudo reference electrode at a scan rate of 50 mV s^{-1}	167
Figure 110.	Solid-state UV Vis spectra of compounds 1-5 as well as the Ligand of 5	167
Figure 111.	Emission spectrum of the ligand of 5 . The intensity is normalized to 1.....	167
Figure 112.	Visualization of the HOMO and LUMO of the optimized structures of compounds 1-5	168
Figure 113.	Solid-state molecular structure of complex 1a in the crystal. Thermal ellipsoids are set to 50 % probability. Selected bond lengths [Å] and angles [°]: P1–O1 1.506(8), P1–C1 1.794(2), P1–C7 1.802(2), P1–C15 1.804(2), Cu1–O1 2.296(8), Cu2–O2 2.236(7), Cu1–N3 1.955(9), Cu1–N4 1.926(9), O1–P1–C1 112.2(5), O1–P1–C7 110.9(5), O1–P1–C15 111.5(5), O1–Cu1–O2 78.9(2), Cu1–O1–Cu2 98.5(3), N3–Cu1–N4 161.9(4), O1–Cu1–N3 101.1(3).....	171
Figure 114.	Solid-state molecular structure of complex 2 in the crystal. Thermal ellipsoids are set to 50 % probability. Anions are omitted for clarity. Selected bond lengths [Å] and angles [°]: P1–O1 1.498(2), P1–C1 1.806(3), P1–C7 1.818(3), P1–C15 1.816(3), Ag1–O1 2.565(2), Ag1–N1 2.222(2), O1–P1–C1 112.6(2), O1–P1–C7 112.6(2), O1–P1–C15 112.7(2), O1–Ag1–O1 ⁱ 88.7(7), Ag1–O1–Ag1 ⁱ 91.3(7), N1–Ag1–N2 ⁱ 172.3(9), O1–Ag1–N1 90.1(8). Symmetry code: $i = 2-x, -y, -z$	172
Figure 115.	Solid state molecular structure of complex 3 in the crystal. Thermal ellipsoids are set to 50 % probability. Anions are omitted for clarity. Selected bond lengths [Å] and angles [°]: P1–O1 1.499(6), P1–C1 1.802(9), P1–C7 1.805(9), P1–C15 1.823(9), Ag1–O1 2.590(6), Ag1–N1 2.190(6), O1–P1–C1 111.5(4), O1–P1–C7 111.1(4), O1–P1–C15 111.7(4), O1–Ag1–O2 88.2(2), Ag1–O1–Ag2 92.0(2), N1–Ag1–N4 167.0(3), O1–Ag1–N1 91.9(2).	172
Figure 116.	Solid-state molecular structure of complex 4 in the crystal. Thermal ellipsoids set to 50 % probability. Selected bond lengths [Å] and angles [°]: P1–O1 1.491(3), P1–C1 1.795(4), P1–C7 1.808(4), P1–C15 1.821(4), Ag1–O1 2.617(3), Ag1–N1 2.280(3), O1–P1–C1 111.8(2), O1–P1–C7 113.2(2), O1–P1–C15 114.5(2), O1–Ag1–O3 ⁱ 163.1(8), Ag1–O1–Ag2 108.4(9), Ag2–O6–Ag3 103.4(9), N1–Ag1–N6 ⁱ 133.3(2), O1–Ag1–N6 ⁱ 106.6(2). Symmetry code: $i = -x, 1-y, 1-z$	173
Figure 117.	$^1\text{H}^1\text{H}$ -COSY and $^1\text{H}^{13}\text{C}$ -HSQC of complex 2 in $\text{MeCN-}d_3$ highlighting the methylene group and the resulting AB part of an ABX spin system.....	174
Figure 118.	Photoluminescence spectrum of 1 at 350 nm illumination, normalized to 1, and a photo of the powder under 366 nm UV illumination.....	174
Figure 119.	Packing of 1a in the crystal. Thermal ellipsoids are set to 50 % probability.	178
Figure 120.	Packing of 1b in the crystal. Thermal ellipsoids are set to 50 % probability.	178
Figure 121.	Packing of 2 in the crystal. Thermal ellipsoids are set to 50% probability.	179
Figure 122.	Packing of 3 in the crystal. Thermal ellipsoids are set to 50% probability.	179
Figure 123.	Molecular structure of the dinuclear complex cation of compound 1 in the crystal; view of the asymmetric unit. Thermal ellipsoids are drawn at 50 % probability level. Solvent molecules and anions are omitted for clarity.	184

Figure 124.	Molecular structure of cluster complex cation 2 in the crystal, view of the asymmetric unit. Thermal ellipsoids are drawn at 50 % probability level. Solvent molecules and anions are omitted for clarity.....	185
Figure 125.	Molecular structure of the cationic complex of 4 in the crystal, view of the asymmetric unit. Ellipsoid representation (left) and stick representation (right). Thermal ellipsoids are drawn at 50 % probability level. Anions are omitted for clarity. Symmetry code: $i = 2-x, 2-y, 1-z$	187
Figure 126.	Molecular structure of the complex cation of compound 5 in the crystal, view of the asymmetric unit. Thermal ellipsoids are drawn at 50 % probability level. Anions are omitted for clarity. Symmetry code: $i = -x, 1-y, -z$	188
Figure 127.	Comparison of the signals for the CH ₂ group in the ¹ H NMR spectra of 1 (left) in CD ₃ CN and the free ligand (right) in CDCl ₃	189
Figure 128.	³¹ P NMR spectrum of 3 in CD ₂ Cl ₂ at -80 °C visualizing the coupling of phosphorus to both silver(I) atoms and a possible molecular structure of 3 in solution.	190
Figure 129.	Molecular structure of compound A in the crystal; view of the asymmetric unit (left). Crystal Packing of A along the <i>b</i> axis (right). Thermal ellipsoids are drawn at 50 % probability level.	197
Figure 130.	Packing of 2 visualizing the π-stacking of the quinaldinyl rings in the 3D-structure of the crystal. Thermal ellipsoids are drawn at 50 % probability level.....	197
Figure 131.	Packing of 4 along the <i>a</i> axis visualizing the π-stacking motifs in the 3D-structure of the crystal. Thermal ellipsoids are drawn at 50 % probability level.....	198
Figure 132.	Packing of 5 along the <i>a</i> axis visualizing the π-stacking of the quinaldinyl rings in the 3D-structure of the crystal. Thermal ellipsoids are drawn at 50 % probability level.....	198
Figure 133.	Crystal structures of the silver(I) complexes highlighting the different coordination motifs.	211
Figure 134.	Crystallized thin films of compound 5-1 under UV light (365 nm). Thin films were prepared by Fraunhofer IAP via spin-coating. Pictures provided by the Fraunhofer IAP.....	211
Figure 135.	Simple OLED devices prepared by Fraunhofer IAP containing selected ligands and zinc(II) complexes in the emissive layer.	212
Figure 136.	Product of the reaction of trimethylpyridinylphosphine oxide with aluminium(III) nitrate in ethanol (left) and the lanthanum(III) nitrate complex of the same ligand in methanol (right).....	212

4.5. List of publications

C. Kirst, N. A. Danaf, F. Knechtel, T. Arczynski, P. Mayer, D. C. Lamb, K. Karaghiosoff: „Methods for elucidating the structural-property relationship in luminescent materials”, *J. Mater. Chem. C* 2021, accepted. DOI: 10.1039/D1TC02634H

C. Kirst, F. Zoller, T. Bräuniger, P. Mayer, D. Fattakhova-Rohlfing, K. Karaghiosoff: „Investigation of structural changes of Cu(I) and Ag(I) complexes utilizing a flexible, yet sterically demanding multidentate phosphine oxide ligand”, *Inorg. Chem.* 2021, **60**, 2437–2445.

C. Kirst, M. Reichel, K. Karaghiosoff: „Coordination complexes of di(2-pyridyl) ketone with copper(I) and their formation in solution and under solvent-free conditions”, *Inorg. Chim. Acta* 2021, **514**, 119951–119962.

C. Kirst, K. Karaghiosoff: „Copper(I) and silver(I) complexes of bridging bis(quinaldinyl)phenylphosphine oxide ligand”, *Phosphorus Sulfur Silicon Relat. Elem.* 2020, **195**, 918–923.

P. Sanz Camacho, D. McKay, D. M. Dawson, C. Kirst, J. R. Yates, T. F. G. Green, D. B. Cordes, A. M. Z. Slawin, J. D. Woollins, S. E. Ashbrook: „Investigating Unusual Homonuclear Intermolecular “Through-Space” J Couplings in Organochalcogen Systems”, *Inorg. Chem.* 2016, **55**, 10881–10887.

C. Kirst, B. E. Bode, D. B. Cordes, P. S. Nejman, A. M. Z. Slawin, K. Karaghiosoff, J. D. Woollins: „Diphosphane 2,2'-binaphtho[1,8-de][1,3,2]-dithiaphosphinine and the easy formation of a stable phosphorus radical cation”, *Dalton Trans.* 2016, **45**, 6348–6351.

D. G. Piercey, D. E Chavez, S. Heimsch, C. Kirst, T. M. Klapötke, J. Stierstorfer: „An Energetic N-Oxide and N-Amino Heterocycle and its transformation to 1,2,3,4-Tetrazine-1-oxide”, *Propellants Explos. Pyrotech.* 2015, **40**, 491–497.

4.6. List of conference contributions

C. Kirst, K. Karaghiosoff: „Coinage metal complexes of a novel, flexible, hemilabile phosphine ligand”, EWPC 17: 17th European Workshop on Phosphorus Chemistry, France, Rennes, 2020. Poster presenter

C. Kirst: „d¹⁰-Metal complexes of novel, hemilabile phosphine oxide ligand”, PBSi 2019: International Conference on Phosphorus, Boron and Silicon, Italy, Rome, 2019. Oral presenter

C. Kirst: „Zinc and phosphorus – magical combination for new luminescent materials”, XXIVth International Krutyń Summer School 2019, Poland, Krutyń, 2019. Oral presenter

C. Kirst, M. Ebeling, L. Horndasch, K. Karaghiosoff: „Efficient one-pot-synthesis of dichlorophosphines – a possible pathway towards challenging compounds”, International Conference on Heteroatom Chemistry (ICHAC), Czech Republic, Prague, 2019. Poster presenter

C. Kirst, M. Reichel, K. Karaghiosoff: „Neue Di(2-pyridyl)keton-Komplexe mit Cu(I) – Bildung von zyklischen sechsgliedrigen, seitenverknüpften Cu₃X₃-Clustern (X = Hal)“, 15th Coordination Chemistry Conference, Germany, Munich, 2019. Poster presenter

C. Kirst: „Functionalized phosphines – The magic of phosphorus”, DFF e.V. System Integration Platform, Member Assembly, Working Group Meeting, Germany, Potsdam, 2018. Oral presenter